AD-A280 084

EDGEWOOD

RESEARCH, DEVELOPMENT & ENGINEERING CENTER

U.S. ARMY CHEMICAL AND BIOLOGICAL DEFENSE COMMAND

ERDEC-SP-019

PROCEEDINGS OF THE 1993 SCIENTIFIC CONFERENCE ON OBSCURATION AND AEROSOL RESEARCH

DTIC
ELECTE
JUN 0 8 1994
S F D

Janice E. Rhodes
Sarah J. Wall

BATTELLE EDGEWOOD OPERATIONS
Edgewood, MD 21040

March 1994

Approved for public release; distribution is unlimited.

DTIC QUALITY INSPECTED 4

CUM SCIENTIA DEFENDIMUS

Aberdeen Proving Ground, MD 21010-5423

94-17281

94 7 038

Disclaimer

The findings in this report are not to be construed as an official Department of the Army position unless so designated by other authorizing documents.

REPORT DOCUMENTATION PAGE

Form Approved
OMB No. 0704-0188

Public reporting burden for this collection of information is estimated to average 1 hour per response, including the time for reviewing instructions, searching existing data sources, gathering and maintaining the data needed, and completing and reviewing the collection of information. Send comments regarding this burden estimate or any other aspect of this collection of information, including suggestions for reducing this burden, to Washington Headquarters Services, Directorate for Information Operations and Reports, 1215 Jefferson Davis Highway, Suite 1204, Arlington, VA 22202-4302, and to the Office of Management and Budget, Paperwork Reduction Project (0704-0188), Washington, DC 20503.

1. AGENCY USE ONLY *(Leave blank)*

2. REPORT DATE
1994 March

3. REPORT TYPE AND DATES COVERED
Final, 93 Jun - 93 Jun

4. TITLE AND SUBTITLE
Proceedings of the 1993 Scientific Conference on Obscuration and Aerosol Research

5. FUNDING NUMBERS
PR-10161102A71A

6. AUTHOR(S)
Rhodes, Janice E.; and Wall, Sarah J. (Compilers)

7. PERFORMING ORGANIZATION NAME(S) AND ADDRESS(ES)
Battelle, Edgewood Operations, 2113 Emmorton Park Road, Suite 200, Edgewood, MD 21040

8. PERFORMING ORGANIZATION REPORT NUMBER
ERDEC-SP-019

9. SPONSORING/MONITORING AGENCY NAME(S) AND ADDRESS(ES)
DIR, ERDEC, ATTN: SCBRD-RTB, APG, MD 21010-5423

10. SPONSORING/MONITORING AGENCY REPORT NUMBER

11. SUPPLEMENTARY NOTES
POC: Edward Stuebing, SCBRD-RTB, (410) 671-3089

12a. DISTRIBUTION/AVAILABILITY STATEMENT
Approved for public release; distribution is unlimited.

12b. DISTRIBUTION CODE

13. ABSTRACT *(Maximum 200 words)*

In this report, 26 papers presented at the 1993 Scientific Conference on Obscuration and Aerosol Research are included under the headings of Aerosol Dynamics, Aerosol Characterization Methods, and Optical Properties of Aerosols.

14. SUBJECT TERMS

Obscurants	Aerosols	Extinction	Transmission
Obscuration	Aerosol	Absorption	Infrared
Scattering	Sizing	Smoke	(Continued on page 2)

15. NUMBER OF PAGES
486

16. PRICE CODE

17. SECURITY CLASSIFICATION OF REPORT	18. SECURITY CLASSIFICATION OF THIS PAGE	19. SECURITY CLASSIFICATION OF ABSTRACT	20. LIMITATION OF ABSTRACT
UNCLASSIFIED	UNCLASSIFIED	UNCLASSIFIED	UL

14. Subject Terms (Continued)

Electromagnetic scattering
Millimeter wave radiation
Submillimeter wave radiation
Visible radiation
Electromagnetic waves
Spherical particles
Mie scattering
Rayleigh scattering
Raman scattering
Concentration sampling
Particle dynamics
Diffusive mixing
Aerosol growth
Nucleation
Smoke generation
Aerosol generation
Photoionization
Conductivity
Chemical characterization
Phosphorus smoke
Fluorescence
Aerosol clusters
Spheres
Cylinders
Rough particles
Irregular particles
Nonspherical particles
Particle aggregates
Particle chains
Infrared emission
Cooperative scattering
Dependent scattering
Multiple scattering
Radiative transfer
Coagulation
Condensation
Liquid drop
Drop growth
Fog oil smoke
Diesel oil smoke
Particle mechanics
Atmospheric optics
Atmospheric dispersion
Cloud dynamics
Scavenging
Aerosol collectors
Aerosol elimination
Aerosol characterization
Particle sizing
Hygroscopic smokes
Particle size distribution
Particle orientation distribution
Optical constants
Optical properties
Anomalous diffraction
Attenuated total reflection
Reflection spectroscopy
ATR
Far-infrared
Refractive index
Index of refraction
Inversion
Inversion techniques
Gypsum
Natural minerals
Minerals
Metal
Metallic particles
Powdered minerals
Complex refractive index
Effective media
High energy laser
Particles
Aerosol particles
SERS
Surface Enhanced Raman Scattering
Dielectric particles
Conducting particles
Cylindrical particles
Fibers
Conducting fibers
Gas-aerosol reactions
Transport phenomena
Aerosol measurement
Spheroids
Laser pulses
Optical pulses
Pulse propagation
Clouds
Laser
Radiation transport
Fourier analysis
Plume mechanics
Light
Plumes
Properties

PREFACE

The 1993 U.S. Army Edgewood Research, Development and Engineering Center (Edgewood RDEC) Scientific Conference on Obscuration and Aerosol Research was held 22 - 24 June 1993 at the Edgewood Area Conference Center of Aberdeen Proving Ground, MD. The Conference is held annually, the last full week in June, under the direction of Dr. Edward Stuebing, Team Leader, Aerosol Sciences and Technology. This report was authorized under project number 1O161102A71A, Research in CW/CB Defense.

The Conference is an informal forum for scientific exchange and stimulation among investigators in the wide variety of disciplines required for aerosol research, including a description of an obscuring aerosol and its effects. The participants develop some familiarity with the U.S. Army aerosol and obscuration science research programs and also become personally acquainted with the other investigators and their research interests and capabilities. Each attendee is invited to present any aspect of a topic of interest and may make last minute changes or alterations in his presentation as the flow of ideas in the Conference develops.

While all participants in the Conference are invited to submit papers for the proceedings of the Conference, each investigator, who is funded by the U.S. Army Research Program, is requested to provide one or more written papers that document specifically the progress made in his funded effort in the previous year and indicating future directions. Also, the papers for the proceedings are collected in the Fall to allow time for the fresh ideas that arise at the Conference to be incorporated. Therefore, while the papers in these proceedings tend to closely correspond to what was presented at the Conference, there is not an exact correspondence.

The reader will find the items relating to the Conference itself, photographs, the list of attendees, and the agenda in the appendixes following the papers and in the indexes pertaining to them.

The use of trade names or manufacturers' names in this report does not constitute an official endorsement of any commercial products. This report may not be cited for purposes of advertisement.

Reproduction of this document in whole or in part is prohibited except with permission of the Director, U.S. A[illegible] [illegible]ewood Research, Development and Engineering Center, ATTN: SCBRD-h[illegible] [illegible]lding E-5951, Aberdeen Proving Ground, MD 21010-5423. However, [illegible]e Defense Technical Information Center and the National Technical Information Service are authorized to reproduce this document for U.S. Government purposes.

This report has been approved for release to the public.

Accesion For
NTIS CRA&I ☑
DTIC TAB ☐
Unannounced ☐
Justification
By
Distribution /
Availability Codes
Dist | Avail and / or Special
A-1

Blank

TABLE OF CONTENTS

Page

I. AEROSOL DYNAMICS

A. PARTICLE FORMATION AND TRANSPORT

CARBON AEROSOL GENERATION IN ELECTRIC DISCHARGE
J. Kretzschmar, J.R. Brock 11

NUCLEATION AND COAGULATION OF SINGLE MAGNETIC DOMAIN IRON GRAINS
J.A. Nuth, O. Berg, J. Faris, P. Wasilewski 21

COSMIC DUST ANALOG SIMULATION IN A MICROGRAVITY ENVIRONMENT: THE STARDUST PROGRAM
F. Ferguson, L.U. Lilleleht, J. Nuth, J.R. Stephens, E. Bussoletti, L. Carotenuto, L. Colangeli, P. Dell'Aversana, F. Mele, V. Mennella, C. Mirra 31

B. PARTICLE DISSEMINATION, TRANSPORT AND DEPOSITION

A NUMERICAL SIMULATION OF TURBULENT DISPERSION
A. Hadad, M. Stiassnie, M. Poreh 37

ELECTRODYNAMIC LEVITATION OF MICROPARTICLES IN A GAS FLOW
E.E. Allison, B.R.F. Kendall 41

MODELING AND MEASUREMENT OF THE EFFECTIVE DRAG COEFFICIENT IN DECELERATING AND NON-ACCELERATING TURBULENT GAS-SOLIDS DILUTE PHASE FLOW OF LARGE PARTICLES IN A VERTICAL TRANSPORT PIPE
H. Littman, M.H. Morgan 47

A NEW HYBRID METHOD TO SOLVE THE MAXWELL EQUATIONS FOR ABSORPTION AND SCATTERING OF ELECTROMAGNETIC RADIATION BY A DIELECTRIC PARTICLE
M.K. Choi, J.R. Brock 49

EXPLOSIVE DISSEMINATION OF OBSCURANTS FOR THE PROTECTION OF MEN AND MATERIAL, PLASMA PRODUCTION, INTERMEDIATE REACTIONS, DISPERSION BY WIND OVER NONFLAT TERRAIN, AND EXTINCTION PROPERTIES OF FIBER, SPHEROID, AND COMPLEX PARTICLES IN AN AEROSOL OVER THE COMPLETE RANGE OF INTERROGATING ELECTROMAGNETIC RADIATION
D.K. Cohoon 65

II. AEROSOL CHARACTERIZATION METHODS

A. SAMPLING, NEPHELOMETRY AND INVERSION

QUASI-BINARY DECISION MAKING: A SPEEDUP
W. Cai, X. Li, M Lax 101

SPHERICAL AND NON SPHERICAL AEROSOL AND PARTICULATE CHARACTERIZATION USING OPTICAL PATTERN RECOGNITION TECHNIQUES
M.S. Marshall, R.E. Benner, R.K. Meyer 115

OPERATION OF THE BREEZE TUNNEL TO DETERMINE MASS EXTINCTION COEFFICIENTS
G.A. Sehmel, R. Bonfante, D.R. Banks, E. Catalano, W.G. Rouse 129

ANGULAR DISTRIBUTION OF THE FORWARD LIGHT SCATTERING FROM A QUARTZ FIBER
C. Oh, G.G. Padmabandu, E.S. Fry 147

SCATTERING OF PHASE CONJUGATED LIGHT BY A STATIONARY PARTICLE
C. Oh, K.T. Andrews, E.S. Fry, G.J. Dunning, M.L. Minden, D.M. Pepper 155

PORTABLE HIGH-THROUGHPUT LIQUID-ABSORPTION AEROSOL SAMPLER
A. Akinyemi, A. Birenzvige, R. Torres, S. Zaromb 165

SUFFICIENCY OF USING A CONTINUUM OF FREQUENCIES TO SOLVE THE ELECTROMAGNETIC INVERSE PROBLEM 173
O.I. Sindoni, D.K. Cohoon

COMPUTER CODES FOR SOLVING THE SPHERE INVERSION PROBLEM
D.K. Cohoon 177

COMPUTER LEARNING AND RAPID ANALYSIS OF METHANE COMBUSTION
M. Frenklach, S. Sun, D.K. Cohoon 305

B. SPECTROSCOPY OF SINGLE PARTICLES AND AEROSOLS

CAVITY-QED ENHANCEMENT OF FLUORESCENCE YIELDS IN MICRODROPLETS
M.D. Barnes, W.B. Whitten, J.M. Ramsey 329

FLUCTUATION SPECTROSCOPY FOR SMALL INCLUSIONS IN A LEVITATED MICRODROPLET
B.V. Bronk, M.J. Smith, S. Arnold 347

INCOHERENT SCATTERING OF SEMICLASSICAL PARTICLES AND THE RELAXATION FUNCTION
M.H. Lee 359

IDENTIFICATION OF INDIVIDUAL MICROORGANISMS BY A MICROSPHERE FLUORESCENCE IMMUNOASSAY
W.B. Whitten, M.J. Shapiro, J.M. Ramsey, B.V. Bronk . . . 363

III. OPTICAL PROPERTIES OF AEROSOLS

REMOTE BIOLOGICAL SENSING BY CIRCULAR POLARIZATION TRANSMISSOMETRY
D.L. Rosen 371

PASSIVE REMOTE SENSING OF MICROORGANISMS USING OPTICAL ACTIVITY AND SUNLIGHT
D.L. Rosen, J.D. Pendleton 379

CREEPING WAVES: A MISSING INGREDIENT IN VARIATIONAL TRIAL FIELDS
B.J. Stoyanov, R.A. Farrell 387

APPLICATION OF THE EXACT SOLUTION FOR INFINITE CYLINDER SCATTERING TO FINITE CYLINDER PROBLEMS
R.T. Wang 409

THE RESPONSE OF N LAYER BIANISOTROPIC CYLINDRICAL STRUCTURES TO OBLIQUELY INCIDENT ARBITRARILY POLARIZED PLANE WAVE ELECTROMAGNETIC RADIATION
D.K. Cohoon 427

SCATTERING AND ABSORPTION BY SPHERES CONTAINING ARBITRARILY LOCATED SPHERICAL INHOMOGENEITIES
K.A. Fuller 443

INDEXES FOR THESE PROCEEDINGS

A. Index of Authors 475
B. Index of Author's Organizations 477

APPENDIXES FOR THESE PROCEEDINGS

A. Photograph of 1993 Conference Attendees 479
B. List of 1993 Attendees 481
C. Conference Agenda 483

PROCEEDINGS OF THE 1993 SCIENTIFIC CONFERENCE ON OBSCURATION AND AEROSOL RESEARCH

I. AEROSOL DYNAMICS

Moderator: Janon Embury

U.S. Army Edgewood Research,
Development and Engineering Center
Attn: SCBRD-RTB
Aberdeen Proving Ground MD

Blank

CARBON AEROSOL GENERATION IN ELECTRIC DISCHARGE

J. Kretzschmar and J. R. Brock
Department of Chemical Engineering
University of Texas/Austin 78712-1062

RECENT PUBLICATIONS, SUBMITTALS FOR PUBLICATION AND PRESENTATIONS

"A theoretical investigation of low pressure particle impaction in a highly underexpanded sonic impinging slit jet", J. Aerosol Sci. **24**, 31-44, (1993) (with P. S. Chang and I. Trachtenberg)

""Formation of nanoparticles by laser ablation of aerosol particles",Appl. Phys.Lett. .submitted(1993) (with C-B Juang, H. Kai,. M. F. Becker, J. Keto)

"Particle formation by homogeneous nucleation in rapidly expanding flows" *Proceedings of the 1990 CRDEC Scientific Conference on Obscuration and Aerosol Research*, CRDEC, U. S. Army, 1991 (with B. J. Jurcik).

"Particle formation by binary homogeneous nucleation in supersonic flows" *Proceedings of the 1991 CRDEC Scientific Conference on Obscuration and Aerosol Research*, CRDEC, U. S. Army, 1992 (with B. J. Jurcik).

"Formation of graphite and diamond fibers in corona discharges" *Proceedings of the 1991 CRDEC Scientific Conference on Obscuration and Aerosol Research*, CRDEC, U. S. Army, 1992.

"Laser-assisted liquid film etching",Appl. Phys. Lett..**62** 3345(1993).(with P. Lim and I. Trachtenberg)

"Finite element solution of the Maxwell equations for absorption and scattering of electromagnetic radiation by a coated dielectric particle", Appl. Opt. (1993). (with Choi and Liebman).

"Numerical simulation of particle formation and growth in rapidly expanding axisymmetric flows", J. Phys. Chem. **97**,323-331 (1993) (with B. J. Jurcik)

"Feasibility of finite element solution of the Maxwell equations for absorption and scattering of electromagnetic radiation by a dielectric particle", J. Comput. Physics, submitted, 1993 (with Choi and Liebman).

"A new hybrid method to solve the Maxwell equations for absorption and scattering of electromagnetic radiation by dielectric particles", submitted for publication,1993. (with Choi).

"Finite element solution of the Maxwell equations for absorption and scattering of electromagnetic radiation by dielectric particles", SPIE Meeting, Los Angeles, CA, April 1993.

ABSTRACT
A study is underway to determine optimum conditions for generating carbon aerosol in corona discharge in JP-8 vapor as a possible improved replacement technology for the VEESS. Preliminary experiments and results are presented. A theoretical analysis of corona discharge dynamics is given along with directions for future research.

INTRODUCTION

Vehicle Engine Exhaust Smoke Systems (VEESS) were incorporated onto a majority of U. S. Army combat vehicles (M1, M2/M3, M60, M551, and M48) by development efforts of the U. S. Army Chemical Research, Development and Engineering Center (CRDEC) and with the respective combat vehicle's production contractors during the late 1970s to early 1980s[1] The purpose of the VEESS is to provide combat vehicles with an onboard screening smoke system supplementing the rapid short duration smoke provided by launched screening smoke grenades. The VEESS uses the vehicle exhaust system to vaporize fuel to produce smoke.

The Vehicle Engine Exhaust Smoke System (VEESS) operated with diesel fuel DF-2 or materials with similar or lower vapor pressures was found in the TRAC VEESS Study to be an essential element in increasing effectiveness and protection of armored vehicles on the battlefield. TRAC found that VEESS gave significant statistical increases in force effectiveness, in M1A1 system effectiveness and gave significant statistical decreases in force vulnerability and in BMP and DVO equipped FST effectiveness.

Recently, the "Fuel Standardization on the Battlefield" policy was adopted that replaces diesel fuel (DF-2) with aviation turbine fuel (JP-8), with initial fielding of JP-8 to begin in Europe during 1987. Stocks of DF-2 will be exhausted prior to 1990. A field trial was carried out at Dugway Proving Ground during September 1986, where fog oil, DF-2 and JP-8 smoke yields were compared. The study was carried out under stable atmospheric conditions with ambient temperatures in the range 41 to 70 ^{o}F. This study showed that, while Fog Oil and DF-2 produced an acceptable smoke, the M1 VEESS produced an ineffective smoke when JP-8 was used. JP-8 fuel is a petroleum cut somewhat lighter than kerosene and heavier than gasoline. The mean molecular weight of JP-8 is around 160, considerably less than that for diesel fuel (~200) and for Fog Oil (~300) . For this reason, JP-8 has a vapor pressure at STP around five times greater than that of diesel DF-2, thereby accounting for the ineffectiveness of JP-8 smoke. Therefore, the planned introduction of JP-8 as the single battlefield fuel will make the current VEESS ineffective.

For these reasons this research was initiated to identify optimum conditions for generating carbon aerosol in corona discharge from JP-8 vapor as a possible improved replacement technology for the VEESS system. This research is composed of two major parts. The first part consists of demonstration of carbon aerosol generation from JP-8 in corona discharge, and the other is modeling carbon aerosol generation in the DC corona discharge with the view of optimizing aerosol production from JP-8. In experimental investigation of carbon aerosol generation, optical emission spectroscopy is used to identify the species responsible for carbon formation, whose concentrations can be found by actinometry. Raman spectroscopy can also used to identify the type of carbon aerosol formed in the discharge. The aerosol characteristics can be examined by Scanning Electron Microscopy (SEM) and Transmission Electron Microscopy (TEM).

Modeling of the DC corona discharge process will be done numerically to calculate the active species concentrations (which include ions, electrons, and neutrals), potential distribution, the electrical field distribution, and total conduction currents. From these modeled concentrations, particular solutions will be compared with actual experimental results obtained from optical emission spectroscopy.

II. THEORETICAL BACKGROUND

1. Corona Discharge

A corona is a weakly luminous gaseous discharge that appears in the neighborhood of electrified points or thin wires, where the field is greatly enhanced. Ionization of the gas takes place only locally where the gas emits light. The electric current is closed by a flux of charges of

---

[1]R. J. Lepito and G. Rubel, *JP-8 Impact on the Vehicle Engine Exhaust Smoke System (VEESS)*, SMCCR_MUS (70-1r) 30 September 1988.

a specific sign (depending on the polarity of the point) that are produced in the self-sustaining discharge zone at the point and are transported by a relatively weak field to the other electrode. Little if any radiation is emitted from the outer region.

A corona discharge occurs only if the field is sharply nonuniform. The field near one or both electrodes must be larger than in the rest of the gap. This situation typically arises when the characteristic size r of the electrodes is much smaller than the interelectrode distance d, i.e.--, r<<d. Thus, a corona discharge system consists of high-field active electrodes or surfaces surrounded by ionization regions where free charges are produced; low-field drift regions where charged particles drift and react; and low-field passive electrodes mainly acting as charge collectors.

To initiate a corona, a certain rather high voltage is required, that depends on the specific conditions. The corona discharge belongs to the group of self-sustained discharges; the conditions under which it appears reflect the physical mechanism of reproduction of elements in that region of the enhanced field where ionization occurs. The mechanism of multiplication of electrons is essentially dependent on the polarity of the electrode surrounded by the corona. If this electrode is the cathode (the corona is then said to be negative), then avalanche multiplication takes place. The secondary process is the e-emission from the cathode. In principle , the ignition of a negative corona does not differ from the so-called Townsend discharge. The variety of behavior in discharges is summarized in Table 1, below.

Table 1. Classification of dc gas discharges

Discharge type	Field and potential distribution	Feedback mechanism and cathode fall volt.
Townsend	Essentially Laplacian	Feedback to cathode by photons, positive ions, and metastables, needing a high cathode fall voltage Vc >> Vi
Glow (Corona)	Space charge dominated, with a concentrated cathode fall and a non-LTE or LTE* positive column	
Arc, Spark		Feedback to cathode via thermal or field electron emission

LTE: Local thermodynamic equilibrium

1. Experimental Work.

The experimental arrangement proposed for study of growth of carbon fibers in the corona discharge is shown in Fig. 1. This system is designed to provide information on those charged species responsible for growth of fibrous carbon. Additional experiments have been done and the arrangement is indicated by the schematic diagram of Fig. 2. This was used to collect bulk samples of carbon aerosol formed in corona discharge Samples of several grams of aerosol were collected and sent to RDEC for testing as an ir-vis obscurant, as was done by

Dr. J. Embury. The samples were produced by passing a mixture of diesel fuel vapor in nitrogen through the domain of a negative corona discharge. The arrangement shown depended on impaction for collection of the produced carbon aerosol; the efficiency of impaction was very low, so that much larger amounts of aerosol were produced than collected (collection rate was ~0.18 gm/min., production rate was~10 times this). The corona was operated at a total power of ~14-23 watts. with a hydrocarbon flow rate of ~ 50 cc/min. this corresponds to a hydrocarbon molal flow rate of ~0.0022 g-moles/min., or of diesel vapor ~0.446gm/min which, taking into account the low impaction efficiency, indicates a conversion efficiency of vapor to carbon aerosol considerably greater than ~ 40% .

2. Mechanism of the corona discharge

2.1 Townsend coefficient (primary ionization coefficient)

When electrons are liberated from a cathode in a point to plane gap, they gain their equilibrium energy distribution in the field in the gas rapidly, after traveling some small distance x_o. As they proceed toward the anode along the x-direction, defined here as the direction of the applied field E at a pressure p, they will produce ionization. After ionization by an electron, two new electrons are created that start with nearly zero energy and quickly gain enough energy to ionize anew. There are thus four new electrons after the second ionizing event; these again ionize and create eight. Thus the one initial electron, starting from the cathode, on advancing x_o cm in the field direction, will have created $n=\exp(\alpha x_o)$ electrons. On arrival at the anode (at x=d), there will be $n=\exp(\alpha d)$ new electrons. Since these move with a high drift velocity, they will reach the anode, leaving their positive ion companions virtually at the place where they were created. The positive ions then gradually drift toward the cathode. The quantity α, called the first Townsend coefficient, or coefficient for ionization by electron impact, represents the number of new electrons created per centimeter path in the field direction. One electron and its progeny of $\exp(\alpha d)$ electrons on arrival at the anode constitute what is termed an "electron avalanche".

2.2 Secondary Electron Emission

When an energetic species strikes a surface, one of the possible results is that an electron will be ejected. The number of electrons ejected per incident species is called the secondary electron coefficient. Secondary electron emission is observed for impact by ions, electrons, photons and neutrals (both ground state and metastable); each will have a different coefficient and a different energy dependence. Secondary electron emission from a cold cathode produces breakdown of discharge gaps and also sustains small dc currents that are incapable of substantial heating of the cathode or of creating such a strong field at the cathode that thermionic field emission develops.

The most important among the various secondary mechanisms is the ion-electron emission. It is characterized by a coefficient γ_i , the number of electrons emitted per incident positive ion. The relatively small kinetic energies that ions acquire in discharges are ineffective for knocking out electrons, and the main mechanism for secondary electron emission on impact is that the field of an ion approaching a surface to within a distance of atomic dimensions transforms a potential well on the surface into a potential barrier. If this barrier is low and narrow because the field is very strong, on the order of that around nuclei, an electron from the metal immediately tunnels into the ion and neutralizes it. If the energy released is greater than the work function of the cathode, $e\Phi$, it may be spent on ejecting another electron.

These secondary electron emission processes are important in discharges, because each of them can contribute electrons to the discharge and help to offset the electron loss processes.

3. Modeling the DC Corona Discharge

An accurate description of the DC corona discharge--i.e., the ion and electron densities and currents, is essential in simulation of the corona discharge processes. In this research, we focus on fluid or continuum models of ion and electron kinetics and transport. The continuum model consist of equations of conservation and Poisson's equation. When modeling unmagnetized plasmas, equations of conservation are combined with Poisson's equation to describe the self-consistent, local electric field. The basic assumption made in deriving this model is that charged

particle transport is at LTE, as indexed by E/p--that is, the collisional mean free path is small compared to the distances over which voltage and gas density change significantly. A continuum model provides estimates for average quantities such as densities and fluxes. The continuum model is summarized below.

The magnitude and shape of the local electric field depends on both the applied field and the space charge distribution according to Poisson's equation.

$$\nabla^2 V = -\nabla E = \frac{q}{\varepsilon_o} \left(n_e - n_p \right)$$

where n_p and n_e are positive ion and electron densities, respectively, V is the electrostatic potential, whose gradient, E, is the electric field. Ion densities are given, in turn, by equations of continuity:

$$\frac{\partial n_p}{\partial t} + \nabla . \Gamma_p = F$$

$$\frac{\partial n_e}{\partial t} + \nabla . \Gamma_e = F$$

where Γ is the flux, and F is the source strength:.

$$F = \alpha \left| \Gamma_e \right|$$

where α, the first Townsend coefficient (Fig. 2), is expressed as:

$$\alpha = A\ p \exp\left(\frac{-B}{(E/p)^r} \right).$$

Both A and B are constants that depend on the type of gas and the pressure; r depends on the nature of the gas. Note that this form for the ionization function means that the ionization rate will be largest where both the electric field and the electron flux are large. Since the dependence on the field is exponential, this means that the ionization rate will be maximum in the sheath.

III. EXPERIMENTS

1. Experimental Procedures

A schematic diagram of the experimental apparatus to be used for the study of carbon fiber growth in a DC corona discharge is shown in Fig. 3. The reactor is made of polycarbonate in order to contain the electric field within the chamber. The system is comprised of a point to plane arrangement where the electrode spacing is set by the operator. The cathode wire is made of nickel, and the powered electrode is made of chromium and an aluminum plate is the grounded electrode. These electrodes will be powered by a Spellman PHSR regulated high voltage DC power generator, providing between 3000 - 5000 volts at 0-5mA. Evacuation of the chamber will be accomplished by an Edwards 40 two stage pump, creating an effective pressure of 760 to 1 torr. The pressure is varied in order to study its effect on the discharge chemistry. The feed gas will be a variable mixture of JP-8 vapor and nitrogen. All flow rate measurements will be made with rotameters.

A schematic diagram of the basic setup for optical emission spectroscopy (OES) and Raman spectroscopy is shown in Fig. 4. Both the OES and Raman spectra of the corona discharge will be obtained with a Tracor Northern TN-6500 optical multichannel spectrum analyzer connected to a Tracor model 6121 512 element intensified diode array detector. The optical system is coupled to the emissions through a fiber optic cable or a Gaertner micrometer microscope attached to a sapphire viewport. The fiber optic cable is connected to a 0.22m SPEX 1681 spectograph that includes the diode detector. The monochromator contains a diffractive

grating of 1200 grooves/mm which will allow approximately 0.12 nm/diode resolution. The Raman portion of the analysis to be done on the generated carbon incorporates in addition a Spectra-Physics 164 argon ion laser and a Raman notch filter (omega optical) which will be placed between the reactor and the monochromator to eliminate the laser line.

IV. Preliminary results

A one dimensional continuum model for the DC discharge has been derived and solved. This continuum model consists of the equations of continuity for both ions and electrons and Poisson's equation. The DC simulation results are presented in Figs. 3-8. Fig. 3 is a plot of particle densities, showing the region of quasi-neutrality in the bulk. The peak ion density is around 1.8×10^9 cm^{-3}. The electric potential and electric field distributions are shown in Figs. 4 and 5. The electric field varies linearly through the ionization region and then becomes nearly zero in the drift region. The total current density is plotted in Fig. 6. The total current density is a constant across the domain of a DC discharge. The total current indicated is around 0.184 mA/cm^2. Ionization rate is shown in Fig.7. After the ionization region, the ions and electrons drift to the anode. The effect of pressure on the calculated ion density is shown in Fig. 8, indicating higher values of ion density and decreases in the size of the ionization region, as pressure increases.

ACKNOWLEDGMENTS

This work was supported by RDEC, U.S. Army. We thank Dr. Janon Embury and Dr. E. Stuebing for helpful discussions on this problem.

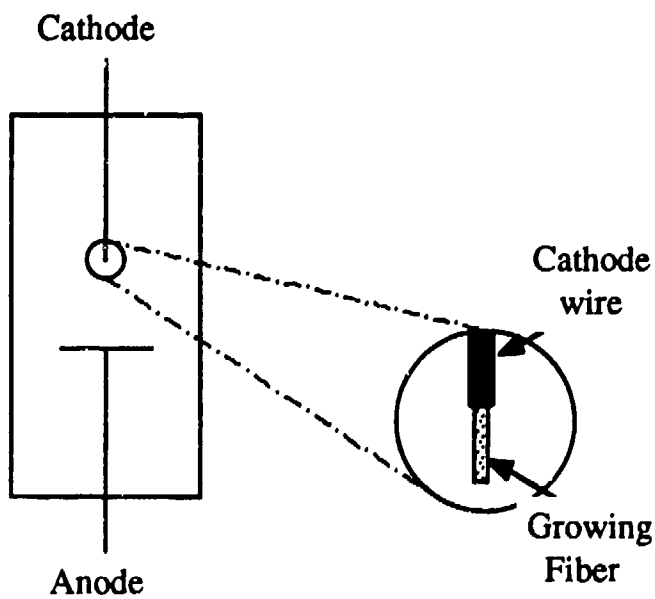

Fig. 1. The configuration of the point to plane corona discharge and detail for proposed study of fiber growth.

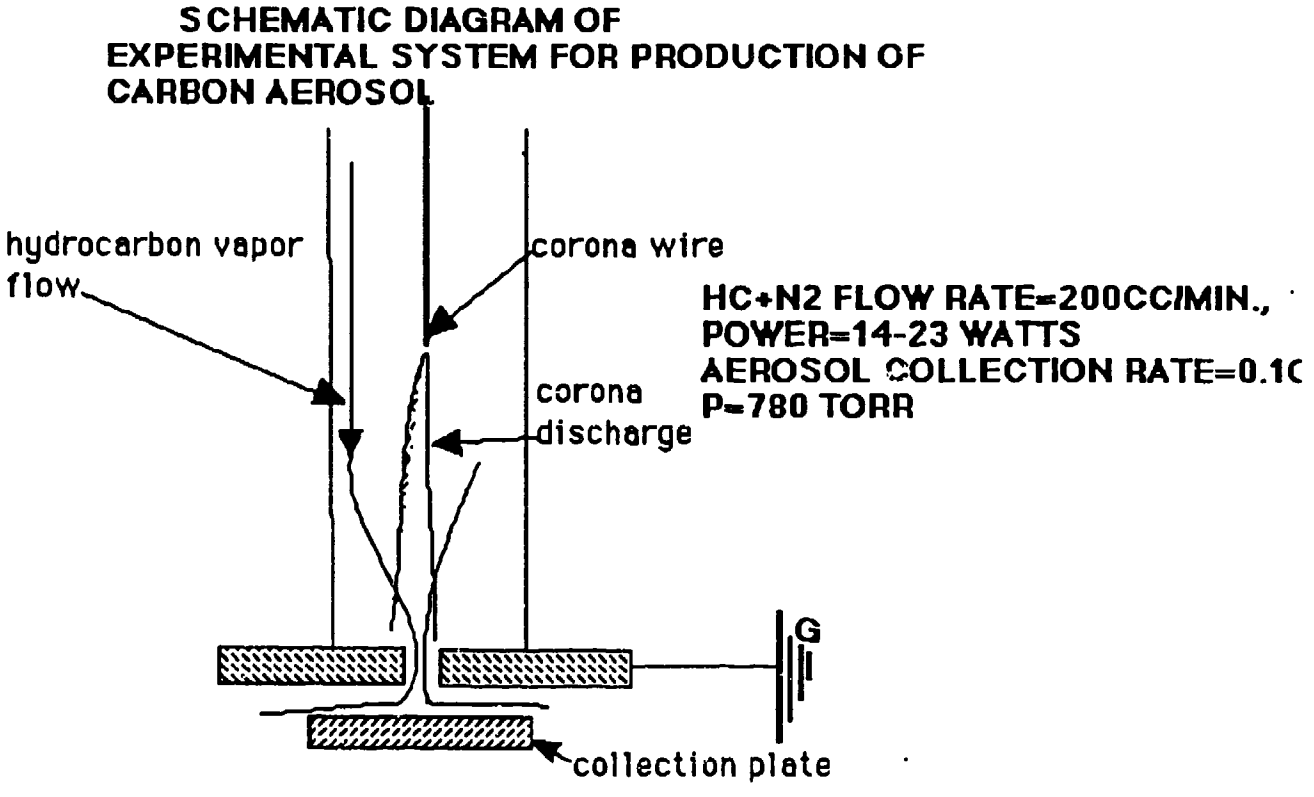

Fig. 2 schematic diagram of experimental system used for collection of carbon aerosol formed in corona discharge.

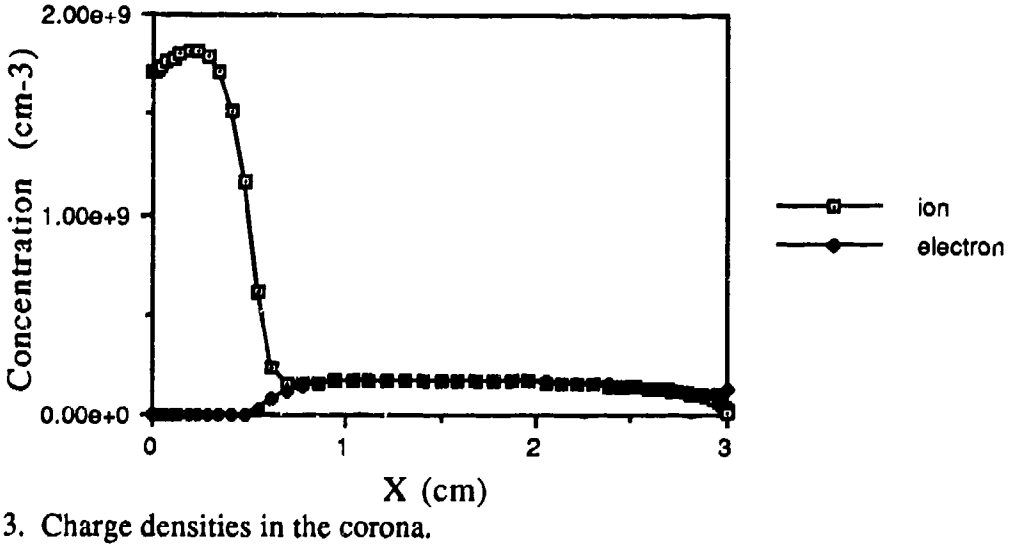

FIG. 3. Charge densities in the corona.

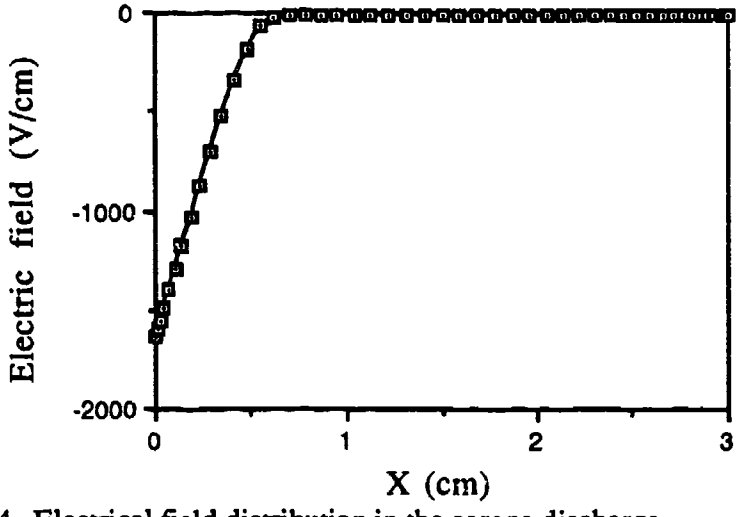

Fig. 4. Electrical field distribution in the corona discharge

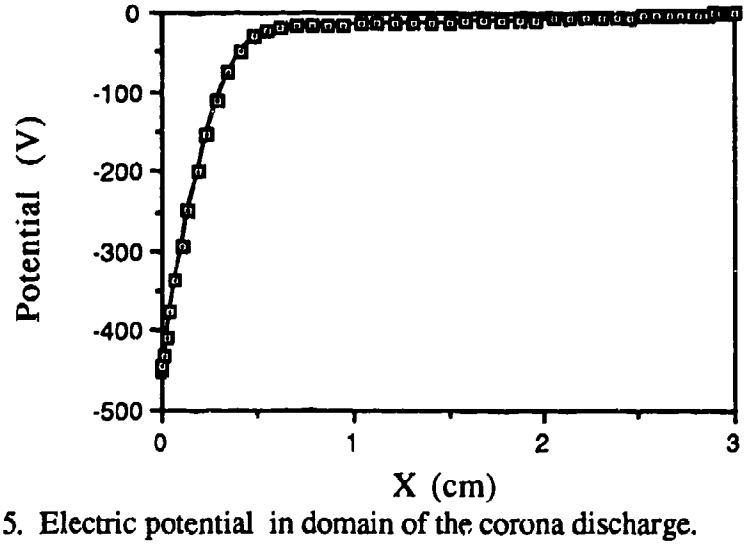

Fig. 5. Electric potential in domain of the corona discharge.

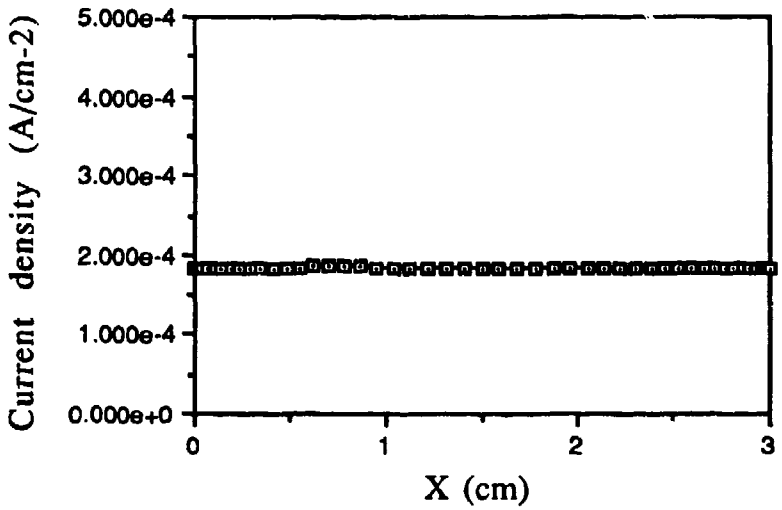

Fig. 6. Total current density in domain of the corona discharge.

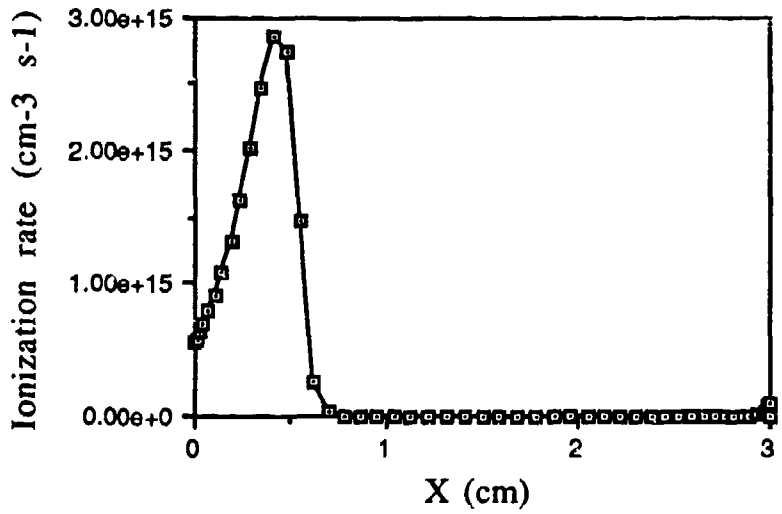

Fig. 7. Ionization rate in corona discharge.

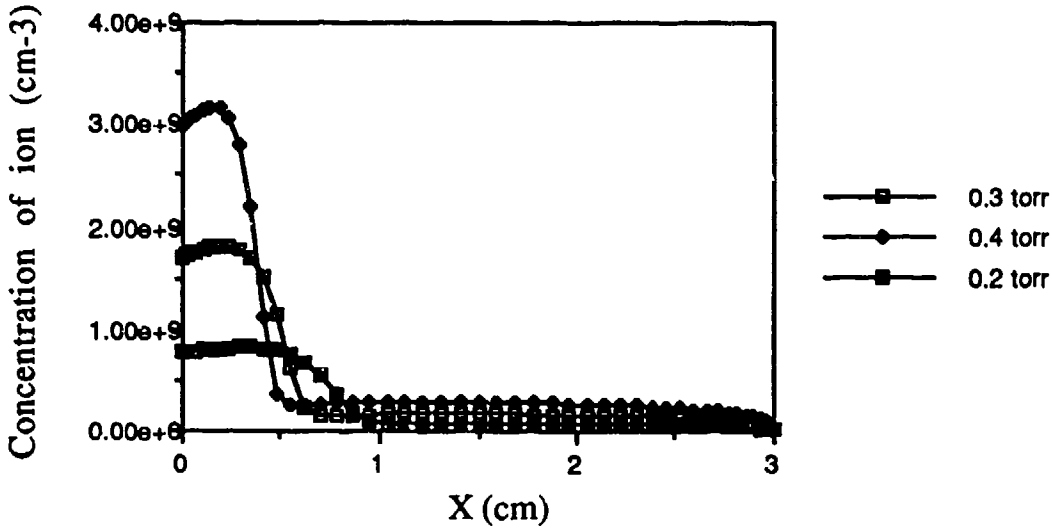

Fig. 8. Ion densities in corona discharge.

Nucleation and Coagulation of Single Magnetic Domain Iron Grains

Joseph A. Nuth III[1], Otto Berg[2], James Faris[1]
and Peter Wasilewski[1]

[1]Astrochemistry Branch, Code 691, NASA-Goddard Space Flight Center
Greenbelt, MD 20771, [2]Calvert Institute, Port Republic, MD 20676

ABSTRACT

We report the results of a series of experiments in which single domain iron particles (20-50 nm radius) were condensed from the gase phase in the presence of a magnetic field. Coagulation of these particles was extremely efficient and resulted in the formation of long chains of single particles. The remanent magnetization of the chains was a few percent of saturation and these chains were magnetically hard: a field of 1650 gauss was required to demagnetize one half of the saturation remnance in our samples. Our results are completely consistent with the enhanced coagulation efficiency expected of strong magnetic dipoles. We suspect that these particles will have a very flat spectral response and should therefore be very efficient absorbers of microwave radiation.

INTRODUCTION

The thermal decomposition of iron pentocarbonyl at temperatures in excess of ~ 500 K can be utilized to form nanometer-scale iron particles, if the decomposition occurs under reducing conditions. In this study we report on the results of a series of experiments in which very small iron grains produced via thermal decomposition and vapor phase nucleation rapidly coagulated into long (~ 10 cm) strands which formed an interconnected web. At progressively lower iron pentacarbonyl concentrations the particles formed shorter (~ 2-3 cm) thread-like strands and small (~ 1mm) "dustballs" on increasingly longer timescales.

In the following sections we will briefly describe our experimental apparatus, the phenomenology of our experimental results and the results of both microscopic and magnetic analyses of the iron particles. We will then present an explanation for the extraordinarily high coagulation efficiency which we observe in our experiments and which can also explain the unique morphology of the final aggregate. We conclude by speculating on rather unique optical properties which might be expected for these iron webs.

Experiment

In these experiments very small iron particles were produced by flowing iron pentacarbonyl diluted in hydrogen through a furnace at temperatures in excess of 500 K at total pressures on the order of 100 torr. The furnace consists of an aluminum oxide tube which passes through the center of a 5.6 cm diameter graphite bar. The graphite bar is heated by passing a low voltage AC of between 500 [illegible] amperes through it. This latter is sufficient power to heat the furnace to temperatures in excess of 1500 K. The overall geometry of the system is shown in Figure 1.

In previous experiments (Rietmeijer and Nuth, 1991; Nelson et al., 1989) this apparatus has been used to generate copious quantities of 10-20 nm radius metal and metal oxide

particles from volatile precursors such as silane, trimethyl aluminum, iron carbonyl and/or titanium tetrachloride diluted in hydrogen or helium and allowed to react with oxygen or nitrous oxide as appropriate. In all of the previous experiments the resulting particles slowly settled out of the hydrogen or helium carrier gas and were collected on a copper surface at approximately 300 K. In all of our previous experiments using this system, coagulation has been minimal and detectable only by using electron microscopy to study grain morphology. No evidence for particle coagulation has ever been visually observable during the experiment.

In these experiments, a flowing gas mixture of ~ 10 mole percent iron carbonyl diluted in hydrogen through the furnace at temperatures in excess of 500 K resulted in the initial formation of a cloud of iron particles as expected. However, several seconds after the initial particles were observed to form, the cloud suddenly gelled into an interconnected mass of "webs" (see Figure 2). Dilution of the iron carbonyl by roughly a factor of 100 resulted in the formation of shorter (2-3 cm) "streamers" several tens of seconds after initiation of the experiment. These floated in the gas stream and usually stuck to the chamber walls rather than settle out onto the collector. Further dilution by another factor of 10 resulted in the formation of very small (~ 1 mm) roughly spherical dustballs occuring several minutes into the experiment. We have run several hundred experiments in this apparatus and have never before observed such phenomena.

One obvious hypothesis was that the freshly nucleated iron particles became magnetized in the high field associated with to the furnace and that this lead to the increased coagulation efficiency observed in our experiments. To test this hypothesis we ran several experiments in which we first preheated the furnace to ~ 1000 K in a pure hydrogen flow and the turned off the current to the graphite furnace prior to starting the flow of iron carbonyl. These experiments produced copious quantities of iron particles as the furnace cooled at a rate of ~ 100 K per minute. No evidence for coagulation was observed during the ~5 minutes available to initiate formation of the iron particles and for the 3 to 4 minutes subsequent to our stopping the iron carbonyl flow as the particles gently settled out of the carrier gas.

Subsequent SEM analyses of these particles confirmed that they were "normal smokes", 10-25 nm in radius and coagulated into short chains only 10-20 particles long. We attempted to perform a series of experiments in which the iron particles condensed above the Curie Point by bringing the furnace to ~ 1300 K prior to starting the flow of iron carbonyl. Unfortunately the temperature gradient downstream of the furnace is extremely high (>500 K/inch) as is the magnetic field generated by the high electrical current used to heat the furnace to this temperature (~ 1200 Amps). We were therefore unable to observe grains formed at high temperature but which passed through the Curie Point at very low magnetic field strength. In each of these experiments we formed copious quantities of webs quite rapidly.

We performed several experiments in which iron spiderwebs were collected on glass slides covered in non-magnetic epoxy. The strands appeared to sink evenly into the epoxy which was then allowed to solidify in vacuo: thus the iron strands were collected without exposure to the atmosphere and were the subject of later magnetic analyses.

The magnetic remanance (RM) of the iron webs collected in epoxy and dried in vacuo was measured using a liquid helium cooled superconducting magnetometer. The samples were then subjected to a 10,000 Gauss (0.1 Tesla) magnetic field and the saturation remnant magnetization (SIRM) measured on the same superconducting magnetometer. The ratio (REM) of the remnant magnetization in the web samples produced in the flow system to the saturation magnetic remnance for each of the three samples is given in Table 1. REM

values of a few percent suggest that the remnance acquisition mechanism is extremely efficient. The magnetic remnance in the web samples was acquired as the result of exposure to a magnetic field estimated to be at most 35-90 Gauss just outside the furnace, although no field measurements were made. This estimate was based on the geometry of the system and the 500-1200 ampere AC current typically used to heat the furnace.

Alternating field demagnetization studies were also performed on the web samples: the results were identical for three samples and are presented in Figure 3. A field of 1650 Gauss (165 mT) was required to demagnetize one-half of the saturation remnance in the samples, indicating that the material making up the web is magnetically hard. These chains appear to be magnetically harder than a non-interacting dispersion of iron spheres in a copper matrix with a size distribution between ~ 20-35 nm (Wasilewski, 1981). It may be that the coagulation of the initial distribution of spheres into sintered chains (see below) allows an approximation to stable single domain behavior in strings containing tens of iron particles.

The morphology of the web was studied using optical microscopy, scanning electron microscopy and transmission electron microscopy. The web consisted of intersecting continuous strands a fraction of a millimeter thick and 4-5 inches long (the collection chamber is 4" in diameter). Individual strands consist of many kinked smaller strands of iron particles ~ 20-50 nm in diameter and many hundreds of particles long (Figure 4). Individual particles were connected to their neighbors in head-to-tail chains at angles usually between about 90 and 180°. Very few triplets were observed at angles of either 90 or 180°; the vast majority appear to form at angles on the order of 130°-150°. Individual particle boundaries show evidence for much more than simple "sticking"; some evidence is observed for martensitic transformation at the joints, some joints have deformed into contact planes and the chains show evidence for a continuous overgrowth of a metal oxide layer. We suggest that these grains underwent some degree of contact welding due to the interaction of both surface tension and magnetic dipole forces shortly after or during coagulation.

Discussion

The iron particles produced in these experiments are within the size-range predicted to behave as single magnetic domain particles (Butler and Banerjee, 1975) provided that they are not perfect spheres. Single-domain particles should be very easily magnetized in the 35-90 gauss field present throughout most of the experiments and such particles will then behave as dipole magnets. A dipole in the presence of a non-uniform magnetic field-e.g. that produced by another dipole - will experience a maximum force at an angle which maximizes the divergence of the field (Purcell, 1965). If the sticking cross-section is maximized at an angle to the magnetic pole which maximizes the attractive force between the dipoles then it would not be unexpected to observe that the average angle between any three individual particles is less than 180°. In general one would predict that the pole of one particle would be attracted to a point ~ 45° from the pole of a second. A few triplets could therefore form at angles as small as 90° while a few others could join at 180°. However, the vast majority of grains would be expected to form at angles of ~ 135° or so as is observed.

A first estimate for the increase in efficiency one might expect for the coagulation of magnetic dipoles as compared to the coagulation of a similar size distribution of unmagnetized iron spheres can be made by calculating the increase in interaction distance, or effective radius for magnetic dipoles. For unmagnetized iron spheres, the effective collision cross section is proportional to the square of the geometric radius of the particles. For magnetic dipoles, attracted to one another by a force which varies as the inverse square

of the particle separation (Weast, 1972), the increase in effective particle radius can be calculated by using the analogous increase in the effective radius of celestial bodies due to gravitational forces.

For gravitational focusing of interacting planetessimals the increased effective radius (R) of the target is given by (Opik, 1975)

$$R = a\left(1 + V_e^2 / V_o^2\right)^{1/2} \tag{1}$$

where a is the geometric radius of the target, V_e is the escape velocity of the target and V_o is the initial velocity of the impactor. The escape velocity for gravitational interactions is given by

$$V_e = \left(\frac{2GM}{r}\right)^{1/2} \tag{2}$$

where G is the gravitational constant M is the mass of the target body and r is the initial separation of the two planetessimals.

The magnetic analogy to gravitational focusing can be constructed by comparison of the force between two interacting magnetic dipoles and that between two gravitationally interacting bodies, e.g.

$$F_{grav} = \frac{GM_1M_2}{r^2} \qquad F_{Mag} = \frac{m_1m_2}{\mu r^2} \tag{3}$$

where M_1 and M_2 are the masses of the celestial bodies, m_1 and m_2 are the magnetic pole strengths, r is the particle separation and μ is the magnetic permeability equal to unity in a vacuum. The equivalent "escape velocity" for two interacting magnetic dipoles is therefore given by

$$V_e = \left(\frac{2m_1m_2}{M\mu r}\right)^{1/2} \tag{4}$$

where M is the reduced mass of the dipoles.

The average particle separation, r, can be obtained from the initial number density, n_o, of single domain iron grains so that

$$r = \left(\frac{3}{4\pi n_o}\right)^{1/3} \tag{5}$$

$$V_e = \left[\frac{2m_1m_2}{M\mu}\left(\frac{3}{4\pi n_o}\right)^{-1/3}\right]^{1/2} \tag{6}$$

and $$R = a\left(1 + 2\left(\frac{4\pi}{3}\right)^{1/3} \frac{m_1 m_2}{M\mu} \frac{n_o}{V_o^2}^{1/3}\right)^{1/2}. \qquad (7)$$

For 20 nm radius single domain iron particles with a density of 7.86 g/cm^3 and bulk saturation magnetization of 1720 emu/cm^3, M is approximately 2.5 x 10^{-16} g, M_1 equals M_2 and is approximately 1.7 x 10^{-3} esu. For an initial number density of 10^6 cm^{-3}, a relative velocity on the order of 1 cm/s and $\mu \approx 1$, R ≈ 4 cm, an enhancement in effective radius by a factor of ~2 x 10^6.

An increase (or decrease) in the initial number density of dipoles has little effect on the enhancement factor, due to the $n_0^{1/6}$ dependence of R derived in equation (7). The largest effect of decreasing n_0 will be to increaase the average time between collisions and decrease the mass available for coagulation. This appears to be consistent with our observations that smaller scale aggregates formed on longer timescales as the initial concentration of iron carbonyl in the flow was decreased.

In the above calculation, we assumed that the single domain iron spheres were completely magnetized and therefore that M_1 equaled M_2. Equation 7 shows that R is directly proportioned to M. Accordingly, a slight variation in the pole strength will have little effect on the enhancement expected in the experiments. However, there is experimental evidence to suggest that the grains were probably magnetized to nearly saturation. The magnetic remnance of the web was found to be a few percent of the saturation value. The coagulation process for magnetic dipoles should tend to force "North-to-South" pole contact on grounds of energy minimization, and this would therefore force the cancellation of the remnant field of individual particles. If the average angle between dipole triplets were 180° one would expect very little remanance for macroscopic samples of the web. Since the average angle between triplets lies between 130°-150° as noted above, the observed remnance is due to incomplete cancellation of the magnetization of the individual particles. Because cancellation of the remnant field of a large number of dipoles in the webs is expected to have occurred with some reasonable efficiency, an observed remnant field of a few percent for the microscopic samples implies a much larger initial degree of magnetization for individual particles. Our assumption of complete magnetization is therefore likely to lead to only a relatively small numerical error in calculation of R if individual particles were actually magnetized to only ~ 20-50% of their theoretical maximum.

The optical properties of random aggregates of conducting spheres has been discussed by Wright (1987) for open clusters of varying fractal dimension. In general the absorption cross section is proportioned to a power of the frequency: the exact value of the power varies between 0.6 and 1.4 over more than two decades in frequency for aggregates of fractal dimension, D, between ~1.7 and 2.5. The lower the fractal dimension, the flatter the spectrum and thus the lower the calculated exponent. As an example the ratio of the absorption cross section at 1 micron compared to the absorption cross section at 1 millimeter for spheres, D=3: aggregate, D=2.5: aggregate, D=1.7 is 1704:10:1, respectively (Wright, 1987). If the absorption cross section at 1 micron is the same for each of the above cases, the open fractal aggregates have enormously enhanced long wavelength absorption.

As noted by Kim and Brock (1987) in their discussions of the formation of ferromagnetic particles from solution via cation reduction by borohydride ions, the fractal dimension of a linear chain of particles is one, and the more ferromagnetic particles tend to form lower fractal dimension aggregates under the influence of an external field. From Figure 4 it is obvious that the fractal dimension of individual strands produced in our experiments is quite low; these aggregates are not really linear chains but are really more like highly kinked strings which have become intertwined to some degree. Because one would expect that the fractal dimension of "head-to-tail" chains of magnetic dipoles should be nearly 1 and because Wright (1987) has demonstrated that lower fractal dimension aggregates appear to have "flatter" spectra than higher dimension aggregates, one would predict that the long wavelength absorption cross section for an aggregate of magnetized, single domain iron grains should be considerably more than 2000 times that for spherical particles of equal mass.

Conclusions

Magnetically-hard, open nets of very small iron metal grains rapidly form via coagulation in a laboratory system in which large scale coagulation has never before occurred. We have shown that magnetically induced dipole-dipole interactions between the magnetized iron grains increase the grain coagulation efficiency by several orders of magnitude and probably also increase the strength of the interparticle bonds in the aggregate. We hypothesize that the optical absorption cross section for an aggregate of magnetically interacting single domain particles should show considerable enhancement at long wavelength (> 1 mm) when compared to an equal mass of iron spheres.

References

Butler, R. F. and Banerjee, S. K., 1975, J. Geophys. Res., 80, 252-259.

Kim, S. G. and Brock, J. R., 1987, J. Coll. Interface Sci., 116, 431-443.

Nelson, R., Thiemens, M., Nuth, J. and Donn, B., 1989, Proc. Lun. Plan. Sci. Conf., 19, pp. 559-563.

Öpik, E. J., 1975, Interplanetary Encounters, Technical Report #75-009 (University of Maryland, College Park) pp. 49-51.

Purcell, E. M., 1965, Electricity and Magnetism: Berkeley Physics Course - Volume 2 (McGraw-Hill, NY) pp. 367-369.

Rietmeijer, F. and Nuth, J., 1991, Proc. Lun. Plan. Sci. Conf., 21, 591-599.

Wasilewski, P. J., 1981, in Shock Waves and high Strain Rate Phenomena in Metals, M. A. Meyers and L. E. Murr (eds.) (Plenum Press, NY).

Weast, R. C., 1972, Handbook of Chemistry and Physics - 53rd Edition (CRC Press, Cleveland) p. F-80.

Wright, E. L., 1987, Astrophys. J., 320, 818-824.

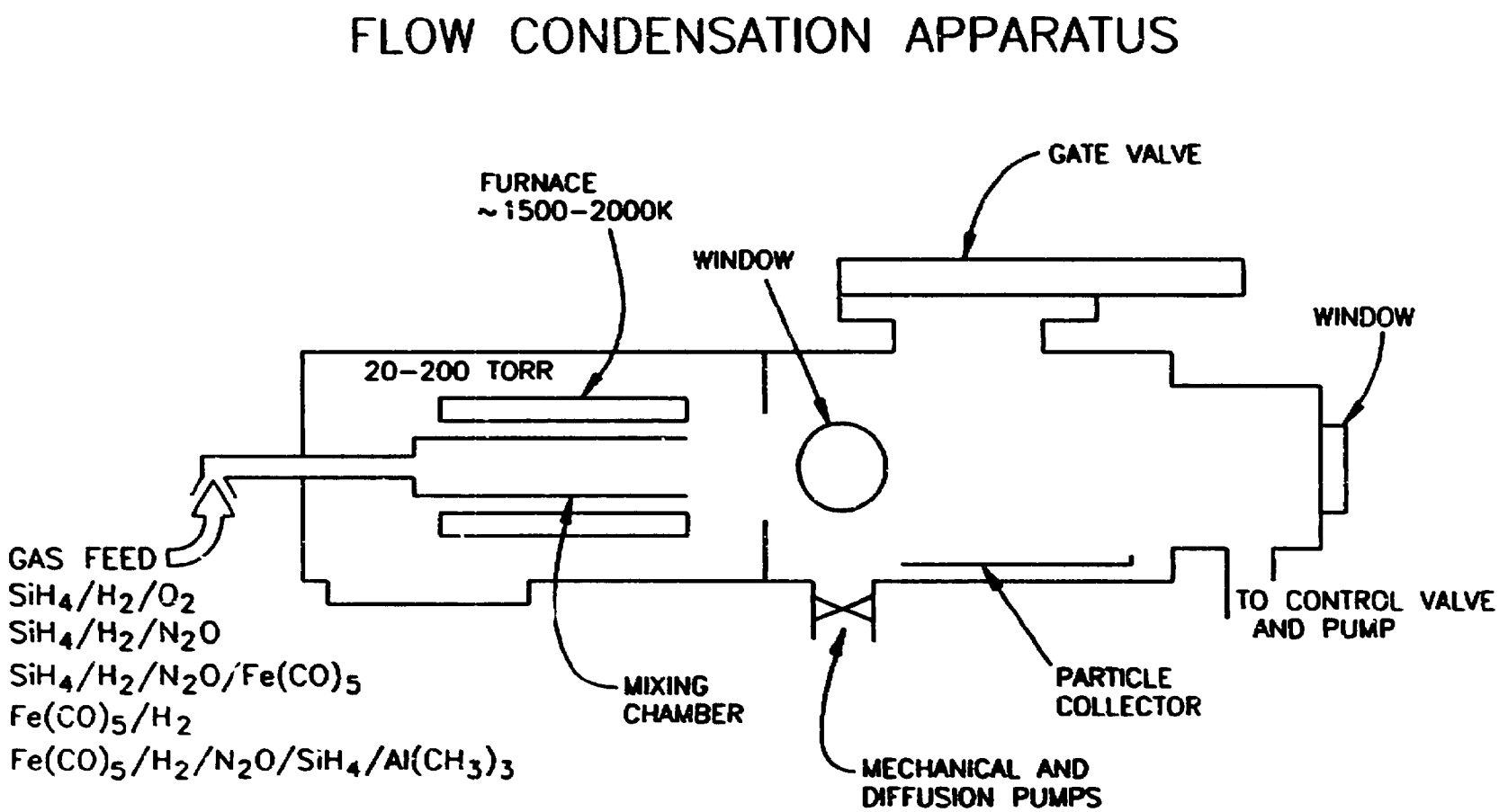

Figure 1. A schematic drawing of the experimental apparatus.

Figure 2 A photograph of "webs" of coagulated iron particles taken through the side port of the apparatus. The diameter of the window through which the photo was taken is 4 inches.

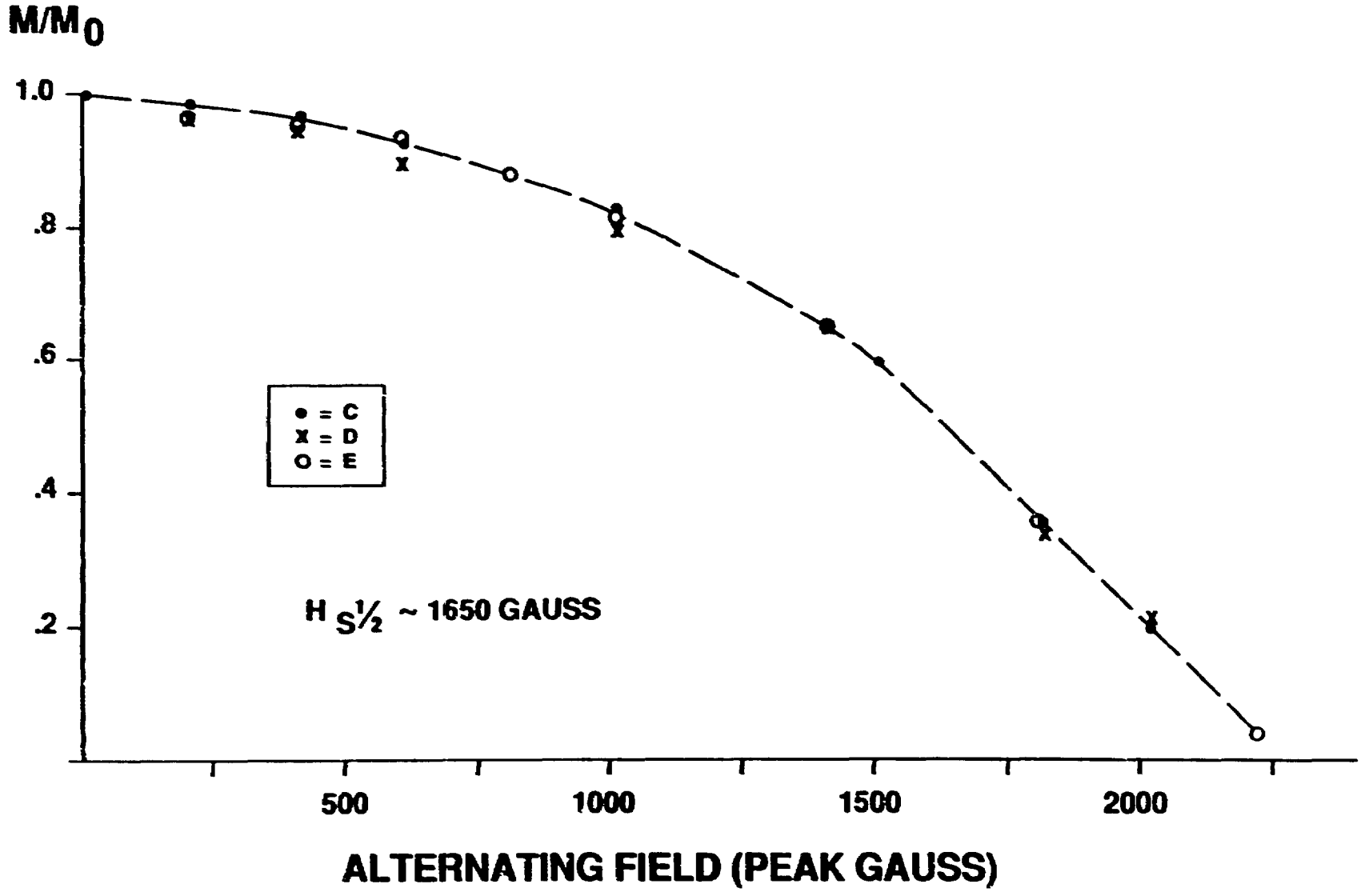

Figure 3. Alternating field demagnitization curves were identical for the three samples studied: the 1650 gauss field required to demagnetize on half of the saturation remnance ($M/M_0 = 0.5$) indicates that the particles making up the web are magnetically hard.

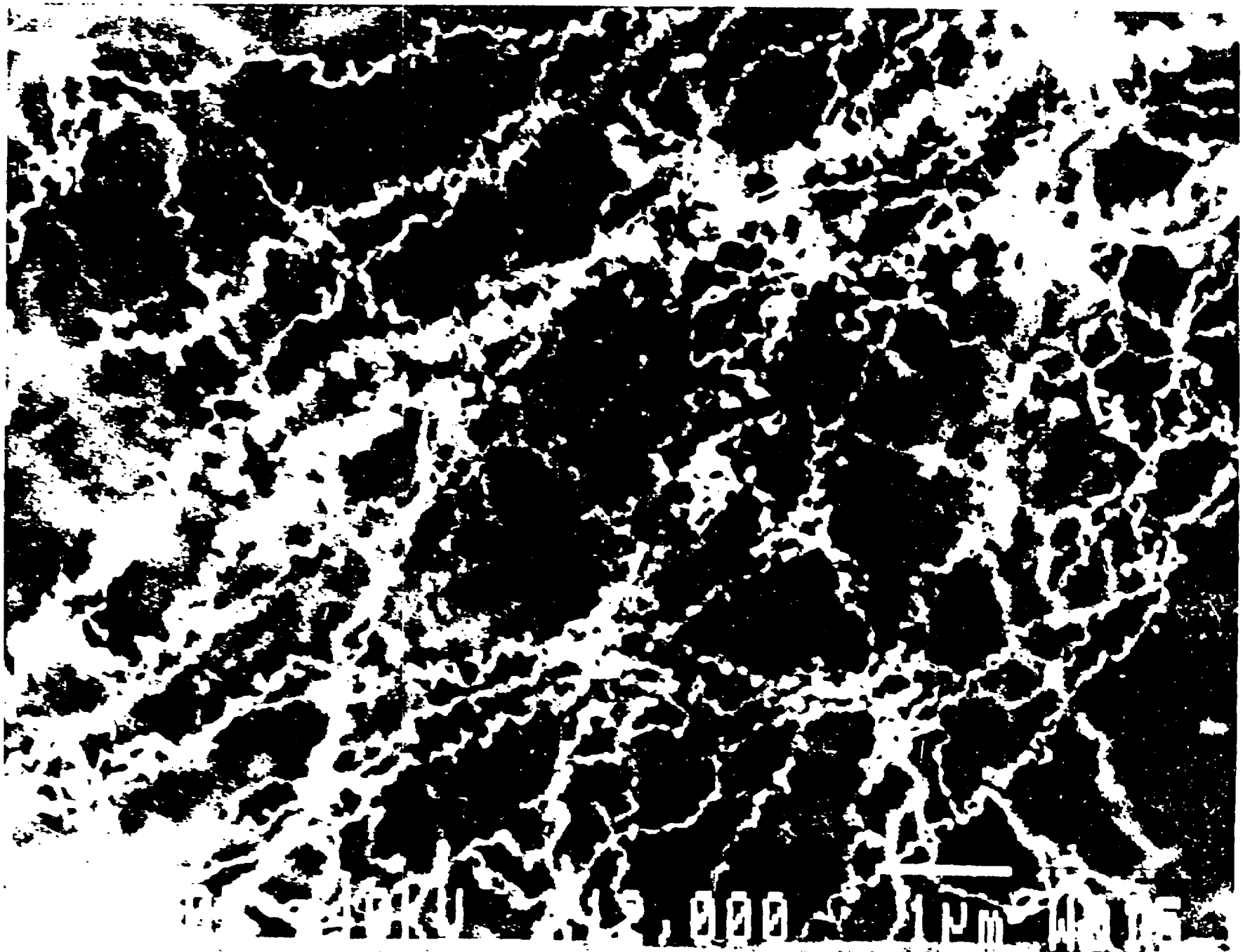

Figure 4 Scanning electron microscope image of a small portion of the web magnified 12000 times at a beam energy of 30 keV. The scale bar is 1 μm.

Cosmic Dust Analog Simulation in a Microgravity Environment: The STARDUST Program

F. Ferguson[1], L. U. Lilleleht[1], J. Nuth[2], J. R. Stephens[3], E. Bussoletti[4,7], L. Carotenuto[5], L. Colangeli[6], P. Dell'Aversana[5], F. Mele[5], V. Mennella[7], C. Mirra[5]

[1]University of Virginia, Charlottesville (VA), [2]NASA Goddard Space Flight Center, Greenbelt (MD), [3]Matrix, Santa Fè (NM), [4]Istituto Universitario Navale, Naples (I), [5]MARS Center, Naples (I), [6]Università di Cassino, Cassino, (I), [7]Osservatorio Astronomico di Capodimonte, Naples (I)

ABSTRACT

We have undertaken a project called STARDUST which is a collaboration with Italian and American investigators. The goals of this program are to study the condensation and coagulation of refractory materials from the vapor and to study the properties of the resulting grains as analogs to cosmic dust particles. To reduce thermal convective currents and to develop valuable experience in designing an experiment for the Gas-Grain Simulation Facility aboard Space Station, Freedom we have built and flown a new chamber to study these processes under periods of microgravity available on NASA's KC-135 Research Aircraft. Preliminary results from flights with magnesium and zinc are discussed.

INTRODUCTION

Small cosmic dust particles play an important role in several stages of stellar evolution. Major components of these interstellar grains are refractories such as silicates and carbides which condense in the outflows of red-giant stars. These refractory materials play a crucial role in the chemistry of the interstellar medium by serving as sites for chemical reactions and as regulators of the temperature in denser clouds by absorbing and re-emitting light. Furthermore, the condensation and later coagulation of such grains will lead to insights into the formation of larger bodies such as planetesimals and planets.

To understand how refractory particles form and grow we have undertaken a project called STARDUST as a collaboration between Italian and American investigators. The goals of this program are to study the processes of condensation and coagulation of refractory materials from the vapor and to study the size, morphology, mechanical strength, and optical properties of the resulting grains as analogs to the more complex cosmic dust particles. An important first step in this project is the production of a quiescent suspension of monodisperse, refractory particles. There is evidence that particles formed by nucleation and condensation of vapor are uniform in size with only a few, if any, aggregate clumps at the onset of formation. Although the nucleation of a few refractory systems has been investigated in terrestrial laboratories, accurate studies of the interaction between the fine-grained particulates are greatly hampered by particle settling effects. Resuspension of small particles by a burst of gas or by other mechanical motion will result in fast-moving, shearing flows and the break-up of some particles, while other aggregates formed during the settling process may never break up. Thus uniform, quiescent suspensions of monodisperse particles in a low pressure gas are difficult, if not impossible to achieve by the injection or resuspension of previously characterized particulates. Yet such well-characterized suspensions are ideal starting points for many of the more interesting particle interaction experiments envisioned for the Gas-Grain Simulation Facility on Space Station Freedom. It should be possible, however, to produce such suspensions by the direct condensation of refractory vapors under controlled conditions in a microgravity environment. The studies necessary to predict both the size distribution and characteristics of the particles produced by such a method may also yield high quality data on the vapor phase nucleation of refractory materials.

Previous experiments on condensation of refractory material from the vapor have also been affected by thermal convective currents arising from the high temperatures needed to produce such vapors. As a result we have designed and built a new apparatus which can be operated aboard NASA's KC-135 Research Aircraft. This aircraft flies in a series of parabolic arches and may produce approximately 23 seconds of weightlessness per parabola, thereby reducing thermal convective currents. This

microgravity environment is not expected to affect the condensation process itself; rather it should provide a quiescent environment for condensation and coagulation which is easier to model and more suitable for producing uniform suspensions of condensed particles. These experiments also provide valuable information on the production of such refractory suspensions under sustained microgravity and are in fact crucial steps in the development of coagulation experiments for the Gas-Grain Simulation Facility for the investigation of the coagulation, mechanical strength, and optical properties of aggregates of refractory particles. It is believed that during extended periods of weightlessness suspended particles could coalesce into very different structures than are formed in a 1g gravitational field--perhaps producing "fluffy" or "fractal-like" structures. These resulting open and porous structures could have very unusual optical and mechanical properties. It is impossible to form such aggregates on the ground since any force applied to arrest their settling is likely to crush these undoubtedly fragile structures. The periods of weightlessness on the KC-135 are unfortunately too short to study more than just the initial stages of coagulation, yet these flights will provide excellent experience in producing uniform, quiescent suspensions and developing *in situ* techniques for characterizing the particles and monitoring their interactions.

PREVIOUS WORK

In addition to providing valuable experience in the production of suspensions of refractory particles from the vapor, experiments on condensation in a microgravity environment may also provide useful information on the nucleation of these materials. Most of the experiments in refractory nucleation have been performed with two types of apparatus--the shock tube technique and the gas evaporation method. The results of both types of experiments are the same: none of the experimental data agree with Classical Nucleation Theory or its modifications such as the Lothe-Pound formulation. To date, only Hale's Scaled Nucleation theory has compared successfully with any experimental nucleation data, and only for two gas evaporation studies of silver and SiO[2]. Hale's theory predicts a relationship between the critical supersaturation, S_C, and the condensation temperature, T, as follows:

$$\ln(S_C) = \Gamma\Omega^{3/2}\left[\frac{T_C}{T} - 1\right]^{3/2} \qquad (1)$$

for a flux of particles of $1/cm^3$-s[3]. In this expression the quantities Γ and Ω are essentially constant and T_C is the critical temperature of the material. Equation (1) works quite well with many volatile substances such as water and alcohols, and for the experimental data for silver and SiO. Only a handful of refractory compounds have been studied and more experimental data or additional refractory substances are needed to test the validity of this or other theories.

EXPERIMENTAL APPARATUS

To study the condensation of refractory vapors and the coagulation of the resulting grains we have designed and built the chamber shown in Figure 1. It consists of a cylindrical vacuum chamber separated into two sections. The upper section contains the material to be studied within an alumina crucible and surrounded by a set of graphite resistive heaters and insulation. The lower half of the chamber is the viewing region of the apparatus. The graphite heaters serve two purposes: they produce the refractory vapor and establish a temperature gradient in the viewing region. A laser beam strikes a rotating, multifaceted mirror and produces a two-dimensional fan of illumination within the chamber. When vapors from the heater assembly diffuse into the viewing region, the fan of laser light illuminates only a cross-section of the condensed smoke particles. The pressure, acceleration level and temperatures throughout the chamber are recorded using a computerized data acquisition system.

RESULTS

To date, we have conducted experiments with only two metals: magnesium and zinc. These two materials are not especially important in astrophysical environments, although magnesium is one of the more abundant metals in such systems. We have chosen these elements for our initial experimental

studies because of their relatively high vapor pressures. As we develop our apparatus we will study more refractory, and therefore more relevant substances such as iron metal and magnesium and iron silicates. We have tried to apply Hale's Scaled Nucleation theory to the experimental results for both magnesium and zinc, but the data and the theory do not agree. According to Hale's theory, a plot of $(LnS)^{2/3}$ vs. (1/T) should yield a straight line and the ratio of the slope of this line to the negative of the intercept should yield the critical temperature of the material. Thus far, application of the scaled theory to the magnesium and zinc data have yielded unreasonably low critical temperatures. Just recently, we have re-examined shock tube data for iron, bismuth and lead in the form suggested by Hale and found similarly low critical temperatures, at times even below the boiling point[4]. Therefore we are currently re-examining the apparatus, the models of the data, and the theory to understand this discrepancy.

The immediate major goal of our work is the production of uniform suspensions of refractory particles. Although we do not yet have a quantitative way of rating the uniformity of the cloud of smoke particles, by eye the clouds obtained in zero-g appear to be quite uniform. Figure 2 shows a comparison between the smoke clouds formed under terrestrial and zero-g conditions. Each figure is a digitized video image of the viewing region of the chamber taken during experimental runs with magnesium. The source of vapor is a spout which appears as a bright spot at the top-center of each image. The figure under 1g shows a cloud which is nonuniform and exhibits convective swirls. The image obtained in zero-g shows what appears to be a uniform suspension of particles. Surrounding the vapor spout there is a region which is free of particles. During an experimental run in zero-g the smoke cloud slowly moves away from the vapor source, but this particle-free zone remains essentially stationary. In our nucleation experiments we are trying to measure the temperature and vapor concentration at the interface between this particle-free and particle-rich region.

We have not quantitatively measured the size distribution of the smoke particles within the cloud during individual parabolas. We have collected particles on SEM grids from various locations with the chamber. Figure 3 is a set of SEM micrographs from an experiment with zinc metal. The particles in these micrographs appear to be spherical and rather uniform--both of which are desirable in the design of a coagulation experiment. In some cases there are aggregates of these small particles which are branched and chain-like. These particles may be the initial stages of some of the fractal-like particles we are interested in growing. Some of the nonuniformity of the particles could be due to the changing conditions and different times in which they adhered to the SEM grid. During a typical flight, we undergo approximately 40 parabolic arches; we do not yet have a method of collecting particles from an individual parabola or from specific regions of the smoke cloud. We are in the process of designing a more sophisticated particle collection facility to eliminate this problem.

FUTURE WORK

Refractory species over a range of volatilities will be investigated to study the basic mechanism of the nucleation and condensation phenomenon. Thus far we have studied magnesium and zinc, species with relatively high vapor pressures. Examples of intermediate volatility species are SiO and iron and these materials are being planned for later experiments. Eventually we also want to study "super refractory" species such as carbon, silicon carbide and aluminum oxide. These compounds cannot be vaporized from standard crucibles and will require significant modifications to the existing apparatus. Not only will higher vapor source temperatures be required but the method of producing vapor will have to be redesigned as well.

A sampling system for extracting particles from the chamber during the experiment, and the capability for *in situ* particle characterization will also need to be developed. These would help to differentiate between the design change effects and those caused by the extended exposure of the condensate

particles to the varying environmental conditions in the chamber through the series of parabolic maneuvers.

CONCLUSIONS

We have presented an overview of the STARDUST program, a program with long-term goals which include studying the condensation, coagulation, and physical and optical properties of refractory particles as analogs to cosmic dust grains. We have made good progress towards these goals by producing uniform suspensions of particles from the vapor. The next step is to develop a more sophisticated method of characterizing the resulting particles and improving the data collection and analysis of the nucleation of these particles.

REFERENCES

1. E. Bussoletti and L. Colangeli, "Cosmic Dust: from Space to Laboratory," *Rivista del Nuovo Cimento*, Bologna, **13**, 1-70 (1990).

2. B. N. Hale, P. Kemper, J. A. Nuth, "Analyses of Experimental Nucleation Data for Silver and SiO Using Scaled Nucleation Theory," *J. Chem. Phys.* **91** p. 4314, (1989).

3. B. N. Hale, "Application of Scaled Homogeneous Nucleation-Rate Formalism to Experimental Data at $T << T_C$," *Physical Review A* **33** 4156, (1986).

4. J. A. Nuth, F. T. Ferguson, "Nucleation of Solids from the Gas Phase," *Proceedings from the Fourth Symposium on Nucleation and Crystallization*, Atlanta, Georgia, Preprint, (1992).

5. G. Fogelman, J. L. Huntington, D. E. Schwartz, and M. L. Fonda, *Gas-Grain Simulation Facility: Fundamental Studies of Particle Formation and Interactions*, NASA CP-10026, (1989).

6. D. J. Frurip, S. H. Bauer, "Homogeneous Nucleation in Metal Vapors. 3. Temperature Dependence of the Critical Supersaturation Ratio for Iron, Lead and Bismuth," *J. of Phys. Chem.*, **81** p.1001,(1977).

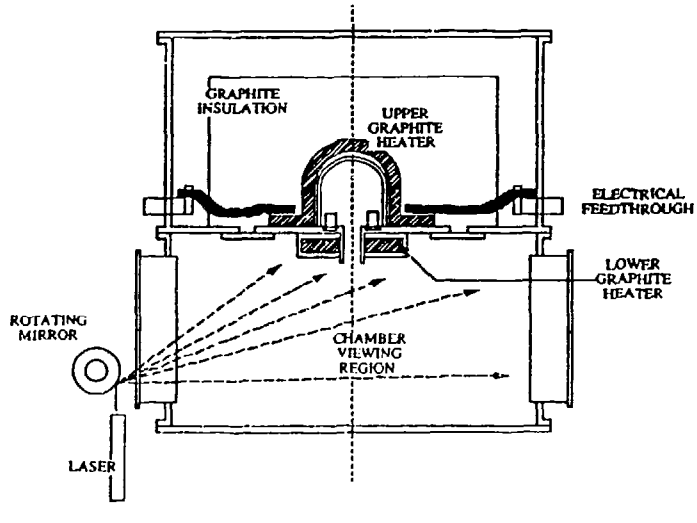

FIGURE 1. Experimental chamber used on NASA's KC-135 aircraft.

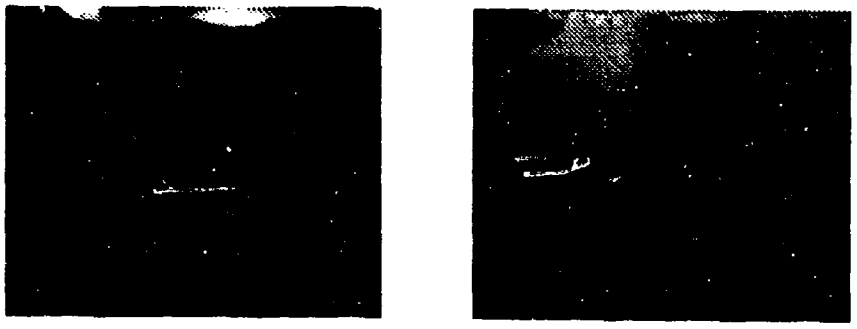

(a) (b)

FIGURE 2. Digitized video images from experimental runs with magnesium at (a) 1-g and (b) microgravity.

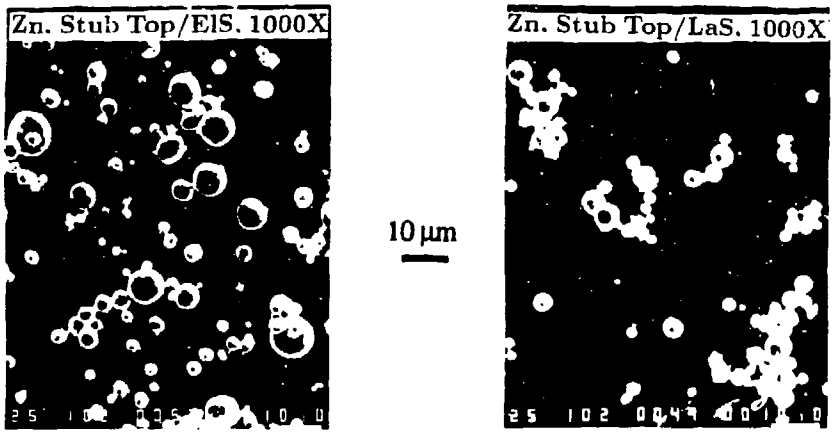

FIGURE 3. SEM micrographs of zinc particles at 1000X magnification. Note aggregates which look like the initial stages of growth of fractal-like particles.

Blank

B. PARTICLE DISSEMINATION, TRANSPORT AND DEPOSITION

A NUMERICAL SIMULATION OF TURBULENT DISPERSION

A. Hadad, M. Stiassnie, M. Poreh
Department of Civil Engineering, Technion, Haifa 32000, Israel

RECENT PUBLICATIONS, SUBMITTALS FOR PUBLICATION, AND PRESENTATION:

Hadad, A., M. Stiassnie, M. Poreh and J. E. Cermak (1992a): Some Fractal Properties of Integrated Concentration Fluctuations, Proceedings of the 1992 CRDEC Scientific Conference on Obscuration and Aerosol Research.

Poreh, M. and J. E. Cermak (1992b): On the Similarity of Line Integrated Concentration Fluctuations Across Plumes Diffusing in Grid-generated Turbulence, Proceedings of the 1992 CRDEC Scientific Conference on Obscuration and Aerosol Research.

Poreh, M., A. Hadad and J. E. Cermak (1993a): Fluctuations of Line Integrated Concentrations Across Plumes Diffusion in Grid Generated Turbulence and in Shear Flows, *Boundary Layer Meteorology*, Vol. 62, 1993, pp. 247-267.

Hadad A., M. Stiassnie, M. Poreh and J. E. Cermak (1993b): Fractal Aspects of Integrated Concentration Fluctuations, *Boundary Layer Meteorology*, Vol. 62, 1993, pp. 291-302.

ABSTRACT

The paper presents numerical simulation of dispersion in a turbulent flow field created by superposition of Taylor-Green vortices. Good agreement between the simulations and measurements are found.

BACKGROUND

The prediction of dispersion of contaminants in turbulent flows is of considerable basic and practical interest. We have attempted to simulate the dispersion of inert scalar tracers in a homogeneous turbulent flow obtained by superposition of Taylor-Green (TG) vortices (Taylor and Green [1]). Each TG vortex is described by:

$$\tilde{u}_i = 4\sqrt{2/3}\ \sin[\phi_o + 2\Pi\ (i - 1)/3] \sum_{j=1}^{3} \cos[\Pi\delta_{ij}/2 - k\tilde{x}_j]\ ;\ i = 1,\ 2,\ 3. \qquad (1)$$

Such a flow satisfies the continuity equation for a constant piezometric pressure. Superposition of eight TG vortices with different sizes, different phase values ϕ_o, different orientations and positions, so that the energy spectral density of the turbulence E(k) satisfied the -5/3 law: $E(k) = E_o\ k^{-5/3}$ in a given range $k_L < k < k_2$, where k_L is the wave number related to the mesh size of a grid and k_2 is the wave number associated with dissipation length, was used to simulate slowly decaying grid-generated turbulence described in Poreh et al. [2]. The dispersion of a puff of 10^4 tracer particles initially located at a small volume was then calculated numerically.

TYPICAL RESULTS

Figure 1 shows the shape of the puff at different times (T) for a given experiment. Figure 2 shows the superposition of 26 puffs of 1000 particles at T = 1 s. We have also calculated the integrated concentration (IC) fluctuations across the puffs and compared their statistical properties with those measured by Poreh et al. [2]. A very good agreement between the calculated and measured values were found. Figure 3 shows, for example, the measured and calculated values of the relative rms value of the integrated vertical integrated concentrations (VIC) across a plume.

It was also noted that the typical shapes of the instantaneous puffs were very similar to the shape of photographed puffs and was not similar at all to that of Gaussian puffs, which are often used to describe the shape of puffs and instantaneous plumes.

CONCLUSIONS

The use of Taylor Green vortices for studying the dynamics of diffusion in turbulent flows appears to be of considerable value. It is proposed to study the simultaneous diffusion of puffs of different species from different sources and to calculate the correlation between the local concentrations, which could be used to estimate the possibility of a chemical reaction between the two species.

REFERENCES

1. Taylor, G. I. and A. E. Green (1937) Mechanism of the Production of Small Eddies From Large Ones, *Proc. R. Soc. Lon.*, A158, 499-511.

2. Poreh, M., A. Hadad and J. E. Cermak (1993) Fluctuations of Line Integrated Concentrations Across Plumes Diffusion in Grid Generated Turbulence and in Shear Flows, *Boundary Layer Meteorology*, Vol. 62, 1993, pp. 247-267.

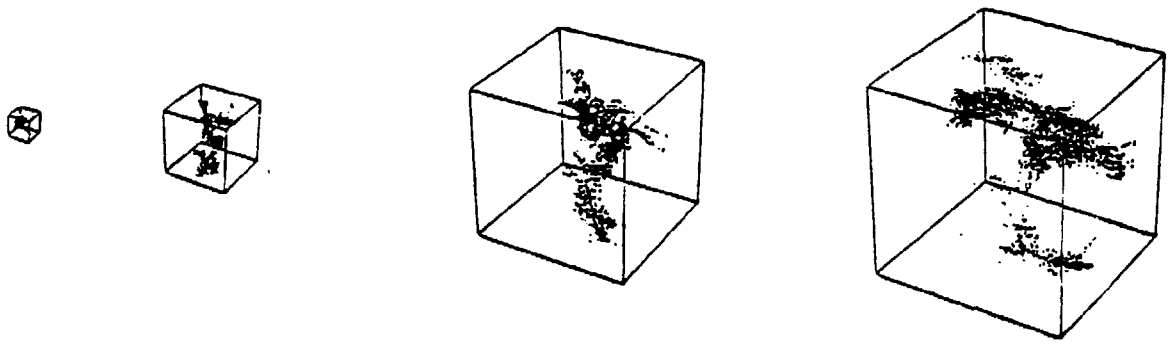

FIGURE 1. PROPORTIONAL (3-D) VIEW OF A TRACER PUFF DISPERSION IN THE FLOW FIELD AT T = 0.25, 0.50, 0.75 AND 1.00 SECONDS.

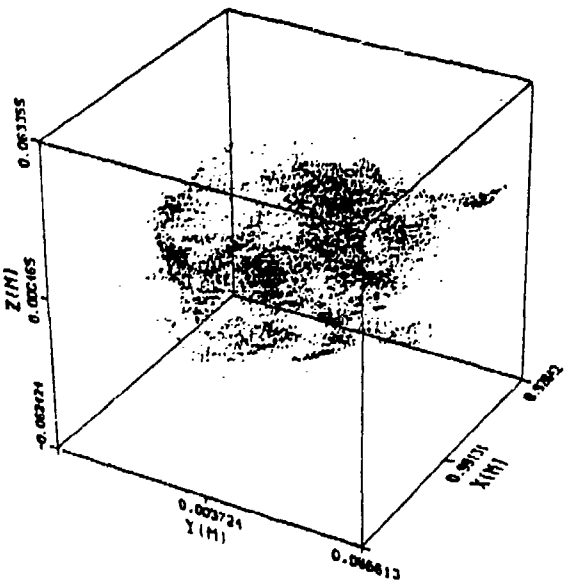

FIGURE. 2. AVERAGE PUFF OBTAINED BY A SUPERPOSITION OF 26 DIFFERENT PUFFS OF 10^3 PARTICLES EACH AT T = 1 S.

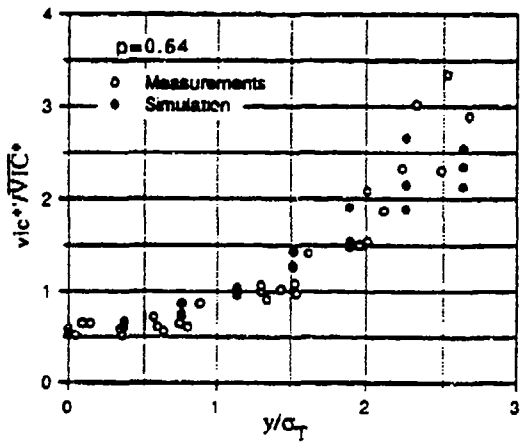

FIGURE 2. THE DISTRIBUTION OF THE INTENSITY FLUCTUATIONS OF THE VERTICAL INTEGRATED CONCENTRATIONS (VIC).

Blank

ELECTRODYNAMIC LEVITATION OF MICROPARTICLES IN A G .S FLOW

E.E. Allison and B.R.F. Kendall

Department of Physics
The Pennsylvania State University
UniversityPark, PA 16802

RECENT PUBLICATIONS, SUBMITTALS FOR PUBLICATION, AND PRESENTATIONS:

E.E. Allison, B.R.F. Kendall, B.V. Bronk, and D.S. Weyandt, "Manipulation of Microparticles in Multiphase Levitation Traps", Proceedings of the 1992 CRDEC Scientific Conference on Obscuration and Aerosol Research.

ABSTRACT

An electrodynamic levitation trap is used to suspend charged microparticles in a horizontally-flowing gas of known velocity and viscosity. Orthogonal DC electric fields permit both gravitational and Stokes drag forces to be balanced independently, allowing determination of the particle's mass, diameter and charge. Future work will investigate the influence of humid gas flows on the size of levitated microdroplets.

INTRODUCTION

Electrodynamic levitation traps were originally developed by Wuerker[1], et al, in connection with fusion research in the late 1950's. Under the simplest condition of a single particle in an evacuated trap, particle motion is described by a set of Mathieu differential equations. If the magnitude and frequency of the AC drive voltage to the trap are in the stable range for a given particle charge-to-mass ratio, stable levitation will occur. If the trap is not evacuated the stability limits for levitation are extended due to the damping effect of the air on particle motion. DC cross-fields may be added to the AC levitation fields to position particles within the trap and to compensate for external forces such as gravity or the drag force of a flowing gas.

EQUIPMENT DESCRIPTION

A cubical trap geometry with six planar electrodes and two-phase AC drive as described by Kendall[2], et al, was used for this work. The cell and its co-ordinate axes are shown in *Figure 1*. The inside dimension of the trap was 3.2 cm on a side. The front and back faces were constructed of transparent conductive glass allowing levitated microparticles to be observed by microscope or video camera. Gas entered the trap through a porous copper wall to prevent turbulence, and exited from the mesh-covered opposite face. The top and bottom electrodes, which in this cell design do not require AC drive, were made of solid insulated aluminum plates with 1.3 cm diameter holes bored through their centers and covered with fine wire mesh. Microparticles were charged and injected into the trap through the hole in the top electrode while the hole in the bottom electrode was used to illuminate the microparticle via a helium-neon or argon laser.

AC signals on the order of 1kV rms with 60 degree phase difference were used to drive the two pairs of vertical electrodes. The DC cross-fields were superimposed upon these signals (in the case of the x and y fields) or applied directly (in the case of the z field).

Particles used in the initial experiments were glass beads of nominal 10 micron radius. They were launched from an aluminum cup, with a small hole in the bottom, which was mounted above the hole in the top electrode of the trap. It was elevated to approximately 15-20 kV during particle launching which charged the beads and caused some to be expelled from the launcher into the trap. Later work will involve liquid droplets.

The controlled air flow was passed through the trap in the positive y direction.

Figure 2 shows the levitation trap and the apparatus connected to it for use in aerosol studies.

DETERMINATION OF PARTICLE SIZE

It is assumed that the microparticles are spherical and of radius r, mass m, charge q and known density ρ. It is further assumed that the gas flow, of known velocity U and known viscosity η, is low enough for Stokes' Law to be valid (Reynolds number less than one).

With a levitated particle brought to the center of the cell by a vertical field E_z, we have

$$qE_z = mg = 4/3\ \pi r^3 \rho g. \tag{1}$$

The gas flow is then turned on and the particle recentered using a horizontal field:

$$qE_y = 6\pi\eta r U. \tag{2}$$

Eliminating q, we obtain

$$r^2 = \frac{9E_z\eta U}{2E_y\rho g}. \tag{3a}$$

Because of the three-axis symmetry of this type of cell, the ratio of fields must be the same as the ratio of the applied DC voltages, so that finally

$$r^2 = \frac{9V_z\eta U}{2V_y\rho g}. \tag{3b}$$

This gives the radius, and hence the mass.

PRELIMINARY RESULTS

The first measurements indicated particle radii spread over the range 5-15 microns. Analysis of the actual size distribution of these nominally 10 micron radius particles showed that they actually covered this wide range. After sieving to reduce the range to 10-12.5 microns, consistent results were obtained.

The volume flow rate was varied over the range 0-40 cm^3/second and plotted against the corresponding cross-field voltage V_y. The result was a straight line, confirming the validity of equation (2) above. This linear range appears to continue up to the highest flow velocities so far used, which correspond to a Stokes drag force of seven times the particle's weight. It was noted that the x and z crossfields required no adjustments over the full flow range, indicating that the gas flow was accurately aligned with the y axis.

In the early experiments there was evidence of a non-uniform (but stable) flow distribution over the cross-section of the cell, necessitating an additional correction factor to obtain central velocity from volume flow rate. The general effectiveness of the porous-wall inlet in reducing turbulence was, however, confirmed by reversing the flow direction so that the gas entered through the metal electrode mesh. This produced severe instability.

Modifications to the inlet system are currently being carried out. Further measurements will then be made using particles of more accurately known sizes.

REFERENCES

1. R.F. Wuerker, H. Shelton and R.V. Langmuir, Journal of Applied Physics Vol. 30, 342 (1959)

2. B.R.F. Kendall, D.S. Weyandt and M.F. Vollero, Proceedings of the 1991 CRDEC Scientific Conference on Obscuration and Aerosol Research.

3. E.E. Allison, B.R.F. Kendall, B.V. Bronk, and D.S. Weyandt, Prodeedings of the 1992 CRDC Scientific Conference on Obscuration and Aerosol Research.

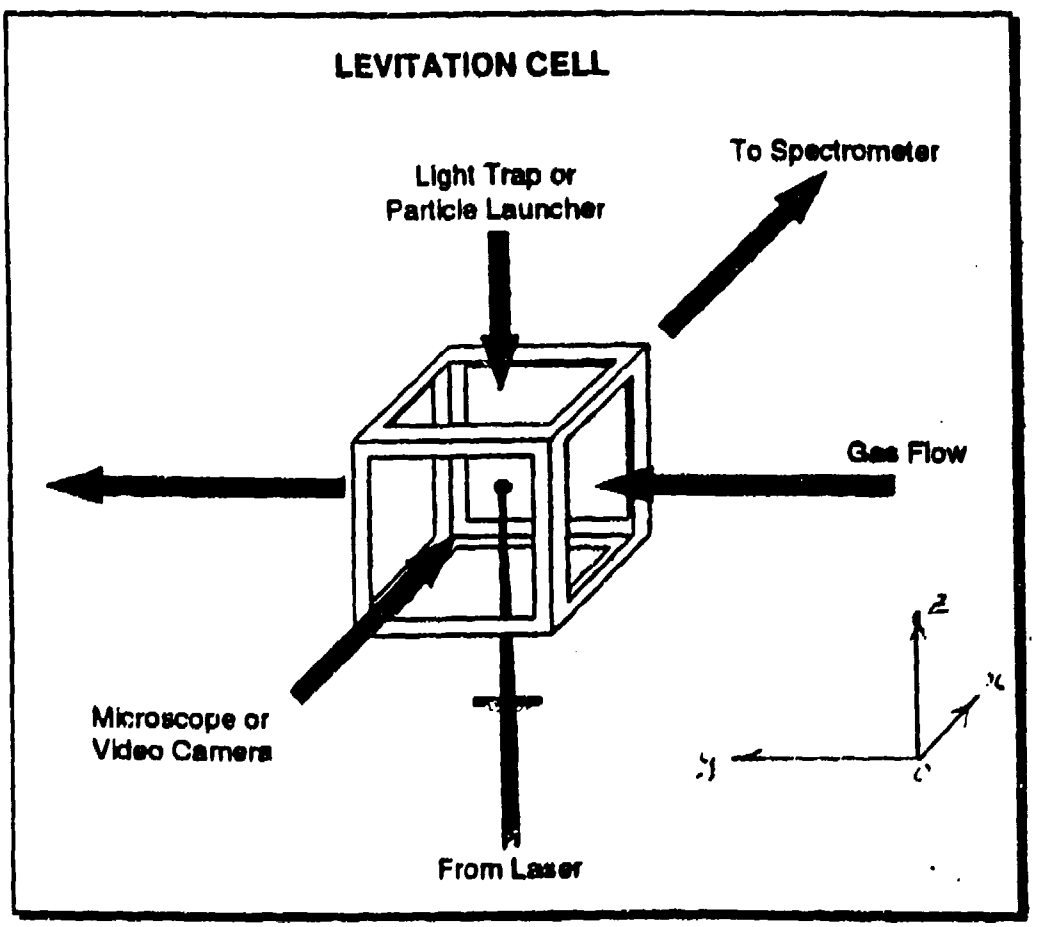

Figure 1. Two-phase cell and co-ordinate axes.

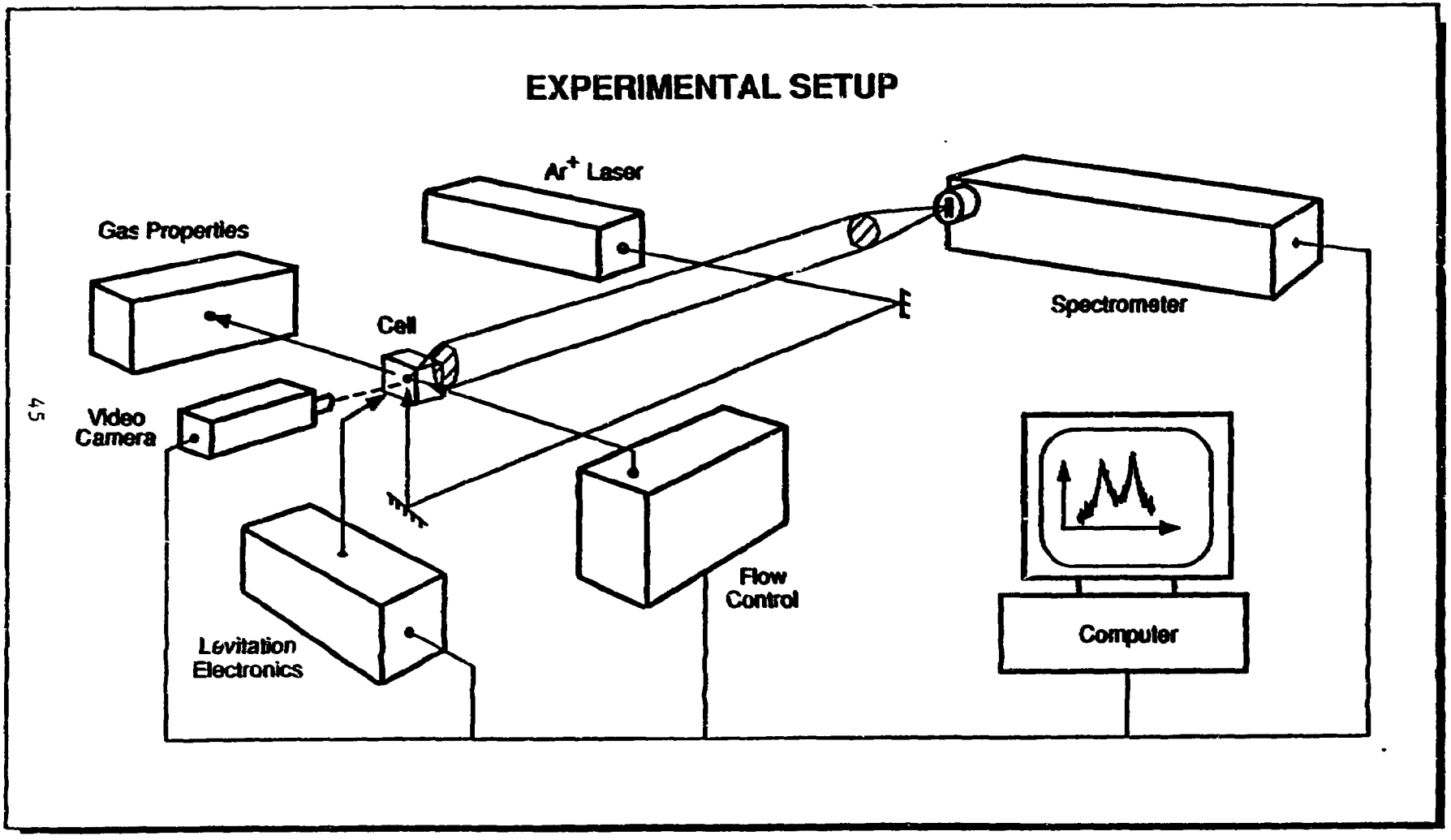

Figure 2. Apparatus for aerosol studies.

Blank

Modeling and Measurement of the Effective Drag Coefficient in Decelerating and Non-Accelerating Turbulent Gas-Solids Dilute Phase Flow of Large Particles in a Vertical Transport Pipe

by

H. Littman and M. H. Morgan, III
Department of Chemical Engineering
Rensselaer Polytechnic Institute
Troy, N.Y. 12180-3590

Abstract

The one-dimensional modeling of decelerating and non-accelerating turbulent dilute phase flow has been studied by transporting 1 mm glass spheres with air in a 28.45 mm grounded stainless steel pipe. The two-fluid model used to analyze the data employs the continuity and individual phase momentum balances from the model of Nakamura and Capes (1). Slip Reynolds numbers for the particles ranged from 471 to 986 and the pipe Reynolds number was of the order of 20000. The loading ratio varied from 5.6 to 17.1.

Evidence is presented to support the existence of a particle free region near the wall making it possible to neglect particle-wall friction effects in the modeling. Fluid-wall friction effects were then modeled assuming turbulent flow in a pipe without particles

The non-acceleration drag coefficient, C_{dn}, correlates as $9.56 \times 10^4/Re_p^{1.96}$ or $\frac{4}{3}\frac{\varepsilon\, Ar}{Re_p^2}$. It decreases from values essentially the same as those on the standard drag curve to values significantly below that curve. C_{dn} is 0.13 when Re_p equals 986, a result attributed to freestream turbulence.

The slip velocity decreases with distance from the pipe inlet so that relative to the gas phase the particle phase is decelerating. The deceleration drag coefficient was correlated by the equation

$$C_{dd} = \{C_{dn} + (4/3)K\, \varepsilon_{NA}[(\rho_p/\rho_f)-1][d_p(-dU_R/dt)/U_R^2]\}[(1-\varepsilon_{NA})/(1-\varepsilon)]$$

where $K = 1.021 - 0.0188\,(\rho_p c_2/\rho_f c_1)$.

The effect of electrostatic forces on the drag coefficient and particle-wall friction factor are also discussed. Full text of paper will appear shortly in the Journal *Powder Technology.*

Reference

1. Nakamura, K. and C.E. Capes, "Vertical Pneumatic Conveying: A Theoretical Study of Uniform and Annular Particle Flow Models," Can. J. Chem. Eng. (1973) 51, 39-46.

Nomenclature

Ar	Archimedes number $= \dfrac{d_p^3 \rho_f (\rho_p - \rho_f) g}{\mu^2}$
c_1	Superficial gas phase velocity, $\dfrac{G_f}{\rho_f}$, m/s
c_2	Superficial particle phase velocity, $\dfrac{G_p}{\rho_p}$, m/s
C_{dd}	Effective particle drag coefficient in decelerating flow
C_{dn}	Effective particle drag coefficient in non-accelerating flow
d_p	Particle diameter, m
G_f	Mass flux of fluid phase, kg/m^2s
G_p	Mass flux of particle phase, kg/m^2s
Re_p	Slip Reynolds number $= d_p U_R/\upsilon$
t	time
U_R	Slip velocity, (u-v), m/s

Greek Symbols

$\varepsilon'(\zeta)$	$= d\varepsilon/d\zeta$
ρ_f	Fluid density, kg/m^3
ρ_p	Particle density, kg/m^3

Subscripts

d	Decelerating
NA	non-accelerating

A NEW HYBRID METHOD TO SOLVE THE MAXWELL EQUATIONS FOR ABSC..PTION AND SCATTERING OF ELECTROMAGNETIC RADIATION BY A DIELECTRIC PARTICLE

Moon Kyu Choi and J. R. Brock
Chemical Engineering Department
University of Texas, Austin, Texas 78712-1062

RECENT PUBLICATIONS, SUBMITTALS FOR PUBLICATION AND PRESENTATIONS

"A theoretical investigation of low pressure particle impaction in a highly underexpanded sonic impinging slit jet", J. Aerosol Sci. 24, 31-44, (1993) (with P. S. Chang and I. Trachtenberg)

""Formation of nanoparticles by laser ablation of aerosol particles",Appl. Phys.Lett. .submitted(1993) (with C-B Juang, H. Kai,. M. F. Becker, J. Keto)

"Particle formation by homogeneous nucleation in rapidly expanding flows" *Proceedings of the 1990 CRDEC Scientific Conference on Obscuration and Aerosol Research*, CRDEC, U. S. Army, 1991 (with B. J. Jurcik).

"Particle formation by binary homogeneous nucleation in supersonic flows" *Proceedings of the 1991 CRDEC Scientific Conference on Obscuration and Aerosol Research*, CRDEC, U. S. Army, 1992 (with B. J. Jurcik).

"Formation of graphite and diamond fibers in corona discharges" *Proceedings of the 1991 CRDEC Scientific Conference on Obscuration and Aerosol Research*, CRDEC, U. S. Army, 1992.

"Laser-assisted liquid film etching",Appl. Phys. Lett.,62 3345(1993).(with P. Lim and I. Trachtenberg)

"Finite element solution of the Maxwell equations for absorption and scattering of electromagnetic radiation ny a coated dielectric particle", Appl. Opt. (1993). (with Choi and Liebman).

"Numerical simulation of particle formation and growth in rapidly expanding axisymmetric flows", J. Phys. Chem. 97,323-331 (1993) (with B. J. Jurcik)

"Feasibility of finite element solution of the Maxwell equations for absorption and scattering of electromagnetic radiation by a dielectric particle", J. Comput. Physics, submitted, 1993 (with Choi and Liebman).

"A hybrid method to solve the Maxwell equaations for absorption and scattering of electromagnetic radiation by a dielectric particle", submitted for publication,1993. (with M-K Choi).

"Finite element solution of the Maxwell equations for absorption and scattering of electromagnetic radiation by dielectric particles", SPIE Meeting, Los Angeles, CA, April 1993.

ABSTRACT

The problem of scattering and absorption of electromagnetic radiation by particles can be solved analytically for only the simplest cases, but established numerical methods allow a straightforward extension to particles with arbitrary inhomogeneities, shapes, and nonlinear response. The finite element technique recently suggested by L. A. Liebman, M. K. Choi and J. R. Brock [1] had a difficulty in that the boundary condition at infinity needed to be employed at an arbitrarily determined and finite maximum boundary of domain. This difficulty can be removed by applying the boundary element method outside the particle. In this paper, a hybrid method is presented that combines the finite element method applied inside the particle and the boundary element method outside the particle and is applied to the problem of a dielectric sphere of arbitrary size parameter. Numerical results showing good agreement with analytical solutions for size parameters of 2.97 to 21 and light wavelength of 10.591 μm, are given. Results obtained suggest that the hybrid method has promise for analytically intractable scattering/absorption problems and show that the Debye amplitude formulation of the problem offers advantages in a numerical scheme. We plan to extend this method to anisotropic particles of various shapes as well as to nonlinear problems.

I. INTRODUCTION

Mie theory exactly describes the absorption and scattering of a plane electromagnetic wave by an isotropic, dielectric sphere of arbitrary size and refractive index [2]. This conceptually simple analytical solution is well known, but it involves cumbersome computations. However, many problems of interest do not readily admit analytical calculation. If a systematic numerical rather than an analytical approach is taken, its extension to particles with arbitrary inhomogeneities, arbitrary shapes, and nonlinear response is apparent since the general governing equations and the solution technique are preserved.

For comparable electromagnetic wave scattering problems in radio and microwave engineering, differential methods have been used predominantly [3]. Finite difference methods and finite element methods are typical differential solution techniques, and both can be applied to the Maxwell equations in their time-domain or frequency-domain form. While these methods have been applied in various disciplines for some time [4,5,6,7,8,9,10], they have not been adapted in a straightforward way to study the absorption and scattering of light by small particles.

In the majority of past work, problems have been solved in terms of vector field variables (**E**,**H**) that are oscillatory in nature over the infinite domain of the scattering problem. The difficulty of modeling these oscillations is removed here by reformulating the problem in terms of the Debye amplitude (DA) functions, described below. Another complication in scattering problems is the treatment of the particle surface and the determination of the internal fields. This issue has been considered in previous time-domain [9] and frequency-domain [8] solution methods, although past investigations have involved perfect conductors (no internal fields).

Recently a finite element technique was devised to deal with the present problem by L.A. Liebman **et al** [1]. Because the boundary condition at infinity had to be used at an arbitrarily chosen finite boundary, the finite element method as applied entailed an inherent error at this maximum boundary of domain. A sufficiently large computational domain may not be feasible because of limitations in available computer memory. The larger the particle size, the larger the computational domain should be since the larger region outside the particle is influenced by scattering. Moreover the smaller the wavelength of light, the more oscillatory the light wave, and denser meshes are required. Consequently, the finite element method was employed to yield correct solutions for small size parameters. A new idea is to introduce the boundary element method outside the particle to remove the boundary condition at infinity. Although one can apply the boundary element method inside the particle, also, for a linear problem, we retain the finite element method inside the particle with a view to extending the present investigation to a nonlinear problem. This combination of the finite element method and the boundary element method, termed the hybrid method, has several advantages over the conventional finite element technique. First of all, the hybrid method enables the removal of the boundary condition at infinity. Secondly, since the calculation is limited to the real boundary of the particle surface and its interior, the memory storage requirement is greatly reduced. This hybrid method has been explored recently in acoustic wave investigation [11]. Here, our new hybrid method is applied to solve electromagnetic wave propagation, followed by presentation of results of comparisons between analytical and numerical solutions.

II. FORMULATION OF SCATTERING AND ABSORPTION BY A DIELECTRIC SPHERE

In the general case, the problem consists of a particle of arbitrary (but specified) size, shape, and composition surrounded by a material that is also of arbitrary composition; a beam of light with arbitrary characteristics illuminates the particle. Given the scatterer and the incident field, the object is to determine the field in both the internal and external regions.

It is assumed that the incident field associated with the light source is that of a plane harmonic wave, and that the scatterer does not perturb the field's source. Plane waves are good approximations of incident fields in scattering problems, with an exception being a field due to a tightly focused laser beam whose local beam diameter is close to or smaller than the size of the particle it is illuminating. As waves that are not time-harmonic can be constructed by Fourier synthesis if the particle and surrounding media are linear, this assumption is not overly restrictive; for linear interactions, arbitrarily time-dependent electromagnetic fields can be obtained by a

superposition of sinusoidal steady states. The materials are assumed to be *homogeneous*, *linear*, and *isotropic* which means that their phenomenological coefficients (conductivity (σ), magnetic permeability (μ), and electric susceptibility (χ)) are independent of position, fields, and direction. The medium surrounding the particle is also infinite and nonabsorbing.

Figure 1 depicts an electromagnetic wave incident on an arbitrary particle. The incident field ($\mathbf{E}^i$, $\mathbf{H}^i$) induces a field ($\mathbf{E}^{II}$, $\mathbf{H}^{II}$) inside the particle and gives rise to a scattered field ($\mathbf{E}^s$, $\mathbf{H}^s$) in the surrounding medium. The total field in the external region ($\mathbf{E}^I$, $\mathbf{H}^I$) is obtained by superposition. The electric and magnetic vectors in both the internal and external regions must satisfy the macroscopic Maxwell equations which govern the behavior of electromagnetic fields at interior points. Taking the harmonic time dependence to be $e^{-i\omega t}$ for all fields and assuming no free charge, the Maxwell equations are reduced to a set of vector wave equations for the electric field, **E** and magnetic field, **H**,

$$\nabla^2\mathbf{E} + k^2\mathbf{E} = 0 \tag{1}$$

$$\nabla^2\mathbf{H} + k^2\mathbf{H} = 0 \tag{2}$$

where

k = wave number; $k = \omega\sqrt{\varepsilon\mu}$; ε = complex permittivity.

As the fields, **E** and **H** are only required to satisfy the Maxwell equations in regions throughout which the physical properties (characterized by ε and μ) are continuous, the fields must satisfy boundary conditions at the interface between the particle and the surrounding medium. Since ε and μ change abruptly over a region of atomic dimensions, macroscopically the boundary between homogeneous materials is a sharp discontinuity. The requirements at the boundary are obtained by considering the Maxwell equations in their integral form and applying Gauss' theorem [12,13]. Doing so gives

$$\hat{\mathbf{n}} \times (\mathbf{E}^I - \mathbf{E}^{II}) = 0 \tag{3}$$

$$\hat{\mathbf{n}} \times (\mathbf{H}^I - \mathbf{H}^{II}) = 0 \tag{4}$$

where

$\hat{\mathbf{n}}$ = unit normal to the particle/medium interface, directed outward from the particle (II) to the medium (I),

which is the condition that the tangential components of the electromagnetic fields are continuous across the boundary. Equations (3) and (4) constitute a necessary and sufficient condition to ensure energy conservation through the interface [2].

Thus, the problem to be considered is: Given a particle and $\mathbf{E}^i$, determine $\mathbf{E}^s$ and $\mathbf{E}^{II}$ so that the Maxwell equations (1) and (2) are satisfied in the particle and surrounding medium and so that the boundary conditions (3) and (4) are satisfied on the interface. The problem to be solved consists of a plane polarized wave incident on a dielectric particle; only linear scattering is considered. Assuming $\exp(-i\omega t)$ dependence for all fields, the electric and magnetic fields, **E** and **H**, must satisfy the vector wave equations both inside and outside the particle, with a requirement that the tangential components of **E** and **H** must be continuous across the surface of the particle and the Sommerfeld radiation condition requires that the scattered fields represent divergent traveling waves as $r \rightarrow \infty$.

III. SOLUTION METHOD

By introducing two auxiliary scalar functions, the electric and magnetic Debye potentials, u and v, in the usual way [14,15,16], it is possible to reduce the vector wave equations to a set of uncoupled scalar wave equations.

A. Debye amplitude functions

Since the field variables are oscillatory in nature over the infinite domain it is advantageous to reformulate the problem once again, this time in terms of a generalized amplitude function which eliminates the oscillations due to the incident field [17]; use of these Debye amplitude functions

(DAs) is desirable in a numerical approach. As demonstrated here and in the previous publication [1], we have found no important degradation in accuracy in recalculating the field observables, such as for example the source function, from the DAs. The Debye potentials are expressed in terms of the amplitude functions as

$$u = \frac{\cos\phi \sin\theta}{(k^I)^2} f_1(r,\theta) \frac{e^{ik^I r}}{r} \tag{5}$$

$$v = \left(\frac{\varepsilon}{\mu}\right)^{1/2} \frac{\sin\phi \sin\theta}{(k^I)^2} f_2(r,\theta) \frac{e^{ik^I r}}{r}. \tag{6}$$

where the superscript "I" denotes the exterior region and the superscript "II" will denote the interior region and $k^2 = \omega^2\varepsilon\mu$. The newly introduced function, $f_i\ (r,\theta)$ is the DA. It should be noted that the formulation of Eqs. (5) and (6) inherently restricts one to the consideration of only axisymmetric problems. For asymmetric cases the ϕ dependence of the Debye potentials cannot be factored out explicitly and one must solve for $f_i\ (r,\theta,\phi)$.

By substituting Eqs. (5) and (6) into their respective scalar wave equation, it can be shown that the interior problem to be solved is

$$-\nabla^2 (f_1 e^{ik^I r}) - \frac{2\cot\theta}{r^2} e^{ik^I r} \frac{\partial f_1}{\partial\theta} + \frac{2}{r} e^{ik^I r}\left(\frac{\partial f_1}{\partial r} + ik^I f_1\right) - e^{ik^I r} f_1 \left(k^2 - \frac{2}{r^2}\right) = 0 \tag{7}$$

$$\left(\frac{\varepsilon}{\mu}\right)^{1/2}\left(-\nabla^2 (f_2 e^{ik^I r}) - \frac{2\cot\theta}{r^2} e^{ik^I r} \frac{\partial f_2}{\partial\theta} + \frac{2}{r} e^{ik^I r}\left(\frac{\partial f_2}{\partial r} + ik^I f_2\right) - e^{ik^I r} f_2 \left(k^2 - \frac{2}{r^2}\right)\right) = 0 \tag{8}$$

where the inclusion of the (ε/μ) factor and the retention of the exponential factors is arbitrarily done for convenience in applying the boundary conditions. The boundary conditions are, in terms of the Debye potentials:

$$i\,\omega\,\varepsilon^I (ru^I)_{r=a} = i\,\omega\,\varepsilon^{II} (ru^{II})_{r=a} \tag{9}$$

$$\frac{\partial}{\partial r}(ru^I)_{r=a} = \frac{\partial}{\partial r}(ru^{II})_{r=a} \tag{10}$$

$$i\,\omega\,\mu^I (rv^I)_{r=a} = i\,\omega\,\mu^{II} (rv^{II})_{r=a} \tag{11}$$

$$\frac{\partial}{\partial r}(rv^I)_{r=a} = \frac{\partial}{\partial r}(rv^{II})_{r=a} \tag{12}$$

Equations (9) through (12) are formulated for a spherical particle, with radius "a". For the general nonspherical problem, Eqs. (9) - (12) must be satisfied at all (x,y) on the particle surface and the partial derivatives are given by $\nabla f \cdot \mathbf{n}$.

B. Finite element approximation

Using Galerkin's method [18] for constructing the finite element approximation, the

solutions to (7) and (8) are sought over a grid as in Fig. 2 having N_n nodes. The Debye amplitude functions, f_1 and f_2 are of the form

$$f(r,\theta) = \sum_{j=1}^{N_n} f_j \Phi_j(r,\theta) \tag{13}$$

and the weight functions are given by

$$v(r,\theta) = \sum_{j=1}^{N_n} v_j \Phi_j(r,\theta) \tag{14}$$

where

$f(r,\theta)$ = either f_1 or f_2

f_j = either $f_1(r_j,\theta_j)$ or $f_2(r_j,\theta_j)$, appropriately

N_n = number of nodes in the finite element grid

$v(r,\theta)$ = either v_1 or v_2

v_j = either $v_1(r_j,\theta_j)$ or $v_2(r_j,\theta_j)$, appropriately

$\Phi_j(r,\theta)$ = global basis functions.

Substituting (13) and (14) into the weak form of (7) or (8) gives a system of linear algebraic equations that can be represented by

$$\sum_{j=1}^{N_n} K_{ij} f_j = F_i, \qquad i = 1, 2, \ldots, N_n \tag{15}$$

where K_{ij} represents a component of the $N_n \times N_n$ *stiffness matrix* **K** and F_i represents an element of the $N_n \times 1$ *load vector* **F**.

In this study the finite elements are nine-node Lagrange quadrilaterals [19] and the elemental area integrations are calculated using Gaussian quadrature of order 3×3. The line integrals along elemental boundaries are determined using second-order Gauss quadrature.

C. Boundary Element Method

Theoretically the original domain of this problem is infinite. As the radial distance, r, approaches infinity, the Sommerfeld radiation condition [13] applies:

$$\lim_{r\to\infty} r\left(\frac{\partial u^I}{\partial r} - ik u^I\right) = 0 \tag{16a}$$

$$\lim_{r\to\infty} r\left(\frac{\partial v^I}{\partial r} - ik v^I\right) = 0. \tag{16b}$$

By using Green's second identity the scalar wave equations outside the particle and the above radiation condition can be transformed to a pair of surface integral equations [20],

$$-2\pi u^I_k = \int\left(-u^I \frac{\partial g}{\partial n} + g \frac{\partial u^I}{\partial n}\right) dS - 4\pi u^{(i)} \tag{17a}$$

$$-2\pi v^I_k = \int\left(-v^I \frac{\partial g}{\partial n} + g \frac{\partial v^I}{\partial n}\right) dS - 4\pi v^{(i)}, \tag{17b}$$

where g is the Green's function for the Helmholtz equation, expressed by

$$g = \frac{\exp(i\, k^I\, |x-x_k|)}{|x-x_k|} \tag{18}$$

with the position vector **x** and the outward normal **n** on the particle surface. The subscript, k signifies the position of point force for the Green's function, and the superscript, (i) represents the incident light. The Debye potentials of incident light are expressed [17] as

$$u^{(i)} = \frac{\cos\phi}{(k^I)^2\, r} W \tag{19a}$$

$$v^{(i)} = \frac{\sin\phi}{(k^I)^2\, r} W \tag{19b}$$

where

$$W(r,\theta) = \frac{\exp(ik^I r \cos\theta)}{\sin\theta} - \cot\left(\frac{\theta}{2}\right)\frac{\exp(ik^I r)}{2} - \tan\left(\frac{\theta}{2}\right)\frac{\exp(-ik^I r)}{2}. \tag{20}$$

Since there is an integrable singularity at the point force of Green's function, one may have difficulty evaluating Eqs. (17) numerically. It is noted, however, that the Green's function for the Helmholtz equation can be divided into two parts, one for the Laplace equation and the other for the remainder [21].

$$g = \frac{\exp(\, i\, k^I\, |x-x_k|) - 1}{|x-x_k|} + \frac{1}{|x-x_k|}\,. \tag{21}$$

The first portion is nonsingular and may be integrated in the ϕ direction using standard Gaussian quardrature. The second is the Green's function for the Laplace equation. For an axisymmetric Laplace equation the surface integrals involving integrable singularities can be easily treated analytically around the point force in terms of elliptic integrals of the first and second kind [22]. Equations (17) can be evaluated numerically for a body of revolution by linearly discretizing the surface in the spherical coordinate system. Since, for validation purposes, only a spherical shape is treated here, the surface is exactly expressed by linear elements. With two nodes used on each element in the direction of the spherical angle, θ, the Debye potentials, u^I and v^I and their derivatives are also approximated linearly.

Only the interior fields are discussed here; however, in principle scattered fields can be easily calculated at a specific position of the exterior region by the following equations:

$$-4\pi\, u^I_k = \int\left(-u^I \frac{\partial g}{\partial n} + g\, \frac{\partial u^I}{\partial n}\right) dS \;-\; 4\pi\, u^{(i)} \tag{22a}$$

$$-4\pi\, v^I_k = \int\left(-v^I \frac{\partial g}{\partial n} + g\, \frac{\partial v^I}{\partial n}\right) dS \;-\; 4\pi\, v^{(i)}\,, \tag{22b}$$

where the singular point x_k for the Green's function, g, lies at the scattering measure position of the exterior region. Once the Debye potentials, u^I and v^I, are calculated on the particle surface by Eqs. (17), one can obtain u^I_k and v^I_k by using them in the surface integrals of Eqs. (22).

D. Lagrange multiplier approach

Some algebraic manipulation of the discretized boundary element formulation and the two

surface boundary conditions yields a new boundary condition on the particle surface in terms of the interior Debye potential amplitude functions. Thus one more equation is made than the number of variables since the FEM formulation inside the particle already gives the same number of equations as that of unknowns. To allow for this characteristic, a Lagrange multiplier approach [18] is taken, adding additional *interface constraint elements* . Since one multiplier, λ is added for each of the surface points, satisfying the additional boundary constraint comes at the cost of increasing both the number of unknowns and the number of linear constraint equations.

The system of equations in (15) must be modified to include the boundary constraint equations, which have the form

$$\mathbf{C}f = \mathbf{p} \tag{23}$$

where

$\mathbf{C}$ = $N_b \times N_n$ constraint matrix made as a new surface boundary condition

f = $N_n \times 1$ vector containing the unknowns f_j

$\mathbf{p}$ = $N_b \times 1$ vector containing $\mathbf{W}$

The problem is now described by

$$\begin{bmatrix} \mathbf{K} & \mathbf{C}^T \\ \mathbf{C} & \mathbf{0} \end{bmatrix} \begin{bmatrix} f \\ \lambda \end{bmatrix} = \begin{bmatrix} \mathbf{F} \\ \mathbf{p} \end{bmatrix} \tag{24}$$

where

λ = $N_b \times 1$ vector containing the multipliers, λ_i

$\mathbf{C}^T$ = the transpose of $\mathbf{C}$.

E. Matrix solution

As all finite element computations presented in this investigation were performed on a Cray Y-MP8/864, the subroutine HCGBLE, part of the Boeing Computer Services mathematical library [23] was used to solve Eq. (24) for f_1 and f_2. The subroutine HCGBLE performs Gaussian elimination with partial pivoting to compute the LU factorization of the first matrix in Eq. (24), which is a general banded matrix having elements that are complex.

F. Calculation of source function

Once one calculates the Debye amplitude functions, f_1 and f_2, the Debye potentials, u and v may be obtained by Eqs. (5) and (6). Then the electric field, $\mathbf{E}$, represented by [14]

$$\mathbf{E} = \nabla \times \left[\nabla (ru) \times \hat{\mathbf{r}} \right] + i\omega\mu \nabla \times \left(rv\hat{\mathbf{r}} \right), \tag{25}$$

can be calculated at every point in the domain by approximating the differentiation by central difference. Since the absorption of radiation by dielectric particles is of particular interest here, the source function, defined by $|\mathbf{E}|^2$, should be investigated.

IV. RESULTS AND DISCUSSIONS

For validation of the computational techniques, initial investigations have been performed for a linearly polarized plane harmonic wave incident on a spherical particle, by varying the size parameter, $x = 2\pi a/\lambda$, and the refractive index of the particle. The particle was isolated and surrounded by air, assumed to have a refractive index of 1.0. The size parameters studied ranged from 2.97 to 21, which covered various situations including three different water droplets and an unspecified aerosol particle, and 10.6 μm for the wavelength of light. The input parameters for four different cases are summarized in Table I.

Comparisons between analytical and numerical solutions are presented for the four different examples in Figs. 3-8. The results for the first three cases were obtained using a 20x60 uniform mesh and required ~546 seconds of Cray YMP CPU time (including output time for results, with a code that has not been fully vectorized) to determine f_1, f_2, the source function, and the error measure called L^2-norm (defined later) over the entire computational domain. The last example for

a 35 μ water drop required a 40x60 mesh and 422 seconds of CPU time. The figures show the source functions obtained numerically and those from the Mie solution along the z-axis which is coincident with the direction of propagation of the light. The particle is centered at the origin which is at the center of the plot, and the z-axis shows distances in micrometers. By comparing the solid line of the Mie solution and the numerical points, excellent agreement between the two solutions can be noted.

It is not necessary to rely on subjective impressions of agreement between exact and numerical solutions; a quantitative measure of the error of the numerical solution over its domain is given by the L^2-norm, which is defined for complex functions as

$$L^2 = \left[\int_{\Omega} (e\, e^*)\, dA\right]^{1/2} \tag{26}$$

where e is the difference between the analytical (exact) and the numerical solution and e^* is the complex conjugate of e. The better the numerical approximation, the closer L^2-norm is to zero. The L^2-norms for the source functions are 2.42×10^{-5}, 1.086×10^{-4}, 1.59×10^{-5}, and 3.00×10^{-4}, respectively for the four different examples. The corresponding values for the L^2 -norm obtained by FEM only were 2.907×10^{-4}, 7.417×10^{-4}, 1.89×10^{-4}, and 8.527×10^{-3}. A dramatic reduction of L^2 -norms is therefore obtained by switching to the hybrid method from FEM.These results are summarized in Table 1 below.

TABLE 1

Example	Particle material	Refractive index of particle	Wavelength of light	Size parameter, x	L^2 -norm of source function
I (Fig. 3)	water	1.179 + i 0.071	10.6 μm	2.97	2.42×10^{-4}
IV (Fig. 4)	arbitrary	1.87 + i 0.15	10.6 μm	5.93	1.09×10^{-4}
V (Fig. 5)	ice	1.097 + i 0.134	10.6 μm	2.97	1.59×10^{-5}
II(Fig. 6)	water	1.179 + i 0.071	10.6 μm	21	3.00×10^{-4}

V. CONCLUSIONS

For the hybrid method, it is demonstrated that the computation times are not prohibitive and that the relationship between CPU time and size parameter, x is favorable. Additionally, the L^2-norms do not increase excessively with increasing x, demonstrating, for examples studied so far, that the accuracy of the solutions, with sufficient mesh refinement, need not degrade with increasing size parameter. These findings support the idea that much larger spherical particles as well as more complex scatterers can be studied without modifying the underlying solution technique presented here.

ACKNOWLEDGMENTS

This work was supported by RDEC, U.S. Army. We thank Dr. Dave Pendleton for the use of his Mie code for the analytical solutions employed here for comparison, and Dr. O. I. Sindoni for helpful discussions.

REFERENCES

1. L. A. Liebman, M. K. Choi, and J. R. Brock, On Feasibility of Finite Element Solution of the Maxwell Equations for Absorption and Scattering of Electromagnetic Radiation by a Dielectric Particle, *J. Comput. Phys.*, submitted.
2. C. F. Bohren and D. R. Huffman, *Absorption and Scattering of Light by Small Particles* (Wiley, New York, 1983).
3. R. H. T. Bates, Analytical constraints on electromagnetic field computations, *IEEE Trans.*

Microwave Theory Tech. **MTT-23**, 605-623 (1975).

4. A. Taflove, Review of the formulation and applications of the finite difference time-domain method for numerical modeling of electromagnetic wave interactions with arbitrary structures, *Wave Motion* **10**, 547-582 (1988).
5. A. Taflove, Numerical solution of steady-state electromagnetic scattering problems using time dependent Maxwell's equations, *IEEE Trans. Microwave Theory Tech.* **MTT-23**, 623-630 (1975).
6. A. Taflove and K. R. Umashankar, Review of FD-TD numerical modeling of electromagnetic wave scattering and radar cross section *Proc. IEEE* **77**, 682-699 (1989).
7. K. R. Umashankar and A. Taflove, A novel method to analyze electromagnetic scattering of complex objects, *IEEE Trans. Electromagn. Compat.* **EMC-24**, 397-405 (1982).
8. D. R. Lynch, K. D. Paulsen and J. W. Strohbehn, Finite element solution of Maxwell's equations for hyperthermia treatment planning, *J. Comput. Phys.* **58**, 246-269 (1985).
9. D. R. Lynch and K. D. Paulsen, Time-domain integration of the Maxwell equations on finite elements, *IEEE Trans. Antennas Propagat.* **38**, 1931-1942 (1990).
10. W. Kerner, A. Jakoby and K. Lerbinger, Finite-element semi-discretization of linearized compressible and resistive MHD, *J. Comput. Phys.* **66**, 332-355 (1986).
11. I-Tai Lu and H. K. Jung, A hybrid (boundary elements)-(finite elements)-ray-mode method for wave scattering by inhomogeneous scatterers in a waveguide, *J. Acoust. Soc. Am.*. **87** (3), 988-996 (1990).
12. J. D. Jackson, *Classical Electrodynamics* , 2nd ed. (Wiley, New York, 1975).
13. J. A. Stratton, *Electromagnetic Theory* (McGraw-Hill, New York, 1941).
14. M. Born, and E. Wolf, *Principles of Optics* (Pergamon, London, 1959).
15. M. Kerker, *The Scattering of Light and Other Electromagnetic Radiation* (Academic Press, New York, 1969).
16. F. Borghese, P. Denti, G. Toscano, and O. I. Sindoni, Electromagnetic scattering by a cluster of spheres, *Appl. Opt.* **18**, 116-120 (1979).
17. R. T. Ling, Application of computational fluid dynamics methods to a numerical study of electromagnetic wave scattering phenomena, *J. Appl. Phys.*, **64**, 3785 (1988).
18. E. B. Becker, G. F. Carey, and J. T. Oden, *Finite Elements: An Introduction (Vol. 1)* (Prentice-Hall, Englewood Cliffs, New Jersey, 1981).
19. G. F. Carey, and J. T. Oden, *Finite Elements: Computational Aspects (Vol. III)* (Prentice-Hall, Englewood Cliffs, New Jersey, 1984).
20. Y.-H. Pao and C.-C. Mow, *Diffraction of Elastic Waves and Dynamic Stress Concentrations* (The Rand Corporation, New York, New York, 1973).
21. A. F. Seybert, B. Soenarko, F. J. Rizzo and D. J. Shippy, A Special Integral Equation Formulation for Acoustic Radiation and Scattering for Axisymmetric Bodies and Boundary Conditions, *J. Acoust. Soc. Am.* **80** (4), 1241-1247 (1986).
22. J. L. Hess, Calculation of Potential Flow About Bodies of Revolution Having Axes Perpendicular to the Free-Stream Direction, *J. Aerospace Sci.* **29**, 726-742 (1962).
23. BCSLIB, *BCSLIB Mathematical/Statistical Library. Advanced Subprograms in Release 12*, Boeing Computer Services, Pub. No. 20462-0516 (1989).

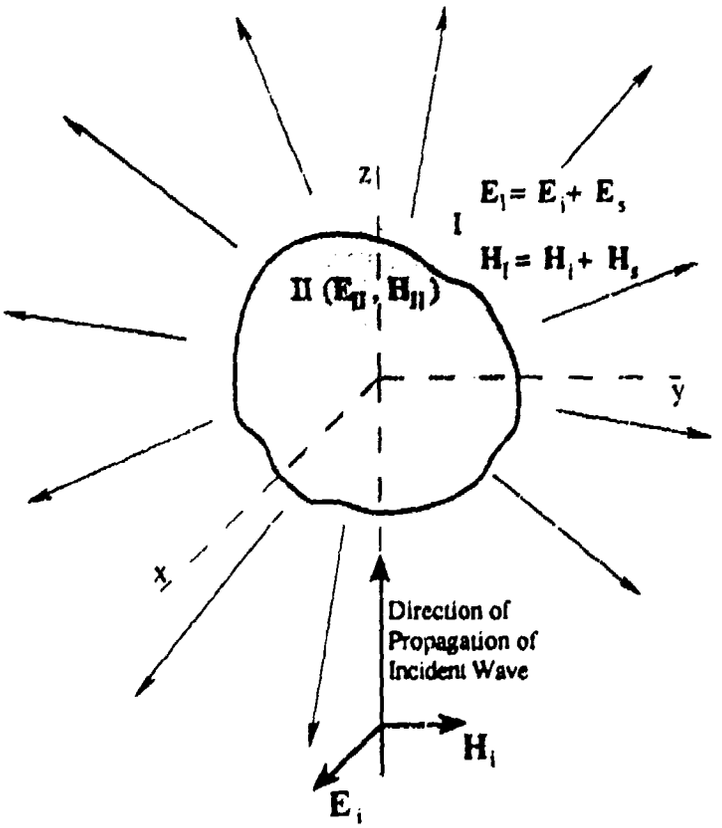

Fig. 1. Absorption and scattering by an arbitrary particle.

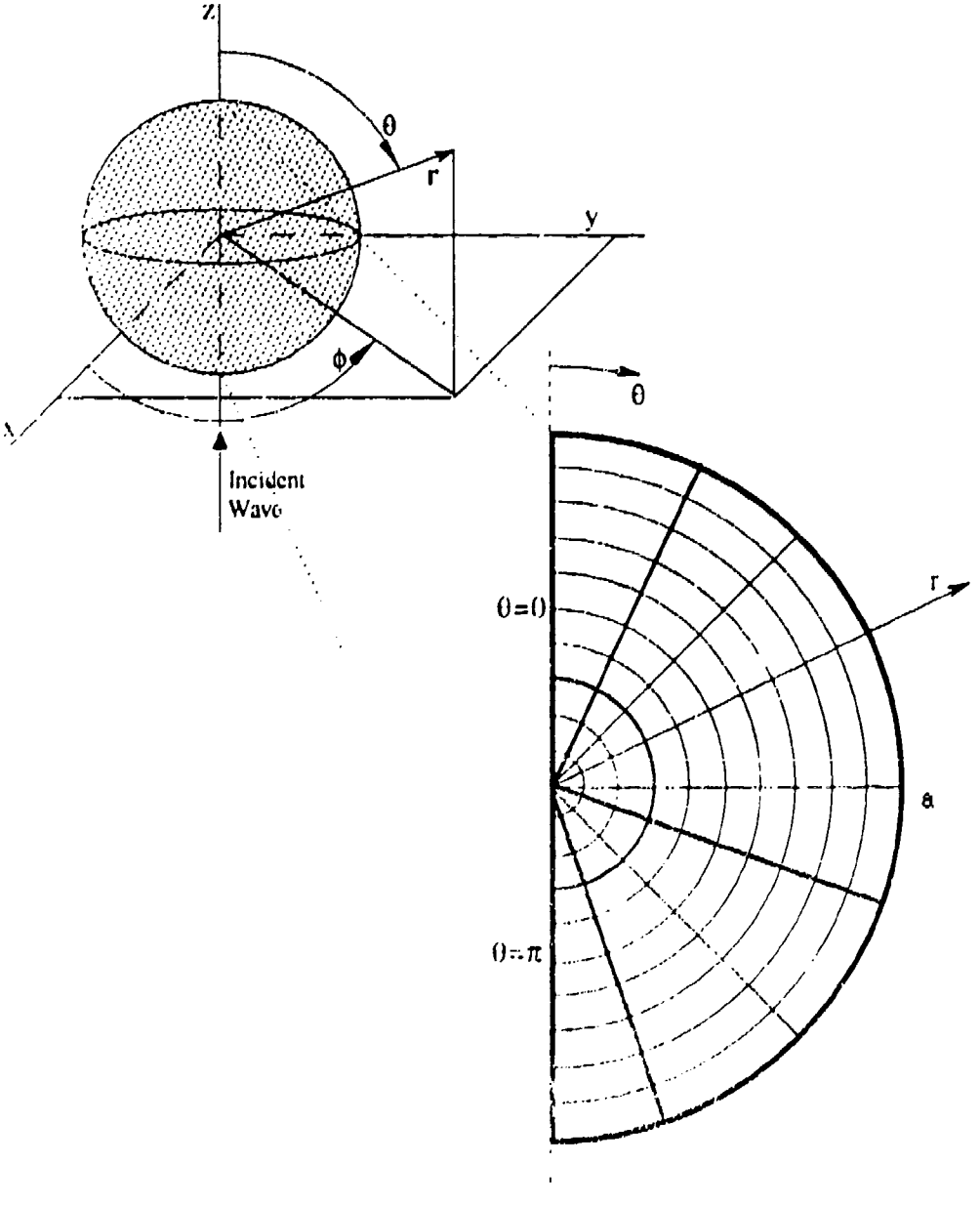

Fig. 2. Typical domain and grid for finite element computations..

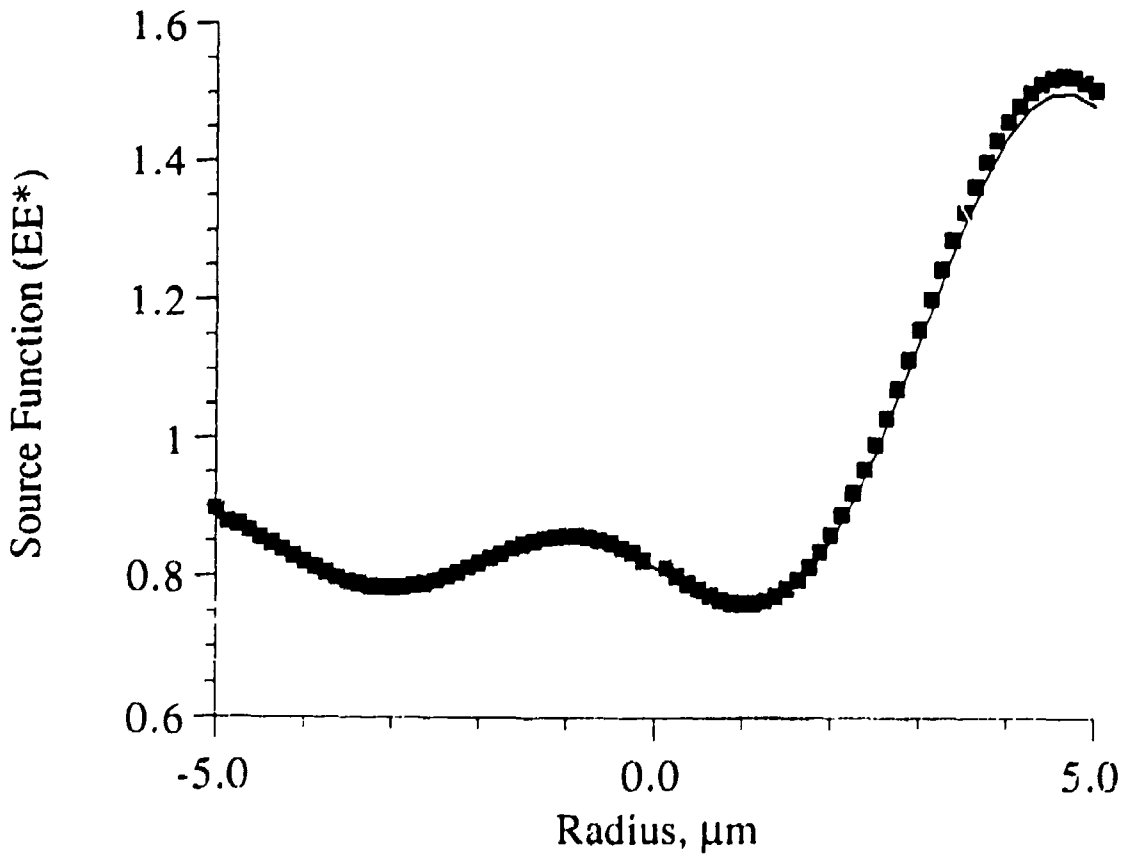

Fig. 3. Source functions calculated along the z-axis from numerical (points) and Mie (solid line) solutions for Debye amplitude functions for a water droplet of diameter 10 μm surrounded by air, illuminated by a 10.6 μm polarized plane wave (example I in Table I).

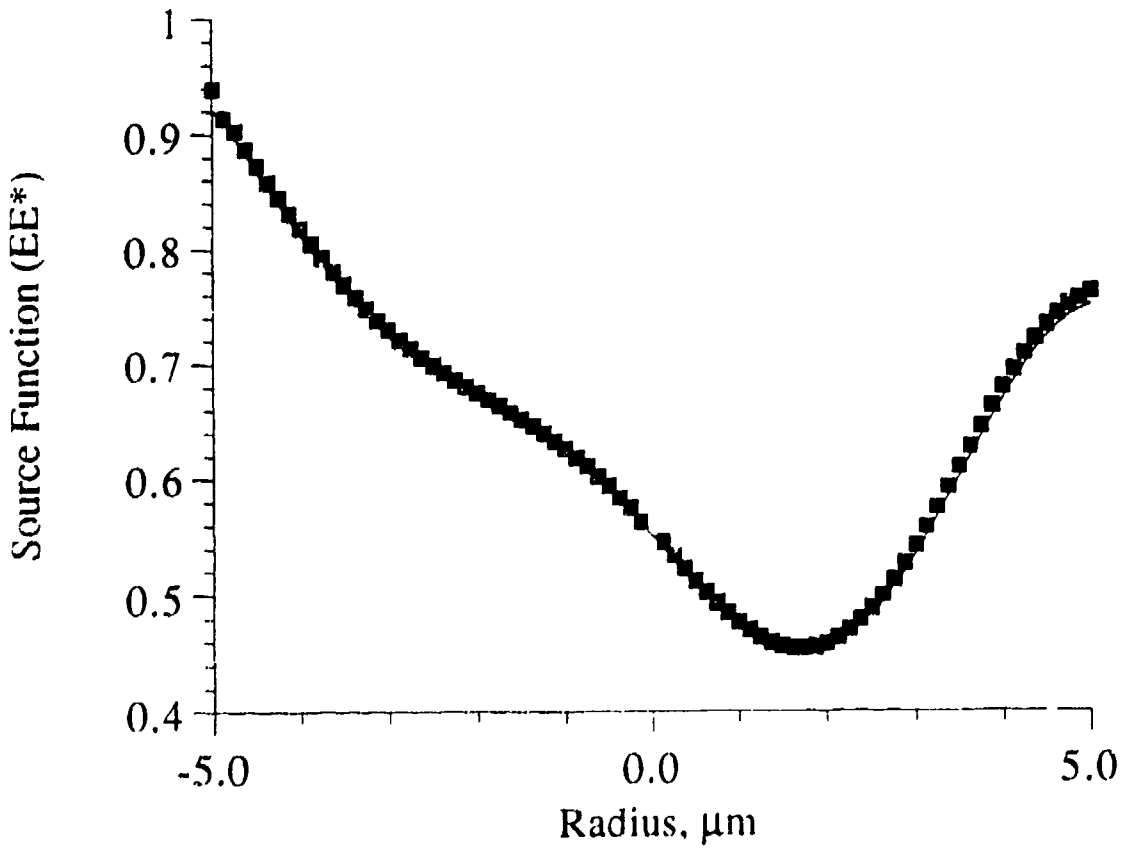

Fig. 4. Source functions calculated along the z-axis from numerical (points) and Mie (solid line) solutions for Debye amplitude functions for an unspecified aerosol particle of diameter 20 μm surrounded by air, illuminated by a 10.6 μm polarized plane wave (example II in Table I).

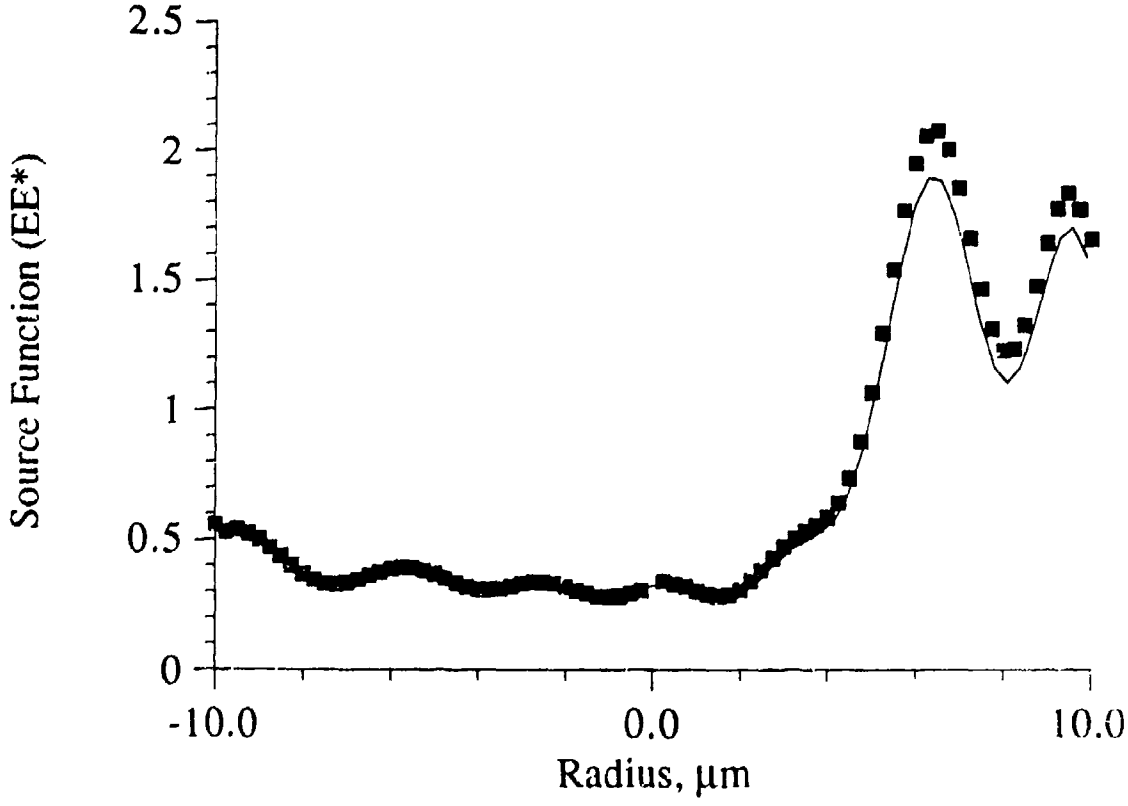

Fig. 5. Source functions calculated along the z-axis from numerical (points) and Mie (solid line) solutions for Debye amplitude functions for an ice particle of diameter 10 µm surrounded by air, illuminated by a 10.6 µm polarized plane wave (example III in Table I).

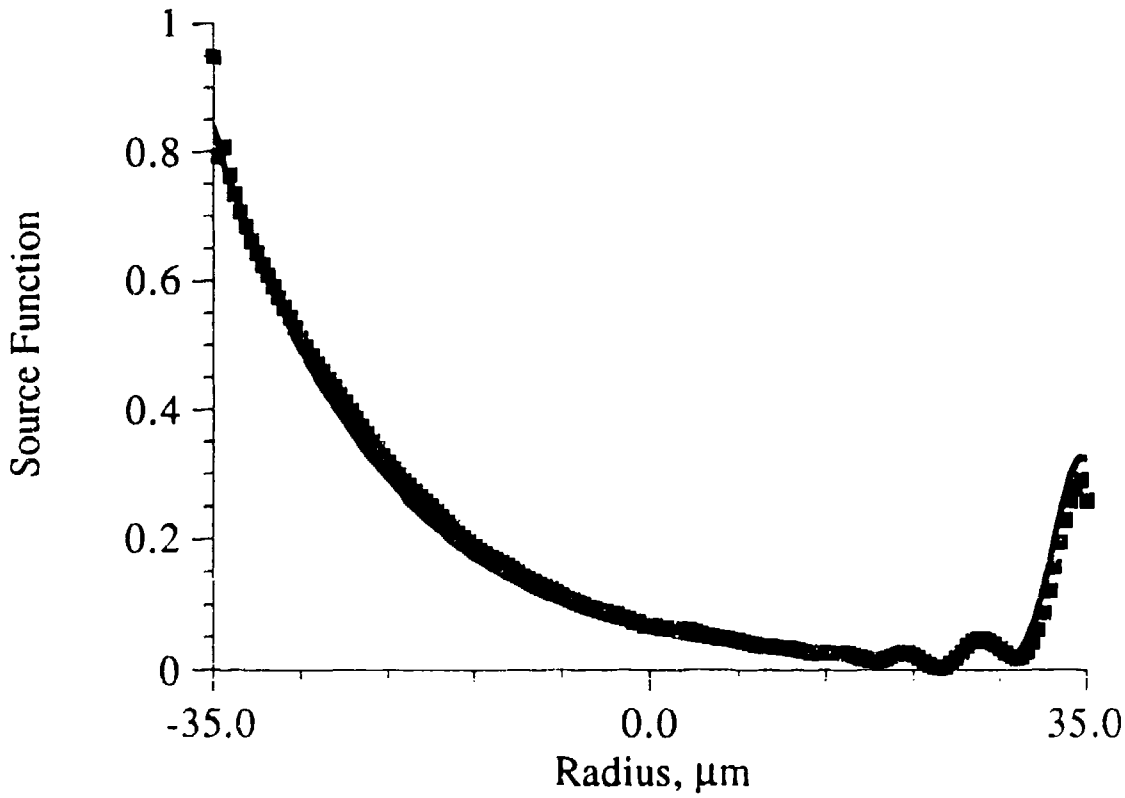

Fig. 6. Source functions calculated along the z-axis from numerical (points) and Mie (solid line) solutions for Debye amplitude functions for a water drop of diameter 70 µm surrounded by air, illuminated by a 10.591 µm polarized plane wave (example IV in Table I).

Blank

Explosive Dissemination of Obscurants for the Protection of Men and Material, Plasma Production, Intermediate Reactions, Dispersion by Wind over Nonflat Terrain, And Extinction Properties of Fiber, Spheroid, and Complex Particles in an Aerosol over the Complete Range of Interrogating Electromagnetic Radiation

D. K. Cohoon

September 21, 1993

This work has three parts. We are going analyze explosions, chemical reactions in clouds, fiber and flake fallout rates and the bouyancy of dispersed clouds of materials and the ability of this cloud of material to obscure men and material from interrogating electromagnetic radiation over the entire frequency band of detection and imaging devices.

We consider a bounded three dimensional body with full tensor bianisotropy covered with impedance sheets.

We conclude with a general surface integral equation formulation which will permit analysis of a complex of homogeneous structures whose regions of homogeneity of electromagnetic properties may be as general as the interiors of diffeomorphs of N handled spheres.

Contents

1 Explosive Dissemination and Dispersion in a Wind

2 Treating Extinction and Absorption
- 2.1 Classes of Tensor Materials
- 2.2 Integral Equations and Bianisotropy

3 Exact Finite Rank Integral Equation Methods
- 3.1 Examples of Spaces of Approximation

3.2 The Standard but Nonoptimal Discretization

4 Exact Solutions of Integral Equations
4.1 Machine Precision in Integral Equation Methods

5 Layered Materials
5.1 Magnetic Slab Integral Equation

6 Discretization of an Integral Equation
6.1 Piecewise Linear Approximation

7 Surface Integral Equation Methods
7.1 Combined Field Integral Equations

8 Potential Benefits

References

1 Explosive Dissemination and Dispersion in a Wind

We give here a modification, for an exploding grenade source, of a fairly simple model of drift of a cloud was developed of obscurants was developed by Peterson and Seinfeld ([42]) which includes a horizontal and verticle drift term and a general fall out term, a kind of simple heat-like equation with a cooling term which represents the fall out of the obscurant with mean concentration $c(x, y, z, t)$ that is given by

$$\frac{\partial c}{\partial t} + \overline{u}\frac{\partial c}{\partial x} - w_s \cdot \frac{\partial c}{\partial z} = \frac{\partial}{\partial y}\left(K_H \frac{\partial c}{\partial y}\right) \frac{\partial}{\partial z}\left(K_V \frac{\partial c}{\partial z}\right) - k \cdot c$$

where

$$\begin{aligned}
\overline{u} &= \text{the mean wind speed in the x direction} \\
w_s &= \text{the settling velocity} \\
K_H &= \text{the horizontal eddy diffusivity} \\
K_V &= \text{the vertical eddy diffusivity} \\
k &= \text{the first order rate constant for the removal of the species}
\end{aligned}$$

The exploding grenade is a point source boundary condition at x equal to zero that is given by

$$c(0, y, z, t) = \frac{Q_1}{\overline{u}} \cdot \delta(y)\delta(z - zs)\delta(t)$$

where

$$\delta \;=\; \text{the dirac delta function}$$

It makes sense that at infinite lateral distance the concentration approaches zero so that

$$\underset{y \to \infty}{LIM} \; c(x, y, z, t) \;=\; 0$$

and

$$\underset{y \to -\infty}{LIM} \; c(x, y, z, t) \;=\; 0$$

There is assumed to be an elevated inversion base $z = H_a$ which inhibits vertical turbulent mixing at which we have

$$\underset{z \to H_a}{LIM} \left(\frac{\partial c}{\partial z}\right) \;=\; 0$$

The obscurant may be removed by deposition across a layer at height $z = z_a$ through deposition with deposition velocity v_d so that

$$\underset{z \to z_a}{LIM} \left(K_V \frac{\partial c}{\partial z} + w_s c\right) \;=\; v_d c$$

While this model does not have all of the physical details, it is sensible in a sense, is easily understood, and has the advantages of

- giving an immediate sense of progress on the solution of the explosive dispersion problem,
- having an exact analytical solution that could be run over a wide range of parameters with almost no computer cost, and
- serving as an exact benchmark for general numerical codes whose accuracy might be questioned as the programming was being developed initially.

A similar equation was considered by Seigneur and Saxena ([51]) which includes reactions and is given by

$$\frac{\partial C_i}{\partial t} \;=\; \frac{\partial}{\partial y}\left(K_y \frac{\partial C_i}{\partial y}\right) \;+\; \frac{\partial}{\partial z}\left(K_z \frac{\partial C_i}{\partial z}\right) \;+$$

$$R_i(C_1, \cdots, C_N, k_1, \cdots, k_M) \;+\; T_i(C_i, n(r)) \;+\; S_i$$

where

S_i = emission rate of smoke from the grenade
C_i = ensemble and spatially averaged concentration of species i
N = the total number of species
R_i = the reaction rate of species i and
k_i = the kinetic rate constants

If we drop the reaction rate term and use S_i as a dirac delta source term for the explosion, this could be solved exactly using transforms and convolution operations.

The motion of smoke over non flat terrain could use the model of Hunt ([29]) to describe motion over a hill.

The recent powder dispersion by an explosion analysis given by Lipanov ([35]) will probably give a rigorous method of treating the problem and the solution would be benchmarked by our exact solutions.

We consider in this paper general methods for solving electromagnetic scattering problems that have promise for reducing computation time while increasing accuracy. While one of the methods involves integral equation formulations, method differs from the popular method of moment computations in that instead of guessing at the accuracy by requiring a certain sampling rate, the solution of the integral equation, using the exact finite rank integral equation methods described in this paper, is obtained to computing machine precision as it is possible to do with ordinary differential equation codes with the proper scaling of variables.

The general explosion problem and dispersion problem require solution of a free boundary value problem ([19]) involving at least the mass conservation, momentum conservation, and energy conservation equation with a relation involving pressure and temperature that includes a complete description of all chemical reactions (a reaction diffusion equation). No exact solution exists for this coupled system of partial differential equations, but some robust numerical methods have been developed by many workers ([18], [31], [39], [48])

2 Treating Extinction and Absorption

The main idea is to know how well particles in a cloud extinguish and absorb electromagnetic radiation.

The electromagnetic scattering problem is what is mathematically called a transmission problem which in this case involves solving the Faraday ([45]) and Ampere ([40]) Maxwell equations inside and outside the aerosol particle. Recently, McCartin and Dicello ([38]), Rappaport and Smith ([45]) have worked out a method of attacking the transmission problem for the Faraday and Ampere Maxwell equations that one considers numerically and directly for general anisotropic materials ([38]) and for cylinders([45]) using a FDFD (finite difference frequency domain) technique when these bodies are subjected to obliquely incident electromagnetic radiation.

The difficult problem of treating a fiber, which can be modeled reasonably as a finite length cylinder ([47]) is especially important. One method uses the Mie solution and expands the field inside the fiber in terms of vector spherical harmonics ([6]), does the same for the incoming and scattered fields outside the fiber and then tries to match the boundary conditions on the surface of the fiber by solving a large systems of linear equations, which is the extended boundary condition. There is nothing theoretically wrong with the concept, but existing computers have been unable to treat accurately the fibers which are very long in comparison with the diameter of the fiber.

There are other ways to see how which fiber length to diameter might give the cloud

with the desired properties. This can be carried out by exactly solving the problem of the scattering of electromagnetic radiation by a prolate spheroid. Some new works on this subject have been developed. Sinha and MacPhie ([54]) and Cooray ([13] and [12]) have extended the older works and have worked out details of the use of vector *spheroidal* wave functions in describing the interaction of electromagnetic radiaion; the hope is that the electromagnetic fields inside and outside the spheroid will be very accurately described with just a few terms of the series. Just as with the Mie solution the complete story of total absorbed power and total scattered power can be determined without solving a large system of linear equations.

Integral equation formulations ([53]) can be used to describe the interaction of radiation with finite cylinders (which is a reasonable way to describe an arbitarily oriented fiber), or any other shape for that matter. If one could accurately solve these integeral equations, where the a priori unknown induced electromagnetic field appears inside an integral operator, then one could use boundary conditions to get the total field just outside the body, one could subtract off the incident field and get the scattered field and by a careful integration of the Poynting vector over the surface of the finite cylinder one could, in exactly the same manner as one easily solves these problems for spheres, find the total absorbed power and the total scattered power for a fiber with an arbitrary orientation. Finite cylinders have been nicely described as bodies of revolution (Mautz ([37]) and (Glisson and Wilton [20]) which reduce this problem to that of solving a one dimensional integral equation for each of the Fourier modes of the field. This is a very sensible thing to do as it is far better to solve 1000 times, 100 equations in 100 unknowns that to solve one system involving 100,000 equations, the number of operations being roughly 1000 times 100^3 or one billion operations versus $100,000^3$ (or one quadrillion) operations, which is the reason that massively parallel computers have been suggested by Cwik, Partee, and Jean Patterson ([14]) as a method of handling these extremely difficult problems. This seems to be the best approach to treating the problem of fibers. In what follows here we will discuss the general problem and methods of carrying out efficient and highly accurate solutions of the one dimensional integral equations which we derive from the surface integral equations which are described in the following sections. This method can be used to describe coated fibers, coated flakes, coated doughnut shaped aerosol particles, and can be benchmarked easily against anyone's multilayer sphere code.

If you look at the fibers that actually make up the cloud, under a microscope, they look like finite cylinders except that in portions of their surface the coating is peeling off like a bad paint job and the hybrid finite element method by Boyse and Seidl for treating near bodies of revolution ([3]) could probably be valuable.

We develop here some new methods for formulating and solving integral equations describing the interaction of electromagnetic radiation with complex materials. Such interaction problems, for currently used methods, such as the method of moments, are beyond the capability of existing computers, because each subunit of the particle communicates radiatively with every other part which makes it impossible to use any time of small wavelength approximations. The body as a whole is electromagnetically large, while intricate subunits may be of the order of a wavelength and thereby be in the *difficult* wavelength region. You don't really know which approximating techniques are valid until you solve the original problem accurately. Thus, accurate solutions, and especially exact solutions

for specific shapes.

2.1 Classes of Tensor Materials

The most general linearly responding material is the bianisotropic material ([34], p 91) defined by the equations,

$$curl\begin{pmatrix}\vec{E}\\ \vec{H}\end{pmatrix} = i\ \omega\cdot\begin{pmatrix}0 & -1\\ 1 & 0\end{pmatrix}\cdot\left[\begin{pmatrix}\bar{\bar{\epsilon}} & \bar{\bar{\xi}}\\ \bar{\bar{\zeta}} & \bar{\bar{\mu}}\end{pmatrix}\cdot\begin{pmatrix}\vec{E}\\ \vec{H}\end{pmatrix} + \begin{pmatrix}\vec{J}\\ \vec{J}_m\end{pmatrix}\right] \tag{2.1.1}$$

(It is easy to see which interchanges leave the above system of equations invariant; this gives us a way of checking complex codes) The bianisotropic relations are embodied in the relationship ([34], p 91)

$$\begin{pmatrix}\vec{D}\\ \vec{B}\end{pmatrix} = \begin{pmatrix}\bar{\bar{\epsilon}} & \bar{\bar{\xi}}\\ \bar{\bar{\zeta}} & \bar{\bar{\mu}}\end{pmatrix}\cdot\begin{pmatrix}\vec{E}\\ \vec{H}\end{pmatrix} \tag{2.1.2}$$

The biisotropic relations ([34], p 92) are

$$\vec{D} = \epsilon\vec{E} + ((\chi - i\kappa)\sqrt{(\mu_0\cdot\epsilon_0)})\cdot\vec{H} \tag{2.1.3}$$

and

$$\vec{B} = (\chi + i\kappa)\sqrt{(\mu_0\cdot\epsilon_0)}\vec{E} + \mu\vec{H} \tag{2.1.4}$$

If in equations (2.1.3) and (2.1.4) the above two equations we set χ equal to zero, then we obtain the *Pasteur* medium.

The *gyroelectric* medium ([2], p 341) is a special case of an anisotropic medium where the permittivity tensor for a wave propagating in the direction of the z axis has the form

$$\bar{\bar{\epsilon}} = \begin{pmatrix}\epsilon_{(x,x)} & \epsilon_{(x,y)} & 0\\ \epsilon_{(y,x)} & \epsilon_{(y,y)} & 0\\ 0 & 0 & \epsilon_{(z,z)}\end{pmatrix} \tag{2.1.5}$$

A different type of material is a general type of *gyrotropic* material ([2], page 342) where the permittivity has the form,

$$\bar{\epsilon} = \begin{pmatrix}\epsilon_{(x,x)} & \epsilon & 0\\ \epsilon & \epsilon_{(y,y)} & \epsilon_{(y,z)}\\ 0 & \epsilon_{(z,y)} & \epsilon_{(z,z)}\end{pmatrix} \tag{2.1.6}$$

A third type of anisotropic material is ([2], p 344) are the *biaxial* and the *uniaxial* material where the permittivity tensors respectively have the form,

$$\bar{\bar{\epsilon}} = \begin{pmatrix}\epsilon_x & 0 & 0\\ 0 & \epsilon_y & 0\\ 0 & 0 & \epsilon_z\end{pmatrix} \tag{2.1.7}$$

and

$$\bar{\bar{\epsilon}} = \begin{pmatrix}\epsilon & 0 & 0\\ 0 & \epsilon & 0\\ 0 & 0 & \epsilon_z\end{pmatrix} \tag{2.1.8}$$

which serve to characterize the optical properties of many types of crystaline materials.

2.2 Integral Equations and Bianisotropy

Bianisotropic materials, because of their greater complexity, have greater potential for creating materials with prescribed or desired absorption, transmission, and reflection properties. Chiral properties are a special case of bianisotropic materials. With chiral materials there is a special scalar ξ_c (Jaggard and Engheta, p 173) such that

$$\vec{D} = \epsilon \cdot \vec{E} + i\xi_c \vec{B} \tag{2.2.1}$$

and

$$\vec{B} = \mu \cdot \vec{H} - i\xi_c \mu \cdot \vec{E} \tag{2.2.2}$$

With the more general bianisotropic materials described in (Lindell [34]) there are tensors $\overline{\overline{\xi}}$ and $\overline{\overline{\zeta}}$ such that $\vec{D}$ and $\vec{B}$ are related to $\vec{E}$ and $\vec{H}$ by the 6 by 6 matrix embodied in equation (2.1.2). Here the Faraday Maxwell equation has, for time harmonic radiation, the form

$$curl(\vec{E}) \;=\; -\; i\omega\vec{B} \tag{2.2.3}$$

while the Ampere Maxwell equation has the form

$$curl(\vec{H}) \;=\; i\omega\vec{D} \;+\; \overline{\overline{\sigma}} \cdot \vec{E} \tag{2.2.4}$$

Using these notions we make Maxwell's equations look like the standard Maxwell equations with complex sources by introducing the generalized electric and magnetic current densities by the relations,

$$curl(\vec{E}) \;=\; i\omega\mu_0\vec{H} \;-\; \vec{J}_m \tag{2.2.5}$$

and

$$curl(\vec{H}) \;=\; i\omega\epsilon_0\vec{E} \;+\; \vec{J}_e \tag{2.2.6}$$

where the $\vec{J}_e$ appearing in equation (2.2.6) is defined by

$$\vec{J}_e \;=\; i\omega\overline{\overline{\epsilon}} \cdot \vec{E} \;+\; i\omega\overline{\overline{\xi}} \cdot \vec{H} \;-\; i\omega\epsilon_0\vec{E} \tag{2.2.7}$$

and the $\vec{J}_m$ appearing in equation (2.2.5) is defined by

$$\vec{J}_m \;=\; i\omega\left[\overline{\overline{\mu}} \cdot \vec{H} \;+\; \overline{\overline{\zeta}} \cdot \vec{E} \;-\; \mu_0\vec{H}\right] \tag{2.2.8}$$

We can think of the current densities (2.2.7) and (2.2.8) as stimulators of radiation in ambient space and use the Maxwell equations (2.2.5) and (2.2.6) to formulate the resolution of the interaction problem as the solution of integral equations. We, however, need to use the current densities given by (2.2.7) and (2.2.8) to define electric and magnetic charge densities ρ_e and ρ_m by the relations,

$$div(\vec{J}_e) \;+\; \frac{\partial\rho_e}{\partial t} \;=\; 0 \tag{2.2.9}$$

and

$$div(\vec{J}_m) \;+\; \frac{\partial\rho_m}{\partial t} \;=\; 0 \tag{2.2.10}$$

We now use the electric and magnetic current densities given by (2.2.7) and (2.2.8) and the electric and magnetic charge densities given by (2.2.9) and (2.2.10), respectively, to develop a coupled system of integral equations describing the interaction of electromagnetic radiation with a bounded bianisotropic body Ω. The electric field integral equation is given by

$$\begin{aligned}\vec{E} - \vec{E}^i = & -grad\left(\int_\Omega \frac{div(\vec{J}_e)}{\omega\epsilon_0} G(r,s)dv(s)\right) \\ & + \frac{i}{\omega\epsilon_0} grad\left(\int_{\partial\Omega} (\vec{J}_e \cdot \vec{n}) G(r,s)da(s)\right) \\ & - i\omega\mu_0 \int_\Omega \vec{J}_e G(r,s)dv(s) + \\ & - curl\left(\int_\Omega \vec{J}_m G(r,s)dv(s)\right) \end{aligned} \tag{2.2.11}$$

If the material is nonmagnetic, then there is no nonzero magnetic current density and we could derive a magnetic field integral equation directly from (2.2.11) simply using Maxwell's equations. The general magnetic field integral equation may be expressed as

$$\begin{aligned}\vec{H} - \vec{H}^i = & -grad\left(\int_\Omega \frac{div(\vec{J}_m)}{\omega\mu_0} G(r,s)dv(s)\right) \\ & - \frac{i}{\omega\mu_0} grad\left(\int_{\partial\Omega} (\vec{J}_m \cdot \vec{n}) G(r,s)da(s)\right) \\ & - i\omega\epsilon_0 \int_\Omega \vec{J}_m G(r,s)dv(s) + \\ & + curl\left(\int_\Omega \vec{J}_e G(r,s)dv(s)\right) \end{aligned} \tag{2.2.12}$$

where G(r,s) is the rotation invariant, temperate fundamental solution of the Helmholtz equation,

$$(\Delta + k_0^2)G = \delta \tag{2.2.13}$$

given by

$$G(r,s) = \frac{exp(-ik_0 \mid r - s \mid)}{4\pi \mid r - s \mid} \tag{2.2.14}$$

Substituting (2.2.7) and (2.2.8) into equations (2.2.11) and (2.2.12) we obtain, the coupled integral equations for bianisotropic materials. The electric field integral equation for a bianisotropic material is given by,

$$\begin{aligned}\vec{E} - \vec{E}^i = & \\ -grad & \left(\int_\Omega \frac{div(i\omega\left[\bar{\bar{\epsilon}} \cdot \vec{E} + \bar{\bar{\xi}} \cdot \vec{H} - \epsilon_0 \vec{E}\right])}{\omega\epsilon_0} G(r,s)dv(s)\right) \\ + \frac{i}{\omega\epsilon_0} grad & \left(\int_{\partial\Omega} (i\omega\left[\bar{\bar{\epsilon}} \cdot \vec{E} + \bar{\bar{\xi}} \cdot \vec{H} - \epsilon_0 \vec{E}\right] \cdot \vec{n}) G(r,s)da(s)\right)\end{aligned}$$

$$-i\omega\mu_0 \int_\Omega i\omega \left[\overline{\overline{\epsilon}} \cdot \vec{E} + \overline{\overline{\xi}} \cdot \vec{H} - \epsilon_0 \vec{E}\right] G(r,s)dv(s) +$$

$$- curl \left(\int_\Omega i\omega \left[\overline{\overline{\mu}} \cdot \vec{H} + \overline{\overline{\zeta}} \cdot \vec{E} - \mu_0 \vec{H}\right] G(r,s)dv(s) \right) \tag{2.2.15}$$

and the magnetic field integral equation for a bianisotropic material is given by

$$\vec{H} - \vec{H}^i = - grad \left(\int_\Omega \frac{div(i\omega \left[\overline{\overline{\mu}} \cdot \vec{H} + \overline{\overline{\zeta}} \cdot \vec{E} - \mu_0 \vec{H}\right])}{\omega\mu_0} G(r,s)dv(s) \right)$$

$$-\frac{i}{\omega\mu_0} grad \int_{\partial\Omega} (i\omega \left[\overline{\overline{\mu}} \cdot \vec{H} + \overline{\overline{\zeta}} \cdot \vec{E} - \mu_0 \vec{H}\right] \cdot \vec{n}) G(r,s)da(s)$$

$$-i\omega\epsilon_0 \int_\Omega (i\omega \left[\overline{\overline{\mu}} \cdot \vec{H} + \overline{\overline{\zeta}} \cdot \vec{E} - \mu_0 \vec{H}\right]) G(r,s)dv(s) +$$

$$+ curl \left(\int_\Omega i\omega \left[\overline{\overline{\epsilon}} \cdot \vec{E} + \overline{\overline{\xi}} \cdot \vec{H} - \epsilon_0 \vec{E}\right] G(r,s)dv(s) \right) \tag{2.2.16}$$

In the subsequent sections we shall explore methods of resolving these integral equations on existing computers using novel, powerful analytical methods of solution.

3 Exact Finite Rank Integral Equation Methods

While we have obtained exact solutions for layered materials, most of the problems are so complex that one must formulate the interaction problems using integral equations. The primary focus of this report is to describe the design of complex materials using an improvement of classical spline methods (Tsai, Massoudi, Durney, and Iskander, pp 1131-1139). This paper is unusual in that comparisons are made between internal fields predicted from moment method computations and Mie solution computations. Successful comparisons have been made for linear basis functions without enhancement by *exact finite rank integral equation* theory. However, as the scattering bodies become more complex the computational requirements become larger and larger. With *exact finite rank integral equation* theory if one has a discretization that enables one to closely approximate the solution, then refinements can be made by a convergent iterative process based on the concept that the norm of the difference between an approximate integral operator and the actual integral operator is simply smaller than one, not necessarily close enough to give answers of acceptable accuracy. Then the answer is improved by an iterative process to any desired precision without the use of additional computer memory.

3.1 Examples of Spaces of Approximation

Solving the electromagnetic transmission problem by finding solutions of Maxwell's equations inside and outside a penetrable scatterer which satisfy boundary conditions and radiation conditions requires functions on a continuum, the problem is from a practical

point of view a discrete one and involves estimation of the values of induced and scattered electric and magnetic vectors in the interior and the exterior of the scattering body. Thus, it is important to understand methods of determining the accuracy with which a solution of a discrete approximation of an integral equation formulation of an electromagnetic interaction problem can be obtained. We specifically need to formulate a space of approximates and a projection operator onto this space of approximates and formulate a finite rank approximation of the original infinite rank integral equations (2.2.15) and (2.2.16) such that the precise solution of this approximate equation is exactly the projection onto the space of approximates of the solution of the original infinite rank integral equation. We further need to develop a means of correcting our solution so that we may exactly determine by iteration the difference $f - Pf$ between the solution f of the original equation and the projection Pf of this solution onto the space of approximates, possibly by an iterative scheme or a series expansion. In this section we illustrate (i) pulse basis function methods, (ii) linear interpolation, (iii) higher order spline interpolation, and (iv) a completetely novel L^∞ norm method of approximating the field components with combinations of trignomometric functions of the local spatial variables using carefully selected frequencies.

We now explain linear interpolation. A common example would be to approximate the space V of functions which are continuous on $[a, b]$ by members of a set

$$S = \{[x_0, x_1), [x_1, x_2), \cdots, [x_{n-1}, x_n]\} \tag{3.1.1}$$

where

$$a = x_0 < x_1 < \cdots < x_n = b \tag{3.1.2}$$

and to define the projection operator of linear interpolation, for the partition defined by equation (3.1.1) by the rule,

$$Pf(x) = f(x_{i-1})\left(\frac{x_i - x}{x_i - x_{i-1}}\right) + f(x_i)\left(\frac{x - x_{i-1}}{x_i - x_{i-1}}\right) \tag{3.1.3}$$

if x belongs to the subinterval from x_{i-1} to x_i and we note that if this is the case then since

$$(Pf)(x_{i-1}) = f(x_{i-1}) \cdot 1 + 0 \tag{3.1.4}$$

and since

$$(Pf)(x_i) = 0 + f(x_i) \cdot 1 \tag{3.1.5}$$

it follows from equations (3.1.3), (3.1.4), and (3.1.5) that

$$P^2 f = Pf \tag{3.1.6}$$

Another simple example is Fourier series or an eigenfunction expansion in the spatial variables. Suppose that V is a set of functions defined on $\mathbf{R}^n$ which are square integrable with respect to Lebesgue measure ν multiplied by a positive function ρ and valued in a Hilbert space X with norm $|\cdot|_X$ with two measurable and square integrable functions f and g being equivalent on an open set,

$$\Omega \subset \mathbf{R}^n, \tag{3.1.7}$$

if and only if

$$\int_\Omega \left(| (f-g)(x) |_X^2 \right) \rho(x) d\nu(x) \;=\; 0 \tag{3.1.8}$$

and where the square integrability with respect to the ordinary Lebesgue measure multiplied by ρ means that

$$\int_\Omega \left(| f(x) |_X^2 \right) \rho(x) d\nu(x) \;<\; \infty \tag{3.1.9}$$

We say that two Hilbert space valued functions f and g are orthogonal if and only if

$$\int_\Omega \{ f(x) \cdot g(x) \} \rho(x) d\nu(x) \;=\; 0 \tag{3.1.10}$$

where

$$(f(x), g(x))_X \;=\; f(x) \cdot g(x) \tag{3.1.11}$$

is the inner product of the Hilbert space elements $f(x)$ and $g(x)$ so that the square of the norm of the function f is

$$| f |_X^2 \;=\; \int_\Omega \{ f(x) \cdot f(x) \} \rho(x) d\nu(x) \tag{3.1.12}$$

If

$$F \;=\; \{ \phi_i : i \in \mathcal{I} \} \tag{3.1.13}$$

is a finite set of pairwise orthogonal functions in the space V of functions from Ω into the Hilbert space X, then

$$Pf(x) \;=\; \sum_{i \in \mathcal{I}} \left[\frac{\int_\Omega f(y) \cdot \phi_i(y) \rho(y) d\nu(y)}{\int_\Omega \phi_i(y) \cdot \phi_i(y) \rho(y) d\nu(y)} \right] \phi_i(x) \tag{3.1.14}$$

The projection operator defined by equation (3.1.14) yields a generalized Fourier series approximation of functions; which is the basis of Mie like solutions of electromagnetic problems.

The next approximation scheme that is often used in electromagnetic analysis is the pulse basis function method. The pulse basis function method has been used by Guru and Chen [22], Hagmann and Gandhi [23], Hagmann and Levine [25], and Livesay and Chen [36] to predict the results of electromagnetic radiation with complex structures by decomposing the body into cells within each of which the induced electric vector is assumed to be a constant and charge densities are also assumed to be piecewise constant. The pulse basis function method makes use of the concept of the partition of an open set Ω of $\mathbf{R}^n$.

We have defined for each x in $\mathbf{R}^n$ and each positive number $r > 0$ the set

$$B(x, r) \;=\; \{ y \in \mathbf{R}^n \;:\; | x - y | \;<\; r \} \tag{3.1.15}$$

to be the ball of radius r centered at x. We let Ω be an open set in $\mathbf{R}^n$ whose closure is bounded.

Definition 3.1 *A partition of Ω is a set $\mathcal{P}(\Omega)$ of pairs (V_i, x_i) where $i \in \mathcal{I}$ and the ball, $B(x_i, r)$ is contained in V_i for some positive number r,*

$$\bigcup_{i \in \mathcal{I}} V_i = \Omega \tag{3.1.16}$$

and

$$\mu_n(V_j \bigcap V_k) = 0 \ (j \neq k) \tag{3.1.17}$$

whenever (V_i, x_i) and (V_j, x_j) are distinct members of the partition, $\mathcal{P}(\Omega)$ and μ_n is the standard Lebesgue measure on $\mathbf{R}^n$ where we let

$$\mathcal{P}_1 = \{V_i : (V_i, x_i) \in \mathcal{P}(\Omega) \text{ for some } x_i \in V_i\} \tag{3.1.18}$$

and we define the characteristic functions,

$$\chi_{V_i}(x) = \begin{cases} 1 & x \in V_i \\ 0 & x \text{ is not a member of } V_i \end{cases} \tag{3.1.19}$$

to be the characteristic functions or pulse functions associated with the sets V_i in $\mathcal{P}(\Omega)_1$. The sets V_i are called cells in a cellular decomposition of Ω.

Next we define the projection operators associated with this partition of an open set in Euclidean n dimensional space.

Definition 3.2 *We define the projection operator P associated with the partition,*

$$\mathcal{P}(\Omega) = \{(V_i, x_i) : x_i \in V_i, \ i \in \mathcal{I}, \ V_i \subset \Omega\} \tag{3.1.20}$$

by the rule,

$$Pf(x) = \sum_{V_i \in \mathcal{P}(\Omega)_1} [\chi_{V_i}(x) \cdot f(x_i)] \tag{3.1.21}$$

for all functions,

$$f : \Omega \to \mathbf{C}^m \tag{3.1.22}$$

where $\mathbf{C}^m$ denotes complex m dimensional space.

We prove the following.

Proposition 3.1 *If $\mathcal{F}(\Omega, \mathbf{C}^m)$ is any topological vector space of functions from Ω into $\mathbf{C}^m$ which includes all functions of the form,*

$$x \to \chi_V(x)\vec{u} \tag{3.1.23}$$

where

$$V \in \mathcal{P}(\Omega)_1 \tag{3.1.24}$$

and

$$\vec{u} \in \mathbf{C}^m \tag{3.1.25}$$

then the mapping P defined by equation (3.1.21) is an endomorphism of this topological vector space which satisfies

$$PP = P \tag{3.1.26}$$

3.2 The Standard but Nonoptimal Discretization

Kun Mu Chen meticulously analyzed the electric field volume integral equation in the work he directed in ([36]) and correctly formulated the electric field volume integral equation for a nonmagnetic body as,

$$(\vec{E} - \vec{E}^i)(p,\omega) = \frac{i\omega^2}{c^2}\int_\Omega \left(\frac{(\epsilon-\epsilon_0)-i\sigma/\omega}{\epsilon_0}\right)\overline{\overline{G}}(p,q)\cdot\vec{E}(q)dv(q) \tag{3.2.1}$$

where

$$\overline{\overline{G}} = \left(\overline{\overline{I}} + \left(\frac{1}{k_0^2}\right) grad(grad)\right)\left(\frac{exp(ik_0 \mid p-q \mid)}{4\pi \mid p-q \mid}\right) \tag{3.2.2}$$

What is done in practice is to apply the projection operator to the a priori unknown field $\vec{E}$ that appears under the integral and to also apply it also to both sides of the integral equation (3.2.1) to obtain the approximate equation

$$(P^x\vec{E} - P^x\vec{E}^i) = \frac{i\omega^2}{c^2}\int_\Omega \left(\frac{(\epsilon-\epsilon_0)-i\sigma/\omega}{\epsilon_0}\right)P^x\overline{\overline{G}}(x,y)\cdot(P^y\vec{E})dv(y) \tag{3.2.3}$$

where $\overline{\overline{G}}$ is defined by equation (3.2.2). The so called method of moments was developed in the early 1900s by mathematicians and is simply the weak topology approximation; as currently applied it is an attempt to do a better job of getting a more acceptable solution of the clearly nonoptimal approximation represented by equation (3.2.3). With the method of moments one obtains $3N$ equations for the $3N$ unknonws representing the electric vector in the N cells into which the scattering body Ω is decomposed by simply multiplying both sides of equation (3.2.3) by a function of x, often the characteristic function of the cell V_i, where i ranges from 1 to N, and integrating both sides of the new equation with respect to x

4 Exact Solutions of Integral Equations

We show in this section a method of creating a computerizable approximate to the original infinite rank integral equation. After multiplying all terms of the integral equation by the same invertible matrix, if necessary, we can reduce the coupled $\vec{E}$ and $\vec{H}$ integral equation to one of the form described in the following section.

4.1 Machine Precision in Integral Equation Methods

We show in this section how to correct our errors in an integral equation method, so that we can obtain, by doing more processing but not using excessive memory, an answer whose precision is close to that of the particular computing machine being used. Letting

f be a vector valued function defined on an open set Ω of $\mathbf{R}^3$ and having values belonging to a Banach space, X, which represents the set of values of the electric and magnetic field vector within the scattering body and having enough regularity that boundary values are defined. Suppose that the functions f that we consider all satisfy the condition,

$$f \in \mathcal{E}(\Omega, X), \tag{4.1.1}$$

that they belong to a Banach space of functions from Ω into X. We further suppose that we define a projection operator,

$$P : \mathcal{E}(\Omega, X) \rightarrow \mathcal{E}(\Omega, X) \tag{4.1.2}$$

We let $\mathcal{B}(X)$ denote a Banach space of operators mapping X into itself and let K be a function,

$$K : \Omega \times \Omega \rightarrow \mathcal{B}(X) \tag{4.1.3}$$

which in practice will represent the integral operator acting on the values of the electric and magnetic field vectors in the interior and on the surface of the scattering body. One way this can be handled is to assume enough regularity in the space of functions, $\mathcal{E}(\Omega, X)$ in which we are seeking the solution (and in the space of approximations within which we are attempting to find a solution that is reasonably close to actual solution), that the required boundary values are defined. Related to this basic projection operator, which may be defined in one of the ways described in the previous section, or in other ways, we define the operator Q^x on functions from Ω into X by the rule,

$$P \int_\Omega K(x,y)(Pf)(y)d\nu(y) = \int_\Omega Q^x K(x,y)(Pf)(y)d\nu(y) \tag{4.1.4}$$

We can reduce our original problem to that of solving an integral equation of the form,

$$f(x) - g(x) = \lambda T f(x) \tag{4.1.5}$$

where

$$Tf(x) = \int_\Omega K(x,y)f(y)d\nu(y) \tag{4.1.6}$$

and f may represent a two tuple consisting of the electric and magnetic vectors and g represents the result of applying an invertible linear transformation two a two tuple consisting of the electric and magnetic vectors of the incoming radiation. We define the operator L by the rule

$$L = PTPf(x) \tag{4.1.7}$$

where P is a projection operator onto a space of approximates, and define the correction operator N by the rule,

$$Nf(x) = Tf(x) - Lf(x) \tag{4.1.8}$$

Normally we require that P is a good enough approximator that solving the equation (3.2.3) will give us a satisfactory solution. However, with *exact finite rank integral equation* theory we need only assume that P is good enough so that if N is defined by (4.1.8) that then the operator norm inequality,

$$max\,\{|\lambda|\,|N|_\Omega\ ,\ |\lambda|\,|(P-I)N|_\Omega\} < 1 \tag{4.1.9}$$

Thus, it follows that

$$T = L + N \tag{4.1.10}$$

The usual approximate integral equation has the form

$$f_a = Pg = \lambda PTf_a \tag{4.1.11}$$

where f_a satisfies the condition,

$$f_a \in P(\mathcal{E}(\Omega, X)), \tag{4.1.12}$$

What is usually done is to assume that f_a is close enough to f to accurately represent the solution of the original infinite rank integral equation (4.1.5). We can, if inequality (4.1.9) is satisfied, define the bounded linear operator

$$G_\lambda = \sum_{k=1}^{n} \lambda^{k-1} N^k \tag{4.1.13}$$

so that it will follow that since formally and in fact,

$$(I - \lambda N) \cdot (I + \lambda N + \lambda^2 N^2 + \cdots) f = f \tag{4.1.14}$$

that by combining equations (4.1.13) and (4.1.14) that

$$(I - \lambda N)(I + \lambda G_\lambda) f = f \tag{4.1.15}$$

in view of the the geometric series relationship and the identity

$$(I + \lambda G_\lambda) = (I + \lambda N + \lambda^2 N^2 + \cdots) \tag{4.1.16}$$

for all functions f satisfying the relationship (4.1.1). Thus, we can in view of the relationship (4.1.10) deduce that

$$\lambda T = \lambda N + \lambda L \tag{4.1.17}$$

Equation (4.1.17) then means that we can express the original integral equation (4.1.5) in the form

$$f = g + \lambda N f + \lambda L f \tag{4.1.18}$$

Rearranging terms in equation (4.1.18) we see that

$$(I - \lambda N) f = g + \lambda L f \tag{4.1.19}$$

Combining equations (4.1.19) and (4.1.15) and equation (4.1.13) we deduce that

$$f = g + \lambda L f + \lambda G_\lambda (g + \lambda L f +) \tag{4.1.20}$$

Now if we simply combine equation (4.1.20) and equation (4.1.18) we deduce that

$$\lambda N f = \lambda G_\lambda (g + \lambda L f) \tag{4.1.21}$$

We would now like to apply the projection operator P to both sides of equation (4.1.20) making use of the fact that P is idempotent, equalling its square, and equation (4.1.7)

$$PL = L \tag{4.1.22}$$

to obtain the relation

$$Pf = Pg + \lambda Lf \lambda P(G_\lambda(g + \lambda Lf) \tag{4.1.23}$$

Substituting equation (4.1.21) into equation (4.1.23) we see that

$$Pf = Pg + \lambda Lf + \lambda PNf \tag{4.1.24}$$

Thus, if we define

$$L_{(K,P)} = \tag{4.1.25}$$

then in view of equation (4.1.7) and (4.1.25) we see that

$$Lf = L_{(K,P)}Pf \tag{4.1.26}$$

Now we see that equations (4.1.24) and (4.1.26) imply that

$$Pf = Pg + \lambda PL_{(K,P)}Pf + \lambda PNf \tag{4.1.27}$$

While equation (4.1.27) is not a finite rank integral equation, it suggests that an approximate finite rank integral equation

$$Pf_a = Pg + \lambda PL_{(K,P)}Pf_a + \lambda PNPf_a \tag{4.1.28}$$

might give a better approximation to the solution than the traditional approximation given by equation (4.1.11). We shall go much farther than this, however, and reduce the equation (4.1.24) to a true finite rank integral equation whose solution will be the projection Pf of the exact solution f of the original infinite rank integral equation (4.1.5) onto the space of approximates. This will permit us to achieve our ultimate objective of representing the solution f exactly in terms of Pf and the stimulating fields g by an exact formula. Going back to equation (4.1.19) and making use of equation (4.1.14) we obtain

$$f = \sum_{k=0}^{\infty} \left[(\lambda N)^k (g + \lambda Lf)\right] \tag{4.1.29}$$

Operating on both sides of equation (4.1.29) with N and then applying λP to both sides of this equation, we see that

$$\lambda PNf = \sum_{k=0}^{\infty} \left[(\lambda N)^k (g + \lambda Lf)\right] \tag{4.1.30}$$

Now, simply substituting equation (4.1.30) into equation (4.1.27) we get the finite rank integral equation,

$$Pf = Pg +$$

$$\lambda P L_{(K,P)} P f \;+\; \lambda P N \left[\sum_{k=0}^{\infty} (\lambda N)^k \left(g \;+\; \lambda L_{(K,P)} P f \right) \right] \qquad (4.1.31$$

Now collecting terms in equation (4.1.31) involving Pf and those involving g and Pg we obtain the relationship

$$Pf \;=\; Pg \;+ \lambda P N \left[\sum_{k=0}^{\infty} (\lambda N)^k g \right] \;+$$

$$\lambda P \left(L_{(K,P)} \;+\; N \left[\sum_{k=0}^{\infty} (\lambda N)^k \right] \lambda L_{(K,P)} \right) Pf \qquad (4.1.32)$$

Our first objective is now achieved since [illegible] ion (4.1.32) is a truly finite rank integral equation in the unknown member Pf of a finite dimensional vector space. The computer program giving a solution of equation (4.1.32) would provide us with coefficients of the basis vectors of this finite dimensional vector space that are needed to represent the solution Pf of equation (4.1.32). In other words, the linear combination of basis vectors of the vector space which is the image of the projector P is the exact value, Pf, of the projection of the exact value of the solution, f, of the original infinite rank integral equation, (4.1.5). From this point on we assume that Pf is known.

To finish off this section we use our exactly determined value of Pf that was obtained by solving equation (4.1.32) under the assumption that $I - \lambda L$ is invertible on the image of the projection operator P, where L is defined by equation (4.1.7). We begin by subtracting the right sides of equations (4.1.18) and (4.1.24) obtaining the relationship,

$$(f \;-\; Pf) \;=\; (g \;-\; Pg) \;+\; \lambda (I - P) N f \qquad (4.1.33)$$

Collecting the terms involving f in equation (4.1.33) and moving the known function Pf over on the right side, we obtain the equation,

$$[I - \lambda (I - P) N] f \;=\; (g \;-\; Pg \;+\; Pf) \qquad (4.1.34)$$

The inequality (4.1.9) then enables us to invert the operator acting on the f in the left side of equation (4.1.34) by applying the geometric series operator

$$S \;=\; \sum_{k=0}^{\infty} (\lambda (I - P) N)^k \qquad (4.1.35)$$

to both sides of equation (4.1.34). Thus, once we solve equation (4.1.32) for Pf we can correct ourselves by expressing the exact value of f as

$$f \;=\; \sum_{k=0}^{\infty} (\lambda (I - P) N)^k \{ g \;-\; Pg \;+\; Pf \} \qquad (4.1.36)$$

Thus, without using a[illegible] memory we can with a good enough start and enough iteration correct our solution to within computer accuracy.

5 Layered Materials

We have formulated some one dimensional scattering problems associated with magnetic materials, and solutions obtained from the differential equation formulations have been substituted into the integral equations and have been shown to satisfy them exactly. For magnetic materials, a single integral equation was obtained and the significance of surface values of the derivative of the electric vector were shown to be important. For higher order splines all terms arising in a matrix representation of the integral equation formulation of the problem, and all iterates of the integrals could be computed exactly. Using distribution theory concepts, we have combined the electric and magnetic field integral equations for the case of a plane wave that is incident normally on the magnetic slab.

5.1 Magnetic Slab Integral Equation

Magnetic materials, particularly lossy ferromganetic fibers or carbon fibers with a ferromagnetic coating should have a very strong tendency to extinguish microwaves. It is therefore important to be able to treat the interaction of radiation with magnetic materials. What is described here is an exact solution of the problem of describing the interaction of radiation with a magnetic slab. Distribution theory is actually needed to formulate and solve the integral equation for a magnetic slab.

We consider in this section radiation normally incident on a magnetic slab, and assume that the electric vector of the incident radiation has the form

$$\vec{E}^i = E_0 exp(-ik_0 z)\vec{e}_x \tag{5.1.1}$$

so that the magnetic vector of the incident radiation defined by the Maxwell equation,

$$\begin{aligned} -i\omega\mu_0 \boldsymbol{H}^i &= curl(\vec{E}^i) = \\ & -\vec{e}_y\left(-\frac{\partial}{\partial z}\right)E_0 exp(-ik_0 z) \\ &= -ik_0 E_0 exp(-ik_0 z)\vec{e}_y \end{aligned} \tag{5.1.2}$$

is after dividing both sides of equation (5.1.2) by $-i\omega\mu$ is given by

$$\boldsymbol{H}^i = \left(\frac{k_0 E_0}{\omega\mu_0}\right) exp(-ik_0 z)\vec{e}_y \tag{5.1.3}$$

Within the magnetic slab, where the permittivity ϵ, the permeability μ, and the conductivity σ are diagonal tensors in Cartesian coordinates, the first Maxwell equation has the form,

$$\begin{aligned} curl(\boldsymbol{H}) = & (i\omega\epsilon_x + \sigma_x)E_x\vec{e}_x + (i\omega\epsilon_y + \sigma_y)E_y\vec{e}_y \\ & + (i\omega\epsilon_z + \sigma_z)E_z\vec{e}_z \end{aligned} \tag{5.1.4}$$

However, if the stimulating electric vector has only an x component, then the same is true of the reflected, induced, and transmitted radiation, and, thus, we may assume that within the slab that this is also true. Hence, we assume that within the slab,

$$\vec{E} = g(z)exp(-i\omega t)\vec{e}_x = E_x\vec{e}_x \tag{5.1.5}$$

Since then

$$curl(\vec{E}) \;=\; -\vec{e}_y\left(-\frac{\partial}{\partial z}\right)E_x \;=\; -i\omega\mu_y H_y\vec{e}_y \tag{5.1.6}$$

we conclude that

$$H_y = \frac{i}{\omega\mu_y}\frac{\partial E_x}{\partial z} \tag{5.1.7}$$

Using (3.4) we conclude that

$$curl(\boldsymbol{H}) = \vec{e}_x\left(-\frac{\partial}{\partial z}\right)H_y \tag{5.1.8}$$

which implies that

$$\begin{aligned} &curl(\boldsymbol{H}) = \\ &\vec{e}_x\left[\left(\frac{i}{\omega\mu_y^2}\mu_y^{(1)}(z)\right)\frac{\partial E_x}{\partial z} - \frac{i}{\omega\mu_y}\frac{\partial^2 E_x}{\partial z^2}\right] \\ &= \vec{e}_x(i\omega\epsilon_x + \sigma_x)E_x \end{aligned} \tag{5.1.9}$$

Thus, multiplying all terms of this last equation by $i\omega\mu_y$ we see that

$$\begin{aligned} &\frac{\partial^2 E_x}{\partial z^2} - \frac{\mu_y^{(1)}(z)}{\mu_y(z)}\frac{\partial E_x}{\partial z} \\ &= (-\omega^2\mu_y\epsilon_x + i\omega\mu_y\sigma_x)E_x \end{aligned} \tag{5.1.10}$$

We are, therefore, seeking an impulse response of the equation,

$$\begin{aligned} &\frac{\partial^2 E_x}{\partial z^2} + \omega^2\mu_0\epsilon_0 E_x = \\ &\frac{\mu_y^{(1)}}{\mu_y}\frac{\partial E_x}{\partial z} + (\omega^2(\mu_0\epsilon_0 - \mu_y\epsilon_x) + i\omega\mu_y\sigma_x)E_x \end{aligned} \tag{5.1.11}$$

We introduce the variable

$$\tau = \omega^2\mu_y\epsilon_x - i\omega\mu_y\sigma_x - \omega^2\mu_0\epsilon_0, \tag{5.1.12}$$

where we agree that ϵ, μ, and σ take their free space values outside the slab, and assume that $E - E^i$ has the form,

$$E - E^i = c\int_{-\infty}^{\infty}\tau E_x exp(-ik_0\mid z - \xi\mid)d\xi$$

$$+ b \int_{-\infty}^{\infty} \frac{\mu_y^{(1)}(\tilde{z})}{\mu_y(\tilde{z})} \frac{\partial E_x}{\partial \tilde{z}} exp(-ik_0 \mid z - \tilde{z}) \mid d\tilde{z} \tag{5.1.13}$$

where we write the global magnetic permeability via the relationship

$$\mu_y(z) = (Y(z) - Y(z - L))(\tilde{\mu}_y - \mu_0) + \mu_0 \tag{5.1.14}$$

where

$$Y(z) = \begin{cases} 1 & \text{if } z \geq 0 \\ 0 & \text{if } z < 0 \end{cases} \tag{5.1.15}$$

is the Heaviside function and

$$Y^{(1)}(z) = \delta(z) \tag{5.1.16}$$

is the Dirac delta function and where we think of μ as the permeability at any point and think of $\tilde{\mu}$ as the value of permeability inside the slab. Thus, with this definition and recognizing the tangential component of the magnetic field as being proportional to the reciprocal of the the magnetic permeability times the derivative of the electric vector with respect to z in view of the relationship

$$H_y = \frac{i}{\omega \mu_y} \frac{\partial E_x}{\partial z}$$

and seek a representation of the form,

$$E_x - E^i = c \int_0^L \tau E_x exp(-ik_0 \mid z - \tilde{z} \mid d\tilde{z}$$

$$+ b \int_0^L \frac{\mu_y^{(1)}(\tilde{z})}{\mu_y(\tilde{z})} \frac{\partial E_x}{\partial \tilde{z}} exp(-ik_0 \mid z - \tilde{z} \mid) d\tilde{z}$$

$$+ b \left(1 - \frac{\mu_0}{\mu_y(0)}\right) \frac{\partial E_x}{\partial z}(0) exp(-ik_0 z)$$

$$- b \left(1 - \frac{\mu_0}{\mu_y(L)}\right) \frac{\partial E_x}{\partial z}(L) exp(ik_0 z) exp(-ik_0 L) \tag{5.1.17}$$

Theorem 5.1 *If E_x satisfies (5.1.17) and E_x is twice continuously at points inside and outside the slab, then (a) outside the slab $E - E^i$ has the representation*

$$E - E^i = \begin{cases} C^r exp(ik_0 z) & \text{for } z < 0 \\ \\ C^t exp(-ik_0 z) & \text{for } z > L \end{cases} \tag{5.1.18}$$

where C^r is the reflection coefficient, and C^t is the coefficient defining the transmitted radiation (c) if a function E_x that is differentiable inside and outside the slab satisfies the integral equation, then E_x is continuous on the entire real line, and furthermore, if $H - H^i$ is determined from (5.1.17) via the relationship

$$H - H^i = \frac{-i}{2\omega\mu_0} \int_0^L \tau E_x exp(-ik_0(z - \tilde{z}) d\tilde{z}$$

$$+ \frac{i}{2\omega\mu_0}\int_z^L \tau E_x exp(-ik_0(\tilde{z}-z)d\tilde{z}$$

$$+ \frac{i}{2\omega\mu_0}\int_0^z \frac{\mu_y^{(1)}(z)}{\mu_y}\frac{\partial E_x}{\partial \tilde{z}} exp(-ik_0(z-\tilde{z}))d\tilde{z}$$

$$+ \frac{-i}{2\omega\mu_0}\int_z^L \frac{\mu_y^{(1)}(z)}{\mu_y}\frac{\partial E_x}{\partial \tilde{z}} exp(-ik_0(\tilde{z}-z))d\tilde{z}$$

$$+ \frac{i}{2\omega\mu_0}\left(1-\frac{\mu_0}{\mu_y(0)}\right)\frac{\partial E_x}{\partial z}(0)exp(-ik_0 z)$$

$$+ \frac{i}{2\omega\mu_0}\left(1-\frac{\mu_0}{\mu_y(L)}\right)\frac{\partial E_x}{\partial z}(L)exp(ik_0 z)exp(-ik_0 L) \tag{5.1.19}$$

and $H - H^i$ is continuous across the boundaries of the magnetic slab. Furthermore, the classical solutions of the integral equation (5.1.17) are solutions of Maxwell's equations provided that

$$b = \frac{i}{2k_0} \tag{5.1.20}$$

and

$$c = -\frac{i}{2k_0} \tag{5.1.21}$$

Proof. Equations (5.1.20) and (5.1.21), which represent the evaluation of the parameters in the integral equation (5.1.17) follows by substituting (5.1.17) into Maxwell's equations. We begin by computing the first and second partial derivatives of E_x with respect to z from the integral equations and we then use these expressions to show that (5.1.20) and (5.1.21) are needed in order that Maxwell's equations be satisfied. We find, upon breaking up the integral from 0 to L into the integral from 0 to z plus the integral from z to L and differentiating, that

$$\frac{\partial E}{\partial z} - \frac{\partial E^i}{\partial z} = c\tau E_x - c\tau E_x$$

$$c(-ik_0)\int_0^z \tau E_x exp(-ik_0(z-\tilde{z})d\tilde{z}+$$

$$c(ik_0)\int_z^L \tau E_x exp(-ik_0(\tilde{z}-z)d\tilde{z}+$$

$$b\frac{\mu_y^{(1)}}{\mu_y}\frac{\partial E_x}{\partial \tilde{z}}\mid_{\tilde{z}=z} - b\frac{\mu_y^{(1)}}{\mu_y}\frac{\partial E_x}{\partial \tilde{z}}\mid_{\tilde{z}=z} +$$

$$(-ik_0)b\int_0^z \frac{\mu_y^{(1)}(\tilde{z})}{\mu_y(\tilde{z}}\frac{\partial E_x}{\partial \tilde{z}}exp(-ik_0(z-\tilde{z})d\tilde{z}$$

$$+(ik_0)b\int_z^L \frac{\mu_y^{(1)}(\tilde{z})}{\mu_y(\tilde{z}}\frac{\partial E_x}{\partial \tilde{z}}exp(-ik_0(\tilde{z}-z)d\tilde{z}$$

$$+(-ik_0)b\left(1-\frac{\mu_0}{\mu_y(0)}\right)\frac{\partial E_x}{\partial z}(0)exp(-ik_0 z)$$

$$-(ik_0)b\left(1-\frac{\mu_0}{\mu_y(L)}\right)\frac{\partial E_x}{\partial z}(L)exp(ik_0 z)exp(-ik_0 L) \qquad (5.1.22)$$

We now take the derivative of both sides of this last equation with respect to z obtaining

$$\frac{\partial^2 E}{\partial z^2} - \frac{\partial^2 E^i}{\partial z^2} =$$

$$c(-ik_0)^2\int_0^z \tau E_x exp(-ik_0(z-\tilde{z}))d\tilde{z} + (-ik_0)c\tau E_x$$

$$-(ik_0)c\tau E_x + c(ik_0)^2\int_z^L \tau E_x exp(-ik_0(\tilde{z}-z))d\tilde{z} +$$

$$(-ik_0)b\frac{\mu_y^{(1)}(\tilde{z})}{\mu_y(\tilde{z})}\frac{\partial E_x}{\partial \tilde{z}}\mid_{\tilde{z}=z} + (-ik_0)^2 b\int_0^z \frac{\mu_y^{(1)}(\tilde{z})}{\mu_y(\tilde{z}}\frac{\partial E_x}{\partial \tilde{z}}exp(-ik_0(z-\tilde{z})d\tilde{z} +$$

$$-(ik_0)b\frac{\mu_y^{(1)}(\tilde{z})}{\mu_y(\tilde{z})}\frac{\partial E_x}{\partial \tilde{z}}\mid_{\tilde{z}=z} + (-ik_0)^2 b\int_z^L \frac{\mu_y^{(1)}(\tilde{z})}{\mu_y(\tilde{z}}\frac{\partial E_x}{\partial \tilde{z}}exp(-ik_0(\tilde{z}-z)d\tilde{z}$$

$$+(-ik_0)^2 b\left(1-\frac{\mu_0}{\mu_y(0)}\right)\frac{\partial E_x}{\partial z}(0)exp(-ik_0 z)$$

$$-(ik_0)^2 b\left(1-\frac{\mu_0}{\mu_y(L)}\right)\frac{\partial E_x}{\partial z}(L)exp(ik_0 z)exp(-ik_0 L) \qquad (5.1.23)$$

We now make use of the fact that

$$-k_0^2(E-E^i) = -k_0^2\left\{c\int_0^L \tau E_x exp(-ik_0 \mid z-\tilde{z} \mid d\tilde{z}\right.$$

$$+b\int_0^L \frac{\mu_y^{(1)}(z)}{\mu_y}\frac{\partial E_x}{\partial \tilde{z}}exp(-ik_0 \mid z-\tilde{z} \mid)d\tilde{z}$$

$$+b\left(1-\frac{\mu_0}{\mu_y(0)}\right)\frac{\partial E_x}{\partial z}(0)exp(-ik_0z)$$

$$-b\left(1-\frac{\mu_0}{\mu_y(L)}\right)\frac{\partial E_x}{\partial z}(L)exp(ik_0z)exp(-ik_0L)\Bigg\} \tag{5.1.24}$$

and substitute it into our equation for the difference between the second partial derivatives of the stimulated and incident electric field vectors. Rewriting (5.1.23) to make this substitution transparent we see that

$$\frac{\partial^2 E}{\partial z^2}-\frac{\partial^2 E^i}{\partial z^2}=$$

$$-(k_0)^2\Bigg\{c\int_0^z \tau E_x exp(-ik_0(z-\tilde{z}))d\tilde{z}$$

$$+c\int_z^L \tau E_x exp(-ik_0(\tilde{z}-z))d\tilde{z}$$

$$+b\int_0^z \frac{\mu_y^{(1)}(\tilde{z})}{\mu_y(\tilde{z}}\frac{\partial E_x}{\partial \tilde{z}}exp(-ik_0(z-\tilde{z})d\tilde{z}$$

$$+b\int_z^L \frac{\mu_y^{(1)}(\tilde{z})}{\mu_y(\tilde{z}}\frac{\partial E_x}{\partial \tilde{z}}exp(-ik_0(\tilde{z}-z)d\tilde{z}$$

$$+b\left(1-\frac{\mu_0}{\mu_y(0)}\right)\frac{\partial E_x}{\partial z}(0)exp(-ik_0z)$$

$$-b\left(1-\frac{\mu_0}{\mu_y(L)}\right)\frac{\partial E_x}{\partial z}(L)exp(ik_0z)exp(-ik_0L)\Bigg\}$$

$$-2(ik_0)c\tau E_x+2(-ik_0)b\frac{\mu_y^{(1)}(z)}{\mu_y(z)}\frac{\partial E_x}{\partial z} \tag{5.1.25}$$

Simplifying the above equation we find that

$$\frac{\partial^2 E}{\partial z^2}-\frac{\partial^2 E^i}{\partial z^2}=-k_0^2(E_x-E_x^i)$$

$$-2cik_0\tau E_x-2ik_0b\frac{\mu_y^{(1)}(z)}{\mu_y(z)}\frac{\partial E_x}{\partial z} \tag{5.1.26}$$

We next simplify this equation by making use of the fact that the electric vector, E_x^i, of the incident radiation satisfies the free space Helmholtz equation

$$\frac{\partial^2 E^i}{\partial z^2}+k_0^2E^i=0 \tag{5.1.27}$$

Substituting this into the previous equation we find that

$$\frac{\partial^2 E_x}{\partial z^2}+k_0^2E_x=$$

$$- \; 2cik_0\tau E_x - 2ik_0 b\frac{\mu_y^{(1)}(z)}{\mu_y(z)}\frac{\partial E_x}{\partial z} \tag{5.1.28}$$

We now need to select c and b in the above equation so that the equation is identical to equation (5.1.11) where τ is given by

$$\begin{aligned}\tau &= \omega^2\mu_y\epsilon_x - i\omega\mu_y\sigma_x - \omega^2\mu_0\epsilon_0 \\ &= k^2 - k_0^2 = k^2 - \omega^2\mu_0\epsilon_0\end{aligned} \tag{5.1.29}$$

We see that we need

$$-\,2ik_0 b = 1 \tag{5.1.30}$$

and

$$2ik_0 c = 1 \tag{5.1.31}$$

In order to define the operations we note here that, while it is true that we cannot in general multiply distributions, certain orders of distributions can act upon spaces larger than the infinitely differentiable functions. For example, order 0 distributions can act on the continuous functions with compact support, and order one distributions can act on the differentiable functions with compact support, et cetera which will enable us to define the product of an order 0 distribution u and a continuous function f by the rule,

$$(uf, \phi) = (u, f\phi) \tag{5.1.32}$$

where ϕ is a test function. However, the function uf is not a general distribution, but is a continous linear functional on the space of continous functions with compact support. The integral equation is then derived by recognizing that in view of equation (5.1.9) that

$$\begin{aligned}&\frac{\partial^2 E_x}{\partial z^2} + k_0^2 E_x = \\ &-\,i\omega\mu_y^{(1)}(z)H_y - \tau E_x\end{aligned} \tag{5.1.33}$$

By convolving the fundamental solution of the left side of this equation with the right side we obtain the integral equation. Since, as we have shown ([9], [33]), every solution of the integral equation is a solution of Maxwell's equations and the solutions of the integral equation satisfy automatically the Silver Mueller radiation conditions and tangential components of the electric and magnetic vectors are automatically continuous across the boundaries, the solution of the integral equation is necessarily the solution of Maxwell's equations. Since the solution to this electromagnetic interaction problem is unique, the function space under consideration is the space of functions which are, along with their derivatives, continuous up to the boundaries. When the slab is nonmagnetic, then uniqueness may be proven in the function space ([33], pp 69-130) consisting of all vector valued functions ϕ such that

$$\int_\Omega |\,\phi\,|^2\,dv + \int_\Omega |\,curl(\phi)\,|^2\,dv < \infty \tag{5.1.34}$$

6 Discretization of an Integral Equation

To approximate the integral equations on a computer with a finite memory, we divide the slab with which the radiation is interacting into thin wafers separated by planes whose normals are perpendicular to the planes defining the boundaries of the slab.

6.1 Piecewise Linear Approximation

We consider approximate integral equations of the form

$$\vec{E}(z) - \vec{E}^{i}(z) =$$

$$\sum_{j=1}^{N} \int_{z_{j-1}}^{z_j} \left\{A_j + B_j(y - z_j^*)\right\} K(z,y)dy +$$

$$\sum_{j=1}^{N} \int_{z_{j-1}}^{z_j} B_j L(z,y)dy +$$

$$F(z)B_1 - G(z)B_N \tag{6.1.1}$$

where we suppose that the numbers z_j are defined by

$$0 = z_0 < z_1 < \ldots < z_{j-1} < z_j < \ldots < z_N = L \tag{6.1.2}$$

and that within the subinterval (z_{j-1}, z_j), the electric vector is approximated by

$$\vec{E} = (A_j + B_j(z - z_j^*))\vec{e}_x, \tag{6.1.3}$$

where the constants A_j and B_j contain the $exp(i\omega t)$ time dependence. We have a separate equation for each value of z. At this stage there are several methods to obtain a matrix equation from this continuum of approximate equations. One obvious method is point matching by selecting two points ζ_{2j-1} and ζ_{2j} in the subinterval $[z_{j-1}, z_j]$. This gives us a system of $2N$ equations in $2N$ unknowns, which have the form

$$E(\zeta_{2\ell-q+1}) - E^{i}(\zeta_{2\ell-q+1}) =$$

$$A_\ell + B_\ell(\zeta_{2\ell-q+1} - z_\ell^*) - E^{i}(\zeta_{2\ell-q+1}) =$$

$$\sum_{j=1}^{N} \int_{z_{j-1}}^{z_j} \left\{A_j + B_j(y - z_j^*)\right\} K(\zeta_{2\ell-q+1}, y)dy +$$

$$\sum_{j=1}^{N} \int_{z_{j-1}}^{z_j} B_j L(\zeta_{2\ell-q+1}, y)dy +$$

$$F(\zeta_{2\ell-q+1})B_1 - G(\zeta_{2\ell-q+1})B_N \tag{6.1.4}$$

Defining

$$\delta_{(j,\ell)} = \begin{cases} 1 & j = \ell \\ 0 & j \neq \ell \end{cases} \tag{6.1.5}$$

We now use the delta function notation to rewrite the previous equation to make it look like a matrix equation. We find that

$$\begin{aligned}
&\sum_{j=1}^{N} \delta_{(j,\ell)} \{A_j + B_j(\zeta_{2\ell-q+1} - z_\ell^*)\} \\
&- \sum_{j=1}^{N} \left\{ A_j \int_{z_{j-1}}^{z_j} K(\zeta_{2\ell-q+1}, y)dy \; + \right. \\
&\left. B_j \int_{z_{j-1}}^{z_j} (y - z_j^*) K(\zeta_{2\ell-q+1}, y)dy \right\} - \\
&\sum_{j=1}^{N} \delta_{(j,1)} B_j F(\zeta_{2\ell-q+1}) + \\
&\sum_{j=1}^{N} \delta_{(j,1)} B_j G(\zeta_{2\ell-q+1}) = E^i(\zeta_{2\ell-q+1})
\end{aligned} \tag{6.1.6}$$

We now represent this last equation in the matrix form

$$T\begin{pmatrix} A_1 \\ B_1 \\ A_2 \\ B_2 \\ \cdot \\ \cdot \\ \cdot \\ A_N \\ B_N \end{pmatrix} = T\bar{\xi} = \begin{pmatrix} E^i(\zeta_1) \\ E^i(\zeta_2) \\ E^i(\zeta_3) \\ E^i(\zeta_4) \\ \cdot \\ \cdot \\ \cdot \\ E^i(\zeta_{2N-1}) \\ E^i(\zeta_{2N}) \end{pmatrix} \tag{6.1.7}$$

We now describe the entries of the matrix T. Note that if we define

$$\xi_{2j-1+p} = \begin{cases} A_j & p = 0 \\ B_j & p = 1 \end{cases} \tag{6.1.8}$$

that then the system of equations may be expressed more compactly in the form

$$\sum_{j=1}^{N}\left(\sum_{p=0}^{1} T_{(2\ell-1+q,2j-1+p)}\xi_{2j-1+p}\right) =$$

$$E^i(\zeta_{2\ell-q+1})) \tag{6.1.9}$$

where $q\epsilon\{0,1\}$. If $p = 0$, then for each $q\epsilon\{0,1\}$ we have

$$T_{(2\ell-1+q,2j-1+p)} = \delta_{(j,\ell)} - \int_{z_{j-1}}^{z_j} K(\zeta_{2\ell-q+1}, y)dy \tag{6.1.10}$$

On the other hand if $p = 1$, then again for each $q\epsilon\{0,1\}$ we have

$$\begin{aligned} T_{(2\ell-1+q,2j-1+p)} &= \delta_{(j,\ell)}(\zeta_{2\ell-q+1} - z_\ell^*) \\ - \int_{z_{j-1}}^{z_j} K(\zeta_{2\ell-q+1}, y)dy &- \int_{z_{j-1}}^{z_j} L(\zeta_{2\ell-q+1}, y)dy \\ - \delta_{(j,1)}F(\zeta_{2\ell-q+1}) &+ \delta_{(j,N)}G(\zeta_{2\ell-q+1}) \end{aligned} \tag{6.1.11}$$

Therefore, the solution of the matrix equation (6.1.7)

$$T\bar{\xi} = \vec{E}^i \tag{6.1.12}$$

then gives parameters in an approximate representation of the electric vector of the induced electromagnetic field.

7 Surface Integral Equation Methods

In this section we shall show how in the case where the irradiated structure consists of homogneous regions which are delimited by diffeomorphisms of the interior of spheres in

three dimensional space to represent the solution of the scattering problem as the solution of two combined field integral equations with integral operators formed from from the Green's functions defined on opposite sides of the separating surfaces. The surface integral equation methods reduce the computational complexity in the sense that they require discretization electric and magnetic fields defined on a surface rather than on a region of three dimensional space.

7.1 Combined Field Integral Equations

Consider a set Ω in $\mathbf{R}^3$ with boundary surface $\partial\Omega$ on which are induced electric and magnetic surface currents $\vec{J}_j$ and $\vec{M}_j$. If we have a simple $N+1$ region problem, where we have N inside and a region outside all N bounded homogenous aerosol particles corresponds to the region index j being equal to 1 and the region inside corresponds to j values ranging from 2 to $N+1$, then if the propagation constant k_j in region j is defined also by a function k_j, naturally defined on a Riemann surface as the square root of,

$$k_j^2 = \omega^2\mu\epsilon - i\omega\mu\sigma \tag{7.1.1}$$

For a Debye medium (Daniel, [17]) the branch cuts are along the imaginary ω axis. For a Lorentz medium particle (Brillouin, [4], [55]) the branch cuts are in the upper half of the complex ω plane parallel to the real axis. where μ, ϵ, and σ are functions of frequency that assure causality and that the radiation does not travel faster than the speed of light in vacuum. There are two Helmholtz equations, one for the interior of the particle and the other for the exterior, defined by

$$(\Delta + k_j^2)G_r = 4\pi\delta \tag{7.1.2}$$

where G_j is the temparate, rotationally invariant, fundamental solution ([28]) of the Helmholtz operator. We let

$$J_1 = J = -J_2 \tag{7.1.3}$$

and

$$M_1 = M = -M_2 \tag{7.1.4}$$

where we assume that the surface $S_{(1,2)}$ separates region 1 and region 2. We generalize equations (7.1.3) and (7.1.4) inductively by saying that for any surface $S_{(j,\tilde{j})}$ separating region j from region $\tilde{j}$ where

$$j < \tilde{j} \tag{7.1.5}$$

we have

$$J_j = J = -J_{\tilde{j}} \tag{7.1.6}$$

and

$$M_j = M = -M_{\tilde{j}} \tag{7.1.7}$$

We define

$$\mathcal{I} = \left\{(j,\tilde{j}) : S_{(j,\tilde{j})} \text{ is a separating surface}\right\} \tag{7.1.8}$$

where j is less than $\tilde{j}$. We get a single coupled, combined field integral equation which describes the interaction of radiation with the conglomerate aerosol particle or cluster given by

$$\vec{n} \times \vec{E}^{inc} = \vec{n} \times \sum_{(j,\tilde{j})\in\mathcal{I}} \left\{ \left(\frac{i\omega}{4\pi}\right) \int_{S_{(j,\tilde{j})}} \int \vec{J}(\tilde{r}) \left(\mu_j \cdot G_j(r,\tilde{r}) + \mu_{\tilde{j}} \cdot G_{\tilde{j}}(r,\tilde{r})\right) da(\tilde{r}) \right.$$

$$+ \frac{i}{4\pi\omega} grad \left\{ \int_{S_{(j,\tilde{j})}} \int (div_s \cdot \vec{J}) \left[\frac{G_j(r,\tilde{r})}{\epsilon_j} + \frac{G_{\tilde{j}}(r,\tilde{r})}{\epsilon_{\tilde{j}}}\right] da(\tilde{r}) \right\} +$$

$$\left. \left(\frac{1}{4\pi}\right) curl \left(\int_{S_{(j,\tilde{j})}} \int \vec{M}(\tilde{r}) \cdot \left(G_j(r,\tilde{r}) + G_{\tilde{j}}(r,\tilde{r})\right) da(\tilde{r}) \right) \right\} \tag{7.1.9}$$

In addition to equation (7.1.9) we need equation involving the magnetic vector H^{inc} of the stimulating electromagnetic field which is given by

$$\vec{n} \times \vec{H}^{inc} = \vec{n} \times \sum_{(j,\tilde{j})\in\mathcal{I}} \left\{ \left(\frac{i\omega}{4\pi}\right) \int_{S_{(j,\tilde{j})}} \int \vec{M}(\tilde{r}) \left(\epsilon_1 \cdot G_j(r,\tilde{r}) + \epsilon_2 \cdot G_{\tilde{j}}(r,\tilde{r})\right) da(\tilde{r}) \right.$$

$$+ \left(\frac{i}{4\pi\omega}\right) grad \left\{ \int_{S_{(j,\tilde{j})}} \int (div_s \cdot \vec{M}) \left[\frac{G_j(r,\tilde{r})}{\mu_j} + \frac{G_{\tilde{j}}(r,\tilde{r})}{\mu_{\tilde{j}}}\right] da(\tilde{r}) \right\} +$$

$$\left. \frac{1}{4\pi} curl \left(\int_{S_{(j,\tilde{j})}} \int \vec{J}(\tilde{r}) \cdot \left(G_j(r,\tilde{r}) + G_{\tilde{j}}(r,\tilde{r})\right) da(\tilde{r}) \right) \right\} \tag{7.1.10}$$

Once the coupled combined field system (7.1.9) and (7.1.10) is solved for $\vec{J}$ and $\vec{M}$, the surface electric and magnetic currents respectively and we define the surface electric charge density by ([20], p 7)

$$\rho^e(\tilde{r}) = \frac{i}{\omega} \left[div_s \cdot \vec{J}(\tilde{r})\right] \tag{7.1.11}$$

and the surface magnetic charge density

$$\rho^m(\tilde{r}) = \frac{i}{\omega} \left[div_s \cdot \vec{M}(\tilde{r})\right] \tag{7.1.12}$$

where div_s is the surface divergence. Now for each region index j we define

$$\mathcal{J}(j) = \left\{\tilde{j} : (j,\tilde{j}) \in \mathcal{I}\right\} \tag{7.1.13}$$

where $\mathcal{I}$ is the set of all indices of separating surfaces defined by (7.1.8). We now need to be able to express the electric and magnetic fields inside and outside the scattering body. We first define the vector potentials $\vec{A}_j$ and $\vec{F}_j$ by the rules, ([20] [37])

$$\vec{A}_j = \sum_{\tilde{j}\in\mathcal{J}(j)} \left[\frac{\mu_j}{4\pi} \int_{S_{(j,\tilde{j})}} \int \vec{J}_j(\tilde{r}) \cdot G_j(r,\tilde{r}) da(\tilde{r})\right] \tag{7.1.14}$$

$$\vec{F}_j = \sum_{\tilde{j}\in\mathcal{J}(j)} \left[\left(\frac{\epsilon_j}{4\pi}\right) \int_{S_{(j,\tilde{j})}} \int \vec{M}_j(\tilde{r}) \cdot G_j(r,\tilde{r}) da(\tilde{r})\right] \tag{7.1.15}$$

The scalar potentials are defined in terms of the electric charge density (7.1.11) and magnetic charge density (7.1.12) by the rules,

$$\Phi_j(\tilde{r}) = \sum_{\tilde{j}\in\mathcal{J}(j)} \left[\left(\frac{1}{4\pi\epsilon_j}\right)\int_{S_{(j,\tilde{j})}}\int \rho_j^e(\tilde{r})G_j(r,\tilde{r})da(\tilde{r})\right] \tag{7.1.16}$$

and

$$\Psi_j(\tilde{r}) = \sum_{\tilde{j}\in\mathcal{J}(j)} \left[\left(\frac{1}{4\pi\mu_j}\right)\int_{S_{(j,\tilde{j})}}\int \rho_j^m(\tilde{r})G_j(r,\tilde{r})da(\tilde{r})\right] \tag{7.1.17}$$

We now can define the electric and magnetic vectors inside the region j in terms of these potentials (7.1.14), (7.1.15), (7.1.16), and (7.1.17) by the rules,

$$\vec{E}_j = -i\omega\vec{A}_j(r) - grad(\Phi_j(r) + \frac{1}{\epsilon_j}curl(\vec{F}_j)(r) \tag{7.1.18}$$

and

$$\vec{H}_j = -i\omega\vec{F}_j(r) - grad(\Psi_j(r) + \frac{1}{\mu_j}curl(\vec{A}_j)(r) \tag{7.1.19}$$

Similar equations apply outside the body, by there the fields represented are the differences $\vec{E}_1^s$ and $\vec{H}_1^s$ between the total electric and magnetic vectors and the electric vector $\vec{E}^{inc}$ and the magnetic vector $\vec{H}^{inc}$ of the incoming wave that is providing the stimulation. Thus ([20]) we see that outside the body,

$$\vec{E}_1^s = -i\omega\vec{A}_1(r) - grad(\Phi_1(r) + \frac{1}{\epsilon_1}curl(\vec{F}_1)(r) \tag{7.1.20}$$

and

$$\vec{H}_1^s = -i\omega\vec{F}_1(r) - grad(\Psi_1(r) + \frac{1}{\mu_1}curl(\vec{A}_1)(r) \tag{7.1.21}$$

These equations generalize the formulation of Glisson ([20]) to a three dimensional structure whose regions of homogeneity are diffeomorphisms of the interior of the sphere or a torus in $\mathbf{R}^3$. If the scattering structure is not a body of revolution, then the region may be a diffeomorph of an N handled sphere.

8 Potential Benefits

The fact that the implementation of these ideas would provide a machine precision integral equation formulation of electromagnetic interaction problems means that using carefully designed sources one could develop a means of focusing microwaves on a cancer tumor within the human body, and destroy the tumor by raising its temperature 4 degrees without harming the nearby normal tissue. This would bring the cost of harmless cancer treatment down to the level the working person.

The fact that this problem can be solved for anisotropic structures means that we have a practical means of optimally designing liquid crystal television sets and video displays.

thereby making the home environment less hazardous for inner city children who spend so much time with television and those who work with video display monitors. The reprogramming of these new safer devices will stimulate the economy by providing many new jobs.

The successful determination of an order $N^{2+\epsilon}$ matrix inversion algorithm, will assist us in the development of dynamical system models kinetic type models of world peace, which will include models that provide this nation and other nations with resource management plans for economic and ecological stability and medical care and food distribution as well as optimal running of coorporations and the design of very large systems. Also, the key part of the globally convergent homotopy method, with its myriad of design application potentials such the design of a magnet and irradiation configuration that would increase the absorption efficiency of a plasma in a fusion reactor by a factor of a billion or so, is the inversion of matrices.

The implementation of the explosion models would give us a way of tracking the results of effluent from power plants and show the efficacy or safety flaws in the design of installations for burning toxic materials.

References

[1] Barber, P. W., Om P. Gandhi, M. J. Hagmann, Indira Chatterjee. "Electromagnetic Absorption in a Multilayer Model of Man" *IEEE Transactions on Biomedical Engineering. Volume BME - 26, Number 7* (1979) pp 400-405

[2] Barkeshi, S. "Eigenvalues and Eigenvectors of General Gyroelectric Media" *IEEE Transactions on Antennas and Propagation. Volume 40, Number 3* (March, 1992) pp 340 - 344

[3] Boyse, W. E. and A. A. Seidl. "A Hybrid Finite Element Method for Near Bodies of Revolution" *IEEE Transactions on Magnetics. Volume 27, No. 5* (September, 1991) pp 3833 - 3836

[4] Brillouin, Leon. *Wave Propagation and Group Velocity.* New York: Academic Press (1960).

[5] Burr, John G., David K. Cohoon, Earl L. Bell, and John W. Penn. Thermal response model of a Simulated Cranial Structure Exposed to Radiofrequency Radiation. *IEEE Transactions on Biomedical Engineering. Volume BME-27, No. 8* (August, 1980) pp 452-460.

[6] Barrera, R. G., G. A. Estevez, and J. Giraldo. "Vector Spherical Harmonics and Their Application to Magnetostatics" *Journal of Physics. Vol 6* (1985) pp 287 - 294

[7] Calderon, A. P. and A. Zygmund. "On the Existence of Certain Singular Integrals" *Acta Mathematica Volume 88* (1985) pp 85-139

[8] Cohen, L. D., R. D. Haracz, A. Cohen, and C. Acquista. "Scattering of light from arbitrarily oriented finite cylinders." *Applied Optics. Volume 21* (1983) pp 742 - 748.

[9] Cohoon, D. K. "Uniqueness of Solutions of Electromagnetic Interaction Problems Associated with Scattering by Bianisotropic Bodies Covered with Impedance Sheets" *IN* Rassias, George M. (Editor) *The Mathematical Heritage of C. F. Gauss* Singapore: World Scientific (1991) pp 119-132

[10] Cohoon, D. K., J. W. Penn, E. L. Bell, D. R. Lyons, and A. G. Cryer. *A Computer Model Predicting the Thermal Response to Microwave Radiation SAM-TR-82-22* Brooks AFB, Tx 78235: USAF School of Aerospace Medicine. (RZ) Aerospace Medical Division (AFSC) (December, 1982).

[11] Colton, David and Rainer Kress. *Integral Equation Methods in Scattering Theory* New York: John Wiley and Sons (1983)

[12] Cooray, M. F. R. and I. R. Ciric. "Electromagnetic scattering by a system of two parallel dielectric prolate spheroids" *Canadian Journal of Physics. Volume 68* (1990) pp 376 - 384.

[13] Cooray, M. Francis and Ioan R. Ciric. "Electromagnetic wave scattering by a system of two spheroids of arbitrary orientation" *IEEE Transactions on Antennas and Propagation. Vol. 37, No. 5* (May, 1989) pp 608 - 618.

[14] Cwik, Tom, Jonathan Partee, and Jean Patterson. "Method of Moment Solutions to Scattering Problems in a Parallel Processing Environment" *IEEE Transactions on Magnetics, Volume 27, No. 5* (September, 1991) p 3837.

[15] Dalmas, J. "Diffusion d'une onde electromagnetique par un ellipsoide de revolution allonge de conduction infinie en incidence non axiale" *Optica Acta, Vol 28, No. 7* (1981) pp 933 - 948

[16] Dalmas, J. and R. Deleuil. "Diffusion d'une onde electromagnetique par un ellipsoide de revolution allonge et par un demi ellipsoide pose sur un plan en incidence axiale" *Optica Acata, Vol 27, No. 5* (1980) pp 637 - 649

[17] Daniel, Vera V. *Dielectric Relaxation* New York: Academic Press (1967).

[18] Ewing, Richard E. "Mathematical Modeling and Large Scale Computing in Energy and Environmental Research" *IN* R. E. Ewing, K. I. Gross, and C. F. Martin (Editors) *The Merging of Disciplines: New Directions in Pure, Applied, and Computational Mathematics* New York: Springer Verlag (1985)

[19] Friedman, Avner. *Free Boundary Value Problems* New York: Wiley (1982)

[20] Glisson, A. K. and D. R. Wilton. "Simple and Efficient Numerical Techniques for Treating Bodies of Revolution" University of Mississippi: University, Mississippi USA 38677 *RADC-TR-79-22*

[21] Gohberg, I. C. and I. A. Feldman. *Convolution Equations and Projection Methods for their Solution* Providence: American Mathematical Society (1974)

[22] Guru, Bhag Singh and Kun Mu Chen. "Experimental and theoretical studies on electromagnetic fields induced inside finite biological bodies" *IEEE Transactions on Microwave Theory and Techniques. Volume MTT-24, No. 7* (1976).

[23] Hagmann, M. J. and O. P. Gandhi. "Numerical calculation of electromagnetic energy deposition in man with grounding and reflector effects" *Radio Science Volume 14, Number 6* (1979) pp 23 -29

[24] Hagmann, M. J. and O. P. Gandhi. "Numerical calculation of electromagnetic energy deposition for a realistic model of man." *IEEE Transactions on Microwave Theory and Techniques Volume MTT-27, Number 9* (1979) pp 804-809.

[25] Hagmann, M. J. and R. L. Levin. "Nonlocal energy deposition - - problem in regional hyperthermia" *IEEE Transactions on Biomedical Engineering. Volume 33* (1986) pp 405 - 411.

[26] Haracz, Richard, D. Leonard D. Cohen, and Ariel Cohen. "Scattering of linearly polarized light from randomly oriented cylinders and spheroids." *Journal of Applied Physics. Volume 58, Number 9* (November, 1958) pp 3322 - 3327.

[27] Hochstadt, Harry. *The Functions of Mathematical Physics.* New York: Dover(1986).

[28] Hörmander, Lars. *Linear Partial Differential Operators* New York: Academic Press (1963)

[29] Hunt, J. C. R. and J. S. Puttick and W. H. Snyder. "Turbulent diffusion from a point source in stratified and neutral flows around a three dimensional hill – part I diffusion equation analysis" *Atmospheric Environment. Vol 13* (1979) pp 1227 - 1239.

[30] Jaggard, D. L. and N. Engheta. *Chirosorb^{TM}* as an invisible medium. Electronic Letters. Volume 25, Number 3 (February 2, 1989) pp 173-174.

[31] Jain, Romesh K. *Generation of Body Fitted Grids for Two Dimensional Interior Problems by the Solution of a System of Poisson Equations using Multigrid Methods* Darmstadt: Gesellschaft fur Mathematik und Datenverarbeitung mbH (1987)

[32] Kleinman, R. E. "Low frequency electromagnetic scattering" In P. L. Uslenghi (Ed) *Electromagnetic Scattering* New York: Academic Press (1978)

[33] Li, Shu Chen. Interaction of Electromagnetic Fields with Simulated Biological Structures. Ph.D. Thesis(Temple University, Department of Mathematics 038-16, Philadelphia, Pa 19122) (1986). 454 pages

[34] Lindell, Ismo V. and Ari J. Viitanen. "Duality Transformations for General Bi-Isotropic (Nonreciprocal Chirai) Media" *IEEE Transactions on Antennas and Propagation, Volume 40, No. 1* (January, 1992) pp 91 -95

[35] Lipanov, A. M. and A. V., Vakhrushev. "Problem of Powder material dispersion by an explosion" *Soviet Applied Mechanics. Volume 27 No. 2* (1991) pp 154 - 160

[36] Livesay, D. E. and Kun-Mu Chen. "Electromagnetic fields induced inside arbitrarily shaped biological bodies" *IEEE Transactions on Microwave Theory and Techniques. Volume MTT-22, Number 12* (1974) pp 1273 - 1280.

[37] Mautz, J. R. and R. F. Harrington. "Radiation and Scattering from bodies of revolution" *Applied Science Research. Volume 20* (June, 1969) pp 405-435.

[38] McCartin, B. J. and J. F. Dicello. "Three Dimensional Finite Difference Frequency Domain Scattering Computation Using the Control Region Approximation" *IEEE Transactions on Magnetics, July 1989* pp 3092 - 3094.

[39] McCormick, Stephen F. "Multilevel Projection Methods for Partial Differential Equations" Philadelphia, PA: Society for Industrial and Applied Mathematics (1992)

[40] Mendoza, Eric. "Ampere's experimental proof of his law of induction: $I_2 \sim I_1$" *Journal of Physics 6* (1985) pp 281 - 286

[41] Neittaanmaki, Pekka and Jukka Saranen. "Semi - discrete Galerkin approximation methods applied to initial boundary value problems for Maxwell's equations in anisotropic inhomogeneous media." *Proceedings of the Royal Society of Edinburgh. Volume 89 A* (1981) pp 125 - 133.

[42] Peterson, Thomas W. and John H. Seinfeld. "Mathematical Model for Transport, Interconversion, and Removal of Gaseous and Particulate Air Pollutants - Application to the Urban Plume" *Atmospheric Environment, Volume 11* (1977) pp 1171 - 1184

[43] Ramm, A. G. "Numerical solution of integ quations in a space of distributions." *Journal of Mathematical Analysis and Applications. Volume 110* (1980) pp 384-390

[44] Ramm, A. G. *Theory and applications if some new classes of integral equations* New York: Springer Verlag (1980)

[45] Rappaport, Carey M. and Edward B. Smith. "Anisotropic FDFD Computed on Conformal Meshes" *IEEE Transactions on Magnetics. Volume 27, Number 5* (September, 1991)

[46] Rappaport, C. M. and B. J. McCartin. "FDFD Analysis of Electromagnetic Scattering in Anisotropic Media Using Unconstrained Triangular Meshes" *IEEE Transactions on Antennas and Propagation, Volume AP-39, No. 3* (March, 1991) pp 334 - 349

[47] Ruppin, R. "Electromagnetic Scattering From Finite Dielectric Cylinders" *Journal of Physics D. Applied Physics 23* (1990) pp 757 - 763

[48] Russell, T. F. *An Incomplete Iterated Characteristic Finite Element Method for a Miscible Displacement Problem* Chicago: University of Chicago Ph.D. Thesis (1980)

[49] Saranen, Jukka. "On generalized harmonic fields in domains with anisotropic homogeneous media." *Journal of Mathematical Analysis and Applications. Volume 88, Number 1* (1982) pp 104 - 182.

[50] Saranen, Jukka. *Some remarks about the convergence of the horizontal line method for Maxwell's equations* Jyvaskyla 10, Finland: University of Jyvaskyla Department of Mathematics. Report 23 (1980)

[51] Seigneur, Christian and Pradeep Saxena. "Diffusion and Reaction of Pollutants in Stratus Clouds: Application to Nocturnal Acid Formation in Plumes" *Environmental Science Technology. Volume 19* (1985) pp 821 - 828.

[52] Sheih, C. M. "Mathematical Modeling of Particulate Thermal Coagulation and Transport Downstream of an Urban Area Source" *Atmospheric Environment, Volume 11* (1977) pp 1185 - 1190.

[53] Shepherd, J. W. and A. R. Holt. "The scattering of electromagnetic radiation from finite dielectric circular cylinders." *Journal of Physics A. Math. Gen. 16* (1983) pp 651-652.

[54] Sinha, B. P. and R. H. MacPhie. "On Electromagnetic Plane Wave Scattering by a Prolate Spheroid" *Canadian Journal of Physics. Volume 58*(1980) pp 25 - 30.

[55] Sherman, George C. and Kurt Edmund Oughston. "Description of pulse dynamics in Lorentz media in terms of energy velocity and attenuation of time harmonic waves." *Physical Review Letters, Volume 47, Number 20* (November, 1981) pp 1451 - 1454.

[56] Shifrin, K. S. *Scattering of Light in a Turbid Medium.* Moscow - Leningrad: Gosudarstvennoye Izdatel'stvo Tekniko - Teoreticheskoy Literatury Moscow Leningrad (1951)

[57] Tsai, Chi-Taou, Habib Massoudi, Carl H. Durney, and Magdy F. Iskander. A Procedure for Calculating Fields Inside Arbitrarily Shaped, Inhomogeneous Dielectric Bodies Using Linear Basis Functions with the Moment Method. *IEEE Transactions on Microwave Theory and Techniques, Volume MTT-34, Number 11* (November, 1986) pp 1131-1139.

[58] Uzunoglu, N. K. and N. G. Alexopoulos and J. G. Fikioris. "Scattering from thin and finite dielectric cylinders" *Journal of the Optical Society of America. Volume 68, Number 2* (1978) pp 194 - 197.

[59] Uzunoglu, N. K. and A. R. Holt. "The scattering of electromagnetic radiation from dielectric cylinders" *Journal of Physics A. Math. Gen. Volume 10, Number 3*

[60] Whittaker, E. T. and G. N. Watson. *A Course of Modern Analysis* London: Cambridge University Press (1986)

II. AEROSOL CHARACTERIZATION METHODS

Moderator: Jerold Bottiger

U.S. Army Edgewood Research,
Development and Engineering Center
Attn: SCBRD-RTB
Aberdeen Proving Ground MD

Blank

A. SAMPLING, NEPHELOMETRY AND INVERSION

QUASI-BINARY DECISION MAKING: A SPEEDUP

Wei Cai, Xiao-shen Li, and M. Lax

Department of Physics, City College of the City University of New York, New York, New York 10031

RECENT PUBLICATIONS

[a]P. Hu, M. Lax, "Quasi-Binary Decision Making: An Update" Proceedings of the 1992 CRDEC Scientific Conference on Obscuration and Aerosol Research.

[b]P. Hu, M. Lax, "Quasi-Binary Decision Making Using Light Scattering", in Proceedings of the 1991 CRDEC Scientific Conference on Obscuration and Aerosol Research.

[c]P. Hu, M. Lax, "Single Scattering Inversion Problem", in Proceedings of the 1990 CRDEC Scientific Conference on Obscuration and Aerosol Research.

[d]B. Yudanin, M. Lax, "POST Adaptation for a Numerical Solution of the Spherically-Symmetric Riemann Problem," J. Mod. Phys. 4, 285-298 (1990).

[e]B. Yudanin, P. Hu, M. Lax, "Numerical Solution of the Riemann Problem in the Presence of an External Energy Source", in Proceedings of the 1988 CRDEC Scientific Conference on Obscuration and Aerosol Research.

[f]M. Lax, B. Yudanin, "Early-Time Hydrodynamic Response to Pulsed Laser Radiation," Digest - Intl. Conf. on Optical and Millimeter Wave Propagation and Scattering in the Atmosphere. Florence, Italy, 1986.

[g]B. Yudanin, M. Lax, "Hydrodynamical Response to Uniform Laser Absorption in a Droplet," in Proceedings of the CRDC 1985 Scientific Conference on Obscuration and Aerosol Research, edited by R. H. Kohl and D. Stroud (1985).

ABSTRACT

Can a very limited number (5-20) of polarized light scattering measurements from spherical droplets be used to distinguish between a uniform droplet and one with a shell-like structure (described by only two indices of refraction)? Can it be done if the shell inner radius is 90% of the outer radius, and if the uniform droplets have an index of 1.33? What if the measurements have errors of 5% or 10%? Can it be done if the droplet radii are permitted to range from .1μ to 10μ. Conversely, what measurement information (with what accuracy) is needed to make decisions within a given range of parameters? How are these answers affected by limitations of computer time and available disk space?

1. Redefinition of the Problem

If one starts with an enormous permitted range of parameters, a limited number of measurements with limited accuracy, and finite computational strength, one will be unable to solve the decision problem. We have therefore chosen to reverse the question. With a given amount of measurement information, e.g. five intensities, over what range of permitted parameters will a decision be possible?

During this initial phase, the amount of computation is modest. However, a shell is, in full generality, a point in a four parameter space (two radii and two indices). We have found that each added parameter multiplies both the computation time, and the required storage by a factor of 100. We start, however, by assuming that we have an arbitrary amount of CPU time available, and ask if a solution can be obtained at all.

The problem can be rephrased in a useful way by asking with a given amount of resources (number of measurements and computer time) over what range of parameters is such a discrimination possible?

2. Why is the Problem So Hard?

Although our problem is one of detection, namely the choice of sphere or shell, this is preceded by an estimation problem: Assuming that the scatterer is a sphere, what is the best

parameter set $\eta = R, m$ that fits the observed data? Here R is the sphere radius, and m is the index of refraction of the sphere.

Then, one must assume that the scatterer is a shell described by the four parameter set: $\eta = R_{out}, R_{in}, m_{shell}, m_{core}$. Again, estimate the point η, now in a four parameter space that best fits the data. Finally, one must ask is the fit to the sphere sufficiently better than to the shell (or vice-versa) that we can make a clear decision as to the nature of the scatterer.

The Estimation Problem

In our preliminary work, a least squares estimation procedure is used. We calculate the (theoretical) scattering intensities $I(\theta_i, \eta^k)$ over the permissible space in η. For k=1 this is the two dimensional space of the radius R_s and index m_s of a sphere. For k=2, η ranges over the permissible values in the four dimensional space $R_{out}, m_{out}, R_{in}, m_{in}$, where the shell is bounded by the inner and outer radii, the core is bounded by the inner radius, and $m_{out} = m_{shell}$ and $m_{in} = m_{core}$. With $I(\theta_i, \eta^*)$ the experimental intensity at angle θ_i and (unknown parameters η^*) the function

$$v(\eta^k) = \left(\sum_{i=1}^{M} [\bar{I}(\theta_i, \eta^*) - I(\theta_i, \eta^k)]^2\right) \tag{1}$$

to be minimized over the domain of η^k. In our simulation, we actually start from a particular point η^* and then add noise comparable to that in the measurement process (5 or 10%).

To illustrate how difficult the minimization procedure is, we consider the spherical case and plot the logarithm

$$F(\eta^1) = \ln v(\eta^1) \tag{2}$$

Because our parameter space extends to $R/\lambda = 8$ or size parameter of about 50, $v(\eta)$ oscillates rapidly, and over a wide range of amplitudes. The use of the logarithm is needed to make the plot in Fig. 1 feasible. The difficulty of locating the minimum in the figure is evident.

The Decision Problem

Let us describe the results of performing the minimization procedure by

$$\nu_k = \min_{\eta^k} \nu(\eta^k) \tag{3}$$

where ν_1 describes the best fit using spherical parameters and ν_2 describes the best fit using shell parameters. We then found it expedient to introduce a single decision parameter:

$$R = \log_{10}(\nu_1/\nu_2) \tag{4}$$

By employing Bayesian procedures, or a version of maximum likelihood methods[1] we arrived at a decision algorithm, namely a way to compute a parameter $\bar{R}$ such that $R > \bar{R}$ implies the choice of a shell, and the converse implies the choice of a sphere. This parameter will, in general, be close to zero.

3. Previous results

The first attempt[1] compared a sphere with known radius of 2.5μ and an index between 1.33 and 1.55 with a shell of outer radius 2.5μ and inner radius between 1.76 and 2.2μ. The core index was assumed to be 1.33 and the shell index 1.55. Both cases have only one free parameter, and 5 measurements were found sufficient to distinguish between the two cases.

Another case considered was a sphere with index an a shell with indices 1.33 an 1.55. The radius of the sphere an the outer radius of the shell were assumed identical. The inner radius was assumed to be .9 of the outer radius of the shell and the latter was assumed to be identical to that of the uniform sphere. The latter was permitted the wide range from Again 5 measurements were found adequate for this one parameter case.

Our second attempt[2] was made with a two parameter description of the sphere and a three parameter description of the shell. This was accomplished by assuming that the outer radius of the shell was known. The parameters, and the results are shown in Fig. 2.

Because of the third parameter, we felt it necessary to use 12 intensity measurements. Moreover, an increase of a factor of 100 in computing time was needed. The calculation was therefore shifted to a Cray.

By precomputing a table of Bessel functions and using interpolation to get the desired values during a least-square parameter determination, the computation time was reduced from 20 hours on a Cray to 2 hours on a Cray.[2] The small overlap between the two peaks in Fig. 2 demonstrates that the region of indecision is small.

We then turn to the case of a shell described by two radii and two indices. Another increase of a factor 100 in CPU time was needed. Calculations initiated by Po Hu attempted to reduce the large CPU time (even on the Cray) by making use of vectorization and dealing with 1,000 drops simultaneously.

The calculations were extended to the case of a four parameter description of the shell by using only a random sample of points in the four parameter space.[3] The results shown in Figure 3 using 1,000 "experimental" droplets and 12 measurements on each demonstrate that a decision is feasible for the parameter ranges shown in the figure.

4. Need for a New Procedure

The procedure of calculating 1,000 droplets simultaneously to take advantage of vectorization on a Cray was useful to test feasibility. It is an unacceptable procedure to use in the field. There one wishes to compute one drop at a time, and determine whether or not it is a shell. It is not acceptable to wait for 1,000 droplets before one begins computing.

One of us (ML) then proposed precomputing as much as possible. It does not matter how long the precomputation takes, as long as the testing of an individual droplet can be done in nearly real time, by comparing with precomputed data.

What about the limiting case, in which one precomputes everything? Table I shows that we used about 70 million sample points in the 4 dimensional parameter space of the shell. For each such point, we need 12 measurements. This information takes a Gigaword of storage. That is difficult but not prohibitive. But to search such a huge database seems prohibitive.

We then sought a compromise. Can we use a precomputed database to obtain part of the information about the particular droplet, for example, the permissible range of outer radius? The final least squares fit on a particular droplet can then be made by doing those Mie scattering calculations only within the permitted ranges.

5. The Cai Procedure

Wei Cai came up with an ingenious way of storing the precalculated data in such a way

that it is economical of computer space, and is quickly searchable. All points of a fine mesh in the two or four dimensional parameter space are chosen, and twelve Mie scattering intensities are computed for each point. However, the intensities (which take a word each) are not recorded. Instead, the intensity range is divided up into 80 regions each corresponding to a 10% range of intensities. One file is associated with each of these intensity ranges. At the same time, see Table 1, the parameter space of 69,120,000 points is divided up into 960,000 cells, each of which contains 72 points. Each file will contain 960,000*2 bytes, since each pair of bytes (an "address" for one cell) will hold 12 pieces of intensity information in bit form. If any of the 72 points within that cell gives an intensity in the range for file 51, for measurement 3, then the third bit in the address for that cell in file 51 will be set to 1, otherwise to 0.

Thus 12 pieces of information about 69,120,000 points that would take 829 Megawords to store, are summarized in 80 files requiring a total of 154 Megabytes (a factor 80 reduction on a Cray). The price one pays for this, is that the Mie scattering must be recomputed as needed.

For a given set of 12 measurements one can then determine which cells contain possible fits by searching the above files. Note that we don't store the intensities themselves which require a word apiece, but only bits that reveal where such intensities may be found. Compatibility with all 12 measurements eliminates most cells, leaving only a small fraction. For these cells, say 1/1000 of the total number, one can perform the Mie scattering calculations and determine which of the individual points gives the best fit.

The computation of the database takes many hours of Cray CPU time. But that is irrelevant. The search and minimization over the restricted set of cells can now be performed in seconds. And this is the only part that need be performed on an actual test droplet. Our preliminary results show that a factor 1,000 reduction has been made in the vital second stage of the calculation.

Note that by using a larger number of cells, and a smaller number of points within each cell, the final minimization will be faster. This trade off, however, requires (1) more disk space available than the 150 Mbytes we have used, and (2) the time for selecting the permissible cells increases.

We start with a discrete space containing about 70 million points (69,120,000), see table I. When we ask which point in this 4D space gives the best fit to the "measured" data, we often find an exact match to the starting point. We can't expect the fit to be perfect because noise has been added to the intensity calculate by Mie scattering to provide the "experimentally

measured" data.

6. Results of Calculations Using the New Procedure

The tables I and II, separately, indicate how the parameter spaces of 2D and 4D are divided. Optimization for division into cells and choosing the number of points in each cell is that the time for selecting permissible cells should nearly equal the time for detailed Mie scattering calculations. Due to limitation of our hard disk space, in our design the latter is still about 3 times of former. Most of the running time in building a 4D database is expended on the Mie scattering calculation at all 69,120,000 points in parameter space. It takes 38000 seconds on CRAY-YMP. This precomputation is done once. Having the database, if a pseudo-experimental data is given, suppose with a $\pm 5\%$ noise, it takes only 10 seconds to search the database to determine which cells are possible. Then it takes another 28 seconds (on average) to do the detailed Mie scattering calculation on points inside these possible cells, and to find the best fitting point in the parameter space. Since only about 1/1000 of cells (on average) are found to be permissible, a factor of 1000 reduction has been made. With a $\pm 10\%$ noise, about 78 (average) seconds are needed, since more files need to be searched and more cells are possible. Compared with the 4D case, the running time for the 2D case is negligible, so we can cover the 2D parameter space with many points.

We found that in most of 4D cases, the best fitting points obtained are exactly the points we started with as pseudo-data. Among 1000 tries, no mismatches were found for $\pm 5\%$ noise case and 8 mismatches for $\pm 10\%$ noise case were found, but at points close to the starting points. Because of very fine meshes in the 2D space, there are many mismatches, but all are near the starting points. We can assert from above results that, at least for the assigned range of parameters, especially $4 < R/\lambda < 8$, inversion could be successful. The reason for this, we think, is that strong oscillations of intensity with parameters is of benefit for inversion. For very small drops, inversion may be difficult as shown by Bottiger.[4]

Fig. 4 and Fig. 5 show the event distribution as a function of $\log_{10}(\nu_1/\nu_2)$, separately, for noise $\pm 5\%$ and for noise $\pm 10\%$, with ν_1 the minimum fitting error for sphere case and ν_2 the minimum fitting error for shell case. We see that no crossing appears, so all decisions (total 4000 tries) for distinguishing a shell or a uniform sphere in our tests are correct. Since we do a search of possible cells before do a least square fit, it is possible, when the input pseudo-data is

shell-like (4D), that not a single cell in 2D space is actually possible! This is true for 963 events among 1000 for noise ±5%) and 648 for noise ±10%, as shown on the right side of Fig. 4 and Fig. 5.. Certain shell data are thus found almost impossible to match with any spherical parameters.

7. Conclusions

The impossible dream of doing the calculation on a portable computer in nearly real time seems to be within reach. For this stage, it would be desirable to have a fast workstation with an extra disk of 1 or 2 Gbytes to hold our special database. Such disks are now quite inexpensive (slightly more than $1,000 per Gbyte. But we also need a fast CPU so that the turnaround time in testing is reasonable. Further improvement, of another factor of 10 is needed to realize the dream. Part of this may be achieved by optimizing the code. Part may be achieved by choosing the most favorable angles at which to make the measurements. See figure 4. Another part may come from the increased speed of today's (and tomorrow's) workstation. Can we guarantee success? Of course not. But the success, so far, suggests that an attempt at further improvements is worthwhile.

8. Acknowledgements

This work was supported principally by the Army Research Office, and by CRDEC (the Chemical Research Development and Engineering Center at Edgewood Arsenal). Incidental support was also received from the Department of Energy.

[1]P. Hu and M. Lax, "Single Scattering Inversion Problem", in Proceedings of the 1990 CRDEC Scientific Conference on Obscuration and Aerosol Research.

[2]P. Hu, M. Lax, "Quasi-Binary Decision Making Using Light Scattering", in Proceedings of the 1991 CRDEC Scientific Conference on Obscuration and Aerosol Research.

[3]P. Hu, M. Lax, "Quasi-Binary Decision Making: An Update" Proceedings of the 1992 CRDEC Scientific Conference on Obscuration and Aerosol Research.

[4]J. R. Bottiger, "Sizing spheres with the submicron particle analyzer" Proceedings of the 1991 CRDEC Scientific Conference on Obscuration and Aerosol Research, p125.

TABLE I. INVERSION FOR SHELL-LIKE DROP (4D)

	range	divisions	cells	points
inner-index	1.33-1.55	40	20	2
outer-index	1.6 - 1.8	40	20	2
in/out radius	0.7 – 0.9	90	30	3
outer radius	4 - 8 (R/λ)	480	80	6
Totals		69,120,000	960,000	72
Running on CRAY-YMP for noise ± 5% (Sec)	(†)38000		(%)10 + 28 = 38	
Running on CRAY-YMP for noise ± 10% (Sec) for noise ± 10%	(†)38000		17 + 61 = 78	
Size of database		960000*2*80=153,600,000 bytes		

(†) Direct use of the Mie formula to find the point best fitting 12 "experimental" intensities takes 38000 seconds.

(%) Average time for searching possible cells is 10 sec, for scanning the best point is 28 sec.

A speed-up by a factor ≈ 1000 for noise ±5%; 500 for ±10%.

TABLE II. INVERSION FOR SPHERE-LIKE DROP (2D)

	range	divisions	cells	points
index	1.33-1.8	500	100	5
radius	4 - 8 (R/λ)	2000	200	10
Totals		1,000,000	20,000	50
Running on CRAY-YMP for noise ± 10% (Sec)	(†)38000		7	
Size of database		20,000*2*80=3,200,000 bytes		

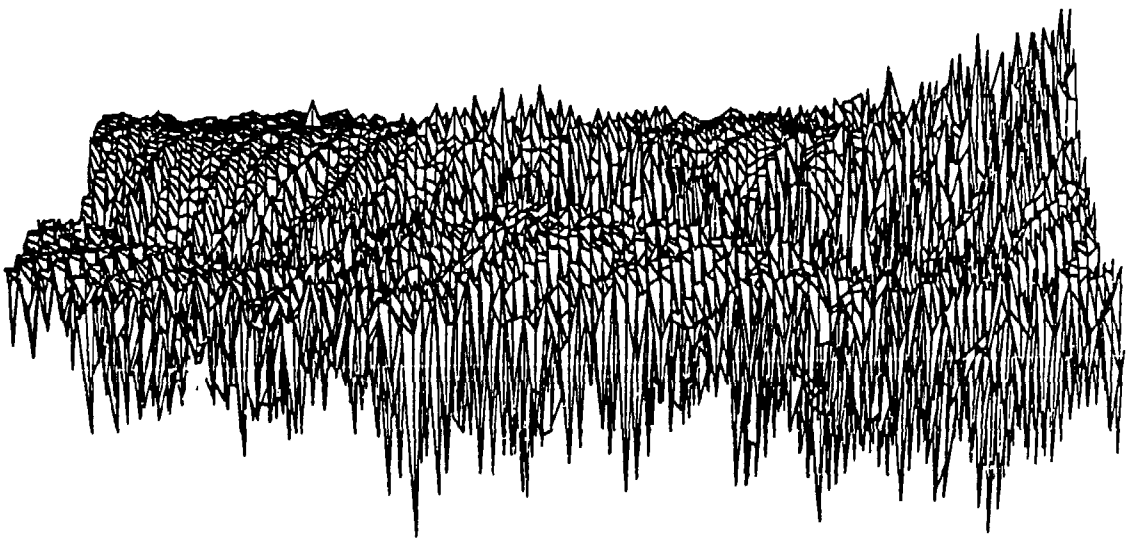

Fig. 1. Function $F=\ln(\sum_{i=1}^{M}[\tilde{i}(\theta_i,\eta^*)-i(\theta_i,\eta^0)]^2)$ is plotted over the permitted parameter space. The source intensities $\tilde{i}(\theta_i,\eta^*)$ are generated from a parameter point for a uniform sphere $m^*=1.515$ and $r^*/\lambda=6.98$. The fitting hypothesis is chosen as the correct hypothesis (uniform sphere), and the permitted parameter range is $m_s=[1.33,1.8]$ and $r_s/\lambda=[4,8]$. 100 mesh points are taken for both m_s and r_s. This figure displays the difficulty of finding a global minimum when large size parameters are permitted.

TWO-THREE PARAMETER FIT

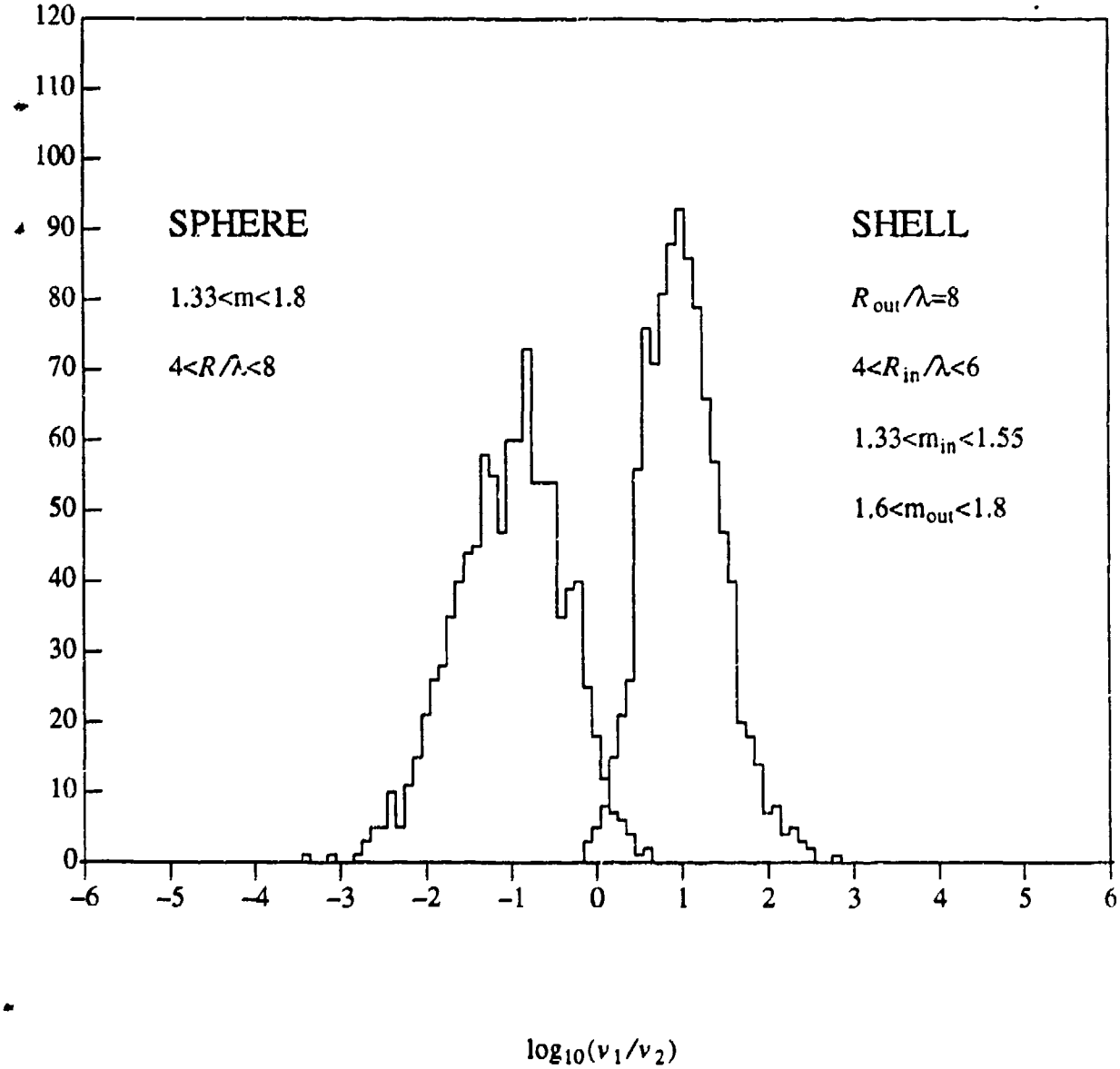

Fig. 2. Histograms based on 1000 droplets.
Fits based on H and V polarized detection at θ=90, 105, 120, 135, 150, 165.

TWO-FOUR PARAMETER FIT

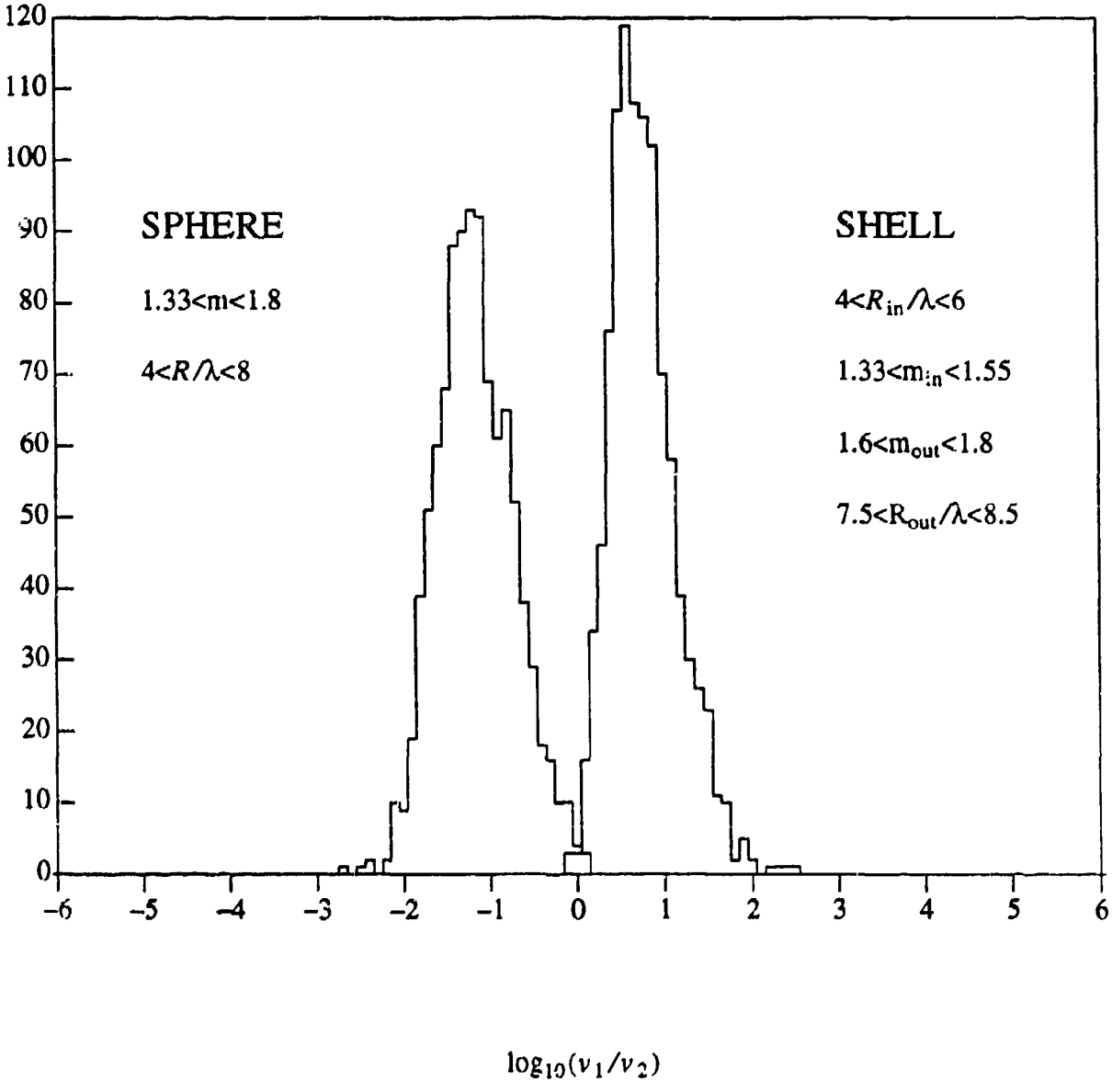

Fig. 3. Histograms based on 1,000 droplets.
Fits based on H and V polarized detection at θ=90, 105, 120, 130, 145, 160.

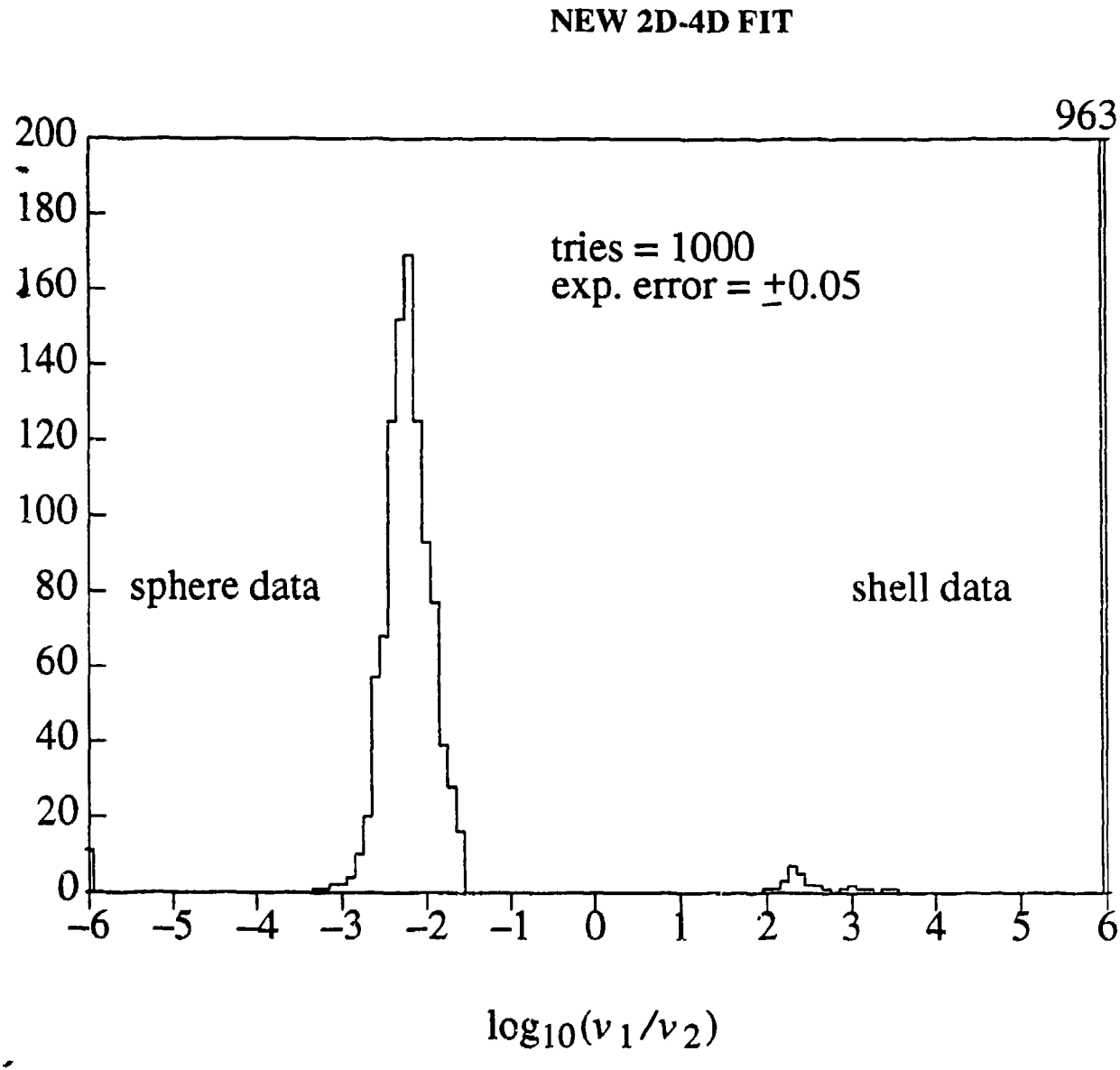

Fig. 4. Histograms (1,000 sphere droplets, 1,000 shell droplets)
Fits based on H and V polarized detection at θ=115, 125, 135, 145, 155, 165 .

For shell data, there are no mis-match cases.
For sphere data, there are 47 mis-match cases.
The output" point is always in the neighborhood of the input point.

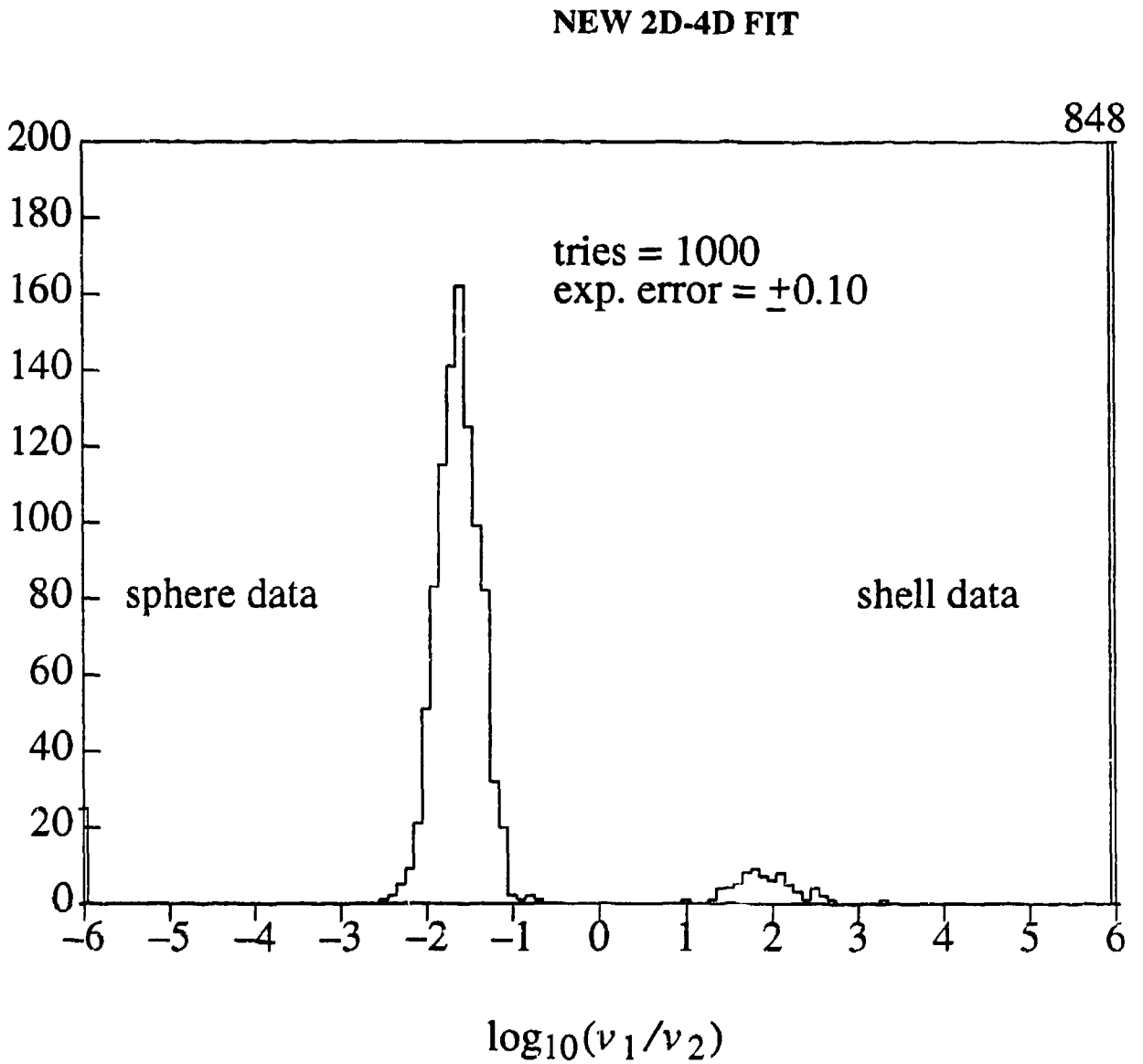

Fig. 5. Histograms (1,000 sphere droplets, 1,000 shell droplets)
Fits based on H and V polarized detection at θ=115, 125, 135, 145, 155, 165 .

For shell data, there are 8 mis-match cases.
For sphere data, there are 221 mis-match cases.
The output point is always in the neighborhood of the input point.

SPHERICAL AND NONSPHERICAL AEROSOL AND PARTICULATE CHARACTERIZATION USING OPTICAL PATTERN RECOGNITION TECHNIQUES

Martin S. Marshall

US Army Dugway Proving Ground
Instrumentation Branch
Dugway, UT 84022

Robert E. Benner and Ronald K. Meyer

University of Utah
Electrical Engineering Department
Salt Lake City, UT 84112

RECENT PUBLICATIONS AND PRESENTATIONS

Martin S. Marshall, Robert E. Benner and Ronald K. Meyer, "Smoke and Obscurant Characterization using a Holographic Ring-Wedge Detector and Optical Neural Networks," *Smoke/Obscurant Symposium XVII*, April 1993.

Martin S. Marshall and Robert E. Benner, "Spherical and Nonspherical Particle Characterization using a Holographic Ring-Wedge Detector-Optical Neural Network Combination," *Optical Information Processing Systems and Architectures IV*, B. Javidi, Editor, Proc. SPIE **1772**, 251-257 (1992).

Marshall, M. S., and R. E. Benner, "Sizing Opaque Spherical Particles using Classical Matched Filters and Holographic Ring Detectors," Opt. Eng. **31**, 947-955 (1992).

ABSTRACT

This study includes three standard classes of unclassified military smokes and obscurants: 1) Standard liquid aerosol smokes, 2) Fibrous obscurants, and 3) Infrared obscurants. Digital and optical implementations of the holographic ring detector directly coupled into an optical neural network are studied as a means of increasing the speed of the decision process for particle characterization. Additional work completed utilizing a holographic ring-wedge detector and an optical neural network combination for characterizing the particulates is included in this study is described. The latter method has the ability to simultaneously recognize and distinguish the spherical and nonspherical particle groups and to give a size range for spherical particles. Single holographic optical elements fabricated to perform the same functions as a ring detector and a simple two-layer, feedforward optical neural network are evaluated. Future work will include expanding the capabilities of the system to include more particulate types and to develop a field competent system.

INTRODUCTION

Since the introduction of complex spatial filtering using the classical matched filter[1] (CMF), the optical correlator has been used for numerous functions[2-5], but its potential for particle sizing has not yet been fully exploited. Particle sizing is important for many applications including quality control, atmospheric chemistry, cell sorting[4,5], and smoke testing[6,7]. Other optical methods for particle sizing include direct imaging[8], holographic imaging[8,9], Fraunhofer diffraction[10,11], and light scattering[12-14].

The use of a ring-wedge detector (RWD) and a neural network (NN) software package combination for pattern recognition has been introduced by George et al.[15] who briefly mention four possible applications of a RWD-NN combination. More recently a RWD was used to drive a series of LEDs, laser diodes or a 1-D spatial light modulator as the input to an optical neural network[16] (ONN) and an optical associative processor[17-18]. Yee and Ho[19] used the outputs from a laser velocimetry particle sizing instrument as the inputs to a NN software package for the recognition and classification of environmental, bacterial, and artificial aerosols based on aerodynamic particle size distributions. The wedge regions of the detector can give an indication of the shape of a particle independent of the size. We have previously demonstrated[20] sizing opaque spherical particles using computer-generated holographic ring detectors (HRDs). By directly coupling the outputs of a HRD into an optical processor, the decision process in determining the particle size could be performed optically. This would simplify the algorithms of the data collection computer and effectively increase the potential speed of the particle characterization system.

Dugway Proving Ground is involved in testing military smokes and obscurants and would like to monitor and characterize the smokes present at various points on a grid in real time. At the very least, Dugway would like to identify the smokes and obscurants and count the number of particles present each second. It is also desirable for the instrumentation used to be a stand-alone, PC-based data acquisition system to integrate effectively with currently available systems of the Instrumentation Branch.

Initially, Dugway is interested in the three standard classes of unclassified military smokes and obscurants: 1) Standard liquid aerosol smokes, 2) Fibrous obscurants, and 3) Infrared obscurants. The liquid aerosol smokes[6] in the first class can be broken up into two groups. The first group consists of the hygroscopic smokes which react with water vapor in air to produce white smoke droplets which are highly obscurant at visible wavelengths. These obscurants include phosphorus-derived smokes, FS (chlorosulfonic acid and free sulfur trioxide) smokes, HC (zinc oxide and hexachloroethane aluminum) smokes, and FM (titanium tetrachloride) smokes. The second group is disseminated in liquid form to produce droplets which are not dependent on the relative humidity of the atmosphere. This group includes fog oil, diesel fuel oil, and polythylene glycol smokes. All of the standard aerosol smokes included in both of these groups making up this class of liquid aerosol smokes form highly opaque spherical droplets, typically confined to the range between 0.1 μm and 15 μm.

ing additional information[7] available on fog oil smokes, an estimate can be found on the number particles per second that would need to be characterized to handle the high particulate concentrations utilized by Dugway. Taking the average particle diameter to be at least 1.0 μm, the density of fog oil given as 0.9 g/cm^3, the maximum fog oil concentration reported in the data as 321 mg/m^3, and a typical flow rate for present particle sizing instruments of one cubic foot per minute, an estimated upper limit of one million particles per second must be measurable. This rate would tax even the fastest light scattering instruments available at the present time.

The fibrous obscurants are made from what looks like thin, black thread with a diameter of 6 μm, cut into 1/4 inch (6.35 mm) or 1/8 inch (3.175 mm) lengths. The fibers are then compressed side-by-side into a network which looks very much like a black hockey puck. To disseminate the fibers, the puck is put into a disseminator, analogous to a blender, which separates the individual fibers and disperses them into air.

The Infrared obscurant group consists of highly irregular brass and graphite flakes designed to block the infrared wavelengths. The materials look like a fine gold or blackish-grey powder. For this study only brass flakes will be used. It was possible to isolate individual samples of the brass flakes for study in the lab where the graphite would tend to smear and decompose into a finer powder.

METHODS AND MATERIALS

For this study two holographic optical element (HOE) were fabricated and implemented in the Fourier plane P_2 of the standard 4f optical correlator, see Fig. 1. The first HOE was designed to perform the same function as a HRD directly coupled into an ONN. The HRD part of the HOE has the same dimensions as described in our previous paper[20]. For simplicity a two-layer feedforward ONN will be considered with nine inputs and nine fully connected outputs where the nine outputs from the HRD will be the nine inputs to the ONN. This ONN is the simple associative memory vector-matrix multiplier. Table I lists the expected inputs to the ONN and Table II lists the desired outputs from the ONN. The best interconnection weights for the ONN must be determined. If Table I defines the input matrix **X** and Table II defines the output matrix **Y** = **I**, where matrix **I** is the identity matrix, then the desired interconnection weights are the single memory matrix **M**, such that **MX** = **I**.

The inputs listed in Table I are normalized so that the sum of the inputs (i.e., the total intensity out of the HRD) is equal to one. There are three justifications for this normalization. First, it is an easily realizable and measurable normalization. Second, the total output of the HRD can easily be sampled and used as a bias input required for many NN implementations. Finally, this bias establishes the threshold value to be used at the output of the ONN for determining which outputs are high and which are low. Computer experiments which included this additional bias term as an input to the ONN to determine the interconnection weights for this two-layer feedforward ONN

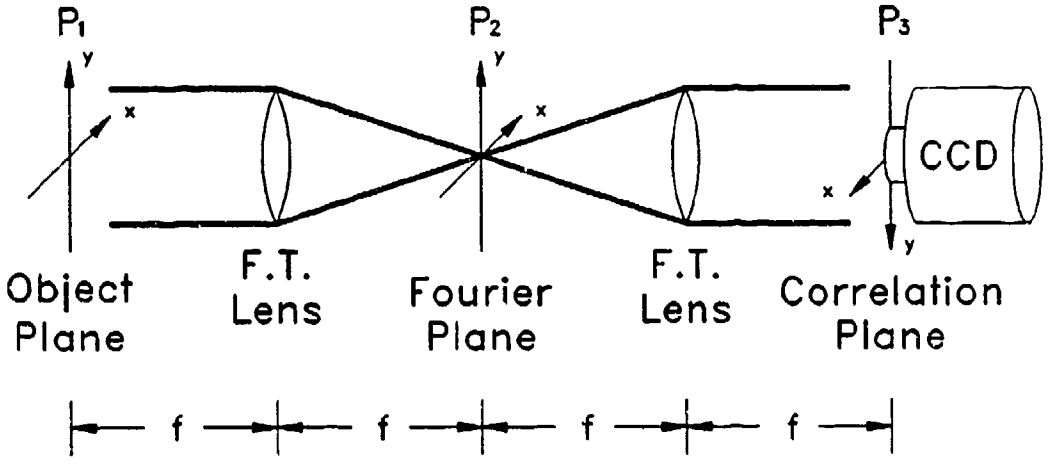

Figure 1. The standard 4f optical correlator.

Table I. NORMALIZED INPUTS FROM THE HRD INTO THE ONN

Ring Number	28 μm Particle	35 μm Particle	43 μm Particle	50 μm Particle	60 μm Particle	70 μm Particle	85 μm Particle	100 μm Particle	115 μm Particle
1	0.0683	0.0995	0.1431	0.1866	0.2386	0.2779	0.2363	0.0846	0.0068
2	0.0965	0.1343	0.1803	0.2174	0.2388	0.2224	0.0990	0.0098	0.1045
3	0.1398	0.1804	0.2154	0.2258	0.1850	0.1033	0.0124	0.1495	0.3025
4	0.1638	0.1871	0.1826	0.1471	0.0614	0.0085	0.1299	0.2879	0.1472
5	0.1678	0.1586	0.1092	0.0504	0.0050	0.0664	0.2129	0.0891	0.0453
6	0.1639	0.1123	0.0367	0.0045	0.0582	0.1460	0.0650	0.0736	0.1619
7	0.1248	0.0435	0.0043	0.0437	0.1077	0.0568	0.0693	0.1301	0.0434
8	0.0622	0.0061	0.0617	0.0970	0.0311	0.0571	0.0904	0.0899	0.0860
9	0.0127	0.0781	0.0668	0.0274	0.0742	0.0616	0.0847	0.0855	0.1023

Table II. DESIRED OUTPUT FROM THE ONN

Ring Number	28 μm Particle	35 μm Particle	43 μm Particle	50 μm Particle	60 μm Particle	70 μm Particle	85 μm Particle	100 μm Particle	115 μm Particle
1	1.0	0.0	0.0	0.0	0.0	0.0	0.0	0.0	0.0
2	0.0	1.0	0.0	0.0	0.0	0.0	0.0	0.0	0.0
3	0.0	0.0	1.0	0.0	0.0	0.0	0.0	0.0	0.0
4	0.0	0.0	0.0	1.0	0.0	0.0	0.0	0.0	0.0
5	0.0	0.0	0.0	0.0	1.0	0.0	0.0	0.0	0.0
6	0.0	0.0	0.0	0.0	0.0	1.0	0.0	0.0	0.0
7	0.0	0.0	0.0	0.0	0.0	0.0	1.0	0.0	0.0
8	0.0	0.0	0.0	0.0	0.0	0.0	0.0	1.0	0.0
9	0.0	0.0	0.0	0.0	0.0	0.0	0.0	0.0	1.0

did not show any significant advantages over computer experiments that did not include this bias term. Therefore, the bias was not included as an input to the HRD-ONN fabricated for this study but was used to normalize the outputs of the ONN.

Using the standard error back-propagation algorithm as implemented by NeuralWare, Inc.[21] in the *NeuralWorks Professional II: Neural Computing* software package results in the memory matrix

$$M = \begin{bmatrix} -5.7 & 6.7 & -3.8 & 0.8 & 1.2 & 1.4 & 4.3 & 3.0 & -3.2 \\ 7.3 & -9.4 & 8.1 & -1.4 & 3.8 & 0.1 & -2.1 & -12.0 & -3.9 \\ -10.2 & 16.7 & -13.0 & 8.7 & -4.8 & 2.1 & -4.5 & 5.5 & 6.6 \\ 7.7 & -9.9 & 9.8 & -3.8 & 3.0 & -3.3 & -0.8 & -0.2 & -10.4 \\ -4.4 & 5.4 & -1.2 & -2.7 & 0.7 & -4.8 & 8.5 & -1.8 & 7.6 \\ 5.1 & -1.4 & -2.5 & 4.1 & -5.6 & 8.2 & -7.0 & -0.2 & -4.9 \\ -0.2 & -2.2 & 1.8 & -5.5 & 6.0 & -4.8 & 3.0 & 3.5 & 5.5 \\ 2.8 & -2.3 & -2.1 & 5.7 & -5.3 & 2.8 & -1.1 & -0.5 & -1.0 \\ -1.2 & -2.7 & 4.0 & -4.8 & 1.9 & -0.6 & 0.7 & 3.6 & 4.6 \end{bmatrix} \quad (1)$$

for this HRD-ONN computer experiment. Figure 2 depicts the outputs from the HRD-ONN expected as a function of input particle diameter with a memory matrix **M** using the standard error back-propagation method given by Eq. 1. Next the interconnection weights for matrix **M** are set to integers so that the positive numbers become integers from 0 and 15, and the negative numbers become integers from 0 to -15. The integers 0 to 15 were chosen because they can be represented with a four-bit integer and represents a typical resolution for most HOE fabrication methods. The matrix **M** represented by Eq. 1 becomes

$$M = \begin{bmatrix} -5 & 5 & -3 & 0 & 1 & 1 & 3 & 2 & -2 \\ 6 & -8 & 7 & -1 & 3 & 0 & -1 & -10 & -3 \\ -9 & 15 & -11 & 7 & -4 & 1 & -4 & 4 & 5 \\ 6 & -8 & 8 & -3 & 2 & -2 & 0 & 0 & -9 \\ -3 & 4 & -1 & -2 & 0 & -4 & 7 & -1 & 6 \\ 4 & -1 & -2 & 3 & -5 & 7 & -6 & 0 & -4 \\ 0 & -1 & 1 & -4 & 5 & -4 & 2 & 3 & 4 \\ 2 & -2 & -1 & 5 & -4 & 2 & -1 & 0 & 0 \\ -1 & -2 & 3 & -4 & 1 & 0 & 0 & 3 & 4 \end{bmatrix} \quad (2)$$

after setting the interconnection weights to integers. Figure 3 depicts the outputs from the HRD-ONN expected as a function of input particle diameter with a memory matrix **M** using the standard error back-propagation method with integer

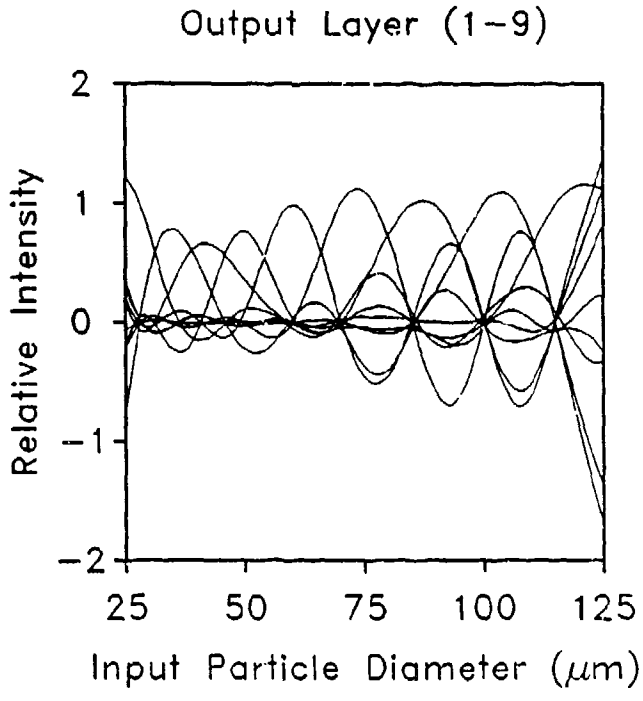

Figure 2. Responses for the output layer nodes as a function of spherical particle diameter using the standard error back-propagation method.

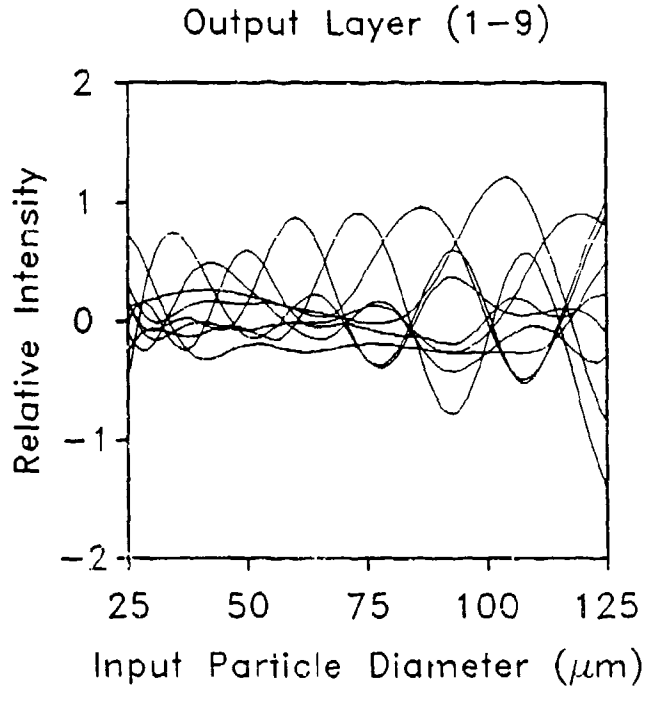

Figure 3. Responses for the output layer nodes as a function of spherical particle diameter using the digitized interconnection weights.

interconnections given by Eq. 2.

A bipolar representation for the interconnection weights was used, meaning that the positive and negative weights were treated separately. Positive values are deflected to a different point than the negative values. At the output two peaks must be measured, one for the positive values and one for the negative values, and the difference between the measured intensities gives the final answer. To provide varying interconnection magnitudes each ring is divided into 32 sections and only the required number of sections equal to the digitized interconnection weight has a grating within that area. The maximum any one output requires is 15 of the 32 sections. This sectioning method works for perfectly spherical particles only. A better method would be to modulate the magnitude of the grating over the entire ring to minimize the effects of possible intensity fluctuations. However, this modulation requires higher resolution capabilities in the fabrication process which are not available using our photoreduction method.

The second HOE was designed to perform the same function as a holographic ring-wedge detector (HRWD) directly coupled into an ONN. The dimensions of the ring sections were identical to the ring sections of the fist HOE and eight 45° wedge sections were included. Ternary-valued (i.e., ± 1 and 0) interconnection weights were used so that entire ring sections would be used and sigmoid transfer functions were electronically implemented at the output nodes of the ONN. Two output nodes were included representing when brass flakes or fibers were introduced at the Object plane P_1 in addition to the previous nine output nodes representing the nine spherical particle size ranges. The matrix **M** becomes

$$\mathbf{M} = \begin{bmatrix} 0 & 0 & 0 & 0 & 10 & 10 & 0 & 0 & -100 \\ 0 & 0 & 0 & 10 & 0 & 0 & 0 & -100 & 0 \\ 0 & 0 & 10 & 0 & 0 & 0 & -100 & 0 & 0 \\ 0 & 0 & 10 & 0 & 0 & -100 & 0 & 0 & 0 \\ 0 & 10 & 0 & 0 & -100 & 0 & 0 & 0 & 0 \\ 10 & 0 & 0 & -100 & 0 & 0 & 0 & 0 & 0 \\ 10 & 0 & -100 & 0 & 0 & 0 & 0 & 0 & 0 \\ 0 & -100 & 0 & 10 & 0 & 0 & 0 & 0 & 0 \\ -100 & 0 & 10 & 0 & 0 & 0 & 0 & 0 & 0 \end{bmatrix} \tag{3}$$

for the ring sections connected to the nine output nodes representing the spherical particles. Figure 4 depicts the outputs from the HRWD-ONN expected as a function of input particle diameter with a memory matrix **M** using the sigmoid transfer function method with ternary-valued interconnections given by Eq. 3.

To fabricate the HOEs, an HP compatible plotter was used to produce an enlarged version of the desired HOE. The plot was then photoreduced onto Kodak High Speed

Holographic Film SO-253. In the photoreduction process the object and image distances are chosen so that the image of the filter is reduced by the same amount that it was enlarged during the plotting process. The lenses used were Fourier transform lenses with an inside diameter of 7.2 cm and a focal length of 37.4 cm.

EXPERIMENTAL RESULTS

The output of the correlator was recorded for 25 μm, 35 μm, 50 μm, 70 μm and 100 μm particles, and with fibers and brass flakes for the HRWD-ONN. Precision drilled pinholes were used to simulate the spherical particles. Figure 5 gives the results using the HRD-ONN with the solid lines representing the integrated intensity for each output neuron as predicted by the computer experiment program. The high-low bars represent the range of integrated intensities measured for the input particle. Figure 6 gives the results using the HRWD-ONN for the nine outputs representing the spherical particle size ranges with the solid lines representing the integrated intensity for each output neuron as predicted by the computer experiment program after an electronically implemented sigmoid function was applied. For all five spherical particle sizes utilized, it is expected that there will be one output neuron easily distinguishable from the rest. All integrated intensities were normalized by the bias terms.

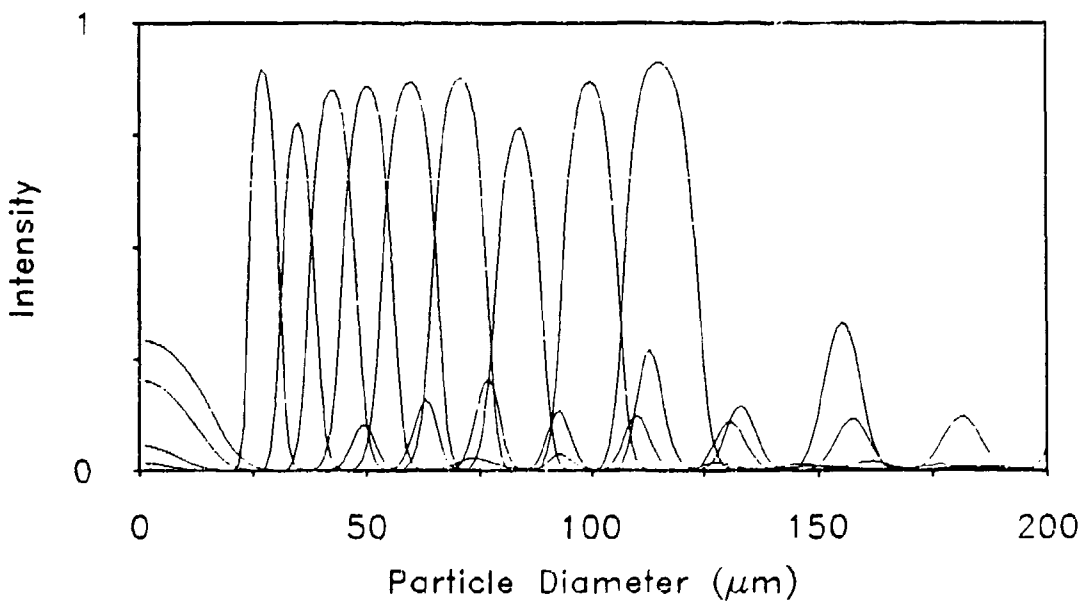

Figure 4. Responses for the output layer nodes as a function of spherical particle diameter using the ternary-valued interconnection weights and a sigmoid transfer function.

CONCLUSIONS

In spite of the various limitations and approximations, the HRD-ONN worked quite well. Using a winner-takes-all (WTA) algorithm, the HRD-ONN correctly identified all five spherical particle sizes introduced at the input plane. There are many HRD-ONN combinations that could be considered. The purpose of using an ONN is to improve the overall speed of the particle characterization instrument. Photoreduction was used to fabricate the HRD-ONN used for this study. Unfortunately, photoreduction has an inherent size-resolution trade-off restriction. This severely limited the complexity of the HRD-ONNs that were considered. A higher resolution, large area method such as

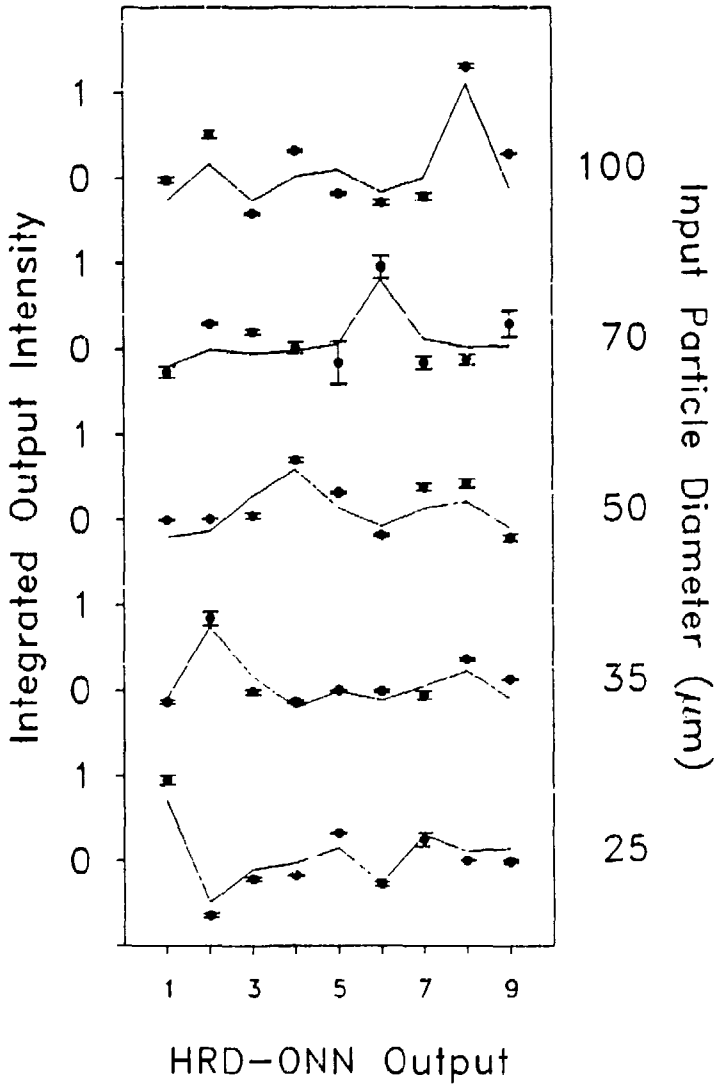

Figure 5. Solid lines represent the HRD-ONN computer experiment intensities integrated over the correlation peak. High-low bars represent the range of integrated intensities measured.

Electron-beam fabrication would be ideal for this application. The nine input, nine output HRD-ONN was adequate for evaluation purposes and performed as predicted. However, for a field competent system the HRD-ONN would need to have better size range capabilities and better output control.

The HRWD-ONN correctly identified each particle type and size range for the spherical particles. In addition, the HRWD-ONN had better output control than the HRD-ONN and does not suffer as greatly from the size-resolution trade-off problem. The main disadvantage with the HRWD-ONN is that part of the decision process was removed from the ONN since we required the computer to implement the sigmoid transfer

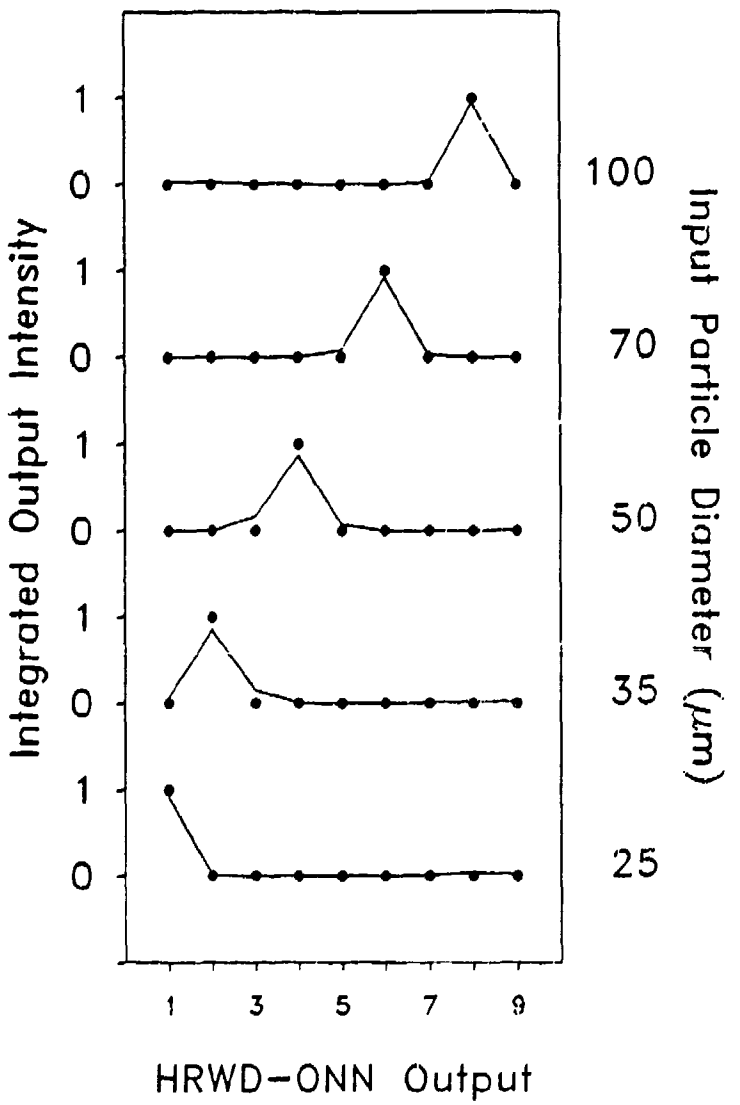

Figure 6. Solid lines represent the HRWD-ONN computer experiment intensities integrated over the correlation peak with a sigmoid transfer function applied.

function on the recorded measured outputs of the ONN. Solutions to this problem could include using an optical implementation of the transfer function or use a computer that could implement the transfer function on all eleven output nodes at the desired rate of one million particles per second.

Much work still needs to be accomplished. Future work could include developing a field competent system, based on the principles demonstrated in this paper, capable of characterizing high obscurant concentrations. Figure 7 depicts an optical layout we are investigating capable of achieving the desired one million particles per second rate. Further work could also include expanding the capabilities of the system to characterize a larger set of particulates or generalizing the capabilities of the system to characterize an arbitrary spherical or nonspherical particle against an established set of reference shapes.

ACKNOWLEDGMENTS

We thank the U.S. Army Dugway Proving Ground and the University of Utah Laser Institute for support of this research. We also acknowledge the assistance of James W. Dyer and Charles E. DeWitt.

REFERENCES

1. A. VanderLugt, "Signal Detection by Complex Spatial Filtering," IEEE Trans. Inf. Theory **IT-10**, 139-145 (1964).

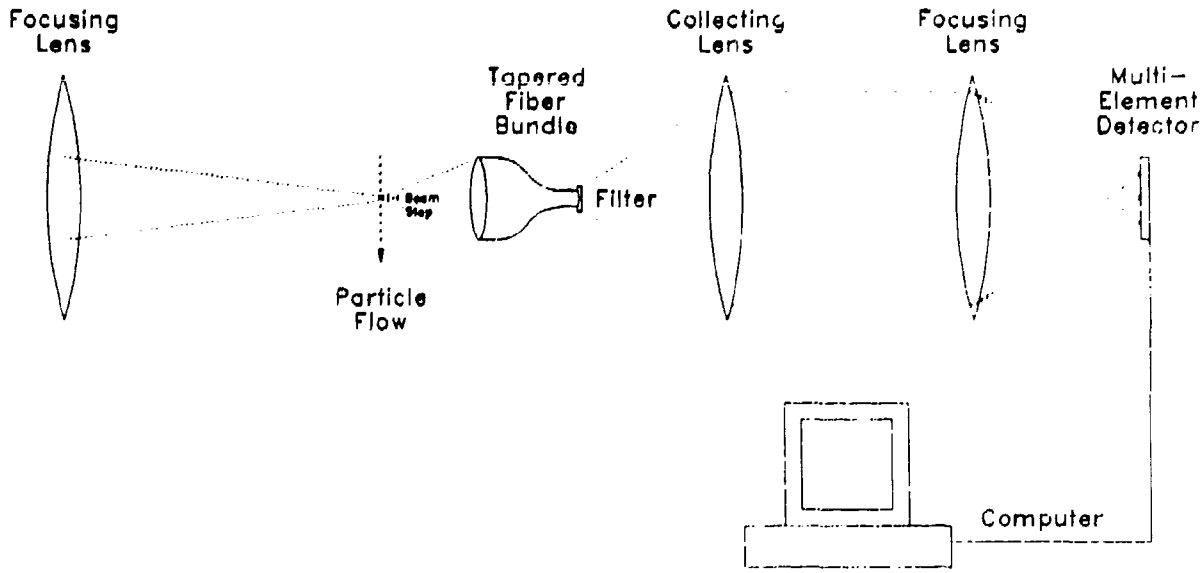

Figure 7. Optical layout for future compact field system.

2. D. P. Casasent, "Coherent Optical Pattern Recognition: A Review," Opt. Eng. **24**, 26-32 (1985).

3. D. Vukicevic, N. Demoli, and L. Bistricic, "VanderLugt Filter Optimization for Metrology in Industrial and Scientific Research," *2nd European Congress in Optics Applied to Metrology*, M. Grossman and P. Meyrueis, Editors, Proc. SPIE 210, 54-64 (1979).

4. J. Cairns, Jr., K. L. Dickson, P. Pryfogle, S. P. Almeida, S. K. Case, J. M. Fournier, and H. Fujii, "Determining the Accuracy of Coherent Optical Identification of Diatoms," Water Res. Bull. **15**, 1770-1775 (1979).

5. S. P. Almeida, S. K. Case, J. M. Fournier, H. Fujii, J. Cairns, Jr., K. L. Dickson, and P. Pryfogle, "Analysis of Algae Using Coherent Optical Processing," Proc. of ICO-11 Conference, Madrid, Spain (1978).

6. M. E. Milham and D. H. Anderson, *Obscuration Sciences Smoke Data Compendium: Standard Smokes*, Special Publication ARCSL-SP-82024 (US Army Aberdeen Proving Ground, Maryland, 1983).

7. J. C. Liljegren, W. E. Dunn, G. E. DeVaull, and A. J. Policasto, *Field Study of Fog-Oil Smokes*, (University of Illinois, Urbana, 1986).

8. B. J. Thompson, "Droplet Characteristics with Conventional and Holographic techniques," *Liquid Particle Size Measurement Techniques*, STP 848, J. M. Tishkoff, R. D. Ingebo and J. B. Kennedy, Editors, 111-122 (American Society for Testing and Materials, Philadelphia, 1984).

9. P. H. Malyak and B. J. Thompson, "Obtaining Particle Velocity and Displacement from Double-Exposure Holograms Using Optical and Digital Processing," *Particle Sizing and Spray Analysis*, N. Chigier and G. W. Stewart, Editors, Proc. SPIE 573, 2-11 (1985).

10. E. D. Hirleman, "Particle Sizing by Optical, Nonimaging Techniques," *Liquid Particle Size Techniques*, STP 484, J. M. Tishkoff, R. D. Ingebo and J. B. Kennedy, Editors, 35-60 (American Society for Testing and Materials, Philadelphia, 1984).

11. E. D. Hirleman and P. A. Dellenback, "Adaptive Fraunhofer Diffraction Particle Sizing Instrument Using a Spatial Light Modulator," Appl. Opt. **28**, 4870-4878 (1989).

12. H. C. van de Hulst, *Light Scattering by Small Particles* (Dover, New York, 1981).

13. C. F. Bohren and D. R. Huffman, *Absorption and Scattering of Light by Small*

Particles (Wiley, New York, 1983).

14. W. M. Farmer, "Particle Sizing Interferometer Nephelometry," *Particle Sizing and Spray Analysis*, N. Chigier and G. W. Stewart, Editors, Proc. SPIE 573, 37-46 (1985).

15. George, N., S. Wang, and D. L. Venable, "Pattern Recognition Using the Ring-Wedge Detector and Neural-Net Software," *Optical Pattern Recognition II*, H. J. Caulfield, Editor, Proc. SPIE 1134, 12-47 (1985).

16. Casasent, D. P., and E. Barnard, "Adaptive-Clustering Optical Neural Net," Appl. Opt. **29**, 2603-2615 (1990).

17. Telfer, B., and D. P. Casasent, "Ho-Kashyap Optical Associative Processors," Appl. Opt. **29**, 1191-1202 (1990).

18. Casasent, D. P., and B. Telfer, "Ho-Kashyap Advanced Pattern Recognition Heteroassociative Processors," *Optical Information Processing Systems and Architectures II*, B. Javidi, Editor, Proc. SPIE 1347, 16-31 (1990).

19. Yee, E., and J. Ho, "Neural Network Recognition and Classification of Aerosol Particle Distributions Measured With a Two-Spot Laser Velocimeter," Appl. Opt. **29**, 2929-2938 (1990).

20. Marshall, M. S., and R. E. Benner, "Sizing Opaque Spherical Particles using Classical Matched Filters and Holographic Ring Detectors," Opt. Eng. **31**, 947-955 (1992).

21. NeuralWare, Inc., *NeuralWorks Professional II: Neural Computing* (Pittsburgh, 1989).

Blank

OPERATION OF THE BREEZE TUNNEL TO DETERMINE MASS EXTINCTION COEFFICIENTS

George A. Sehmel

Pacific Northwest Laboratory[1]
Battelle Boulevard
Richland, Washington 99352

R. Bonfante, D. R. Banks, E. Catalano, and W. G. Rouse

Edgewood Research, Development and Engineering Center
Aberdeen Proving Ground, Maryland 21010

RECENT PUBLICATIONS, SUBMITTALS FOR PUBLICATION, AND PRESENTATIONS:

G. A. Sehmel, D. R. Banks, J. J. Novad, R. Bonfante, R. D. Swannack, and M. W. Ligotke. 1992. Breeze Tunnel Performance of XM56 Carbon-Flake Generation for Attenuation of CO_2 and HeNe Laser Transmission in May and October 1992 Trials. PNL-8430, Pacific Northwest Laboratory, Richland, Washington.

G. A. Sehmel, J. F. Embury, and H. R. Carlon. 1993. Extinction of Laser Radiation by Man-Made Graphite-Flake Aerosols. Paper issued by the U.S. Army Edgewood Research Development and Engineering Center at Aberdeen Proving Ground, MD. For inclusion in the Proceedings for the Electromagnetic Wave Propagation Panel, 52nd Specialists' Meeting on Atmospheric Propagation Effects Through Natural and Man-Made Obscurants for Visible to MM-Wave Radiation, 17-21 May 1993, Spain.

G. A. Sehmel, R. Bonfante, D. R. Banks, E. Catalano, and W. G. Rouse. 1993. Operation of the Breeze Tunnel to Determine Mass Extinction Coefficients. PNL-SA-22650. Presented at the Scientific Conference on Obscuration and Aerosol Research, 22-24 June 1993, Aberdeen Proving Ground, MD.

G. A. Sehmel, R. D. Swannack, M. W. Ligotke, W. G. Rouse, and R. Bonfante. 1993. ASM-MM Breeze Tunnel Experiments - August 1991. ERDEC-CR-016, U. S. Army Edgewood Research, Development and Engineering Center, Aberdeen Proving Ground, MD.

G. A. Sehmel, W. G. Rouse, and R. Bonfante. 1993. Compact-Disc-Generator Breeze Tunnel Trials in 1991. PNL-SA-2229. Presented at the U.S. Army Smoke/Obscurants Symposium XVII, 13-16 April 1993, Laurel, MD.

G. A. Sehmel, W. G. Rouse, R. Bonfante, R. D. Swannack, and M. W. Ligotke. 1992. Breeze Tunnel Performance of Compact-Disc Carbon-Fiber Generation for Attenuation of 35-GHz and 94 GHz Radar Transmission. PNL-8351, Pacific Northwest Laboratory, Richland, Washington.

ABSTRACT

The breeze tunnel at the Edgewood Research, Development and Engineering Center (Edgewood RDEC) at Aberdeen Proving Ground, Maryland, is a unique facility for determining the efficacy of released smoke/obscurants in flowing air as a function of controlling variables. Optimum material feed characteristics and generator operating conditions can be determined. The facility allows investigation of the effects of different generator operating variables, airborne concentrations, and airborne particle sizes on mass extinction coefficients. During trials in the breeze tunnel, obscurants have been released from the compact-disc-generator, the IR-Log generator, and the XM56 generator. Obscurant release rates have ranged from an instantaneous puff to a continuous release of 10 lb/min. Extinction can be measured in the visual, infrared, and millimeter ranges of the electromagnetic spectrum. Experimental conditions allow calculation of mass extinction coefficients as a function of generator variables, including material release rates. Average mass extinction coefficients address attenuation from obscurants, both single primary particles and aggregates. The breeze tunnel facility can accommodate trials by clients from within Edgewood RDEC, the Department of the Army, and the Department of Defense (DoD).

INTRODUCTION

The U.S. Army Edgewood Research, Development and Engineering Center (Edgewood RDEC) operates a breeze tunnel within building E5584 at the Edgewood area of the Aberdeen Proving Ground, Maryland. A generator releasing obscurant into the inlet of the breeze tunnel is shown in Figure 1. The obscurant generator system can be located in front of the inlet (as shown in Figure 1) or within the inlet of the breeze tunnel.

One purpose of the breeze tunnel is to determine the efficacy of obscurant generators and released obscurants. The breeze tunnel has a nominal wind speed of 2.2 m/s (5 mph). The cross section of the tunnel is 4.27 m x 4.27 m (14 ft by 14 ft), and the length is 53.0 m (174 ft). Figure 2 is a plan view of the breeze tunnel, showing locations of the laser and radar lines of sight and of the filter transporters used to determine airborne mass concentrations. (Airborne mass concentrations are required for calculation of mass extinction coefficients from transmittance.) During particle generation, release efficacy can be investigated with CO_2 and HeNe lasers and 35- and 94-GHz radar and with airborne mass concentration samplers near the opposite end of the breeze tunnel.

Use of the breeze tunnel for obscurant trials minimizes environmental concerns during development of obscurant programs. After an obscurant is released into the breeze tunnel, obscuration can be measured within the visual, infrared, and millimeter ranges of the electromagnetic spectrum. Environmental concerns during trials are minimized because airborne particles are removed by a bag-house filter system before air is released to the environment.

The breeze tunnel is large enough to test at design release rates. In contrast to open air trials that are dependent on wind direction, expensive, and subject to escalating environmental regulations, the breeze tunnel allows trials under controlled and repeatable conditions because air flow is unidirectional and constant.

---

[1]Pacific Northwest Laboratory is operated for the U.S. Department of Energy by Battelle Memorial Institute under Contract DE-AC06-76RLO 1830.

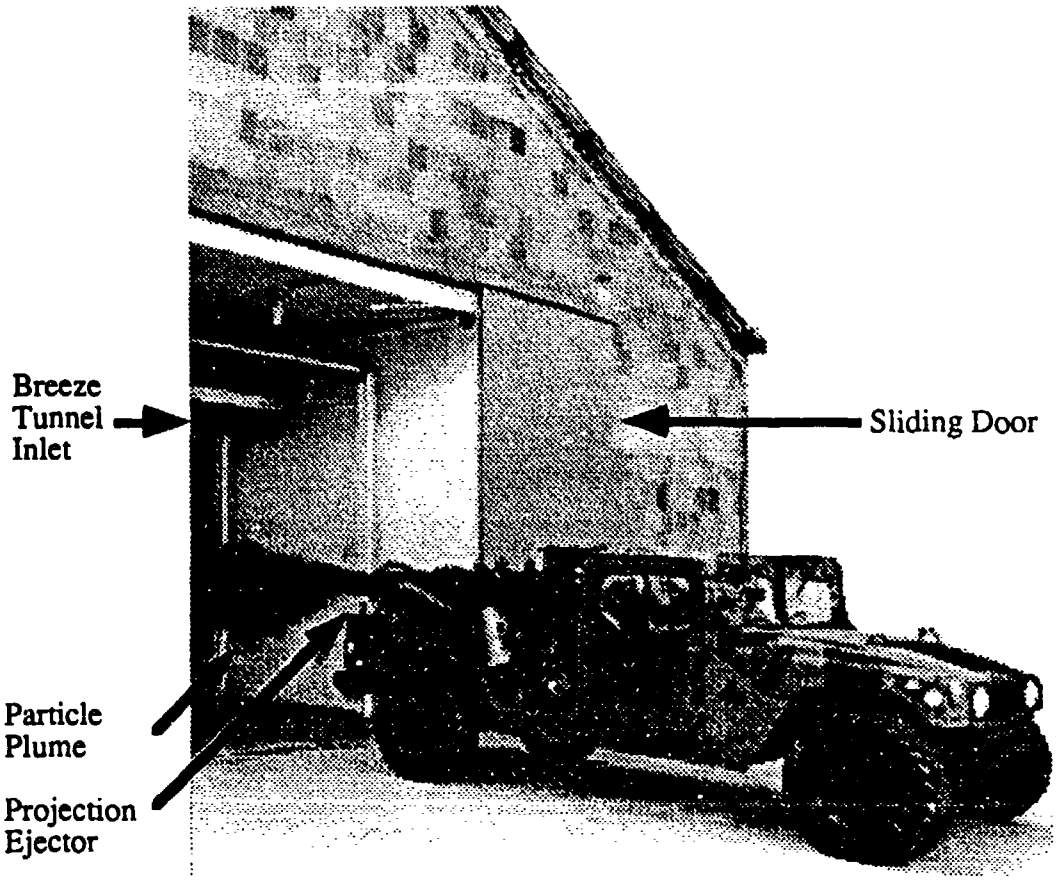

FIGURE 1. Obscurant Release Into the 4.27 m x 4.27 m (14 ft x 14 ft) Cross-Section Inlet of the Breeze Tunnel

Obscurants are released by the obscurant developer or contractor. Pacific Northwest Laboratory (PNL) and Edgewood RDEC staff have operated the data acquisition system for 35- and 94-GHz radar and for CO_2 (10.6-μm wave length) and HeNe (0.63-μm wave length) lasers. PNL staff have operated the sampling transporter to determine airborne mass concentrations during trials, and have analyzed and synthesized information from the data collected during trials (Sehmel et al., 1992a, b, 1993a, b). Synthesis has addressed 1) mass extinction coefficients derived from transmittance and average airborne particle mass concentrations, 2) the dependence of mass extinction coefficients on particle size, 3) aggregation of airborne particles, and 4) the extinction yield per unit mass of obscurant released.

The breeze tunnel facility can accommodate trials by clients from within Edgewood RDEC, the Department of the Army, and the Department of Defense (DoD). Clients have three options for using the tunnel: use just the facility, setting up project-specific equipment and instrumentation; use the facility with its instrumentation; or use the facility, its instrumentation, and its support personnel to develop the experimental plan, run the equipment, and analyze the data. This paper describes the facility and outlines the calculation of mass extinction coefficients and alpha yield with the intent of encouraging trials by other DoD clients in the breeze tunnel facility.

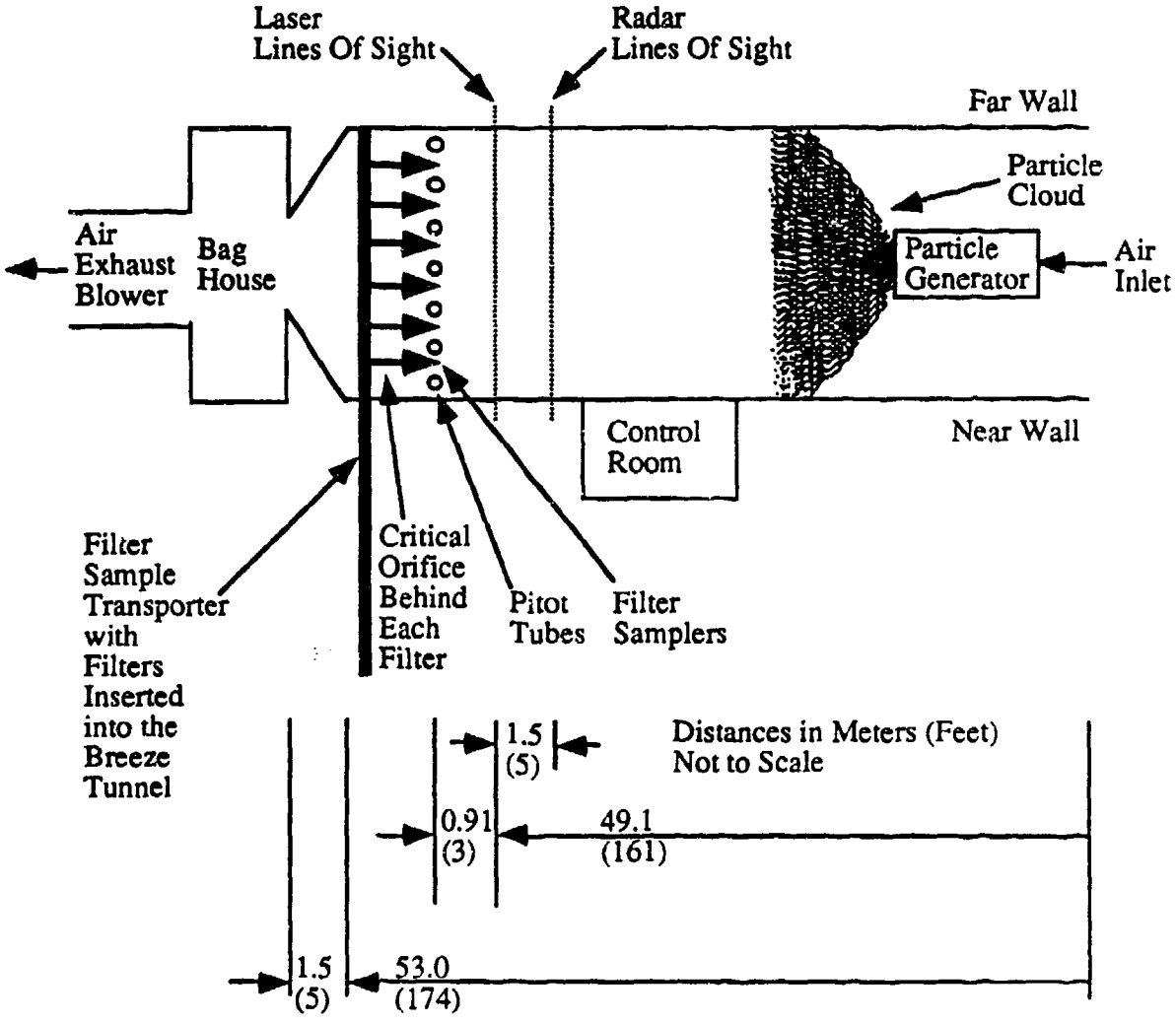

FIGURE 2. Plan View of Breeze Tunnel with Positions of the Lasers, Radar, and Transporter for Filter Samplers for Average Mass Concentration

BREEZE TUNNEL TEST EQUIPMENT

As shown in Figures 1 and 2, obscurant can be released near and within the air inlet of the breeze tunnel. Positions of lasers, radar, and transporter for filter samplers for determining average concentrations within the breeze tunnel are included in Figure 2. The data acquisition computer is in the control room outside the tunnel along the near wall.

Important features of the breeze tunnel include the following:

- radar to measure transmission
- lasers and power meters to measure transmission
- filter transporters to measure airborne concentrations
- pitot tubes to measure wind speed
- sensors to automatically record temperature and humidity
- computer control system for data acquisition during trial operation.

To evaluate mass extinction coefficients, airborne particle mass concentrations are measured at six filter locations along the middle filter transporter shown in Figure 3. Each filter transporter has three pipes oriented along a vertical plane. The middle pipe size is 1-in., and the other pipes are 1-1/4-in. The middle pipe is a sliding pipe supported by bearings on the upper and lower pipes. The middle pipe has pipe connections for filter samplers and supplies vacuum to the six filer samplers. Connections (1/8-in. pipe nipples) along the side of this middle pipe supply vacuum to the filter holders (in-line holder, Gelman model 1235 for 47 mm filters)[1].

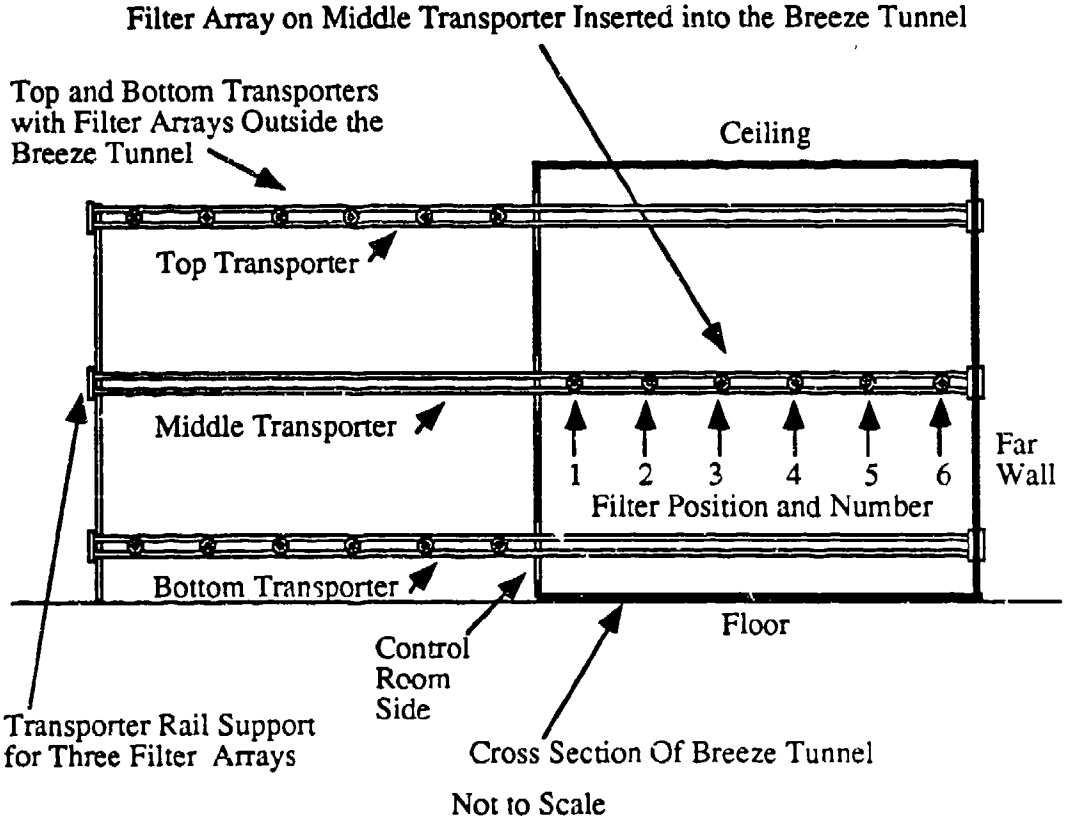

FIGURE 3. Schematic of Three Filter Transporters with the Middle Transporter Inserted in the Breeze Tunnel

There is a maximum of two lasers at each measurement location. These can be either CO_2 or HeNe lasers or one of each. The measurement location is 49.1 m (161 ft) from the inlet of the breeze tunnel. The radar path length is the 4.27-m (14-ft) width of the tunnel. The laser path length is adjustable, either the entire 4.27-m width of the tunnel or shorter distances. For example, a 1.07-m-wide (3.5-ft-wide) interval in the center of the tunnel has been used. The 1.07-m path length was created by containing the laser beam within aluminum tubes that extended 1.60 m (5.25 ft) from either side of the tunnel.

[1]Gelman Sciences, 600 S. Wagner Road, Ann Arbor, MI 48103-9019.

Radar transmission at 35 and 94 GHz, laser transmission with CO_2 and HeNe lasers, airborne mass concentration (using filter array on the middle filter transporter), and wind speed are all measured along approximately the same line of sight. The distance between the radar transceivers is about 0.36 m (14 in.). Radar transmission is measured at a distance of about 1.5 m (5 ft) upwind from the laser measurement location. Airborne concentrations and wind speed are measured 0.91 m (3 ft) downwind of the lasers. Laser transmission, concentrations, and wind speed across the width of the breeze tunnel are measured at a height of 2.16 m (7 ft 1 in.). Radar transmission is measured at a height of about 1.5 m (5 ft).

Extinction coefficients are calculated from transmission results, and airborne mass concentrations measured along the middle filter transporter. For the 4.27-m (14-ft) laser path length, an average concentration is calculated from all six filter sample locations along the filter array for the middle filter transporter. For the 1.07-m (3.5-ft) laser path length, the average concentration is calculated from only the central two filter samplers.

Breeze Tunnel Geometry

As shown in Figure 1, the tunnel inlet is immediately behind the building's sliding doors, which are adjacent to a driveway. The edges of the opening for the sliding doors are at the tunnel floor, walls, and ceiling. The size of the door, and thus the cross section of the breeze tunnel, is 4.27 m x 4.27 m (14 ft by 14 ft). The tunnel length extends at full size 53.0 m (174 ft) from the inlet. The tunnel walls then converge in a distance of 1.5 m (5 ft) into the 1.8 m x 1.8 m (6 ft x 6 ft) framework for a bag house, where air is cleaned in a bag filter system and exhausted through a blower at slightly greater distances. An automatic carbon-dioxide fire extinguishing system[1] is installed in the baghouse. An exhaust blower draws air through the tunnel and bag house and exhausts filtered air through a stack.

Radar Transmission Measurement

Radar frequencies are 35 and 94 GHz. The radar system[2] was originally constructed by Stuart (1984) for the Chemical Research and Development Center (CRDEC) and has been modified by CRDEC and Edgewood RDEC. Radar transmitters are located outside the breeze tunnel near the wall opposite the control room (Figure 2). Radar transmission across the tunnel is measured with transceivers outside the breeze tunnel and near the wall adjacent to the control room. The radar signal passes through plastic windows in both walls. Radar lines of sight extend horizontally across the width of the breeze tunnel and perpendicular to its walls.

Each radar transmitter has a calibrator to set the radar output from 0 to 30 dB in 1-dB increments. The computer program calibrates the radar by measuring the voltage output of the transceiver as a function of the signal attenuation in decibels. The calibration yields information on decibel power transmitted versus the voltage output of the transceiver.

[1] Kidde, Inc., Fire Suppression Operations, Wake Forest NC 27587.

[2] Constructed for Edgewood RDEC (formerly CRDEC) by Franklin Institute, 20th Street and Parkway, Philadelphia, 19103.

Radar transceivers measure transmission as a function of time across the breeze tunnel. The purpose of the transceiver is to measure the reduction in received power at the transceiver (i.e., the reduction in voltage) when obscurant is present in the breeze tunnel. Calibration data allow conversion of transceiver voltages to attenuation in decibels. The reduction in decibels is a fraction of the decibel measurement in the absence of the obscurant, i.e., the baseline transmission before and after material generation.

Laser Transmission Measurement

Laser lines of sight are horizontal, extending across the entire width of the breeze tunnel and perpendicular to the tunnel walls. The lasers are outside the breeze tunnel and near the far wall. The laser signal passes through an opening in the far wall, crosses the tunnel, and exits through an opening in the near wall.

Two types of lasers are used, a 5.5-W CO_2 laser with a wavelength of 10.6 μm and a 35-mW HeNe laser with a wavelength of 632.8 nm. The CO_2 lasers are Laser Photonics[1] model CL-AOVO. (To improve the temperature stability of the CO_2 lasers, these air-cooled CO_2 lasers are currently being replaced with water-cooled CO_2 lasers, Laser Photonics model CL-75W000.) The HeNe lasers are Spectra-Physics[2] model 127-355. At each laser location, the distance between the laser lines of sight is 11 cm (4.5 in.) along a horizontal plane. The HeNe laser was 11 cm downwind (toward the baghouse of the tunnel) of the CO_2 laser.

Transmission is calculated from the reduction in voltage that occurs when obscurant is present in the tunnel. Transmission is calculated as a fraction of the power-meter voltage in the absence of the obscurant, i.e., a fraction of baseline transmission before and after material generation.

Transmission across the tunnel is measured with power meters outside the tunnel and adjacent to the near wall. There is one power meter for each laser. Power meters are Laser Precision Corporation[3] model RKP5710 radiometers with RKP575 pyroelectric probes. These power meters have a 14-decade dynamic range (10^{-11} to 10^{3}). Scale ranges are 200 μW, 2 mW, 20 mW, 200 mW, 2 W, and 10 W. The analog output voltage for each power meter is received by the computer data acquisition system over a Hewlett-Packard[4] interface bus (HPIB).

Airborne Concentration Measurement

Airborne concentrations (in mg/m^3 air) are time-averages for collection of particles on filter samplers over the sampling interval. The filter sample locations relative to the near wall of the breeze tunnel are listed in Table I. The filter spacing is approximately 0.6 m (2 ft).

As illustrated in Figure 3, airborne concentrations can be measured at six filter locations along three filter transporters for filter arrays. Each transporter has a sliding rail that includes filter supports, filters, vacuum supply, and a critical orifices (Anderson-Forester model PL-629)[5] for

[1] Laser Photonics, 12351 Research Parkway, Orlando, FL 32826.
[2] Spectra-Physics Laser Products Division, 1250 W. Middlefield Road, Mountain View, CA 94039-7013.
[3] Laser Precision Corporation, 1231 Hart Street, Utica, NY 13052.
[4] Hewlett-Packard, Inc., 8245 North Union Boulevard, Colorado Springs, CO 80920.
[5] Anderson-Forester, 6250 Joyce Drive, Golden, CO 80403.

TABLE I. Filter Positions near Laser and Radar Lines of Sight for Collection of Airborne Mass Concentration

Location	Incremental Distance Between Locations m	(in.)	Cumulative Distance from Wall near Computer Room m	(ft)
Near wall				
	0.56	(22)		
Filter 1			0.56	(1.83)
	0.61	(24)		
Filter 2			1.17	(3.83)
	0.61	(24)		
Filter 3			1.78	(5.83)
	0.72	(28.5)		
Filter 4			2.50	(8.21)
	0.61	(24)		
Filter 5			3.11	(10.21)
	0.61	(24)		
Filter 6			3.72	(12.21)
	0.55	(21.5)		
Far wall			4.27	(14)

each filter sample to control air flow and to maintain a constant sampling rate. As shown in Figure 3, the middle sliding rail is inserted into the breeze tunnel to collect material for calculation of mass extinction coefficients.

The sampling height for the middle transporter is 2.16 m (7 ft 1 in.) and approximates the heights for the lasers and radar. The simultaneous use of the bottom and top filter transporter allow investigation of concentration variations as a function of height, heights of 0.91 m (3 ft) and 3.43 m (11 ft 3 in.), respectively.

In order to calculate mass extinction coefficients, airborne concentrations are measured with isokinetic air samplers along the middle transporter. Each sampler is connected to an in-line filter holder for a 47-mm-diameter filter. An isokinetic sampler is a metal tube with a beveled inlet edge to improve sampling. Isokinetic inlet diameters of 0.84 cm (0.33 in.) and 1.88 cm (0.74 in.) have been used. Particles flow through 3.3 cm (1.3 in.) and 6.1 cm (2.4 in.) lengths of metal tube, respectively. The sampling rate is constant and assumed to be isokinetic throughout each trial.

After particle collection, the sliding rail is withdrawn from the breeze tunnel and the filters are removed for gravimetric analysis. Filters are weighed in a room cooled by refrigerated air conditioning.

Airborne Particle Size Measurement

An Andersen[1] ambient-particle cascade impactor (non-viable) is used to determine average size distributions as a function of airborne particle diameter. The impactor has been located with the inlet about 15 cm (6 in.) below filter number one on the filter array for the middle filter transporter (see Figure 3 with transporter inserted into the breeze tunnel) and between the control room side of the breeze tunnel and filter number one, about 15 cm (6 in.) from filter number one. The diameter of the inlet tube to the impactor is 1.6 cm (5/8 in.). At a sampling flow rate of 18.8 L/min, the aerodynamic particle diameters for 50% collection at successive impactor stages were 11.3, 7.2, 4.9, 3.4, 2.2, 1.1, 0.66, and 0.44 μm.

The sampling time for particle collection is adjusted to allow sufficient material to be collected above gravimetric detection limits, but not so long as to cause overloading. Particles are collected on pre-weighed collection plates placed on each stage. Gravimetric analysis is used to determine particle collection on each collection site. The limit of accuracy for gravimetric analysis is about 0.050 mg.

Size distributions for trials are assumed to be lognormal distributions by mass. The aerodynamic mass median diameter (AMMD) and D84 particle diameter characterize the log-normal distribution. By definition, 50% of the mass is greater than the AMMD and 50% is less. Eighty-four percent of the cumulative particle mass has diameters less than D84. The geometric standard deviation (GSD) is the ratio D84/AMMD. The smaller the value of GSD, the narrower is the size distribution.

Velocity Measurement

Air velocity in the breeze tunnel is measured with Dwyer[2] 166-12-CF pitot tubes. A velocity profile is obtained by an array of seven pitot tubes. These are mounted horizontally across the tunnel at approximately the level of the laser lines of sight. Table II lists the position of each pitot tube. Filter samplers are approximately midway between adjacent pitot tubes.

Each pitot tube is connected to an MKS[3] model 220BD pressure transducer. The analog output of the transducer is multiplexed to the computer data acquisition system by means of multiplex input cards. Output of the pressure transducer is 0 to ± 10 volts for 0 to ± 1.4 cm (0 to ± 0.54 inches) of water. At an air flow rate of 2.2 m/s (5 mph) in the tunnel, the system is expected to provide an output pressure of 0.3 mm (0.012 inches) of water or 0.22 volts.

Two control relays provide control of the calibration valves for the pressure transducers. These relays zero the transducer (and clean the pitot tubes) and set the transducer span. A computer-controlled valve system calibrates the pressure transducers. The valves can be controlled to

1) connect ambient pressure to both sides of the pressure transducer (at the same time providing air pressure to clear possible obstructions from both the impact and reference ports of the pitot tube),

[1] Graseby Andersen, 4801 Fulton Industrial Boulevard, Atlanta, GA 30336-2003.
[2] Dwyer Instruments Inc. P.O. Box 373, Michigan City, IN 46360.
[3] MKS Instruments, Inc., 6 Shattuck Road, Andover, MA 01810.

TABLE II. Pitot Tube Positions near Laser and Radar Lines of Sight for Measurement of Wind Speed

Location	Incremental Distance Between Locations m	(in.)	Cumulative Distance from Wall near Computer Room m	(ft)
Near wall				
	0.23	(9.25)		
Pitot tube 1			0.23	(0.77)
	0.61	(24)		
Pitot tube 2			0.84	(2.77)
	0.61	(24)		
Pitot tube 3			1.45	(4.77)
	0.77	(30)		
Pitot tube 4			2.22	(7.27)
	0.61	(24)		
Pitot tube 5			2.83	(9.27)
	0.61	(24)		
Pitot tube 6			3.44	(11.27)
	0.61	(24)		
Pitot tube 7			4.05	(13.27)
	0.22	(8.75)		
Far wall			4.27	(14)

2) connect a micrometer-sized manometer to the impact side of the pressure transducer while maintaining the reference side of the transducer at ambient pressure, or

3) connect the transducer to the pitot tube.

Temperature and Humidity Measurements

Temperature and humidity are measured within the tunnel inlet and 4.6 m (15 ft) from it. Air is sampled at the 2.1-m (7-ft) height adjacent to the near wall. Temperature and humidity are measured with an EG&G[1] model 911 digital humidity system. Data are stored by the computer data acquisition system.

Computer Control System

Data acquisition and storage are computer controlled. The computer stores real-time data for radar transmission and wind speed. Figure 4 is a block diagram of the system's computer hardware and instrumentation. A Hewlett-Packard (HP) 310 computer with 5 megabytes of random access memory (RAM) is used for primary system control and data acquisition. An HP 9133 combined 10-megabyte hard disk drive and 3-1/2-in. floppy disk drive is used for program and data storage. The program and menu data are stored on the hard drive. Data are stored to the 3-1/2-in. floppy drive and printed to an HP 2225A ink-jet printer. All data input

[1]EG&G, 151 Bear Hill Road, Waltham, MA 02154.

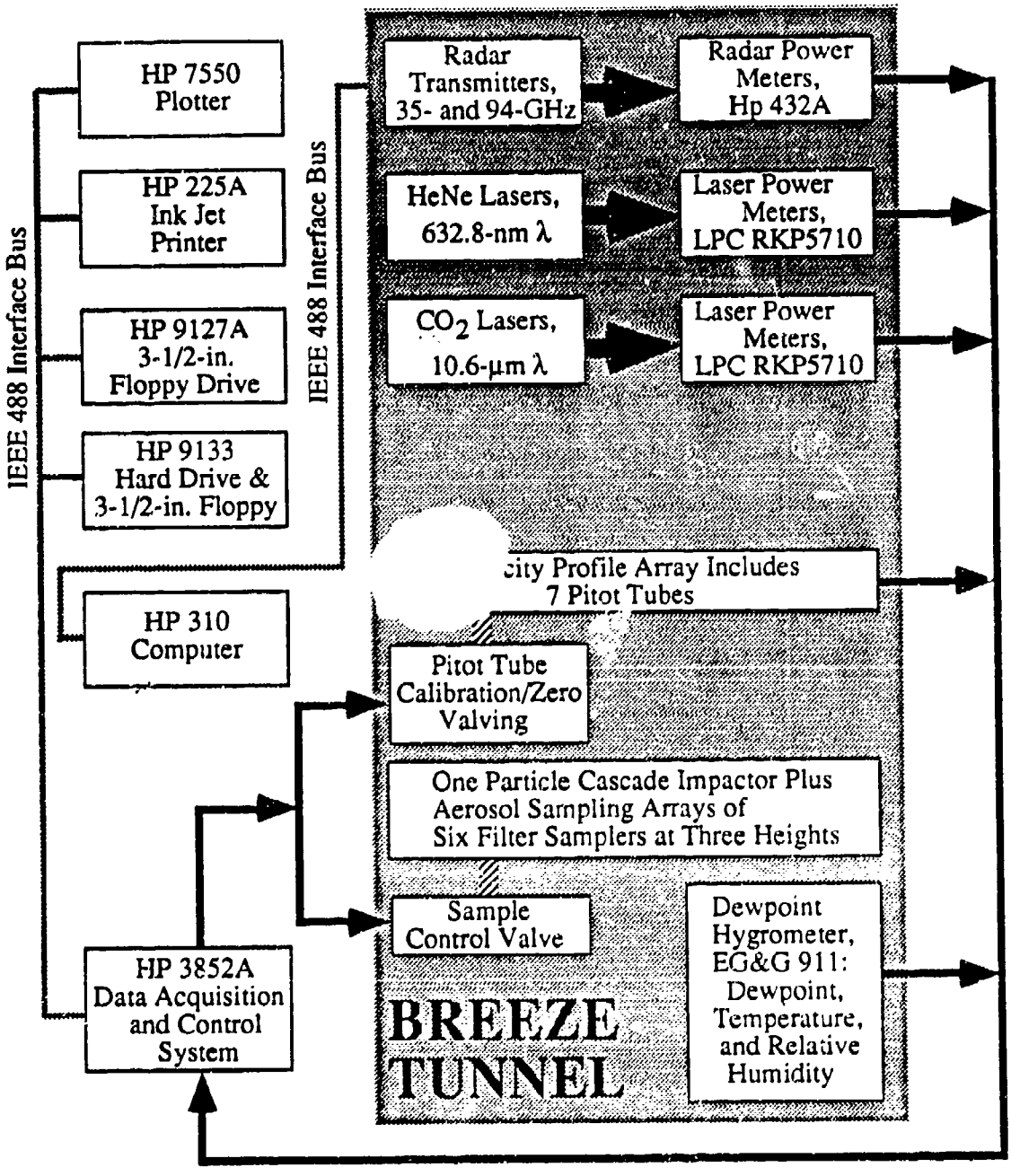

FIGURE 4. Block Diagram of the Computer Hardware and Instrumentation

to the system are analog and are read into the computer by means of an HP 3852A data acquisition system that contains an HP 44702A voltmeter and two HP 44711A, 24-channel high-speed multiplex input cards. System control is provided through the HP data acquisition system by means of an HP 44725A, 16-channel general purpose switching output card. Output control for the two radar systems is provided by means of an IOtech[1] HPIB 488-to-RS232 converter.

A menu-driven data acquisition and control program acquires and stores transmission data from lasers and radar, as well as velocity, temperature, and relative humidity. Array menus are used to make all system assignments (such as the electrical assignments of data monitors and system control components), to enter monitor calibration values, and to make protocol parameter assignments (such as data acquisition timing values). A "comment" selection allows the operator to type comments to a computer file. If the protocol requires that data be taken while the operator is in the comment menu, the comment is interrupted while the data are taken.

All protocol information (such as measurement timing), instrument calibration, measurement data, event times (such as time of start of generation of the obscurant and aerosol filter collection times), and comments made by the operator or the computer are saved to a 3-1/2-in. floppy disk. Protocol, calibration, and other information that may apply to a series of trials is stored to the hard drive and copied to the floppy disk. Immediately after a trial series, the operator makes a backup of the floppy disk and write-protects and stores the original separately from the backup disk and printouts.

CALCULATION OF MASS EXTINCTION COEFFICIENTS AND ALPHA YIELD

The following sections list the equations to calculate mass extinction coefficients and alpha yield. The calculation of mass extinction coefficients requires laser transmission and airborne particle concentration.

Mass Extinction Coefficient Calculation

Transmittance at wavelength λ, T_λ, is a function of the mass extinction coefficient at that wavelength, α_λ (in m^2/g), and the concentration path length, CL (in g/m^2). The mass extinction coefficient quantifies the degree of extinction of radiant energy propagating through airborne smoke/obscurant particles. The CL value is the integral of concentration along the path through the obscurant cloud, a product of concentration (C) and path length (L).

The Beer-Lambert relationship between transmittance, extinction coefficient, and concentration path length (CL) is

$$T/T_o = \exp(-\alpha CL) \qquad (1)$$

[1] IOtech, PO Box 391345, Cleveland, OH 44139-9846.

where T/T_o = normalized transmission of transmitted (T) to incident (T_o) radiation (T/T_o is also called transmission or transmittance)
α = mass extinction coefficient
CL = concentration integrated along the path of propagation (m^2/g)
C = obscurant concentration (g/m^3)
L = laser path length (m).

The mass extinction coefficient is equal to

$$\alpha = -\overline{\ln(T/T_0)} \,/\, \overline{(C\,L)}. \tag{2}$$

Alpha Yield Calculation

A figure of merit for an obscurant material release is the alpha yield, or extinction yield per gram of material released, which is calculated for the laser line of sight. The larger the alpha yield, the greater is the efficacy of release of the obscurant material. The units of alpha yield are $m^2/g_{actual\ release}$.

Alpha-yield estimates require simplifying assumptions. The expression for alpha yield is obtained by combining Equation (1) and an equation for mass balance. The mass-balance equation is

$$m\,Y = C\,A\,v \tag{3}$$

where m = mass released rate (g/s)
Y = yield of airborne material per unit mass released ($g_{airborne}/g_{actual\ release}$)
A = cross-sectional area of the breeze tunnel (m^2)
v = velocity (m/s).

It is assumed that the yield (Y) is equal to 1.0 and that the airborne concentration [$C = (mY)/(Av)$] and velocity are uniform across the tunnel's cross section. The average concentration is measured.

A concentration value is needed to calculate alpha yield. Therefore, to predict concentration, Equation (1) is rearranged to

$$C = -\ln(T/T_o) \,/\, (\alpha\,L). \tag{4}$$

Then to determine the alpha yield, the concentration C from Equation (4) is substituted into Equation (3),

$$m\,Y = -A\,v\,\ln(T/T_o) \,/\, (\alpha\,L), \tag{5}$$

and the equation is rearranged to

$$\alpha\,Y = -A\,v\,\ln(T/T_o) \,/\, (m\,L). \tag{6}$$

Thus alpha yield depends on the cross-sectional area of the breeze tunnel, average wind speed, release rate, tunnel width, normalized transmission, and the assumption of uniform airborne concentrations across the cross section.

DATA ANALYSIS PROCEDURE

The data analysis procedure is summarized here; details are included in trial reports (Schmel et al., 1992a, b, 1993a, b, c). Before analysis, data files are converted from the binary format of the HP computer in the breeze tunnel to an ASCII format and then transferred to a Macintosh[1] computer. Data analysis procedures use commercial software.

This section includes discussions of baseline voltages, and average transmission. The section on baseline voltages describes the procedure to adjust the drift in baseline during a trial. The section on transmission describes the procedure to evaluate average transmission during sampling for airborne concentration.

Baseline Voltage Calculation

Transmission, T/T_o, is the ratio of voltages from the laser and radar power meters (radar voltages are converted to decibels of attenuation). The ratio is the voltage during material release to the baseline voltage in the absence of airborne material. During baseline times before and after release of obscurant, the average baseline voltages are expected to be equal. However, the laser and radar systems do not always satisfy expectations for a constant baseline voltage, and usually they are not equal. Baseline voltages vary because of the effects of variations in ambient temperature on the stability of laser and radar electronics, and because of laser movement caused by mechanical instability of the laser supports.

Consequently, there are three baseline periods. The initial baseline occurs before obscurant reaches the laser line of sight. The trial baseline occurs during passage of the obscurant cloud. The final baseline occurs after passage of the cloud. Average voltages are calculated for the initial and final baselines. The trial baseline is represented by a linear interpolation between the initial and final baselines.

To calculate transmission during cloud passage, experimental voltages are divided by baseline voltage ratios, $(\text{Volts}_{\text{Power Meter}})/(\text{Volts}_{\text{during baseline}})$. The term in the denominator considers three periods for voltages: an initial baseline before particle release, the baseline during particle release, and a final baseline after particle release. A linear interpolation is used to predict the variation in baseline voltages between the initial and final baselines. The voltage adjustment equation for the initial baseline is

$$\text{Transmission} = (\text{Volts}_{\text{Power Meter}}) / (\text{Baseline}_{\text{Initial}}). \tag{7}$$

For the final baseline,

$$\text{Transmission} = (\text{Volts}_{\text{Power Meter}}) / (\text{Baseline}_{\text{Final}}). \tag{8}$$

[1] Apple Computer, Inc., 20525 Mariani Avenue, Cupertino, CA 95014.

Ratios are also used to calculate transmission during material release. The analysis procedure is to divide experimental voltages as a function of time by baseline values calculated by linear interpolation between the end of the initial baseline and the start of the final baseline. The voltage adjustment equation during material release is

$$\text{Transmission} = (\text{Volts}_{\text{Power Meter}}) / (\text{Baseline}_{\text{Interpolated}}). \tag{9}$$

Average Transmission Calculation

Mass extinction coefficients are calculated from the average transmission during sampling for mass concentration. Average transmission is the average of the time-weighted natural logarithm of transmission (T/T_o). The time-weighted average is

$$(T/T_o)_{avg} = \exp(\{ \Sigma [\ln(T/T_o)_i \Delta t_i] \} / \{ t_S - t_F \}). \tag{10}$$

where t = time for recording laser power meter voltage (s)
t_S = time that sampling for average airborne mass concentration started (s)
t_F = time that sampling for average airborne mass concentration ended (s).

A constant transmission value is optimal for calculating mass extinction coefficients. However, the term "constant" describes an idealized obscurant cloud. In practice, transmission often continues to change. During plume passage, transmission initially decreased and then tended toward a constant value, with fluctuations around that value.

During a trial, the operator watches the control-room computer screen to estimate when constant transmission begins, but also to ensure that a sample is taken during obscurant release. Sampling during constant transmission is desired to improve the accuracy of mass extinction coefficients calculated from the measured airborne mass concentration.

ILLUSTRATIVE RESULTS

Prior reports have discussed average laser transmission, aerodynamic particle diameter, mass concentration, alpha yield, mass extinction coefficients, and dependency of mass extinction coefficients on aerodynamic mass median diameter (AMMD). Sections on aerodynamic particle diameter summarize AMMD and geometric standard deviation (GSD) for trials. For millimeter-wave obscurants, airborne particle aggregation is inferred by comparing regions of transmission at 94 GHz with those of transmission at 35 GHz. Sections on mass concentration summarize average concentrations across the breeze tunnel. Sections on alpha yield summarize alpha yield based on feed rates. Sections on mass extinction coefficients summarize mass extinction coefficients for the attenuation of CO_2 and HeNe laser spectra, and the dependency on mass concentration. Sections on mass extinction coefficients summarize the dependency of mass extinction coefficients on AMMD.

The sections that follow illustrate results that might be expected from trials in the breeze tunnel. These sections illustrate normalized transmission and the dependency of mass extinction coefficients on the aerodynamic particle diameter. For these trials, the mass extinction coefficient for attenuation of CO_2 laser spectra ranged from 0.44 to 1.60 m^2/g, and airborne concentration ranged from 0.03 to 1.9 g/m^3.

Mass extinction coefficients were calculated based on the average normalized transmission (T/T_o) during sampling for airborne mass concentration, and based on the average measured mass concentration. The T_o is the transmission when obscurant is not airborne. The average concentration was assumed to be the arithmetic average of concentrations measured along the middle sample transporter. The average transmission during sampling for airborne mass concentration was used in equation (2) to calculate the mass extinction coefficient from the Beer-Lambert relationship between transmittance, extinction coefficient, and concentration path length.

Normalized Transmission

Normalized transmission for one trial is shown as a function of time in Figure 5. Included in the figure is a horizontal line that represents the time of sampling for average airborne mass concentrations and the average concentration [see equation (10)]. This average transmission was used in equation (2) to calculate the mass extinction coefficient.

Dependency on Aerodynamic Particle Size

As shown in Figure 6, mass extinction coefficients have been found to be a function of the aerodynamic mass median diameter (AMMD), and mass extinction coefficients decreased as the AMMD increased. For these trials, the AMMD ranged from 2.80 to 7.49 μm.

SUMMARY

The breeze tunnel allows the control of variables that are essential to evaluating mass extinction coefficients for airborne obscurant particles in a flowing air stream and the efficacy of the generators at a target generation rate of 10 lb/min. There is some residual uncertainty in the precision of evaluating average mass extinction coefficients because of transient variations in release mechanisms at the particle generator. Such variations also occur during field releases, but variations in wind flow during field experiments cause much greater uncertainty. Field trials can be considered tests of the influence of short-term meteorology on the released particles (airborne concentrations often change rapidly as a function of time and within the laser line of sight), rather than tests of the efficacy of the particles to obscure.

In breeze tunnel trials, air flow is reproducible and always suitable for trials: unidirectional and constant. For breeze tunnel trials with nearly collocated lasers, radar, and concentration samplers, the precision and accuracy of experimental mass extinction coefficients are reliable and are not influenced by the experimental vagaries in wind flow that confound results from field experiments.

The breeze tunnel is a unique facility to determine the efficacy of released particles in flowing air as a function of the controlling variables. Optimum material feed characteristics and generator operating conditions can be determined. The facility allows investigation of the effects of different generator operating variables, airborne concentration, and airborne particle size on mass extinction coefficients for particles moving in a flowing air stream.

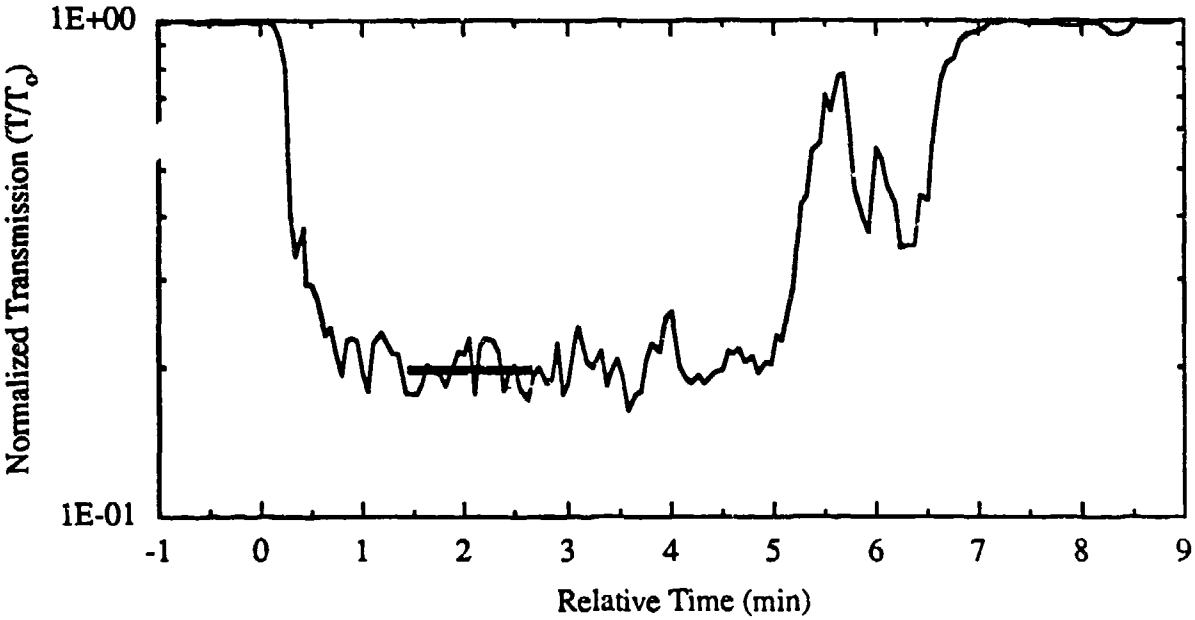

Horizontal line is time and average ln(T/T$_o$) during sampling

FIGURE 5. Normalized Transmission for CO_2 Laser Spectra Attenuation for a 3.5-ft Path Length and Average Transmission During Sampling for Airborne Mass Concentration

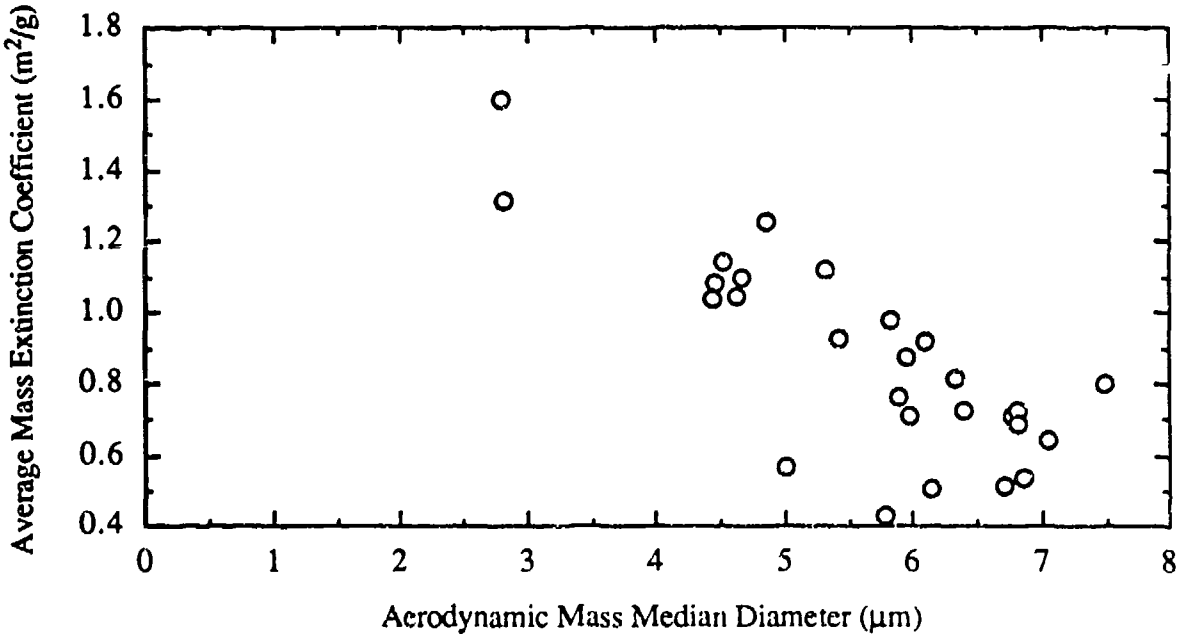

FIGURE 6. Average Mass Extinction Coefficients for Attenuation of CO_2 Laser Spectra as a Function of Aerodynamic Mass Median Diameter

REFERENCES

G. A. Sehmel, W. G. Rouse, R. Bonfante, R. D. Swannack, and M. W. Ligotke. 1992a. Breeze Tunnel Performance of Compact-Disc Carbon-Fiber Generation for Attenuation of 35- and 94-GHz Radar Transmission. PNL-8351, Pacific Northwest Laboratory, Richland, Washington.

G. A. Sehmel, D. R. Banks, J. J. Novad, R. Bonfante, R. D. Swannack, and M. W. Ligotke. 1992b. Breeze Tunnel Performance of XM56 Carbon-Flake Generation for Attenuation of CO_2 and HeNe Laser Transmission in May and October 1991 Trials. PNL-8430, Pacific Northwest Laboratory, Richland, Washington.

G. A. Sehmel, R. D. Swannack, M. W. Ligotke, W. G. Rouse, and R. Bonfante. 1993a. ASM-MM Breeze Tunnel Experiments - August 1991. ERDEC-CR-016, U. S. Army Edgewood Research, Development and Engineering Center, Aberdeen Proving Ground, MD.

G. A. Sehmel, D. R. Banks, J. J. Novad, R. Bonfante, E. G. Kuffel, R. D. Swannack, and M. W. Ligotke. 1993b. XM56 Carbon-Flake Breeze Tunnel Experiments in March and June to July 1992 Trials. PNL-8578, Pacific Northwest Laboratory, Richland, Washington.

G. A. Sehmel, W. G. Rouse, E. S. Catalano, R. Bonfante, E. G. Kuffel, R. D. Swannack, and M. W. Ligotke. 1993c. IR Log Generator Trials Using Brass Flakes in the Breeze Tunnel During August 1991. PNL-8625, Pacific Northwest Laboratory, Richland, Washington.

J. G. Stuart. 1984. Radiometers to Measure Attenuation and Phase Shift at 35 GHz and at 95 GHz. F-C5772, The Franklin Institute, Philadelphia, Pennsylvania 19103.

ANGULAR DISTRIBUTION OF THE FORWARD LIGHT SCATTERING FROM A QUARTZ FIBER

Choonghoon Oh, G. G. Padmabandu, and Edward S. Fry

Department of Physics
Texas A & M University
College Station, Texas 77843-4242

RECENT PUBLICATIONS, SUBMITTALS, AND PRESENTATIONS:

A) Edward S. Fry, G. G. Padmabandu, and Choonghoon Oh, "Coherent Effects in Forward Scattering", in Ocean Optics XI, G. D. Gilbert, Editor, Proc. SPIE 1750, 170-177 (1992).

B) Edward S. Fry, G. G. Padmabandu, and Choonghoon Oh, "Angular Measurement of the Forward Light Scattering from a Quartz Fiber", Proceedings of the 1992 CRDEC Scientific Conference on Obscuration and Aerosol Research, October, 1992.

C) Choonghoon Oh, G. G. Padmabandu, and Edward S. Fry, "Angular Distribution of the Forward Light Scattering from a Quartz Fiber", submitted to Applied Optics, September, 1993.

D) Choonghoon Oh, "Measurement of Forward Light Scattering Using a Barium Titanate Crystal as a Novelty Filter", Ph.D. Thesis, Texas A&M University (August, 1993).

E) Choonghoon Oh, Kelly T. Andrews, Edward S. Fry, G. J. Dunning, M. L. Minden, and D. M. Pepper, "Scattering of Phase Conjugated Light by a Stationary Particle", submitted to the proceedings of the 1993 Edgewood RDEC Scientific Conference on Obscuration and Aerosol Research (these proceedings).

F) Edward S. Fry, G. G. Padmabandu, and Choonghoon Oh, "Angular Distribution of Electromagnetic Scattering Near Zero Degrees", presented at the 1993 Edgewood RDEC Scientific Conference on Obscuration and Aerosol Research, June, 1993.

G) Choonghoon Oh, Kelly T. Andrews, Edward S. Fry, G. J. Dunning, M. L. Minden, and D. M. Pepper, "Scattering of Phase Conjugated Light by a Stationary Particle", presented at the annual meeting of the Optical Society of America , Toronto, October, 1993.

H) G. J. Dunning, M. L. Minden, D. M. Pepper, Choonghoon Oh, Kelly T. Andrews, and Edward S. Fry, "On the Propagation of Phase-Conjugate Fields Through Dynamically Scattering Media", presented at the annual meeting of the Optical Society of America , Toronto, October, 1993.

I) Kelly T. Andrews, Choonghoon Oh, Edward S. Fry, "Scattering of Phase Conjugated Light by a Stationary Micron-Sized Dielectric Particle", presented at the Texas Section Meeting of the American Physical Society, College Station, TX, October, 1993.

J) Kelly T. Andrews and Edward S. Fry, "Light Scattering Mueller Matrix Measurements of Micron Sized Spheres", presented at the Texas Section Meeting of the American Physical Society, Houston, TX, November, 1992. Ms. Andrews won an award for "Outstanding Paper Presented by a Graduate Student" for this paper.

ABSTRACT

Using a new technique based on the fanning of a coherent light beam in a photorefractive $BaTiO_3$ crystal, the angular distribution of forward light scattering by quartz fibers of radii from 15 μm to 30 μm has been successfully measured. Data have been obtained over the angular range 0° to 0.3°, and are in good agreement with theory.

INTRODUCTION

Light scattering by small particles has been the subject of intense investigations for many decades. However, virtually all experimental work to date has been limited to angles from near forward to backward directions.[1] The limiting experimental factor in measurement of forward scattering is the unscattered incident wave that is superimposed on the scattered wave.[2]

There has not been much experimental success in separating these two waves in the forward direction. Most extensive are the microwave analog techniques that have been used to measure light scattering in all directions including 0°.[3, 4] In this approach microwave radiation is scattered by macroscopically constructed targets in order to simulate light scattering by micron-size particles at optical frequencies. In a direct optical measurement, Spinrad used a special low-angle scattering meter to measure volume-scattering functions down to angles as small as 0.1° from the forward direction.[5, 6] Forward-scattering measurements from an isolated sphere have been made recently by using the Guoy phase shift that occurs at the waist of a focused Gaussian beam.[7] However, that method is applicable only to particles so small that the scattering phase shift can be neglected in the analysis. Recently, we reported the first measurements of light scattering at 0° by single micron sized quartz fibers,[8] and the first observations of coherent scattering at 0° by a suspension of particles.[9] For this previous work we developed a novel technique based on the fanning of a coherent light beam in a photorefractive $BaTiO_3$ crystal to separate the scattered light in the forward direction from the strong unscattered incident beam. The present work reports an extension of the single particle measurements to higher angular resolution, including angular distribution measurements near zero degrees.

II. THEORETICAL BACKGROUND

Light scattering by a right circular cylinder is given by,[1]

$$\begin{pmatrix} E_{s,par} \\ E_{s,per} \end{pmatrix} = e^{i3\pi/4} \sqrt{\frac{2}{\pi kr}}\, e^{ikr} \begin{pmatrix} T_1 & 0 \\ 0 & T_2 \end{pmatrix} \begin{pmatrix} E_{i,par} \\ E_{i,per} \end{pmatrix}. \qquad (1)$$

Here, E_i and E_s are the incident and scattered fields, respectively; and *per* and *par* represent the polarization of the fields perpendicular and parallel to the cylinder axis, respectively. Discussion in this paper centers on T_2, but the same argument holds for T_1. Eq. (1) shows that there is an intrinsic phase shift of $3\pi/4$ between the scattered field and the incident field. We have taken this phase shift into account when measuring the scattering amplitude $T_2(\theta)$ for small angles, including zero degrees.

By using a novelty filter based on photorefractive beam fanning in $BaTiO_3$ we have succeeded in reducing the background intensity due to the unscattered beam so that it is comparable to, or even smaller than, the intensity of the scattered field.[8, 10] The concept is based on the fact that at low intensities, beam fanning can take a long time (even seconds or longer) to establish. Fields that are undergoing phase and amplitude changes on a much shorter time scale do not undergo appreciable fanning. Consequently, if the scattering particle(s) move sufficiently fast, the fields scattered by them do not undergo fanning in a $BaTiO_3$ crystal, whereas the steady incident field is fanned out of the forward direction. Forward scattering from surface imperfections in windows, lenses, etc. does not contribute a background to forward scattering measurements since this scattering is also fanned out of the forward direction (i.e. these scatterers are stationary).

III. EXPERIMENTAL APPARATUS

Fig. 1 schematically illustrates our experimental setup for angular resolved measurements of forward scattering by a quartz fiber. The cw Ar^+ laser beam (514.5 nm), whose intensity was kept below 2 mW/cm^2, is polarized in the plane of the figure. This plane also contains the *c*-axes of two $BaTiO_3$ crystals; these axes are oriented symmetrically, as indicated by

the arrows. Each is a 0°-cut crystal in the form of a cube with dimensions 5×5×5 mm^3.

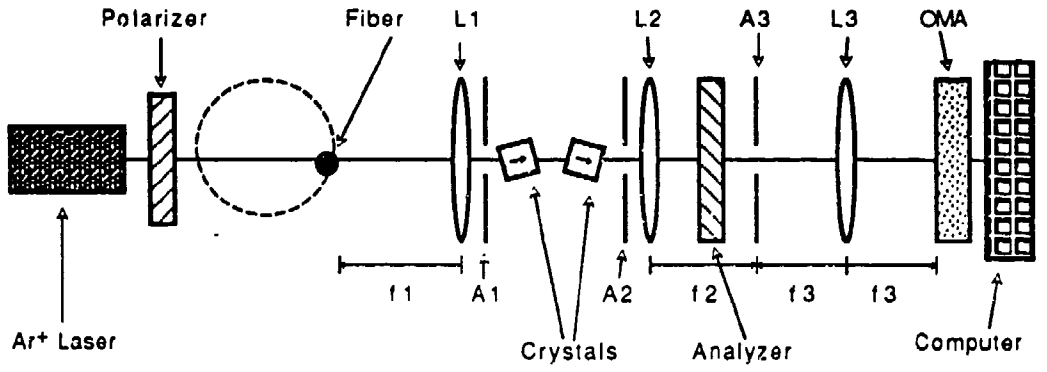

Figure 1. Schematic of the experimental apparatus.

To introduce a time dependence to the scattered light, the quartz fiber is mounted on a 1 rpm synchronous motor that rotates it in a circle of radius 3 cm so that it traverses the beam twice in each revolution. Adjustable apertures A1, A2 and A3 define the angular acceptance and shield both the crystals and the detector from stray light. Lens L1 collects forward scattered light over a small angular range and collimates it prior to passage through the $BaTiO_3$ crystals. Lens L2 focuses the transmitted light onto a pinhole (aperture 3), and lens L3 re-collimates it so that the transverse intensity profile in the detector plane corresponds to the angular distribution of the scattered light.

Most of the light incident on the first crystal is fanned out by it. However, because of the asymmetric nature of beam fanning some of the light is left of one side of the beam.[8, 10] Much of this remaining light is fanned out by the second crystal, leaving a background intensity in the forward direction that corresponds to less than 1% of the incident light intensity. As the fiber crosses the laser beam a pulse of scattered light is

generated in this dark background. The angular distribution of this pulse is measured with an optical multichannel analyzer (OMA) which has 1024 detection elements in a 1 inch length. This signal is recorded in a computer and compared with the results of theoretical calculations.

IV. EXPERIMENTAL RESULTS

Because the background intensity is not exactly zero, what is actually measured is the interference pattern between the scattered field $E_s(x)$ and the unscattered background field $E_b(x)$. If forward scattering is measured with the apparatus of Fig. 2, the intensity distribution $I(x)$ in the detector plane will have the form

$$I(x) = I_b(x) + I_s(x) + 2(\hat{\varepsilon}_s \cdot \hat{\varepsilon}_i)\sqrt{I_b(x) I_s(s)}\,\cos[\phi(x)]. \qquad (2)$$

Here $I_b(x) = |\vec{E}_b(x)|^2$ and $I_s(x) = |\vec{E}_s(x)|^2$; $\hat{\varepsilon}_s$ and $\hat{\varepsilon}_i$ are unit vectors representing the polarizations of the scattered and the incident fields, respectively; $\phi(x)$ is the phase difference between the two fields; and x is the position on the detection plane. There is, of course a one-to-one correspondence between x and the scattering angle θ. According to Eq. (1) the phase difference between the scattered field and the incident field is

$$\phi(\theta) = 3\pi/4 + \phi_0(\theta) + kr\left(\frac{1}{\cos\theta} - 1\right). \qquad (3)$$

Here $\phi_0(\theta)$ is the phase of $T_2(\theta)$ and the last term is the phase difference between a plane wave and a cylindrical wave at the detector plane. At and near zero degrees, the phase factor, $\phi_0 + 3\pi/4$, generally has only small fluctuations around a mean value $3\pi/4$ radian. Therefore, $I(x)$ is mainly the interference between a plane wave and a cylindrical wave.

Fig. 2 shows a typical measurement of the forward scattering from a quartz fiber. The horizontal axis is the scattering angle in degrees and the vertical axis is the intensity in arbitrary units. The thick curve is the measurement and the thin curve is the calculation based on the measured unscattered background. Two fitting parameters were used: the amplitude of the scattered field at 0°, and the position corresponding to 0°. The angular uncertainty obtained was ≈0.005°.

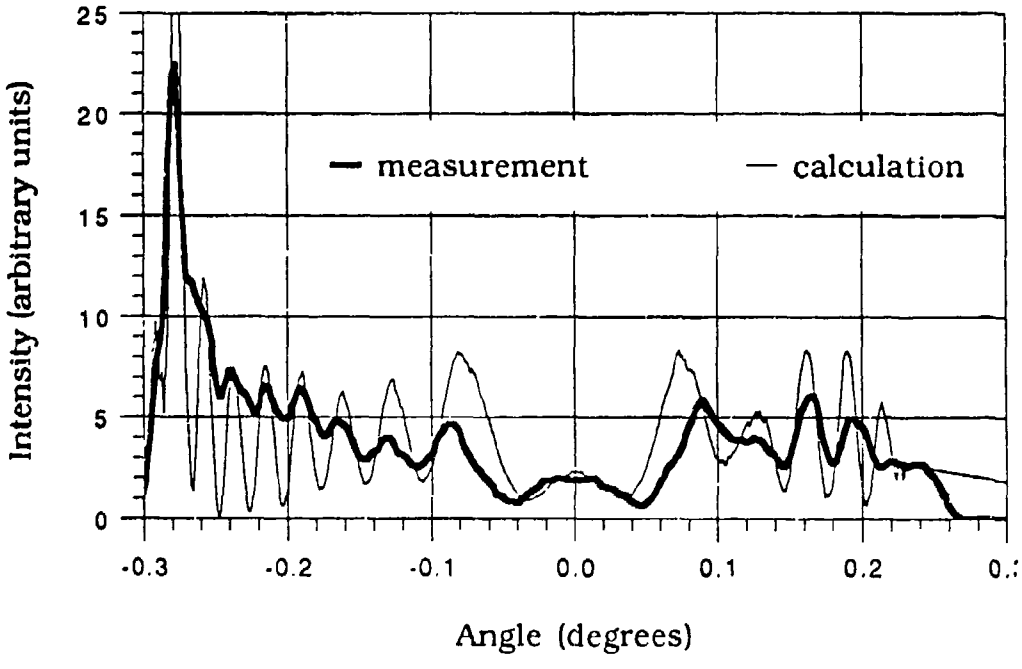

Figure 2. Angular distribution of forward scattering by a quartz fiber. The oscillatory structure is a consequence of interference with the residual unscattered light.

REFERENCES

1. C. F. Bohren and D. R. Huffman, "Absorption a[illegible] Scattering of Light by Small Particles," (Wiley Interscience, New York, [illegible] 1), .

2. H. C. Van de Hulst, "Light Scattering by Small Particles," (Dover, New York, 1981), pp. 30,55,304.

3. A. C. Lind, R. T. Wang, and J. M. Greenberg, "Microwave Scattering by Nonspherical Particles," Appl. Opt. 4, 1555-1561 (1965).

4. R. T. Wang and J. M. Greenberg, "Scattering by Spheres with Non-isotropic Refractive Indices," Appl. Opt. 15, 1212-1217 (1976).

5. R. W. Spinrad, "Measurement of the volume scattering function at near forward angles for suspended oceanic particulates," in Ocean Optics V, M.B. White and R.E. Stevenson, ed., Society Photo-Optical Instrumentation Engineers 160, (San Diego, CA, 1978), pp. 18-22.

6. R. W. Spinrad, J. R. V. Zaneveld, and H. Pak, "Volume scattering function of suspended particulate matter at near-forward angles: a comparison of experimental and theoretical values," Appl. Opt. 17, 1125-1130 (1978).

7. J. S. Batchelder and M. A. Taubenblatt, "Interferometric detection of forward scattered light from small particles," Appl. Phys. Lett. 55, 215-217 (1989).

8. G. G. Padmabandu, C. Oh, and E. S. Fry, "Measurement of light scattering at 0° by micrometer-size quartz fibers," Opt. Lett. 17, 169-171 (1992).

9. E. S. Fry, G. G. Padmabandu, and C. Oh, "Coherent Effects in Forward Scattering," in Ocean Optics XI, G.D. Gilbert, ed., Society Photo-Optical Instrumentation Engineers 1750, (San Diego, CA, 1992), pp. 170-177.

10. C. Oh, "Measurement of Forward Light Scattering Using a [illegible]arium Titanate Crystal as a Novelty Filter," Ph.D. Thesis, Texas A&M University (1993).

SCATTERING OF PHASE CONJUGATED LIGHT BY A STATIONARY PARTICLE

Choonghoon Oh, Kelly T. Andrews, and Edward S. Fry

Department of Physics, Texas A & M University
College Station, TX 77843-4242

and

G. J. Dunning, M. L. Minden, and D. M. Pepper

Hughes Research Laboratories
3011 Malibu Canyon Road,
Malibu, CA 90265

RECENT PUBLICATIONS, SUBMITTALS, AND PRESENTATIONS:

These are itemized in these proceedings in the paper: Choonghoon Oh, Kelly T. Andrews, Edward S. Fry, G. J. Dunning, M. L. Minden, and D. M. Pepper, "Scattering of Phase Conjugated Light by a Stationary Particle".

ABSTRACT

Experimental observations of the angular distributions due to scattering of a phase conjugate reflected beam by a quartz fiber are reported. It is shown that the scattered intensity due to the phase conjugate beam is less than that due to a beam reflected by a normal mirror.

INTRODUCTION

It is well known that phase conjugated light can correct the phase distortions introduced by a phase distorting medium.[1,2] There have been numerous experimental demonstrations of this phenomenon using various phase distorters and phase conjugating media.[3]

Here we report the experimental observations of this phenomenon using light scattering by a micron-sized particle. In an ideal case, if all the light scattered by a small particle is reflected back toward the particle by a phase conjugator, its phase should be corrected after interacting with the particle the second time; in principle, the incident wave would be recovered. In an experimental situation, generation of a phase conjugate reflection of all the scattered light is probably not reasonable, or of practical interest. Thus the precise form of the incident wave is generally not recoverable. However, when light is scattered by a particle with radius larger than the wavelength, the scattering probability in the forward direction is so large that most of the scattered intensity is confined in the forward direction.[4] Therefore in practice we can approximately reproduce the ideal situation by phase conjugating a large portion of the forward scattered light.

In the present work, a portion of the light scattered in the forward direction by a quartz fiber is retroreflected by a phase conjugator and re-scattered by the fiber. The angular distribution of this scattering is compared with that due to retroreflection by a normal mirror.

EXPERIMENTAL APPARATUS

The experimental arrangements are schematically illustrated in Figs. 1 and 2. A micron-size quartz fiber, whose axis is perpendicular to the plane of figure, is used as a scattering sample. The 514.5 nm line of a cw Ar^+ laser is polarized in the plane of incidence (plane of the figure). A 0°-cut $BaTiO_3$ crystal is used as a self-pumped phase conjugator.[5] The crystal is a cube whose edge dimension is approximately 5 mm, and its c-axis is in the plane of incidence. The intensities of the laser beam and the retroreflected beam are monitored throughout the experiment with detectors 2 and 1, respectively. The phase conjugate reflectivity of the

crystal is estimated from these readings, and it was typically about 30% relative to the mirror reflection. The retroreflected light going back into the laser cavity is minimized by a neutral density filter. The angular distribution of the scattered light is measured with a photomultiplier tube (PMT) mounted on a rotating arm.

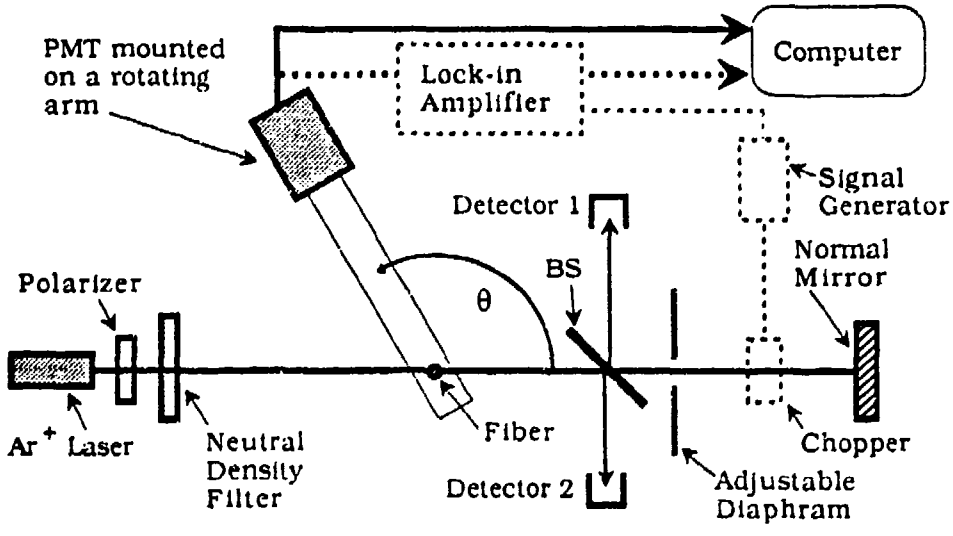

Figure 1. Apparatus schematic with normal mirror. The chopper and lock-in are used in the second set of experiments.

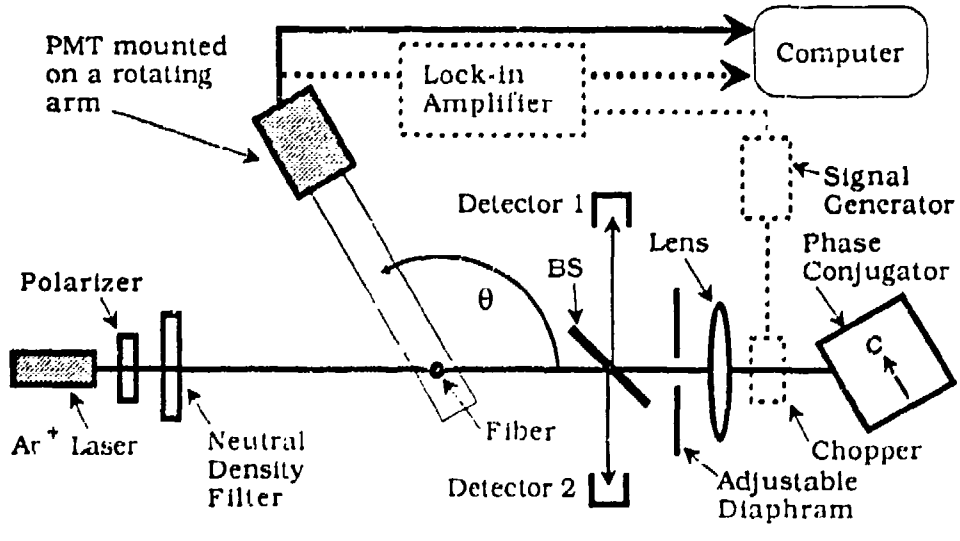

Figure 2. Apparatus schematic with phase conjugate mirror. The chopper and lock-in are used in the second set of experiments.

To calibrate the fiber size, the angular distribution of the scattered intensity is measured without a retroreflector and the radius of the fiber is determined by fitting this data to the theoretical calculations for the angular scattering function of an infinite dielectric cylinder.[4] For all the work to be described here, the fiber was a quartz cylinder with a radius of 19.8 μm.

Two sets of experiments were performed. In the first set, the output of the photomultiplier was recorded directly by the computer and the data were then manipulated to separate the scattering by the incident and the retroreflected beams. In the second set, the retroreflected beam passed through a chopper and the photomultiplier output was processed by a lock-in amplifier tuned to the chopper frequency (as indicated by the dashed components in Figs. 1 and 2). The lock-in output is proportional to the intensity of the light scattered from the retroreflected beam.

FIRST EXPERIMENTAL RESULTS (DIRECT MEASUREMENTS)

Initially, the angular distribution of the scattered intensity is measured without a retroreflector. Both the light scattered in the forward direction and the incident laser beam are then retroreflected with a normal mirror, as shown in Fig. 1, and the angular distribution of the scattered light is measured again. Since this first set of experiments does not employ the chopper, data for scattering from the retroreflected beam are obtained from these two angular distributions by subtracting the initial one from the latter one. Fig. 3 shows the results for the 19.8 μm radius quartz fiber. Data for scattering from the incident laser beam (obtained in the absence of a retroreflected beam) are plotted as a function of scattering angle θ. Data for scattering from the retroreflected beam (obtained by subtracting the two angular distributions) are plotted as a function of $180°-\theta$, so that forward scattering for the retroreflected beam can be easily compared to the incident beam scattering.

As expected, the scattering of light reflected by a normal mirror has a structure almost identical to that produced by the incident laser beam. Due both to the reflections at the beam splitter and to the less than perfect reflection at the mirror, some light is lost; this accounts for the

differences in amplitude. In addition, at the larger angles there are some anomalously large oscillations. With respect to these, we recall that the scattered intensity distribution observed with the phase conjugate reflected light was obtained by subtracting two independent data sets. In the calculation of these differences, a small mismatch in the recorded scattering angles was observed. This mismatch is believed to have produced a systematic error that is responsible for these discrepancies at the larger scattering angles.

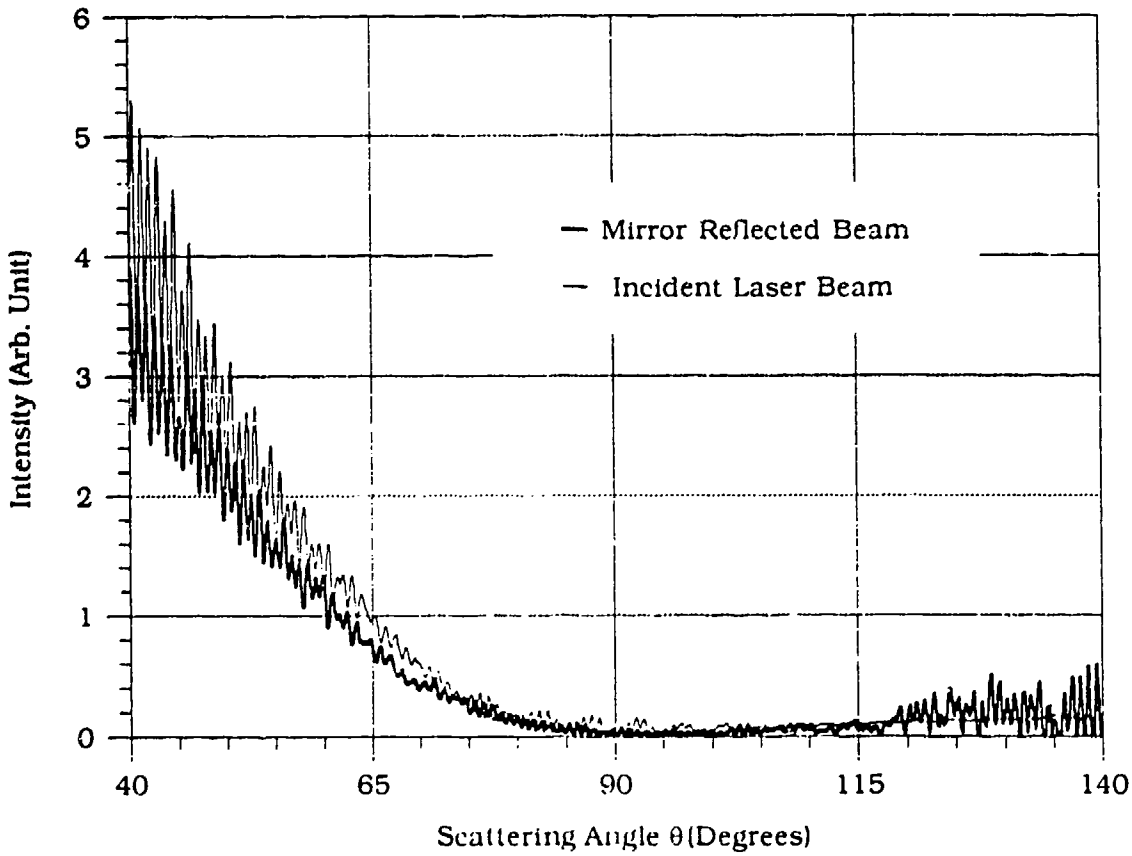

Figure 3. The scattered intensity distribution for the incident laser and for the reflection by a normal mirror. Fiber radius is 19.8 μm, wavelength is 514.5 nm, and polarization is perpendicular to the fiber axis and parallel to the plane of incidence.

Next, the conventional mirror is replaced by a $BaTiO_3$ crystal, as in Fig. 2. The forward scattered light is collected by a lens placed in front of the crystal. The position of the lens is adjusted so that the forward scattered light within a full cone angle of about 10° is incident on the front face of the crystal. This light together with the incident laser beam

is then self phase conjugated in the $BaTiO_3$ crystal. The phase conjugation of forward scattered light is confirmed by checking that the diffraction pattern of the fiber at detector 1 is the same as the pattern produced by the original beam at detector 2. The angular distribution of the total intensity scattered by the fiber is then measured. As before, the scattered intensity distribution due to the phase conjugate reflected light is determined by subtracting the angular distribution of the scattered intensity without the retroreflection from that observed with the phase conjugate reflector in place. In order to normalize this difference to the signal due to the normal mirror, it was multiplied by the signal observed at detector 1 with a normal mirror reflector and divided by the signal observed at detector 1 with a phase conjugate reflector. Fig. 4 shows the intensity distributions for scattering from the incident laser beam and from the phase conjugate reflection.

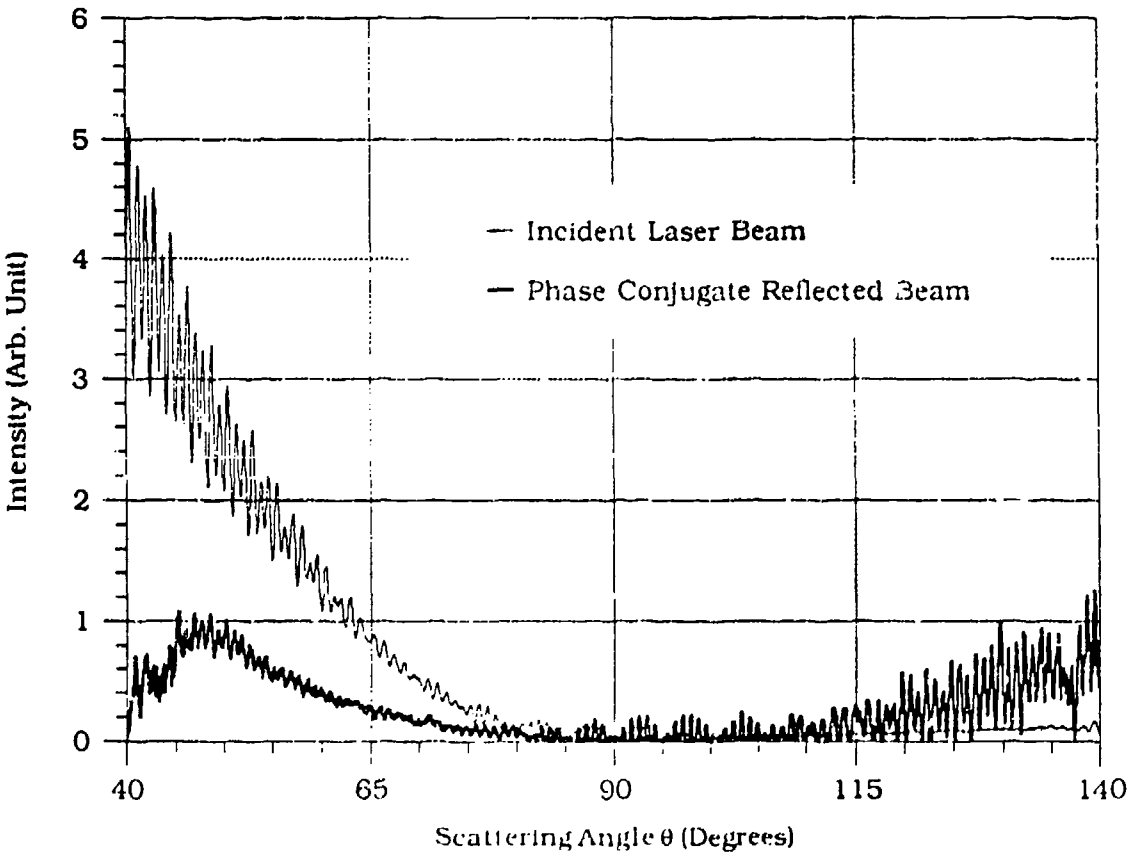

Figure 4. The scattered intensity distribution for the incident laser and for a phase conjugate reflection. Fiber radius is 19.8 μm, wavelength is 514.5 nm, and polarization is perpendicular to the fiber axis and parallel to the plane of incidence.

The structure of the angular distribution produced by the scattering of phase conjugate reflected light is significantly different from that produced by the scattering of light reflected by a normal mirror. In particular, note the suppression of scattering at small angles. However, the anomalous oscillations observed at the larger angles in the last experiment are also present here. Again, this is believed to be a systematic error arising in the subtraction process.

SECOND EXPERIMENTAL RESULTS (CHOPPER BASED)

This systematic error was eliminated, and the data subtraction procedure was avoided in a second set of experiments. In these, the effects due to the scattering of retroreflected light were separated from those due to the scattering of the incident laser beam by placing a mechanical chopper in front of the retroreflector. This chopper modulates the intensity of the retroreflected light and thereby produces a modulation in the intensity of the scattering from the retroreflected beam. The PMT signal due to the intensity of the scattered light is amplified using a lock-in amplifier synchronized to the chopper frequency. These additional components are indicated by dashed lines in Figs. 1 and 2. As before, signals due to scattering from the incident beam are obtained in the absence of a retroreflected beam, but in this second set of measurements, the signals due to scattering from the retroreflected beam are given directly by the lock-in output.

First, a normal mirror is used to retroreflect the incident beam and the scattered light. The chopper is turned on and the angular scattering function of the mirror reflected light is measured. In order to provide a calibration for the lock-in output, these data are matched to the data for the mirror reflected light in Fig. 3 and a calibration factor is obtained. Results for the intensity distributions of the scattering from the incident laser beam and from the beam produced by reflection from a normal mirror are shown in Fig. 5. These data are analogous to those in Fig. 3.

As expected, the scattering of mirror reflected light shows structure similar to that of the incident laser beam. Note that the anomalously large scattering that appears at large values of θ in Figs. 3 and 4 is absent here. Specifically, when using the lock-in technique there is no

need to take the difference between two independent data sets, and this introduction of uncertainty in the data is absent. Also, note that due to the long time constant of the lock-in amplifier some of the detailed structure is partially suppressed.

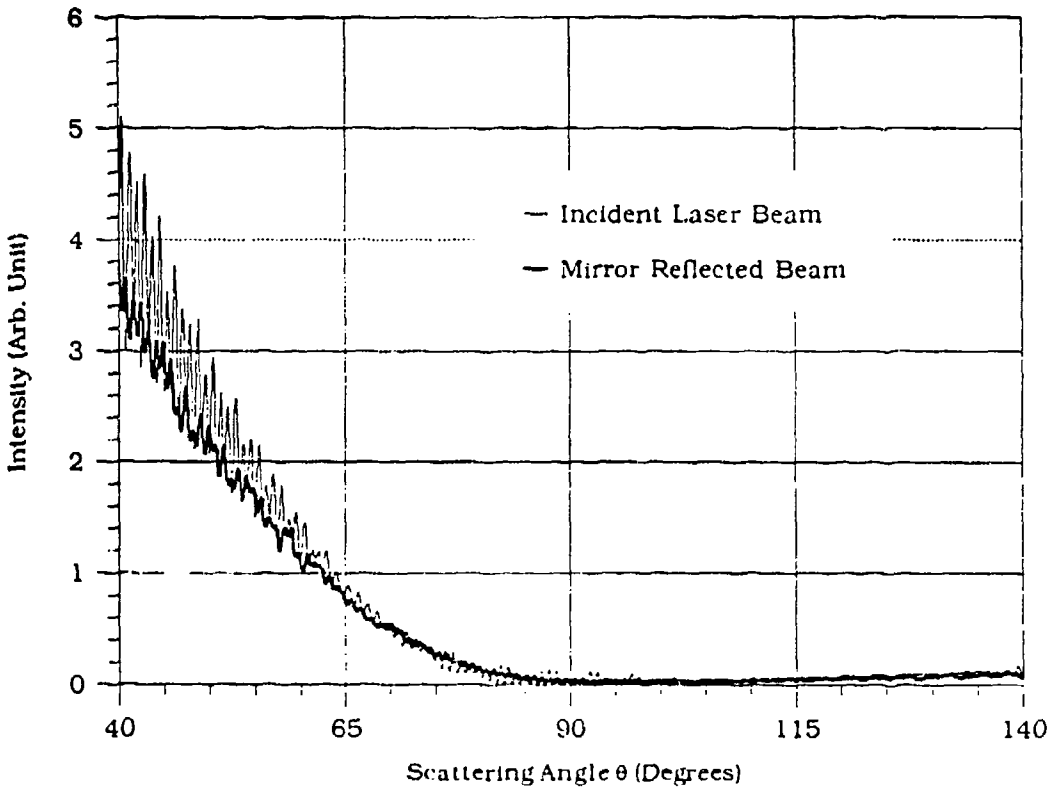

Figure 5. The scattered intensity distribution for the incident laser and for the reflection by a normal mirror. The latter is measured using the chopper and the lock-in (Fig. 1). Fiber radius is 19.8 μm, wavelength is 514.5 nm, and polarization is perpendicular to the fiber axis and parallel to the plane of incidence.

Next, the normal mirror is replaced by a $BaTiO_3$ crystal. As in the first set of experiments, the forward scattered light is collected by a lens placed in front of the crystal. The position of the lens is again adjusted so that forward scattered light within a full cone angle of ≈10° is incident on the front face of the crystal. The mechanical chopper is placed between the lens and the crystal as shown in Fig. 2. The chopper apertures are large enough to allow a full 10° cone of forward scattered light to pass through them. The chopper is turned on and the angular scattering

function of the phase conjugate reflected light is then measured. In order to normalize to the signal due to a normal mirror, the lock-in signal is multiplied by the calibration constant (as in Fig. 5) and by the ratio of the signals at detector 1 due to the mirror and conjugator (as in Fig. 4). Results for the intensity distributions of the scattering from the incident laser beam and from the beam produced by phase conjugate reflection are shown in Fig. 6. These data are analogous to those shown in Fig. 4.

Again, the angular distribution of the scattering from the phase conjugate reflection shows a significantly different structure compared to that from a normal mirror reflection. As in Fig.4, the scattering is suppressed at small angles, but here it is also observed to be suppressed at large scattering angles. As before, the anomalously large scattering observed in Fig. 4 at large values of θ is absent here.

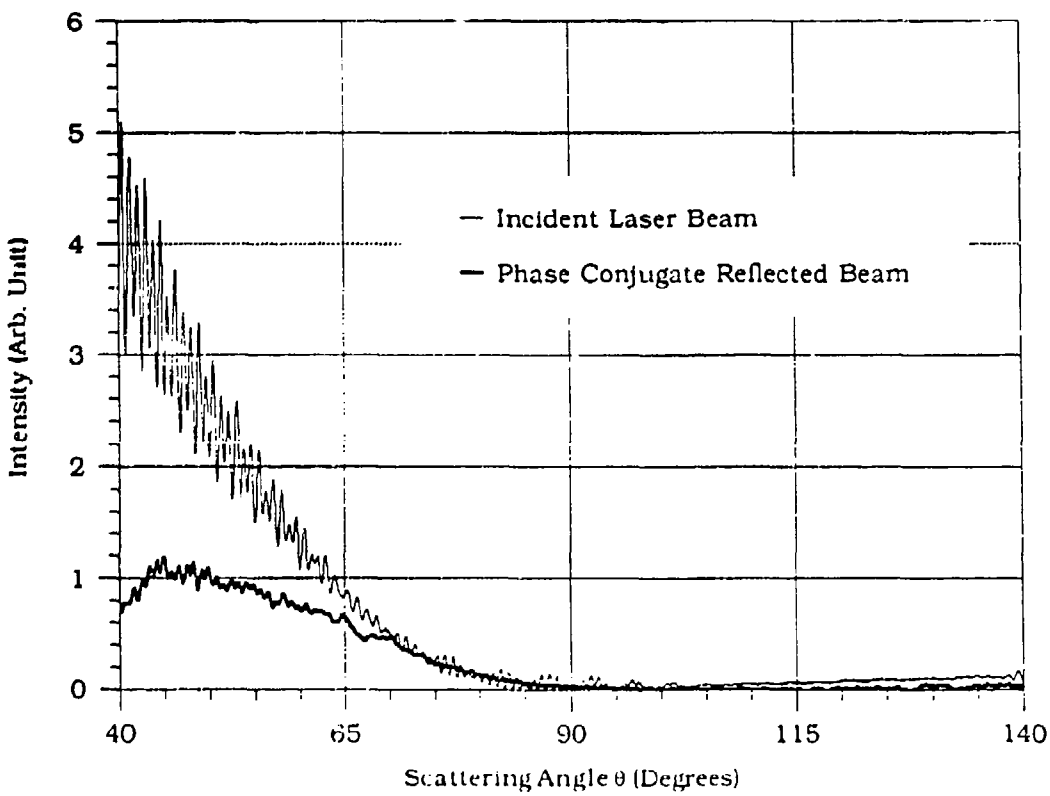

Figure 6. The scattered intensity distribution for the incident laser and for a phase conjugate reflection. The latter is measured using the chopper and the lock-in (Fig. 2). Fiber radius is 19.8 μm, wavelength is 514.5 nm, and polarization is perpendicular to the fiber axis and parallel to the plane of incidence.

SUMMARY

A simple physical interpretation of the suppression of the scattering from a phase conjugate beam can be given. When the incident light is scattered by a fiber of radius 19.8 μm, most of the scattered light is confined to a small cone in the forward direction. Thus, phase conjugation of light scattered into the full angle of 10° is enough to simulate an almost ideal situation of phase conjugating all the scattered light. After the interaction between the fiber and the phase conjugated light the incident wave is approximately recovered; hence, the angular distribution of the scattering from the phase conjugated beam is suppressed.

In conclusion, we have observed that if forward scattered light is reflected by a phase conjugator, the angular scattering it produces is suppressed relative to that produced upon reflection by a normal mirror. However, quantitative relationships have not yet been obtained. This research was supported by the Office of Naval Research, under contract N00014-93-C-0011.

REFERENCES

1. C. Giuliano, Physics Today, 27 (April 1981).
2. B. Ya. Zel'dovich, N. A. Mel'nikov, N. F. Pilipetskii, and V. V. Ragul'skii, JETP Lett. **25**, 35 (1977).
3. J. Feinberg and K. R. MacDonald, in *Photorefractive Materials and Their Applications II, P. Gunter and J. P. Huignard, eds. (Springer-Verlag, New York, 1988)*, P. 151.
4. C. F. Bohren and D. R. Huffman, *Absorption and Scattering of Light by Small Particles (Wiley Interscience, New York, 1981).*
5. J. Feinberg, Opt. Lett., **7**, 486 (1982).

PORTABLE HIGH-THROUGHPUT LIQUID-ABSORPTION AEROSOL SAMPLER

Agnes Akinyemi, Amnon Birenzvige, Ricardo Torres, and Solomon Zaromb

U. S. Army Edgewood RDE Center
Code SCBRD-RTE
Aberdeen Proving Ground, Maryland 21010-5423

RECENT PUBLICATIONS, SUBMITTALS FOR PUBLICATION, AND PRESENTATIONS

S. Zaromb and R. W. Bozen, U.S. Patent 5,173,264, Dec. 22, 1992.

S. Zaromb, J. Alcaraz, D. Lawson, and C. S. Woo, J. Chromatogr., **643**:107-115, 1993.

Agnes Akinyemi, Amnon Birenzvige, Ricardo Torres, and Solomon Zaromb, "Portable High-Throughput Liquid-Absorption Aerosol Sampler," Presented at the 1993 Edgewood RDEC Scientific Conference on Obscuration and Aerosol Research, June 22-24, 1993.

ABSTRACT

An improved portable high-throughput liquid-absorption air sampler [PHTLAAS] was recently developed at Argonne National Laboratory's Environmental Safety and Health Division for monitoring tritium in air. This PHTLAAS is being evaluated for use as an aerosol sampler. Respirable particulates are dispersed in a wind tunnel and their concentrations measured in both the sampled air and the collected particulate-enriched liquid. The particulate-enriched liquid can be tested for biological materials by several alternative techniques. In initial experiments with aerosols of Bacillus subtilis var. niger [BG] spore agglomerates of 4 μm geometric-mean aerodynamic-mass diameter [with a geometric standard deviation of 1.735] dispersed in a wind tunnel, the PHTLAAS was tested at an air sampling rate of 230 L/min. The collection efficiency of the first tested PHTLAAS, as measured by the standard bacteriological assay for BG, was found to be 85(+10,-14)%. Experiments are in progress to verify the initial results, eliminate or minimize possible sources of error, check the reproducibility of the collection efficiency measurements, and determine the dependence of collection efficiency on particle size [using monodisperse fluorescent particles in the 0.3-15 μm range], air sampling rate [200-250 L/min], operating conditions [temperature, relative humidity, etc.], and geometrical features.

INTRODUCTION

A recently developed high-throughput liquid-absorption air sampler[1,2] [HTLAAS] was evaluated primarily for the detection of

analyte vapors in trace concentrations.[3] The HTLAAS comprises a glass tube, 6 cm I.D., through which air passes at a rate of 600-700 L/min in a swirling, highly turbulent motion, which facilitates rapid transfer of trace constituents to a liquid film covering the inner walls of the tube and being drained from the bottom at an average rate of 0.1-1 mL/min. The pressure drop through the glass tube is only about 30 cm of water, as compared with 100-260 cm in earlier large-air-volume liquid scrubbers.[4,5]

The advantages of the HTLAAS for rapid and/or ultrasensitive detection and analysis of trace air contaminants result from (a) the high air-sampling rate, (b) an appreciable analyte collection efficiency (40-60%) for both vapors and aerosols, and (c) the low volume of collected liquid absorbent. These three features combine to reduce the lower detection limit [LDL] of available analytical instrumentation by a factor of >1000 and/or to permit faster sampling and far more rapid on-site air monitoring than were previously practicable. For instance, LDLs of alkaloid vapors $\approx 1:10^{13}$ by volume have been achieved using the HTLAAS with liquid chromatography and electrochemical detection.[3]

Other attractive features of the HTLAAS include its applicability to both vapors and aerosols, applicability to most analytes, and compatibility with most analytical devices, particularly those geared for the detection of analytes in liquid, especially aqueous, samples.

To determine whether the HTLAAS can also collect particles or droplets from aerosols, a corn oil mist (0.3 to 3 μm droplets) was produced by a Laskin nozzle. The relative concentrations of these droplets at the sampler inlet and outlet were measured with a Model TDA-2EL light-scattering photometer (Air Techniques., Inc., Baltimore, MD). The difference in the photometer readings yielded an aerosol collection efficiency of 42-48%.[3]

A portable HTLAAS [PHTLAAS] was first developed for field use with funding from the U. S. Customs Service.[6] An improved, streamlined PHTLAAS was subsequently devised at Argonne National Laboratory's Environmental Safety and Health Division for monitoring tritium in air.[7] The streamlined PHTLAAS has a glass tube with an I.D. of 2.7 cm and samples air at a rate of 150-250 L/min, which still permits it to reduce the LDL and/or the sampling time for trace air contaminants of most air analyzers [operating at sampling rates of ≤3 L/min] by two or more orders of magnitude. The PHTLAAS is made of simple and inexpensive components. Its total weight, excluding the power pack, is only about 700 g. The weight of the power pack depends on the choice of batteries and their replacement frequency. The required power is <40 watts. The PHTLAAS has maximum dimensions of 10 cm diameter and about 50 cm total length.

The PHTLAAS is now being evaluated for use as an aerosol sampler. Respirable particulates are dispersed in a wind tunnel and their concentrations measured in both the sampled air and the collected

particulate-enriched liquid. These measurements will yield the dependencies of the sampler's collection efficiency on particulate size [in the 0.3-15 μm range], air sampling rate [in the range of 150-250 L/min], other operational parameters [initial liquid volume, sampling time, ambient temperature and relative humidity, etc.], and sampler design.

The particulate-enriched liquid can be analyzed for biological particles by standard biological assay techniques, by immunoassay methods or by fluorescence detection.

EXPERIMENTAL APPROACH

To measure the efficiency of collection of an i-th species, ϵ_I, it is necessary to determine the volume of the sampled air $V_A = F_A t$, where F_A is the flow rate of the sampled air and t is the sampling time, the concentrations C_{IA} = weight of i-th species per volume of air and C_{IL} = weight of i-th species per volume of liquid, and the volume of the collected liquid v_L. A materials balance then yields:

$$\epsilon_I = C_{IL} v_L / C_{IA} t F_A \qquad [1].$$

The liquid volume v_L is measured with a graduated pipette and the sampling time t with a timer. To measure F_A, a low-rate [0-2 L/min] flowmeter, connected to a probe hole situated 1 cm above the glass tube, was first calibrated against a primary standard [orifice flowmeter for 140-700 L of air/min connected in series with the PHTLAAS, Fig. 1] and thereafter served as a secondary standard. The problem reduced then to measuring the concentration ratio C_{IL}/C_{IA} of Equation 1.

An airflow rate of 230 L/min was used in initial experiments with aerosols of Bacillus subtilis var. niger [BG] spore agglomerates of 4 μm geometric-mean aerodynamic-mass diameter [with a geometric standard deviation of 1.735, as measured by an aerodynamic particle sizer, Model APS 3310, TSI, St. Paul, MN] dispersed in a wind tunnel [WT]. Several procedures were tested for measuring the concentration C_{IA} of the particulates in the WT. Placed near the air inlet of the PHTLAAS were the following two isokinetic probes:

PROBE MATERIAL	AIR FLOW RATE L/MIN
Plain Gelman No. 60173 Supor-450 modified polysulfone 0.45-μm-pore-size, 47-mm-diameter, membrane filter	17
Packed absorbent cotton [Fig. 2]	3.8

After a 15-minute sampling period, the membrane filter was placed in a bottle containing 5 mL of filtered 12% saline solution, whereas the cotton was submerged in a bottle containing 50 mL of 0.85% saline. To dislodge and disperse the collected particulates, the bottle containing the filter was sonicated for 1 min, vortexed using a Maxi Mix II Thermolyne Vortex Mixer for 1 min, and then shaken intensely in a mechanical shaker for at least 10 min. The cotton was vortexed and shaken in the same way, without prior sonication. The particle concentrations from the filter were first measured with an Elzone model 282PC particle counter [Particle Data, Inc., Elmhurst, IL] and so were the concentrations C_{IL} of the particulates collected in the liquid samples obtained with the PHTLAAS. However, particulates emanating from the shaken filter interfered with the Elzone measurements. In an alternative procedure, the suspensions of BG spores from the membrane filter, the cotton, and the PHTLAAS were subjected to successive dilutions in 0.85% saline solution and assayed on tryptose agar using standard microbiological dilution and plating techniques. The resulting colony counts yielded the concentrations of viable BG spores in the original liquid samples. This method is practically free from interferences, as the unique appearance of BG colonies permits easy discrimination from any bacterial contaminants. The results obtained by this method are reported in the next section.

A third procedure for obtaining BG counts is based on an immunoassay approach. However, the first attempt to use this procedure yielded qualitative rather than quantitative results.

PRELIMINARY RESULTS AND THEIR DISCUSSION

The first collection efficiency measurements followed a methodology that was based on the following assumptions:

Assumption 1: A 0.45-μm-pore-size, 47-mm-diameter,cellulose acetate membrane filter [Metricell GN-6, Gelman Part No. 63069], with an isokinetic intake, that had been designed and used in previous wind tunnel [WT] experiments collects and releases nearly 100% of any BG spores entering at its inlet.

Assumption 2: The concentration profile of particulates within the WT's center region does not vary appreciably from point to point.

The validity of Assumption 1 was cast into doubt when the first two measurements yielded efficiencies of >200% and >2,000%. It appears that the cellulose acetate filter does not release all the spores that are retained by the membrane and that the more recently used modified polysulfone filter may be more suitable for the present tests. Following a suggestion made by Gail Hatfield [ERDEC], the absorbent cotton filter of Fig. 2, that had been reported to collect BG spores with an efficiency of >99.95%[4,8] was used as an isokinetic calibration standard in lieu

of the membrane filter. This procedure yielded an erroneous collection efficiency of 13±2%, most recently revised to 85(+10,-14)% [vide infra], for a PHTLAAS of intermediate [19 cm] glass tube length operating at an air flow rate of 230 L/min.

As a rough check of the accuracy of the absorbent cotton standard, the input rate of BG spores was compared with the amount collected. Surprisingly, a calculation assuming that the spores were uniformly distributed throughout the cross section of the WT yielded an apparent collection efficiency of about 400% for the absorbent cotton filter. This result suggested that the above Assumption 2 may yield highly erroneous results. Subsequent scans of the horizontal and vertical concentration profiles in the WT revealed large point-to-point variations in particulate concentrations, which imply that our above-cited first collection efficiency value of 13±2% may have been in serious error.

To minimize such errors, changes were effectuated in the aerosol mixing chamber [near the air inlet of the WT], which have resulted in a major improvement in the particle concentrations profile in the test section of the tunnel. Also worked out was a computer program that permits rapid and accurate scanning of the concentration profiles in the test section of the WT with the aid of a TSI Model 3755 Laser Particle Counter. The scanning was performed within a cross section of the tunnel at a height of 12.5 cm from the base plane horizontally and at the vertical mid-plane of the tunnel vertically. Also obtained [with a Solomat MPM 500e Environmental Monitor] were the wind velocity profiles at a height of 12.5 cm above the base of the tunnel test section. The horizontal and vertical positions corresponding to relatively small [±15%] point-to-point variations in particulate concentrations and wind velocities were found to be in the range of 8-23 cm [preferably 12-18 cm] from the front door of the test section at a height of 8-18 cm [preferably 13 cm] from the base. Therefore, subsequent measurements were performed with the sampler inlets placed at these optimal locations.

With the improvement in the concentration profile, it was possible to resume the collection efficiency measurements with BG spore agglomerates. A rerun of these measurements yielded a collection efficiency of 82(+10,-14)%. Moreover, a comparison of the number of BG spores collected by the cotton filter with the number expected from the rate of injection, assuming a uniform distribution throughout the cross section of the WT, yielded 100% agreement. These encouraging results must be verified through several repeat runs.

CONCLUDING REMARKS

The measured collection efficency value of 85% could have been due mainly to the larger particle sizes in the sampled mass distribution. Therefore, experiments are in progress to verify the initial results, eliminate or minimize possible sources of error, check the reproducibility of the collection efficiency measurements, and determine the dependence of collection efficiency on particle size [using monodisperse fluorescent particles in the 0.3-15 μm range], air sampling rate [200-250 L/min], operating conditions [temperature, relative humidity, etc.], and geometrical features.

ACKNOWLEDGEMENTS

Fig. 2 was prepared and provided by Gail E. Hatfield of ERDEC. Thanks are due to Mr. Hatfield for pointing out the usefulness of the cotton absorber for measuring the concentration of BG spores in air.

REFERENCES

1. S. Zaromb and W. Prepejchal, U.S. Patent 4,977,095, Dec. 11, 1990.

2. S. Zaromb and R. W. Bozen, U.S. Patent 5,173,264, Dec. 22, 1993.

3. S. Zaromb, J. Alcaraz, D. Lawson, and C. S. Woo, J. Chromatogr., **643**:107-115, 1993.

4. L. M. Buchanan, J. B. Harstad, J. C. Phillips, E. Lafferty, C. M. Dahlgren, and H. M. Decker, Appl. Microbiol., 23(6):1140-1144, 1972.

5. F. P. Errington and E. O. Powell, J. Hyg.(Cambridge), **67**:387-399, 1969.

6. S. Zaromb, J. Alcaraz, D. Lawson, and W. E. Johnson, "Portable High-Throughput Liquid-Absorption Air and Aerosol Sampler," paper presented at the 2nd Annual Hazardous Waste and Hazardous Materials Management Conference and Exhibition, Haztech International, Pittsburgh, May 14-16, 1991.

7. S. Zaromb, D. Reilly, M. Robinet, A. Justus, and W. Munyon, unpublished work, Argonne National Laboratory, 1992.

8. J. B. Harstad, H. M Decker, C. E. Mick, and C. R. Phillips, Protection Branch Report of Test No. 5-68, Department of the Army, Fort Detrick, Frederick, MD 21701, February 1968. Copy only obtainable upon approval of the releasing authority.

FIG. 1. FLOW RATE CALIBRATION SET-UP

[SCALE 1:4]

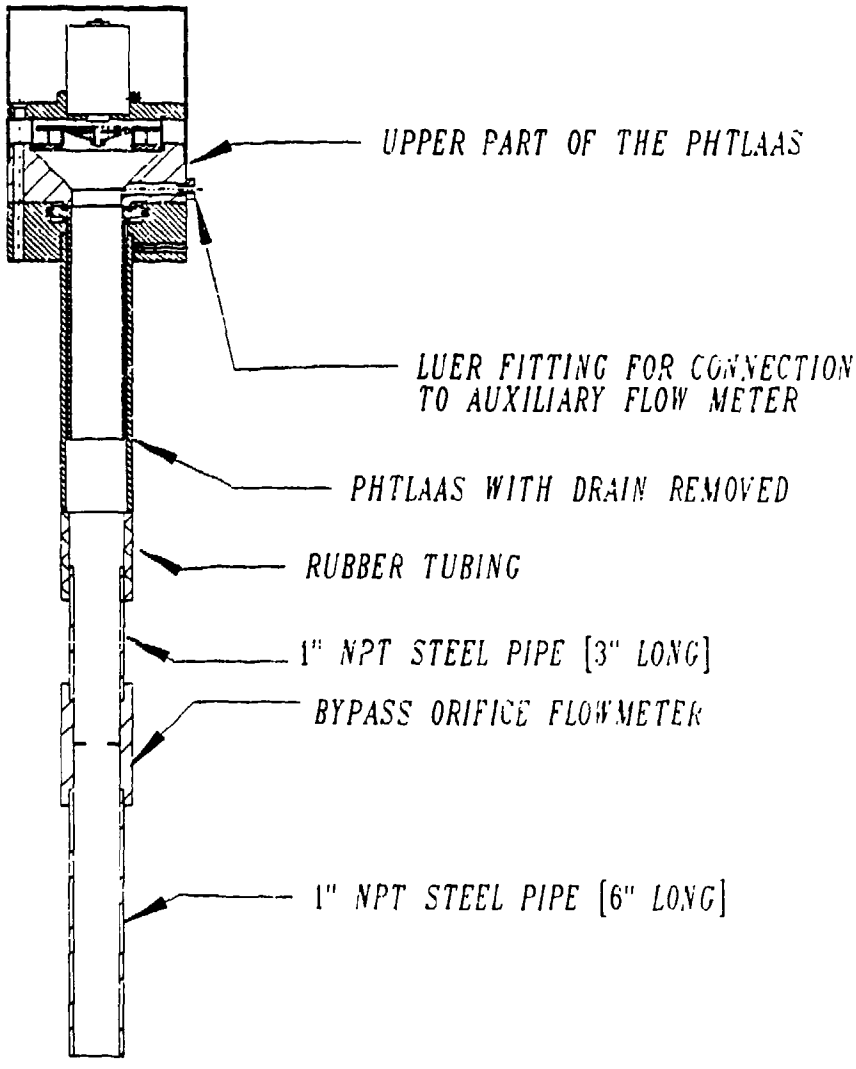

FIG. 2 COTTON COLLECTOR ASSEMBLY

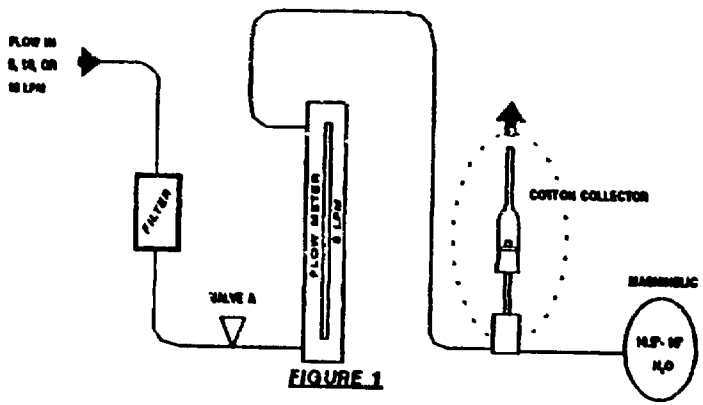

FIGURE 1

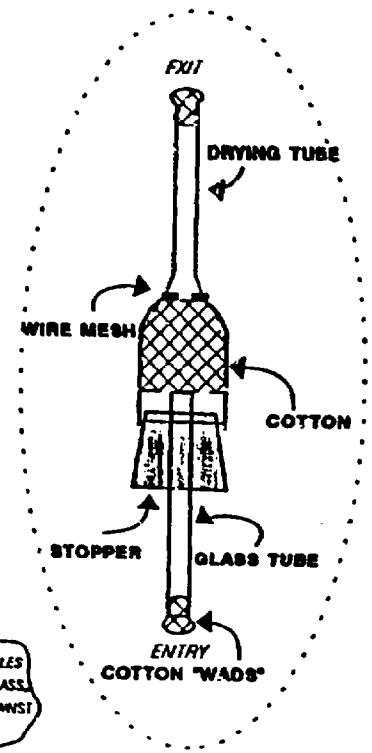

FIGURE 2

PREPARATION

1 INSERT WET COLLECTOR INTO APPARATUS AS SHOWN ABOVE.

2 REMOVE FROM STOPPER AND INSERT MESH AND COTTON AS SHOWN IN FIGURE 2, FILLING TO WITHIN ½" OF OPEN END OF DRYING TUBE (1 PIECE IF POSSIBLE)
NOTE. GLASS TUBE PROTUDES ¼" BEYOND STOPPER AND CONTACTS COTTON.

3 PACK, ADD OR REMOVE COTTON UNTIL A FLOW RATE OF 5 LPM IS ACHIEVED AT 14.5 - 16" H_2O PRESSURE
VALVE A USED TO REGULATE PRESSURE AND FLOW

BE CAREFUL TO AVOID WRINKLES (LEAKAGE PATHS) AGAINST GLASS. DO NOT APPLY PRESSURE AGAINST COTTON WHEN MEASURING

4 INSERT COTTON "WADS" INTO ENDS OF ENTRY AND EXIT TUBES

5 AUTOCLAVE THEN OVEN DRY FOR 8 HOURS AT 120°C

SAMPLING

1. SETUP VACUUM LINE WITH 5 LPM CRITICAL ORFICE
2. REMOVE COTTON "WADS" FROM ENTRY AND EXIT TUBES
3. INSERT DRYING TUBE END INTO VACUUM LINE AND GLASS TUBE INTO SAMPLING PROBE (PROBE SHOULD PROVIDE ISOKINETIC SAMPLING)
4. AFTER TAKING SAMPLE FOR TEST SPECIFIC PERIOD, REINSERT COTTON "WADS"
5. USING STERILE TECHNIQUE REMOVE COTTON FROM DRYING TUBE AND PLACE INTO STERILE 50 ml 0.85% SALINE BLANK. SHAKE ON SHAKER FOR 10 MINUTES. **PLATE, INCUBATE AND COUNT.**

Sufficiency of Using a Continuum of Frequencies to Solve the Electromagnetic Inverse Problem

O.I. Sindoni and D. K. Cohoon

We show the possibility of using a tunable source with frequencies ranging over an interval of frequencies to recover remotely the structure of a complex aerosol from the scattered radiation.

1 Inverse Problem

There are two approaches to the inverse scattering problem. One is to use a single interrogating frequency but use a continuum of angles of incidence and directions of polarization. A second is to use one direction of propagation of the interrogating radiation and one angle of polarization but use all frequencies ω which lie between a smaller frequency ω_1 and a larger frequency ω_2. We show that the latter approach constitutes an imbedding, in the sense of differential topology ([5]) of the scattering problems into the space of scattered electromagnetic fields for both complexes of perfect conductors and a collection of dielectric scatterers. In Sindoni et al. ([8]) we find numerical evidence for the use of multiple frequencies to characterize complex clusters of dielectric spheres even when individual spheres in a cluster are close enough to each other that cooperative scattering strongly influences the scattered radiation fields.

1.1 Uniqueness of the Inverse for Perfect Conductors

The theorem which follows is adapted from a known theorem ([3], p 189).

Theorem 1.1 *Let D_1 and D_2 be two bounded perfect conductors whose connected components are each diffeomorphisms of the interior of a sphere such that for one fixed direction and one fixed polarization of the incoming field, but for all frequencies ω between the smaller frequency ω_1 and the larger frequency ω_2, the scattered electric field far field patterns coincide. Then D_1 is equal to D_2*

The proof is extremely simple. The electric field $\vec{E}$ satisfies

$$\Delta\vec{E} + k^2\vec{E} = 0 \tag{1.1.1}$$

where k is the free space propagation constant, denoted by k_0 in the next section, which is ω/c with ω being the frequency and c denoting the vacuum speed of light. Now outside the perfect conductor and outside $D_1 \bigcup D_2$ we have $\vec{E}$ is equal to $\vec{E}^s + \vec{E}^i$. We let $\vec{F}$ be the partial derivative of $\vec{E}$ with respect to k and note that taking the partial derivatives of all terms of the Ampere Maxwell equation with respect to k implies that

$$curl\left(\frac{\partial\vec{H}}{\partial k}\right) = i\epsilon_0 c\vec{E} + ik\epsilon_0 c\vec{F} \tag{1.1.2}$$

which tells us that $div(\vec{F})$ is zero as we already know that the divergence of $\vec{E}$ and the divergence of any curl is zero. In view of Green's theorem then we conclude that if D_1 and D_2 were different and if G were the complement of the union of D_1 and D_2 and if D^* were the part of space that was not in G or in D_2 which would be nonempty if there were a part of D_1 that was not totally inside of D_2, that then

$$0 = 2k_0\int_{D^*} \mid \vec{E} \mid^2 dxdydz = \int_{D^*}(\vec{F}\cdot\Delta\vec{E} - \vec{E}\cdot\Delta\vec{F})dxdydz \tag{1.1.3}$$

This will mean that $\vec{E}$ vanishes everywhere in D^* and by analyticity of $\vec{E}$ this means that $\vec{E}$ vanishes everywhere outside of the union of D_1 and D_2 and since this means that

$$\vec{E} = \vec{E}^i + \vec{E}^s = 0 \tag{1.1.4}$$

and since $\vec{E}^s$ satisfies the Silver Mueller radiation conditions at infinity that the incoming radiation $\vec{E}^i$ being equal to $-\vec{E}^s$, in view of (1.1.4) also satisfies the Silver Mueller radiation conditions ([2]). This is a contradiction since the incoming radiation, being a plane wave, certainly does not satisfy the Silver Mueller radiation conditions.

1.2 Dielectric Scatterers

For simplicity of discussion we consider an isotropic dielectric, we suppose, following Tai ([9]) that

$$\overline{\overline{G}}_0 = \left[\overline{\overline{I}} + \frac{1}{k_0^2}grad_q grad_p\right]\Phi(p,q) \tag{1.2.1}$$

where

$$\Phi(p,q) = \frac{exp(ik_0 \mid p-q \mid)}{\mid p-q \mid} \tag{1.2.2}$$

Then

$$\left[curl(curl) - k_0^2\right]\overline{\overline{G}}_0 = \overline{\overline{I}}\delta(p-q) \tag{1.2.3}$$

where $\overline{\overline{I}}$ is the identity dyadic and δ is the Dirac delta function, acutally a distribution with a one point support, whose integral is 1 and whose support is the origin of three dimensional space. In this setting in an operator sense the integral equation of electromagnetic scattering for a dielectric scatterer indexed by j can be expressed in the form

$$\vec{E} = \vec{E}^i + k_0^2 T_j \vec{E} \tag{1.2.4}$$

where if $\epsilon_r^{(j)}(q)$ is the relative permittivity function describing the jth scatterer, then the integral operator for the jth scatterer is given by

$$T_j \vec{E}_j =$$

$$\int_{R^3} \left(\epsilon_r^{(j)}(q) - 1\right) \vec{E}_j \overline{\overline{G}}_0(p,q) dv(q) \tag{1.2.5}$$

where we use the fact that $\epsilon_r^{(j)}(q)$ is equal to 1 outside the scatterer causing the integral (1.2.5) to vanish outside the scattering body. The integral gives the fields outside the scattering body and inside the scattering body if interpreted in the principal value sense. If we suppose that we have two scatterers, scatterer 1 and scatterer 2, giving the same scattered radiation, then a subtraction yields the equation

$$T_1 \vec{E}_1 - T_2 \vec{E}_2 = \vec{0} \tag{1.2.6}$$

A problem with using (1.2.6) directly to conclude that $\epsilon_r^{(1)}$ is equal to $\epsilon_r^{(2)}$ and that consequently the two dielectric scatterers are really the same is that inside the integrals in (1.2.6) we have the products of $\epsilon_r^{(j)}(q) - 1$ and $\vec{E}_j$ for j equal to 1 and 2 instead of a single unknown. However, now we make use of the continuum of values of k_0 or ω/c where ω is the frequency and c is the vacuum speed of light which means that by analytic continuation we can extend values of k_0 to zero and we note that

$$\| \left(\overline{\overline{I}} + k_0^2 T_j\right)^{-1} - \overline{\overline{I}} \| = O(k_0^2) \tag{1.2.7}$$

as k_0 goes to zero since for small values of k_0 we can express the inverse as a Born series via the relationship

$$\left(\overline{\overline{I}} + k_0^2 T_j\right)^{-1} = \overline{\overline{I}} - k_0^2 T_j + k_0^4 T_j^2 - \cdots \tag{1.2.8}$$

which means since we can always certainly replace $\vec{E}_j$ in equation (1.2.6) by

$$\vec{E}_j = \left(\overline{\overline{I}} + k_0^2 T_j\right)^{-1} \vec{E}^i \tag{1.2.9}$$

and then using (1.2.7) as k_0 goes to zero and dividing all terms of (1.2.6) by k_0^n and letting k_0 go to zero we derive a simpler sequence of relationships using the expansion of $\overline{\overline{G}}_0$ in vector spherical harmonics as in ([9]) and ([7], pp 1776 - 1783 or as in my student's Ph.D thesis ([6]) and conclude by orthogonality that we have an infinite sequence of expressions of the form

$$\int_{R^3} (\epsilon_r^{(1)}(q) - \epsilon_r^{(2)}(q)) \mid r_q \mid^n \Psi_{(m,n)}(\theta_q, \phi_q) dv(q) = 0 \tag{1.2.10}$$

where (r_q, θ_q, ϕ_q) is the spherical coordinate representation of the point q in the scatterer and where the $\Psi_{(m,n)}$ will be derived from the Dyadic expansion of $\overline{\overline{G}}_0$ in ([9]) in terms of vector spherical harmonics. This is based upon the Cauchy integral theorem relationship

$$\frac{1}{2\pi i}\int_C \left(\frac{1}{k^n}\right)\left\{\sum_{j=0}^{\infty} a_j k^j\right\} dk \;=\; a_{n-1} \tag{1.2.11}$$

where each a_{n-1} is an integral of a combination of spherical harmonics multiplied by the difference $(\epsilon_r^{(1)} - \epsilon_r^{(2)})(q)$. As the spherical harmonics are complete, it will be impossible that all these a_{n-1} terms are zero unless $\epsilon_r^{(1)}(q)$ is equal to $\epsilon_r^{(2)}(q)$ which will mean that scatterer 1 is the same as scatterer 2.

References

[1] Bayliss, A. "On the Use of Coordinate Stretching in the Numerical Computation of High Frequency Scattering" *Journal of Sound and Vibration, Volume 60, Number 4* (1978) pp 543 - 553

[2] Bayliss, A. and Eli Turkil. "Radiation Boundary Conditions for Wavelike Equations" *Communications of Pure and Applied Mathematics, Volume XXXII* (1980) pp 707 - 725

[3] Colton, David and Ranier Kress. "Inverse Acoustic and Electromagnetic Theory" New York: Springer Verlag (1992)

[4] Borghese, F., P. Denti, R. Saija, G. Toscano, and O. I. Sindoni. "Extinction Coefficients for a Random Dispersion of Small Stratefied Spheres and a Random Dispersion of their Binary Aggregates" *Journal of the Optical Society of America. Volume 4* (October, 1987) pp 1984 - 1991

[5] Kelley, John. *General Topology* New York: Van Nostrand (1955)

[6] Li, Shu Chen. *The Bioeffects of Electromagnetic Radiation* Ph.D Thesis for the Temple University Mathematics Department 038-16 Philadelphia, PA 19122

[7] Morse, Philip M. and Herman Feshbach. *Methods of Theoretical Physics. Volume II* New York: McGraw Hill (1953) pp 1776-1783

[8] Sindoni, O.I., F. Borghese, P. Denti, R. Saija, and G. Toscano. "Multiple Scattering Approach to the Electromagnetic Scattering from Dielectric Nonspherical Objects" *IN* Varadan, V. V. and V. K. Varadan. *Multiple Scattering of Waves in Random Media and by Random Rough Surfaces* University Park, PA 16802: The Pennsylvania State University, 227 Hammond Building (1987) pp 479 - 489

[9] Tai, C. T. *Dyadic Green's Functions in Electromagnetic Theory* Singapore: Intex Educational Publishers (1971)

Computer Codes for Solving the Sphere Inversion Problem

D. K. Cohoon

This paper gives a description and listing [illegible] computer code which will help us look inside a nonmagnetic layered spherical particle [illegible] recover the layer thicknesses and electrical properties (permittivities) of these layers just by looking at the scattered radiation resulting from exposing the layered spherical particle to a single plane wave electromagnetic radiation source of a single plane wave monochromatic polarized source so that the interrogating radiation has (i) one frequency, (ii) one angle of incidence and (iii) only one polarization. A Levinberg-Marquardt algorithm is used for the inversion

Contents

1 INTRODUCTION

2 The Inverse Problem Computer Code

3 COEF subroutine

4 COEFAS subroutine

5 DPMPAR subroutine

6 EVEC or Electric Vector Determination Subroutine

7 EVCSC for Scattered Radiation

8 EVCINC for the electric vector of the incoming radiation

9 EVSPHD helps compute Mueller matrix entries

10 ENORM

11 Mueller and amplitude scattering matrix entry determination

12 MMEVEI

13 BTERAD inversion by the scattered radiations radial component

14 PROPGF – propagation constants in all layers

15 Bessel function subroutine BJYH

16 GAUSS – a volume integral of power density

17 GETEC for obtaining expansion coefficients

18 Jacobian Determination

19 FUNAL – a function that gives α expansion coefficients

20 FNBET for β expansion coefficients

21 SURINC – accurate surface integration routine

22 FNTST for testing SURINC

23 FUNC – a test function for minimization

24 Getting Letters and Numbers

25 Minimization routine LMDIF

26 LMDIFF driver routine for LMDIF

27 Minimum value of an integer array

28 FUNCD – the function of sphere parameters

29 Test Function FNT18 of the Minimization Routine

30 Miminzation subroutine LMPAR

31 QRFAC – matrix factorization routine

32 QRSOLV – simultaneous solution of linear equations

33 Machine constants in single precision

34 PROPG – the propagation constants FKP

35 Legendre Functions

36 CSMCOM.f – the COMMON block

37 MAKE FILE

38 INPUT DATA SET

39 OUTPUT DATA

40 Applicability

1 INTRODUCTION

The computer code listed here solves the forward scattering problem for an N layer sphere implementing the Mie solution and then performs validating checks and solves the inverse scattering problem by considering that the output of the Mie solution program which is the set of expansion coefficients representing the scattered radiation is a vector valued function and minimizing the difference between these values and the measured or otherwise determined expansion coefficients representing the radiation scattered from the sphere with a priori unknown properties.

It is therefore essential to be sure that there is no error of any significance in the computer solution of the forward scattering problem. The validity of the answers are checked by comparing tangential components of electric and magnetic vectors on opposite sides of layer boundries. We check the energy balance by computing the total energy entering the sphere minus the total energy scattered away in two different ways. The standard method, which is the method of computing the total absorbed power for an aerosol particle of any shape, is the integration of the Poynting vector dotted with the inward directed normal over the surface of the sphere. The second method uses the local concept of power per unit volume at any point in any layer and carries out the volume integral of this power per unit volume over all the layers of the sphere. These two results must be the same if the Mie solution program is working correctly. Since these comparisons are made with the vector spherical harmonics, this is not quite enough. We also make sure that the electric vector of the incoming radiation which is given by a simple formula in Cartesian coordinates of the form

$$\vec{E}^{i} = E_0 exp(-ik_0 \cdot x - i\omega t) \cdot \vec{e}_x$$

is accurately represented by the expression in vector spherical harmonics for the number of vector spherical harmonics that we are using on the surface of the sphere. Thus, by the uniqueness theorem in ([1]) we are sure that the forward scattering problem has been correctly solved by the computer program. Next we determine Mueller matrix entries and the scattering amplitude matrix. If the noise in measurement is represented as a multiple of higher order vector spherical harmonics, we show via the computer program that inner products with lower order vector spherical harmonics integrated over the outer surface of the sphere will completely eliminate this noise as the lower order expansion coefficients of the scattered radiation are recovered to nearly full machine precision by a Gaussian

quadrature over the surface of the sphere or over a surrounding sphere that is concentric with the scattering sphere. Finally, we use a Levinberg Marquardt algorithm to recover the sphere properties from the scattered radiation.

This routine hypothesizes a sphere with a number of layers and radii of delimiting spheres, and electromagnetic properties of these layers, solves the forward problem along a search path determined by the Levinberg Marquardt algorithm until the calculated expansion coefficients and the expansion coefficients that represent the electromagnetic radiation scattered from the real sphere are as close as possible. When INFO = 2 or INFO = 4 is printed in the output, this means that the minimization procedure has been successful usually to all of the decimal places printed. Ideally, measurement noise should be removed before using this program to recover the sphere properties.

2 The Inverse Problem Computer Code

The following is a computer code that tests various aspects of procedures to recover the properties of scattering spheres from the scattered electromagnetic fields and a knowledge of the incoming field.

```
c
      PROGRAM CSM
c     ELECTROMAGNETIC ENERGY DEPOSITION IN A CONCENTRIC SPHERE.
c
     IMPLICIT REAL*8 (A-H, O-Z)
```

```
      COMPLEX*16 ERADI,ETHETI,EPHII,CEXOLD,CI,ZOLD,
     1 ERADIN,ETHEIN,EPHIIN,ALPNM,BETNM
c     COMPLEX*16 FKP(10), CEX, ANP(1000), BNP(1000), ALPNP(1000),
c    1           BETNP(1000), BJNP(500), BHNP(500), Z
c     COMMON /COEFF/ANP, BNP, ALPNP, BETNP
c     COMMON FKP, BJNP, BHNP, CEX, BDP, P, DP, SIGP, EO, TIME, R,
c    1       THETA, PHI, STOPR, NC, NORG, NMIN
      INCLUDE 'CSMCOM.f'
      EXTERNAL FUNCD,FNT18
      COMMON /PRICOM/IPRINT,IENTR
      COMMON /FNCOM/IPRNDX
      DIMENSION  SBDP(9),XARRAY(18),FVEC(20),IWK(18),
     1 WK(470)
c     M = 20
c     MDB4 = 5
c     N = 18
c     LWA = M*N+5*N + M
c   are used in CALL FUNC
      IPRNDX = 1234
      ZERO = 0.D0
      ONE = 1.D0
      CI = DCMPLX(ZERO,ONE)
      IPESIN = 0
c     This last statement initializes a printing index
*     CALL ERRSET(208, 0, -1, 1)     WHAT DOES THIS DO?
c     OPEN(5,FILE='C:\DATA\CSM.DAT')
c     OPEN(6,FILE='C:\DATA\CSMOUT1.DAT')
c     OPEN(7,FILE='C:\DATA\CSMBNP.DAT')
      OPEN(3,FILE='ICSM.d')
      OPEN(26,FILE='CCSMOUT1.DAT',STATUS='UNKNOWN')
      OPEN(7,FILE='CSMCMBNP.DAT',STATUS='UNKNOWN')
      OPEN(16,FILE='OCOMPDEN.DAT',STATUS='UNKNOWN')
      OPEN(70,FILE='O-M11.DAT',STATUS='UNKNOWN')
      OPEN(71,FILE='O-M12.DAT',STATUS='UNKNOWN')
      OPEN(74,FILE='O-M33.DAT',STATUS='UNKNOWN')
      OPEN(75,FILE='O-M34.DAT',STATUS='UNKNOWN')
      OPEN(77,FILE='O-M43.DAT',STATUS='UNKNOWN')
      OPEN(76,FILE='GAUSSPRI DAT',STATUS='UNKNOWN')
      OPEN(37,FILE='ALPHACF.DAT',STATUS='UNKNOWN')
      OPEN(38,FILE='BETACF.DAT',STATUS='UNKNOWN')
      REWIND(37)
      REWIND(38)
      REWIND(16)
```

```
      REWIND(3)
      REWIND(26)
      REWIND(7)
      REWIND(70)
      REWIND(71)
      REWIND(74)
      REWIND(75)
      REWIND(77)
      REWIND(76)
      IPRINT = 0
      IENTR = 0
      IPRDIA = 0
      PIE=3.141592653589793D0
      RAD=180.D0/PIE
      EPS0=8.85416D-12
      VEL=2.997924562D8
      VELOCI = VEL
* READ IN CONTROL PARAMETERS
    5 READ(3,10,END=1110) FREQ, EO, TIME, STOPR, NORG, NOCR
      WRITE(*,*)FREQ,' = FREQ'
      WRITE(*,*)EO,' = EO'
      WRITE(*,*)TIME,' = TIME'
      WRITE(*,*)STOPR,' = STOPR'
      WRITE(*,*)NOCR,' = NOCR'
      WRITE(16,*)FREQ,' = FREQ'
      WRITE(16,*)EO,' = EO'
      WRITE(16,*)TIME,' = TIME'
      WRITE(16,*)STOPR,' = STOPR'
      WRITE(16,*)NOCR,' = NOCR'
   10 FORMAT(4E10.0, 2I5)
* COMPUTE COMPLEX TIME VARIATION
      OMEGA=2.D6*PIE*FREQ
      ARG=-OMEGA*TIME
      CEX=DCMPLX(COS(ARG),DSIN(ARG))
* READ DIELECTRIC PROPERTY PARAMETERS
      READ(3,20) (EPSP(I), SIGP(I), I=1,NORG)
   20 FORMAT(6E10.0)
* COMPUTE COMPLEX PROPAGATION CONSTANT
      FAC1=OMEGA/VEL
      WRITE(*,*)NORG,' = NORG'
      DO 30 I=1,NORG
 FAC2=EPSP(I)/2.D0
 FAC3=SQRT(1.D0+(1.D0/(EPS0*OMEGA)**2)*(SIGP(I)/EPSP(I))**2)
```

```
 REKP=FAC1*SQRT(FAC2*(FAC3+1.D0))
 FIMKP=FAC1*SQRT(FAC2*(FAC3-1.D0))
 FKP(I)=DCMPLX(REKP,FIMKP)
 WRITE(26,*)'FKP(',I,') = ',FKP(I)
   30 CONTINUE
      FKP(NORG+1)=DCMPLX(FAC1,0.D0)
       WRITE(26,*)' FKP(',NORG+1,') =',FKP(NORG+1)
      WRITE(*,*)NORG+1,' = NORG+1'
      WRITE(*,*)FKP(NORG+1),' = FKP(NORG+1)'
c READ RADII OF SURFACE BOUNDARIES
      READ(3,20) (SBDP(I), I=1,NORG)
      DO 35 I=1, NORG
 WRITE(16,*)SBDP(I),' = LAYER BOUNDARY no ',I
 BDP(I)=SBDP(I)/1.D2
   35 CONTINUE
* PRINT OUT TITLE AND BASIC INPUT DATA
      WRITE(26,40) FREQ, EO, TIME, NORG
   40 FORMAT('  ELECTROMAGNETIC ENERGY DEPOSITION IN A CONCENTRIC',
     1  ' SPHERE.'/'  *** SPHERICAL BESSEL FUNCTIONS CALCULATED ',
     2  'USING SUBROUTINE CBSSLJ ***',/
     3  ' FREQUENCY =',F9.2,' MHZ      FIELD ',
     4  'STRENGTH =',F7.2,' V/M     TIME =',F7.2,' SEC'/,
     5     ' NUMBER ',
     5  'OF REGIONS =',I3)
      WRITE(26,41) (EPSP(I), I=1,NORG)
   41 FORMAT(' RELATIVE DIELECTRIC CONSTANTS =',9(F7.2,2X))
      WRITE(26,42) (SIGP(I), I=1,NORG)
   42 FORMAT(' CONDUCTIVITIES (MHO/M) =',9(F7.3,2X))
      WRITE(26,43) (SBDP(I), I=1,NORG)
   43 FORMAT(' SURFACE BOUNDARIES (CM) =',9(F7.3,2X))
* COMPUTE SERIES EXPANSION COEFFICIENTS FOR ELECTRIC FIELDS
      CALL PROPG
      CALL COEF
c*******************************************
      NC = NMIN
      NORGPO = NORG+1
      DO 3801 IR = 1,NORGPO
      NSUM = (IR-1)*NMIN
      WRITE(37,3788)IR,NORG,NMIN,NSUM
c
      WRITE(38,3788)IR,NORG,NMIN,NSUM
      DO 3701 IC = 1,NMIN
      IRMTMP = (IR-1)*NMIN + IC
```

```
      WRITE(37,*)ALPNP((IR-1)*NMIN+IC),' = ALPNP(IR,',IC,')'
c
      WRITE(38,*)BETNP((IR-1)*NMIN+IC),' = BETNP(IR,',IC,')'
 3701 CONTINUE
 3788 FORMAT(I5,' = IR',I5,' = NORG',I5,' = NMIN',I5,' = NSUM')
 3801 CONTINUE
      WRITE(76,*)NC,' = NC = NMIN after CALL COEF'
c     CALL COEF(ANP, BNP, ALPNP, BETNP) expansion coefficients
c  are passed through common
      WRITE(*,*)' We have just completed call to COEF'
      DO 873 LLL=1,NMIN
 WRITE(7,874) LLL, BNP(LLL)
  874   FORMAT(' LLL = ',I3,3X,'BNP = (',E14.7,',',E14.7,')')
  873 CONTINUE
c     CLOSE(7)
c     CLOSE(5)
c     JJ=3
c     IF (JJ.EQ.3) THEN
c       STOP
c     ENDIF
      WRITE(16,*)NOCR,' = NOCR'
      WRITE(16,*)NMIN,' = NMIN'
c
      WRITE(76,*)NOCR,' = NOCR'
      WRITE(16,45)
   45 FORMAT('0')
      WRITE(16,5401)
 5401 FORMAT(' NREG','  NCC',6x,'SAVR',4x,'THETA',6x,'PHID',
     1'  Power Density')
      WRITE(*,*)NOCR,' = NOCR'
      DO 70 I=1,NOCR
      WRITE(*,*)I,' = no I of NOCR = ',NOCR
* READ DEFINING CHARACTERISTICS OF INTERIOR POINTS AT WHICH
* ABSORBED-POWER DENSITIES ARE TO BE COMPUTED.
c     READ(3,50) NREG, R, THETAD, PHID
      WRITE(*,*)' Carrying out READ(3,*)NREG,R,THETAD,PHID'
      READ(3,*) NREG, R, THETAD, PHID
   50 FORMAT(I5,3E10.3)
      SAVR=R
      R=R/1.D2
      THETA=THETAD/RAD
      PHI=PHID/RAD
      Z=FKP(NREG)*R
```

```
c     WRITE(*,*)' We are about to CALL BJYH'
      NCOLD = NMIN
      NCC = NMIN
      CALL BJYH(BJNP, BHNP, Z, NCC, STOPR)
      WRITE(76,*)NCC,' = NCC after CALL BJYH'
      NCC = NCC-2
      IF (NCC.GT.NMIN) NCC=NMIN
      CALL PL(THETA, NMIN, P, DP)
* ABSORBED-POWER DENSITY AT GIVEN POINT INTERIOR TO P-TH REGION
      NC = NCC
      CALL EVEC(NREG, PD)
      NC = NMIN
c       ,Z) is passed through COMMON
      PD=.5D0*SIGP(NREG)*PD
* PRINT OUT PARTICULARS OF INTERIOR POINT OF REGION P
c     WRITE(6,60) NREG, SAVR, THETAD, PHID, PD
c  60 FORMAT(' REGION',I2,' INTR. POINT: RADIUS =',F7.3,' CM  THETA',
c    1  ' =',F7.2,' DEG  PHI =',F7.2,' DEG  ABSORBED POWER DENSITY =',
c    2  F12.8,' W/M**3')
      WRITE(16,60)NREG,NCC,SAVR,THETAD,PHID,PD
   60 FORMAT(2I5,E10.3,E10.3,E10.3,1PD15.7)
   70 CONTINUE
      NN=NORG*NMIN
      FAC=2.D0*PIE/(FAC1*FAC1)
      QS=0.D0
      QT=0.D0
      DO 90 N=1,NMIN
 FACN=2.D0*N+1.D0
 QT=QT+FACN*REAL(ALPNP(NN+N)+BETNP(NN+N))
 QS=QS+FACN*(ABS(ALPNP(NN+N))**2+ABS(BETNP(NN+N))**2)
   90 CONTINUE
      QA=FAC*(ABS(QT)-QS)
* TOTAL ABSORBED POWER
      TOTPOW=2.65441D-3*E0**2*QA/2.D0
* AVERAGE ABSORBED POWER DENSITY
      PAVG=TOTPOW/(4.D0*PIE*BDP(NORG)**3/3.D0)
* PRINT AVERAGE ABSORBED-POWER DENSITY AND TOTAL ABSORBED POWER
      WRITE(16,100)PAVG, TOTPOW
      WRITE(*,100)PAVG,TOTPOW
  100 FORMAT('0',9X,'AVERAGE ABSORBED-POWER DENSITY =',1PD13.5,' W/M**3'
     1    /'0',9X,'TOTAL ABSORBED POWER =',D13.5,' WATT.')
c*****GOTO 5********original code stopped here*****
  110 CONTINUE
```

```
      WRITE(*,*)' About to call GAUSS'
      LSTART = 1
      TPGAU = GAUSS(LSTART)
      WRITE(16,*)TPGAU,' total absorbed power by vol integration'
      WRITE(*,*)TPGAU,' total absorbed power by vol integration'
      WRITE(*,*)' TOTPOW = ',TOTPOW
      WRITE(*,*)' completed the call to GAUSS'
c     We are about to test the EVECSC.f routine
      R = BDP(NORG)
      NP = NORG+1
      PI = 3.14159265358979323D0
      THETA = PI/3.D0
      PHI = PI/4.D0
      Z = FKP(NORG+1)*R
      ZOLD=Z
      CALL BJYH(BJNP,BHNP,Z,NC,STOPR)
      NC = NC-2
      IF(NC.GT.NMIN) THEN
 NC = NMIN
      ENDIF
c******************************
c
      CALL PL(THETA,NC,P,DP)
      CALL EVEC(NP,PD)
      CALL EVCSC(NP,PDSC)
      CALL EVCINC(NP,PDIN,ERADIN,ETHEIN,EPHIIN)
c     We have called PROPG and COEF prior to entering
c   this block
c*****************************************
c  e_x = sin(theta)cos(phi)e_r + cos(theta)cos(phi)e_theta -
c        sin(theta)e_phi
c  which means that the representation of the incident field
c  which is polarized in the direction of the positive x axis
c  in spherical coordinates is given by
c         ERADI = SIN(THETA)*COS(PHI)
c         ETHETI = COS(THETA)*SIN(PHI)
c         EPHII = SIN(THETA)
      CEXOLD = CEX
      Z = ZOLD
      CEX = CEX*EXP(+CI*Z*COS(THETA))
c     In this code we follow Stratton and use an
c   exp(-i omega t) time dependence.
      ERADI = SIN(THETA)*COS(PHI)*EO*CEX
```

```
      ETHETI = COS(THETA)*COS(PHI)*E0*CEX
      EPHII = -SIN(PHI)*E0*CEX
      WRITE(*,*)ERADI,' = ERADI(E radial exact by CSM.f)'
      WRITE(*,*)ERADIN,' = ERADIN (E radial in by EVCINC.f)'
      WRITE(*,*)ERADSC,' = ERADSC (E radial scat from EVCSC.f)'
      WRITE(*,*)ETHETI,' = ETHETI (E theta in exact by CSM.f)'
      WRITE(*,*)ETHEIN,' = ETHEIN (E theta in from EVCINC)'
      WRITE(*,*)ETHESC,' = ETHESC (E theta scat from EVCSC.f)'
c
      WRITE(*,*)EPHII,' = EPHII (E phi exact formula)'
      WRITE(*,*)EPHIIN,' = EPHIIN (E phi in from EVCINC.f)'
      WRITE(*,*)EPHISC,' = EPHISC (E phi scat from EVCSC.f)'
      CEX = CEXOLD
      WRITE(*,*)ERADI+ERADSC,' = ERADI+ERADSC'
      WRITE(*,*)ERAD,' = ERAD'
c
      WRITE(*,*)ETHETI+ETHESC,' = ETHETI+ETHESC'
      WRITE(*,*)ETHETA,' = ETHETA'
c
      WRITE(*,*)EPHII+EPHISC,' = EPHII+EPHISC'
      WRITE(*,*)EPHI,' = EPHI'
      IFARMU = 1
      R2MU = 10.D0*BDP(NORG)
c     We are about to calculate Mueller matrix entries at a point
c  10 radii out from the outer radius of the sphere
      WRITE(*,*)' We are about to call MMEVEI'
      WRITE(*,*)CEX,' = CEX before CALL MMEVEI'
      CALL MMEVEI(PHID,IFARMU,R2MU)
      WRITE(*,*)' We have finished CALL MMEVEI'
c     We are calling modular amplitude scattering matrix subroutine
c
c     We are now getting the expansion coefficients of the scattered
c   radiation numerically and making a comparison with the exact
c   formula based on making use of the boundary conditions which
c   require that the tangential components of the electric and
c   magnetic vectors be continuous across the boundary.
      NVAL = 2
      RADIUS = 1.0D0*BDP(NORG)
      WRITE(*,8961)
 8961 FORMAT(' Layer no',8x,' radius',5x,' thickness')
      DO 8963 IL = 1,NORG
      IF(IL.EQ.1) THEN
  THICK(IL) = 0.D0
```

```
      ELSE
  THICK(IL) = BDP(IL)-BDP(IL-1)
      ENDIF
      WRITE(*,8962)IL,BDP(IL),THICK(IL)
 8962 FORMAT(I9,1PD15.7,D15.7)
 8963 CONTINUE
c     Calling the routine to get the expansion coefficients
c  of the scattered radiation numerically.
      CALL GETEC(RADIUS,ALPNM,BETNM)
c
c     We are now going to check out our ability to create a function
c   which produces the expansion coefficients of the scattered radiation
      M = 20
      MDB4 = 5
      N = 18
c   are used in CALL FUNC
      NORGF = NORG
      FRACR = 1.000000D0
      FRACEP = 1.00000D0
      FRACSG = 1.00000D0
 8754 FORMAT(1PD15.7,2D15.7)
      DO 8761 I = 1,NORG
      XARRAY(I) = FRACR
      XARRAY(NORG+I) = FRACEP
      XARRAY(2*NORG+I)=FRACSG
 8761 CONTINUE
      CALL FUNC(M,N,XARRAY,FVEC,IFLAG)
c
      WRITE(*,*)' Test of subroutine FUNC'
      WRITE(*,8758)
 8758 FORMAT(8x,'FVEC(I)',1x,'ALPFN or BETFN',
     1 1x,'ALPNP or BETNP')
      DO 8762 I = 1,MDB4
      WRITE(*,8763)FVEC(I),REAL(ALPFN(NORGF*NMINF+I)),
     1 REAL(ALPNP(NORGF*NMINF+I))
      WRITE(*,8763)FVEC(MDB4+I),DIMAG(ALPFN(NORGF*NMINF+I)),
     1 DIMAG(ALPNP(NORGF*NMINF+I))
      WRITE(*,8763)FVEC(2*MDB4+I),REAL(BETFN(NORGF*NMINF+I)),
     1 REAL(BETNP(NORGF*NMINF+I))
      WRITE(*,8763)FVEC(3*MDB4+I),DIMAG(BETFN(NORGF*NMINF+I)),
     1 DIMAG(BETNP(NORGF*NMINF+I))
 8763 FORMAT(1PD15.7,D15.7,D15.7)
 8762 CONTINUE
```

```
c     We are testing our ability to use LMDIFF to recover
c   values of a  function which cause the function to be
c   minimized.  The function is called FNT18
      N = 18
      M = 20
      LSCRIP = M*N+5*N+M
      WRITE(*,*)LSCRIP,' = M*N+5*N+M for FNT18'
      EPSL = 1.D-9
      TOLL = 1.D-8
      FACTOR = 1.D2
c
      READ(3,7732)T18FRA
      WRITE(*,*)' Calling LMDIFF with T18FRA=',T18FRA
      IF((T18FRA.LE.0.D0).OR.(T18FRA.GT.2.D0)) THEN
 WRITE(*,*)' Stopping program in CSM.f'
 STOP
      ENDIF
c
 7732 FORMAT(1PD15.7)
      DO 7733 IX=1,N
  XARRAY(IX) = FLOAT(IX)*T18FRA
 7733 CONTINUE
      ICALLF = 0
      WRITE(*,*)FACTOR,' = FACTOR before CALL LMDIFF with FNT18'
      CALL LMDIFF(FNT18,M,N,XARRAY,FVEC,EPSL,TOLL,
     1 INFO,IWK,WK,LSCRIP,FACTOR)
      WRITE(*,*)FACTOR,' = FACTOR after CALL LMDIFF with FNT18'
      WRITE(*,*)ICALLF,' = no of function calls to FNT18'
      WRITE(*,*)INFO,' = INFO after call LMDIFF with FNT18'
      WRITE(*,7290)
 7290 FORMAT(6x,'XARRAY(I)',5x,'XARRAY(NORG+I)',
     1 3x,'XARRAY(2*NORG+I)')
      DO 7295 I = 1,NORG
c
      WRITE(*,7291)XARRAY(I),XARRAY(NORG+I),XARRAY(2*NORG+I)
 7291 FORMAT(1PD15.7,4x,D15.7,4x,D15.7)
 7295 CONTINUE
      WRITE(*,*)' Printing out FVEC values from FNT18'
      MDB4 = M/4
      IF(MDB4*4.EQ.M) THEN
       DO 7298 IM = 1,MDB4
       WRITE(*,7297)FVEC(IM),FVEC(MDB4+IM),FVEC(2*MDB4+IM),
     1  FVEC(3*MDB4+IM)
```

```
 7297  FORMAT(1PD15.7,3D15.7)
 7298  CONTINUE
       ENDIF
c******
c      We are now testing our ability to recover the
c  original values of radii and electromagnetic properties
c
c      READ from 3 values of FRACR, FRACEP, FRACSG
       READ(3,8754)FRACR,FRACEP,FRACSG
c
       WRITE(*,*)'  FRACR,FRACEP,FRACSG = '
       WRITE(*,8754)FRACR,FRACEP,FRACSG
       DO 8798 I = 1,NORG
       XARRAY(I) = FRACR
       XARRAY(NORG+I) = FRACEP
       XARRAY(2*NORG+I)=FRACSG
 8798 CONTINUE
       N = 18
       M = 20
       LSCRIP = M*N+5*N+M
       MDB4 = 5
       WRITE(*,*)LSCRIP,' = WA array dimension'
       IF(LSCRIP.GT.470) THEN
 WRITE(*,*)LSCRIP,' = WA length is too small'
 WRITE(16,*)LSCRIP,' = WA length is too small'
 WRITE(*,*)' Stopping before CALL LMDIFF in CSM.f'
 WRITE(16,*)' Stopping before CALL LMDIFF in CSM.f'
 STOP
       ENDIF
       EPSL= 1.D-9
       TOLL= 1.D-5
c*********reading in EPSL and TOLL from the data set
       READ(3,8767)EPSL,TOLL,FACTOR
 8767 FORMAT(1PD15.7,D15.7,D15.7)
       WRITE(*,8768)EPSL,TOLL
 8768 FORMAT(1PD15.7,D15.7,' = EPSL,TOLL')
       WRITE(*,8769)FACTOR
 8769 FORMAT(1PD15.7,' = FACTOR just before call LMDIFF in CSM.f')
       ICALLF = 0
       WRITE(*,*)' About to CALL LMDIFF(FUNCD,M,N,XARRAY,FVEC, '
c*********************************************************
       IPRNDX = 1234
c      This will cause the printing of the initial values
```

```
c     of EPSP,SIGP, and BDP in FUNCD
      CALL LMDIFF(FUNCD,M,N,XARRAY,FVEC,EPSL,TOLL,
     1 INFO,IWK,WK,LSCRIP,FACTOR)
c**********
      WRITE(*,*)FACTOR,' = FACTOR after CALL LMDIFF with FUNCD'
      WRITE(*,*)ICALLF,' = no of function calls'
      WRITE(16,*)ICALLF,' = no of function calls'
      WRITE(*,*)' Completed the call to LMDIFF in CSM.f'
      WRITE(*,*)INFO,' = INFO after call LMDIFF'
      WRITE(16,*)' Completed the call to LMDIFF in CSM.f'
      WRITE(16,*)INFO,' = INFO after call LMDIFF'
      DO 8872 I = 1,NORGF
      IF(I.EQ.1) THEN
 WRITE(*,8869)XARRAY(I)*BDP(I),BDP(I)
 WRITE(16,8869)XARRAY(I)*BDP(I),BDP(I)
      ELSE
c*********
 WRITE(*,8869)BDPFN(I-1)+XARRAY(I)*THICKF(I),
     1  BDP(I-1)+THICK(I)
 WRITE(16,8869)BDPFN(I-1)+XARRAY(I)*THICKF(I),
     1  BDP(I-1)+THICK(I)
      ENDIF
 8869 FORMAT(1PD15.7,D15.7,' = radii (approx and orig)')
      WRITE(*,8870)XARRAY(NORG+I)*EPSP(I),EPSP(I)
      WRITE(16,8870)XARRAY(NORG+I)*EPSP(I),EPSP(I)
 8870 FORMAT(1PD15.7,D15.7,' = EPS (approx and orig)')
      WRITE(*,8871)XARRAY(2*NORG+I)*SIGP(I),SIGP(I)
      WRITE(16,8871)XARRAY(2*NORG+I)*SIGP(I),SIGP(I)
 8871 FORMAT(1PD15.7,D15.7,' = COND (approx and orig)')
 8872 CONTINUE
      WRITE(*,*)' Printing out FVEC values from FUNCD'
      MDB4 = M/4
      IF(MDB4*4.EQ.M) THEN
       DO 9298 IM = 1,MDB4
       WRITE(*,9297)FVEC(IM),FVEC(MDB4+IM),FVEC(2*MDB4+IM),
     1  FVEC(3*MDB4+IM)
 9297  FORMAT(1PD15.7,3D15.7)
 9298  CONTINUE
      ENDIF
      IF(MDB4*4.NE.M) THEN
 DO 8883 I = 1,M
 WRITE(*,8881)FVEC(I),I
 WRITE(16,8881)FVEC(I),I
```

```
8881   FORMAT(1PD15.7,' = FVEC(',I5,')')
8883   CONTINUE
     ENDIF
     GOTO 5
1110 CONTINUE
     CLOSE(UNIT=16)
     CLOSE(UNIT=26)
     CLOSE(UNIT=7)
     CLOSE(UNIT=3)
     CLOSE(UNIT=70)
     CLOSE(UNIT=71)
     CLOSE(UNIT=74)
     CLOSE(UNIT=75)
     CLOSE(UNIT=77)
     CLOSE(UNIT=76)
     STOP
     END
```

This is the end of the driver program.

3 COEF subroutine

The next subroutine enables us to determine the expansion coefficients of the electromagnetic field. The variables ALPNP and BETNP are mulipliers of outgoing spherical waves, while ANP and BNP are multipliers if spherical waves converging towards the center of the sphere.

```
      SUBROUTINE COEF
c     SUBROUTINE COEF(ANP,BNP,ALPNP,BETNP) exp coefficients passed
c through common CSMCOM.f
* GENERATE EXPANSION COEFFICIENTS
      IMPLICIT REAL*8 (A-H, O-Z)
c*************************************************************
c     Several variables are passed through CSMCOM.f the common
c     These include FKP(NLAYPO), the propgagation constants
c                   ANP(NLAYPO*NZ)
c                   BNP(NLAYPO*NZ)
c                   ALPNP(NLAYPO*NZ)
c                   BETNP(NLAYPO*NZ)
c                   BJNP(NZ)
c                   BHNP(NZ)
c    and CEX,Z (the Bessel function argument),BDP(NLAYPO), the
c    layer radii(meters),Z = FKP(J)*BDP(J),EPSP(NLAYER),
c    SIGP(NLAYER) (conductivity in mhos per meter), STOPR
```

```
c
c*********************************************************
      COMPLEX*16
     1             BJHP1(1000),
     2           BJHP2(1000), SJNP1(500), DELNP, SNT11, SNT12, SNT21,
     3           SNT22, TNT11, TNT12, TNT21, TNT22, ETAP1, ETAP2,
     4           ZEP1, ZEP2, SNP11, SNP12, SNP21, SNP22, TNP11, TNP12,
     5           TNP21, TNP22, DEL1, DEL2, SHNP1(500), RATIO,
     6           DELNPE,CI,ZTEMP,ZPLUS,DELEXA
      COMPLEX*16 DELTAA(11)
c     COMMON FKP, BJNP, BHNP, CEX, BDP, P, DP, SIGP, EO, TIME, R,
c    1       THETA, PHI, STOPR, NC, NORG, NMIN
      INCLUDE 'CSMCOM.f'
c      DIMENSION NTER(10), BDP(9), SIGP(9), P(101), DP(500)
       DIMENSION NTER(10)
* COMPUTE COEFICIENTS AN1, BN1, ANN, BNN, ALPN1, BETN1, ALPNN, & BETNN
      DATA JJK/0/
c*********************************
      ONE = 1.D0
      ZERO = 0.D0
      JOLD = 0
      CI = CMPLX(ZERO,ONE)
      N1=0
      N2=0
      IPRINT = 0
      IPSET2 = 0
      IPSET3 = 0
      IPSET4 = 0
      JOLD1 = 0
      JOLD2 = 0
      IF(NORG.GT.10) THEN
 WRITE(*,1007)
 1007 FORMAT(' A value of NORG = ',I5, ' was entered'/
     1' We are stopping the program in COEF')
 STOP
      ENDIF
      NORGP1 = NORG + 1
      WRITE(*,*)FKP(NORGP1),' = FKP(NORG+1) in COEF'
      DO 300 NR = 1,NORG
c      At this stage we have computed all the
c  values of FKP(NR) and we now wish to compute
c  the Wronskians
   DELTAA(NR)  = CI*(FKP(NR)*BDP(NR))**(-2)
```

```
  WRITE(*,3001)NR,DELTAA(NR)
3001     FORMAT(' DELTAA(',I5,') = ',2D20.10)
 300 CONTINUE
     DO 15 NR=1, NORG
Z=FKP(NR)*BDP(NR)
ZPLUS = FKP(NR+1)*BDP(NR)
CALL BJYH(BJNP, BHNP, Z, N, STOPR)
DO 5 I=1,N
  SJNP1(I)=BJNP(I)
  SHNP1(I)=BHNP(I)
   5   CONTINUE
Z=FKP(NR+1)*BDP(NR)
CALL BJYH(BJNP, BHNP, Z, NN, STOPR)
NMIN=MINO(N,NN)
NTER(NR)=NMIN
N2=N2+NMIN
DO 10 I=1, NMIN
  BJHP1(N1+I)=SJNP1(I)
  BJHP1(N2+I)=SHNP1(I)
  BJHP2(N1+I)=BJNP(I)
  BJHP2(N2+I)=BHNP(I)
  10   CONTINUE
N1=N1+2*NMIN
N2=N2+NMIN
  15 CONTINUE
     NMIN=MINN(NTER,NORG)
     NMIN=NMIN-2
     DO 17 I=1,NMIN
ALPNP(I)=DCMPLX(0.D0, 0.D0)
BETNP(I)=DCMPLX(0.D0, 0.D0)
  17 CONTINUE
     NSUM=NORG*NMIN
     DO 30 I=1, NMIN
JJ=0
KK=0
II1=I+1
II2=2*I+1
SNT11=DCMPLX(1.D0, 0.D0)
SNT12=DCMPLX(0.D0, 0.D0)
SNT21=SNT12
SNT22=SNT11
TNT11=SNT11
TNT12=SNT12
```

```
      TNT21=SNT12
      TNT22=SNT11
      DO 27 J=1, NORG
        ZPLUS = FKP(J+1)*BDP(J)
        Z = FKP(J)*BDP(J)
        KK=KK+NTER(J)
        ETAP1=(II1*BJHP1(JJ+I)-I*BJHP1(JJ+I+2))/II2
        ETAP2=(II1*BJHP2(JJ+I)-I*BJHP2(JJ+I+2))/II2
        ZEP1=(II1*BJHP1(KK+I)-I*BJHP1(KK+I+2))/II2
        ZEP2=(II1*BJHP2(KK+I)-I*BJHP2(KK+I+2))/II2
c             DELNP=BJHP1(JJ+I+1)*ZEP1-BJHP1(KK+I+1)*ETAP1
        DELNPE = CI*(FKP(J)*BDP(J))**(-2)
c             IF(IPRINT.LT.14) THEN
c               IPRINT = IPRINT+1
c               WRITE(*,*)DELNP,' = DELNP'
c               WRITE(*,*)DELNPE,' = DELNPE'
c             ENDIF
        DELNP = DELNPE
        RATIO=FKP(J+1)/FKP(J)
        SNP11=(ZEP1*BJHP2(JJ+I+1)-RATIO*BJHP1(KK+I+1)*ETAP2)/DELNP
        SNP12=(ZEP1*BJHP2(KK+I+1)-RATIO*BJHP1(KK+I+1)*ZEP2)/DELNP
        SNP21=(RATIO*BJHP1(JJ+I+1)*ETAP2-ETAP1*BJHP2(JJ+I+1))/DELNP
        SNP22=(RATIO*BJHP1(JJ+I+1)*ZEP2-ETAP1*BJHP2(KK+I+1))/DELNP
        ZTEMP=SNT11
        SNT11=SNT11*SNP11+SNT12*SNP21
        SNT12=ZTEMP*SNP12+SNT12*SNP22
        ZTEMP=SNT21
        SNT21=SNT21*SNP11+SNT22*SNP21
        SNT22=ZTEMP*SNP12+SNT22*SNP22
        TNP11=(RATIO*ZEP1*BJHP2(JJ+I+1)-BJHP1(KK+I+1)*ETAP2)/DELNP
        TNP12=(RATIO*ZEP1*BJHP2(KK+I+1)-BJHP1(KK+I+1)*ZEP2)/DELNP
        TNP21=(BJHP1(JJ+I+1)*ETAP2-RATIO*ETAP1*BJHP2(JJ+I+1))/DELNP
        TNP22=(BJHP1(JJ+I+1)*ZEP2-RATIO*ETAP1*BJHP2(KK+I+1))/DELNP
        IF (JJK.EQ.0) THEN
          WRITE(7,*)' I, RATIO, ZEP1, DELNP, ETAP2'
          WRITE(7,*)ZPLUS/Z,' = ZPLUS/Z'
          JJK=2
        ENDIF
        IF (I.LT.6) THEN
          WRITE(7,759) I, RATIO, ZEP1, DELNP,    ?2
      759       FORMAT('I = ',I3,2X,4('(',E12.5,',',E12.5,')',2X))
        ENDIF
        ZTEMP=TNT11
```

```
  TNT11=TNT11*TNP11+TNT12*TNP21
  TNT12=ZTEMP*TNP12+TNT12*TNP22
  ZTEMP=TNT21
  TNT21=TNT21*TNP11+TNT22*TNP21
  TNT22=ZTEMP*TNP12+TNT22*TNP22
  JJ=JJ+2*NTER(J)
  KK=KK+NTER(J)
  27   CONTINUE
 ANP(I)=SNT11-(SNT12*SNT21)/SNT22
 BNP(I)=TNT11-(TNT12*TNT21)/TNT22
 LL=NSUM+I
 ANP(LL)=DCMPLX(1.D0, 0.D0)
 BNP(LL)=DCMPLX(1.D0, 0.D0)
 ALPNP(LL)=-SNT21/SNT22
 BETNP(LL)=-TNT21/TNT22
  30 CONTINUE
     IF (NORG.EQ.1) RETURN
* COMPUTE COEFICIENTS AN2,...,AN(N-1);       BN2,...,BN(N-1);
*                     ALPN2,...,ALPN2(N-1);  BETN2,...BETN2(N-1)
     JJ=0
     KK=0
     MM1=0
     MM2=NMIN
     NRGM1=NORG-1
     DO 45 J=1, NRGM1
c
  Z = FKP(J)*BDP(J)
  ZPLUS = FKP(J+1)*BDP(J)
 KK=KK+NTER(J)
 DO 40 I=1, NMIN
  II1=I+1
  II2=2*I+1
  ETAP1=(II1*BJHP1(JJ+I)-I*BJHP1(JJ+I+2))/II2
  ETAP2=(II1*BJHP2(JJ+I)-I*BJHP2(JJ+I+2))/II2
  ZEP1=(II1*BJHP1(KK+I)-I*BJHP1(KK+I+2))/II2
  ZEP2=(II1*BJHP2(KK+I)-I*BJHP2(KK+I+2))/II2
c        DELNP=BJHP1(JJ+I+1)*ZEP1-BJHP1(KK+I+1)*ETAP1
  DELNPE  = CI*(FKP(J)*BDP(J))**(-2)
c        IF(IPSET2.LT.14.AND.J.NE.JOLD) THEN
c           JOLD = J
c           IPSET2 = IPSET2 + 1
c           WRITE(*,*) DELNP,' = DELNP just before SPN11 calc'
c           WRITE(*,*) DELNPE,' = DELNPE'
```

```
c          ENDIF
   DELNP = DELNPE
   RATIO=FKP(J+1)/FKP(J)
   SNP11=(ZEP1*BJHP2(JJ+I+1)-RATIO*BJHP1(KK+I+1)*ETAP2)/DELNP
   SNP12=(ZEP1*BJHP2(KK+I+1)-RATIO*BJHP1(KK+I+1)*ZEP2)/DELNP
   SNP21=(RATIO*BJHP1(JJ+I+1)*ETAP2-ETAP1*BJHP2(JJ+I+1))/DELNP
   SNP22=(RATIO*BJHP1(JJ+I+1)*ZEP2-ETAP1*BJHP2(KK+I+1))/DELNP
   DEL1=SNP11*SNP22-SNP12*SNP21
   IF(IPSET3.LT.10.AND.JOLD1.NE.J) THEN
      WRITE(*,*) DEL1,' = DEL1'
c
      DELEXA = (FKP(J+1)/FKP(J))*(-CI)/(ZPLUS**2)
      WRITE(*,*)DELEXA,' = DELEXA'
      WRITE(*,*)J,' = J'
      IPSET3 = IPSET3 + 1
      JOLD1 = J
   ENDIF
   TNP11=(RATIO*ZEP1*BJHP2(JJ+I+1)-BJHP1(KK+I+1)*ETAP2)/DELNP
   TNP12=(RATIO*ZEP1*BJHP2(KK+I+1)-BJHP1(KK+I+1)*ZEP2)/DELNP
   TNP21=(BJHP1(JJ+I+1)*ETAP2-RATIO*ETAP1*BJHP2(JJ+I+1))/DELNP
   TNP22=(BJHP1(JJ+I+1)*ZEP2-RATIO*ETAP1*BJHP2(KK+I+1))/DELNP
   DEL2=TNP11*TNP22-TNP12*TNP21
   IF(IPSET4.LT.10.AND.JOLD2.NE.J) THEN
      WRITE(*,*) DEL2,' = DEL2'
      DELEXA = (FKP(J+1)/FKP(J))*(-CI)/(ZPLUS**2)
      WRITE(*,*)DELEXA,' = DELEXA'
      IPSET4 = IPSET4 + 1
      JOLD2 = J
      WRITE(*,*)J,' = J'
   ENDIF
   NN1=MM1+I
   NN2=MM2+I
   ANP(NN2)=(ANP(NN1)*SNP22-ALPNP(NN1)*SNP12)/DEL1
   BNP(NN2)=(BNP(NN1)*TNP22-BETNP(NN1)*TNP12)/DEL2
   ALPNP(NN2)=(-ANP(NN1)*SNP21+ALPNP(NN1)*SNP11)/DEL1
   BETNP(NN2)=(-BNP(NN1)*TNP21+BETNP(NN1)*TNP11)/DEL2
   40   CONTINUE
 JJ=JJ+2*NTER(J)
 KK=KK+NTER(J)
 MM1=MM1+NMIN
 MM2=MM2+NMIN
   45 CONTINUE
      RETURN
```

```
      END
```

4 COEFAS subroutine

This subroutine generates the expansion coefficients of the scattered radiation outside the N layer sphere as a function of a hypothesized number of layers and hypothesized layer properties. This is called by function FUNCD which is an EXTERNAL variable that is used as an argument in a Levinberg Marquardt subroutine LMDIFF which then attempts to recover the actual sphere properties which will match the actual expansion coefficients of the scattered radiation.

```
      SUBROUTINE COEFAS
c through common CSMCOM.f
* GENERATE EXPANSION COEFFICIENTS
      IMPLICIT REAL*8 (A-H, O-Z)
c*************************************************************
c     Several variables are passed through CSMCOM.f the common
c     These include FKPF(NLAYPO), the propgagation constants
c                   ANPFN(NLAYPO*NZ)
c                   BNPFN(NLAYPO*NZ)
c                   ALPFN(NLAYPO*NZ)
c                   BETFN(NLAYPO*NZ)
c                   BJNP(NZ)
c                   BHNP(NZ)
c    and CEX,Z (the Bessel function argument),BDPFN(NLAYPO), the
c    layer radii(meters),Z = FKPF(J)*BDPFN(J),EPSPF(NLAYER),
c    SIGPF(NLAYER) (conductivity in mhos per meter), STOPR
c
c*************************************************************
      COMPLEX*16
     1             BJHP1(1000),
     2           BJHP2(1000), SJNP1(500), DELNP, SNT11, SNT12, SNT21,
     3           SNT22, TNT11, TNT12, TNT21, TNT22, ETAP1, ETAP2,
     4           ZEP1, ZEP2, SNP11, SNP12, SNP21, SNP22, TNP11, TNP12,
     5           TNP21, TNP22, DEL1, DEL2, SHNP1(500), RATIO,
     6           DELNPE,CI,ZTEMP,ZPLUS,DELEXA
      COMPLEX*16 DELTAA(11)
      INCLUDE 'CSMCOM.f'
       DIMENSION NTER(10)
* COMPUTE COEFICIENTS AN1, BN1, ANN, BNN, ALPN1, BETN1, ALPNN, & BETNN
      DATA JJK/0/
c*********************************
      ONE = 1.DO
```

```
      ZERO = 0.D0
      JOLD = 0
      CI = CMPLX(ZERO,ONE)
      N1=0
      N2=0
      IPRINT = 0
      IPSET2 = 0
      IPSET3 = 0
      IPSET4 = 0
      JOLD1 = 0
      JOLD2 = 0
      IF(NORGF.GT.10) THEN
 WRITE(*,1007)
 1007 FORMAT(' A value of NORGF = ',I5, ' was entered'/
     1' We are stopping the program in COEFAS')
 STOP
      ENDIF
      NORGP1 = NORGF + 1
      DO 300 NR = 1,NORGF
c       At this stage we have computed all the
c  values of FKPF(NR) and we now wish to compute
c  the Wronskians
   DELTAA(NR)  = CI*(FKPF(NR)*BDPFN(NR))**(-2)
c*******  WRITE(*,3001)NR,DELTAA(NR)
 3001     FORMAT(' DELTAA(',I5,') = ',2D20.10)
  300 CONTINUE
      DO 15 NR=1, NORGF
 Z=FKPF(NR)*BDPFN(NR)
 ZPLUS = FKPF(NR+1)*BDPFN(NR)
 CALL BJYH(BJNP, BHNP, Z, N, STOPR)
 DO 5 I=1,N
   SJNP1(I)=BJNP(I)
   SHNP1(I)=BHNP(I)
    5   CONTINUE
 Z=FKPF(NR+1)*BDPFN(NR)
 CALL BJYH(BJNP, BHNP, Z, NN, STOPR)
 NMINF=MINO(N,NN)
 NTER(NR)=NMINF
 N2=N2+NMINF
 DO 10 I=1, NMINF
   BJHP1(N1+I)=SJNP1(I)
   BJHP1(N2+I)=SHNP1(I)
   BJHP2(N1+I)=BJNP(I)
```

```
  BJHP2(N2+I)=BHNP(I)
  10   CONTINUE
N1=N1+2*NMINF
N2=N2+NMINF
  15 CONTINUE
     NMINF=MINN(NTER,NORGF)
     NMINF=NMINF-2
     DO 17 I=1,NMINF
ALPNP(I)=DCMPLX(0.D0, 0.D0)
BETNP(I)=DCMPLX(0.D0, 0.D0)
  17 CONTINUE
     NSUM=NORGF*NMINF
     DO 30 I=1, NMINF
JJ=0
KK=0
II1=I+1
II2=2*I+1
SNT11=DCMPLX(1.D0, 0.D0)
SNT12=DCMPLX(0.D0, 0.D0)
SNT21=SNT12
SNT22=SNT11
TNT11=SNT11
TNT12=SNT12
TNT21=SNT12
TNT22=SNT11
DO 27 J=1, NORGF
  ZPLUS = FKPF(J+1)*BDPFN(J)
  Z = FKPF(J)*BDPFN(J)
  KK=KK+NTER(J)
  ETAP1=(II1*BJHP1(JJ+I)-I*BJHP1(JJ+I+2))/II2
  ETAP2=(II1*BJHP2(JJ+I)-I*BJHP2(JJ+I+2))/II2
  ZEP1=(II1*BJHP1(KK+I)-I*BJHP1(KK+I+2))/II2
  ZEP2=(II1*BJHP2(KK+I)-I*BJHP2(KK+I+2))/II2
c         DELNP=BJHP1(JJ+I+1)*ZEP1-BJHP1(KK+I+1)*ETAP1
  DELNPE = CI*(FKP(J)*BDP(J))**(-2)
c         IF(IPRINT.LT.14) THEN
c           IPRINT = IPRINT+1
c           WRITE(*,*)DELNP,' = DELNP'
c           WRITE(*,*)DELNPE,' = DELNPE'
c         ENDIF
  DELNP = DELNPE
  RATIO=FKPF(J+1)/FKPF(J)
  SNP11=(ZEP1*BJHP2(JJ+I+1)-RATIO*BJHP1(KK+I+1)*ETAP2)/DELNP
```

```
      SNP12=(ZEP1*BJHP2(KK+I+1)-RATIO*BJHP1(KK+I+1)*ZEP2)/DELNP
      SNP21=(RATIO*BJHP1(JJ+I+1)*ETAP2-ETAP1*BJHP2(JJ+I+1))/DELNP
      SNP22=(RATIO*BJHP1(JJ+I+1)*ZEP2-ETAP1*BJHP2(KK+I+1))/DELNP
      ZTEMP=SNT11
      SNT11=SNT11*SNP11+SNT12*SNP21
      SNT12=ZTEMP*SNP12+SNT12*SNP22
      ZTEMP=SNT21
      SNT21=SNT21*SNP11+SNT22*SNP21
      SNT22=ZTEMP*SNP12+SNT22*SNP22
      TNP11=(RATIO*ZEP1*BJHP2(JJ+I+1)-BJHP1(KK+I+1)*ETAP2)/DELNP
      TNP12=(RATIO*ZEP1*BJHP2(KK+I+1)-BJHP1(KK+I+1)*ZEP2)/DELNP
      TNP21=(BJHP1(JJ+I+1)*ETAP2-RATIO*ETAP1*BJHP2(JJ+I+1))/DELNP
      TNP22=(BJHP1(JJ+I+1)*ZEP2-RATIO*ETAP1*BJHP2(KK+I+1))/DELNP
      IF (JJK.EQ.0) THEN
c******       WRITE(7,*)' I, RATIO, ZEP1, DELNP, ETAP2'
c******       WRITE(7,*)ZPLUS/Z,' = ZPLUS/Z'
        JJK=2
      ENDIF
      IF (I.LT.6) THEN
c            WRITE(7,759) I, RATIO, ZEP1, DELNP, ETAP2
  759        FORMAT('I = ',I3,2X,4('(',E12.5,',',E12.5,')',2X))
      ENDIF
      ZTEMP=TNT11
      TNT11=TNT11*TNP11+TNT12*TNP21
      TNT12=ZTEMP*TNP12+TNT12*TNP22
      ZTEMP=TNT21
      TNT21=TNT21*TNP11+TNT22*TNP21
      TNT22=ZTEMP*TNP12+TNT22*TNP22
      JJ=JJ+2*NTER(J)
      KK=KK+NTER(J)
   27   CONTINUE
    ANPFN(I)=SNT11-(SNT12*SNT21)/SNT22
    BNPFN(I)=TNT11-(TNT12*TNT21)/TNT22
    LL=NSUM+I
    ANPFN(LL)=DCMPLX(1.D0, 0.D0)
    BNPFN(LL)=DCMPLX(1.D0, 0.D0)
    ALPFN(LL)=-SNT21/SNT22
    BETFN(LL)=-TNT21/TNT22
   30 CONTINUE
      IF (NORGF.EQ.1) RETURN
* COMPUTE COEFICIENTS AN2,...,AN(N-1);        BN2,...,BN(N-1);
*                     ALPN2,...,ALPN2(N-1);  BETN2,...BETN2(N-1)
      JJ=0
```

```
      KK=0
      MM1=0
      MM2=NMINF
      NRGM1=NORGF-1
      DO 45 J=1, NRGM1
c
   Z = FKPF(J)*BDPFN(J)
 KK=KK+NTER(J)
 DO 40 I=1, NMINF
   II1=I+1
   II2=2*I+1
   ETAP1=(II1*BJHP1(JJ+I)-I*BJHP1(JJ+I+2))/II2
   ETAP2=(II1*BJHP2(JJ+I)-I*BJHP2(JJ+I+2))/II2
   ZEP1=(II1*BJHP1(KK+I)-I*BJHP1(KK+I+2))/II2
   ZEP2=(II1*BJHP2(KK+I)-I*BJHP2(KK+I+2))/II2
c          DELNP=BJHP1(JJ+I+1)*ZEP1-BJHP1(KK+I+1)*ETAP1
   DELNPE  = CI*(FKPF(J)*BDPFN(J))**(-2)
c          IF(IPSET2.LT.14.AND.J.NE.JOLD) THEN
c             JOLD = J
c             IPSET2 = IPSET2 + 1
c             WRITE(*,*) DELNP,' = DELNP just before SPN11 calc'
c             WRITE(*,*) DELNPE,' = DELNPE'
c          ENDIF
   DELNP = DELNPE
   RATIO=FKPF(J+1)/FKPF(J)
   SNP11=(ZEP1*BJHP2(JJ+I+1)-RATIO*BJHP1(KK+I+1)*ETAP2)/DELNP
   SNP12=(ZEP1*BJHP2(KK+I+1)-RATIO*BJHP1(KK+I+1)*ZEP2)/DELNP
   SNP21=(RATIO*BJHP1(JJ+I+1)*ETAP2-ETAP1*BJHP2(JJ+I+1))/DELNP
   SNP22=(RATIO*BJHP1(JJ+I+1)*ZEP2-ETAP1*BJHP2(KK+I+1))/DELNP
   DEL1=SNP11*SNP22-SNP12*SNP21
   IF(IPSET3.LT.10.AND.JOLD1.NE.J) THEN
c****         WRITE(*,*) DEL1,' = DEL1'
c
      DELEXA = (FKPF(J+1)/FKPF(J))*(-CI)/(ZPLUS**2)
c*****        WRITE(*,*)DELEXA,' = DELEXA'
c*****        WRITE(*,*)J,' = J'
      IPSET3 = IPSET3 + 1
      JOLD1 = J
   ENDIF
   TNP11=(RATIO*ZEP1*BJHP2(JJ+I+1)-BJHP1(KK+I+1)*ETAP2)/DELNP
   TNP12=(RATIO*ZEP1*BJHP2(KK+I+1)-BJHP1(KK+I+1)*ZEP2)/DELNP
   TNP21=(BJHP1(JJ+I+1)*ETAP2-RATIO*ETAP1*BJHP2(JJ+I+1))/DELNP
   TNP22=(BJHP1(JJ+I+1)*ZEP2-RATIO*ETAP1*BJHP2(KK+I+1))/DELNP
```

```
   DEL2=TNP11*TNP22-TNP12*TNP21
   IF(IPSET4.LT.10.AND.JOLD2.NE.J) THEN
c****         WRITE(*,*) DEL2,' = DEL2'
c****         DELEXA = (FKPF(J+1)/FKPF(J))*(-CI)/(ZPLUS**2)
c****         WRITE(*,*)DELEXA,' = DELEXA'
      IPSET4 = IPSET4 + 1
      JOLD2 = J
c****         WRITE(*,*)J,' = J'
   ENDIF
   NN1=MM1+I
   NN2=MM2+I
   ANPFN(NN2)=(ANPFN(NN1)*SNP22-ALPFN(NN1)*SNP12)/DEL1
   BNPFN(NN2)=(BNPFN(NN1)*TNP22-BETFN(NN1)*TNP12)/DEL2
   ALPFN(NN2)=
     1     (-ANPFN(NN1)*SNP21+ALPFN(NN1)*SNP11)/DEL1
   BETFN(NN2)=
     1     (-BNPFN(NN1)*TNP21+BETFN(NN1)*TNP11)/DEL2
   40   CONTINUE
 JJ=JJ+2*NTER(J)
 KK=KK+NTER(J)
 MM1=MM1+NMINF
 MM2=MM2+NMINF
   45 CONTINUE
      RETURN
      END
```

This is the end of the COEFAS expansion coefficient determination subroutine.

5 DPMPAR subroutine

This is a subroutine adapted from one written by Alfred Morris to determine the best machine constants for the particular computer being used to solve the problem.

```
      DOUBLE PRECISION FUNCTION DPMPAR(I)
      INTEGER I
C-----------------------
C
C     DPMPAR PROVIDES THE DOUBLE PRECISION MACHINE PARAMETERS FOR
C     THE COMPUTER BEING USED. IT IS ASSUMED THAT THE ARGUMENT
C     I IS AN INTEGER HAVING ONE OF THE VALUES 1, 2, OR 3. IF THE
C     DOUBLE PRECISION ARITHMETIC BEING USED HAS T BASE B DIGITS AND
C     ITS SMALLEST AND LARGEST EXPONENTS ARE EMIN AND EMAX, THEN
C
```

```
C         DPMPAR(1) = B**(1 - T), THE MACHINE PRECISION,
C
C         DPMPAR(2) = B**(EMIN - 1), THE SMALLEST MAGNITUDE,
C
C         DPMPAR(3) = B**EMAX*(1 - B**(-T)), THE LARGEST MAGNITUDE.
C
C     TO DEFINE THIS FUNCTION FOR THE COMPUTER BEING USED, ACTIVATE
C     THE DATA STATMENTS FOR THE COMPUTER BY REMOVING THE C FROM
C     COLUMN 1. (ALL OTHER DATA STATEMENTS IN DPMPAR SHOULD HAVE C
C     IN COLUMN 1.) IF DATA STATEMENTS ARE NOT GIVEN FOR THE COMPUTER
C     BEING USED, THEN THE SUBROUTINE MACH MAY BE USED TO COMPUTE THE
C     VALUES FOR DPMPAR.
C
C-----------------------
C
C     DPMPAR IS AN ADAPTATION OF THE FUNCTION D1MACH, WRITTEN BY P.A.
C     FOX, A.D. HALL, AND N.L. SCHRYER (BELL LABORATORIES). DPMPAR
C     WAS DESIGNED BY B.S. GARBOW, K.E. HILLSTROM, AND J.J. MORE
C     (ARGONNE NATIONAL LABORATORY). THE MAJORITY OF PARAMETER VALUES
C     ARE FROM BELL LABORATORIES.
C
C-----------------------
      INTEGER MCHEPS(4)
      INTEGER MINMAG(4)
      INTEGER MAXMAG(4)
      DOUBLE PRECISION DMACH(3)
      EQUIVALENCE (DMACH(1),MCHEPS(1))
      EQUIVALENCE (DMACH(2),MINMAG(1))
      EQUIVALENCE (DMACH(3),MAXMAG(1))
C
C     MACHINE CONSTANTS FOR THE BURROUGHS 1700 SYSTEM.
C
C     DATA MCHEPS(1) / ZCC6800000 /
C     DATA MCHEPS(2) / Z000000000 /
C
C     DATA MINMAG(1) / ZC00800000 /
C     DATA MINMAG(2) / Z000000000 /
C
C     DATA MAXMAG(1) / ZDFFFFFFFF /
C     DATA MAXMAG(2) / ZFFFFFFFFF /
C
C     MACHINE CONSTANTS FOR THE BURROUGHS 5700 SYSTEM.
C
```

```
C     DATA MCHEPS(1) / 01451000000000000 /
C     DATA MCHEPS(2) / 00000000000000000 /
C
C     DATA MINMAG(1) / 01771000000000000 /
C     DATA MINMAG(2) / 00000000000000000 /
C
C     DATA MAXMAG(1) / 00777777777777777 /
C     DATA MAXMAG(2) / 00007777777777777 /
C
C     MACHINE CONSTANTS FOR THE BURROUGHS 6700/7700 SYSTEMS.
C
C     DATA MCHEPS(1) / 01451000000000000 /
C     DATA MCHEPS(2) / 00000000000000000 /
C
C     DATA MINMAG(1) / 01771000000000000 /
C     DATA MINMAG(2) / 07770000000000000 /
C
C     DATA MAXMAG(1) / 00777777777777777 /
C     DATA MAXMAG(2) / 07777777777777777 /
C
C     MACHINE CONSTANTS FOR THE CDC 6000/7000 SERIES.
C     (OCTAL FORMAT FOR FORTRAN 4 COMPILERS)
C
C     DATA MCHEPS(1) / 15614000000000000000B /
C     DATA MCHEPS(2) / 15010000000000000000B /
C
C     DATA MINMAG(1) / 00014000000000000000B /
C     DATA MINMAG(2) / 00000000000000000000B /
C
C     DATA MAXMAG(1) / 37767777777777777777B /
C     DATA MAXMAG(2) / 37167777777777777777B /
C
C     MACHINE CONSTANTS FOR THE CDC 6000/7000 SERIES.
C     (INTEGER FORMAT FOR FORTRAN 4 AND 5 COMPILERS)
C
      DATA MCHEPS(1) / 248120191970443264 /
      DATA MCHEPS(2) / 234468655599976448 /
C
      DATA MINMAG(1) /    422212465065984 /
      DATA MINMAG(2) /                  0 /
C
      DATA MAXMAG(1) / 576179277326712831 /
      DATA MAXMAG(2) / 562668478444601343 /
```

```
C
C     MACHINE CONSTANTS FOR THE CRAY-1.
C
C     DATA MCHEPS(1) / 03764240000000000000B /
C     DATA MCHEPS(2) / 00000000000000000000B /
C
C     DATA MINMAG(1) / 02000340000000000000B /
C     DATA MINMAG(2) / 00000000000000000000B /
C
C     DATA MAXMAG(1) / 05777777777777777777B /
C     DATA MAXMAG(2) / 00000077777777777776B /
C
C     MACHINE CONSTANTS FOR THE DATA GENERAL ECLIPSE S/200.
C
C     NOTE - IT MAY BE APPROPRIATE TO INCLUDE THE FOLLOWING CARD -
C     STATIC DMACH(3)
C
C     DATA MINMAG/20K,3*0/,MAXMAG/77777K,3*177777K/
C     DATA MCHEPS/32020K,3*0/
C
C     MACHINE CONSTANTS FOR THE HARRIS 220.
C
C     DATA MCHEPS(1),MCHEPS(2) / '20000000, '00000334 /
C     DATA MINMAG(1),MINMAG(2) / '20000000, '00000201 /
C     DATA MAXMAG(1),MAXMAG(2) / '37777777, '37777577 /
C
C     MACHINE CONSTANTS FOR THE HONEYWELL 600/6000 SERIES.
C
C     DATA MCHEPS(1),MCHEPS(2) / 0606400000000, 0000000000000 /
C     DATA MINMAG(1),MINMAG(2) / 0402400000000, 0000000000000 /
C     DATA MAXMAG(1),MAXMAG(2) / 0376777777777, 0777777777777 /
C
C     MACHINE CONSTANTS FOR THE HP 2100
C     THREE WORD DOUBLE PRECISION OPTION WITH FTN4
C
C     DATA MCHEPS(1), MCHEPS(2), MCHEPS(3) / 40000B,       0,    276B /
C     DATA MINMAG(1), MINMAG(2), MINMAG(3) / 40000B,       0,      1 /
C     DATA MAXMAG(1), MAXMAG(2), MAXMAG(3) / 77777B, 177777B, 177776B /
C
C     MACHINE CONSTANTS FOR THE HP 2100
C     FOUR WORD DOUBLE PRECISION OPTION WITH FTN4
C
C     DATA MCHEPS(1), MCHEPS(2) /  40000B,       0 /
```

```
C     DATA MCHEPS(3), MCHEPS(4) /       0,    227B /
C     DATA MINMAG(1), MINMAG(2) /  40000B,       0 /
C     DATA MINMAG(3), MINMAG(4) /       0,       1 /
C     DATA MAXMAG(1), MAXMAG(2) /  77777B, 177777B /
C     DATA MAXMAG(3), MAXMAG(4) / 177777B, 177776B /
C
C     MACHINE CONSTANTS FOR THE HP 9000
C
C     DATA DMACH(1) / .22204460492503131D-15  /
C     DATA DMACH(2) / .22250738585072014D-307 /
C     DATA DMACH(3) / .17976931348623157D+309 /
C
C     MACHINE CONSTANTS FOR THE IBM 360/370 SERIES,
C     THE AMDAHL 470/V6, THE ICL 2900, THE ITEL AS/6,
C     THE XEROX SIGMA 5/7/9 AND THE SEL SYSTEMS 85/86.
C
C     DATA MCHEPS(1),MCHEPS(2) / Z34100000, Z00000000 /
C     DATA MINMAG(1),MINMAG(2) / Z00100000, Z00000000 /
C     DATA MAXMAG(1),MAXMAG(2) / Z7FFFFFFF, ZFFFFFFFF /
C
C     MACHINE CONSTANTS FOR THE IBM PC - MICROSOFT FORTRAN
C
C     DATA MCHEPS(1), MCHEPS(2) / #00000000, #3CB00000 /
C     DATA MINMAG(1), MINMAG(2) / #00000000, #00100000 /
C     DATA MAXMAG(1), MAXMAG(2) / #FFFFFFFF, #7FEFFFFF /
C
C     MACHINE CONSTANTS FOR THE IBM PC - PROFESSIONAL FORTRAN,
C     LAHEY FORTRAN, AND RM FORTRAN
C
C     DATA MCHEPS(1), MCHEPS(2) / Z'00000000', Z'3CB00000' /
C     DATA MINMAG(1), MINMAG(2) / Z'00000000', Z'00100000' /
C     DATA MAXMAG(1), MAXMAG(2) / Z'FFFFFFFF', Z'7FEFFFFF' /
C
C     MACHINE CONSTANTS FOR THE PDP-10 (KA PROCESSOR).
C
C     DATA MCHEPS(1),MCHEPS(2) / "114400000000, "000000000000 /
C     DATA MINMAG(1),MINMAG(2) / "033400000000, "000000000000 /
C     DATA MAXMAG(1),MAXMAG(2) / "377777777777, "344777777777 /
C
C     MACHINE CONSTANTS FOR THE PDP-10 (KI PROCESSOR).
C
C     DATA MCHEPS(1),MCHEPS(2) / "104400000000, "000000000000 /
C     DATA MINMAG(1),MINMAG(2) / "000400000000, "000000000000 /
```

```
C     DATA MAXMAG(1),MAXMAG(2) / "377777777777, "377777777777 /
C
C     MACHINE CONSTANTS FOR THE PDP-11 FORTRAN SUPPORTING
C     32-BIT INTEGERS (EXPRESSED IN INTEGER AND OCTAL).
C
C     DATA MCHEPS(1),MCHEPS(2) /  620756992,          0 /
C     DATA MINMAG(1),MINMAG(2) /    8388608,          0 /
C     DATA MAXMAG(1),MAXMAG(2) / 2147483647,         -1 /
C
C     DATA MCHEPS(1),MCHEPS(2) / 004500000000, 000000000000 /
C     DATA MINMAG(1),MINMAG(2) / 000040000000, 000000000000 /
C     DATA MAXMAG(1),MAXMAG(2) / 017777777777, 037777777777 /
C
C     MACHINE CONSTANTS FOR THE PDP-11 FORTRAN SUPPORTING
C     16-BIT INTEGERS (EXPRESSED IN INTEGER AND OCTAL).
C
C     DATA MCHEPS(1),MCHEPS(2) /   9472,      0 /
C     DATA MCHEPS(3),MCHEPS(4) /      0,      0 /
C
C     DATA MINMAG(1),MINMAG(2) /    128,      0 /
C     DATA MINMAG(3),MINMAG(4) /      0,      0 /
C
C     DATA MAXMAG(1),MAXMAG(2) /  32767,     -1 /
C     DATA MAXMAG(3),MAXMAG(4) /     -1,     -1 /
C
C     DATA MCHEPS(1),MCHEPS(2) / 0022400, 0000000 /
C     DATA MCHEPS(3),MCHEPS(4) / 0000000, 0000000 /
C
C     DATA MINMAG(1),MINMAG(2) / 0000200, 0000000 /
C     DATA MINMAG(3),MINMAG(4) / 0000000, 0000000 /
C
C     DATA MAXMAG(1),MAXMAG(2) / 0077777, 0177777 /
C     DATA MAXMAG(3),MAXMAG(4) / 0177777, 0177777 /
C
C     MACHINE CONSTANTS FOR THE UNIVAC 1100 SERIES.
C
C     DATA MCHEPS(1),MCHEPS(2) / 0170640000000, 0000000000000 /
C     DATA MINMAG(1),MINMAG(2) / 0000040000000, 0000000000000 /
C     DATA MAXMAG(1),MAXMAG(2) / 0377777777777, 0777777777777 /
C
C     MACHINE CONSTANTS FOR THE VAX 11/780
C     (EXPRESSED IN INTEGER AND HEXADECIMAL)
C
```

```
C     DATA MCHEPS(1), MCHEPS(2) /      9472,         0 /
C     DATA MINMAG(1), MINMAG(2) /       128,         0 /
C     DATA MAXMAG(1), MAXMAG(2) /    -32769,        -1 /
C
C     DATA MCHEPS(1), MCHEPS(2) / Z00002500, Z00000000 /
C     DATA MINMAG(1), MINMAG(2) / Z00000080, Z00000000 /
C     DATA MAXMAG(1), MAXMAG(2) / ZFFFF7FFF, ZFFFFFFFF /
C
      DPMPAR = DMACH(I)
      RETURN
C
C     LAST CARD OF FUNCTION DPMPAR.
C
      END
```

This is the end of the routine to maximize accuracy of computation by recognizing the largest and smallest positive numbers represented on the computer.

6 EVEC or Electric Vector Determination Subroutine

This subroutine determines ERAD, ETHETA, and EPHI, which are the radial, colatitudinal or azimuthal components of the electric vector at any prescribed point inside or outside the sphere.

```
      SUBROUTINE EVEC(NP, PD)
* COMPUTE THE RADIAL, COLATITUDE, AND AZIMUTHAL COMPONENTS OF ELECTRIC
* FIELD VECTOR FOR REGION P.
      IMPLICIT REAL*8 (A-H, O-Z)
      COMPLEX*16 CZERO,T,T1,PROD
c
c     COMPLEX*16
c    1            ERAD, ETHETA,
c    2           EPHI, T, T1, PROD
c     COMMON /COEFF/ANP, BNP, ALPNP, BETNP
c     COMMON FKP, BJNP, BHNP, CEX, BDP, P, DP, SIGP, EO, TIME, R,
c    1       THETA, PHI, STOPR, NC, NORG, NMIN
      INCLUDE 'CSMCOM.f'
c     DIMENSION BDP(9), SIGP(9), P(101), DP(500)
c     COMPLEX*16 FKP(10), CEX, ANP(1000), BNP(1000), ALPNP(1000),
c    1           BETNP(1000), BJNP(500), BHNP(500), ERAD, ETHETA,
c    2           EPHI, T, T1, PROD
```

```
      CZERO = DCMPLX(0.D0,0.D0)
      ERAD=DCMPLX(0.D0, 0.D0)
      ETHETA=DCMPLX(0.D0, 0.D0)
      EPHI=DCMPLX(0.D0, 0.D0)
      NCK=0
      NN=(NP-1)*NMIN
      DO 40 N=1,NC
 FAC1=2.D0*N+1.D0
 FAC2=N*(N+1.D0)
 RATIO=FAC1/FAC2
 T=FAC1*P(N)*(BNP(NN+N)*BJNP(N+1)+BETNP(NN+N)*BHNP(N+1))
c       IF (N.LT.11) THEN
c         WRITE(6,456) N, RATIO, T
c456       FORMAT(' N = ',I3,'  RATIO = ',E14.7,3X,'T = (',E14.7,
c    1    ',',E14.7,')')
c        ENDIF
 NCK=NCK+1
 CALL TERM(NCK, T, 1)
 ERAD=ERAD+T
 T=ANP(NN+N)*BJNP(N+1)+ALPNP(NN+N)*BHNP(N+1)
 CALL TERM(NCK, T, 0)
 T1=BNP(NN+N)*((N+1.D0)*BJNP(N)-N*BJNP(N+2))/FAC1+BETNP(NN+N)*
     1     ((N+1.D0)*BHNP(N)-N*BHNP(N+2))/FAC1
 CALL TERM(NCK, T1, 1)
 IF ((THETA.GE.1.D-6).AND.(THETA.LT.3.141592D0)) GOTO 20
 IF (THETA.GE.3.141592D0) GOTO 10
 ETHETA=ETHETA+FAC1/2.D0*T-RATIO*DP(N)*T1
 EPHI=EPHI-RATIO*DP(N)*T+FAC1/2.D0*T1
 GOTO 30
   10   ETHETA=ETHETA+(-1.D0)**(N+1)*FAC1/2.D0*T-RATIO*DP(N)*T1
 EPHI=EPHI-RATIO*DP(N)*T+(-1.D0)**(N+1)*FAC1/2.D0*T1
 GOTO 30
   20   ETHETA=ETHETA+RATIO*P(N)/SIN(THETA)*T-RATIO*DP(N)*T1
 EPHI=EPHI-RATIO*DP(N)*T+RATIO*P(N)/SIN(THETA)*T1
   30   IF(NCK.EQ.4)NCK=0
   40 CONTINUE
      PROD=E0*CEX
      ERAD=-PROD*COS(PHI)/(FKP(NP)*R)*ERAD
      ETHETA=PROD*COS(PHI)*ETHETA
      EPHI=PROD*SIN(PHI)*EPHI
      PD= REAL(ERAD*DCONJG(ERAD))+ REAL(ETHETA*DCONJG(ETHETA))+
     1   REAL(EPHI*DCONJG(EPHI))
      pd=sigp(np)*pd
```

```
      RETURN
      END
```

This assumes that the electric vector of the incoming radiation is polarized along the x axis.

7 EVCSC for Scattered Radiation

This subroutine determines the electric vector of the scattered radiation at any point outside the sphere.

```
      SUBROUTINE EVCSC(NP, PD)
* COMPUTE THE RADIAL, COLATITUDE, AND AZIMUTHAL COMPONENTS OF ELECTRIC
* FIELD VECTOR FOR REGION P.
      IMPLICIT REAL*8 (A-H, O-Z)
      COMPLEX*16 CZERO,T,T1,PROD
      INCLUDE 'CSMCOM.f'
c*************************************************************
c     COMPLEX*16
c    1            ERAD, ETHETA,
c    2           EPHI, T, T1, PROD
c     COMMON /COEFF/ANP, BNP, ALPNP, BETNP
c     COMMON FKP, BJNP, BHNP, CEX, BDP, P, DP, SIGP, E0, TIME, R,
c    1       THETA, PHI, STOPR, NC, NORG, NMIN
c     DIMENSION BDP(9), SIGP(9), P(101), DP(500)
c     COMPLEX*16 FKP(10), CEX, ANP(1000), BNP(1000), ALPNP(1000),
c    1           BETNP(1000), BJNP(500), BHNP(500), ERAD, ETHETA,
c    2           EPHI, T, T1, PROD
c**************************************************************
      CZERO = DCMPLX(0.D0,0.D0)
      ERADSC=DCMPLX(0.D0, 0.D0)
      ETHESC=DCMPLX(0.D0, 0.D0)
      EPHISC=DCMPLX(0.D0, 0.D0)
      NCK=0
      NN=(NP-1)*NMIN
      DO 40 N=1,NC
 FAC1=2.D0*N+1.D0
 FAC2=N*(N+1.D0)
 RATIO=FAC1/FAC2
c       T=FAC1*P(N)*(BNP(NN+N)*BJNP(N+1)+BETNP(NN+N)*BHNP(N+1))
 T=FAC1*P(N)*(BETNP(NN+N)*BHNP(N+1))
c       IF (N.LT.11) THEN
c         WRITE(6,456) N, RATIO, T
```

```
c456        FORMAT(' N = ',I3,'  RATIO = ',E14.7,3X,'T = (',E14.7,
c    1     ',',E14.7,')')
c         ENDIF
 NCK=NCK+1
 CALL TERM(NCK, T, 1)
 ERADSC=ERADSC+T
c        T=ANP(NN+N)*BJNP(N+1)+ALPNP(NN+N)*BHNP(N+1)
 T=ALPNP(NN+N)*BHNP(N+1)
 CALL TERM(NCK, T, 0)
c        T1=BNP(NN+N)*((N+1.D0)*BJNP(N)-N*BJNP(N+2))/FAC1+BETNP(NN+N)*
c    1      ((N+1.D0)*BHNP(N)-N*BHNP(N+2))/FAC1
 T1=BETNP(NN+N)*
     1      ((N+1.D0)*BHNP(N)-N*BHNP(N+2))/FAC1
 CALL TERM(NCK, T1, 1)
 IF ((THETA.GE.1.D-6).AND.(THETA.LT.3.141592D0)) GOTO 20
 IF (THETA.GE.3.141592D0) GOTO 10
 ETHESC=ETHESC+FAC1/2.D0*T-RATIO*DP(N)*T1
 EPHISC=EPHISC-RATIO*DP(N)*T+FAC1/2.D0*T1
 GOTO 30
   10   ETHESC=ETHESC+(-1.D0)**(N+1)*FAC1/2.D0*T-RATIO*DP(N)*T1
 EPHISC=EPHISC-RATIO*DP(N)*T+(-1.D0)**(N+1)*FAC1/2.D0*T1
 GOTO 30
   20   ETHESC=ETHESC+RATIO*P(N)/SIN(THETA)*T-RATIO*DP(N)*T1
 EPHISC=EPHISC-RATIO*DP(N)*T+RATIO*P(N)/SIN(THETA)*T1
   30   IF(NCK.EQ.4)NCK=0
c       TERM computes either I**N or I*I**N and this permits
c   us to achieve more rapid computation with a computed GOTO
c   rather than by using an extra multiplication; an alternative
c   would have been to replace NCK by   NCK mod 4.
   40 CONTINUE
      PROD=E0*CEX
      ERADSC=-PROD*DCOS(PHI)/(FKP(NP)*R)*ERADSC
      IF(IPESIN.EQ.1234) THEN
 WRITE(*,*)NORG,' = NORG'
 WRITE(*,*)NMIN,' = NMIN'
 WRITE(*,*)NORG*NMIN+2,' = NORG*NMIN+2'
 WRITE(*,*)NVAL,' = NVAL'
 WRITE(*,*) BHNP(NVAL+1),' = BHNP(NVAL+1)'
 WRITE(*,*) PROD,' = PROD in EVCSC.f'
 WRITE(*,*) FKP(NP)*R,' = FKP(NP)*R'
 WRITE(*,*) NP,' = NP'
 IPESIN = 0
      ENDIF
```

```
      ETHESC=PROD*DCOS(PHI)*ETHESC
      EPHISC=PROD*DSIN(PHI)*EPHISC
      PD= REAL(ERADSC*DCONJG(ERADSC))+ REAL(ETHESC*DCONJG(ETHESC))+
     1   REAL(EPHISC*DCONJG(EPHISC))
      RETURN
      END
```

8 EVCINC for the electric vector of the incoming radiation

This subroutine gives a spherical harmonic representation of the electric vector of the incoming radiation. It is important to make sure that the incoming radiation is accurately represented by the spherical harmonic expansion. If this is not true, then everything else could match up and you could still be getting incorrect values of the solution. This comparison is printed out.

```
      SUBROUTINE EVCINC(NP, PD,ERADIN,ETHEIN,EPHIIN)
* COMPUTE THE RADIAL, COLATITUDE, AND AZIMUTHAL COMPONENTS OF ELECTRIC
* FIELD VECTOR FOR REGION P.
      IMPLICIT REAL*8 (A-H, O-Z)
      COMPLEX*16 CZERO,T,T1,PROD,ERADIN,ETHEIN,EPHIIN
c
c     COMPLEX*16
c    1            ERADIN, ETHEIN,
c    2           EPHI, T, T1, PROD
c     COMMON /COEFF/ANP, BNP, ALPNP, BETNP
c     COMMON FKP, BJNP, BHNP, CEX, BDP, P, DP, SIGP, EO, TIME, R,
c    1       THETA, PHI, STOPR, NC, NORG, NMIN
      INCLUDE 'CSMCOM.f'
c     DIMENSION BDP(9), SIGP(9), P(101), DP(500)
c     COMPLEX*16 FKP(10), CEX, ANP(1000), BNP(1000), ALPNP(1000),
c    1           BETNP(1000), BJNP(500), BHNP(500), ERAD, ETHETA,
c    2           EPHI, T, T1, PROD
      CZERO = DCMPLX(0.DO,0.DO)
      WRITE(*,*)CZERO,' = CZERO'
      ERADIN=CZERO
      ETHEIN=CZERO
      EPHIIN=CZERO
      NCK=0
      NN=(NP-1)*NMIN
      DO 40 N=1,NC
 FAC1=2.DO*N+1.DO
```

```
 FAC2=N*(N+1.D0)
 RATIO=FAC1/FAC2
 T=FAC1*P(N)*(BNP(NN+N)*BJNP(N+1) )
c       IF (N.LT.11) THEN
c         WRITE(6,456) N, RATIO, T
c456       FORMAT(' N = ',I3,'  RATIO = ',E14.7,3X,'T = (',E14.7,
c    1    ',',E14.7,')')
c        ENDIF
 NCK=NCK+1
 CALL TERM(NCK, T, 1)
 ERADIN=ERADIN+T
 T=ANP(NN+N)*BJNP(N+1)
 CALL TERM(NCK, T, 0)
 T1=BNP(NN+N)*((N+1.D0)*BJNP(N)-N*BJNP(N+2))/FAC1
 CALL TERM(NCK, T1, 1)
 IF ((THETA.GE.1.D-6).AND.(THETA.LT.3.141592D0)) GOTO 20
 IF (THETA.GE.3.141592D0) GOTO 10
 ETHEIN=ETHEIN+FAC1/2.D0*T-RATIO*DP(N)*T1
 EPHIIN=EPHIIN-RATIO*DP(N)*T+FAC1/2.D0*T1
 GOTO 30
   10   ETHEIN=ETHEIN+(-1.D0)**(N+1)*FAC1/2.D0*T-RATIO*DP(N)*T1
 EPHIIN=EPHIIN-RATIO*DP(N)*T+(-1.D0)**(N+1)*FAC1/2.D0*T1
 GOTO 30
   20   ETHEIN=ETHEIN+RATIO*P(N)/SIN(THETA)*T-RATIO*DP(N)*T1
 EPHIIN=EPHIIN-RATIO*DP(N)*T+RATIO*P(N)/SIN(THETA)*T1
   30   IF(NCK.EQ.4)NCK=0
   40 CONTINUE
      PROD=E0*CEX
      ERADIN=-PROD*COS(PHI)/(FKP(NP)*R)*ERADIN
      ETHEIN=PROD*COS(PHI)*ETHEIN
      EPHIIN=PROD*SIN(PHI)*EPHIIN
      PD= REAL(ERADIN*DCONJG(ERADIN))+
     1   REAL(ETHEIN*DCONJG(ETHEIN))+
     1   REAL(EPHIIN*DCONJG(EPHIIN))
      RETURN
      END
      SUBROUTINE TERM(NCK,T,KEY)
* COMPUTE I**NCK*(NTH TERM IN SERIES)
      IMPLICIT REAL*8 (A-H, O-Z)
      COMPLEX*16 T
      IF (KEY.EQ.1) GOTO 20
      GOTO (5, 10, 15, 45), NCK
   20 GOTO (10, 15, 45, 5), NCK
```

```
    5 T=DCMPLX(-DIMAG(T), REAL(T))
      GOTO 45
   10 T=-T
      GOTO 45
   15 T=DCMPLX(DIMAG(T), - REAL(T))
   45 RETURN
      END
```

This is the end of the subroutine to represent the electric vector of the incoming plane wave in terms of vector spherical harmonics.

9 EVSPHD helps compute Mueller matrix entries

This subroutine will help us compute the amplitude scattering matrix.

```
      SUBROUTINE EVSPHD(NP, PD,DETHES,DEPHIS)
* COMPUTE THE RADIAL, COLATITUDE, AND AZIMUTHAL COMPONENTS OF ELECTRIC
* FIELD VECTOR FOR REGION P.
      IMPLICIT REAL*8 (A-H, O-Z)
      COMPLEX*16 CZERO,T,T1,PROD,DETHES,DEPHIS
c
c     COMPLEX*16
c    1            ERAD, ETHETA,
c    2           EPHI, T, T1, PROD
c     COMMON /COEFF/ANP, BNP, ALPNP, BETNP
c     COMMON FKP, BJNP, BHNP, CEX, BDP, P, DP, SIGP, EO, TIME, R,
c    1       THETA, PHI, STOPR, NC, NORG, NMIN
      INCLUDE 'CSMCOM.f'
c     DIMENSION BDP(9), SIGP(9), P(101), DP(500)
c     COMPLEX*16 FKP(10), CEX, ANP(1000), BNP(1000), ALPNP(1000),
c    1           BETNP(1000), BJNP(500), BHNP(500), ERAD, ETHETA,
c    2           EPHI, T, T1, PROD
      CZERO = DCMPLX(0.D0,0.D0)
      ERADSC=DCMPLX(0.D0, 0.D0)
      ETHESC=DCMPLX(0.D0, 0.D0)
      EPHISC=DCMPLX(0.D0, 0.D0)
      NCK=0
      NN=(NP-1)*NMIN
      DO 40 N=1,NC
 FAC1=2.D0*N+1.D0
 FAC2=N*(N+1.D0)
 RATIO=FAC1/FAC2
c       T=FAC1*P(N)*(BNP(NN+N)*BJNP(N+1)+BETNP(NN+N)*BHNP(N+1))
```

```
 T=FAC1*P(N)*(BETNP(NN+N)*BHNP(N+1))
c       IF (N.LT.11) THEN
c         WRITE(6,456) N, RATIO, T
c456       FORMAT(' N = ',I3,'  RATIO = ',E14.7,3X,'T = (',E14.7,
c    1     ',',E14.7,')')
c        ENDIF
 NCK=NCK+1
 CALL TERM(NCK, T, 1)
 ERADSC=ERADSC+T
c       T=ANP(NN+N)*BJNP(N+1)+ALPNP(NN+N)*BHNP(N+1)
 T=ALPNP(NN+N)*BHNP(N+1)
 CALL TERM(NCK, T, 0)
c       T1=BNP(NN+N)*((N+1.DO)*BJNP(N)-N*BJNP(N+2))/FAC1+BETNP(NN+N)*
c    1     ((N+1.DO)*BHNP(N)-N*BHNP(N+2))/FAC1
 T1=BETNP(NN+N)*
     1     ((N+1.DO)*BHNP(N)-N*BHNP(N+2))/FAC1
 CALL TERM(NCK, T1, 1)
 IF ((THETA.GE.1.D-6).AND.(THETA.LT.3.141592DO)) GOTO 20
 IF (THETA.GE.3.141592DO) GOTO 10
 ETHESC=ETHESC+FAC1/2.DO*T-RATIO*DP(N)*T1
 EPHISC=EPHISC-RATIO*DP(N)*T+FAC1/2.DO*T1
 GOTO 30
   10   ETHESC=ETHESC+(-1.DO)**(N+1)*FAC1/2.DO*T-RATIO*DP(N)*T1
 EPHISC=EPHISC-RATIO*DP(N)*T+(-1.DO)**(N+1)*FAC1/2.DO*T1
 GOTO 30
   20   ETHESC=ETHESC+RATIO*P(N)/SIN(THETA)*T-RATIO*DP(N)*T1
 EPHISC=EPHISC-RATIO*DP(N)*T+RATIO*P(N)/SIN(THETA)*T1
   30   IF(NCK.EQ.4)NCK=0
c       This effectively gives us    NCK  MOD 4 for input
c   into TERM.
c
   40 CONTINUE
      PROD=EO*CEX
      ERADSC=-PROD*COS(PHI)/(FKP(NP)*R)*ERADSC
      DETHES=PROD*(-SIN(PHI))*ETHESC
      ETHESC=PROD*COS(PHI)*ETHESC
      DEPHIS = PROD*COS(PHI)*EPHISC
      EPHISC=PROD*SIN(PHI)*EPHISC
      PD= REAL(ERADSC*DCONJG(ERADSC))+ REAL(ETHESC*DCONJG(ETHESC))+
     1   REAL(EPHISC*DCONJG(EPHISC))
      RETURN
      END
```

We compute here the square PD of the length of the lectric vecto. . scattered radiation

and the radial, theta, and phi components of the scattered radiation.

10 ENORM

This determines a vector norm used in solving the inverse problem.

```
      FUNCTION ENORM(N,X)
c     REAL FUNCTION ENORM(N,X)
      INTEGER N
      REAL*8 X(N), ENORM
C     **********
C
C     FUNCTION ENORM
C
C     GIVEN AN N-VECTOR X, THIS FUNCTION CALCULATES THE
C     EUCLIDEAN NORM OF X.
C
C     THE EUCLIDEAN NORM IS COMPUTED BY ACCUMULATING THE SUM OF
C     SQUARES IN THREE DIFFERENT SUMS. THE SUMS OF SQUARES FOR THE
C     SMALL AND LARGE COMPONENTS ARE SCALED SO THAT NO OVERFLOWS
C     OCCUR. NON-DESTRUCTIVE UNDERFLOWS ARE PERMITTED. UNDERFLOWS
C     AND OVERFLOWS DO NOT OCCUR IN THE COMPUTATION OF THE UNSCALED
C     SUM OF SQUARES FOR THE INTERMEDIATE COMPONENTS.
C     THE DEFINITIONS OF SMALL, INTERMEDIATE AND LARGE COMPONENTS
C     DEPEND ON TWO CONSTANTS, RDWARF AND RGIANT. THE MAIN
C     RESTRICTIONS ON THESE CONSTANTS ARE THAT RDWARF**2 NOT
C     UNDERFLOW AND RGIANT**2 NOT OVERFLOW. THE CONSTANTS
C     GIVEN HERE ARE SUITABLE FOR EVERY KNOWN COMPUTER.
C
C     THE FUNCTION STATEMENT IS
C
C       REAL FUNCTION ENORM(N,X)
C
C     WHERE
C
C       N IS A POSITIVE INTEGER INPUT VARIABLE.
C
C       X IS AN INPUT ARRAY OF LENGTH N.
C
C     SUBPROGRAMS CALLED
C
C       FORTRAN-SUPPLIED ... ABS,SQRT
```

```
C
C     ARGONNE NATIONAL LABORATORY. MINPACK PROJECT. MARCH 1980.
C     BURTON S. GARBOW, KENNETH E. HILLSTROM, JORGE J. MORE
C
C     **********
      INTEGER I
      REAL AGIANT,FLOATN,ONE,RDWARF,RGIANT,S1,S2,S3,XABS,X1MAX,X3MAX,
     *     ZERO
      DATA ONE,ZERO,RDWARF,RGIANT /1.0E0,0.0E0,3.834E-20,1.304E19/
      S1 = ZERO
      S2 = ZERO
      S3 = ZERO
      X1MAX = ZERO
      X3MAX = ZERO
      FLOATN = N
      AGIANT = RGIANT/FLOATN
      DO 90 I = 1, N
  XABS = ABS(X(I))
  IF (XABS .GT. RDWARF .AND. XABS .LT. AGIANT) GO TO 70
     IF (XABS .LE. RDWARF) GO TO 30
C
C              SUM FOR LARGE COMPONENTS.
C
        IF (XABS .LE. X1MAX) GO TO 10
    S1 = ONE + S1*(X1MAX/XABS)**2
    X1MAX = XABS
    GO TO 20
   10          CONTINUE
    S1 = S1 + (XABS/X1MAX)**2
   20          CONTINUE
        GO TO 60
   30       CONTINUE
C
C              SUM FOR SMALL COMPONENTS.
C
        IF (XABS .LE. X3MAX) GO TO 40
    S3 = ONE + S3*(X3MAX/XABS)**2
    X3MAX = XABS
    GO TO 50
   40          CONTINUE
    IF (XABS .NE. ZERO) S3 = S3 + (XABS/X3MAX)**2
   50          CONTINUE
   60       CONTINUE
```

```
      GO TO 80
   70    CONTINUE
C
C           SUM FOR INTERMEDIATE COMPONENTS.
C
      S2 = S2 + XABS**2
   80    CONTINUE
   90    CONTINUE
C
C     CALCULATION OF NORM.
C
      IF (S1 .EQ. ZERO) GO TO 100
  ENORM = X1MAX*SQRT(S1+(S2/X1MAX)/X1MAX)
  GO TO 130
  100 CONTINUE
  IF (S2 .EQ. ZERO) GO TO 110
     IF (S2 .GE. X3MAX)
     *         ENORM = SQRT(S2*(ONE+(X3MAX/S2)*(X3MAX*S3)))
     IF (S2 .LT. X3MAX)
     *         ENORM = SQRT(X3MAX*((S2/X3MAX)+(X3MAX*S3)))
     GO TO 120
  110    CONTINUE
     ENORM = X3MAX*SQRT(S3)
  120    CONTINUE
  130 CONTINUE
      RETURN
C
C     LAST CARD OF FUNCTION ENORM.
C
      END
```

This is the end of the matrix norm computation.

11 Mueller and amplitude scattering matrix entry determination

This uses the amplitude scattering matrix entries S_1 and S_2 for the Mie solution to compute the Mueller matrix entries.

```
      SUBROUTINE MUEMTX(I,S1,S2,S11,S21,S33,S34,S43)
C                                                                       *
C  SUBROUTINE MUEMTX  uses amplitude scattering                         *
```

```
C                                                                       *
C  CALCULATE AND RETURN    MUELLER MATRIX ENTRIES FOR SPHERE SCATTER *
C         THE THETA ANGLES GO FROM -180 TO 180 DEGREES.                 *
C           PHI ANGLES ARE 0 AND 90 DEGREES                             *
c   FILES 0-M11.DAT, 0-M12.DAT, 0-M33.DAT, 0-M34.DAT, 0-M43.DAT
c
      IMPLICIT REAL*8 (A-H, O-Z)
      COMPLEX*16 S1,S2
c   These must appear in the calling program
c     OPEN(70,FILE='0-M11.DAT')
c     OPEN(71,FILE='0-M12.DAT')
c     OPEN(74,FILE='0-M33.DAT')
c     OPEN(75,FILE='0-M34.DAT')
c     OPEN(77,FILE='0-M43.DAT')
c     REWIND(70)
c     REWIND(71)
c     REWIND(72)
c     REWIND(74)
c     REWIND(75)
c     REWIND(77)
  S11 = .5D0*(ABS(S1)**2 + ABS(S2)**2)
  S12 = .5D0*(ABS(S2)**2 - ABS(S1)**2)
  S21 = .5D0*(ABS(S2)**2 - ABS(S1)**2)
  S22 = S11
  S33 = REAL(S1*CONJG(S2))
  S34 = DIMAG(S2*CONJG(S1))
  S43 = DIMAG(S1*CONJG(S2))
  S44 = REAL(S1*CONJG(S2))
  WRITE(70,*)I,S11
  WRITE(71,*)I,S12/S11
  WRITE(74,*)I,S33/S11
  WRITE(75,*)I,S34/S11
  WRITE(77,*)I,S43/S11
c     These must appear after we have completed all printing
c  in the calling program
c     CLOSE(UNIT=70)
c     CLOSE(UNIT=71)
c     CLOSE(UNIT=74)
c     CLOSE(UNIT=75)
c     CLOSE(UNIT=77)
c
      RETURN
      END
```

The entries of the 4 by 4 Mueller matrix normalized by the (1,1) entry are computed by this routine.

12 MMEVEI

This calls PL and EVSPHD and computes the amplitude scattering matrix entries that are used by the previous subroutine.

```
      SUBROUTINE MMEVEI(PHID,IFARMU,R2MU)
      IMPLICIT REAL*8(A-H,O-Z)
      COMPLEX*16 ZBFA,DETHES,DEPHIS,EINOLD,
     1 EINPAR,EIPERP,DEIPAR,DEINPE,CI,S1,S2
      INCLUDE 'CSMCOM.f'
      DATA PI/3.14159265358979323D0/
      CI = (0.D0,1.D0)
      OPEN(82,FILE='OMUEL90.DAT')
      OPEN(84,FILE='OMUEL0.DAT')
      REWIND(82)
      REWIND(84)
      RADPD = PI/180.D0
      IF(R2MU.GT.1.D2*BDP(NORG)) THEN
  WRITE(*,*)R2MU,' = R2MU is too large'
  WRITE(*,*)' Stopping program'
  STOP
      ENDIF
      IF(IFARMU.EQ.1) THEN
       ZBFA = FKP(NORG+1)*R2MU
       CALL BJYH(BJNP,BHNP,ZBFA,NC,STOPR,NORG+1)
       IF(NC.GT.NMIN) THEN
  NC = NMIN-2
       ELSE
  NC = NC-2
       ENDIF
c      ZBFA is the complex Bessel Function Argument
c      We call the Bessel functions with this argument
       DO 101 JJ = 1,2
       IF(JJ.EQ.1) THEN
  PHI = 0.D0
  COSPHI = 1.D0
  SINPHI = 0.D0
       ENDIF
       IF(JJ.EQ.2) THEN
```

```
  PHI = PI/2.D0
  COSPHI = 0.D0
  SINPHI = 1.D0
       ENDIF
       DO 100 I = 0,180
       THETAD = FLOAT(I)
       IF(I.EQ.0) THEN
  THETAD = .0001D0
       ENDIF
       IF(I.EQ.180) THEN
  THETAD = 179.999
       ENDIF
       THETA = THETAD*RADPD
       EINOLD = E0*EXP(CI*FKP(NORG+1)*R2MU*COS(THETA))
       EINPAR = EINOLD*COS(PHI)
       EIPERP = EINOLD*SIN(PHI)
       DEIPAR = - EINOLD*SIN(PHI)
       DEINPE = EINOLD*COS(PHI)
       CALL PL(THETA,NC,P,DP)
       CALL EVSPHD(NORG+1,PD,DETHES,DEPHIS)
       IF(JJ.EQ.1) THEN
    S1 = DEPHIS/DEINPE
    S2 = ETHESC/EINPAR
    WRITE(82,*)S1,S2
    CALL MUEMTX(I,S1,S2,S11,S21,S33,S34,S43)
c          This call will cause the Mueller matrix elements to be
c        deposited into files.
       ENDIF
       IF(JJ.EQ.2) THEN
    S1 = EPHISC/EIPERP
    S2 = DETHES/DEIPAR
    WRITE(84,*)S1,S2
       ENDIF
c
  100  CONTINUE
  101  CONTINUE
      ENDIF
      IF(IFARMU.NE.1) THEN
       WRITE(*,*)IFARMU,' = IFARMU is wrong value'
       WRITE(*,*)' Stopping program in MMEVEI'
       STOP
      ENDIF
       CLOSE(UNIT=82)
```

```
      CLOSE(UNIT=84)
      RETURN
      END
```

13 BTERAD inversion by the scattered radiations radial component

The FUNCTION BTERAD uses the radial component of the electric vector of the scattered radiation to determine the β expansion coefficients of the scattered radiation. This routine calls PL and EVCSC.

```
      FUNCTION BTERAD(THETAQ,PHIQ)
      IMPLICIT DOUBLE PRECISION(A-H,O-Z)
      COMPLEX*16 CI,ALERAD,TERM,BTERAD
c     We are using the radial component of the scattered
c  radiation to get the expansion coefficient beta
      INCLUDE 'CSMCOM.f'
      DATA PI/3.14159265358979323D0/
      CI = DCMPLX(0.D0,1.D0)
c     PI = 3.14159265358979323D0
      THETA = THETAQ
      PHI = PHIQ
      CALL PL(THETA,NC,P,DP)
      CALL EVCSC(NORG+1,PD)
      ALERAD = ERADSC*P(NVAL)*DCOS(PHI)
      ALERAD =  FKP(NORG+1)*R*ALERAD/
     1 ((NVAL*(NVAL+1))*(-CEX*E0)*2.D0*PI*(CI**(NVAL+1))*BHNP(NVAL+1))
      IF(IPRDIA.EQ.1234) THEN
 WRITE(*,*)E0*CEX,' = E0*CEX'
 WRITE(*,*)CI**(NVAL+1),' = CI**(NVAL+1)'
 WRITE(*,*)R,' = R'
 WRITE(*,*)BHNP(NVAL+1),' = BHNP(NVAL+1) in BTERAD'
 WRITE(*,*)FKP(NORG+1),' = FKP(NORG+1) in BTERAD'
 TERM = -(CEX*E0/(FKP(NORG+1)*R))*CI**(NVAL+1)*BHNP(NVAL+1)
 WRITE(*,*)TERM,' = '
 WRITE(*,*)' -(CEX*E0/(FKP(NORG+1)*R))*(CI**(NVAL+1)*BHNP)'
 WRITE(*,*)NVAL,' = NVAL'
 IPRDIA = 11
      ENDIF
      BTERAD = ALERAD
      RETURN
      END
```

14 PROPGF – propagation constants in all layers

The subroutine PROPGF determines, as the search is carried out for the sphere which gave the scattered radiation data, the propagation constants FKPF in each of the layers of the sphere that was hypothesized to have caused this scattered radiation. If the permittivity is ϵ, the conductivity is σ, the permeability is μ, and the frequency is ω, then the square of the propagation constant k for an isotropic medium is

$$k^2 = \omega^2\mu\epsilon - i\omega\mu\sigma$$

```
      SUBROUTINE PROPGF
      IMPLICIT REAL*8(A-H,O-Z)
      INCLUDE 'CSMCOM.f'
      VEL = VELOCI
c23456789101112
      FAC1 = OMEGA/VELOCI
      DO 37 I = 1,NORGF
      FAC2 = EPSPF(I)/2.DO
      FAC3 = SQRT( 1.DO +
     1 (1.DO/(EPSO*OMEGA)**2)*(SIGPF(I)/EPSPF(I))**2  )
      REKP = FAC1*SQRT(FAC2*(FAC3+1.DO))
      FIMKP=FAC1*SQRT(FAC2*(FAC3 - 1.DO))
      FKPF(I) = DCMPLX(REKP,FIMKP)
   37 CONTINUE
      NORGP1 = NORGF + 1
c
      FKPF(NORGP1)=DCMPLX(FAC1,0.DO)
      RETURN
      END
```

15 Bessel function subroutine BJYH

The Bessel function routine BJYH creates arrays BJNP and BHNP of Bessel function values at argument Z.

```
      SUBROUTINE BJYH(BJNP, BHNP, Z, N, STOPR)
c COMPUTE SPHERICAL BESSEL FUNCTIONS
      IMPLICIT REAL*8 (A-H, O-Z)
      COMPLEX*16 BJNP(500),BHNP(500),Z,ZT1,T1,ZSQ,TDZ,
     1     XNU, A1, DEN, F, CF, F1, Q
c     The complex variable QP was removed
c   The complex array BYNP(500) was removed
```

```
      NBF=499
      BJNP(1)= SIN(Z)/Z
      BJNP(2)=(BJNP(1)-COS(Z))/Z
      ZT1=DCMPLX(-DIMAG(Z),  REAL(Z))
      T1=EXP(ZT1)/Z
      T1=DCMPLX(DIMAG(T1),- REAL(T1))
      BHNP(1)=T1
      BHNP(2)=DCMPLX(DIMAG(T1),- REAL(T1))*(1.D0-1.D0/ZT1)
      ZSQ=Z*Z
      TDZ=2.D0/Z
      X=1.D0/STOPR
      DO 15 N=3, NBF
XNPH=DFLOAT(N)-.5D0
XNU=-(XNPH+1.D0)*TDZ
A1=XNPH*TDZ
DEN=XNU+1.D0/A1
F=XNU/(DEN*A1)
CF=-TDZ
DO 5 I=2,200
  CF=-CF
  A1=CF*(XNPH+I)
  XNU=A1+1.D0/XNU
  DEN=A1+1.D0/DEN
  F1=XNU/DEN
  F=F*F1
  IF (ABS(ABS(F1)-1.D0).LT.1.D-14) GOTO 10
   5   CONTINUE
  10   BJNP(N)=F*BJNP(N-1)
Q=1.D0/(ZSQ*BJNP(N-1))
BHNP(N)=F*BHNP(N-1)-DCMPLX(-DIMAG(Q),  REAL(Q))
IF (ABS(BJNP(N)).LT.X.OR.ABS(BHNP(N)).GT.STOPR) GOTO 20
  15 CONTINUE
      IF(IPRDIA.EQ.2) THEN
 WRITE(*,*)BHNP(3),' = BHNP(3)'
      ENDIF
      N =N-1
  20 IF (N.LT.5) WRITE (6,25) N,Z
  25 FORMAT(25X,'ONLY',I3,' BESSEL FUNCTIONS FOR Z =',1X,2D12.4)
      RETURN
      END
```

This program stores values of Bessel functions. The number N of Bessel and Hankel functions actually computed is determined by STOPR.

16 GAUSS – a volume integral of power density

The routine GAUSS integrates the power per unit volume over the volume of the sphere.

```
      FUNCTION GAUSS(LSTART)
* FUNCTION GAUSS(LSTART)    Version 5.4   04/4/91    DKC          *
*                                                                  *
* CALCULATE THE TOTAL POWER ABSORBED BY THE SPHERE BY DOING A      *
* VOLUME INTEGRATION OVER THE SPHERE AND AN AREA INTEGRATION       *
* OVER IMPEDANCE SHEETS.  UTILIZE THE GAUSS QUADRATURE METHOD.     *
*                                                                  *
*   Inputs:                                                        *
*                                                                  *
*      LSTART   INTEGER*4    Starting layer for integration.       *
*                                                                  *
*   Inputs (via COMMONs):                                          *
*                                                                  *
*      NORG     INTEGER*4    Number of layers in sphere.           *
*      EPSP()   COMPLEX*16   Permittivities of the layers.         *
*      XMU()    COMPLEX*16   Permeabilities of the layers.         *
*      SIGP()   COMPLEX*16   Conductivities of the layers.         *
*      BDP()    REAL*8       Boundaries of the layers (meters).    *
*      FKP()    COMPLEX*16   Propagation constants in the layers.  *
*      STOPR    REAL*8       Stop computing Bessel functions       *
*                            when value of last Bessel exceeds     *
*                            STOPR or is less than 1/STOPR.        *
*      EO       REAL*8       Scale factor for incident E field.    *
*      ITYPE()  INTEGER*4    Set to 1 if layer has impedance sheet.*
*                                                                  *
*   Outputs:                                                       *
*                                                                  *
*      GAUSS    REAL*8       Total power absorbed in sphere.       *
*                                                                  *
c     FUNCTION GAUSS(LSTART)
c M-POINT GAUSS-LEGENDRE QUADRATURE
      IMPLICIT COMPLEX*16 (A-H, O-Z)
c  Variables are transferred via the following COMMON
      INCLUDE 'CSMCOM.f'
      COMMON /PRICOM/IPRINT,IENTR
c     PARAMETER (NGAUPT=14) is the max number of GAUSS Q points
c  is defined in CSMCOM.f an array of COMMON variables
      REAL*8 ARG2, ARG3, D, GAUSS, PD2, PI, RH, R1, R2
      REAL*8 SINTH,SUM1,SUM2,SUM3,XMUL1,WT, Y, PD, PM, XMUO
```

```
c     DIMENSION BJNP3(4,2*NZ,7), BHNP3(4,2*NZ,7), NTERM(10,2)
c     DIMENSION BJNP3(NZ,2), BHNP3(NZ,2),
      DIMENSION
     1 BJNPA(NZ,NGAUPT,2),BHNPA(NZ,NGAUPT,2),
     2 NTERM(NLAPLO,2),BJNPO(NZ),BHNPO(NZ)
c234567 where NZ is the number of Bessel function orders and
c where  NGAUPT is the no of points at which the Bessel function
c associated with that order is evaluated
c
      DIMENSION NPOINT(9), KEY(10), Y(33), WT(33), ARG2(2), ARG3(2)
*
      DATA PI/3.141592653589793D0/
      DATA NPOINT/2,3,4,5,6,8,10,12,14/
      DATA KEY/1,2,4,6,9,12,16,21,27,34/
      DATA Y/.57735026918963D0,.00000000000000D0,.77459666924148D0,
     &       .33998104358486D0,.86113631159405D0,.00000000000000D0,
     &       .53846931010568D0,.90617984593866D0,.23861918608320D0,
     &       .66120938646626D0,.93246951420315D0,.18343464249565D0,
     &       .52553240991633D0,.79666647741363D0,.96028985649754D0,
     &       .14887433898163D0,.43339539412925D0,.67940956829902D0,
     &       .86506336668898D0,.97390652851717D0,.12523340851147D0,
     &       .36783149899818D0,.58731795428662D0,.76990267419430D0,
     &       .90411725637047D0,.98156063424672D0,.10805494870734D0,
     &       .31911236892789D0,.51524863635815D0,.68729290481169D0,
     &       .82720131506996D0,.92843488366357D0,.98628380869681D0/
c
      DATA WT/.10000000000000D1,.88888888888889D0,.55555555555556D0,
     &        .65214515486255D0,.34785484513745D0,.56888888888889D0,
     &        .47862867049937D0,.23692688505619D0,.46791393457269D0,
     &        .36076157304814D0,.17132449237917D0,.36268378337836D0,
     &        .31370664587789D0,.22238103445337D0,.10122853629038D0,
     &        .29552422471475D0,.26926671931000D0,.21908636251598D0,
     &        .14945134915058D0,.06667134430869D0,.24914704581340D0,
     &        .23349253653835D0,.20316742672307D0,.16007832854335D0,
     &        .10693932599532D0,.04717533638651D0,.21526385346316D0,
     &        .20519846372130D0,.18553839747794D0,.15720316715819D0,
     &        .12151857068790D0,.08015808715976D0,.03511946033175D0/
*
      XMU0=4.D-7*PI
      M1=14
      M2=14
      M3=14
      GAUSS=0.D0
```

```
      L=0
      DO 25 I=1,9
IF (M1.EQ.NPOINT(I)) THEN
  JF1=KEY(I)
  JL1=KEY(I+1)-1
  L=L+1
ENDIF
IF (M2.EQ.NPOINT(I)) THEN
  JF2=KEY(I)
  JL2=KEY(I+1)-1
   L=L+1
ENDIF
IF (M3.EQ.NPOINT(I)) THEN
   JF3=KEY(I)
   JL3=KEY(I+1)-1
   L=L+1
ENDIF
  25 CONTINUE
      IF (L.NE.3) THEN
WRITE(76,*)'GAUSS-PARAMETER ERROR'
WRITE(76,*)'  M1 = ',M1
WRITE(76,*)'  M2 = ',M2
WRITE(76,*)'  M3 = ',M3
GAUSS=0.D0
RETURN
      ENDIF
      PD2=PI/2.D0
       WRITE(76,*)LSTART,' = LSTART IN GAUSS'
       WRITE(*,*)LSTART,' = Starting layer for Gauss Quadrature'
       WRITE(*,*)NORG,' = Ending layer for Gauss Quadrature'
       WRITE(76,*)NORG,' = Ending layer for Gauss Quadrature'
c     We are going to evaluate the Bessel functions at the Gauss
c  quadrature points in all layers
      WRITE(*,*)NC,' = NC'
      WRITE(76,*)NC,' = NC or NC passed through COMMON'
      WRITE(*,*)NMIN,' = NMIN'
      WRITE(76,*)NMIN,' = NMIN as passed through COMMON'
      DO 900 NP=LSTART, NORG
WRITE(*,*)NP,' = current layer number for integration'
ISKIP=1
c
c DO VOLUME INTEGRATION ONLY IF PROPERTIES DIFFER FROM FREE SPACE
c
```

```
   IF (EPSP(NP).NE.1.D0) ISKIP=0
   IF (SIGP(NP).NE.0.D0) ISKIP=0
    5   CONTINUE
 IF (ISKIP.EQ.0) THEN
c*********We are really integrating over LAYER = NP and set
c****the values of R2 and R1
   LAYER=NP
   R2=BDP(NP)
   AM=FKP(NP)
   IF (NP.EQ.1) THEN
     R1=0.D0
   ELSE
     R1=BDP(NP-1)
   ENDIF
   D=(R2-R1)*2.D0
   RH=D/4.D0
   SUM3=0.D0
cxxxxxxxxx
c COMPUTE AND STORE NEEDED BESSEL FUNCTIONS TO SAVE TIME
cxxxxxxxxx
   IF ( NMIN .GT. NZ ) THEN
     WRITE(76,*)'Too many Bessel Functions needed in GAUSS'
     WRITE(*,*)' NMIN exceeded NZ in GAUSS'
     GAUSS=0.D0
   RETURN
   ENDIF
c        J2 is the index for the  Radial variable with
c        JF2 and JL2 being array indices for Gauss Q array
c        for selecting points.
   DO 40 J2=JF2, JL2
     IF (Y(J2).EQ.0.D0) THEN
       ARG2(1)=RH+R1
       I2=1
       WRITE(76,*)ARG2(1),' = ARG2(1)'
       WRITE(76,*)J2,' = J2'
       WRITE(76,*)' Stopping program'
       STOP
     ELSE
       ARG2(1)=RH+Y(J2)*RH+R1
       ARG2(2)=RH-Y(J2)*RH+R1
c
c   Note that ARG2(1) is equal to (B-A)/2 + Y*(B-A)/2 + A =
c  ****                          A + (1+Y)B/2 - (1+Y)A/2 =
```

```
c  ****                          A/2 + B/2 + (Y*(B-A)/2)
c  and similarly
c              ARG2(2) = (A+B)/2  - Y*(B-A)/2
       I2=2
     ENDIF
     WRITE(76,5433)I2,J2,ARG2(1),ARG2(2)
 5433       FORMAT(I5,' = I2',I5,' = J2',1PD15.7,D15.7,' = ARG2(1,2)')
     DO 39 I=1,I2
       Z=AM*ARG2(I)
       IF(ARG2(I).GT.BDP(NORG)) THEN
  WRITE(*,*)' ARG2(I) = ',ARG2(I)
  WRITE(*,*)'  Error in ARG2(I)'
  WRITE(*,*) ' STOPPED in GAUSS'
  STOP
       ENDIF
c              We have two values of Z, one for the left half of the
c       interval corresponding to I = 2 and the other for the right
c       half of the interval of integration I = 1.
c    CALL BJYH2(BJNP2, BHNP2, Z, NCC, STOPR, LAYER)
       LAYER = NP
       CALL BJYH(BJNPO,BHNPO,Z,NCC,STOPR)
c
       IF(NCC.GT.NMIN) THEN
  IF(IPRINT.EQ.0) THEN
    WRITE(*,*)Z,' = Z'
    WRITE(*,*)NCC,' = NCC after CALL BJYH'
  ENDIF
  NCC = NMIN
       ENDIF
       IF(IPRINT.EQ.0) THEN
   WRITE(*,*)NCC,' = NCC after CALL BJYH'
   WRITE(*,*)NC,' = NC before CALL BJYH'
   WRITE(76,*)NCC,' = NCC after CALL BJYH'
   WRITE(76,*)NC,' = NC before CALL BJYH'
   WRITE(76,1132)
 1132            FORMAT(25x,'BJNPO',25x,'BHNPO')
   DO 1134 IBSL = 1,NCC
   WRITE(76,1133)BJNPO(IBSL),BHNPO(IBSL)
 1133            FORMAT(1PD15.7,D15.7,2D15.7)
 1134            CONTINUE
   IPRINT = IPRINT+1
       ENDIF
c               ,LAYER) is not included as argument in BJYH
```

```
c             We are getting spherical Bessel and Hankel functions
c          of orders 1 through NCC with values not exceeding STOPR and
c          are storing them temporarily in BJNPO  and BHNPO
      IIJ=J2-JF2+1
c              J2 is the Gauss Q index and JF2 is the starting index
c              which makes IIJ an index starting at 1 which runs from
c              1 to 14, say, if there are 14 Gauss Q points.
      NTERM(IIJ,I)=NCC
      DO 38 II=1,NCC
c             DO 37 JJ=1,2
    BJNPA(II,IIJ,I)=BJNPO(II)
    BHNPA(II,IIJ,I)=BHNPO(II)
c               This array contains the orders and the arguments
c of the Bessel functions as the orders range from 1 to NCC and the
c arguments range over the Gauss Q points.
   37           CONTINUE
   38          CONTINUE
   39        CONTINUE
   40      CONTINUE
c
c INTEGRATE OVER THETA
c
   DO 85 J3=JF3, JL3
     IF (Y(J3).EQ.0.D0) THEN
       ARG3(1)=PD2
       I3=1
     ELSE
       ARG3(1)=PD2+PD2*Y(J3)
       ARG3(2)=PD2-PD2*Y(J3)
       I3=2
     ENDIF
     DO 84 L=1,I3
       THETA=ARG3(L)
       SINTH=SIN(THETA)
       CALL PL(THETA,NMIN,P,DP)
c
c INTEGRATE OVER RADIUS
c
       SUM2=0.D0
c
       DO 80 J2=JF2, JL2
       IF (Y(J2).EQ.0.D0) THEN
    ARG2(1)=RH+R1
```

```
      I2=1
         ELSE
      ARG2(1)=RH+Y(J2)*RH+R1
      ARG2(2)=RH-Y(J2)*RH+R1
      I2=2
         ENDIF
        DO 79 I=1,I2
      R=ARG2(I)
      Z=AM*R
      IIJ=J2-JF2+1
c                 IIJ runs from 1 to 14 if their are 14 Gauss Q points
      NCC=NTERM(IIJ,I)
c                 NC is the number of Bessel functions
      DO 60 II=1,NCC
c                 II is the order of the Bessel or Hankel function
c                     DO 59 JJ=1,2
c                     K=2*I+JJ-2
          BJNP(II)=BJNPA(II,IIJ,I)
          BHNP(II)=BHNPA(II,IIJ,I)
   59               CONTINUE
   60             CONTINUE
*
* INTEGRATE OVER PHI
*
      SUM1=0.D0
*
      DO 75 J=JF1, JL1
        IF (Y(J).EQ.0.D0) THEN
          PHI=PI
          XMUL1=1.D0
        ELSE
          PHI=PI+Y(J)*PI
          XMUL1=2.D0
        ENDIF
c  We know AM and R and these are passed through COMMON
        IF(IPRINT.EQ.1) THEN
          WRITE(*,*)NP,' = NP'
          WRITE(*,1139)
 1139                FORMAT(25x,'BJNP',25x,'BHNP')
          DO 1142 IBSL = 1,NCC
          WRITE(*,1141)BJNP(IBSL),BHNP(IBSL)
 1141                FORMAT(2(1PD15.7,D15.7))
 1142                CONTINUE
```

```
        IPRINT = IPRINT+1
      ENDIF
      NCOLD = NC
      NC = NCC-2
      CALL EVEC(NP, PD)
      NC = NCOLD
c                     Z) is passed through common
      IF(PD.GT.1.D17) THEN
        WRITE(*,*)Z,' = Z'
        WRITE(*,*)NP,' = NP'
        WRITE(*,*)R,' = R'
        WRITE(*,*)THETA,' = THETA'
        WRITE(*,*)PHI,' = PHI'
        WRITE(*,*)ERAD,' = ERAD'
        WRITE(*,*)ETHETA,' = ETHETA'
        WRITE(*,*)EPHI,' = EPHI'
        WRITE(*,*)' STOPPING program in GAUSS.f'
        STOP
      ENDIF
      PD=E0*E0*.5D0*PD
c                    CALL MVEC(NP, PM, Z)
      PM = 0.D0
c    Assuming a nonmagnetic sphere
c                    PM=E0*E0*.5D0*PM
      SUM1=SUM1+XMUL1*WT(J)*(PD+PM)
   75              CONTINUE
    SUM2 = SUM2+WT(J2)*SUM1*ARG2(I)**2
   79            CONTINUE
   80          CONTINUE
       SUM3=SUM3+WT(J3)*SUM2*SINTH
   84        CONTINUE
   85      CONTINUE
   GAUSS=GAUSS+SUM3*PD2*RH*PI
 ENDIF
  900 CONTINUE
  930 CONTINUE
      ISFLAG=1
      WRITE(*,417) GAUSS
  417 FORMAT(' Total Absorbed Power from Gauss Integration = ',
     1       1PD15.8,' Watts.')
      RETURN
      END
```

The end value of GAUSS is the total absorbed power. The original GAUSS was written

with Earl Bell and John Penn.

17 GETEC for obtaining expansion coefficients

The rou..ne GETEC gives us back expansion coefficients from the electric vector of the scattered radiation.

```
      SUBROUTINE GETEC(RADIUS,ALPNM,BETNM)
      IMPLICIT DOUBLE PRECISION(A-H,O-Z)
      COMPLEX*16  ALPHC,ALPNM,BETNM,BTNM1,BTNM2,BTNM3,BTP12,
     1 BTP23,BTERAD,
     2 CHFR12,CHFR23,CI,CSTNR,CXALPF,FUNAL,SURINC,ZBFA,CFNTST,FNTST
c23456
      INCLUDE 'CSMCOM.f'
      EXTERNAL FUNAL,BTERAD,FNTST
      DATA PI/3.14159265358979323D0/
      CI = (0.D0,1.D0)
      BETNM = CI
c     IPRDIA is a diagnostic printing index
      IPRDIA = 0
c     We are initializing this printing index to zero
c
c     CSTNR is a normalization constant that must be
c    divided into the expansion coefficient determined
c    by numerical integration in order to get the expansion
c    coefficient determined by solving the system of
c    linear equations based on orthogonality relations
       R = RADIUS
      WRITE(*,*)RADIUS,' = RADIUS in GETEC.f'
      WRITE(*,*)BDP(NORG),' = BDP(NORG) in GETEC.f'
      RADPD = PI/180.D0
      IF(RADIUS.LT.BDP(1)) THEN
  WRITE(*,*)RADIUS,' = RADIUS is too small'
      ENDIF
      IF(RADIUS.GT.1.D1*BDP(NORG)) THEN
  WRITE(*,*)RADIUS,' = RADIUS is too large'
  WRITE(*,*)' Stopping program'
  STOP
      ENDIF
       ZBFA = FKP(NORG+1)*RADIUS
       WRITE(*,*)ZBFA,' = ZBFA in GETEC.f'
       IPRDIA = 2
```

```
      CALL BJYH(BJNP,BHNP,ZBFA,NC,STOPR)
      WRITE(*,*)' Finished calling Bessel functions in GETEC.f'
      IPRDIA = 0
      WRITE(*,*)BHNP(3),' = h_2(FKP(NORG+1)*RADIUS)'
      WRITE(*,*)' Finished CALL BJYH in GETEC.f'
      WRITE(*,*)NC,' = NC after CALL BJYH in GETEC.f'
      WRITE(*,*)NMIN,' = NMIN after CALL BJYH in GETEC.f'
      IF(NC.GT.NMIN) THEN
  NC = NMIN-2
      ELSE
  NC = NC-2
      ENDIF
c     ZBFA is the complex Bessel Function Argument
c     We call the Bessel functions with this argument
c
c     We are going to get        :rical value of the expansion
c  coefficients ALPHA and        :he index N equal to NVAL
      ISIND = 0
      NGQPTS = 16
      NVAL = 2
      NSITH = NVAL
      NSIPH = NVAL
      WRITE(*,*)' About to call SURINC with FNTST as arg.'
      CFNTST=SURINC(RADIUS,FNTST,NGQPTS,ISING,NSITH,NSIPH)
      WRITE(*,*)CFNTST/(PI*RADIUS*RADIUS),' ='
      WRITE(*,*)'  (output from SURINC with FNTST)/(PI*RADIUS**2)'
      F2 = 2.D0
      F3 = 3.D0
      EVAL=(2.D0/(2.D0*F2+1.D0))*((F2*(F2+1.D0))**2)
      EVAL3=(2.D0/(2.D0*F3+1.D0))*((F3*(F3+1.D0))**2)
      WRITE(*,*)EVAL,' = exact value of real part'
      WRITE(*,*)EVAL3,' = exact value of imag part'
      ISIND = 0
      WRITE(*,*) ' We are about to call SURINC with FUNAL as arg'
      ALPHC=SURINC(RADIUS,FUNAL,NGQPTS,ISIND,NSITH,NSIPH)
      FN = FLOAT(NVAL)
      CXALPF =
     1 PI*(CI**NVAL)*FN*(FN+1.D0)*R*R*BHNP(NVAL+1)*2.D0
      WRITE(*,*)CXALPF,' = pi*i**N)*N*(N+1)*R**2*H_n(k*R)*2'
      ACX = ABS(CXALPF)
      IF(ACX.EQ.0.D0) THEN
  WRITE(*,*)' Error in GETEC'
  WRITE(*,*)' Stopping in GETEC after ALPHC=SURINC'
```

```
  STOP
      ENDIF
      ALPHC = ALPHC/CXALPF
      WRITE(*,*)ALPHC,' = ALPHC after ALPHC = SURINC'
      WRITE(*,*)' We have finished this call to SURINC in GETEC.f'
c
c     (N+1)!/(N-1)! = (N+1)*N*(N-1)!/(N-1)! = N*(N+1)
      RDEN = NVAL*(NVAL+1)
      IF(RDEN.LE.0.D0) THEN
  WRITE(*,*)NVAL,' = NVAL in GETEC.f'
  WRITE(*,*)' Stopping program in GETEC.f'
  STOP
      ENDIF
      RATIO = (2*NVAL+1)/RDEN
      CSTNR =
     1  (PI*BHNP(NVAL+1))*(CI**NVAL)*FN*(FN+1.D0)*R*R*CI**N
c     ALPHC = ALPHC/CSTNR
      ALPNM = ALPHC
      WRITE(*,*)ALPNM,' = Computed ALPHA expansion coefficient'
      WRITE(*,*)ALPNP(NORG*NMIN+NVAL),' = ALPNP(NORG*NMIN+NVAL)'
      WRITE(*,*)ALPHC/ALPNP(NORG*NMIN+NVAL),' ='
      WRITE(*,*)' ALPHC/ALPNP(NORG*NMIN+NVAL)'
      WRITE(*,*)NORG*NMIN+NVAL,' = NORG*NMIN+NVAL'
      ISIND = 0
      NSITH = 4
      NSIPH = 4
      IPESIN = 1234
      IPRDIA = 1234
      NVAL = 2
      BETNM = SURINC(RADIUS,BTERAD,NGQPTS,ISIND,NSITH,NSIPH)
      BETNM = BETNM/(RADIUS*RADIUS)
c    Diagnostic printing
      WRITE(*,*)NVAL,' = NVAL'
      WRITE(*,*)BETNM,' = BETNM from GETEC.f after call SURINC'
      WRITE(*,*)BETNP(NORG*NMIN+NVAL),' = BETNP(NORG*NMIN +2)'
      WRITE(*,*)BETNM/BETNP(NORG*NMIN+2),' =BETNM/BETNP(N)'
      WRITE(*,*)NORG*NMIN+2,' = NORG*NMIN+2'
      BTNM2 = BETNM
c
      NVAL = 1
      IPESIN = 1234
      IPRDIA = 1234
      ISIND = 0
```

```
c
      BETNM = SURINC(RADIUS,BTERAD,NGQPTS,ISIND,NSITH,NSIPH)
      BETNM = BETNM/(RADIUS*RADIUS)
c     Diagnostic printing
      WRITE(*,*)NVAL,' = NVAL'
      WRITE(*,*)BETNM,' = BETNM from GETEC.f after call SURINC'
      WRITE(*,*)BETNP(NORG*NMIN+1),' = BETNP(NORG*NMIN +1)'
      WRITE(*,*)BETNM/BETNP(NORG*NMIN+1),' =BETNM/BETNP(N)'
      WRITE(*,*)NORG*NMIN+1,' = NORG*NMIN+1'
      BTNM1 = BETNM
      WRITE(*,*)BTNM1/BTNM2,' = BETANM(1)/BETANM(2)'
      BTP12 = BETNP(NORG*NMIN+1)/BETNP(NORG*NMIN+2)
      WRITE(*,*)BETNP(NORG*NMIN+1)/BETNP(NORG*NMIN+2),' = '
      WRITE(*,*)' BETNP(NORG*NMIN+1)/BETNP(NORG*NMIN+2)'
c
      CHFR12 = BHNP(NVAL+2)/BHNP(NVAL+1)
      WRITE(*,*)CHFR12,' = BHNP(NVAL+2)/BHNP(NVAL+1)'
      WRITE(*,*)(BTNM1/BTNM2)*CHFR12,' = BTNM1/BTNM2*CHFR12'
      WRITE(*,*)BTP12*CHFR12,' = Beta1/Beta2 * Hankel2/Hankel1'
c
      NVAL = 3
      IPESIN = 1234
      IPRDIA = 1234
      ISIND = 0
c
      BETNM = SURINC(RADIUS,BTERAD,NGQPTS,ISIND,NSITH,NSIPH)
      BETNM = BETNM/(RADIUS*RADIUS)
c     Diagnostic printing
      WRITE(*,*)NVAL,' = NVAL'
      WRITE(*,*)BETNM,' = BETNM from GETEC.f after call SURINC'
      WRITE(*,*)BETNP(NORG*NMIN+3),' = BETNP(NORG*NMIN +3)'
      WRITE(*,*)BETNM/BETNP(NORG*NMIN+3),' =BETNM/BETNP(N)'
      WRITE(*,*)NORG*NMIN+3,' = NORG*NMIN+3'
      BTNM3 = BETNM
      WRITE(*,*)BTNM2/BTNM3,' = BETANM(2)/BETANM(3)'
      BTP23 = BETNP(NORG*NMIN+2)/BETNP(NORG*NMIN+3)
      WRITE(*,*)BETNP(NORG*NMIN+2)/BETNP(NORG*NMIN+3),' = '
      WRITE(*,*)' BETNP(NORG*NMIN+1)/BETNP(NORG*NMIN+2)'
c
      CHFR23 = BHNP(NVAL+3)/BHNP(NVAL+2)
      WRITE(*,*)CHFR12,' = BHNP(NVAL+3)/BHNP(NVAL+2)'
      WRITE(*,*)(BTNM2/BTNM3)*CHFR23,' = BTNM2/BTNM3*CHFR23'
      WRITE(*,*)BTP23*CHFR23,' = Beta2/Beta3 * Hankel3/Hankel2'
```

```
      RETURN
      END
```

This routine shows the capapility of recovering expansion coefficients from the electric vector of the scattered radiation by comparision with actual known values.

18 Jacobian Determination

The routine FDJAC2 was rewritten by Alfred Morris as a part of a Levinberg Marquardt algorithm. The original was written by Hillstrom, Garbow, and More ([2]). This uses discrete approximations to compute a Jacobian associated with M functions in N independent variables.

```
      SUBROUTINE FDJAC2(FCN,M,N,X,FVEC,FJAC,LDFJAC,IFLAG,EPSFCN,WA)
      INTEGER M,N,LDFJAC,IFLAG
      REAL*8 EPSFCN
      REAL*8 X(N),FVEC(M),FJAC(LDFJAC,N),WA(M)
      EXTERNAL FCN
C     **********
C
C     SUBROUTINE FDJAC2
C
C     THIS SUBROUTINE COMPUTES A FORWARD-DIFFERENCE APPROXIMATION
C     TO THE M BY N JACOBIAN MATRIX ASSOCIATED WITH A SPECIFIED
C     PROBLEM OF M FUNCTIONS IN N VARIABLES.
C
C     THE SUBROUTINE STATEMENT IS
C
C       SUBROUTINE FDJAC2(FCN,M,N,X,FVEC,FJAC,LDFJAC,IFLAG,EPSFCN,WA)
C
C     WHERE
C
C       FCN IS THE NAME OF THE USER-SUPPLIED SUBROUTINE WHICH
C         CALCULATES THE FUNCTIONS. FCN MUST BE DECLARED
C         IN AN EXTERNAL STATEMENT IN THE USER CALLING
C         PROGRAM, AND SHOULD BE WRITTEN AS FOLLOWS.
C
C         SUBROUTINE FCN(M,N,X,FVEC,IFLAG)
C         INTEGER M,N,IFLAG
C         REAL X(N),FVEC(M)
C         ----
C         CALCULATE THE FUNCTIONS AT X AND
C         RETURN THIS VECTOR IN FVEC.
```

```
C         ---
C         RETURN
C         END
C
C         THE VALUE OF IFLAG SHOULD NOT BE CHANGED BY FCN UNLESS
C         THE USER WANTS TO TERMINATE EXECUTION OF FDJAC2.
C         IN THIS CASE SET IFLAG TO A NEGATIVE INTEGER.
C
C       M IS A POSITIVE INTEGER INPUT VARIABLE SET TO THE NUMBER
C         OF FUNCTIONS.
C
C       N IS A POSITIVE INTEGER INPUT VARIABLE SET TO THE NUMBER
C         OF VARIABLES. N MUST NOT EXCEED M.
C
C       X IS AN INPUT ARRAY OF LENGTH N.
C
C       FVEC IS AN INPUT ARRAY OF LENGTH M WHICH MUST CONTAIN THE
C         FUNCTIONS EVALUATED AT X.
C
C       FJAC IS AN OUTPUT M BY N ARRAY WHICH CONTAINS THE
C         APPROXIMATION TO THE JACOBIAN MATRIX EVALUATED AT X.
C
C       LDFJAC IS A POSITIVE INTEGER INPUT VARIABLE NOT LESS THAN M
C         WHICH SPECIFIES THE LEADING DIMENSION OF THE ARRAY FJAC.
C
C       IFLAG IS AN INTEGER VARIABLE WHICH CAN BE USED TO TERMINATE
C         THE EXECUTION OF FDJAC2. SEE DESCRIPTION OF FCN.
C
C       EPSFCN IS AN INPUT VARIABLE USED IN DETERMINING A SUITABLE
C         STEP LENGTH FOR THE FORWARD-DIFFERENCE APPROXIMATION. THIS
C         APPROXIMATION ASSUMES THAT THE RELATIVE ERRORS IN THE
C         FUNCTIONS ARE OF THE ORDER OF EPSFCN. IF EPSFCN IS LESS
C         THAN THE MACHINE PRECISION, IT IS ASSUMED THAT THE RELATIVE
C         ERRORS IN THE FUNCTIONS ARE OF THE ORDER OF THE MACHINE
C         PRECISION.
C
C       WA IS A WORK ARRAY OF LENGTH M.
C
C     SUBPROGRAMS CALLED
C
C       USER-SUPPLIED ...... FCN
C
C       MINPACK-SUPPLIED ... SPMPAR
```

```
C
C       FORTRAN-SUPPLIED ... ABS,AMAX1,SQRT
C
C     ARGONNE NATIONAL LABORATORY. MINPACK PROJECT. MARCH 1980.
C     BURTON S. GARBOW, KENNETH E. HILLSTROM, JORGE J. MORE
C
C     **********
      INTEGER I,J
      REAL*8 EPS,EPSMCH,H,TEMP,ZERO
      REAL*8 SPMPAR,DPMPAR
c     DATA ZERO /0.0E0/
      DATA ZERO /0.0D0/
C
C     EPSMCH IS THE MACHINE PRECISION.
C
      EPSMCH = SPMPAR(1)
c     WRITE(91,*)EPSMCH,' = SPMPAR(1) in FDJAC2'
      EPSMCH = DPMPAR(1)
c     WRITE(91,*)EPSMCH,' = DPMPAR(1) in FDJAC2'
C
c     EPS = SQRT(AMAX1(EPSFCN,EPSMCH))
      EPS = SQRT(DMAX1(EPSFCN,EPSMCH))
      DO 20 J = 1, N
  TEMP = X(J)
  H = EPS*ABS(TEMP)
  IF (H .EQ. ZERO) H = EPS
  X(J) = TEMP + H
  CALL FCN(M,N,X,WA,IFLAG)
  IF (IFLAG .LT. 0) GO TO 30
  X(J) = TEMP
  DO 10 I = 1, M
     FJAC(I,J) = (WA(I) - FVEC(I))/H
   10       CONTINUE
   20    CONTINUE
   30 CONTINUE
      RETURN
C
C     LAST CARD OF SUBROUTINE FDJAC2.
C
      END
```

19 FUNAL – a function that gives α expansion coefficients

The function subroutine FUNAL gives us the α expansion coefficients by making use of orthogonality of the vector spherical harmonics used to represent the electric vector of the scattered radiation.

```
      FUNCTION FUNAL(THETGQ,PHIGQ)
      IMPLICIT DOUBLE PRECISION(A-H,O-Z)
c     This will give us an expansion coefficient ALPNP(NN+N)
c  by performing the integration of the proper function FUNAL
c  over the surface of the sphere
      COMPLEX*16 CI,FUNAL
      INCLUDE 'CSMCOM.f'
      CI = (0.D0,1.D0)
      PI = 3.14159265358979323D0
c
c      There are no more than NZ Legendre functions
c      The particular index is passed through common
c   having the name  COMMON/FALBT/RADOFC,NVAL
c      RADOFC = radius for the function calculation
c      NVAL   = the Legendre function index
       THETA = THETGQ
       NCPO = NC+1
       IF(NCPO.GE.70)THEN
   WRITE(*,*)NC,' = NC in FUNAL.f'
   WRITE(*,*)' Stopping program in FUNAL.f'
   STOP
       ENDIF
       CALL PL(THETA,NCPO,P,DP)
c      Next we call the EVCSC which give us the electric
c  vector of the scattered radiation in the THETA and PHI directions
       PHI = PHIGQ
       SINTH = DSIN(THETA)
       COSTH = DCOS(THETA)
       SINPHI = DSIN(PHI)
       COSPHI = DCOS(PHI)
c
       IF(SINTH.EQ.0.D0) THEN
  WRITE(*,*)THETA,' = THETA'
  WRITE(*,*)PHI,' = PHI'
  WRITE(*,*)' Stopping program in FUNAL.f'
  STOP
```

```
      ENDIF
      IF(IPRDIA.LT.10) THEN
 WRITE(*,*)' About to call EVCSC in FUNAL',NVAL,' = NVAL'
 IPRDIA = IPRDIA + 1
 WRITE(*,*)ALPNP(NORG*NMIN + NVAL),' = ALPNP(NORG*NMIN+NVAL)'
 WRITE(*,8765)COSPHI,SINTH,SINPHI,THETA*180.D0/PI
 WRITE(*,*)BHNP(3),' = BHNP(3) in FUNAL.f'
8765    FORMAT(1PD15.7,3D15.7,' = COSPHI,SINTH,SINPHI,THETA')
      ENDIF
      NP = NORG+1
      R = BDP(NORG)
      CALL EVCSC(NORG+1,PD)
      FUNAL =  (  ( ETHESC*P(NVAL)/SINTH )*COSPHI
     1  - EPHISC*DP(NVAL)*SINPHI )
      RETURN
      END
```

20 FNBET for β expansion coefficients

The function FNBET gives us a function which when integrated over the surface of a sphere gives us the β expansion coefficients of the scattered radiation.

```
      FUNCTION FNBET(THETGQ,PHIGQ)
c     This will give us the expansion coefficient
c     BETNP(NN+N) by performing the integration of
c     the complex valued function FNBET over the surface
c     of the sphere
      IMPLICIT DOUBLE COMPLEX(A-H,O-Z)
      DOUBLE PRECISION THETGQ,PHIGQ,PD,SINTH,COSTH,SINPHI,
     1 COSPHI
      INCLUDE 'CSMCOM.f'
c     RADOFC = radius of the sphere over which the
c   integration is carried out.
c     NVAL   = the Legendre function index
      THETA = THETGQ
      PHI = PHIGQ
      CALL PL(THETA,NC,P,DP)
c     Next we shall call EVCSC which will give us the electric
c   vector of the scattered radiation's components in the
c   THETA and PHI coordinate directions
      COSTH = DCOS(THETA)
      SINTH =DSIN(THETA)
```

```
      COSPHI = DCOS(PHI)
      SINPHI = DSIN(PHI)
      CALL EVCSC(NORG+1,PD)
      FNBET = ETHESC*DP(NVAL)*DCOS(PHI) -
     1  EPHISC*(P(NVAL)/DSIN(THETA))*DSIN(PHI)
      RETURN
      END
```

21 SURINC – accurate surface integration routine

This routine gives a way of accurately integrating any function over the surface of a sphere by Gaussian quadrature.

```
      FUNCTION SURINC(RADIUS,FUNC,NGQPTS,ISIND,NSITH,NSIPH)
c     SURFACE INTEGRAL OF A REAL FUNCTION
      IMPLICIT DOUBLE PRECISION(A-H,O-Z)
      COMPLEX*16 SURINC,CZERO,FUNC,SUMPH,SUMTH
      DIMENSION XI16(16),WT16(16),X16TH(16,28),X16PH(16,28),
     1 W16TH(16,28),W16PH(16,28),
     2 WT12(12),XI12(12)
c     RADIUS = the radius of the sphere over which the surface
c              integral is being carried out
c     FUNC   = a complex valued function of THETA and PHI
c              which is to be integrated over the surface
c              of a sphere
c     NGGPTS = the number of Gaussian Quadrature points used
c              in carrying out the surface integration
c     ISIND  = an index which is set to  0  the first time
c              the suface integration is being carried out
c              and when this is zero and NGQPTS is 16 we
c              carry determination of weights and quadrature
c              points
c     NSITH   =the number of subintervals into which the azimuthal
c              and coordinate range is subdivided
c     NSIPH   =the number of subintervals into which the equatorial
c              coordinate range is subdivided
      DATA XI16/-.98940093499164993 2D0,-.94457502307323257 6D0,
     1          -.86563120238783174 3D0,-.75540440835500303 3D0,
     2          -.61787624440264374 8D0,-.45801677765722738 6D0,
     3          -.28160355077925891 3D0,-.09501250983763744 0D0,
     4          +.09501250983763744 0D0,+.28160355077925891 3D0,
     5          +.45801677765722738 6D0,+.61787624440264374 8D0,
```

```
     6          +.75540440835500303 3D0,+.86563120238783174 3D0,
     7          +.94457502307323257 6D0,+.98940093499164993 2D0/
      DATA WT16/+.02715245941175409 4D0,+.06225352393864789 2D0,
     1          +.09515851168249278 4D0,+.12462897125553387 2D0,
     2          +.14959598881657673 2D0,+.16915651939500253 8D0,
     3          +.18260341504492358 8D0,+.18945061045506849 6D0,
     4          +.18945061045506849 6D0,+.18260341504492358 8D0,
     5          +.16915651939500253 8D0,+.14959598881657673 2D0,
     6          +.12462897125553387 2D0,+.09515851168249278 4D0,
     7          +.06225352393864789 2D0,+.02715245941175409 4D0/
      DATA XI12/-9.81560634246719D-1,-9.04117256370475D-1,
     1          -7.69902674194305D-1,-5.87317954286617D-1,
     2          -3.67831498998180D-1,-1.25233408511469D-1,
     3           1.25233408511469D-1, 3.67831498998180D-1,
     4           5.87317954286617D-1, 7.69902674194305D-1,
     5           9.04117256370475D-1, 9.81560634246719D-1/
      DATA WT12/ 4.71753363865120D-2 , 1.06939325995318D-1,
     1           1.60078328543346D-1, 2.03167426723066D-1,
     2           2.33492536538355D-1, 2.49147045813403D-1,
     3           2.49147045813403D-1, 2.33492536538355D-1,
     4           2.03167426723066D-1, 1.60078328543346D-1,
     5           1.06939325995318D-1, 4.71753363865120D-2/
      DATA PI/3.14159265358979323D0/
c     Other important variables are listed as follows
c     ATH       = the starting point for the Gaussian Quadrature
c                 in the Kth subinterval of the azimuthal THETA
c                 coordinate
c     BTH       = the ending point for the Gaussian quadrature
c                 in the Kth subinterval of the azimuthal THETA
c                 coordinate
c     APH       = the starting point for Gaussian quadrature in the
c                 Lth subinterval of  the equatorial PHI coordinate
c     BPH       = the ending point for Gaussian quadrature in the Lth
c                 subinterval of the equatorial PHI coordinate
c
      WRITE(*,1111)RADIUS,NGQPTS,ISIND,NSITH,NSIPH
 1111 FORMAT(1PD15.7,4I5,' = RADIUS,NGQPTS,ISIND,NSITH,NSIPH')
       ZERO = 0.D0
       CZERO = DCMPLX(ZERO,ZERO)
       IF((NSITH.GT.28).OR.(NSIPH.GT.28)) THEN
 WRITE(*,*)' You used the wrong value of'
 WRITE(*,*)' NSITH or NSIPH'
 WRITE(*,*)' Neither can exceed 28'
```

```
 WRITE(*,*)NSIPH,' = NISPH'
 WRITE(*,*)NSITH,' = NSITH'
 WRITE(*,*)' Stopping program in SURINC'
 STOP
       ENDIF
       IF((NGQPTS.NE.16).AND.(NGQPTS.NE.12)) THEN
 WRITE(*,*)' You used the wrong value of NGQPTS'
 WRITE(*,*)NGQPTS,' = NGQPTS'
 WRITE(*,*)' stopping program in SURINC'
 STOP
       ENDIF
c     The first loop takes care of the case where
c   NGQPTS = 16
      IF((ISIND.EQ.0).AND.(NGQPTS.EQ.16)) THEN
 DO 7 K = 1,NSITH
 ATH = FLOAT(K-1)*PI/FLOAT(NSITH)
 BTH = FLOAT(K)*PI/FLOAT(NSITH)
c
 DO 2 ITH = 1,NGQPTS
 YITH = .5D0*((BTH-ATH)*XI16(ITH) + (BTH+ATH))
 X16TH(ITH,K) = YITH
c       We obtained the ITH Gauss Q pt in the Kth subinterval
 W16TH(ITH,K) = .5D0*((BTH-ATH))*WT16(ITH)
c       We obtained the ITH weight in the Kth subinterval
    2   CONTINUE
c
    7   CONTINUE
c234567
 DO 6 L = 1,NSIPH
 APH = FLOAT(L-1)*2.D0*PI/FLOAT(NSIPH)
 BPH = FLOAT(L)*2.D0*PI/FLOAT(NSIPH)
c
 DO 5 IPH = 1,NGQPTS
 YIPH = .5D0*((BPH-APH)*XI16(IPH) +(BPH+APH))
 X16PH(IPH,L) = YIPH
 W16PH(IPH,L) = .5D0*(BPH- APH)*WT16(IPH)
 IF(W16PH(IPH,L).LT.0.D0) THEN
c
    WRITE(*,*)' ERROR in SURINC'
    WRITE(*,*)IPH,' = IPH'
    WRITE(*,*)L,' = L'
    WRITE(*,*)WT12(IPH),' = WT12(IPH)'
    WRITE(*,*)APH,' = APH'
```

```
      WRITE(*,*)BPH,' = BPH'
      STOP
    ENDIF
c         WRITE(22,1022)L,IPH,X16PH(IPH,L),W16PH(IPH,L)
c1022     FORMAT(I5,I5,1PD15.7,D15.7,' =L,IPH,X16PH(IPH,L)',
c     1   ',W16PH(IPH,L)')
c         We obtained the IPH Gauss Q point in the Lth subinterval
      5   CONTINUE
      6   CONTINUE
        ENDIF
c
c       This loop takes care of the case where NGQPTS = 12
        IF((ISIND.EQ.0).AND.(NGQPTS.EQ.12)) THEN
    DO 127 K = 1,NSITH
    ATH = FLOAT(K-1)*PI/FLOAT(NSITH)
    BTH = FLOAT(K)*PI/FLOAT(NSITH)
c
    DO 122 ITH = 1,NGQPTS
    YITH = .5D0*((BTH-ATH)*XI12(ITH) + (BTH+ATH))
    X16TH(ITH,K) = YITH
c         We obtained the ITH Gauss Q pt in the Kth subinterval
    W16TH(ITH,K) = .5D0*((BTH-ATH))*WT12(ITH)
c         We obtained the ITH weight in the Kth subinterval
  122   CONTINUE
c
  127   CONTINUE
c234567
    DO 126 L = 1,NSIPH
    APH = FLOAT(L-1)*2.D0*PI/FLOAT(NSIPH)
    BPH = FLOAT(L)*2.D0*PI/FLOAT(NSIPH)
c
    DO 125 IPH = 1,NGQPTS
    YIPH = .5D0*((BPH-APH)*XI12(IPH) +(BPH+APH))
    X16PH(IPH,L) = YIPH
    W16PH(IPH,L) = .5D0*(BPH- APH)*WT12(IPH)
    IF(W16PH(IPH,L).LT.0.D0) THEN
      WRITE(*,*)' ERROR in SURINC'
      WRITE(*,*)IPH,' = IPH'
      WRITE(*,*)WT12(IPH),' = WT12(IPH)'
      WRITE(*,*)APH,' = APH'
      WRITE(*,*)BPH,' = BPH'
      STOP
    ENDIF
```

```
c       We obtained the IPH Gauss Q point in the Lth subinterval
  125   CONTINUE
  126   CONTINUE
      ENDIF
c
      SUMTH =  CZERO
      DO 21 K = 1,NSITH
      DO 20 ITH = 1,NGQPTS
      SINTH = DSIN(X16TH(ITH,K))
c     WRITE(22,1122)K,ITH,X16TH(ITH,K),SINTH
c1122 FORMAT(I5,I5,D15.7,D15.7,' = K,ITH,X16TH(ITH,K),SINTH')
      SUMPH =  CZERO
      DO 16 L = 1,NSIPH
      DO 15 IPH = 1,NGQPTS
      SUMPH = W16PH(IPH,L)*FUNC(X16TH(ITH,K),X16PH(IPH,L))+SUMPH
c
c     WRITE(22,*)SUMPH,' = SUMPH'
   15 CONTINUE
   16 CONTINUE
      SUMTH = SUMTH + SUMPH*SINTH*W16TH(ITH,K)
   20 CONTINUE
   21 CONTINUE
      SURINC = SUMTH*(RADIUS*RADIUS)
      RETURN
      END
```

This is the end of the surface integration routine.

22 FNTST for testing SURINC

The following function has a known surface integral and gives us a way of checking SURINC.

```
      FUNCTION FNTST(THETA,PHI)
      IMPLICIT DOUBLE PRECISION(A-H,O-Z)
      COMPLEX*16 FNTST
      DIMENSION P(70),DP(70)
      COMMON /FNPARM/NVAL
      ZERO = 0.D0
      N = 30
      SINTH = DSIN(THETA)
      COSTH = DCOS(THETA)
      CSPH = DCOS(PHI)
```

```
      SNPH = DSIN(PHI)
      CSPHSQ = CSPH*CSPH
      SNPHSQ = SNPH*SNPH
      CALL PL(THETA,N,P,DP)
      NVAL = 2
c
      IF(ABS(SINTH).LT.1.D-4) THEN
 PNOSN =  DP(NVAL)/COSTH
 PNOSNP = DP(NVAL+1)/COSTH
      ELSE
 PNOSN = P(NVAL)/SINTH
 PNOSNP = P(NVAL+1)/SINTH
      ENDIF
c     Just called the Legendre function routine
      RLPT = (DCOS(PHI)*PNOSN)**2 +
     1 (DSIN(PHI)*DP(NVAL))**2
      IF(RLPT.LE.0.D0) THEN
 WRITE(*,*)RLPT,' = ((P(NVAL)/SIN(THETA))*COS(PHI))**2+'
 WRITE(*,*)'   (DP(NVAL)*SIN(PHI))**2 '
 WRITE(*,*)PNOSN,' =  P(NVAL)/SIN(THETA)'
 WRITE(*,*)NVAL,' = NVAL'
 WRITE(*,*)THETA*180.D0/PI,' = THETA*180.D0/PI'
 WRITE(*,*)' Program stopped in FNTST'
 STOP
      ENDIF
      CXPT = CSPHSQ*(PNOSNP**2)+
     1 SNPHSQ*(DP(NVAL+1)**2)
      IF(CXPT.LT.0.D0) THEN
 WRITE(*,*)CXPT,' = PNOSN**2+DP(NVAL)**2'
 WRITE(*,*)' Error in FNTST'
 STOP
      ENDIF
      FNTST = DCMPLX(RLPT,CXPT)
      RETURN
      END
```

23 FUNC – a test function for minimization

This test function has the same structure as FUNCD and simply shows that we get exactly the same values of expansion coefficients as were determined by COEF.

```
      SUBROUTINE FUNC(M,N,XARRAY,FVEC,IFLAG)
```

```
      IMPLICIT REAL*8 (A-H,O-Z)
      INCLUDE 'CSMCOM.f'
      COMMON /FNCOM/IPRNDX
c     NORGF is passed from COMMON CSMCOM.f by MAIN
c     NMINF is passed from COMMON CSMCOM.f by COEF after
c    computing the expansion coefficients
      DIMENSION XARRAY(N),FVEC(M)
      IF(N.LT.3*NORGF) THEN
 WRITE(*,*)' Error in SUBROUTINE FUNC'
 WRITE(*,*)N,' = N'
 WRITE(*,*)NORGF,' = NORGF'
 WRITE(*,*)' Stopping program in FUNC'
 STOP
      ENDIF
c*********************************************
c     N is 3*NORGF
c*********************************************
c     XARRAY contains EPSPF,SIGPF,BDPFN and after we are
c  done FVEC will contain the real parts of the ALPFN, the imag
c  inary parts of the ALPFN, the real parts of the BETFN, and
c  the imaginary parts of the BETFN in the region surrounding
c  the sphere
      IF((NORGF.LT.0).OR.(NORGF.GT.NLAYER)) THEN
  WRITE(*,*)NORGF,' = NORGF in FUNC.f'
  WRITE(*,*)' Stopping program in FUNC.f'
  STOP
      ENDIF
      IF(IPRNDX.EQ.1234) THEN
       WRITE(*,1233)
 1233  FORMAT(4x,'I',7x,'BDPFN(I)',7x,'EPSPF(I)',7x,
     1 'SIGPF(I)')
      ENDIF
      FKPF(NORGF+1) = OMEGA/VELOCI
      DO 30 I = 1,NORGF
      IF(I.EQ.1) THEN
 BDPFN(I) = XARRAY(I)*BDP(I)
      ELSE
 THICKF(I) = THICK(I)*XARRAY(I)
 BDPFN(I) = BDPFN(I-1)+THICKF(I)
      ENDIF
 IF(BDPFN(I).LT.0.D0) THEN
  IFLAG = -1
 ENDIF
```

```
      EPSPF(I) = XARRAY(NORGF+I)*EPSP(I)
c
      IF(EPSPF(I).LT.EPS0) THEN
 IFLAG = -1
      ENDIF
      SIGPF(I) = XARRAY(2*NORGF+I)*SIGP(I)
c
      IF(SIGPF(I).LT.0.D0) THEN
 IFLAG = -1
      ENDIF
      IF(IPRNDX.EQ.1234) THEN
      WRITE(*,1234)I,BDPFN(I),EPSPF(I),SIGPF(I)
 1234 FORMAT(I5,1PD15.7,2D15.7,' in FUNC.f')
      ENDIF
   30 CONTINUE
      IPRNDX = 11
c*******getting a new set of expansion coefficients
      CALL PROPGF
      CALL COEFAS
c*************************************************
c     MDB4 = M/4 is passed through CSMCOM.f
c      and M is a multiple of 4
      IF((4*MDB4.NE.M).OR.(NMINF.LT.MDB4)) THEN
 WRITE(*,*)' Error in SUBROUTINE FUNC'
 WRITE(*,*)MDB4,' = MDB4 which should be M/4'
 WRITE(*,*)M,' = M = no FVEC values'
 WRITE(*,*)NMINF,' = min no of Bessel functions'
 WRITE(*,*)' Stopping program in FUNC'
 STOP
      ENDIF
      DO 40 J = 1,MDB4
      FVEC(J) = REAL(ALPFN(NORGF*NMINF+J))
      FVEC(MDB4+J)=DIMAG(ALPFN(NORGF*NMINF+J))
c
      FVEC(2*MDB4+J) = REAL(BETFN(NORGF*NMINF+J))
      FVEC(3*MDB4+J)=DIMAG(BETFN(NORGF*NMINF+J))
   40 CONTINUE
      RETURN
      END
```

24 Getting Letters and Numbers

The next two routines permit us to get letters and numbers from the screen

```
      SUBROUTINE GETLET(LCHOIC,LANS)
c*****************************************************************
c                                                                *
c SUBROUTINE GETLET(LCHOIC,LANS)                                 *
c                                                                *
c This subroutine gets the CHARACTER*1 variable LANS from the user  *
c and makes certain that LANS is one of the two characters in the   *
c CHARACTER*2 variable LCHOIC.  The routine continues pestering the *
c user until one of the valid choices is input.                  *
c                                                                *
c*****************************************************************
      IMPLICIT REAL*8 (A-H, O-Z)
      CHARACTER LCHOIC*2, LANS*1, LINP*1, L1*1, L2*1
      INTEGER*2 IC
    5 READ(*,10) LINP
c   5 READ 10, LINP
   10 FORMAT(A)
*
* CONVERT INPUT TO UPPER CASE
*
      IF ( IAND(ICHAR(LINP),32) .GT. 0) THEN
 IC=IEOR(ICHAR(LINP),32)
 LANS=CHAR(IC)
      ELSE
 LANS=LINP
      ENDIF
*
* CHECK INPUT FOR VALIDITY
*
      L1=LCHOIC(1:1)
      L2=LCHOIC(2:2)
      IF ( (LANS.NE.L1) .AND. (LANS.NE.L2) ) THEN
 WRITE(*,20) LANS,L1,L2
   20   FORMAT(' ','**** Your response of ',A,' was not valid ****'/
     1          ' Please choose either ',A,' or ',A/
     2          ' Choice ? ')
 GOTO 5
      ENDIF
      END
      SUBROUTINE GETNUM(X)
      IMPLICIT REAL*8 (A-H, O-Z)
    5 READ(*,*,ERR=20) X
```

```
      RETURN
   20 WRITE(*,30)
   30 FORMAT(' **** You must enter a real number here ****'/
     1       ' Please try again ? ')
      GOTO 5
      END
```

25 Minimization routine LMDIF

This minimization routine LMDIF is listed in the following.

```
      SUBROUTINE LMDIF(FCN,M,N,X,FVEC,FTOL,XTOL,GTOL,MAXFEV,EPSFCN,
     *                 DIAG,MODE,FACTOR,NPRINT,INFO,NFEV,FJAC,LDFJAC,
     *                 IPVT,QTF,WA1,WA2,WA3,WA4)
      IMPLICIT REAL*8 (A-H,O-Z)
      INTEGER M,N,MAXFEV,MODE,NPRINT,INFO,NFEV,LDFJAC
      INTEGER IPVT(N)
c     REAL*8 MIN,MAX
      REAL*8 FTOL,XTOL,GTOL,EPSFCN,FACTOR
      REAL*8 X(N),FVEC(M),DIAG(N),FJAC(LDFJAC,N),QTF(N),WA1(N),WA2(N),
     *     WA3(N),WA4(M)
      EXTERNAL FCN
C     **********
C
C     SUBROUTINE LMDIF
C
C     THE PURPOSE OF LMDIF IS TO MINIMIZE THE SUM OF THE SQUARES OF
C     M NONLINEAR FUNCTIONS IN N VARIABLES BY A MODIFICATION OF
C     THE LEVENBERG-MARQUARDT ALGORITHM. THE USER MUST PROVIDE A
C     SUBROUTINE WHICH CALCULATES THE FUNCTIONS. THE JACOBIAN IS
C     THEN CALCULATED BY A FORWARD-DIFFERENCE APPROXIMATION.
C
C     THE SUBROUTINE STATEMENT IS
C
C       SUBROUTINE LMDIF(FCN,M,N,X,FVEC,FTOL,XTOL,GTOL,MAXFEV,EPSFCN,
C                        DIAG,MODE,FACTOR,NPRINT,INFO,NFEV,FJAC,
C                        LDFJAC,IPVT,QTF,WA1,WA2,WA3,WA4)
C
C     WHERE
C
C       FCN IS THE NAME OF THE USER-SUPPLIED SUBROUTINE WHICH
C         CALCULATES THE FUNCTIONS. FCN MUST BE DECLARED
```

```
C         IN AN EXTERNAL STATEMENT IN THE USER CALLING
C         PROGRAM, AND SHOULD BE WRITTEN AS FOLLOWS.
C
C         SUBROUTINE FCN(M,N,X,FVEC,IFLAG)
C         INTEGER M,N,IFLAG
C         REAL X(N),FVEC(M)
C         ----
C         CALCULATE THE FUNCTIONS AT X AND
C         RETURN THIS VECTOR IN FVEC.
C         ----
C         RETURN
C         END
C
C         THE VALUE OF IFLAG SHOULD NOT BE CHANGED BY FCN UNLESS
C         THE USER WANTS TO TERMINATE EXECUTION OF LMDIF.
C         IN THIS CASE SET IFLAG TO A NEGATIVE INTEGER.
C
C       M IS A POSITIVE INTEGER INPUT VARIABLE SET TO THE NUMBER
C         OF FUNCTIONS.
C
C       N IS A POSITIVE INTEGER INPUT VARIABLE SET TO THE NUMBER
C         OF VARIABLES. N MUST NOT EXCEED M.
C
C       X IS AN ARRAY OF LENGTH N. ON INPUT X MUST CONTAIN
C         AN INITIAL ESTIMATE OF THE SOLUTION VECTOR. ON OUTPUT X
C         CONTAINS THE FINAL ESTIMATE OF THE SOLUTION VECTOR.
C
C       FVEC IS AN OUTPUT ARRAY OF LENGTH M WHICH CONTAINS
C         THE FUNCTIONS EVALUATED AT THE OUTPUT X.
C
C       FTOL IS A NONNEGATIVE INPUT VARIABLE. TERMINATION
C         OCCURS WHEN BOTH THE ACTUAL AND PREDICTED RELATIVE
C         REDUCTIONS IN THE SUM OF SQUARES ARE AT MOST FTOL.
C         THEREFORE, FTOL MEASURES THE RELATIVE ERROR DESIRED
C         IN THE SUM OF SQUARES.
C
C       XTOL IS A NONNEGATIVE INPUT VARIABLE. TERMINATION
C         OCCURS WHEN THE RELATIVE ERROR BETWEEN TWO CONSECUTIVE
C         ITERATES IS AT MOST XTOL. THEREFORE, XTOL MEASURES THE
C         RELATIVE ERROR DESIRED IN THE APPROXIMATE SOLUTION.
C
C       GTOL IS A NONNEGATIVE INPUT VARIABLE. TERMINATION
C         OCCURS WHEN THE COSINE OF THE ANGLE BETWEEN FVEC AND
```

```
C         ANY COLUMN OF THE JACOBIAN IS AT MOST GTOL IN ABSOLUTE
C         VALUE. THEREFORE, GTOL MEASURES THE ORTHOGONALITY
C         DESIRED BETWEEN THE FUNCTION VECTOR AND THE COLUMNS
C         OF THE JACOBIAN.
C
C       MAXFEV IS A POSITIVE INTEGER INPUT VARIABLE. TERMINATION
C         OCCURS WHEN THE NUMBER OF CALLS TO FCN IS AT LEAST
C         MAXFEV BY THE END OF AN ITERATION.
C
C       EPSFCN IS AN INPUT VARIABLE USED IN DETERMINING A SUITABLE
C         STEP LENGTH FOR THE FORWARD-DIFFERENCE APPROXIMATION. THIS
C         APPROXIMATION ASSUMES THAT THE RELATIVE ERRORS IN THE
C         FUNCTIONS ARE OF THE ORDER OF EPSFCN. IF EPSFCN IS LESS
C         THAN THE MACHINE PRECISION, IT IS ASSUMED THAT THE RELATIVE
C         ERRORS IN THE FUNCTIONS ARE OF THE ORDER OF THE MACHINE
C         PRECISION.
C
C       DIAG IS AN ARRAY OF LENGTH N. IF MODE = 1 (SEE
C         BELOW), DIAG IS INTERNALLY SET. IF MODE = 2, DIAG
C         MUST CONTAIN POSITIVE ENTRIES THAT SERVE AS
C         MULTIPLICATIVE SCALE FACTORS FOR THE VARIABLES.
C
C       MODE IS AN INTEGER INPUT VARIABLE. IF MODE = 1, THE
C         VARIABLES WILL BE SCALED INTERNALLY. IF MODE = 2,
C         THE SCALING IS SPECIFIED BY THE INPUT DIAG. OTHER
C         VALUES OF MODE ARE EQUIVALENT TO MODE = 1.
C
C       FACTOR IS A POSITIVE INPUT VARIABLE USED IN DETERMINING THE
C         INITIAL STEP BOUND. THIS BOUND IS SET TO THE PRODUCT OF
C         FACTOR AND THE EUCLIDEAN NORM OF DIAG*X IF NONZERO, OR ELSE
C         TO FACTOR ITSELF. IN MOST CASES FACTOR SHOULD LIE IN THE
C         INTERVAL (.1,100.). 100. IS A GENERALLY RECOMMENDED VALUE.
C
C       NPRINT IS AN INTEGER INPUT VARIABLE THAT ENABLES CONTROLLED
C         PRINTING OF ITERATES IF IT IS POSITIVE. IN THIS CASE,
C         FCN IS CALLED WITH IFLAG = 0 AT THE BEGINNING OF THE FIRST
C         ITERATION AND EVERY NPRINT ITERATIONS THEREAFTER AND
C         IMMEDIATELY PRIOR TO RETURN, WITH X AND FVEC AVAILABLE
C         FOR PRINTING. IF NPRINT IS NOT POSITIVE, NO SPECIAL CALLS
C         OF FCN WITH IFLAG = 0 ARE MADE.
C
C       INFO IS AN INTEGER OUTPUT VARIABLE. IF THE USER HAS
C         TERMINATED EXECUTION, INFO IS SET TO THE (NEGATIVE)
```

```
C         VALUE OF IFLAG. SEE DESCRIPTION OF FCN. OTHERWISE,
C         INFO IS SET AS FOLLOWS.
C
C         INFO = 0  IMPROPER INPUT PARAMETERS.
C
C         INFO = 1  BOTH ACTUAL AND PREDICTED RELATIVE REDUCTIONS
C                   IN THE SUM OF SQUARES ARE AT MOST FTOL.
C
C         INFO = 2  RELATIVE ERROR BETWEEN TWO CONSECUTIVE ITERATES
C                   IS AT MOST XTOL.
C
C         INFO = 3  CONDITIONS FOR INFO = 1 AND INFO = 2 BOTH HOLD.
C
C         INFO = 4  THE COSINE OF THE ANGLE BETWEEN FVEC AND ANY
C                   COLUMN OF THE JACOBIAN IS AT MOST GTOL IN
C                   ABSOLUTE VALUE.
C
C         INFO = 5  NUMBER OF CALLS TO FCN HAS REACHED OR
C                   EXCEEDED MAXFEV.
C
C         INFO = 6  FTOL IS TOO SMALL. NO FURTHER REDUCTION IN
C                   THE SUM OF SQUARES IS POSSIBLE.
C
C         INFO = 7  XTOL IS TOO SMALL. NO FURTHER IMPROVEMENT IN
C                   THE APPROXIMATE SOLUTION X IS POSSIBLE.
C
C         INFO = 8  GTOL IS TOO SMALL. FVEC IS ORTHOGONAL TO THE
C                   COLUMNS OF THE JACOBIAN TO MACHINE PRECISION.
C
C       NFEV IS AN INTEGER OUTPUT VARIABLE SET TO THE NUMBER OF
C         CALLS TO FCN.
C
C       FJAC IS AN OUTPUT M BY N ARRAY. THE UPPER N BY N SUBMATRIX
C         OF FJAC CONTAINS AN UPPER TRIANGULAR MATRIX R WITH
C         DIAGONAL ELEMENTS OF NONINCREASING MAGNITUDE SUCH THAT
C
C                T     T           T
C              P *(JAC *JAC)*P = R *R,
C
C         WHERE P IS A PERMUTATION MATRIX AND JAC IS THE FINAL
C         CALCULATED JACOBIAN. COLUMN J OF P IS COLUMN IPVT(J)
C         (SEE BELOW) OF THE IDENTITY MATRIX. THE LOWER TRAPEZOIDAL
C         PART OF FJAC CONTAINS INFORMATION GENERATED DURING
```

```
C         THE COMPUTATION OF R.
C
C       LDFJAC IS A POSITIVE INTEGER INPUT VARIABLE NOT LESS THAN M
C         WHICH SPECIFIES THE LEADING DIMENSION OF THE ARRAY FJAC.
C
C       IPVT IS AN INTEGER OUTPUT ARRAY OF LENGTH N. IPVT
C         DEFINES A PERMUTATION MATRIX P SUCH THAT JAC*P = Q*R,
C         WHERE JAC IS THE FINAL CALCULATED JACOBIAN, Q IS
C         ORTHOGONAL (NOT STORED), AND R IS UPPER TRIANGULAR
C         WITH DIAGONAL ELEMENTS OF NONINCREASING MAGNITUDE.
C         COLUMN J OF P IS COLUMN IPVT(J) OF THE IDENTITY MATRIX.
C
C       QTF IS AN OUTPUT ARRAY OF LENGTH N WHICH CONTAINS
C         THE FIRST N ELEMENTS OF THE VECTOR (Q TRANSPOSE)*FVEC.
C
C       WA1, WA2, AND WA3 ARE WORK ARRAYS OF LENGTH N.
C
C       WA4 IS A WORK ARRAY OF LENGTH M.
C
C     SUBPROGRAMS CALLED
C
C       USER-SUPPLIED ...... FCN
C
C       MINPACK-SUPPLIED ... SPMPAR,ENORM,FDJAC2,LMPAR,QRFAC
C
C       FORTRAN-SUPPLIED ... ABS,AMAX1,AMIN1,SQRT,MOD
C
C     ARGONNE NATIONAL LABORATORY. MINPACK PROJECT. MARCH 1980.
C     BURTON S. GARBOW, KENNETH E. HILLSTROM, JORGE J. MORE
C
C     **********
      INTEGER I,IFLAG,ITER,J,L
      REAL*8 ACTRED,DELTA,DIRDER,EPSMCH,FNORM,FNORM1,GNORM,ONE,PAR,
     *     PNORM,PRERED,P1,P5,P25,P75,P0001,RATIO,SUM,TEMP,TEMP1,
     *     TEMP2,XNORM,ZERO
      REAL*8 SPMPAR,ENORM
c     DATA ONE,P1,P5,P25,P75,P0001,ZERO
c    *     /1.0E0,1.0E-1,5.0E-1,2.5E-1,7.5E-1,1.0E-4,0.0E0/
      DATA ONE,P1,P5,P25,P75,P0001,ZERO
     *     /1.0D0,1.0D-1,5.0D-1,2.5D-1,7.5D-1,1.0D-4,0.0D0/
C
C     EPSMCH IS THE MACHINE PRECISION.
C
```

```
      EPSMCH = SPMPAR(1)
C
      INFO = 0
      IFLAG = 0
      NFEV = 0
C
C     CHECK THE INPUT PARAMETERS FOR ERRORS.
C
      WRITE(*,*)' Checking input parameters in LMDIF'
      IF (N .LE. 0 .OR. M .LT. N .OR. LDFJAC .LT. M
     *    .OR. FTOL .LT. ZERO .OR. XTOL .LT. ZERO .OR. GTOL .LT. ZERO
     *    .OR. MAXFEV .LE. 0 .OR. FACTOR .LE. ZERO) GO TO 300
      IF (MODE .NE. 2) GO TO 20
      DO 10 J = 1, N
  IF (DIAG(J) .LE. ZERO) GO TO 300
   10    CONTINUE
   20 CONTINUE
C
C     EVALUATE THE FUNCTION AT THE STARTING POINT
C     AND CALCULATE ITS NORM.
C
      IFLAG = 1
      CALL FCN(M,N,X,FVEC,IFLAG)
      NFEV = 1
      IF (IFLAG .LT. 0) GO TO 300
      FNORM = ENORM(M,FVEC)
C
C     INITIALIZE LEVENBERG-MARQUARDT PARAMETER AND ITERATION COUNTER.
C
      PAR = ZERO
      ITER = 1
C
C     BEGINNING OF THE OUTER LOOP.
C
   30 CONTINUE
C
c***********************************
c******Changing FACTOR after a large number of calls
c******
      IF((ICHFAC.EQ.0).AND.(ICALLF.GT.IFMXFV)) THEN
 FACTOR = 1.D1*FACTOR
 ICHFAC = 1
      ENDIF
```

```
c*****************************************************
c
c*****************************************************
c*****Determinining the largest value of FVEC*****
      FVMAX = -1.D35
      DO 31 IFV = 1,M
      IF(FVEC(IFV).GT.FVMAX) THEN
    FVMAX = FVEC(IFV)
      ENDIF
   31 CONTINUE
c************Changing FACTOR*****************
      IF((FVMAX.LT.1.D-9).AND.(ICHFAC.EQ.0)) THEN
  FACTOR = 1.D1*FACTOR
  ICHFAC = 1
  WRITE(*,*)' We changed FACTOR when'
  WRITE(*,*)FVMAX,' = FVMAX'
  WRITE(*,*)' and',ICALLF,' = ICALLF'
  WRITE(*,*)' in subroutine LMDIF.f'
      ENDIF
      IF((FVMAX.LT.1.D-11).AND.(ICHFAC.EQ.1)) THEN
  FACTOR = .1D0
  ICHFAC = 2
  WRITE(*,*)' We changed FACTOR when'
  WRITE(*,*)FVMAX,' = FVMAX'
  WRITE(*,*)' and',ICALLF,' = ICALLF'
  WRITE(*,*)' in subroutine LMDIF.f'
      ENDIF
C        CALCULATE THE JACOBIAN MATRIX.
C
  IFLAG = 2
  CALL FDJAC2(FCN,M,N,X,FVEC,FJAC,LDFJAC,IFLAG,EPSFCN,WA4)
  NFEV = NFEV + N
  IF (IFLAG .LT. 0) GO TO 300
C
C        IF REQUESTED, CALL FCN TO ENABLE PRINTING OF ITERATES.
C
  IF (NPRINT .LE. 0) GO TO 40
  IFLAG = 0
  IF (MOD(ITER-1,NPRINT) .EQ. 0) CALL FCN(M,N,X,FVEC,IFLAG)
  IF (IFLAG .LT. 0) GO TO 300
   40    CONTINUE
C
C        COMPUTE THE QR FACTORIZATION OF THE JACOBIAN.
```

```
C
  CALL QRFAC(M,N,FJAC,LDFJAC,.TRUE.,IPVT,N,WA1,WA2,WA3)
C
C        ON THE FIRST ITERATION AND IF MODE IS 1, SCALE ACCORDING
C        TO THE NORMS OF THE COLUMNS OF THE INITIAL JACOBIAN.
C
  IF (ITER .NE. 1) GO TO 80
  IF (MODE .EQ. 2) GO TO 60
  DO 50 J = 1, N
     DIAG(J) = WA2(J)
     IF (WA2(J) .EQ. ZERO) DIAG(J) = ONE
   50       CONTINUE
   60    CONTINUE
C
C        ON THE FIRST ITERATION, CALCULATE THE NORM OF THE SCALED X
C        AND INITIALIZE THE STEP BOUND DELTA.
C
  DO 70 J = 1, N
     WA3(J) = DIAG(J)*X(J)
   70       CONTINUE
  XNORM = ENORM(N,WA3)
  DELTA = FACTOR*XNORM
  IF (DELTA .EQ. ZERO) DELTA = FACTOR
   80    CONTINUE
C
C        FORM (Q TRANSPOSE)*FVEC AND STORE THE FIRST N COMPONENTS IN
C        QTF.
C
  DO 90 I = 1, M
     WA4(I) = FVEC(I)
   90       CONTINUE
  DO 130 J = 1, N
     IF (FJAC(J,J) .EQ. ZERO) GO TO 120
     SUM = ZERO
     DO 100 I = J, M
        SUM = SUM + FJAC(I,J)*WA4(I)
  100          CONTINUE
     TEMP = -SUM/FJAC(J,J)
     DO 110 I = J, M
        WA4(I) = WA4(I) + FJAC(I,J)*TEMP
  110          CONTINUE
  120       CONTINUE
     FJAC(J,J) = WA1(J)
```

```
      QTF(J) = WA4(J)
  130       CONTINUE
C
C        COMPUTE THE NORM OF THE SCALED GRADIENT.
C
  GNORM = ZERO
  IF (FNORM .EQ. ZERO) GO TO 170
  DO 160 J = 1, N
      L = IPVT(J)
      IF (WA2(L) .EQ. ZERO) GO TO 150
      SUM = ZERO
      DO 140 I = 1, J
         SUM = SUM + FJAC(I,J)*(QTF(I)/FNORM)
  140          CONTINUE
c           GNORM = AMAX1(GNORM,ABS(SUM/WA2(L)))
      GNORM = DMAX1(GNORM,ABS(SUM/WA2(L)))
  150       CONTINUE
  160       CONTINUE
  170    CONTINUE
C
C        TEST FOR CONVERGENCE OF THE GRADIENT NORM.
C
  IF (GNORM .LE. GTOL) INFO = 4
  IF (INFO .NE. 0) GO TO 300
C
C        RESCALE IF NECESSARY.
C
  IF (MODE .EQ. 2) GO TO 190
  DO 180 J = 1, N
c           DIAG(J) = AMAX1(DIAG(J),WA2(J))
      DIAG(J) = DMAX1(DIAG(J),WA2(J))
  180       CONTINUE
  190    CONTINUE
C
C        BEGINNING OF THE INNER LOOP.
C
  200    CONTINUE
C
C           DETERMINE THE LEVENBERG-MARQUARDT PARAMETER.
C
      CALL LMPAR(N,FJAC,LDFJAC,IPVT,DIAG,QTF,DELTA,PAR,WA1,WA2,
     *                 WA3,WA4)
C
```

```
C           STORE THE DIRECTION P AND X + P. CALCULATE THE NORM OF P.
C
      DO 210 J = 1, N
         WA1(J) = -WA1(J)
         WA2(J) = X(J) + WA1(J)
         WA3(J) = DIAG(J)*WA1(J)
  210          CONTINUE
      PNORM = ENORM(N,WA3)
C
C           ON THE FIRST ITERATION, ADJUST THE INITIAL STEP BOUND.
C
C           IF (ITER .EQ. 1) DELTA = AMIN1(DELTA,PNORM)
      IF (ITER .EQ. 1) DELTA = DMIN1(DELTA,PNORM)
C
C           EVALUATE THE FUNCTION AT X + P AND CALCULATE ITS NORM.
C
      IFLAG = 1
      CALL FCN(M,N,WA2,WA4,IFLAG)
      NFEV = NFEV + 1
      IF (IFLAG .LT. 0) GO TO 300
      FNORM1 = ENORM(M,WA4)
C
C           COMPUTE THE SCALED ACTUAL REDUCTION.
C
      ACTRED = -ONE
      IF (P1*FNORM1 .LT. FNORM) ACTRED = ONE - (FNORM1/FNORM)**2
C
C           COMPUTE THE SCALED PREDICTED REDUCTION AND
C           THE SCALED DIRECTIONAL DERIVATIVE.
C
      DO 230 J = 1, N
         WA3(J) = ZERO
         L = IPVT(J)
         TEMP = WA1(L)
         DO 220 I = 1, J
     WA3(I) = WA3(I) + FJAC(I,J)*TEMP
  220             CONTINUE
  230          CONTINUE
      TEMP1 = ENORM(N,WA3)/FNORM
      TEMP2 = (SQRT(PAR)*PNORM)/FNORM
      PRERED = TEMP1**2 + TEMP2**2/P5
      DIRDER = -(TEMP1**2 + TEMP2**2)
C
```

```
C           COMPUTE THE RATIO OF THE ACTUAL TO THE PREDICTED
C           REDUCTION.
C
      RATIO = ZERO
      IF (PRERED .NE. ZERO) RATIO = ACTRED/PRERED
C
C           UPDATE THE STEP BOUND.
C
      IF (RATIO .GT. P25) GO TO 240
         IF (ACTRED .GE. ZERO) TEMP = P5
         IF (ACTRED .LT. ZERO)
     *            TEMP = P5*DIRDER/(DIRDER + P5*ACTRED)
         IF (P1*FNORM1 .GE. FNORM .OR. TEMP .LT. P1) TEMP = P1
C              DELTA = TEMP*AMIN1(DELTA,PNORM/P1)
         DELTA = TEMP*DMIN1(DELTA,PNORM/P1)
         PAR = PAR/TEMP
         GO TO 260
  240       CONTINUE
         IF (PAR .NE. ZERO .AND. RATIO .LT. P75) GO TO 250
         DELTA = PNORM/P5
         PAR = P5*PAR
  250          CONTINUE
  260       CONTINUE
C
C           TEST FOR SUCCESSFUL ITERATION.
C
      IF (RATIO .LT. P0001) GO TO 290
C
C           SUCCESSFUL ITERATION. UPDATE X, FVEC, AND THEIR NORMS.
C
      DO 270 J = 1, N
         X(J) = WA2(J)
         WA2(J) = DIAG(J)*X(J)
  270          CONTINUE
      DO 280 I = 1, M
         FVEC(I) = WA4(I)
  280          CONTINUE
      XNORM = ENORM(N,WA2)
      FNORM = FNORM1
      ITER = ITER + 1
  290       CONTINUE
C
C           TESTS FOR CONVERGENCE.
```

```
C
      IF (ABS(ACTRED) .LE. FTOL .AND. PRERED .LE. FTOL
     *          .AND. P5*RATIO .LE. ONE) INFO = 1
      IF (DELTA .LE. XTOL*XNORM) INFO = 2
      IF (ABS(ACTRED) .LE. FTOL .AND. PRERED .LE. FTOL
     *          .AND. P5*RATIO .LE. ONE .AND. INFO .EQ. 2) INFO = 3
      IF (INFO .NE. 0) GO TO 300
C
C           TESTS FOR TERMINATION AND STRINGENT TOLERANCES.
C
      IF (NFEV .GE. MAXFEV) INFO = 5
      IF (ABS(ACTRED) .LE. EPSMCH .AND. PRERED .LE. EPSMCH
     *          .AND. P5*RATIO .LE. ONE) INFO = 6
      IF (DELTA .LE. EPSMCH*XNORM) INFO = 7
      IF (GNORM .LE. EPSMCH) INFO = 8
      IF (INFO .NE. 0) GO TO 300
C
C           END OF THE INNER LOOP. REPEAT IF ITERATION UNSUCCESSFUL.
C
      IF (RATIO .LT. P0001) GO TO 200
C
C        END OF THE OUTER LOOP.
C
   GO TO 30
   300 CONTINUE
C
C     TERMINATION, EITHER NORMAL OR USER IMPOSED.
C
      IF (IFLAG .LT. 0) INFO = IFLAG
      IFLAG = 0
      IF (NPRINT .GT. 0) CALL FCN(M,N,X,FVEC,IFLAG)
      RETURN
C
C     LAST CARD OF SUBROUTINE LMDIF.
C
      END
```

This is the end of the general LMDIF routine.

26 LMDIFF driver routine for LMDIF

Alfred Morris wrote the following driver for the Levenberg Marcquardt program previously listed. The external function FCN is an argument and this routine is to be minimized.

```
      SUBROUTINE LMDIFF(FCN,M,N,X,FVEC,EPSFCN,TOL,INFO,IWA,WA,LWA,
     1 FACTOR)
      IMPLICIT REAL*8(A-H,O-Z)
      INTEGER M,N,INFO,LWA
      INTEGER IWA(N)
      REAL*8 EPSFCN,TOL
      REAL*8 FACTOR,FTOL,GTOL,XTOL,ZERO
      REAL*8 X(N),FVEC(M),WA(LWA)
      EXTERNAL FCN
C     **********
C
C     SUBROUTINE LMDIFF
C
C     THE PURPOSE OF LMDIFF IS TO MINIMIZE THE SUM OF THE SQUARES OF
C     M NONLINEAR FUNCTIONS IN N VARIABLES BY A MODIFICATION OF THE
C     LEVENBERG-MARQUARDT ALGORITHM. THIS IS DONE BY USING THE MORE
C     GENERAL LEAST-SQUARES SOLVER LMDIF. THE USER MUST PROVIDE A
C     SUBROUTINE WHICH CALCULATES THE FUNCTIONS. THE JACOBIAN IS
C     THEN CALCULATED BY A FORWARD-DIFFERENCE APPROXIMATION.
C
C     THE SUBROUTINE STATEMENT IS
C
C       SUBROUTINE LMDIFF(FCN,M,N,X,FVEC,EPSFCN,TOL,INFO,IWA,WA,LWA)
C
C     WHERE
C
C       FCN IS THE NAME OF THE USER-SUPPLIED SUBROUTINE WHICH
C         CALCULATES THE FUNCTIONS. FCN MUST BE DECLARED
C         IN AN EXTERNAL STATEMENT IN THE USER CALLING
C         PROGRAM, AND SHOULD BE WRITTEN AS FOLLOWS.
C
C         SUBROUTINE FCN(M,N,X,FVEC,IFLAG)
C         INTEGER M,N,IFLAG
C         REAL X(N),FVEC(M)
C         ----
C         CALCULATE THE FUNCTIONS AT X AND
C         RETURN THIS VECTOR IN FVEC.
C         ----
C         RETURN
C         END
C
C         THE VALUE OF IFLAG SHOULD NOT BE CHANGED BY FCN UNLESS
C         THE USER WANTS TO TERMINATE EXECUTION OF LMDIFF.
```

```
C         IN THIS CASE SET IFLAG TO A NEGATIVE INTEGER.
C
C       M IS A POSITIVE INTEGER INPUT VARIABLE SET TO THE NUMBER
C         OF FUNCTIONS.
C
C       N IS A POSITIVE INTEGER INPUT VARIABLE SET TO THE NUMBER
C         OF VARIABLES. N MUST NOT EXCEED M.
C
C       X IS AN ARRAY OF LENGTH N. ON INPUT X MUST CONTAIN
C         AN INITIAL ESTIMATE OF THE SOLUTION VECTOR. ON OUTPUT X
C         CONTAINS THE FINAL ESTIMATE OF THE SOLUTION VECTOR.
C
C       FVEC IS AN OUTPUT ARRAY OF LENGTH M WHICH CONTAINS
C         THE FUNCTIONS EVALUATED AT THE OUTPUT X.
C
C       EPSFCN IS AN INPUT VARIABLE USED IN DETERMINING A SUITABLE
C         STEP LENGTH FOR THE FORWARD-DIFFERENCE APPROXIMATION. THIS
C         APPROXIMATION ASSUMES THAT THE RELATIVE ERRORS IN THE
C         FUNCTIONS ARE OF THE ORDER OF EPSFCN. IF EPSFCN IS LESS
C         THAN THE MACHINE PRECISION, IT IS ASSUMED THAT THE RELATIVE
C         ERRORS IN THE FUNCTIONS ARE OF THE ORDER OF THE MACHINE
C         PRECISION.
C
C       TOL IS A NONNEGATIVE INPUT VARIABLE. TERMINATION OCCURS
C         WHEN THE ALGORITHM ESTIMATES EITHER THAT THE RELATIVE
C         ERROR IN THE SUM OF SQUARES IS AT MOST TOL OR THAT
C         THE RELATIVE ERROR BETWEEN X AND THE SOLUTION IS AT
C         MOST TOL.
C
C       INFO IS AN INTEGER OUTPUT VARIABLE. IF THE USER HAS
C         TERMINATED EXECUTION, INFO IS SET TO THE (NEGATIVE)
C         VALUE OF IFLAG. SEE DESCRIPTION OF FCN. OTHERWISE,
C         INFO IS SET AS FOLLOWS.
C
C         INFO = 0  IMPROPER INPUT PARAMETERS.
C
C         INFO = 1  ALGORITHM ESTIMATES THAT THE RELATIVE ERROR
C                   IN THE SUM OF SQUARES IS AT MOST TOL.
C
C         INFO = 2  ALGORITHM ESTIMATES THAT THE RELATIVE ERROR
C                   BETWEEN X AND THE SOLUTION IS AT MOST TOL.
C
C         INFO = 3  CONDITIONS FOR INFO = 1 AND INFO = 2 BOTH HOLD.
```

```
C
C         INFO = 4  FVEC IS ORTHOGONAL TO THE COLUMNS OF THE
C                   JACOBIAN TO MACHINE PRECISION.
C
C         INFO = 5  NUMBER OF CALLS TO FCN HAS REACHED OR
C                   EXCEEDED 200*(N+1).
C
C         INFO = 6  TOL IS TOO SMALL. NO FURTHER REDUCTION IN
C                   THE SUM OF SQUARES IS POSSIBLE.
C
C         INFO = 7  TOL IS TOO SMALL. NO FURTHER IMPROVEMENT IN
C                   THE APPROXIMATE SOLUTION X IS POSSIBLE.
C
C       IWA IS AN INTEGER WORK ARRAY OF LENGTH N.
C
C       WA IS A WORK ARRAY OF LENGTH LWA.
C
C       LWA IS A POSITIVE INTEGER INPUT VARIABLE NOT LESS THAN
C         M*N+5*N+M.
C
C     SUBPROGRAMS CALLED
C
C       USER-SUPPLIED ...... FCN
C
C       MINPACK-SUPPLIED ... LMDIF
C
C     ARGONNE NATIONAL LABORATORY. MINPACK PROJECT. MARCH 1980.
C     BURTON S. GARBOW, KENNETH E. HILLSTROM, JORGE J. MORE
C
C     **********
      INTEGER MAXFEV,MODE,MP5N,NFEV,NPRINT
c*****************************************
c     REAL FACTOR,FTOL,GTOL,XTOL,ZERO
c     DATA FACTOR,ZERO /1.0E2,0.0E0/
c**************smaller factor being used*******
      DATA ZERO/0.D0/
c*********************************************
      INFO = 0
      WRITE(*,*)' We just entered LMDIFF with'
      WRITE(*,*)TOL,' = TOL'
      WRITE(*,*)EPSFCN,' = EPS'
      WRITE(*,*)FACTOR,' = FACTOR'
      WRITE(*,*)LWA,' = LWA'
```

```
C
C     CHECK THE INPUT PARAMETERS FOR ERRORS.
C
      IF (N .LE. 0 .OR. M .LT. N .OR. EPSFCN .LT. ZERO
     *    .OR. TOL .LT. ZERO .OR. LWA .LT. M*N + 5*N + M) GO TO 10
C
C     CALL LMDIF.
C
c**** MAXFEV = 200*(N + 1)***was used to determine the maximum
c********number of iterations allowed to find the minimum of FCN,
c********which is the user supplied function
c**** MAXFEV = 400*(N+1)
      MAXFEV = 800*(N+1)
      IFMXFV = 9*MAXFEV/10
      ICHFAC = 0
c*************************************************************
c******Changes made to get more rapid convergence********
c*************************************************************
      FTOL = TOL
      XTOL = TOL
      GTOL = ZERO
      MODE = 1
      NPRINT = 0
      MP5N = M + 5*N
      WRITE(*,*)MAXFEV,' = MAXFEV in LMDIFF'
      WRITE(*,*)IFMXFV,' = IFMXFV in LMDIFF'
      WRITE(*,*)' IFMXFV causes FACTOR = 10*FACTOR if'
      WRITE(*,*)' in case ICALLF exceeds IFMXFV'
      WRITE(*,*)' We are about to CALL LMDIF in LMDIFF.f'
      CALL LMDIF(FCN,M,N,X,FVEC,FTOL,XTOL,GTOL,MAXFEV,EPSFCN,WA(1),
     *           MODE,FACTOR,NPRINT,INFO,NFEV,WA(MP5N+1),M,IWA,
     *           WA(N+1),WA(2*N+1),WA(3*N+1),WA(4*N+1),WA(5*N+1))
      WRITE(*,*)' We finished CALL LMDIF in LMDIFF.f'
      IF (INFO .EQ. 8) INFO = 4
   10 CONTINUE
      RETURN
C
C     LAST CARD OF SUBROUTINE LMDIFF.
C
      END
```

27 Minimum value of an integer array

The following gives the minimum value of an integer array.

```
      FUNCTION MINN(NRAY, N)
* DETERMINE MINIMUM POSITIVE INTEGER VALUE IN ARRAY NRAY
      DIMENSION NRAY(10)
      IF (N.EQ.1) GOTO 20
      NMIN=NRAY(1)
      DO 10 I=2,N
 NTEMP=NRAY(I)
 IF (NTEMP.LT.NMIN) NMIN=NTEMP
   10 CONTINUE
      MINN=NMIN
      GOTO 30
   20 MINN=NRAY(1)
   30 RETURN
      END
```

28 FUNCD – the function of sphere parameters

This is a vector valued function of sphere parameters that represents the difference between expansion coefficient values created by hypothesized spheres and the actual expansion coefficients.

```
      SUBROUTINE FUNCD(M,N,XARRAY,FVEC,IFLAG)
      IMPLICIT REAL*8 (A-H,O-Z)
      INCLUDE 'CSMCOM.f'
      COMMON /FNCOM/IPRNDX
c     NORGF is passed from COMMON CSMCOM.f by MAIN
c     NMINF is passed from COMMON CSMCOM.f by COEF after
c    computing the expansion coefficients
      DIMENSION XARRAY(N),FVEC(M)
      ICALLF = ICALLF + 1
      IF(N.NE.3*NORGF) THEN
 WRITE(*,*)' Error in SUBROUTINE FUNC'
 WRITE(*,*)N,' = N'
 WRITE(*,*)NORGF,' = NORGF'
 WRITE(*,*)' Stopping program in FUNC'
 STOP
      ENDIF
c*****************************************
```

```
c     N is 3*NORGF
c*********************************************
c     XARRAY contains EPSPF,SIGPF,BDPFN
c  for the core and THICKF(I) if I is an outer
c  layer index and after we are
c  done FVEC will contain the real parts of the ALPFN, the imag
c  inary parts of the ALPFN, the real parts of the BETFN, and
c  the imaginary parts of the BETFN in the region surrounding
c  the sphere
      IF((NORGF.LT.0).OR.(NORGF.GT.NLAYER)) THEN
  WRITE(*,*)NORGF,' = NORGF in FUNC.f'
  WRITE(*,*)' Stopping program in FUNC.f'
  STOP
      ENDIF
      IF(IPRNDX.EQ.1234) THEN
       WRITE(*,*)' Temporary print from FUNCD.f'
       WRITE(*,*)FKP(NORG+1),' = FKP(NORG+1)'
       WRITE(*,*)OMEGA/VELOCI,' = FKPF(NORGF+1)'
       WRITE(*,1233)
 1233  FORMAT(4x,'I',7x,'BDPFN(I)',7x,'EPSPF(I)',7x,
     1 'SIGPF(I)')
      ENDIF
      FKPF(NORGF+1) = OMEGA/VELOCI
      DO 30 I = 1,NORGF
  IF(I.EQ.1) THEN
     BDPFN(I) = BDP(I)*XARRAY(I)
  ELSE
     THICKF(I) = XARRAY(I)*THICK(I)
     BDPFN(I) = BDPFN(I-1)+THICKF(I)
  ENDIF
      IF(THICK(I).LT.0.DO) THEN
 IFLAG = -1
  WRITE(*,*)' Negative thickness in FUNCD'
  WRITE(*,*)I,THICKF(I),' = I, new layer thickness'
  WRITE(*,*)' Stopping program in FUNCD.f'
  STOP
      ENDIF
      IF(BDPFN(I).LT.0.DO) THEN
 IFLAG = -1
 WRITE(*,*)' Negative Radius in FUNCD'
 WRITE(*,*)BDPFN(I),' = BDPFN(I)'
 WRITE(*,*)' Stopping program in FUNCD'
 STOP
```

```
      ENDIF
      IF(ABS(XARRAY(I)).LT..9D0) THEN
c******  This is temporary
  IFLAG = -1
  WRITE(*,8876)XARRAY(I),I,BDPFN(I)
 8876    FORMAT(1PD15.7,' = XARRAY(',I5,') in FUNCD',
     1 D15.7,' = BDPFN(I)')
      ENDIF
      EPSPF(I) = XARRAY(NORGF+I)*EPSP(I)
c
      IF(EPSPF(I).LT.0.D0) THEN
 IFLAG = -1
 WRITE(*,*)' Negative permittivity in FUNCD'
 WRITE(*,*)EPSPF(I),' = EPSPF(I)'
 WRITE(*,*)' Stopping program in FUNCD'
 STOP
c
      ENDIF
      IF(ABS(XARRAY(NORGF+I)).LT.0.9) THEN
  IFLAG = -1
c******
  WRITE(*,8877)XARRAY(NORGF+I),NORGF+I,EPSPF(I)
 8877    FORMAT(1PD15.7,' = XARRAY(',I5,') in FUNCD',
     1 D15.7,' = EPSPF(I)')
      ENDIF
      SIGPF(I) = XARRAY(2*NORGF+I)*SIGP(I)
c
      IF(SIGPF(I).LT.0.D0) THEN
 IFLAG = -1
 WRITE(*,*)' Negative conductivity in FUNCD'
 WRITE(*,*)SIGPF(I),' = SIGPF(I)'
 WRITE(*,*)' Stopping program in FUNCD'
 STOP
c
      ENDIF
      IF(ABS(XARRAY(2*NORGF+I)).LT.0.9) THEN
 IFLAG = -1
c******
  WRITE(*,8878)XARRAY(2*NORGF+I),2*NORGF+I,SIGPF(I)
 8878    FORMAT(1PD15.7,' = XARRAY(',I5,') in FUNCD',
     1 D15.7,' = SIGPF(I)')
      ENDIF
      IF(IPRNDX.EQ.1234) THEN
```

```
      WRITE(*,1234)I,BDPFN(I),EPSPF(I),SIGPF(I)
 1234 FORMAT(I5,1PD15.7,2D15.7,' in FUNCD')
      ENDIF
   30 CONTINUE
c************getting a new set of expansion coefficients
      CALL PROPGF
      CALL COEFAS
c*****************************************************
c       The arrays ALPFN and BETFN analogous to ALPNP and BETNP
c     are produced in COEFAS and passed through CSMCOM.f
c     MDB4 = M/4 is passed through CSMCOM.f
c      and M is a multiple of 4
      IF((4*MDB4.NE.M).OR.(NMINF.LT.MDB4)) THEN
 WRITE(*,*)' Error in SUBROUTINE FUNC'
 WRITE(*,*)MDB4,' = MDB4 which should be M/4'
 WRITE(*,*)M,' = M = no FVEC values'
 WRITE(*,*)NMINF,' = min no of Bessel functions'
 WRITE(*,*)' Stopping program in FUNC'
 STOP
      ENDIF
      IF(IPRNDX.EQ.1234) THEN
 WRITE(*,3455)
 3455   FORMAT(4x,'MDB4',4x,'NMIN',4x,'NORG',3x,'NMINF',
     1   3x,'NORGF')
 WRITE(*,3456)MDB4,NMIN,NORG,NMINF,NORGF
 3456    FORMAT(5I8)
      ENDIF
      DO 40 J = 1,MDB4
      ABSVL = ABS(ALPNP(NORG*NMIN+J))
      FVEC(J) = ( REAL(ALPFN(NORGF*NMINF+J)) -
     1 REAL(ALPNP(NORG*NMIN+J)) )/ABSVL
      FVEC(MDB4+J)=( DIMAG(ALPFN(NORGF*NMINF+J)) -
     1 DIMAG(ALPNP(NORG*NMIN+J)) )/ABSVL
c
      ABSVL = ABS(BETNP(NORG*NMIN+J) )
      FVEC(2*MDB4+J) = ( REAL(BETFN(NORGF*NMINF+J)) -
     1 REAL(BETNP(NORG*NMIN+J)) )/ABSVL
      FVEC(3*MDB4+J)=( DIMAG(BETFN(NORGF*NMINF+J)) -
     1 DIMAG(BETNP(NORG*NMIN + J)) )/ABSVL
   40 CONTINUE
      IPRNDX = 11
      RETURN
      END
```

This is the end of the argument of our minimization routine.

29 Test Function FNT18 of the Minimization Routine

The function FNT18 is a paraboloid-like bowl in 19 dimensional space and the minimization routine finds the bottom of the bowl. This function has exactly the same form as FUNCD.

```
      SUBROUTINE FNT18(M,N,XARRAY,FVEC,IFLAG)
      IMPLICIT REAL*8(A-H,O-Z)
      INCLUDE 'CSMCOM.f'
      DIMENSION XARRAY(N),FVEC(M)
      SUM = 0.D0
      ICALLF = ICALLF + 1
      IF(ICALLF.EQ.1) THEN
WRITE(*,*)' Printing initial XARRAY values from FNT18'
DO 2000 IX = 1,NORG
WRITE(*,1900)XARRAY(IX),XARRAY(NORG+IX),XARRAY(2*NORG+IX)
1900   FORMAT(1PD15.7,2D15.7)
2000   CONTINUE
      ENDIF
      IF(M.NE.20) THEN
WRITE(*,*)' Wrong M value in FNT18'
STOP
      ENDIF
      IF(N.NE.18) THEN
WRITE(*,*)N,' = WRONG N value in FNT18'
STOP
      ENDIF
      DO 20 J = 1,N
       IF(XARRAY(J).LT.0.D0) THEN
IFLAG = -1
       ENDIF
      IF(J.LE.N) THEN
       FVEC(J) = ((XARRAY(J)-FLOAT(J))/FLOAT(J))
      ENDIF
c
       SUM = SUM + FVEC(J)**2
 20 CONTINUE
      FVEC(19) = SUM
      FVEC(20)=SUM+((XARRAY(2)-FLOAT(2))/FLOAT(2))**2
      RETURN
```

```
      END
```

This is the end of the test function listing.

30 Miminzation subroutine LMPAR

This is a linear minimization routine that serves a role in the nonlinear minimization problem. This was rewritten by Alfred Morris.

```
      SUBROUTINE LMPAR(N,R,LDR,IPVT,DIAG,QTB,DELTA,PAR,X,SDIAG,WA1,
     *                 WA2)
      INTEGER N,LDR
      INTEGER IPVT(N)
      REAL*8 DELTA,PAR
      REAL*8 R(LDR,N),DIAG(N),QTB(N),X(N),SDIAG(N),WA1(N),WA2(N)
C     **********
C
C     SUBROUTINE LMPAR
C
C     GIVEN AN M BY N MATRIX A, AN N BY N NONSINGULAR DIAGONAL
C     MATRIX D, AN M-VECTOR B, AND A POSITIVE NUMBER DELTA,
C     THE PROBLEM IS TO DETERMINE A VALUE FOR THE PARAMETER
C     PAR SUCH THAT IF X SOLVES THE SYSTEM
C
C           A*X = B ,     SQRT(PAR)*D*X = 0 ,
C
C     IN THE LEAST SQUARES SENSE, AND DXNORM IS THE EUCLIDEAN
C     NORM OF D*X, THEN EITHER PAR IS ZERO AND
C
C           (DXNORM-DELTA) .LE. 0.1*DELTA ,
C
C     OR PAR IS POSITIVE AND
C
C           ABS(DXNORM-DELTA) .LE. 0.1*DELTA .
C
C     THIS SUBROUTINE COMPLETES THE SOLUTION OF THE PROBLEM
C     IF IT IS PROVIDED WITH THE NECESSARY INFORMATION FROM THE
C     QR FACTORIZATION, WITH COLUMN PIVOTING, OF A. THAT IS, IF
C     A*P = Q*R, WHERE P IS A PERMUTATION MATRIX, Q HAS ORTHOGONAL
C     COLUMNS, AND R IS AN UPPER TRIANGULAR MATRIX WITH DIAGONAL
C     ELEMENTS OF NONINCREASING MAGNITUDE, THEN LMPAR EXPECTS
C     THE FULL UPPER TRIANGLE OF R, THE PERMUTATION MATRIX P,
C     AND THE FIRST N COMPONENTS OF (Q TRANSPOSE)*B. ON OUTPUT
```

```
C     LMPAR ALSO PROVIDES AN UPPER TRIANGULAR MATRIX S SUCH THAT
C
C           T   T                    T
C          P *(A *A + PAR*D*D)*P = S *S .
C
C     S IS EMPLOYED WITHIN LMPAR AND MAY BE OF SEPARATE INTEREST.
C
C     ONLY A FEW ITERATIONS ARE GENERALLY NEEDED FOR CONVERGENCE
C     OF THE ALGORITHM. IF, HOWEVER, THE LIMIT OF 10 ITERATIONS
C     IS REACHED, THEN THE OUTPUT PAR WILL CONTAIN THE BEST
C     VALUE OBTAINED SO FAR.
C
C     THE SUBROUTINE STATEMENT IS
C
C       SUBROUTINE LMPAR(N,R,LDR,IPVT,DIAG,QTB,DELTA,PAR,X,SDIAG,
C                        WA1,WA2)
C
C     WHERE
C
C       N IS A POSITIVE INTEGER INPUT VARIABLE SET TO THE ORDER OF R.
C
C       R IS AN N BY N ARRAY. ON INPUT THE FULL UPPER TRIANGLE
C         MUST CONTAIN THE FULL UPPER TRIANGLE OF THE MATRIX R.
C         ON OUTPUT THE FULL UPPER TRIANGLE IS UNALTERED, AND THE
C         STRICT LOWER TRIANGLE CONTAINS THE STRICT UPPER TRIANGLE
C         (TRANSPOSED) OF THE UPPER TRIANGULAR MATRIX S.
C
C       LDR IS A POSITIVE INTEGER INPUT VARIABLE NOT LESS THAN N
C         WHICH SPECIFIES THE LEADING DIMENSION OF THE ARRAY R.
C
C       IPVT IS AN INTEGER INPUT ARRAY OF LENGTH N WHICH DEFINES THE
C         PERMUTATION MATRIX P SUCH THAT A*P = Q*R. COLUMN J OF P
C         IS COLUMN IPVT(J) OF THE IDENTITY MATRIX.
C
C       DIAG IS AN INPUT ARRAY OF LENGTH N WHICH MUST CONTAIN THE
C         DIAGONAL ELEMENTS OF THE MATRIX D.
C
C       QTB IS AN INPUT ARRAY OF LENGTH N WHICH MUST CONTAIN THE FIRST
C         N ELEMENTS OF THE VECTOR (Q TRANSPOSE)*B.
C
C       DELTA IS A POSITIVE INPUT VARIABLE WHICH SPECIFIES AN UPPER
C         BOUND ON THE EUCLIDEAN NORM OF D*X.
C
```

```
C       PAR IS A NONNEGATIVE VARIABLE. ON INPUT PAR CONTAINS AN
C         INITIAL ESTIMATE OF THE LEVENBERG-MARQUARDT PARAMETER.
C         ON OUTPUT PAR CONTAINS THE FINAL ESTIMATE.
C
C       X IS AN OUTPUT ARRAY OF LENGTH N WHICH CONTAINS THE LEAST
C         SQUARES SOLUTION OF THE SYSTEM A*X = B, SQRT(PAR)*D*X = 0,
C         FOR THE OUTPUT PAR.
C
C       SDIAG IS AN OUTPUT ARRAY OF LENGTH N WHICH CONTAINS THE
C         DIAGONAL ELEMENTS OF THE UPPER TRIANGULAR MATRIX S.
C
C       WA1 AND WA2 ARE WORK ARRAYS OF LENGTH N.
C
C     SUBPROGRAMS CALLED
C
C       MINPACK-SUPPLIED ... SPMPAR,ENORM,QRSOLV
C
C       FORTRAN-SUPPLIED ... ABS,AMAX1,AMIN1,SQRT
C
C     ARGONNE NATIONAL LABORATORY. MINPACK PROJECT. MARCH 1980.
C     BURTON S. GARBOW, KENNETH E. HILLSTROM, JORGE J. MORE
C
C     **********
      INTEGER I,ITER,J,JM1,JP1,K,L,NSING
      REAL*8 DXNORM,DWARF,FP,GNORM,PARC,PARL,PARU,P1,P001,SUM,TEMP,ZERO
      REAL*8 DPMPAR,SPMPAR,ENORM
      DATA P1,P001,ZERO /1.0E-1,1.0E-3,0.0E0/
C
C     DWARF IS THE SMALLEST POSITIVE MAGNITUDE.
C
      DWARF = SPMPAR(2)
      DWARF = DPMPAR(2)
C
C     COMPUTE AND STORE IN X THE GAUSS-NEWTON DIRECTION. IF THE
C     JACOBIAN IS RANK-DEFICIENT, OBTAIN A LEAST SQUARES SOLUTION.
C
      NSING = N
      DO 10 J = 1, N
   WA1(J) = QTB(J)
   IF (R(J,J) .EQ. ZERO .AND. NSING .EQ. N) NSING = J - 1
   IF (NSING .LT. N) WA1(J) = ZERO
  10    CONTINUE
      IF (NSING .LT. 1) GO TO 50
```

```
      DO 40 K = 1, NSING
  J = NSING - K + 1
  WA1(J) = WA1(J)/R(J,J)
  TEMP = WA1(J)
  JM1 = J - 1
  IF (JM1 .LT. 1) GO TO 30
  DO 20 I = 1, JM1
     WA1(I) = WA1(I) - R(I,J)*TEMP
   20       CONTINUE
   30    CONTINUE
   40    CONTINUE
   50 CONTINUE
      DO 60 J = 1, N
  L = IPVT(J)
  X(L) = WA1(J)
   60    CONTINUE
C
C     INITIALIZE THE ITERATION COUNTER.
C     EVALUATE THE FUNCTION AT THE ORIGIN, AND TEST
C     FOR ACCEPTANCE OF THE GAUSS-NEWTON DIRECTION.
C
      ITER = 0
      DO 70 J = 1, N
  WA2(J) = DIAG(J)*X(J)
   70    CONTINUE
      DXNORM = ENORM(N,WA2)
      FP = DXNORM - DELTA
      IF (FP .LE. P1*DELTA) GO TO 220
C
C     IF THE JACOBIAN IS NOT RANK DEFICIENT, THE NEWTON
C     STEP PROVIDES A LOWER BOUND, PARL, FOR THE ZERO OF
C     THE FUNCTION. OTHERWISE SET THIS BOUND TO ZERO.
C
      PARL = ZERO
      IF (NSING .LT. N) GO TO 120
      DO 80 J = 1, N
  L = IPVT(J)
  WA1(J) = DIAG(L)*(WA2(L)/DXNORM)
   80    CONTINUE
      DO 110 J = 1, N
  SUM = ZERO
  JM1 = J - 1
  IF (JM1 .LT. 1) GO TO 100
```

```
      DO 90 I = 1, JM1
         SUM = SUM + R(I,J)*WA1(I)
 90         CONTINUE
100      CONTINUE
      WA1(J) = (WA1(J) - SUM)/R(J,J)
110      CONTINUE
         TEMP = ENORM(N,WA1)
         PARL = ((FP/DELTA)/TEMP)/TEMP
120   CONTINUE
C
C        CALCULATE AN UPPER BOUND, PARU, FOR THE ZERO OF THE FUNCTION.
C
         DO 140 J = 1, N
      SUM = ZERO
      DO 130 I = 1, J
         SUM = SUM + R(I,J)*QTB(I)
130         CONTINUE
      L = IPVT(J)
      WA1(J) = SUM/DIAG(L)
140      CONTINUE
         GNORM = ENORM(N,WA1)
         PARU = GNORM/DELTA
c        IF (PARU .EQ. ZERO) PARU = DWARF/AMIN1(DELTA,P1)
         IF (PARU .EQ. ZERO) PARU = DWARF/DMIN1(DELTA,P1)
C
C        IF THE INPUT PAR LIES OUTSIDE OF THE INTERVAL (PARL,PARU),
C        SET PAR TO THE CLOSER ENDPOINT.
C
c        PAR = AMAX1(PAR,PARL)
c        PAR = AMIN1(PAR,PARU)
         PAR = DMAX1(PAR,PARL)
         PAR = DMIN1(PAR,PARU)
         IF (PAR .EQ. ZERO) PAR = GNORM/DXNORM
C
C        BEGINNING OF AN ITERATION.
C
150   CONTINUE
      ITER = ITER + 1
C
C           EVALUATE THE FUNCTION AT THE CURRENT VALUE OF PAR.
C
c           IF (PAR .EQ  ZERO) PAR = AMAX1(DWARF,P001*PARU)
      IF (PAR .EQ. ZERO) PAR = MAX(DWARF,P001*PARU)
```

```
      TEMP = SQRT(PAR)
      DO 160 J = 1, N
         WA1(J) = TEMP*DIAG(J)
      160       CONTINUE
      CALL QRSOLV(N,R,LDR,IPVT,WA1,QTB,X,SDIAG,WA2)
      DO 170 J = 1, N
         WA2(J) = DIAG(J)*X(J)
      170       CONTINUE
      DXNORM = ENORM(N,WA2)
      TEMP = FP
      FP = DXNORM - DELTA
C
C        IF THE FUNCTION IS SMALL ENOUGH, ACCEPT THE CURRENT VALUE
C        OF PAR. ALSO TEST FOR THE EXCEPTIONAL CASES WHERE PARL
C        IS ZERO OR THE NUMBER OF ITERATIONS HAS REACHED 10.
C
      IF (ABS(FP) .LE. P1*DELTA
     *       .OR. PARL .EQ. ZERO .AND. FP .LE. TEMP
     *            .AND. TEMP .LT. ZERO .OR. ITER .EQ. 10) GO TO 220
C
C        COMPUTE THE NEWTON CORRECTION.
C
      DO 180 J = 1, N
         L = IPVT(J)
         WA1(J) = DIAG(L)*(WA2(L)/DXNORM)
      180       CONTINUE
      DO 210 J = 1, N
         WA1(J) = WA1(J)/SDIAG(J)
         TEMP = WA1(J)
         JP1 = J + 1
         IF (N .LT. JP1) GO TO 200
         DO 190 I = JP1, N
            WA1(I) = WA1(I) - R(I,J)*TEMP
      190          CONTINUE
      200       CONTINUE
      210       CONTINUE
      TEMP = ENORM(N,WA1)
      PARC = ((FP/DELTA)/TEMP)/TEMP
C
C        DEPENDING ON THE SIGN OF THE FUNCTION, UPDATE PARL OR PARU.
C
c        IF (FP .GT. ZERO) PARL = AMAX1(PARL,PAR)
c        IF (FP .LT. ZERO) PARU = AMIN1(PARU,PAR)
```

```
  IF (FP .GT. ZERO) PARL = DMAX1(PARL ,PAR)
  IF (FP .LT. ZERO) PARU = DMIN1(PARU,PAR)
C
C        COMPUTE AN IMPROVED ESTIMATE FOR PAR.
C
c        PAR = AMAX1(PARL,PAR+PARC)
  PAR = MAX(PARL,PAR+PARC)
C
C        END OF AN ITERATION.
C
  GO TO 150
  220 CONTINUE
C
C     TERMINATION.
C
      IF (ITER .EQ. 0) PAR = ZERO
      RETURN
C
C     LAST CARD OF SUBROUTINE LMPAR.
C
      END
```

This is the end of LMPAR.

31 QRFAC – matrix factorization routine

The SUBROUTINE QRFAC computes a QR factorization of the input M by N matrix A.

```
      SUBROUTINE QRFAC(M,N,A,LDA,PIVOT,IPVT,LIPVT,RDIAG,ACNORM,WA)
      INTEGER M,N,LDA,LIPVT
      INTEGER IPVT(LIPVT)
      LOGICAL PIVOT
      REAL*8 A(LDA,N),RDIAG(N),ACNORM(N),WA(N)
C     **********
C
C     SUBROUTINE QRFAC
C
C     THIS SUBROUTINE USES HOUSEHOLDER TRANSFORMATIONS WITH COLUMN
C     PIVOTING (OPTIONAL) TO COMPUTE A QR FACTORIZATION OF THE
C     M BY N MATRIX A. THAT IS, QRFAC DETERMINES AN ORTHOGONAL
C     MATRIX Q, A PERMUTATION MATRIX P, AND AN UPPER TRAPEZOIDAL
C     MATRIX R WITH DIAGONAL ELEMENTS OF NONINCREASING MAGNITUDE,
```

```
C     SUCH THAT A*P = Q*R. THE HOUSEHOLDER TRANSFORMATION FOR
C     COLUMN K, K = 1,2,...,MIN(M,N), IS OF THE FORM
C
C                            T
C          I - (1/U(K))*U*U
C
C     WHERE U HAS ZEROS IN THE FIRST K-1 POSITIONS. THE FORM OF
C     THIS TRANSFORMATION AND THE METHOD OF PIVOTING FIRST
C     APPEARED IN THE CORRESPONDING LINPACK SUBROUTINE.
C
C     THE SUBROUTINE STATEMENT IS
C
C       SUBROUTINE QRFAC(M,N,A,LDA,PIVOT,IPVT,LIPVT,RDIAG,ACNORM,WA)
C
C     WHERE
C
C       M IS A POSITIVE INTEGER INPUT VARIABLE SET TO THE NUMBER
C         OF ROWS OF A.
C
C       N IS A POSITIVE INTEGER INPUT VARIABLE SET TO THE NUMBER
C         OF COLUMNS OF A.
C
C       A IS AN M BY N ARRAY. ON INPUT A CONTAINS THE MATRIX FOR
C         WHICH THE QR FACTORIZATION IS TO BE COMPUTED. ON OUTPUT
C         THE STRICT UPPER TRAPEZOIDAL PART OF A CONTAINS THE STRICT
C         UPPER TRAPEZOIDAL PART OF R, AND THE LOWER TRAPEZOIDAL
C         PART OF A CONTAINS A FACTORED FORM OF Q (THE NON-TRIVIAL
C         ELEMENTS OF THE U VECTORS DESCRIBED ABOVE).
C
C       LDA IS A POSITIVE INTEGER INPUT VARIABLE NOT LESS THAN M
C         WHICH SPECIFIES THE LEADING DIMENSION OF THE ARRAY A.
C
C       PIVOT IS A LOGICAL INPUT VARIABLE. IF PIVOT IS SET TRUE,
C         THEN COLUMN PIVOTING IS ENFORCED. IF PIVOT IS SET FALSE,
C         THEN NO COLUMN PIVOTING IS DONE.
C
C       IPVT IS AN INTEGER OUTPUT ARRAY OF LENGTH LIPVT. IPVT
C         DEFINES THE PERMUTATION MATRIX P SUCH THAT A*P = Q*R.
C         COLUMN J OF P IS COLUMN IPVT(J) OF THE IDENTITY MATRIX.
C         IF PIVOT IS FALSE, IPVT IS NOT REFERENCED.
C
C       LIPVT IS A POSITIVE INTEGER INPUT VARIABLE. IF PIVOT IS FALSE,
C         THEN LIPVT MAY BE AS SMALL AS 1. IF PIVOT IS TRUE, THEN
```

```
C         LIPVT MUST BE AT LEAST N.
C
C       RDIAG IS AN OUTPUT ARRAY OF LENGTH N WHICH CONTAINS THE
C         DIAGONAL ELEMENTS OF R.
C
C       ACNORM IS AN OUTPUT ARRAY OF LENGTH N WHICH CONTAINS THE
C         NORMS OF THE CORRESPONDING COLUMNS OF THE INPUT MATRIX A.
C         IF THIS INFORMATION IS NOT NEEDED, THEN ACNORM CAN COINCIDE
C         WITH RDIAG.
C
C       WA IS A WORK ARRAY OF LENGTH N. IF PIVOT IS FALSE, THEN WA
C         CAN COINCIDE WITH RDIAG.
C
C     SUBPROGRAMS CALLED
C
C       MINPACK-SUPPLIED ... SPMPAR,ENORM
C
C       FORTRAN-SUPPLIED ... AMAX1,SQRT,MINO
C
C     ARGONNE NATIONAL LABORATORY. MINPACK PROJECT. MARCH 1980.
C     BURTON S. GARBOW, KENNETH E. HILLSTROM, JORGE J. MORE
C
C     **********
      INTEGER I,J,JP1,K,KMAX,MINMN
c     REAL AJNORM,EPSMCH,ONE,P05,SUM,TEMP,ZERO
c     REAL SPMPAR,ENORM
      REAL*8 AJNORM,EPSMCH,ONE,P05,SUM,TEMP,ZERO
      REAL*8 SPMPAR,DPMPAR,ENORM
      DATA ONE,P05,ZERO /1.0E0,5.0E-2,0.0E0/
C
C     EPSMCH IS THE MACHINE PRECISION.
C
      EPSMCH = SPMPAR(1)
      EPSMCH = DPMPAR(1)
C
C     COMPUTE THE INITIAL COLUMN NORMS AND INITIALIZE SEVERAL ARRAYS.
C
      DO 10 J = 1, N
  ACNORM(J) = ENORM(M,A(1,J))
  RDIAG(J) = ACNORM(J)
  WA(J) = RDIAG(J)
  IF (PIVOT) IPVT(J) = J
   10    CONTINUE
```

```
C
C     REDUCE A TO R WITH HOUSEHOLDER TRANSFORMATIONS.
C
      MINMN = MINO(M,N)
      DO 110 J = 1, MINMN
  IF (.NOT.PIVOT) GO TO 40
C
C        BRING THE COLUMN OF LARGEST NORM INTO THE PIVOT POSITION.
C
  KMAX = J
  DO 20 K = J, N
     IF (RDIAG(K) .GT. RDIAG(KMAX)) KMAX = K
   20       CONTINUE
  IF (KMAX .EQ. J) GO TO 40
  DO 30 I = 1, M
     TEMP = A(I,J)
     A(I,J) = A(I,KMAX)
     A(I,KMAX) = TEMP
   30       CONTINUE
  RDIAG(KMAX) = RDIAG(J)
  WA(KMAX) = WA(J)
  K = IPVT(J)
  IPVT(J) = IPVT(KMAX)
  IPVT(KMAX) = K
   40    CONTINUE
C
C        COMPUTE THE HOUSEHOLDER TRANSFORMATION TO REDUCE THE
C        J-TH COLUMN OF A TO A MULTIPLE OF THE J-TH UNIT VECTOR.
C
  AJNORM = ENORM(M-J+1,A(J,J))
  IF (AJNORM .EQ. ZERO) GO TO 100
  IF (A(J,J) .LT. ZERO) AJNORM = -AJNORM
  DO 50 I = J, M
     A(I,J) = A(I,J)/AJNORM
   50       CONTINUE
  A(J,J) = A(J,J) + ONE
C
C        APPLY THE TRANSFORMATION TO THE REMAINING COLUMNS
C        AND UPDATE THE NORMS.
C
  JP1 = J + 1
  IF (N .LT. JP1) GO TO 100
  DO 90 K = JP1, N
```

```
      SUM = ZERO
      DO 60 I = J, M
         SUM = SUM + A(I,J)*A(I,K)
   60          CONTINUE
      TEMP = SUM/A(J,J)
      DO 70 I = J, M
         A(I,K) = A(I,K) - TEMP*A(I,J)
   70          CONTINUE
      IF (.NOT.PIVOT .OR. RDIAG(K) .EQ. ZERO) GO TO 80
      TEMP = A(J,K)/RDIAG(K)
c           RDIAG(K) = RDIAG(K)*SQRT(AMAX1(ZERO,ONE-TEMP**2))
      RDIAG(K) = RDIAG(K)*SQRT(DMAX1(ZERO,ONE-TEMP**2))
      IF (P05*(RDIAG(K)/WA(K))**2 .GT. EPSMCH) GO TO 80
      RDIAG(K) = ENORM(M-J,A(JP1,K))
      WA(K) = RDIAG(K)
   80       CONTINUE
   90       CONTINUE
  100    CONTINUE
  RDIAG(J) = -AJNORM
  110    CONTINUE
      RETURN
C
C     LAST CARD OF SUBROUTINE QRFAC.
C
      END
```

32 QRSOLV – simultaneous solution of linear equations

This routine simultaneously solves two linear equations.

```
      SUBROUTINE QRSOLV(N,R,LDR,IPVT,DIAG,QTB,X,SDIAG,WA)
      INTEGER N,LDR
      INTEGER IPVT(N)
      REAL*8 R(LDR,N),DIAG(N),QTB(N),X(N),SDIAG(N),WA(N)
C     **********
C
C     SUBROUTINE QRSOLV
C
C     GIVEN AN M BY N MATRIX A, AN N BY N DIAGONAL MATRIX D,
C     AND AN M-VECTOR B, THE PROBLEM IS TO DETERMINE AN X WHICH
C     SOLVES THE SYSTEM
```

```
C
C           A*X = B ,      D*X = 0 ,
C
C     IN THE LEAST SQUARES SENSE.
C
C     THIS SUBROUTINE COMPLETES THE SOLUTION OF THE PROBLEM
C     IF IT IS PROVIDED WITH THE NECESSARY INFORMATION FROM THE
C     QR FACTORIZATION, WITH COLUMN PIVOTING, OF A. THAT IS, IF
C     A*P = Q*R, WHERE P IS A PERMUTATION MATRIX, Q HAS ORTHOGONAL
C     COLUMNS, AND R IS AN UPPER TRIANGULAR MATRIX WITH DIAGONAL
C     ELEMENTS OF NONINCREASING MAGNITUDE, THEN QRSOLV EXPECTS
C     THE FULL UPPER TRIANGLE OF R, THE PERMUTATION MATRIX P,
C     AND THE FIRST N COMPONENTS OF (Q TRANSPOSE)*B. THE SYSTEM
C     A*X = B, D*X = 0, IS THEN EQUIVALENT TO
C
C                 T        T
C           R*Z = Q *B ,  P *D*P*Z = 0 ,
C
C     WHERE X = P*Z. IF THIS SYSTEM DOES NOT HAVE FULL RANK,
C     THEN A LEAST SQUARES SOLUTION IS OBTAINED. ON OUTPUT QRSOLV
C     ALSO PROVIDES AN UPPER TRIANGULAR MATRIX S SUCH THAT
C
C            T   T                 T
C           P *(A *A + D*D)*P = S *S .
C
C     S IS COMPUTED WITHIN QRSOLV AND MAY BE OF SEPARATE INTEREST.
C
C     THE SUBROUTINE STATEMENT IS
C
C       SUBROUTINE QRSOLV(N,R,LDR,IPVT,DIAG,QTB,X,SDIAG,WA)
C
C     WHERE
C
C       N IS A POSITIVE INTEGER INPUT VARIABLE SET TO THE ORDER OF R.
C
C       R IS AN N BY N ARRAY. ON INPUT THE FULL UPPER TRIANGLE
C         MUST CONTAIN THE FULL UPPER TRIANGLE OF THE MATRIX R.
C         ON OUTPUT THE FULL UPPER TRIANGLE IS UNALTERED, AND THE
C         STRICT LOWER TRIANGLE CONTAINS THE STRICT UPPER TRIANGLE
C         (TRANSPOSED) OF THE UPPER TRIANGULAR MATRIX S.
C
C       LDR IS A POSITIVE INTEGER INPUT VARIABLE NOT LESS THAN N
C         WHICH SPECIFIES THE LEADING DIMENSION OF THE ARRAY R.
```

```
C
C       IPVT IS AN INTEGER INPUT ARRAY OF LENGTH N WHICH DEFINES THE
C         PERMUTATION MATRIX P SUCH THAT A*P = Q*R. COLUMN J OF P
C         IS COLUMN IPVT(J) OF THE IDENTITY MATRIX.
C
C       DIAG IS AN INPUT ARRAY OF LENGTH N WHICH MUST CONTAIN THE
C         DIAGONAL ELEMENTS OF THE MATRIX D.
C
C       QTB IS AN INPUT ARRAY OF LENGTH N WHICH MUST CONTAIN THE FIRST
C         N ELEMENTS OF THE VECTOR (Q TRANSPOSE)*B.
C
C       X IS AN OUTPUT ARRAY OF LENGTH N WHICH CONTAINS THE LEAST
C         SQUARES SOLUTION OF THE SYSTEM A*X = B, D*X = 0.
C
C       SDIAG IS AN OUTPUT ARRAY OF LENGTH N WHICH CONTAINS THE
C         DIAGONAL ELEMENTS OF THE UPPER TRIANGULAR MATRIX S.
C
C       WA IS A WORK ARRAY OF LENGTH N.
C
C     SUBPROGRAMS CALLED
C
C       FORTRAN-SUPPLIED ... ABS,SQRT
C
C     ARGONNE NATIONAL LABORATORY. MINPACK PROJECT. MARCH 1980.
C     BURTON S. GARBOW, KENNETH E. HILLSTROM, JORGE J. MORE
C
C     **********
      INTEGER I,J,JP1,K,KP1,L,NSING
      REAL COS,COTAN,P5,P25,QTBPJ,SIN,SUM,TAN,TEMP,ZERO
      DATA P5,P25,ZERO /5.0E-1,2.5E-1,0.0E0/
C
C     COPY R AND (Q TRANSPOSE)*B TO PRESERVE INPUT AND INITIALIZE S.
C     IN PARTICULAR, SAVE THE DIAGONAL ELEMENTS OF R IN X.
C
      DO 20 J = 1, N
  DO 10 I = J, N
     R(I,J) = R(J,I)
   10       CONTINUE
  X(J) = R(J,J)
  WA(J) = QTB(J)
   20    CONTINUE
C
C     ELIMINATE THE DIAGONAL MATRIX D USING A GIVENS ROTATION.
```

```
C
      DO 100 J = 1, N
C
C        PREPARE THE ROW OF D TO BE ELIMINATED, LOCATING THE
C        DIAGONAL ELEMENT USING P FROM THE QR FACTORIZATION.
C
  L = IPVT(J)
  IF (DIAG(L) .EQ. ZERO) GO TO 90
  DO 30 K = J, N
     SDIAG(K) = ZERO
   30       CONTINUE
  SDIAG(J) = DIAG(L)
C
C        THE TRANSFORMATIONS TO ELIMINATE THE ROW OF D
C        MODIFY ONLY A SINGLE ELEMENT OF (Q TRANSPOSE)*B
C        BEYOND THE FIRST N, WHICH IS INITIALLY ZERO.
C
  QTBPJ = ZERO
  DO 80 K = J, N
C
C           DETERMINE A GIVENS ROTATION WHICH ELIMINATES THE
C           APPROPRIATE ELEMENT IN THE CURRENT ROW OF D.
C
     IF (SDIAG(K) .EQ. ZERO) GO TO 70
     IF (ABS(R(K,K)) .GE. ABS(SDIAG(K))) GO TO 40
        COTAN = R(K,K)/SDIAG(K)
        SIN = P5/SQRT(P25+P25*COTAN**2)
        COS = SIN*COTAN
        GO TO 50
   40       CONTINUE
        TAN = SDIAG(K)/R(K,K)
        COS = P5/SQRT(P25+P25*TAN**2)
        SIN = COS*TAN
   50       CONTINUE
C
C           COMPUTE THE MODIFIED DIAGONAL ELEMENT OF R AND
C           THE MODIFIED ELEMENT OF ((Q TRANSPOSE)*B,0).
C
     R(K,K) = COS*R(K,K) + SIN*SDIAG(K)
     TEMP = COS*WA(K) + SIN*QTBPJ
     QTBPJ = -SIN*WA(K) + COS*QTBPJ
     WA(K) = TEMP
C
```

```
C           ACCUMULATE THE TRANFORMATION IN THE ROW OF S.
C
      KP1 = K + 1
      IF (N .LT. KP1) GO TO 70
      DO 60 I = KP1, N
         TEMP = COS*R(I,K) + SIN*SDIAG(I)
         SDIAG(I) = -SIN*R(I,K) + COS*SDIAG(I)
         R(I,K) = TEMP
   60          CONTINUE
   70       CONTINUE
   80       CONTINUE
   90    CONTINUE
C
C        STORE THE DIAGONAL ELEMENT OF S AND RESTORE
C        THE CORRESPONDING DIAGONAL ELEMENT OF R.
C
  SDIAG(J) = R(J,J)
  R(J,J) = X(J)
  100    CONTINUE
C
C     SOLVE THE TRIANGULAR SYSTEM FOR Z. IF THE SYSTEM IS
C     SINGULAR, THEN OBTAIN A LEAST SQUARES SOLUTION.
C
      NSING = N
      DO 110 J = 1, N
  IF (SDIAG(J) .EQ. ZERO .AND. NSING .EQ. N) NSING = J - 1
  IF (NSING .LT. N) WA(J) = ZERO
  110    CONTINUE
      IF (NSING .LT. 1) GO TO 150
      DO 140 K = 1, NSING
  J = NSING - K + 1
  SUM = ZERO
  JP1 = J + 1
  IF (NSING .LT. JP1) GO TO 130
  DO 120 I = JP1, NSING
     SUM = SUM + R(I,J)*WA(I)
  120       CONTINUE
  130    CONTINUE
  WA(J) = (WA(J) - SUM)/SDIAG(J)
  140    CONTINUE
  150 CONTINUE
C
C     PERMUTE THE COMPONENTS OF Z BACK TO COMPONENTS OF X.
```

```
C
      DO 160 J = 1, N
  L = IPVT(J)
  X(L) = WA(J)
  160    CONTINUE
      RETURN
C
C     LAST CARD OF SUBROUTINE QRSOLV.
C
      END
```

This is the end of the QRSOLV part of the inversion program. This was rewritten by Alfred Morris.

33 Machine constants in single precision

The function SPMPAR gives machine constants in single precision. This was rewritten by Alfred Morris.

```
      FUNCTION SPMPAR(I)
c     REAL FUNCTION SPMPAR(I)
      REAL*8 SPMPAR
      INTEGER I
C-----------------------
C
C     SPMPAR PROVIDES THE SINGLE PRECISION MACHINE PARAMETERS FOR
C     THE COMPUTER BEING USED. IT IS ASSUMED THAT THE ARGUMENT
C     I IS AN INTEGER HAVING ONE OF THE VALUES 1, 2, OR 3. IF THE
C     SINGLE PRECISION ARITHMETIC BEING USED HAS T BASE B DIGITS AND
C     ITS SMALLEST AND LARGEST EXPONENTS ARE EMIN AND EMAX, THEN
C
C         SPMPAR(1) = B**(1 - T), THE MACHINE PRECISION,
C
C         SPMPAR(2) = B**(EMIN - 1), THE SMALLEST MAGNITUDE,
C
C         SPMPAR(3) = B**EMAX*(1 - B**(-T)), THE LARGEST MAGNITUDE.
C
C     TO DEFINE THIS FUNCTION FOR THE COMPUTER BEING USED, ACTIVATE
C     THE DATA STATMENTS FOR THE COMPUTER BY REMOVING THE C FROM
C     COLUMN 1. (ALL OTHER DATA STATEMENTS IN SPMPAR SHOULD HAVE C
C     IN COLUMN 1.) IF DATA STATEMENTS ARE NOT GIVEN FOR THE COMPUTER
C     BEING USED, THEN THE SUBROUTINE MACH MAY BE USED TO COMPUTE THE
C     VALUES FOR SPMPAR.
C
```

```
C-----------------------------
C
C     SPMPAR IS AN ADAPTATION OF THE FUNCTION R1MACH, WRITTEN BY P.A.
C     FOX, A.D. HALL, AND N.L. SCHRYER (BELL LABORATORIES). SPMPAR
C     WAS DESIGNED BY B.S. GARBOW, K.E. HILLSTROM, AND J.J. MORE
C     (ARGONNE NATIONAL LABORATORY). THE MAJORITY OF PARAMETER VALUES
C     ARE FROM BELL LABORATORIES.
C
C-----------------------------
      INTEGER MCHEPS(2)
      INTEGER MINMAG(2)
      INTEGER MAXMAG(2)
      REAL RMACH(3)
      EQUIVALENCE (RMACH(1),MCHEPS(1))
      EQUIVALENCE (RMACH(2),MINMAG(1))
      EQUIVALENCE (RMACH(3),MAXMAG(1))
C
C     MACHINE CONSTANTS FOR THE BURROUGHS 1700 SYSTEM.
C
C     DATA RMACH(1) / Z4EA800000 /
C     DATA RMACH(2) / Z400800000 /
C     DATA RMACH(3) / Z5FFFFFFFF /
C
C     MACHINE CONSTANTS FOR THE BURROUGHS 5700/6700/7700 SYSTEMS.
C
C     DATA RMACH(1) / 01301000000000000 /
C     DATA RMACH(2) / 01771000000000000 /
C     DATA RMACH(3) / 00777777777777777 /
C
C     MACHINE CONSTANTS FOR THE CDC 6000/7000 SERIES.
C     (OCTAL FORMAT FOR FORTRAN 4 COMPILERS)
C
C     DATA RMACH(1) / 16414000000000000000B /
C     DATA RMACH(2) / 00014000000000000000B /
C     DATA RMACH(3) / 37767777777777777777B /
C
C     MACHINE CONSTANTS FOR THE CDC 6000/7000 SERIES.
C     (INTEGER FORMAT FOR FORTRAN 4 AND 5 COMPILERS)
C
      DATA MCHEPS(1) / 26163099085255475 2 /
      DATA MINMAG(1) /    422212465065984 /
      DATA MAXMAG(1) / 576179277326712831 /
C
```

```
C     MACHINE CONSTANTS FOR THE CRAY-1.
C
C     DATA RMACH(1) / 03772240000000000000B /
C     DATA RMACH(2) / 02000340000000000000B /
C     DATA RMACH(3) / 05777777777777777776B /
C
C     MACHINE CONSTANTS FOR THE DATA GENERAL ECLIPSE S/200.
C
C     NOTE - IT MAY BE APPROPRIATE TO INCLUDE THE FOLLOWING CARD -
C     STATIC RMACH(3)
C
C     DATA MINMAG/20K,0/,MAXMAG/77777K,177777K/
C     DATA MCHEPS/36020K,0/
C
C     MACHINE CONSTANTS FOR THE HARRIS 220.
C
C     DATA MCHEPS(1) / '20000000, '00000353 /
C     DATA MINMAG(1) / '20000000, '00000201 /
C     DATA MAXMAG(1) / '37777777, '00000177 /
C
C     MACHINE CONSTANTS FOR THE HONEYWELL 600/6000 SERIES.
C
C     DATA RMACH(1) / 0716400000000 /
C     DATA RMACH(2) / 0402400000000 /
C     DATA RMACH(3) / 0376777777777 /
C
C     MACHINE CONSTANTS FOR THE HP 2100
C
C     DATA MCHEPS(1), MCHEPS(2) / 40000B,    327B /
C     DATA MINMAG(1), MINMAG(2) / 40000B,      1 /
C     DATA MAXMAG(1), MAXMAG(2) / 77777B, 177776B /
C
C     MACHINE CONSTANTS FOR THE HP 9000
C
C     DATA RMACH(1) / .1192093E-06 /
C     DATA RMACH(2) / .5877472E-38 /
C     DATA RMACH(3) / .3402823E+39 /
C
C     MACHINE CONSTANTS FOR THE IBM 360/370 SERIES,
C     THE AMDAHL 470/V6, THE ICL 2900, THE ITEL AS/6,
C     THE XEROX SIGMA 5/7/9 AND THE SEL SYSTEMS 85/86.
C
C     DATA RMACH(1) / Z3C100000 /
```

```
C     DATA RMACH(2) / Z00100000 /
C     DATA RMACH(3) / Z7FFFFFFF /
C
C     MACHINE CONSTANTS FOR THE IBM PC - MICROSOFT FORTRAN
C
C     DATA MCHEPS(1) / #34000000 /
C     DATA MINMAG(1) / #00800000 /
C     DATA MAXMAG(1) / #7F7FFFFF /
C
C     MACHINE CONSTANTS FOR THE IBM PC - PROFESSIONAL FORTRAN,
C     LAHEY FORTRAN, AND RM FORTRAN
C
C     DATA MCHEPS(1) / Z'34000000' /
C     DATA MINMAG(1) / Z'00800000' /
C     DATA MAXMAG(1) / Z'7F7FFFFF' /
C
C     MACHINE CONSTANTS FOR THE PDP-10 (KA OR KI PROCESSOR).
C
C     DATA RMACH(1) / "147400000000 /
C     DATA RMACH(2) / "000400000000 /
C     DATA RMACH(3) / "377777777777 /
C
C     MACHINE CONSTANTS FOR THE PDP-11 FORTRAN SUPPORTING
C     32-BIT INTEGERS (EXPRESSED IN INTEGER AND OCTAL).
C
C     DATA MCHEPS(1) /  889192448 /
C     DATA MINMAG(1) /    8388608 /
C     DATA MAXMAG(1) / 2147483647 /
C
C     DATA RMACH(1) / 006500000000 /
C     DATA RMACH(2) / 000040000000 /
C     DATA RMACH(3) / 017777777777 /
C
C     MACHINE CONSTANTS FOR THE PDP-11 FORTRAN SUPPORTING
C     16-BIT INTEGERS (EXPRESSED IN INTEGER AND OCTAL).
C
C     DATA MCHEPS(1),MCHEPS(2) / 13568,     0 /
C     DATA MINMAG(1),MINMAG(2) /   128,     0 /
C     DATA MAXMAG(1),MAXMAG(2) / 3[illegible]        -1 /
C
C     DATA MCHEPS(1),MCHEPS(2) / 0032400, 0000000 /
C     DATA MINMAG(1),MINMAG(2) / 0000200, 0000000 /
C     DATA MAXMAG(1),MAXMAG(2) / 0077777, 0177777 /
```

```
C
C     MACHINE CONSTANTS FOR THE UNIVAC 1100 SERIES.
C
C     DATA RMACH(1) / 0147400000000 /
C     DATA RMACH(2) / 0000400000000 /
C     DATA RMACH(3) / 0377777777777 /
C
C     MACHINE CONSTANTS FOR THE VAX 11/780
C     (EXPRESSED IN INTEGER AND HEXADECIMAL)
C
C     DATA MCHEPS(1) /     13568 /
C     DATA MINMAG(1) /       128 /
C     DATA MAXMAG(1) /    -32769 /
C
C     DATA MCHEPS(1) / Z00003500 /
C     DATA MINMAG(1) / Z00000080 /
C     DATA MAXMAG(1) / ZFFFF7FFF /
C
      SPMPAR = RMACH(I)
      RETURN
C
C     LAST CARD OF FUNCTION SPMPAR.
C
      END
```

34 PROPG – the propagation constants FKP

The following subroutine determines the propagation constants FKP in all layers of the sphere.

```
      SUBROUTINE PROPG
      IMPLICIT REAL*8(A-H,O-Z)
      INCLUDE 'CSMCOM.f'
c
      VEL = VELOCI
* COMPUTE COMPLEX PROPAGATION CONSTANT
      FAC1=OMEGA/VEL
      WRITE(*,*)NORG,' = NORG'
      DO 30 I=1,NORG
 FAC2=EPSP(I)/2.DO
 FAC3=SQRT(1.DO+(1.DO/(EPSO*OMEGA)**2)*(SIGP(I)/EPSP(I))**2)
 REKP=FAC1*SQRT(FAC2*(FAC3+1.DO))
```

```
FIMKP=FAC1*SQRT(FAC2*(FAC3-1.D0))
FKP(I)=DCMPLX(REKP,FIMKP)
WRITE(26,*)'FKP(',I,') = ',FKP(I)
  30 CONTINUE
     FKP(NORG+1)=DCMPLX(FAC1,0.D0)
     RETURN
     END
```

This is the end of the propagation constant routine.

35 Legendre Functions

The following routine gives an array of associated Legendre functions P_n^1 and their derivatives. This was written with Earl Bell and John Penn.

```
      SUBROUTINE PL(THETA,N,P,DP)
* GENERATE ASSOCIATED LEGENDRE POLYNOMIALS OF ORDER 1 AND DEG N
      IMPLICIT REAL*8 (A-H, O-Z)
      DIMENSION P(70), DP(70)
      SNJ=DSIN(THETA)
      CNJ=DCOS(THETA)
      P(1)=SNJ
      P(2)=3.D0*SNJ*CNJ
      DP(1)=CNJ
      DO 10 M=2,N
 A=M
 MP1=M+1
 P(MP1)=(2.D0*A+1.D0)/A*CNJ*P(M)-(A+1.D0)/A*P(M-1)
 IF((THETA.GE.1.D-6).AND.(THETA.LT.3.141592D0))GOTO 5
 DP(M)=M*MP1/2
 IF (THETA.GE.3.141592D0) DP(M)=(-1.D0)**M*DP(M)
 GOTO 10
    5   DP(M)=(A*CNJ*P(M)-(A+1.D0)*P(M-1))/SNJ
   10 CONTINUE
      RETURN
      END
```

36 CSMCOM.f – the COMMON block

Expansion coefficients, Bessel function values, indices that keep track of the number of times functions are called, and other parameters are passed through the COMMON. You

just need to change the COMMON at this location and recompile to make a run with new variables.

```
c     CSM  common variables
      PARAMETER (NLAPLO=10)
      PARAMETER (NLAYER=9)
      PARAMETER (NZ = 70)
      PARAMETER (NGAUPT=14)
c*****************************************************************
c***     COMMON /MISC/ FKP(NLAPLO),CEX,ANP(NLAPLO*NZ),BNP(NLAPLO*NZ),
c*** 1   ALPNP(NLAPLO*NZ),BETNP(NLAPLO*NZ),BJNP(NLAPLO*NZ),
c*** 2   BHNP(NLAPLO*NZ),Z  is an alternate common
c*****************************************************************
      COMMON/CNSTA/EPSO,OMEGA,VELOCI
      COMMON/CFFUN/ANPFN(NLAPLO*NZ),BNPFN(NLAPLO*NZ),ALPFN(NLAPLO*NZ),
     1 BETFN(NLAPLO*NZ)
      COMMON /COEFF/ANP(NLAPLO*NZ),BNP(NLAPLO*NZ),ALPNP(NLAPLO*NZ),
     1 BETNP(NLAPLO*NZ)
      COMMON /FMISC/FKPF(NLAFLO),BDPFN(NLAYER),SIGPF(NLAYER),
     1 EPSPF(NLAYER),THICKF(NLAPLO),ICALLF,ICHFAC,IFMXFV
      COMMON /MISC/FKP(NLAPLO),BJNP(NZ),BHNP(NZ),
     1 CEX,BDP(NLAYER),P(NZ),DP(NZ),SIGP(NLAYER),
     2 EPSP(NLAYER),THICK(NLAPLO),
     3 EO,TIME,R,THETA,PHI,STOPR,NC,NORG,NMIN,NORGF,NMINF,MDB4
       COMMON /ELECV/ERAD,ETHETA,EPHI,Z
       COMMON /ESCAT/ERADSC,ETHESC,EPHISC,IPESIN
       COMMON /FALBT/RADOFC,NVAL,IPRDIA
      COMPLEX*16 ALPNP,ALPFN,ANP,ANPFN,BNP,BNPFN,
     1 BETNP,BETFN,BJNP,BHNP,CEX,
     2 ERAD,ETHETA,EPHI,Z,ERADSC,ETHESC,EPHISC,FKP,FKPF
      REAL*8 BDP,P,DP,SIGP,EPSP,EO,TIME,R,THETA,PHI,STOPR,
     1    RADOFC,EPSO,OMEGA,VELOCI,BDPFN,SIGPF,EPSPF,THICK,
     2    THICKF
```

Here, the components of the electric vector in spherical coordinates are ERAD, ETHETA, and EPHI and R, THETA, and PHI are the coordinates of a point at which the electric vector was last evaluated. The variable Z is the argument of the last Bessel functions that were evaluated.

37 MAKE FILE

The subroutines can be changed and recompiled separately using the MAKE file listed below.

```
FILES=CSM.f COEF.f COEFAS.f DPMPAR.f EVEC.f EVCSC.f EVCINC.f\
  TERM.f EVSPHD.f ENORM.f MUEMTX.f MMEVEI.f BTERAD.f PROPGF.f\
 BJYH.f GAUSS.f GETEC.f FDJAC2.f FUNAL.f FNBET.f SURINC.f\
 FNTST.f FUNC.f GETLET.f GETNUM.f LMDIF.f LMDIFF.f MINN.f\
 FUNCD.f FNT18.f LMPAR.f QRFAC.f QRSOLV.f SPMPAR.f PROPG.f PL.f
OBJECTS=CSM.o COEF.o COEFAS.o DPMPAR.o EVEC.o EVCSC.o EVCINC.o\
 TERM.o EVSPHD.o ENORM.o MUEMTX.o MMEVEI.o BTERAD.o PROPGF.o\
 BJYH.o GAUSS.o GETEC.o FDJAC2.o FUNAL.o FNBET.o SURINC.o\
 FNTST.o FUNC.o GETLET.o GETNUM.o LMDIF.o LMDIFF.o MINN.o\
 FUNCD.o FNT18.o LMPAR.o QRFAC.o QRSOLV.o SPMPAR.o PROPG.o PL.o
.f.o: ; fort -c $*.f
csm.x:  ${OBJECTS}
  fort -o csm.x ${OBJECTS}
  strip csm.x
```

If, for example, the name of the make file is sphere.m then one could create the executable module csm.x by issuing the command,

```
make -f sphere.m
```

38 INPUT DATA SET

The following is an input data set for analysis of a six layer sphere (a core plus 5 shells). The present common allows treatment of from 1 to 9 layers.

```
1000.0E0     1.0E0     0.0E0    1.0E15    6   22
  60.0E0     0.9E0    76.0E0     1.7E0     45.E0      1.E0
   8.5E0    0.11E0     5.5E0     .08E0     45.E0      1.E0
  5.27E0    5.47E0    5.52E0    5.80E0    5.90E0    6.00E0
  1   1.00D-3   180.0D0     0.0D0
  1    .25D+0   170.0D0     0.0D0
  1    .50D+0   160.0D0     0.0D0
  1    .75D+0   150.0D0     0.0D0
  1   1.00D+0   145.0D0     0.0D0
  1   1.25D+0   140.0D0     0.0D0
  1   1.50D+0   130.0D0     0.0D0
  1   1.75D+0   120.0D0     0.0D0
  1   2.00D+0   110.0D0     0.0D0
  1   2.25D+0   100.0D0     0.0D0
  1   2.50D+0    90.0D0     0.0D0
  1   2.75D+0    80.0D0     0.0D0
  1   3.00D+0    70.0D0     0.0D0
  1   5.27D+0    60.0D0     0.0D0
```

```
  2   5.47D+0     50.0D0      0.0D0
  3   5.52D+0     40.0D0      0.0D0
  4   5.60D+0     30.0D0      0.0D0
  4   5.80D+0     20.0D0      0.0D0
  5   5.90D+0     10.0D0      0.0D0
  6   6.00D+0      0.0D0      0.0D0
  1   3.475861092  99.72494519  199.4498910
  2   5.380805495  99.72494519  199.149891
 0.8000000D0
 1.0010288D0     1.0010388D0     1.0010298D0
1.0000000D-9    1.0000000D-8     0.0000001D0
```

The reader can interpret the meaning of the data values by looking at the READ(3 statements in order in the first program listed in this report. These extracted READ statements are listed in order here.

```
THEREADSTATEMENTS
c READ IN CONTROL PARAMETERS
    5 READ(3,10,END=1110) FREQ, EO, TIME, STOPR, NORG, NOCR
   10 FORMAT(4E10.0, 2I5)
c READ DIELECTRIC PROPERTY PARAMETERS
      READ(3,20) (EPSP(I), SIGP(I), I=1,NORG)
   20 FORMAT(6E10.0)
c READ RADII OF SURFACE BOUNDARIES
      READ(3,20) (SBDP(I), I=1,NORG)
c READ DEFINING CHARACTERISTICS OF INTERIOR POINTS AT WHICH
c ABSORBED-POWER DENSITIES ARE TO BE COMPUTED.
      READ(3,*) NREG, R, THETAD, PHID
c
 7732 FORMAT(1PD15.7)
      READ(3,7732)T18FRA
      WRITE(*,*)' Calling LMDIFF with T18FRA=',T18FRA
      IF((T18FRA.LE.0.D0).OR.(T18FRA.GT.2.D0)) THEN
 WRITE(*,*)' Stopping program in CSM.f'
 STOP
      ENDIF
c
c     READ from 3 values of FRACR, FRACEP, FRACSG
      READ(3,8754)FRACR,FRACEP,FRACSG
 8754 FORMAT(1PD15.7,2D15.7)
c
      WRITE(*,*)'  FRACR,FRACEP,FRACSG = '
      DO 8798 I = 1,NORG
      XARRAY(I) = FRACR
```

```
      XARRAY(NORG+I) = FRACEP
      XARRAY(2*NORG+I)=FRACSG
 8798 CONTINUE
      READ(3,8767)EPSL,TOLL,FACTOR
 8767 FORMAT(1PD15.7,D15.7,D15.7)
```

The last value of the last line of data is FACTOR which is 1 million times smaller than the recommended value. This causes the Levenberg Marquardt algorithm to do a careful search close to the starting value initially.

39 OUTPUT DATA

What follows is one of the shorter output data sets called OCOMPDEN.DAT which gives calculated power densities at the (R, θ, ϕ) points listed in the input data set. We also find a comparison between the total absorbed power as computed by a Poynting vector analysis on the surface of the sphere and by integrating the power per unit volume over all six layers of the sphere.

```
  1.000000000E+003  = FREQ (one billion cycles per second)
  1.00000000  = E0 (one volt per meter)
  0.000000000E+000  = TIME
  1.000000000E+015  = STOPR
 22  = NOCR
  5.27000000  = LAYER BOUNDARY no  1
  5.47000000  = LAYER BOUNDARY no  2
  5.52000000  = LAYER BOUNDARY no  3
  5.80000000  = LAYER BOUNDARY no  4
  5.90000000  = LAYER BOUNDARY no  5
  6.00000000  = LAYER BOUNDARY no  6
 22  = NOCR
 14  = NMIN
0
 NREG  NCC      SAVR     THETA      PHID  Power Density
    1    3  .100E-02  .180E+03  .000E+00  1.2148501E-01
    1   10  .250E+00  .170E+03  .000E+00  1.1301373E-01
    1   12  .500E+00  .160E+03  .000E+00  9.5336480E-02
    1   14  .750E+00  .150E+03  .000E+00  7.7171359E-02
    1   14  .100E+01  .145E+03  .000E+00  5.8909441E-02
    1   14  .125E+01  .140E+03  .000E+00  4.4385801E-02
    1   14  .150E+01  .130E+03  .000E+00  3.7460077E-02
    1   14  .175E+01  .120E+03  .000E+00  3.1037602E-02
    1   14  .200E+01  .110E+03  .000E+00  2.4086524E-02
    1   14  .225E+01  .100E+03  .000E+00  1.7446906E-02
```

```
   1   14  .250E+01  .900E+02  .000E+00  1.2369684E-02
   1   14  .275E+01  .800E+02  .000E+00  9.2487407E-03
   1   14  .300E+01  .700E+02  .000E+00  7.4911854E-03
   1   14  .527E+01  .600E+02  .000E+00  5.8454196E-03
   2   14  .547E+01  .500E+02  .000E+00  1.3243193E-02
   3   14  .552E+01  .400E+02  .000E+00  4.3939251E-03
   4   14  .560E+01  .300E+02  .000E+00  4.7558447E-04
   4   14  .580E+01  .200E+02  .000E+00  2.4503299E-04
   5   14  .590E+01  .100E+02  .000E+00  9.4160065E-05
   6   14  .600E+01  .000E+00  .000E+00  6.9334437E-03
   1   14  .348E+01  .997E+02  .199E+03  2.7546319E-02
   2   14  .538E+01  .997E+02  .199E+03  8.0076588E-02
0          AVERAGE ABSORBED-POWER DENSITY =  1.60618E-02 W/M**3
0          TOTAL ABSORBED POWER =  1.45324E-05 WATT.
 1.453240960E-005  total absorbed power by vol integration
362  = no of function calls
 Completed the call to LMDIFF in CSM.f
2  = INFO after call LMDIFF
 5.2700000E-02  5.2700000E-02 = radii (approx and orig)
 6.0000000E+01  6.0000000E+01 = EPS (approx and orig)
 9.0000000E-01  9.0000000E-01 = COND (approx and orig)
 5.4700000E-02  5.4700000E-02 = radii (approx and orig)
 7.6000000E+01  7.6000000E+01 = EPS (approx and orig)
 1.7000000E+00  1.7000000E+00 = COND (approx and orig)
 5.5200000E-02  5.5200000E-02 = radii (approx and orig)
 4.5000000E+01  4.5000000E+01 = EPS (approx and orig)
 1.0000000E+00  1.0000000E+00 = COND (approx and orig)
 5.8000000E-02  5.8000000E-02 = radii (approx and orig)
 8.5000000E+00  8.5000000E+00 = EPS (approx and orig)
 1.1000000E-01  1.1000000E-01 = COND (approx and orig)
 5.9000000E-02  5.9000000E-02 = radii (approx and orig)
 5.5000000E+00  5.5000000E+00 = EPS (approx and orig)
 8.0000000E-02  8.0000000E-02 = COND (approx and orig)
 6.0000000E-02  6.0000000E-02 = radii (approx and orig)
 4.5000000E+01  4.5000000E+01 = EPS (approx and orig)
 1.0000000E+00  1.0000000E+00 = COND (approx and orig)
```

At the end we find that the minimization program was able to recover the radii of the spheres that separate layers and the permittivity and conductivity of the layers from examining the expansion coefficients of the scattered radiation using only 362 forward scattering solutions.

The following is a listing from a file that is created by WRITE(*,*) commands that describes the recovery of expansion coefficients from integration and gives the propagation constants in all layers. The following is a listing of Bessel and Hankel function values.

```
(  4.78211328 ,  6.333847323E-001 )  = Z
25  = NCC after CALL BJYH
14  = NCC after CALL BJYH
14  = NC before CALL BJYH
1  = NP
   BJNP                          BHNP
-2.4624054E-01  4.2471119E-02 -1.0982323E-01  6.8131434E-03
-8.5106205E-02 -1.2098671E-01 -1.5570898E-02  1.1421268E-01
 1.8389119E-01 -1.1011255E-01  1.0954976E-01  6.4873001E-02
 2.5907535E-01 -1.7184874E-02  1.3696629E-01 -6.2462546E-02
 1.8552786E-01  3.6028465E-02  7.5582111E-02 -1.8082540E-01
 9.2896810E-02  3.8372659E-02 -4.1469422E-02 -2.9050167E-01
 3.5962168E-02  2.2901727E-02 -2.5630656E-01 -4.6346095E-01
 1.1283356E-02  1.0086319E-02 -8.0727371E-01 -8.5698502E-01
 2.9381563E-03  3.5836171E-03 -2.5821012E+00 -1.8486907E+00
 6.3969724E-04  1.0739372E-03 -9.0690603E+00 -4.4068432E+00
 1.1503418E-04  2.7889328E-04 -3.5108388E+01 -1.0668253E+01
 1.6166966E-05  6.3916381E-05 -1.4854467E+02 -2.1565603E+01
 1.3960425E-06  1.3097212E-05 -6.8051430E+02  1.7298640E+00
-8.2149394E-08  2.4229998E-06 -3.3465467E+03  4.9352935E+02
```

We integrate over each layer separately to get the total absorbed power and compare this result with the Poynting vector analysis. The following data shows the comparison of these two calculations.

```
1.453240960E-005  total absorbed power by vol integration
TOTPOW =   1.453240756E-005 = total absorbed power
as determined by the Poynting vector analysis
completed the call to GAUSS
```

The following shows a comparison between the computation of the radial, theta, and phi components of the electric vector by exact formula and by the vector spherical harmonic expansion.

```
 (  0.000000000E+000 ,  0.000000000E+000 )  = CZERO
c*************************************************
 (  4.952630924E-001 ,  3.601589500E-001 )
 = ERADI(E radial by exact formula in CSM.f)
 (  4.952630924E-001 ,  3.601589500E-001 )
 = ERADIN (E radial in by EVCINC.f) (by the series)
c*************************************************
 ( -4.585376045E-002 ,  1.59206685 )
 = ERADSC (E radial scat from EVCSC.f)
c*************************************************
 (  2.859402797E-001 ,  2.079378668E-001 )
```

```
 = ETHETI (E theta by exact formula in CSM.f )
 (  2.859402797E-001 ,  2.079378668E-001 )
 = ETHEIN (E theta in from EVCINC) (by the series)
c*************************************************
 ( -4.003204705E-001 , -2.150255645E-001 )
 = ETHESC (E theta scat from EVCSC.f
c*************************************************
 ( -5.718805594E-001 , -4.158757335E-001 )
 = EPHII (E phi by exact formula)
 ( -5.718805594E-001 , -4.158757335E-001 )
 = EPHIIN (E phi in from EVCINC.f) (by the series)
c*************************************************
 (  5.255407044E-001 ,  4.396722339E-001 )
 = EPHISC (E phi scat from EVCSC.f)
```

In the following we check to see that the boundary condition which says that the tangential components of the electric vector are continuous across the boundary is indeed satisfied on the digital computer.

```
 (  4.494093320E-001 ,  1.95222580 )  = ERADI+ERADSC
 (  4.494093320E-001 ,  1.95222580 )  = ERAD
 ( -1.143801908E-001 , -7.087697742E-003 )  = ETHETI+ETHESC
 ( -1.143801908E-001 , -7.087697742E-003 )  = ETHETA
 ( -4.633985508E-002 ,  2.379650041E-002 )  = EPHII+EPHISC
 ( -4.633985508E-002 ,  2.379650041E-002 )  = EPHI
```

The following are intermediate printouts showing the Mueller matrix call and the testing of the surface integration routine with a function of θ and ϕ whose surface integral is known.

```
  We are about to call MMEVEI
 (  1.00000000 ,  0.000000000E+000 )  = CEX before CALL MMEVEI
  We have finished CALL MMEVEI
 Layer no          radius       thickness
 1  5.2700000E-02  0.0000000E+00
 2  5.4700000E-02  2.0000000E-03
 3  5.5200000E-02  5.0000000E-04
 4  5.8000000E-02  2.8000000E-03
 5  5.9000000E-02  1.0000000E-03
 6  6.0000000E-02  1.0000000E-03
  6.000000000E-002  = RADIUS in GETEC.f
  6.000000000E-002  = BDP(NORG) in GETEC.f
 (  1.25750702 ,  0.000000000E+000 )  = ZBFA in GETEC.f
  Finished calling Bessel functions in GETEC.f
 (  9.402474840E-002 , -2.02467295 )  = h_2(FKP(NORG+1)*RADIUS)
  Finished CALL BJYH in GETEC.f
```

```
16  = NC after CALL BJYH in GETEC.f
14  = NMIN after CALL BJYH in GETEC.f
 About to call SURINC with FNTST as arg.
 6.0000000E-02   16    0    2    2 = RADIUS,NGQPTS,ISIND,NSITH,NSIPH
(  1.440000000E+001 ,  4.114285714E+001 )  =
  (output from SURINC with FNTST)/(PI*RADIUS**2)
 1.440000000E+001  = exact value of real part
 4.114285714E+001  = exact value of imag part
```

We next test the ability of SURINC to extract the expansion coefficients by integrating the inner product of the full electric vector of the scattered radiation with a vector spherical harmonic that is part of the complete orthogonal system that forms a base of the Hilbert space in which the electric vector is represented.

```
  We are about to call SURINC with FUNAL as arg
\par
    The following output shows a comparison between numerically
computed $\alpha$ expansion coeficient using surface integration
of an inner product of the electric vector of the scattered
radiation and a vector spherical harmonic and the coefficient
computed directly by the Mie solution.
\begin{verbatim}
c*********************************************
 ( -1.507217348E-002 , -3.036661101E-002 )
 = Computed ALPHA expansion coefficient
 ( -1.507217348E-002 , -3.036661101E-002 )
 = ALPNP(NORG*NMIN+NVAL) (by exact formula)
 (  1.00000000 , -2.750070753E-016 )  =
  ALPHC/ALPNP(NORG*NMIN+NVAL)
c*********************************************
 86  = NORG*NMIN+NVAL
  6.0000000E-02   16    0    4    4 = RADIUS,NGQPTS,ISIND,NSITH,NSIPH
 6  = NORG
 14  = NMIN
 86  = NORG*NMIN+2
 2  = NVAL
c*****************************************
 ( -2.702826945E-002 ,  8.883191962E-002 )
 = BETNM from GETEC.f after call SURINC
 ( -2.702826945E-002 ,  8.883191962E-002 )
 = BETNP(NORG*NMIN +2) (by exact formula)
 (  1.00000000 ,  7.149399175E-017 )  =BETNM/BETNP(N)
   gives the ratio of the SURINC output and the exact value.
c*********************************************
```

```
 1  = NVAL
 ( -5.323296461E-001 ,  3.592983774E-001 )
 = BETNM from GETEC.f after call SURINC
 ( -5.323296461E-001 ,  3.592983774E-001 )
 = BETNP(NORG*NMIN +1) (by exact formula)
 (  1.000000000E+000 , -3.582105228E-016 )
 =BETNM/BETNP(N) (ratio of SURINC determined and exact values)
 85  = NORG*NMIN+1
c*************************************************
 (  5.37080280 ,  4.35841241 )
 = BETANM(1)/BETANM(2) (numerical expansion coefficient ratio)
 (  5.37080280 ,  4.35841241 )  =
  BETNP(NORG*NMIN+1)/BETNP(NORG*NMIN+2) (exact ratio)
 (  1.89851672 , -6.126018911E-001 )  = BHNP(NVAL+2)/BHNP(NVAL+1)
 (  1.286653062E+001 ,  4.98435490 )
 = BTNM1/BTNM2*CHFR12
 (  1.286653062E+001 ,  4.98435490 )
 = Beta1/Beta2 * Hankel2/Hankel1
c*************************************************
c
c*************************************************
 3  = NVAL
 ( -3.302310388E-004 ,  3.555414103E-003 )
 = BETNM from GETEC.f after call SURINC
 ( -3.302310388E-004 ,  3.555414103E-003 )
 = BETNP(NORG*NMIN +3) (by exact formula)
 (  1.00000000 , -2.161700745E-015 )
 =BETNM/BETNP(N) (ratio of SURINC and exact formula values)
 87  = NORG*NMIN+3
c*************************************************
 (  2.547131556E+001 ,  5.23619751 )  = BETANM(2)/BETANM(3)
 (  2.547131556E+001 ,  5.23619751 )  =
  BETNP(NORG*NMIN+1)/BETNP(NORG*NMIN+2)
 (  1.89851672 , -6.126018911E-001 )  = BHNP(NVAL+3)/BHNP(NVAL+2)
 (  1.774781418E+002 ,  3.647265045E+001 )
 = BTNM2/BTNM3*CHFR23  (SURINC determined ratios)
 (  1.774781418E+002 ,  3.647265045E+001 )
 = Beta2/Beta3 * Hankel3/Hankel2 (exact formula ratios)
c*************************************************
    I        BDPFN(I)        EPSPF(I)        SIGPF(I)
    1  5.2700000E-02  6.0000000E+01  9.0000000E-01 in FUNC.f
    2  5.4700000E-02  7.6000000E+01  1.7000000E+00 in FUNC.f
    3  5.5200000E-02  4.5000000E+01  1.0000000E+00 in FUNC.f
```

```
   4  5.8000000E-02  8.5000000E+00  1.1000000E-01 in FUNC.f
   5  5.9000000E-02  5.5000000E+00  8.0000000E-02 in FUNC.f
   6  6.0000000E-02  4.5000000E+01  1.0000000E+00 in FUNC.f
 Test of subroutine FUNC
FVEC(I) ALPFN or BETFN ALPNP or BETNP
-1.5639835E-01 -1.5639835E-01 -1.5639835E-01
-2.3334588E-01 -2.3334588E-01 -2.3334588E-01
-5.3232965E-01 -5.3232965E-01 -5.3232965E-01
 3.5929838E-01  3.5929838E-01  3.5929838E-01
-1.5072173E-02 -1.5072173E-02 -1.5072173E-02
-3.0366611E-02 -3.0366611E-02 -3.0366611E-02
-2.7028269E-02 -2.7028269E-02 -2.7028269E-02
 8.8831920E-02  8.8831920E-02  8.8831920E-02
-1.3271589E-03 -1.3271589E-03 -1.3271589E-03
-1.2307263E-03 -1.2307263E-03 -1.2307263E-03
-3.3023104E-04 -3.3023104E-04 -3.3023104E-04
 3.5554141E-03  3.5554141E-03  3.5554141E-03
-2.8230504E-05 -2.8230504E-05 -2.8230504E-05
-1.4539905E-05 -1.4539905E-05 -1.4539905E-05
-5.4127263E-06 -5.4127263E-06 -5.4127263E-06
 8.1250403E-05  8.1250403E-05  8.1250403E-05
-4.8707312E-07 -4.8707312E-07 -4.8707312E-07
-2.7316679E-07 -2.7316679E-07 -2.7316679E-07
-7.9921910E-08 -7.9921910E-08 -7.9921910E-08
 1.2649466E-06  1.2649466E-06  1.2649466E-06
c*************************************************
```

Above is a comparison of FUNC created and original expansion coefficients determined by exact formula. We determine sphere properties by allowing arguments of FUNC to range and finding those values which cause a match of known expansion coefficients and those determined by FUNC.

A function similar to FUNC is passed as an EXTERNAL variable argument into the Levinberg Marquardt algorithm subroutine and when the minimization algorithm has recovered the sphere properties the expected differences in expansion coefficient values should be zero. The following table shows the actual values after the minimization program successfully terminated.

```
c*************************************************
  Printing out FVEC values from FUNCD
  9.0901279E-15  1.2844746E-15  4.8402967E-15 -1.2273610E-14
 -3.3157996E-14  2.4561479E-15 -8.8181479E-15  3.2133929E-14
  3.0190224E-14  2.2283261E-14 -6.2852876E-15  4.9189207E-14
 -1.0146840E-13 -4.2892005E-14  2.0803826E-17  8.2216722E-14
 -5.6499749E-14  3.1852208E-14  2.1301647E-15  1.1561364E-13
NOHUPOUT
```

40 Applicability

By removal of noise from the data prior to processing one could possibly transmit field data to a computer with many processors working in parallel to discriminate between layered particles which would probably be man made and could be a source of concern and nonlayered particles such as ordinary water droplets just by using scattering data. Perhaps hundreds of coherent gated laser beams could be created by crystals and could be made to overlap significantly on an arbitrarily small remote volume thereby permitting droplet interrogation at some distance from the cloud droplet or droplets could be sucked into an autofunctioning nephelometer that would transmit its "measurements" to a site that would be capable of processing the measurements.

References

[1] Cohoon, D. K. "On the uniqueness of solutions of electromagnetic interaction problems associated with scattering by bianisotropic bodies" *IN* Rassias, George (Editor) *The Mathematical Heritage of C. F. Gauss.* Singapore: World Scientific Publishing (1991) pp 119 - 132

[2] More, J. J. "The Levinberg-Marquardt Algorithm: Implementation and Theory" *IN* Watson, G. A. (Editor) *Numerical Analysis* New York: Springer Verlag (1977)

Computer Learning and Rapid Analysis of Methane Combustion

Michael Frenklach,
Suyang Sun,
and D. K. Cohoon

March 4, 1993

We show how a computer can learn how to approximate processes in complex chemical reactions with high accuracy. This has applications in the improvement of the design of aircraft engines, power plants, and the processes used for the destruction of toxic chemicals.

We describe the chemistry of methane combustion and the conservation laws associated with a one dimensional flame. Our motivation is to develop a way of understanding chemical reactions occurring in a flame with a view toward reducing harmful emissions.

Contents

1 INTRODUCTION
- 1.1 Uniqueness of the Premixed Flame Problem
- 1.2 Approximations in Concentration Space
- 1.3 Local Chemical Reactions
- 1.4 Chemical Kinetic Differential Equations
- 1.5 Vector Analysis
- 1.6 Energy Equations
- 1.7 EQUATION OF STATE

2 SUMMARY

3 FLAME THEORY
- 3.1 Multicomponent Diffusion
- 3.2 Conservation of Species and Energy

References

1 INTRODUCTION

We try to improve computation time by for each species approximating growth and destruction rates for species of interest in local regions of concentration space. We have exact formulae for the concentrations and try to get the program to learn how to make highly accurate local approximations. The accuracy turns out to be important if you happen to be in a region of concentration space where the net rates are changing from increasing rates to decreasing rates. The situation of a decreasing net rate holds if the positive rate of production arising from an approximation of the forward rates of creation minus the positive rate of destruction is a negative number. Numerical round off error occurs when these two numbers would quite correctly agree to d decimal places and the accuracy of each approximate does not exceed this number of decimal places. If approximations of rates or even if one is numerically solving the full problem one has to be sure that the method of solution has enough accuracy to avoid this type of round off error. A high level of approximation can be achieved with a low order polynomial provided that the domain of the polynomial is a sufficiently small region of chemical concentration space. A high enough order of the method for solving the differential equations must also be used.

The objective of the work is to determine a method of making the flame calculations with great speed and accuracy so that burners can be redesigned to reduce dangerous emissions. We are testing our ideas with a one dimensional premixed flame program. To understand the mathematics associated with the computer program we write out the basic boundary value problem and show that there is only one solution in a space of sufficiently regular functions.

1.1 Uniqueness of the Premixed Flame Problem

In the premixed flame problem we assume that the concentrations of the chemicals quickly reach a steady value and then calculate local concentration of chemical species and temperature. In ([70]) the boundary value problem requires solution of the differential equations giving the mass fraction Y_k of the kth species and the temperature. We begin by

defining the quantities, where

T	=	the temperature
Y_k	=	mass fraction of kth species
p	=	the pressure
W_k	=	molecular weight of kth species
ρ	=	the mass density
$(d/dt)\omega_k$	=	molar production rate of kth species
c_p	=	mixture heat capacity at constant p
$c_{(p,k)}$	=	kth species heat capacity at constant p
V_k	=	kth species diffusion velocity
h_k	=	kth species specific enthalpy
$\overline{W}$	=	the average molecular weight
R	=	the universal gas constant
ϕ	=	reactant stream equivalence ratio
T_u	=	the unburnt temperature, and
$\epsilon_k(\phi)$	=	incoming kth species mass flux fraction

We then solve the differential equations,

$$\frac{dM}{dt}\frac{dY_k}{dx} + \frac{d}{dx}(\rho Y_k V_k) - \frac{d\omega_k}{dt}\cdot W_k = 0 \;(\; k \in \{1, 2, \cdots K\}\;) \tag{1.1.1}$$

and

$$c_p \frac{dM}{dt}\frac{dT}{dx} - \frac{d}{dx}\left(\lambda \frac{dT}{dx}\right) + \sum_{k=1}^{K}\left(\rho \cdot Y_k \cdot V_k \cdot c_{(p,k)}\frac{dT}{dx}\right) + \sum_{k=1}^{K}\frac{d\omega_k}{dt}\cdot h_k W_k = 0 \tag{1.1.2}$$

subject to the boundary conditions,

$$T(0) = 0 \tag{1.1.3}$$

$$\frac{dM}{dt}\cdot Y_k(0) + \rho(0)\cdot Y_k(0)\cdot V_k(0) = \frac{dM}{dt}\cdot \epsilon_k(\phi) \tag{1.1.4}$$

for k in $\{1, 2, \cdots K\}$ and

$$\lambda(0)\frac{dT}{dx}(0) = \sum_{k=1}^{K}\epsilon_k(\phi)\left[h_k(T(0)) - h_k(T_u)\right] \tag{1.1.5}$$

as well as

$$\underset{x \to \infty}{LIM}\left(\frac{dT}{dx}\right) = 0 \tag{1.1.6}$$

and

$$\underset{x \to \infty}{LIM}\left(\frac{dY_k}{dx}\right) = 0 \;\; k = 1, \ldots, K \tag{1.1.7}$$

In practice in a computer program the limits (1.1.6) and (1.1.7) are replaced by precise values at an x that is remote from the initial value.

We now show that under suitable regularity conditions on the temperature T and the mass fractions Y_k there is at most one set of functions T and Y_1 through Y_K which satisfy equations (1.1.2) and (1.1.1) subject to the boundary conditions (1.1) , (1.1.5), and (1.1.4) and the conditions at infinity (1.1.7) and (1.1.6). We let T be the difference of two possibly different temperatures and let Y_k now denote the difference between two possibly different mass fractions of the kth chemical species that appears in the flame. We assume that the *unburnt temperature* T_u is a constant.

We use a variational formulation and dual space arguments to verify uniqueness of the solution of the premixed flame boundary value problem. Letting T now denote the difference between two temperature distributions in a nonunique solution we have upon multiplying all terms of equation (
refeq: xtoinftyoftemperature) by the derivative of T and integrating from x equal zero to x equal ∞ we deduce that

$$\int_0^\infty \left[c_p \frac{dM}{dt} \cdot \frac{dT}{dx} \cdot \frac{dT}{dx} - \frac{dT}{dx} \cdot \frac{d}{dx}\left(\lambda \cdot \frac{dT}{dx}\right)\right] dx +$$

$$\sum_{k=1}^{K} \int_0^\infty \left(\rho \cdot Y_k \cdot V_k \cdot c_{(p,k)} \frac{dT}{dx}\right) \cdot \frac{dT}{dx} dx = 0 \qquad (1.1.8)$$

Integrating the high order derivative term in (1.1.8) we deduce that

$$\int_0^\infty \left[c_p \frac{dM}{dt} \cdot \left(\frac{dT}{dx}\right)^2 \cdot \right] dx - \frac{1}{2} \cdot \underset{x \to \infty}{LIM} \left(\lambda \cdot \frac{dT}{dx}\right)^2 +$$

$$+ \lambda \cdot \left(\frac{dT}{dx}(0)\right)^2 + \sum_{k=1}^{K} \int_0^\infty \left[\rho \cdot Y_k \cdot V_k \cdot c_{(p,k)} \left(\frac{dT}{dx}\right)^2\right] dx = 0 \qquad (1.1.9)$$

As the integrated term involving the derivative of temperature at 0 is positive and the temperature derivative goes to zero far away from the flame, we see that equation (1.1.9), which is a sum of nonnegative terms being equal to zero, tells us that the temperature difference is identically zero.

It is even easier to show that there is at most one solution of the concentration equation as these equations are first order. The uniqueness of the solution of this equation based on the uniqueness of the solution of the Cauchy problem since the differential equation (1.1.1) has the same form as the differential equation.

$$\frac{dY_k}{dx} + f(x, Y_k) = 0 \qquad (1.1.10)$$

subject to the initial condition (1.1.4) which may be transformed into the initial condition

$$Y_k(0) = A \qquad (1.1.11)$$

1.2 Approximations in Concentration Space

We approximate the chemical reactions of methane by relating the rates $(\partial/\partial t)\omega_{(p,i)}$ of production of species i, the rates $(\partial/\partial t)\omega_{(d,i)}$ of destruction of species i to the logarithms of the concentrations X_j of all participating species on sufficiently small compact subsets of concentration space by the rule,

$$\ell n\left(\frac{\partial\omega_{(p,i)}}{\partial t}\right) = a_0 + \sum_{j=1}^{N} a_j \cdot \ell n(X_j) + \sum_{j}^{N}\left[\sum_{k}^{N}\left[a_{(j,k)}\ell n(X_j)\cdot \ell n(X_k)\right]\right] \tag{1.2.1}$$

If we let the positive quantity A_0 be defined by

$$a_0 = \ell n(A_0) \tag{1.2.2}$$

then

$$\ell n((\partial/\partial t)\omega_{(p,i)}) = \ell n\left(A_0\cdot\left(\prod_{j=1}^{N} X_j^{a_j}\right)\cdot\left[\prod_{j=1}^{N}\left[\prod_{k=1}^{N} X_j^{a_{(j,k)}\cdot \ell n(X_k)}\right]\right]\right) \tag{1.2.3}$$

This would mean that the positive rate of production of species i is given by

$$((\partial/\partial t)\omega_{(p,i)}) = \left(A_0\cdot\left(\prod_{j=1}^{N} X_j^{a_j}\right)\cdot\left[\prod_{j=1}^{N}\left[\prod_{k=1}^{N} X_j^{a_{(j,k)}}\cdot \ell n(X_k)\right]\right]\right) \tag{1.2.4}$$

which is not the usual form of a chemical rate. However, we can approximate this rate with arbitrary accuracy by a polynomial of degree two in the logarithms of the concentrations just by making the domain of approximation a sufficiently small compact subset of concentration space. Furthermore, if these approximates of production rates and destruction rates are sufficiently accurate, then we could approximate the net production rate by

$$\frac{\partial\omega_i}{\partial t} = \frac{\partial\omega_{(p,i)}}{\partial t} - \frac{\partial\omega_{(d,i)}}{\partial t} \tag{1.2.5}$$

even though the actual chemical reaction rates are those described in the next section. By comparison of the exact rates with these approximate rates we can have the computer find zones of accuracy of the approximations by comparing the exact formulae for the rates with the approximate formula over the specific compact subset of concentration space. By computer learning, then we run the actual program whenever we move during the course of solution into a domain of concentration space for which we do not have an approximation scheme of known accuracy.

To estimate accuracy numerically over a compact subset of a higher dimensional concentration space we need a design for a computer experiment (Sacks [64]) to decide how to sample a region of concentration space to compare our exact formulae and the approximating chemical reaction rates and to validate the use of these approximating rates in a faster code with the rates used in the n[illegible]neral flame code.

1.3 Local Chemical Reactions

A summary of the literature treating the complex methane combustion reactions including

- hydrogen oxygen reactions,
- carbon monoxide and hydroxyl reactions
- HCO radical reactions,
- CH and CH_2 radical reactions,
- CH_3 radical and oxygen molecule reactions,
- CH_3O and CH_2OH reactions, and
- methane reactions

and the associated rates are given in the paper of Frenklach, Wang, and Rabinowitz ([29])

The paper of Smooke and Giovangigli ([70]) and Peters ([59]) describe methane combustion. The smallest number of key reactions ([70]) that are considered are 25. Our purpose here is to write down the differential equations describing the rates at which the concentrations of the chemicals involved in these reactions change. We begin by writing down the chemical reactions. A forward reaction involving the hydrogen free radical is

$$H^{\cdot} + O_2 \rightarrow OH^{\cdot} + O^{\cdot} \tag{1.3.1}$$

with a skelatal rate coefficient given by

$$k_{(1,f)} = 2. \times 10^{14} \times T^0 \times exp(-16800/(R \cdot T))$$

and the associated backward reaction is

$$OH^{\cdot} + O^{\cdot} \rightarrow H^{\cdot} + O_2 \tag{1.3.2}$$

whose skelatal rate coefficient is given by

$$k_{(1,b)} = 1.575 \times 10^{13} \times T^0 \times exp(-690/(R \cdot T))$$

An oxygen radical and the hydrogen molecule interact to form a hyroxyl and a hydrogen radical in the reaction

$$O^{\cdot} + H_2 \rightarrow OH^{\cdot} + H^{\cdot} \tag{1.3.3}$$

with a skelatal rate constant of

$$k_{(2,f)} = 1.8 \times 10^{10} \times T \times exp(-8826/(R \cdot T))$$

The corresponding backward reaction is

$$OH^{\cdot} + H \rightarrow O^{\cdot} + H_2 \tag{1.3.4}$$

with skelatal rate constant

$$k_{(2,b)} = 8 \times 10^9 \times T \times exp(-6760/(R \cdot T))$$

The hydrogen molecule and hydroxyl radical combine to form a water molecule and a hydrogen radical in the reaction

$$H_2 + OH^{\cdot} \rightarrow H_2O + H^{\cdot} \tag{1.3.5}$$

with skelatal rate constant

$$k_{(3,f)} = 1.17 \times 10^9 \times T^{1.3} \times exp(-3626/(R \cdot T))$$

The associated backwards reaction is

$$H_2O + H^{\cdot} \rightarrow H_2 + OH^{\cdot} \tag{1.3.6}$$

with skelatal rate constant

$$k_{(3,b)} = 5.09 \times 10^9 \times T^{1.3} \times exp(-18588/(R \cdot T))$$

Two hydroxyl radicals can combine to form an oxygen radical and water in the reaction

$$OH^{\cdot} + OH^{\cdot} \rightarrow O^{\cdot} + H_2O \tag{1.3.7}$$

with a skelatal rate constant given by ([70])

$$k_{(4,f)} = 6 \times 10^8 \times T^{1.3} \times$$

The reverse reaction has the form

$$O^{\cdot} + H_2O \rightarrow OH^{\cdot} + OH \tag{1.3.8}$$

where the skelatal rate constant has the form.

$$k_{(4,b)} = 5.9 \times 10^9 \times T^{1.3} \times exp(-17029/(R \cdot T))$$

There are several reactions where a substance called M representing other molecular moieties stimulates a reaction just by collision. The first of these has the form

$$H^{\cdot} + O_2 + M \rightarrow HO_2mbox + M \tag{1.3.9}$$

with a skelatal rate constant given by

$$k_{(5,f)} = 2.3 \times 10^{18} \times T^{-0.8}$$

$$H^{\cdot} + HO_2^{\cdot} \rightarrow OH^{\cdot} + OH \tag{1.3.10}$$

with a skelatal rate constant of

$$k_{(6,f)} = 1.5 \times 10^{14} \times exp(-1004/(R \cdot T))$$

The same two radicals may produce a different response given by

$$H^{\cdot} + HO_2^{\cdot} \rightarrow H_2 + O_2 \tag{1.3.11}$$

with a skelatal rate constant of

$$k_{(7,f)} = 2.5 \times 10^{13} \times exp(-700/(R \cdot T))$$

Another reaction with radicals which reproduces water and oxygen molecules is

$$OH^{\cdot} + HO_2^{\cdot} \rightarrow H_2O + O_2 \tag{1.3.12}$$

with an associated skelatal rate constant of

$$k_{(8,f)} = 2. \times 10^{13} \times exp(-1000/(R \cdot T))$$

When methane burns in air, carbon monoxide can be produced and this can react with a hydroxyl radical to give back carbon dioxide and a hyrdogen radical as indicated by the relation,

$$CO^{\cdot} + OH^{\cdot} \rightarrow CO_2 + H^{\cdot} \tag{1.3.13}$$

whose skelatal rate constant is

$$k_{(9,f)} = 1.51 \times 10^{7} \times T^{1.3} \times exp(758/(R \cdot T))$$

A backward reaction has the form

$$CO_2 + H^{\cdot} \rightarrow CO^{\cdot} + OH^{\cdot} \tag{1.3.14}$$

with a skelatal rate constant of

$$k_{(9,b)} = 1.51 \times 10^{7} \times T^{1.3} \times exp(-22337/(R \cdot T))$$

A hot methane interaction with a moiety M giving two radicals is denoted in the relation,

$$CH_4 + M \rightarrow CH_3^{\cdot} + H^{\cdot} + M \tag{1.3.15}$$

with a skelatal rate constant of

$$k_{(10,f)} = 6.3 \times 10^{14} \times T^{0} \times exp(-104000/(R \cdot T))$$

and the backward reaction is

$$CH_3^{\cdot} + H^{\cdot} + M \rightarrow CH_4 + M \tag{1.3.16}$$

with a rate constant of

$$k_{(10,b)} = 5.2 \times 10^{12} \times T^{0} \times exp(1310/(R \cdot T))$$

A reaction with methane and a hydrogen radical which can produce a CH_3 radical and hydrogen gas is

$$CH_4 + H^{\cdot} \rightarrow CH_3 + H_2 \tag{1.3.17}$$

with a rate constant of

$$k_{(11,f)} = 2.2 \times 10^{14} \times T^3 \times exp(-8750/(R \cdot T))$$

The reverse reaction is

$$CH_3 + H_2 \rightarrow CH_4 + H^{\cdot} \tag{1.3.18}$$

with a rate constant of

$$k_{(11,b)} = 9.570 \times 10^2 \times T^3 \times exp(-8750/(R \cdot T))$$

Another methane reaction is

$$CH_4 + OH \rightarrow CH_3 + H_2O \tag{1.3.19}$$

with a rate constant of

$$k_{(12,f)} = 1.6 \times 10^6 \times T^{2.1} \times exp(-2460/(R \cdot T))$$

and the backward reaction is

$$CH_3 + H_2O \rightarrow CH_4 + OH^{\cdot} \tag{1.3.20}$$

with a rate constant of

$$k_{(12,b)} = 3.020 \times 10^5 \times T^{2.1} \times exp(-17422/(R \cdot T))$$

A reaction between a CH_3 radical and an oxygen radical is

$$CH_3^{\cdot} + O^{\cdot} \rightarrow CH_2O + H^{\cdot} \tag{1.3.21}$$

with a rate constant given by

$$k_{(13,f)} = 6.8 \times 10^{13}$$

A reaction reducing CH_2O concentration is

$$CH_2O + H^{\cdot} \rightarrow HCO^{\cdot} + H_2 \tag{1.3.22}$$

with a rate constant given by

$$k_{(14,f)} = 2.5 \times 10^{13} \times T^0 \times exp(-3991/(R \cdot T))$$

A second reaction reducing CH_2O concentration is

$$CH_2O + OH^{\cdot} \rightarrow HCO^{\cdot} + H_2O \tag{1.3.23}$$

with a rate constant of

$$k_{(15,f)} = 3. \times 10^{13} \times T^0 \times exp(-1195/(R \cdot T))$$

A reaction involving the reduction of concentration of the hydrogen radical is

$$HCO^{\cdot} + H \rightarrow CO + H_2 \tag{1.3.24}$$

with a rate constant of

$$k_{(16,f)} = 4. \times 10^{13} \times T^0 \times exp(-0/(R \cdot T))$$

A hot collision reaction involving the $HCO^{\cdot}$ radical bumping into the molecular moiety M is

$$HCO^{\cdot} + M \rightarrow CO^{\cdot} + H^{\cdot} + M \tag{1.3.25}$$

has the reaction rate ([70])

$$k_{(17,f)} = 1.6 \times 10^{14} \times T^0 \times exp(-14700/(R \cdot T))$$

The CH_3 radical and the oxygen molecule have the reaction

$$CH_3 + O_2 \rightarrow CH_3O^{\cdot} + O^{\cdot} \tag{1.3.26}$$

whose rate constant ([70]) is

$$k_{(18,f)} = 7. \times 10^{12} \times T^0 \times exp(-25652/(R \cdot T))$$

A reaction involving the CH_3^{O}. radical and the hydrogen radical given by

$$CH_3O^{\cdot} + H^{\cdot} \rightarrow CH_2O + H_2 \tag{1.3.27}$$

has the rate constant ([70])

$$k_{(19,f)} = 2. \times 10^{13}$$

A hot interaction of the $CH_3O^{\cdot}$ radical with another unchanged moiety M is

$$CH_3O^{\cdot} + M \rightarrow CH_2O + H^{\cdot} + M \tag{1.3.28}$$

has the reaction rate

$$k_{(20,f)} = 2.4 \times 10^{13} \times exp(-28812/(R \cdot T))$$

The $HO_2^{\cdot}$ radical interacts with itself in the reaction

$$HO_2^{\cdot} + HO_2^{\cdot} \rightarrow H_2O_2 + O_2 \tag{1.3.29}$$

with the reaction rate

$$k_{(21,f)} = 2. \times 10^{12}$$

Hydrogen peroxide interacts with a hot moiety M according to the reaction.

$$H_2O_2 + M \rightarrow OH^{\cdot} + OH^{\cdot} + M \tag{1.3.30}$$

with a rate constant given by

$$k_{(22,f)} = 1.3 \times 10^{17} \times exp(-45500/(R \cdot T)) Hydrogen\ peroxide$$

In a higher order interaction two hydroxyl radicals together collide with a molecular moiety M in the reaction

$$OH + OH + M \rightarrow H_2O_2 + M \tag{1.3.31}$$

with a rate constant of

$$k_{(22,b)} = 9.86 \times 10^{14} \times exp(5070/(R \cdot T))$$

Hydrogen peroxide can interact with a hydroxyl radical in the reaction,

$$H_2O_2 + OH^{\cdot} \rightarrow H_2O + HO_2^{\cdot} \tag{1.3.32}$$

with a rate constant of

$$k_{(23,f)} = 1. \times 10^{13} \times exp(-1800/(R \cdot T))$$

The reverse reaction that creates hydrogen peroxide is

$$H_2O + HO_2^{\cdot} \rightarrow H_2O_2 + OH^{\cdot} \tag{1.3.33}$$

and has the rate constant

$$k_{(23,b)} = 1. \times 10^{13} \times exp(-32790/(R \cdot T))$$

The hydroxyl radical and a hydrogen ion react by a hot collision with another molecular moiety M by the reaction.

$$OH^{\cdot} + H^{\cdot} + M \rightarrow H_2O + M \tag{1.3.34}$$

with a rate constant of

$$k_f = 2.2 \times 10^{22} \times T^{-2}$$

In the last reaction that we consider two hydrogen ions interact with a molecular moiety M in the reaction

$$H^{\cdot} + H^{\cdot} + M \rightarrow H_2 + M \tag{1.3.35}$$

1.4 Chemical Kinetic Differential Equations

We have to solve the chemical kinetic differential equations very accurately. In the previous section we listed 35 chemical reactions involving 14 molecules or molecular moeities and the unaffected hot third body [M] which collides with a reagent or reagents but itself is unchanged during the reaction. The local chemistry is described by 14 ordinary differential equations at each spatial point but the concentrations as a whole are described by reaction diffusion equations. Using the notation of the previous section the ordinary differential equation for hydrogen ion or $[H^{\cdot}]$ concentration is

$$\frac{d[H]}{dt} = -k_{(1,f)}[H^{\cdot}] \cdot [O_2] + k_{(1,b)}[OH^{\cdot}] \cdot [O^{\cdot}]$$

$$- k_{(2,b)}[OH^{\cdot}] \cdot [H]^{\cdot} + k_{(2,f)}[O^{\cdot}] \cdot [H_2] - k_{(3,b)}[H_2O] \cdot [H^{\cdot}] + k_{(3,f)}[H_2] \cdot [OH^{\cdot}] +$$

$$- k_{(5,f)}[H^{\cdot}] \cdot [O_2] \cdot [M] - k_{(6,f)} \cdot [H^{\cdot}][H_2O] - k_7[H^{\cdot}] \cdot [HO_2] +$$

$$k_{(9,f)}[CO^{\cdot}] \cdot [OH^{\cdot}] - k_{(9,b)}[CO_2] \cdot [H^{\cdot}] +$$

$$+ k_{(10,f)} \cdot [CH_4][M] - k_{(10,b)} \cdot [CH_3^{\cdot}] \cdot [H] \cdot [M]$$
$$- k_{(11,f)} \cdot [CH_4][H] + k_{(11,b)} \cdot [CH_3^{\cdot}] \cdot [H_2]$$
$$+ k_{(13,f)} \cdot [CH_3^{\cdot}] \cdot [O^{\cdot}] - k_{(14,f)} \cdot [CH_2O] \cdot [H^{\cdot}]$$
$$- k_{16} \cdot [HCO^{\cdot}] \cdot [H^{\cdot}] + k_{17} \cdot [HCO^{\cdot}] \cdot [M]$$
$$- k_{19} \cdot [CH_3O] \cdot [M] + k_{20} \cdot [CH_3O^{\cdot}] \cdot [M]$$
$$- k_{24} \cdot [OH^{\cdot}] \cdot [H^{\cdot}] \cdot [M]$$
$$- k_{25} \cdot [H]^2 \cdot [M] \qquad (1.4.1)$$

The ordinary differential equation for the oxygen molecule concentration is

$$\frac{d[O_2]}{dt} = - k_{(1,f)} \cdot [H][O_2^{\cdot}] + k_{(1,b)} \cdot [OH^{\cdot}][O^{\cdot}]$$
$$- k_5 \cdot [H^{\cdot}] \cdot [O_2] \cdot [M] + k_8 \cdot [OH^{\cdot}] \cdot [HO_2^{\cdot}]$$
$$- k_{18}[CH_3^{\cdot}] \cdot [O_2] + k_{21} \cdot [HO_2^{\cdot}]^2 \qquad (1.4.2)$$

The differential equation for the hydroxyl radical $[OH]$ is given by

$$\frac{d}{dt}[OH^{\cdot}] = k_{(1,f)}[H^{\cdot}][O_2] - k_{(1,b)}[OH^{\cdot}][O^{\cdot}]$$
$$+ k_{(2,f)}[O][H_2] - k_{(2,b)}[H_2][OH^{\cdot}] - k_{(3,f)}[H_2][OH^{\cdot}] + k_{(3,b)}[H_2O][H^{\cdot}]$$
$$- k_{(4,f)}[OH^{\cdot}]^2 + k_{(4,b)}[O^{\cdot}][H_2O] + k_{(6,f)}[H][HO_2^{\cdot}] - k_{(9,f)}[CO^{\cdot}][OH^{\cdot}]$$
$$k_{(9,b)}[CO_2][H^{\cdot}] - k_{(12,f)}[CH_4][OH^{\cdot}] + k_{(12,b)}[CH_3^{\cdot}][H_2O] - k_{(15,f)}[CH_2O][OH^{\cdot}]$$
$$+ k_{(22,f)}[H_2O_2][M] - k_{(22,b)}[OH^{\cdot}]^2[M^{\cdot}] - k_{(23,f)}[H_2O_2][OH^{\cdot}]$$
$$+ k_{(23,b)}[H_2O][HO_2^{\cdot}] - k_{(24,f)}[OH^{\cdot}][H^{\cdot}][M^{\cdot}] \qquad (1.4.3)$$

The differential equation for the oxygen radical is given by

$$\frac{d}{dt}[O^{\cdot}] = k_{(1,f)} \cdot [H^{\cdot}][O_2] - k_{(1,b)} \cdot [OH^{\cdot}][O^{\cdot}] - k_{(2,f)} \cdot [O^{\cdot}][H_2]$$
$$+ k_{(2,b)} \cdot [OH^{\cdot}][H^{\cdot}] + k_{(4,f)} \cdot [OH^{\cdot}]^2 -$$
$$k_{(13,f)} \cdot [CH_3^{\cdot}][O^{\cdot}] + k_{(18,f)} \cdot [CH_3][O_2] \qquad (1.4.4)$$

The differential equation for hydrogen gas is

$$\frac{d}{dt}[H_2] = - k_{(2,f)} \cdot [O^{\cdot}][H_2] + k_{(2,b)}[OH^{\cdot}][H^{\cdot}] - k_{(3,f)}[H_2][OH^{\cdot}] + k_{(3,b)}[H_2O][H^{\cdot}]$$
$$+ k_{(7,f)}[H^{\cdot}][HO_2^{\cdot}] + k_{(11,f)}[CH_4][H^{\cdot}] - k_{(11,b)}[CH_3^{\cdot}][H_2] + k_{(14,f)}[CH_2O][H^{\cdot}]$$
$$+ k_{(16,f)}[HCO^{\cdot}][H^{\cdot}] + k_{(19,f)}[CH_3O^{\cdot}][H^{\cdot}] + k_{(25,f)}[H^{\cdot}]^2[M] \qquad (1.4.5)$$

The differential equation for water vapor is given by

$$\frac{d}{dt}[H_2O] = k_{(3,f)}[H_2][OH^{\cdot}] - k_{(3,b)}[H_2O][H^{\cdot}] + k_{(4,f)}[OH^{\cdot}]^2 - k_{(4,b)}[O^{\cdot}][H_2O]$$

$$+ k_{(8,f)}[OH^{\cdot}][HO_2^{\cdot}] + k_{(12,f)}[CH_4][OH^{\cdot}] - k_{(12,b)}[CH_3^{\cdot}][H_2O] + k_{(15,f)}[CH_2O][OH^{\cdot}]$$
$$+ k_{(23,f)}[H_2O_2][OH] + k_{(24,f)}[OH^{\cdot}][H^{\cdot}][M] - k_{(23,b)}[H_2O][HO_2] \quad (1.4.6)$$

The differential equation for the carbon monoxide radical is given by

$$\frac{d}{dt}[CO^{\cdot}] = - k_{(9,f)}[CO^{\cdot}] \cdot [OH^{\cdot}] + k_{(9,b)}[CO_2][H^{\cdot}]$$
$$+ k_{(6,f)}[HCO^{\cdot}][H^{\cdot}] + k_{(17,f)}[HCO^{\cdot}][M] \quad (1.4.7)$$

The differential equation for carbon dioxide is

$$\frac{d}{dt}[CO_2] = k_{(9,f)}[CO^{\cdot}][OH^{\cdot}] - k_{(9,b)}[CO_2][H^{\cdot}] \quad (1.4.8)$$

The differential equation for methane is

$$\frac{d}{dt}[CH_4] =$$
$$- k_{(10,f)}[M][CH_4] + k_{(10,b)}[CH_3^{\cdot}][H^{\cdot}][M]$$
$$- k_{(11,f)}[CH_4][H^{\cdot}] + k_{(11,b)}[CH_3^{\cdot}][H_2]$$
$$- k_{(12,f)}[CH_4][OH^{\cdot}] + k_{(12,b)}[CH_3^{\cdot}][H_2O] \quad (1.4.9)$$

The differential equation for the methyl group radical is

$$\frac{d}{dt}[CH_3^{\cdot}] = k_{(10,f)}[CH_4][M] - k_{(10,b)}[CH_3^{\cdot}][H^{\cdot}][M] + k_{(11,f)}[CH_4][H^{\cdot}]$$
$$- k_{(11,b)}[CH_3^{\cdot}][H_2O] + k_{(12,f)}[CH_4][OH^{\cdot}] - k_{(12,b)}[CH_3^{\cdot}][H_2O] -$$
$$k_{(13,f)}[CH_3^{\cdot}][O^{\cdot}] - k_{(18,f)}[CH_3^{\cdot}][O_2] \quad (1.4.10)$$

The differential equation for $[CH_2O]$ is

$$\frac{d}{dt}[CH_2O] = k_{(13,f)} \cdot [CH_3^{\cdot}] \cdot [O^{\cdot}] - k_{(14,f)} \cdot [CH_2O] \cdot [H^{\cdot}] - k_{(15,f)} \cdot [CH_2O] \cdot [OH^{\cdot}]$$
$$+ k_{(19,f)} \cdot [CH_3O^{\cdot}] \cdot [H^{\cdot}] + k_{(20,f)} \cdot [CH_3O^{\cdot}] \cdot [M] \quad (1.4.11)$$

Next we look at the differential equation for the $[HCO^{\cdot}]$ radical.

$$\frac{d}{dt}[HCO^{\cdot}] = - k_{16} \cdot [HCO^{\cdot}] \cdot [H^{\cdot}] - k_{17} \cdot [HCO^{\cdot}] \cdot [M]$$
$$+ k_{14} \cdot [CH_2O] \cdot [H^{\cdot}] + k_{15} \cdot [CH_2O] \cdot [OH^{\cdot}] \quad (1.4.12)$$

The ordinary differential equation for the $[CH_3O^{\cdot}]$ radical is

$$\frac{d}{dt}[CH_3O^{\cdot}] = k_{18} \cdot [CH_3^{\cdot}] \cdot [O_2] - k_{19} \cdot [CH_3O^{\cdot}] \cdot [H^{\cdot}] - k_{20} \cdot [CH_3O^{\cdot}] \cdot [M] \quad (1.4.13)$$

The 14th and last differential equation involves hydrogen peroxide and is given by

$$\frac{d}{dt}[H_2O_2] = k_{21} \cdot [HO_2^{\cdot}]^2 - k_{(22,f)} \cdot [H_2O_2][M] +$$

$$k_{(22,b)} \cdot [OH^{\cdot}]^2 \cdot [M] \; - \; k_{(23,f)} \cdot [H_2O_2] \cdot [OH^{\cdot}] \; + \; k_{(23,b)} \cdot [H_2O] \cdot [HO_2^{\cdot}] \tag{1.4.14}$$

Using higher order ordinary differential equation solvers, we can in a short period of time obtain rates of creation or destruction of species to machine precision, 10 or 12 decimal places. We may if we wish attempt to model these rates locally by polynomials in the logarithms of the concentrations. By restriction of the domain in concentration space this is always possible. Over a range of temperatures and concentrations we develop a repretoire of approximations which in a highly accurate manner represent the actual rates over compact subsets of the space whose points represent logarithms of concentrations.

1.5 Vector Analysis

The material derivative of a function f is defined by

$$\frac{Df}{Dt} = \frac{\partial f}{\partial t} + \frac{\partial f}{\partial x}\frac{\partial x}{\partial t} + \frac{\partial f}{\partial y}\frac{\partial y}{\partial t} + \frac{\partial f}{\partial z}\frac{\partial z}{\partial t} \tag{1.5.1}$$

Thus, the material derivative is, if we define,

$$\vec{v} = \frac{\partial x}{\partial t}\vec{e}_x + \frac{\partial y}{\partial t}\vec{e}_y + \frac{\partial z}{\partial t}\vec{e}_z \tag{1.5.2}$$

given by

$$\frac{D}{Dt} = \frac{\partial}{\partial t} + (\vec{v} \cdot grad) \tag{1.5.3}$$

where $\vec{v}$ is the velocity of a point in the fluid. We define the velocity as

$$\vec{v} = u\vec{e}_x + v\vec{e}_y + w\vec{e}_z \tag{1.5.4}$$

An important identity involving the dyadic product of two vectors $\vec{A}$ and $\vec{B}$ is

$$div(\vec{A}\vec{B}) = div(\vec{A})\vec{B} + (\vec{A} \cdot grad)\vec{B} \tag{1.5.5}$$

Another important quantity is the tensor or dyadic quantity quantity obtained by taking the gradient of a vector field given by

$$grad(\vec{A}) \; = \; \sum_{i=1}^{n} \left(\frac{\partial A_j}{\partial x_i} \right) \vec{e}_i \vec{e}_j \tag{1.5.6}$$

Any vector field $\vec{U}$ is necessarily a curl plus a gradient given by

$$\vec{U} \; = \; grad(\phi) \; + \; curl(\vec{v}) \tag{1.5.7}$$

This is true for any C^{∞} function defined on an open set in $\mathbf{R}^n$ with values in $\mathbf{C}^n$ for n equal to three or seven, and can be seen from the following lemma ([19]).

Lemma 1.1 *If n is three or seven, then for every open set Ω in $\mathbf{R}^n$ and for every vector field $\vec{F}$ in $C^{\infty}(\Omega, \mathbf{C}^n)$ there is a vector field $\vec{G}$ in the same space such that*

$$\vec{F} = grad(div(\vec{G})) + curl(curl(-\vec{G})) \tag{1.5.8}$$

where if n is equal to seven the curl is defined by the rule,

$$curl(\vec{E}) =$$

$$\sum_{i=1}^{7}\left[\left(\frac{\partial E_{i+3}}{\partial x_{i+1}} - \frac{\partial E_{i+1}}{\partial x_{i+3}}\right) + \right.$$

$$\left.\left(\frac{\partial E_{i+6}}{\partial x_{i+2}} - \frac{\partial E_{i+2}}{\partial x_{i+6}}\right) + \left(\frac{\partial E_{i+5}}{\partial x_{i+4}} - \frac{\partial E_{i+4}}{\partial x_{i+5}}\right)\right]\vec{e}_i \tag{1.5.9}$$

where $\vec{e}_i$ is the unit vector in the direction of the ith coordinate axis in 7 dimensional space and

$$E_{i+7} = E_i \tag{1.5.10}$$

1.6 Energy Equations

If we suppose that the velocity of a fluid point is $\vec{v}$ in terms of its scalar components u, v, and w as in (1.5.4) then for a class of fluids we define the viscous dissipation function Φ by the rule.

$$\Phi = \mu\left[2\left\{\left(\frac{\partial u}{\partial x}\right)^2 + \left(\frac{\partial v}{\partial y}\right)^2 + \left(\frac{\partial w}{\partial z}\right)^2\right\} + \right.$$

$$\left(\frac{\partial v}{\partial x} + \frac{\partial u}{\partial y}\right)^2 + \left(\frac{\partial w}{\partial y} + \frac{\partial v}{\partial z}\right)^2$$

$$\left. + \left(\frac{\partial u}{\partial z} + \frac{\partial w}{\partial x}\right)^2 - \frac{2}{3}\left(\frac{\partial u}{\partial x} + \frac{\partial v}{\partial y} + \frac{\partial w}{\partial z}\right)^2\right] \tag{1.6.1}$$

In these terms the energy equation is given by (Anderson, Tannehill, and Pletcher [1], pages 188-189).

$$\frac{\partial}{\partial t}\left\{\rho e + \frac{\rho\vec{v}\cdot\vec{v}}{2}\right\} =$$

$$-\,div(\rho e\vec{v}) \;+\; \vec{f}\cdot\vec{v} +$$

$$div(\overline{\overline{\Pi}}\cdot\vec{v}) \;-\; div\left(\left(\frac{\rho\vec{v}\cdot\vec{v}}{2}\right)\vec{v}\right) +$$

$$div(\overline{\overline{K}}grad(T)) + \left(\frac{\partial}{\partial t}\right)Q_{in} + \left(\frac{\partial}{\partial t}\right)Q_{out} \tag{1.6.2}$$

We define the enthalpy h as (see Anderson [1], p 188)

$$h = e + \frac{p}{\rho} \tag{1.6.3}$$

where

$e =$ the internal energy including quantum states,
$p =$ the pressure, and
$\rho =$ the density.

To telescope the terms in the energy equation we make use of the vector identity

$$grad(\vec{A}\cdot\vec{B}) = \vec{A}\times curl(\vec{B}) + \vec{B}\times curl(\vec{A}) \; + \\ (\vec{B}\cdot grad)\vec{A} + (\vec{A}\cdot grad)\vec{B} \tag{1.6.4}$$

to observe that

$$\rho\vec{v}\cdot grad\left(\frac{\vec{v}\cdot\vec{v}}{2}\right) = \\ \rho\vec{v}\cdot\{\vec{v}\times curl(\vec{v}) + \vec{v}\cdot grad(\vec{v})\} \tag{1.6.5}$$

Interchanging the dot and cross product in equation (1.6.5) we see that since for an arbitrary vector field $\vec{v}$

$$\vec{v}\cdot(\vec{v}\times curl(\vec{v})) = (\vec{v}\times\vec{v})\cdot curl(\vec{v}) = \vec{0} \tag{1.6.6}$$

it follows that

$$\rho\vec{v}\cdot grad\left(\frac{\vec{v}\cdot\vec{v}}{2}\right) = \rho\vec{v}\cdot\{(\vec{v}\cdot grad)(\vec{v})\} \tag{1.6.7}$$

We can then collapse terms in equation (1.6.2) by observing that the momentum equation implies that

$$\vec{v}\cdot\rho(\vec{v}\cdot grad)\vec{v} = \\ -\rho\frac{\partial\vec{v}}{\partial t}\cdot\vec{v} \\ + \rho\vec{f} - grad(p)\cdot\vec{v} + div(\overline{\overline{\tau}})\cdot\vec{v} \tag{1.6.8}$$

Thus, using equation (1.5.1) and equations (1.6.7) and (1.6.8) the energy equation (1.6.2) may be rewritten in the form.

$$\rho\frac{Dh}{Dt} = \frac{Dp}{Dt} + \\ \left(\frac{\partial}{\partial t}\right)Q_{in} + \left(\frac{\partial}{\partial t}\right)Q_{out} + \\ \Phi - div(\overline{\overline{K}}grad(T)) \tag{1.6.9}$$

where $(\partial/\partial t)\,Q_{in}$ is the internal power density distribution function and Φ is the dissipation function representing the work done by the viscous forces of the fluid. The term representing the transfer by radiation from one part of the fluid to another is given by (Siegel and Howell [68], page 689)

$$\left(\frac{\partial}{\partial t}\right)Q_{out} - div\left(\frac{16\sigma T^3}{3a_R}\cdot grad(T)\right) \tag{1.6.10}$$

This equation may be interpreted as providing a radiation flux across a surface defined by

$$k_r = \frac{16\sigma T^3}{3a_R}. \tag{1.6.11}$$

where a_R is the Rosseland mean absorption coefficient (Siegel [68], p 504 and Rosseland) and where σ (Siegel [68], page 25) is the hemispherical total emissive power of a black surface into vacuum having a value of

$$\sigma = 5.6696\times10^{-8}\ \text{Watts}\ /\ (meters^2\ {}^\circ K) \tag{1.6.12}$$

Using equation (1.6.10) and equation (1.6.2) we see that

$$\rho\frac{De}{Dt} = \left(\frac{\partial}{\partial t}\right) Q_{in} + \left(\frac{\partial}{\partial t}\right) Q_{out} +$$

$$(-p div(\vec{v})) - div(\overline{\overline{K}} grad(T)) + \Phi \tag{1.6.13}$$

where Φ is the viscous dissipation function given by equation (1.6.1)

1.7 EQUATION OF STATE

In the energy equation (1.6.13) the perfect fluid assumption ([1], p 189) would yield

$$\epsilon = c_v T, \tag{1.7.1}$$

where c_v is the specific heat at constant volume, and if we define

$$\gamma = \frac{c_p}{c_v} \tag{1.7.2}$$

where c_p is the specific heat at constant pressure, then the pressure p, the internal energy ϵ and the density ρ are related by ([1], p 189)

$$p = (\gamma - 1)\rho\epsilon \tag{1.7.3}$$

2 SUMMARY

Using the definition of velocity (equation 1.5.4) and the equation of state (1.7.3) we see that the number of equations is 5, allowing 3 equations for the three components of the momentum, and while the intial variables are ρ, u, v, w, p, ϵ, and T, we see that since the temperature T is related to ϵ and since pressure is a function of ρ and ϵ, we see that there are now exactly 5 unknowns.

3 FLAME THEORY

Flame theory can be considered as a system of partial differential equations ([46]) involving

- conservation of mass,
- species creation, diffusion, and transport,
- conservation of momentum,
- conservation of energy, and

- equations of state.

We need several defintions of terms for the formulation of the equations. The variables are

t	=	time
T	=	temperature
ρ	=	density of mixture
Y_k	=	concentration of species k
c_p	=	specific heat of the mixture
$c_{(p,k)}$	=	specific heat of species k
$\vec{u}$	=	velocity of mixture
$D_{(j,k)}$	=	(j,k) entry of species diffusion tensor
$\vec{V}_k$	=	diffusion velocity of species k
Ψ	=	$r^2 \cdot \vec{u}$ equals the stream function for transport down a tube described in cylindrical coordinates, where
r	=	the distance from the axis of the cylinder, and
$\frac{\partial \omega_k}{\partial t}$	=	molar rate of production of species k.

Here, the specific heat of species k and the specific heat of the mixture are related by ([39])

$$c_p = \sum_{k=1}^{n} \left(\frac{\rho_k}{\rho} \right) \cdot c_{(p,k)} \tag{3.0.1}$$

where ρ_k is the density of species k

3.1 Multicomponent Diffusion

One of the more recent developments are the concepts ([22], [46]) of mole fraction differential pressure gradients with the idea that even as a gas is moving along a pipe or a jet aircraft engine with velocity $\vec{u}$ the species or molecular entities are diffusing with individual velocities $\vec{V}_k$ as a result of weighted mole fraction pressure gradients $\vec{d}_k$ and temperature gradients If we suppose that

$$\begin{aligned} p &= \text{pressure} \\ X_k &= \text{mole fraction of species k, and} \\ Y_k &= \text{mass fraction of species k} \end{aligned} \tag{3.1.1}$$

then the weighted mole fraction differential pressure gradient is ([46]) given by

$$\vec{d}_k = grad(\vec{X}_k) + (X_k - Y_k) \cdot grad(p) \tag{3.1.2}$$

and if we let

$$\begin{aligned} W_k &= \text{molecular weight of species k} \\ \overline{W} &= \text{mixture average molecular weight} \\ D_k^T &= \text{the species k thermal diffusion coefficient} \end{aligned} \tag{3.1.3}$$

then the Dixon - Lewis species k diffusion velocity ([22], [46]) (for k running from 1 to N) is given by

$$\vec{V}_k = \left(\frac{1}{X_k \overline{W}}\right) \cdot \left(\sum_{j=1}^{N} W_j D_{(k,j)} \vec{d}_j\right) - \left(\frac{D_k^T}{\rho \cdot Y_k}\right)\left(\frac{grad(T)}{T}\right) \tag{3.1.4}$$

Then using equation (3.1.4) we see that the species k diffusion flux is given by

$$\vec{j}_k = \rho \cdot Y_k \cdot \vec{V}_k \tag{3.1.5}$$

The overall gas velocity contribution of the species k flux is given by

$$J_k = \rho \cdot Y_k \vec{u} \tag{3.1.6}$$

3.2 Conservation of Species and Energy

Using the species diffusion flux (3.1.5) and the species transport flux (3.1.6) and the idea that if the partial derivative with respect to time of ω_k is the molar rate of production of species k from chemical reactions that then the species conservation equation is

$$\rho \frac{\partial Y_k}{\partial t} = div(\vec{j}_k) + div(\rho \cdot Y_k \cdot \vec{u}) + \frac{\partial \omega_k}{\partial t} \tag{3.2.1}$$

where the species diffusion flux $\vec{j}_k$ is given by equation (3.1.5)

The chemical kinetics and species creation processes are an integral part of flame modeling and can be used to describe soot particle nucleation and growth and to understand the type and kind of dangerous materials that can be formed during burning processes (Frenklach and Wang, [31]); in particular we can describe the formation of the PAH, polycyclic aromatic hydrocarbons nucleation and coagulation or growth in premixed flames ([30], [32], [33], [35]). Microscopic equations can account for surface growth of soot particles; the soot formation mechanisms, in spite of intensive study have only recently come to be understood. As a consequence we better understand just how very dangerous to health these particles really are.

We now turn our attention to the development of energy flux using the concept of enthalpy which is defined by equation (1.6.3), the universal gas constant, R, and the concept of the partial pressure p_k of species k and the concept of the energy e_k possessed by species k to define the enthalpy of species k and the total stress tensor $\overline{\overline{\Pi}}$ to give an energy flux defined by

$$\begin{aligned} \vec{q} = & \sum_{j=1}^{N} \left(\vec{j}_k h_k\right) - \overline{\overline{K}} grad T - \\ & \sum_{k=1}^{N} \left(\frac{RT}{W_k X_k}\right) D_k^T \cdot \vec{d}_k + \\ & (\rho \cdot e)\vec{u} + \left(\frac{\rho(\vec{u} \cdot \vec{u})}{2}\right)\vec{u} + \overline{\overline{\Pi}} \cdot \vec{u} \end{aligned} \tag{3.2.2}$$

Then if we define

$$\frac{\partial Q_{internal}}{\partial t} = \text{rate of chemical and radiative heat production}$$

to be the heat produced by chemical reactions and the electromagnetic radiation power density term while we let

$$\frac{\partial Q_{out}}{\partial t} = \text{the rate of radiative transfer of heat to the outside}$$

which includes terms like the one on the right side of equation (1.6.10) describing radiation leaving from flames to all other parts of the reacting system. The energy equation is given by

$$\frac{\partial}{\partial t}\left\{\rho\epsilon + \rho\left(\frac{\vec{u}\cdot\vec{u}}{2}\right)\right\} = div(\vec{q}) + \frac{\partial Q_{internal}}{\partial t} + \frac{\partial Q_{out}}{\partial t} \tag{3.2.3}$$

References

[1] Anderson, Dale A. *Computational Fluid Mechanics and Heat Transfer* New York: McGraw Hill (1984).

[2] Armstrong, Robert L. and Andrew Zardecki. "Propagation of High Energy Laser Beams Through Metallic Aerosols" *Applied Optics. Volume 29. Number 12* (April 20, 1990) pp 1786-1792

[3] *Explosions in Air* Austin, Texas: University of Texas Press (1973)

[4] Barton, J. P., D. R. Alexander, and S. A. Schaub. "Internal fields of a spherical particle illuminated by a tightly focused laser beam: focal point positioning effects at resonance." *Journal of Applied Physics. Volume 65 No. 8* (April 15, 1989) pp 2900-2906

[5] Barton, J. P., D. R. Alexander, and S. A. Schaub. "Internal and near surface electromagnetic fields for a spherical particle irradiated by a focused laser beam" *Journal of Applied Physics. Volume 64 no 4* (1988) pp 1632-1639.

[6] Belts, V. A., O. A. Volkovitsky, A. F. Dobrovolksy, E. V. Ivanov, Y. V. Nasedkin, L. N. Pavlova "Intensive CO_2 laser pulse transmission through droplet and ice crystal fogs" *IN* Kaye, A. S. and A. C. Walker. *Gas flow and chemical lasers. 1984. Proceedings of the Fifth International Symposium* Oxford, England: Gas Flow and Chemical Laser Symposium (August, 1984) pp 20-24

[7] Benedict, Robert P. *Gas Dynamics* New York: John Wiley (1983)

[8] Birkhoff, Garrett. *Hydrodynamics. A Study in Logic Fact, and Similitude* New York: Dover (1950)

[9] Biswas, A., H. Latifi, R. L. Armstrong, and R. G. Pinnick. "Time resolved spectroscopy of laser emission from dye doped droplets" *Optics Letters. Volume 14. No. 4* (February 15, 1989) pp 214-216

[10] Bloembergen, N. *Nonlinear Optics* New York: W. A. Benjamin (1965)

[11] Caledonia, G. E. and J. D. Teare. "Laser beam hygroscopic aerosol interactions" *Transactions of the ASME Journal of Heat Transfer. Vol 99* (May, 1977) pp 281-286.

[12] Carls, J. C. and J. R. Brock. "Explosive vaporization of single droplets by lasers: comparison of models with experiments." *Optics Letters. Volume 13, No. 10* (October, 1988) pp 919-921

[13] Chang, Randolph and E. James Davis. "Knudsen Aerosol Evaporation" *Journal of Colloid and Interface Science. Volume 54, No. 3* (March, 1976) pp 352-363.

[14] Chitanvis, Shirish M. "Explosion of Water Droplets" *Applied Optics, Vol 25, No. 11* pp 1837-1839

[15] Chow, S. N., J. Mallet-Paret, and J. A. Yorke. Finding zeros of maps: homotopy methods that are constructive with probability one. *Math. Comp. Volume 32* (1978) pp 887-889.

[16] Chevaillier, Jean Phillipe, Jean Fabre, and Patrice Hamelin. "Forward scattered light intensities by a sphere located anywhere in a Gaussian beam" *Applied Optics, Vol. 25, No. 7* (April 1, 1986) pp 1222-1225.

[17] Chevaillier, Jean Phillippe, Jean Fabre, Gerard Grehan, and Gerard Gousbet. "Comparison of diffraction theory and generalized Lorenz-Mie theory for a sphere located on the axis of a laser beam." *Applied Optics. Vol 29, No. 9* (March 20, 1990) pp 1293-1298.

[18] Chylek, Petr, Maurice A. Jarzembski, Vandana Srivastava, and Ronald G. Pinnick. "Pressure Dependence of the Laser Induced Breakdown Thresholds of Gases and Droplets" *Applied Optics Volume 29, Number 15* (May 20, 1990) pp 2303-2306

[19] Cohoon, D. K. On the uniqueness of Solutions of Electromagnetic Interaction Problems Associated with Scattering by Bianisotropic Bodies IN Rassias, George. *The Mathematical Heritage of C. F. Gauss* Singapore: World Scientific Publishing (1991) pp 119 - 132.

[20] Cross, L. A. "High repitition rate, high resolution back lit, shadow, and schlieren photography of gaseous and liquid mass transport phenomena and flames" *International Congress on Instrumentation in Aerospace Simulation Facilities Dayton Ohio 1981* Dayton, Ohio: ICIASF 1981 Record (September 30, 1981)

[21] Davis, E. James and Asit K. Ray. "Determination of diffusion coefficients by submicron droplet evaporation"

[22] Dixon - Lewis, G. "Flame Structure and Flame Reaction Kinetics II. Transport Phenomena in Multicomponent Systems" *Proceedings of the Royal Society A. Volume 307* (1968) pp 111 - 135.

[23] Dixon - Lewis, G. "Towards a quantitatively consistent scheme for the oxidation of hydrogen, carbon monoxide, formaldehyde and methane in flames" *IN* Warantz, J. and W. Jäger, (Editors) *Complex Chemical Reaction Systems. Mathematical Modeling and Simulation* New York: Springer Verlag (1987)

[24] Eringen, A. Cemal, and S. Suhubi S. Erdogan. *Elastodynamics. Volume I. Finite Motions* New York: Academic Press (1974)

[25] Eringen, A. Cemal, and S. Suhubi S. Erdogan. *Elastodynamics. Volume II Linear Theory* New York: Academic Press (1975)

[26] Ewing, W., Maurice Wenceslas, S. Jardetzky, and Frank Press. *Elastic Waves in Layered Media* New York: McGraw Hill (1957)

[27] Eyring, Henry, and Mu Shik Jhon *Significant Liquid Structures* New York: John Wiley and Sons (1969)

[28] Fisher, I. Z. *Statistical Theory of Liquids* Chicago: The University of Chicago Press(1961)

[29] Frenklach, Michael, Hai Wang, and Martin Rabinowitz. "Optimization and analysis of large chemical kinetic mechanisms using the solution mapping method — combustion of methane" *Progress Energy Combustion Science. Volume 18* (1992) pp 47 - 73

[30] Frenklach, Michael and Hai Wang. "Detailed Modeling of Soot Particle Nucleation and Growth. *Twentythird Symposium (International) on Combustion. The Combustion Institute* (1990) pp 1559 -1556.

[31] "On the driving force of PAH production" *Twenty Second Symposium (International) on Combustion /The Combustion Institute* (1988) pp 1075 - 1082.

[32] Frenklach, Michael and Stephen J. Harris. "Aerosol Dynamics Modeling Using the Method of Moments" *Journal of Colloid and Interface Science, Volume 118, No. 1* (July, 1987) pp 252 -261

[33] Frenklach, Michael. "Dynamics of Discret Distribution for Smoluchowski Coagualation Model" *Journal of Colloid and Interface Science, Volume 108, No. 1* (November, 1985) pp 237 - 242.

[34] Frenklach, Michael. "Computer Modeling of Infinite Reaction Sequences: A Chemical Lumping" *Chemical Engineering Science, Volume 40, Number 10* (1985) pp 1843 - 1849.

[35] Frenklach, Michael, David W. Clary, William Gardner, and Stephen Stein. "Detailed Kinetic Modeling of Soot Formation in Shock Tube Pyrolysis of Acetylene" *Twentieth Symposium (International) on Combustion /The Combustion Institute* (1984) pp 887 - 901

[36] Miller, James A. and Robert J. Kee. "Chemical Kinetics and Combustion Modeling" *Ann. Rev. Phys. Chem. Volume 41* (1990) pp 345 - 387 and

[37] Garcia, C. B. and W. I. Zangwill. Pathways to Solutions, Fixed Points, and Equilibria. Englewood Cliffs, NJ: Prentice Hall(1981)

[38] Glickler, S. L. "Propagation of a 10.6 μ laser through a cloud including droplet vaporization" *Applied Optics, Volume 10, No. 3* (March, 1971) pp 644-650

[39] Gosman, A. D., W. M. Pun, A. K. Runchal, D. B. Spalding, and M. Wolfshtein (Eds) *Heat and Mass Transfer in Recirculating Flows* New York: Academic Press (1969)

[40] Hochstadt, Harry. *The Functions of Mathematical Physics.* New York: Dover(1986).

[41] Hörmander, Lars. *Linear Partial Differential Operators* New York: Academic Press (1963)

[42] Hsu, Yih-Yun, and Robert W. Graham. *Transport Processes in Boiling and Two Phase Systems* New York: McGraw Hill(1976)

[43] Incropera, Frank P. and David P. Dewitt. *Fundamentals of Heat Transfer* New York: John Wiley and Sons (1981)

[44] Jaluria, Yogesh. *Natural Convection, Heat and Mass Transfer.* New York: Pergamon Press (1980)

[45] Kogelnik, H. and T. Li. "Laser beams and resonators" *Applied Optics, Volume 5, Number 10* (October, 1966) pp 1550-1566

[46] Kee, R. J., and J. A. Miller "A structured approach to the computational modeling of chemical kinetics and molecular transport in flowing systems" Albuquerque, NM 81185: Sandia National Laboratories (February, 1992)

[47] Kee, R. J., J. F. Grcar, M. D. Smooke, and J. A. Miller. *A Fortran Program for Modeling Steady Laminar One Dimensional Premixed Flames SAND85-8240 UC 401* Albuquerque, New Mexico: Sandia National Laboratories (April, 1992)

[48] Kozaki, Shogo. "Scattering of a Gaussian Beam by a Homogeneous Dielectric Cylinder" *Journal of Applied Physics Volume 53, No. 11* (November, 1982) pp 7195-7200

[49] Liou, K. N., S. C. Ou Takano, A. Heymsfield, and W. Kreiss. "Infrared transmission through cirrus clouds: a radiative model for target detection" *Applied Optics. Volume 29, Number 13* (May 1, 1990) pp 1886-1896

[50] Luikov, A. V. and Yu A. Mikhailov. *Theory of Energy and Mass Transfer* New York: Pergamon Press (1965)

[51] Mackowski, D. W., R. A. Altenkirch, and M. P. Menguc. "Internal absorption cross sections in a stratified sphere" *Applied Optics. Volume 29, Number 10* (April 1, 1990) pp 1551-1559

[52] Majda, Andrew. *The Stability of Multi Dimensional Shock Fronts* Providence, Rhode Island: Memoires of the AMS. Volume 41, Number 275 (January, 1983)

[53] Margolis, Stephen B. and Gregory Sivashinsky. "On Spinning Propagation of Cellular Flames" *Combustion Science and Technology. Volume 69* (1990) pp 99 - 131

[54] Margolis, Stephen B. and Bernard J. Matkowsky. "New Modes of Quasi Periodic Combustion Near a Degenerate Hopf Bifurcation Point" *SIAM Journal of Applied Mathematics. Volume 48, No 4* (August, 1988) pp 828 - 853

[55] Monson, B . Vyas Reeta, and R. Gupta. "Pulsed and CW Photothermal Phase Shift Spectroscopy in a Fluid Medium: Theory" *Applied Optics. Volume 28, No. 13* (July, 1989) pp 2554-2561.

[56] Mugnai, Alberto and Warren J. Wiscombe. "Scattering from nonspherical Chebyshev Particles. I Cross Sections, Single Scattering Albedo, Asymmetry factor, and backscattered fraction" *Applied Optics. Volume 25, Number 7* (April 1, 1986) pp 1235-1244.

[57] Odishaw, Hugh. *Research in Geophysics. Volume II. Solid Earth and Interface Phenomena* Cambridge Massachusetts: The MIT Press (1964).

[58] Park, Bae-Sig, A. Biswas, and R. L. Armstrong. "Delay of explosive vaporization in pulsed laser heated droplets" *Optics Letters. Volume 15, No. 4* (February 15, 1990) pp 206-208

[59] Peters, N. "Numerical and Asymptotic Analysis of Systematically Reduced Reaction Schemes for Hydrocarbon Flames" Aachen, West Germany: Institut fur Allgemeine Mechanik (preprint)

[60] Pinnick, R. G., Abhijit Biswas, Robert L. Armstrong, S. Gerard Jennings, J. David Pendleton, and Gilbert Fernandez. "Micron size droplets irradiated with a pulsed CO_2 laser: Measurement of Explosion and Breakdown Thresholds" *Applied Optics. Volume 29, No. 7* (March 1, 1990) pp 918-925

[61] Pinnick, R. G., S. G. Jennings, Petr Chylek, Chris Ham, and W. T. Grandy "Backscatter and Extinction in Water Clouds" *Journal of Geophysical Research. Vol 88, No. C11* (August 20, 1983) pp 6787-6796

[62] Richardson, C. B., R. L. Hightower, and A. L. Pigg. "Optical measurement of the evaporation of sulfuric acid droplets" *Applied Optics. Volume 25, Number 7* (April 1, 1986) pp 1226-1229

[63] Rosseland, S. *Theoretical Astrophysics. Atomic Theory and the Analysis of Stellar Atmospheres and Envelopes* Oxford, England: Clarendon Press (1936)

[64] Sacks, Jerome, Susannah B. Schiller and William Welch "Designs for Computer Experiments" *Technometrics. Volume 41, Number 1* (February, 1989) pp 41 - 47

[65] Schaub, S. A., D. R. Alexander, J. P. Barton, and M. A. Emanuel "Focused laser beam interactions with methanol droplets: effects of relative beam diameter" *Applied Optics. Volume 28, No. 9* (May 1, 1989) pp 1666-1669

[66] Schiffer, Ralf. "Perturbation approach for light scattering by an ensemble of irregular particles of arbitrary material" *Applied Optics. Volume 29, Number 10* (April 1, 1990) pp 1536-1550

[67] Siegel, R. "Radiative Cooling Performance of a Converging Liquid Drop Radiator." *Journal of Thermophysics and Heat Transfer. Volume 3, Number 1* (January, 1989) pp 46-52.

[68] Siegel, Robert, and John R. Howell. *Thermal Radiation Heat Transfer* New York: Hemisphere Publishing Company (1981)

[69] Smoller, Joel. *Shock waves and reaction diffusion equations* New York: Springer Verlag (1983)

[70] Smooke, Mitchell D. and Vincent Giovangigli. "Simplified Transport and Reduced Chemistry Models of Premixed and Nonpremixed Combustion" *IN* Smooke, M. D. (Ed) *Lecture Notes in Physics 384* New York: Springer Verlag (1991)

[71] Svetyurov, D. E. "State of transfer of radient energy accompanied by evaporation of a disperse medium" *Soviet J. Quantum Electronics Volume 3, No. 1* (July August, 1973) pp 33-36

[72] Temam, Roger. *Sur la Stabilite et la Convergence de la Methode Des Pas Fractionnaires. Theses presentee a la faculte des sciences de L'Universite de Paris pour obtenir le grade de docteur es sciences mathematiques* Paris, France: Institut Henri Poincare (Juin, 1967)

[73] Tsai, Wen Chung and Ronald J. Pogorzelski. "Eigenfunction solution of the scattering of beam radiation fields by spherical objects" *Journal of the Optical Society of America. Volume 65, Number 12* (December, 1975) pp 1457-1463.

[74] Trefil, J. S. *Introduction to the Physics of Fluids and Solids* New York: Pergamon Press, Inc. (1975)

[75] Tzeng, H. M., K. F. Wall, M. B. Long, and R. K. Chang. "Laser emission from individual droplets at wavelengths corresponding to morphology dependent resonances" *Optics Letters. Volume 9, Number 11* (1984) pp 499-501

[76] Volkovitsky, O. A. "Peculiarities of light scattering by droplet aerosol in a divergent CO_2 laser beam" *Applied Optics. Volume 26, Number 24* (December 15, 1987) pp 5307-5310

[77] von Mises, Richard, Hilda Geiringer, and G. S. S. Ludford. *Mathematical Theory of Compressible Fluid Flow* New York: Academic Press (1958)

[78] Warantz, J. "Rate Coefficients in the C/H/O System" *IN* Gardner, W. C. (Editor) *Combustion Chemistry* New York: Springer Verlag (1984) (Chapter V)

[79] Wasow, Wolfgang. *Asymptotic Expansions for Ordinary Differential Equations* New York: John Wiley (1965)

[80] White, J. E. *Seismic Waves, Radiation, Transmission, and Antennuation* New York: McGraw Hill (1965)

[81] Whittaker, E. T. and G. N. Watson. *A Course of Modern Analysis* London: Cambridge University Press (1986).

[82] Zardecki, A. and J. David Pendleton. "Hydrodynamics of water droplets irradiated by a pulsed CO_2 laser." *Applied Optics. Volume 28, No. 3* (February 1, 1989) pp 638-640

[83] Zel'dovich, Ya B. and Yu P. Raizer. *Physics of Shock Waves and High Temperature Thermodynamic Phenomena* New York: Academic Press (1966)

B. SPECTROSCOPY OF SINGLE PARTICLES AND AEROSOLS

Cavity-QED Enhancement of Fluorescence Yields in Microdroplets

Michael D. Barnes, William B. Whitten, and J. Michael Ramsey

Analytical Chemistry Division
Oak Ridge National Laboratory
Mail Stop 6142
Oak Ridge, Tennessee 37831

RECENT/SUBMITTED PUBLICATIONS

(1) M. D. Barnes, W. B. Whitten, and J. M. Ramsey, "Enhanced Fluorescence Yields Through Cavity-QED Effects in Microdroplets," J. Opt. Soc. Am. B. submitted, July, 1993.

(2) M. D. Barnes, K. C. Ng, W. B. Whitten, and J. M. Ramsey, "Detection of Single Rhodamine 6G Molecules in Levitated Microdroplets," Anal. Chem. **65**, 2360 (1993).

(3) M. D. Barnes, W. B. Whitten, S. Arnold, and J. M. Ramsey, "Homogeneous Linewidths of Rhodamine 6G at Room Temperature from Cavity-Enhanced Spontaneous Emission Rates," J. Chem. Phys. **97**, 7842 (1992).

Abstract

Measurements of the integrated fluorescence yield of Rhodamine 6G (R6G) in levitated microdroplets (4 to 16 μm diameter) display a size dependence which is attributed to a decreased probability per excitation cycle of photochemical bleaching as a result of cavity-enhanced spontaneous emission rates. The average number of fluorescence photons detected per molecule in 4 μm droplets (where emission rate enhancement has been previously demonstrated) is shown to be approximately a factor of 2 larger than the yield measured for larger droplets where emission rate enhancement does not occur. Within some simple approximations, these results suggest that essentially no emission rate inhibition occurs in this system. A mechanism based on spectral diffusion is postulated for the apparent absence of cavity-inhibited emission and is illustrated by Monte Carlo calculations using time-dependent lineshape functions.

Introduction

One of the fundamental sensitivity limitations in the fluorescence detection of single dye molecules in solution[1] is the finite number of photons which can be emitted by the molecule before irreversible photochemical bleaching occurs, or fluorescence yield. The fluorescence yield is directly proportional to the spontaneous emission rate,[2,3] however, in bulk solution, the emission rate of a particular molecule is essentially fixed for a given solvent. It is now well-known that the spontaneous emission rate of atoms or molecules can be modified (enhanced or inhibited) by placing the emitting species in a small-volume optical enclosure.[4,5] Recently, it has been shown that the spontaneous emission rate can be significantly enhanced in a microdroplet environment for dye molecules[6] and chelated ions[7] through coupling of emission into morphology dependent resonances (MDRs) of the droplet. This effect could, in principle, increase the fluorescence yield for dye molecules thereby increasing sensitivity. However, since the emission profile overlaps several droplet MDRs, cavity-inhibited emission[8,9,10,11] was also initially expected to occur; thus it was unclear whether the combination of emission rate enhancement and inhibition would result in a net increase in the fluorescence yield.

Here we show that a significant increase in the fluorescence yield for R6G in 4 and 5 μm diameter glycerol microdroplets relative to the photon yield for larger droplets (> 10 μm diameter). These results indicate that the combined effects of emission rate enhancement and inhibition do not cancel completely. Using the previously measured emission rate constants,[6] the relative fraction of molecules whose emission rate is inhibited is estimated to be very nea zero. We propose a model based on spectral diffusion[12] in which the transition frequency is not fixed but undergoes random shifts[13] as it is perturbed by the motion of the solvent in response to the change in the dipole moment of the chromophore upon excitation. On roughly the same time-scale as the (free-space) radiative lifetime, the width of a spectral line becomes dynamically broadened which allows the excited state to sample a progressively larger range of frequencies which eventually encompasses at least one droplet MDR.

Fermi's golden rule,[14] given in Eq. (1), provides a basic understanding of how emission rates may be modified in small-volume

optical cavities. The rate of spontaneous emission from state j to state i can be estimated from the expression

$$A_{i\to j} = \frac{2\pi}{\hbar^2} \langle i \mid \mathbf{H}_{ij} \mid j \rangle^2 \rho(\omega) \qquad (1)$$

where $\langle i \mid H_{ij} \mid j \rangle$ is the (volume-normalized) Hamiltonian matrix element representing the atom-field interaction, and $\rho(\omega)$ is the density of final photon states at the emission frequency ω. In bulk media, $\rho(\omega)$ is essentially a constant over a small range of optical frequencies so the emission rate will be approximately independent of ω. When the dimensions of the optical enclosure become comparable to the emission wavele[illegible] the vacuum photon state density becomes redistributed[15] so that ρ [illegible] ich larger than the free-space value when ω corresponds to a cavity reso[illegible]e. Conversely, $\rho(\omega)$ is much smaller than the free-space value when ω is non-resonant. Therefore, the emission rate may be enhanced or inhibited depending on whether the emission frequency corresponds with a cavity resonance provided the cavity resonance spacing is much larger than the spectral linewidth.[16]

For optical transitions, this condition implies cavity dimensions on the order of microns which can be satisfied by using micron-sized high-refractive index liquid droplets.Cavity effects in microdroplets are well known and arise from morphology dependent resonances (MDRs)[17] of the droplet which occur at specific values of the size-parameter, X, defined as $X = 2\pi r / \lambda$, where r is the radius of the sphere and λ is the wavelength of light. These resonances have very high Q's (10^3 - 10^8) and processes such as stimulated emission[18] and lasing[19,20] as well as enhanced energy transfer[21] have been reported in droplets. Recently, Campillo and co-workers[7] have reported enhancement (and inhibition) of the spontaneous emission rate for chelated europium ions in a stream of falling (10 μm diam.) ethanol droplets and demonstrated the unique frequency dependence of the enhanced emission.

In our previous investigation of the temporal distribution of fluorescence emission from R6G in levitated microdroplets,[6] the fluorescence decay kinetics observed for larger droplets (≥ 10 μm diam.) were found to be essentially the same as

in bulk solution. For smaller droplets (4 - 8 μm diam.) however, the fluorescence decay showed two distinct decay components: a slow component with essentially the same time constant as the bulk, and a second much faster decay component whose relative amplitude and decay constant increased with decreasing droplet size. The increase in the decay constant of the fast component with decreasing droplet size was consistent with the expectation that the enhancement should be proportional to the free spectral range.[14] Analysis of these results showed that a 12-fold increase in the spontaneous emission rate constant occurs for R6G in 4 μm diameter glycerol droplets over the decay constant measured in bulk solution.

Because the emission profile overlaps several droplet resonances, it was initially expected that an inhibited rate component should also occur due to emission at frequencies between the cavity resonances. However no inhibited emission was observed, and it was originally assumed that the absence of an inhibited rate component was due to experimental parameters in the time-correlated photon counting apparatus which emphasized the short-time behavior of the fluorescence emission. We have further investigated the question of cavity-inhibited emission of dye molecules in liquid microdroplets by examining the integrated fluorescence yield as a function of droplet size. Since the number of fluorescence photons emitted per molecule should be proportional to the rate constant for spontaneous emission averaged over all molecules in the droplet, the fluorescence yield should be sensitive to the relative fraction of molecules with enhanced and inhibited emission rates as well as the magnitude of emission rate enhancement and inhibition. For droplet diameters between 7 and 16 μm, the average fluorescence yield was observed to be independent of droplet size, while approximately a two-fold increase in the fluorescence yield was measured for 4 μm diameter droplets relative to the larger sizes. These results suggest that the combined effects of enhanced and inhibited emission rates do not cancel completely and further suggest that the fraction of molecules with an inhibited emission rate is very small.

Experimental

The experimental apparatus is similar to that previously described1 except that a second photomultiplier has been added to increase sensitivity. Briefly, a three-electrode structure similar to that employed in ion-trap mass spectrometers is used

to levitate glycerol droplets.[22] Two f/1 collection optics view the droplet at +/- 135° with respect to the direction of propagation of the (cw) Ar^+ excitation laser. The laser was horizontally polarized, with an intensity at the droplet of about 500 W/cm^2. A nominal total measurement time of 200 seconds was used to accurately determine the mean background level. R6G concentrations in glycerol ranged from 1 to 4 x 10-9 M, corresponding to about 100 molecules in the smallest droplets and a few thousand molecules in the largest ones.

Droplets were produced from a piezoelectric pipet[23] with a 40 μm diameter orifice. Control over the droplet diameter was obtained by diluting the R6G/glycerol solutions with varying amounts of water. Droplets leave the pipet with approximately the same diameter as that of the pipet orifice and, after rapid evaporation of the water, a glycerol droplet is left whose volume is roughly proportional to the degree of dilution. Droplet diameters were determined with an estimated uncertainty of ≈ 10 % by measuring the distance between reflected and refracted glare-spots[24] from laser illumination using an eyepiece reticle with rulings corresponding to 1 μm. At the end of a fluorescence measurement, the mean background is subtracted from the data set and the integrated fluorescence signal is normalized by dividing by the number of molecules in the droplet calculated from the concentration and droplet diameter. This normalized signal represents the average number of fluorescence photons emitted per molecule which we term the fluorescence yield.

Results and Discussion

Figure 1 shows the fluorescence count rate at both detectors versus time for a 10 μm glycerol droplet containing ≈ 1000 R6G molecules. The total number of fluorescence photons after background subtraction for this droplet was 5.5 x 10^6, giving a fluorescence yield of 5500 photons/molecule. Figure 2 shows the average fluorescence yield as a function of droplet diameter. About 10 droplets of a given size were analyzed and the error bars represent +/- 1 σ. For droplet diameters between 7 and 20 μm, the average fluorescence yield is 4800 photons/molecule and is independent of diameter. At droplet diameters of 5 and 4 μm, average fluorescence yields were determined to be 8900 and 10500 photons per molecule, respectively. Even though the relative uncertainty for the smaller droplets is larger due to the higher relative error in the diameter measurement, the increase in the average fluorescence yield of about a factor of 2 is clearly significant.

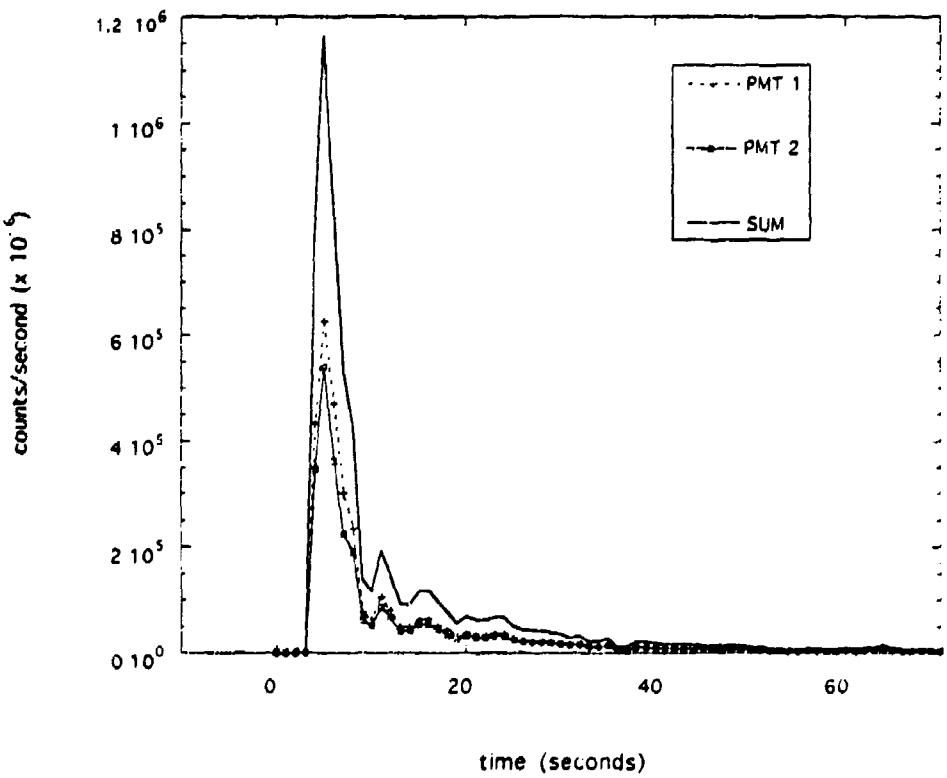

Figure 1. Typical two-channel fluorescence data for R6G (concentration was 3.16 x 10^{-9} M) in a 10 μm glycerol droplet. The integrated signal is 5.5 x 106 counts. Dividing by the number of molecules in the droplet(= 1000) gives a fluorescence yield of 5500 photons/molecule.

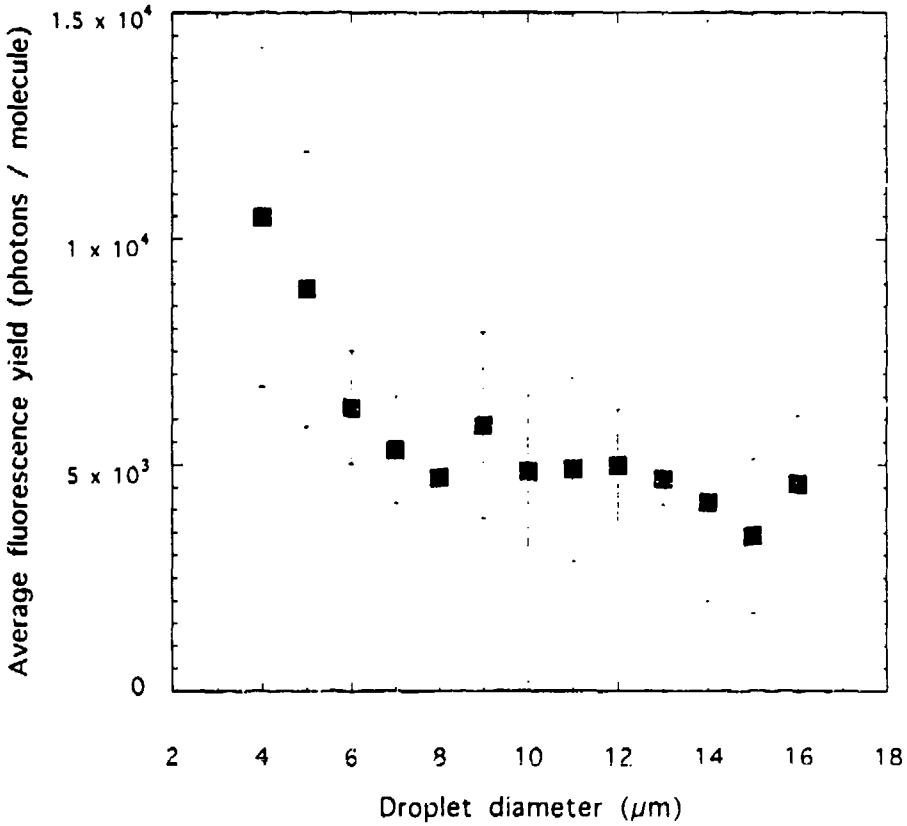

Figure 2. Average fluorescence yield vs. droplet size. Symbols represent an average yield from several droplets of the same size. Error bars are +/- 1 σ.

An estimate of the relative amplitude of cavity-inhibited spontaneous emission can be obtained by relating the observed increase in fluorescence yield for R6G in 4 μm droplets to the emission rate averaged over all molecules in the droplet. As shown by Hirshfeld,[3] the integrated fluorescence yield, Φ, is proportional to the ratio A_{sp}/k_{pb} where A_{sp} is the spontaneous emission rate and k_{pb} is the photobleaching rate. Assuming that k_{pb} is unaffected by changes in photon state density (i.e., due only to the local solvent-chromophore environment), we can write an approximate expression for Φ in terms of the inhibited and enhanced emission rate constants, A_i and A_e, and their respective fractions f_i and f_e as

$$\Phi = \Phi_{bulk}[\,(A_i/A_b)f_i + (A_e/A_b)f_e + f_b] \qquad (2)$$

where Φ_{bulk} represents the average fluorescence yield in the bulk (droplet diameters > 10 μm), and A_b and f_b represent the bulk emission rate constant and the respective fraction. The quantity inside the square brackets in Eqn. 2 thus represents the average emission rate (relative to the bulk) over all molecules in the droplet.

If photon emission occurs with roughly equal probability over the free-spectral range (but with different time dependence), it is easily shown that the quantity inside the square brackets in Eq. 2 is equal to 1. That is, the enhancement and inhibition effects exactly cancel and no net increase in the photon yield can occur. The value of Φ for 4 μm droplets can also be estimated in the other limit where the inhibited fraction, f_i, is equal to zero. The decay constants Ae and Ab are known from our fluorescence lifetime measurements, and the fraction of molecules in the droplet which interact with the droplet MDRs can be estimated from the ratio of mode-volume to droplet volume.[19,25] For a 4 μm diameter glycerol droplet, this ratio is approximately 8%, so that $f_e \approx 0.08$. Substituting a value of 12 for (A_e/A_b),[6] the fluorescence yield in the limit where $f_i \approx 0$ should be 1.9 times larger than the bulk. The agreement of the measured average fluorescence yield (for R6G in 4 μm droplets) with the latter limit suggests that the fraction of molecules with an inhibited emission rate is very small. Thus, there must be some mechanism by which the excited state can sample a frequency range large enough to couple emission into the

droplet resonances.

Recently, solvent-chromophore dynamics in liquids have been probed by several different experimental techniques.[12,26,27,28,29] Using time-resolved fluorescence depolarization measurements, Stein and Fayer[12] have shown that the perturbation of the excited state dipole by the solvent results in a dynamical broadening of a spectral line on the same time scale as the radiative lifetime of the chromophore. These authors make the distinction between the fast (fs) thermal motions of the solvent, which give rise to the pure homogeneous dephasing, and the much slower (ns) response of the solvent to the change in the dipole moment of the chromophore upon excitation. The latter process gives rise to spectral diffusion which causes dynamical (time-dependent) broadening of the spectrum. Similar behavior has been also observed in the solid state at cryogenic temperatures by Moerner and co-workers[30] where perturbations due to conformational changes in the host crystal produce center frequency shifts in the fluorescence excitation spectra of single guest molecules.

In the picture described by Stein and Fayer, the spectral linewidth in solution is not fixed, but changes with time. Following an excitation pulse at time near $t = 0$, the linewidth is the homogeneous width that arises from (femtosecond) collisional dephasing due to thermal motion of the solvent molecules. As $t \rightarrow \infty$, the chromophore has sampled the entire range of solvent-dipole configurations and the transition can occur at essentially any frequency with some probability give by the inhomogeneous profile. The rate at which the width of a dynamically broadened line changes depends on how fast the solvent molecules can respond to the change in the dipole moment of the chromophore after excitation. From Stein and Fayer's value for the solvent relaxation rate for glycerol at room temperature, the dynamic width is estimated to reach 1/2 of the inhomogeneous width (≈ 600 cm^{-1}) in a time of roughly 1 fluorescence lifetime (3.6 ns). Thus, the excited state can eventually sample a large enough frequency range to access a cavity resonance irrespective of the initial transition frequency.

These dynamical solvent-chromophore interactions should strongly affect the distribution of emission frequencies and emission times for dye molecules in a liquid microcavity. Consider a transition which has a (nonresonant) center frequency, ω_χ, in

the midpoint between two cavity resonance frequencies. At time t≈0 following excitation, the density of photon states in the range of frequencies within the homogeneous width is small thereby inhibiting emission of a photon. As the spectral line becomes dynamically broadened, there is a significant probability that the emission can occur at a new frequency, ω_c', near a cavity resonance frequency where the photon state density is much higher. This would result in virtually all photon emission to occur near the cavity resonance frequencies provided that the spectral diffusion is sufficiently rapid. Thus, in this scenario, very few photons would be emitted at non-resonant frequencies and thus at an inhibited rate.

In order to illustrate this effect, Monte Carlo calculations were performed to model the distribution of emission times and frequencies in a system where the transition frequency is allowed to randomize on the same time scale as the radiative lifetime. A dynamic width function was approximated[31] using Stein and Fayer's experimental measurement of the solvent relaxation rate for glycerol at room temperature which defines the spectral width as a function of time. The initial (homogeneous) width was taken to be 100 cm^{-1} fwhm, and the inhomogeneous width at $t = \infty$ was taken to be 600 cm^{-1} fwhm.[12] A "clock" was incremented in 20 picosecond steps, and after each time step a decision was made whether to end the calculation based on a comparison of the integrated emission probability to a random number.

In the Wigner - Weisskopf approximation,[32] the probability of photon emission has a time dependence given by

$$P_{emit}(\omega,t) = 1 - \exp[-\gamma(\omega)\, t] \tag{3}$$

where we have incorporated a frequency dependence in the decay constant, $\gamma(\omega)$, expressed as

$$\gamma(\omega) = \frac{\rho_{cav}(\omega)}{\rho_{bulk}(\omega)}\, \gamma_0 \tag{4}$$

where $\rho_{cav}(\omega)$ and $\rho_{bulk}(\omega)$ are the cavity and bulk density-of-states functions

respectively, and γ_0 is the decay constant in bulk glycerol (0.27 ns-1).

The approximate photon state density function for the cavity was constructed by assuming a cavity Q of 10^3 and a Lorentzian form for the resonance and a resonance spacing of 700 cm^{-1}; values which should be realistic for a 4 μm glycerol droplet.[33] We further assumed that, over the frequency range of interest, $\rho_{bulk}(\omega) \approx$ constant. These functions for the cavity and bulk medium were then constrained so that

$$\int_{\Delta_c} \rho_{cav}(\omega)\, d\omega = \int_{\Delta_c} \rho_{bulk}(\omega)\, d\omega \tag{5}$$

where Δc is the free spectral range.

In calculating the emission probability, the argument, $\gamma(\omega)$, in Eqn. 3 was taken to be an average over the homogeneous lineshape function, $L(\omega, \omega_c)$, expressed as

$$L(\omega, \omega_c) = \frac{\Gamma}{2\pi\left[(\omega - \omega_c)^2 + (\Gamma/2)^2\right]} \tag{6}$$

where ω_c is the center transition frequency, and Γ is the homogeneous width. The ratio, $\rho_{cav}(\omega_c) / \rho_{bulk}(\omega_c)$ in Eqn. 4 was then replaced by an average value $\langle\rho_{cav}(\omega_c)\rangle/\rho_{bulk}(\omega_c)$ given by

$$\frac{\langle\rho_{cav}(\omega_c)\rangle}{\rho_{bulk}(\omega_c)} = \frac{\int_0^\infty \rho_{cav}(\omega)\, L(\omega,\omega_c)\, d\omega}{\int_0^\infty \rho_{bulk}(\omega)\, L(\omega,\omega_c)\, d\omega} \tag{7}$$

The integrated emission probability was computed at each time step using Eqns. 3 and 7 and compared to a random number generated at the start of the calculation. If the random number is larger, a new center frequency, ω_c', is randomly selected from the time-dependent lineshape function whose width is determined by the dynamic width function using standard Monte Carlo sampling techniques.[34] This "diffusion" in frequency space is then continued until the integrated emission probability becomes

greater than the random number and a record is made of the frequency and the time at which the emission occurred.

To illustrate the effect of spectral diffusion in a microcavity environment, two different spectral origins (center frequencies) were chosen. In the first (resonant) case, the origin was chosen to correspond to a cavity resonance, and in the second (non-resonant) case, the origin was located in between two resonances. Figure 3 shows the distribution of emission times for both resonant and non-resonant center frequencies. In both cases, the emission time distribution is described well by single exponential decay with time constants significantly smaller than the bulk decay constant. As expected, the decay constant for the non-resonant case (γ = 0.87 ns-1) is slightly smaller than for the resonant case (γ = 1.05 ns-1). Because the transition frequency is not fixed, the result of spectral diffusion in a microcavity is that virtually all emission is coupled out through the resonances.

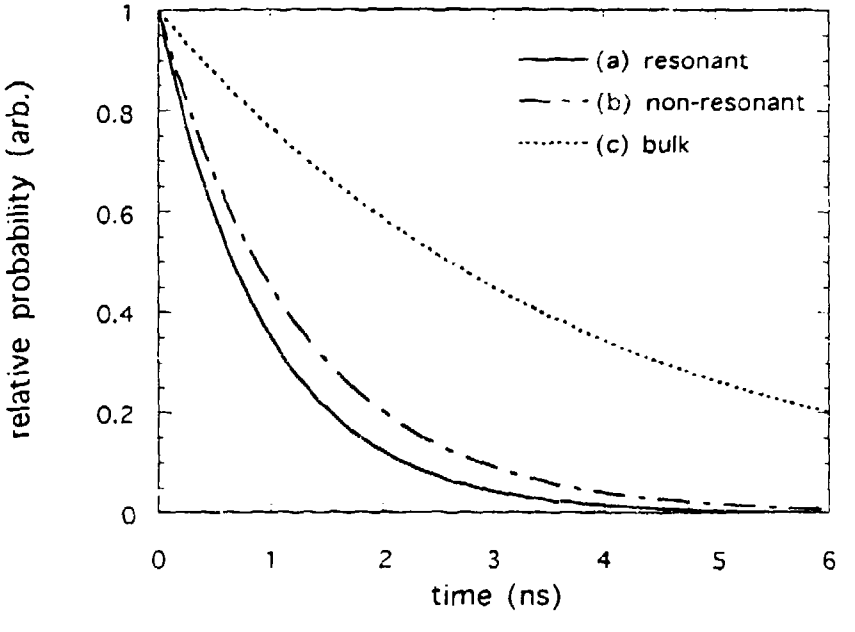

Figure 3. Monte Carlo simulation of emission time distributions for resonant (a), and non-resonant (b) center frequencies. A step size of 20 picoseconds was used with 20000 samples and a homogeneous linewidth of 100 cm^{-1}. Curves are single-exponential fits to the calculated emission time histograms, with decay constants of 1.03 and 0.85 ns^{-1} for the resonant and non-resonant cases respectively. The dashed curve (c) shows the "bulk" emission time distribution for comparison.

This is further illustrated by the simulated distribution of emission frequencies shown in Figure 4. For both resonant and non-resonant cases, the emission frequency distribution maps the cavity resonances with virtually no probability of emission in the 'inhibited' region between the resonances. Similar emission frequency distributions have also been observed experimentally in Fabry-Perot microcavities by Yokoyama and coworkers.[35] Dispersed emission from these structures clearly mapped the cavity resonances and shows very little (if any) emission intensity at non-resonant frequencies

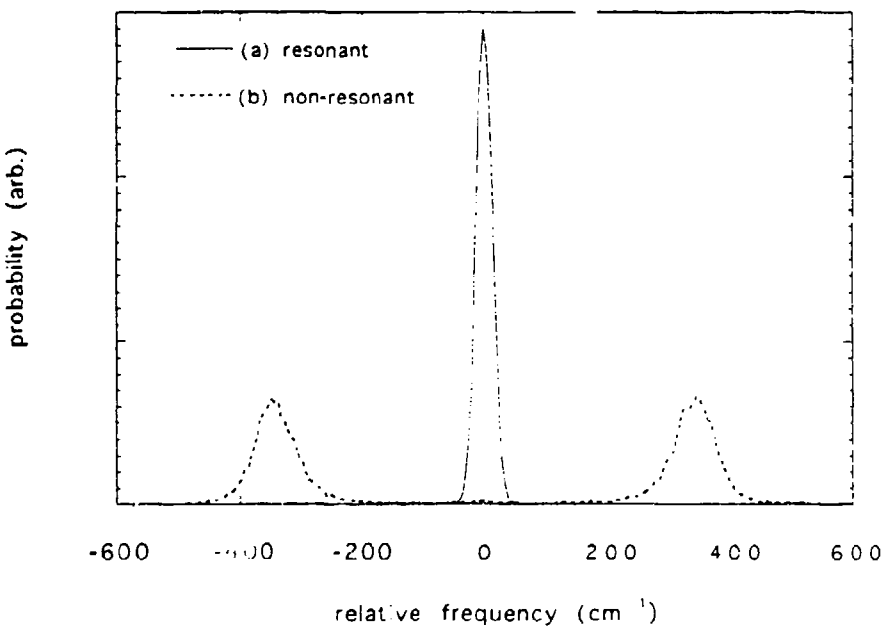

Figure 4. Simulated emission frequency distributions for resonant (a), and non-resonant (b) center frequencies. Both distributions have been normalized to give unit area. The origin of the time-dependent transition frequency distribution was set to zero for both cases. Note that for both (a) and (b), there is negligible probability of photon emission in between the cavity resonances.

The purpose of these calculations was to qualitatively illustrate the effect of solvent-chromophore dynamics on the emission properties of dye molecules in liquid microcavities. We believe that these simulations, in which the transition frequency is

not constrained to be fixed, demonstrate the effect of spectral diffusion in a microcavity environment. Elimination of emission rate inhibition through spectral diffusion is consistent with both the absence of an inhibited component in the previously measured fluorescence decay kinetics and the increased fluorescence yield in the 4 and 5 μm droplets reported here. If one assumes that the fraction of molecules whose emission is inhibited is small compared to the enhanced fraction (an assumption which appears justified on the basis of our model calculations), Eq. 2 predicts that the increase in fluorescence yield should be approximately a factor of 2 which is in good agreement with the experimental results. It therefore seems likely that spectral diffusion strongly influences the distribution of emission frequencies so that emission preferentially occurs near cavity resonances.

If the inhibited emission rate component in our system is truly eliminated through spectral diffusion, it seems important to account for the observation of inhibited emission of chelated europium ions reported by Campillo, et al.[7] In the case of chelated europium species the observed d $\rightarrow$ f transitions involve electrons which are shielded from solvent perturbations. That is, in a case where there is very little inhomogeneous broadening, spectral diffusion cannot occur thus "fixing" the transition frequency. In such a case it seems likely that inhibited emission can occur. In addition, the requirement for elimination of cavity-inhibited emission through spectral diffusion is that the solvent reorganization occur on the same time scale as the excited state lifetime. If the solvent response time is much longer than the free-space radiative lifetime (i.e., in a glass or solid matrix), it then seems likely that, in such a case, the distribution of emission times will show an inhibited component.

Summary and Conclusions

Measurements of R6G fluorescence yields in microdroplets have revealed a size dependence which is attributed to a net decrease in the probability per absorption-emission cycle of photochemical bleaching. This effect derives from an increase in the average spontaneous emission rate as a result of coupling of emission into droplet MDRs. A two-fold increase in the average number of fluorescence photons detected per molecule has been observed for R6G in 4 μm droplets over the yield measured at larger diameters which is interpreted in terms of a net increase in the average spontaneous emission rate. These results are consistent with previously

measured R6G fluorescence decay kinetics in microdroplets and suggest that the relative amplitude of cavity-inhibited emission in this system is very small. We have proposed a mechanism based on randomization of transition frequencies on a time-scale comparable to the excited state lifetime, illustrated by simple Monte Carlo calculations, which can account for the virtual elimination of cavity-inhibited emission in this system. It is also clear from these results that cavity-QED effects associated with microdroplets offer a substantial sensitivity advantage for fluorescence detection of single molecules.

Acknowledgements

This research was sponsored by the U.S. Department of Energy, Office of Basic Energy Sciences, under contract DE-AC05-84OR21400 with Martin Marietta Energy Systems. MDB acknowledges an appointment to the ORNL postdoctoral research associate program administered by the Oak Ridge Institute for Science and Education and Oak Ridge National Laboratory. The authors would also like to thank Steven C. Hill for many helpful discussions.

References

[1] W. B. Whitten, J. M. Ramsey, B. V. Bronk, and S. Arnold, Anal. Chem. **63**, 1027 (1991); K. C. Ng, W. B. Whitten, J. M. Ramsey, and S. Arnold, *ibid.* 64, 2914 (1992); M. D. Barnes, K. C. Ng, W. B. Whitten, and J. M. Ramsey, *ibid.* 65, 2360 (1993).

[2] P. Pringsheim, *Fluorescence and Phosphorescence* (Interscience, New York, 1949).

[3] T. Hirschfeld, Appl. Opt. **15**, 3135 (1976).

[4] E. M. Purcell, Phys. Rev. **69**, 681 (1946).

[5] S. Haroche, and D. Kleppner, Phys. Today **42** (1), 24 (1989); S. E. Morin, Q. Wu, and T. W. Mossberg, Opt. Photonics News **3**, 8 (1992), and references cited therein.

[6] M. D. Barnes, W. B. Whitten, S. Arnold, and J. M. Ramsey, J. Chem. Phys. **97**, 7842 (1992).

[7] H-B. Lin, J. D. Eversole, C. D. Merrit, and A. J. Campillo, Phys. Rev. A **45**, 6756 (1992).

[8] D. Kleppner, Phys. Rev. Lett. **47**, 233 (1981); R. G. Hulet, E. S. Hilfer, and D. Kleppner, *ibid* **59**, 2955 (1987).

[9] F. DeMartini, G. Innocenti, G. R. Jacobvitz, and P. Mataloni, Phys. Rev. Lett. **59**, 2955 (1987).

[10] W. Jhe, A. Anderson, E. A. Hinds, D. Meschede, L. Moi, and S. Haroche, Phys. Rev. Lett. **58**, 666 (1987).

[11] D. J. Heinzen, J. J. Childs, J. E. Thomas, and M. S. Feld, Phys. Rev. Lett. **58**, 1320 (1987).

[12] A. D. Stein, and M. D. Fayer, J. Chem. Phys. **97**, 2948 (1992).

[13] R. Kubo, Adv. Chem. Phys. **15**, 101 (1969).

[14] E. Fermi, Rev. Mod. Phys. **4**, 87 (1932).

[15] S. C. Ching, H. M. Lai, and K. Young, J. Opt. Soc. Am. B. **4**, 1995 (1987).

[16] H. Yokoyama, and S. D. Brorson, J. Appl. Phys. **66**, 4801 (1989).

[17] See S. C. Hill, and R. E. Benner, in *Optical Effects Associated With Small Particles*, edited by P. W. Barber and R. K. Chang (World Scientific, Singapore, 1988).

[18] A. J. Campillo, J. D. Eversole, and H-B. Lin, Phys. Rev. Lett. **67**, 437 (1991).

[19] H-M. Tzeng, K. F. Wall, M. B. Long, and R. K. Chang, Opt. Lett. **9**, 499 (1984).

[20] H-B. Lin, J. D. Eversole, and A. J. Campillo, J. Opt. Soc. Am. B **9**, 43 (1992).

[21] L. M. Folan, S. Arnold, and S. Druger, Chem. Phys. Lett. **118**, 322 (1985); S. Arnold, and L. M. Folan, Optics Lett. **14**, 387 (1989).

[22] R. F. Weurker, H. Shelton, and R. V. Langmuir, J. Appl. Phys. **30**, 342 (1959).

[23] S. Arnold, and L. M. Folan, Rev. Sci. Instrum. **57**, 2250 (1986).

[24] A. Ashkin, and J. M. Dziedzic, Appl. Opt. **20**, 1803 (1981).

[25] P. T. Leung, and K. Young, J. Chem. Phys. **89**, 2894 (1988)

[26] C. J. Bardeen, and C. V. Shank, Chem. Phys. Lett. **203**, 535 (1993).

[27] B. Sauter, and C. Bräuchle, Chem. Phys. Lett. **204**, 157 (1993).

[28] M. J. E. Morgenthaler, S. R. Meech, and K. Yoshihara, Chem. Phys. Lett. **197**, 537 (1992).

[29] E. T. J. Nibbering, D. A. Wiersma, and K. Duppen, Phys. Rev. Lett. **66**, 2464 (1991).

[30] W. P Ambrose, Th. Basche', and W. E. Moerner, J. Luminescence **53**, 62 (1992); Th. Basche', W. P Ambrose, and W. E. Moerner, J. Opt. Soc. Am. B **9**, 829 (1992); W. P. Ambrose, and W. E.

Moerner, Nature (London) **349**, 225 (1991).

[31] From inspection of Fig. 1 in Ref. 8, the approximate fun[illegible] form for the dynamic width function d(Δw)/dt corresponding to a solvent relaxation rat[illegible] was chosen to be $0.5(t/\tau_r)^{-0.4}$, where τ_r is the free-space radiative lifetime.

[32] V. Weisskopf, and E. P. Wigner, Z. Phys. **63**, 54 (1930).

[33] P. Chylek, J. Opt. Soc. Am. **66**, 285 (1976).

[34] M. Karplus, R. N. Porter, and R. D. Sharma, J. Chem. Phys. **43**, 3259 (1965).

[35] H. Yokoyama, M. Suzuki, and Y. Nambu, Appl. Phys. Lett. **58**, 2598 (1991).

Fluctuation Spectroscopy for Small Inclusions in a Levitated Microdroplet*

by Burt V. Bronk and Michael J. Smith
U.S.Army E.R.D.E.C., A.P.G., MD 21010-5423
and
Steve Arnold, N.Y. Polytechnic University
333 Jay Street, Brooklyn, N.Y., 11201

Recent Publications and Presentations

"Photon-correlation spectroscopy for small spherical inclusions in a micrometer-sized electrodynamically levitated droplet", B. V. Bronk, M. J. Smith and S. Arnold, Optics Letters **18**, 93-95 (1993).

"Photon Correlation Spectroscopy of Microorganisms in a Spherical Microdroplet", B. V. Bronk, M. J. Smith, and W. P. Van De Merwe, SPIE Proceedings Vol. **1884**, Proceedings of "Static and Dynamic Light Scattering in Medicine and Biology", 192-201, (1993).

Abstract:

Micron-sized droplets of saturated sodium chloride solution were captured in an electrodynamic levitator. Both pure droplets and droplets with one-half micron sub-particles ('guests') were studied by means of 90 degree polarized light scattering and fluorescence. Large fluctuations appear when guest particles are present. In order to eliminate confusion of the fluctuations with morphological resonances, host droplets were brought to thermodynamic equilibrium with a moist atmosphere and maintained at constant diameter for several days. Analysis of the correlation function for the intensity of the scattered light showed decay times of ~ 9 msec which have a good correspondence with the physical parameters of the solution and the size of the subparticles. Longer characteristic times are measures of morphological features of the electric field intensity in the host particles. A new phenomenon was observed when the exit polarizer was crossed to the input polarization. Scattered light corresponding to light from the guest particles was visualized mainly from a shell near the exterior of the sphere and not from the interior of the host droplet.

* This talk was presented at the 1992 Scientific Conference on Obscuration and Aerosol Research but was not included in that years proceedings.

Introduction:

Since the development of the quadrupole levitation balance, (1-3) studies of the spectroscopic characteristics of levitated micron-sized droplets have become an active field of investigation. In the recent past IR, fluorescence, and Raman spectroscopies (4-8) have been demonstrated. Of particular interest are the morphological resonances for electromagnetic (laser) excitation, which allow highly efficient transfer of energy between molecules in microdroplets seperated by distances far larger than those characteristic for Foerster transfer(9). The variety of experiments using these electrodynamically isolated micron-sized droplets suggests that applications not possible in other microanalytical systems will arise for this "world's smallest test-tube". In one recent example, the possibility of using a sufficiently small droplet consisting of a non-fluorescent solvent as host with one or a few fluorescent molecules present was shown to allow sufficient sensitivity to detect the presence of a single molecule of rhodamine (10). Up to now, many studies have concentrated on pure droplets, but it is expected that composite particles are not unusual in naturally occurring aerosols. Composite particles are also of interest with respect to the problem of detection and identification of unknown particles captured from an aerosol. For example, a method has been devised to reproducibly add measured picoliter amounts of a known liquid in to an unknown particle captured in an electromagnetic balance (11). By this means, various chemicals can be added sequentially to test an unknown aerosol particle whose properties are then analyzed by optical probing of the composite droplet consisting of unknown particles and known liquids surrounding them. The composite droplet would remain levitated free of substrate interference and be available for further tests. In the present communication we discuss our experiments showing that fluctuations in scattered light may be used to reveal the presence of subparticle guests in a host droplet and that analysis of these fluctuations can give an indication of the size of the guests.

Methods:

Droplets with diameters in the twenty to forty micron range were generated into a damp atmosphere with a microparticle generator (Uniphoton, Brooklyn, N.Y.) These were captured in a hyperbolic quadrupole balance which has been described and shown previously (2,4) . The trap is contained in a sealed chamber with a resevoir attached so that the droplet may be brought into equilibrium with a damp atmosphere making

maintainence of droplets of saturated salt solution at constant diameter for periods of several days routine. Laser light polarized in the scattering plane is directed toward the particle through a port in the chamber. Scattered or fluorescent light is measured at 90 degrees through a 1/16 inch "pinhole" to reduce background and is quantitated by photon counting. The exit polarizer is mounted in a rotating frame so that it can easily be switched between alignments either in the scattering plane (par) or perpendicular (perp) to the scattering plane. The signal from a Hamamatsu R928P phototube is transmitted with amplification to a Stanford Research Systems SR-400 photon counter and thence to a PC for analysis. The guest particles were 0.46 micron fluoresbrite spheres (Polysciences, Warrington, PA, catalog #18720) at a 1/40 dilution from a 2.5% solids suspension into room temperature saturated salt water. This gives a suspension of about 1.2 x 10E10 guest particles/ml as was verified by microscope counting. After one day in the working suspension, 80 to 90% of the particles were still singles. This concentration corresponds to an average of 168 particles in a 30 micron droplet. The diameter of the particle was estimated to within 10% by the geometrical model of the distance between glare spots (12). Changes in mass were monitored to ~0.1% by following the DC balancing voltage. Laser light of 633 nm wavelength is used for all the scattering experiments except as noted in Figure 1. 514 nm laser light is used for exciting fluorescence. A bandpass filter (560 nm, half-width 10 nm) and a long pass filter transmitting less than 0.1% below 530nm and 90% above 580 nm were used to monitor fluorescence.

Results and Discussion:

In Figure 1 photon counts are plotted as a function of time for two different experiments with saturated salt water droplets of approximately the same size (~25 microns). The droplets are very slowly evaporating. The upper graph is for a neat droplet. The lower graph is for a droplet with guest particles. The usual resonance structure is seen in both graphs, but the presence of guests produces large random fluctuations on top of the intrinsic structure. From these graphs it is clear that the presence of resonances may interfere with analysis of the fluctuations. In Figure 2 photon counts are shown vs time for a neat salt water droplet coming to equilibrium. Some remaining Mie-like structure is seen in the first part of the graph, but after 1500 seconds, the droplet is virtually constant in size. Small size changes did occur (~2 %) overnight due to temperature changes in the laboratory, but the droplet again came to apparent equilibrium after a couple hours at constant temperature. The fluctuations remaining in the graph after equilibrium is reached are random noise probably from the laser source. For the

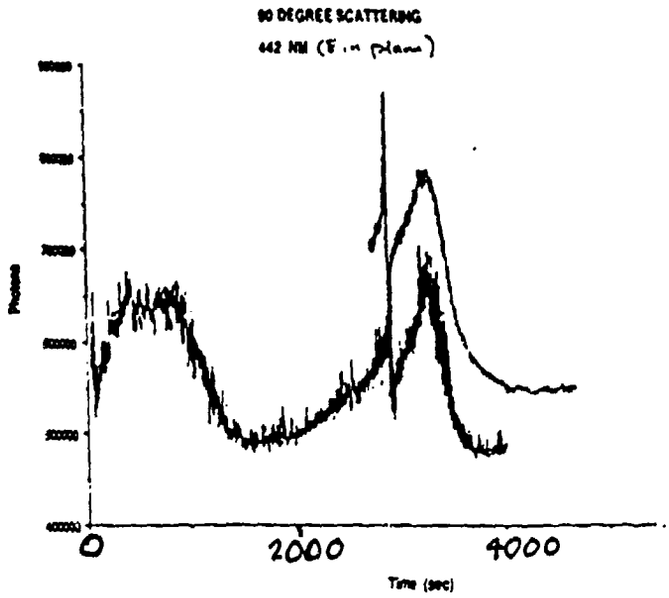

Figure 1 Ninety degree scattering from slowly evaporating levitated microdroplets with no subparticles (upper graph) or with subparticle inclusions (lower graph).

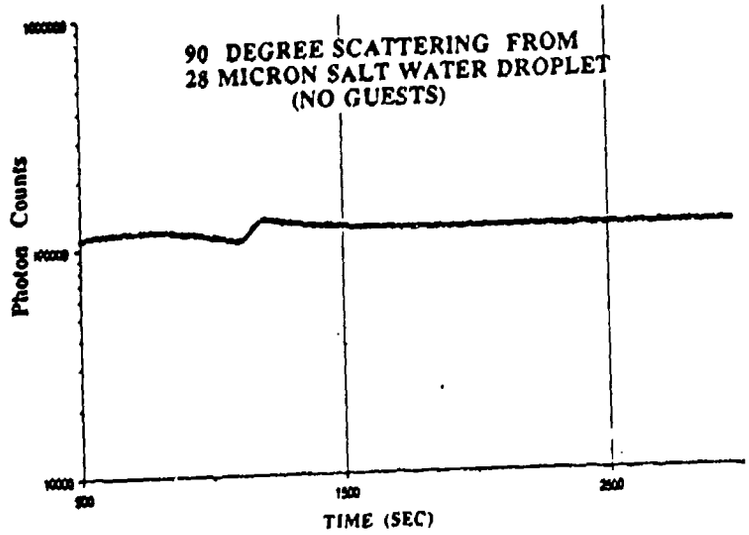

Figure 2 Ninety degree scattering from a neat microdroplet as it comes to thermal equilibrium with a moist atmosphere.

remainder of the experiments, care was taken to have the droplet in this quasi-equilibrium condition.

In Figure 3 the profile of fluorescence counts/sec vs time is shown over a period of several minutes. There is a break in the graph at a time when the phototube was removed to check that the droplet was still well centered. Fluorescence counts drop off rather rapidly as the dye in the guest particles is photoconverted to a non-fluorescing species. Since the host droplet remains at a constant size, we hypothesize that the large upward fluctuation in photon counts occur when guest particles wander into "hot" spots of electromagnetic intensity.

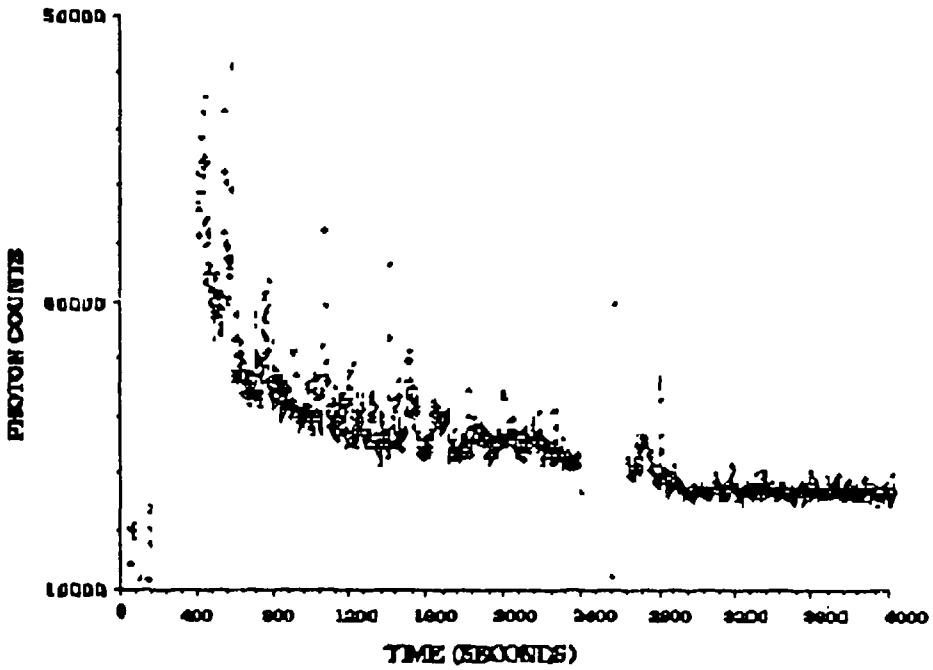

Figure 3 Fluorescent counts from dyed fluoresbrite guest particles contained in levitated nonfluorescent host droplet.

It is interesting to pause to consider a consequence of the breaking of the symmetry of a neat host droplet by the guests contained in it. In Figure 4, the upper sketch shows the path of light scattered by a homogeneous sphere. The laser is to the left. The polarization state is

described by the following matrix equation.

$$\begin{bmatrix} E_{xs} \\ E_{ys} \end{bmatrix} = \begin{bmatrix} S_2 & S_3 \\ S_4 & S_1 \end{bmatrix} \begin{bmatrix} E_{xi} \\ E_{yi} \end{bmatrix} \tag{1}$$

where the input polarization vector on the right side of the equation is transformed into the output vector on the left by the scattering matrix, **S.** Suppose we look at the scattered component perpendicular to the scattering plane.

$$E_{ys} = S_4 E_{xi} + S_1 E_{yi}$$

Now invert all the physical components of photons and the scattering sphere in the **xz** plane. Then we have

$$-E_{ys} = S'_4 E_{xi} - S'_1 E_{yi}$$

but **S'** = **S** by the invariance of a homogeneous sphere, hence $S'_4 = S_4 = 0$. S'_3 is similarly zero so the par and perp components of a scattered photon do not mix on scattering from a homogeneous sphere.

Next we consider the same homogeneous on an element by element basis. The lower figure uses geometric optics to show the refraction of light at the sphere's surface to scatter from two small symmetrically placed subspheres selected from the homogeneous substance of the droplet. The incoming light is polarized perp to the scattering plane in the example shown. After refraction followed by scattering from the two elements chosen we see that the perp components reinforce, whereas the cross-polarized par components cancel in phase. From the earlier symmetry argument there must be a combination of one or more elements canceling the cross-polarized component for every subsphere of a homogeneous sphere.

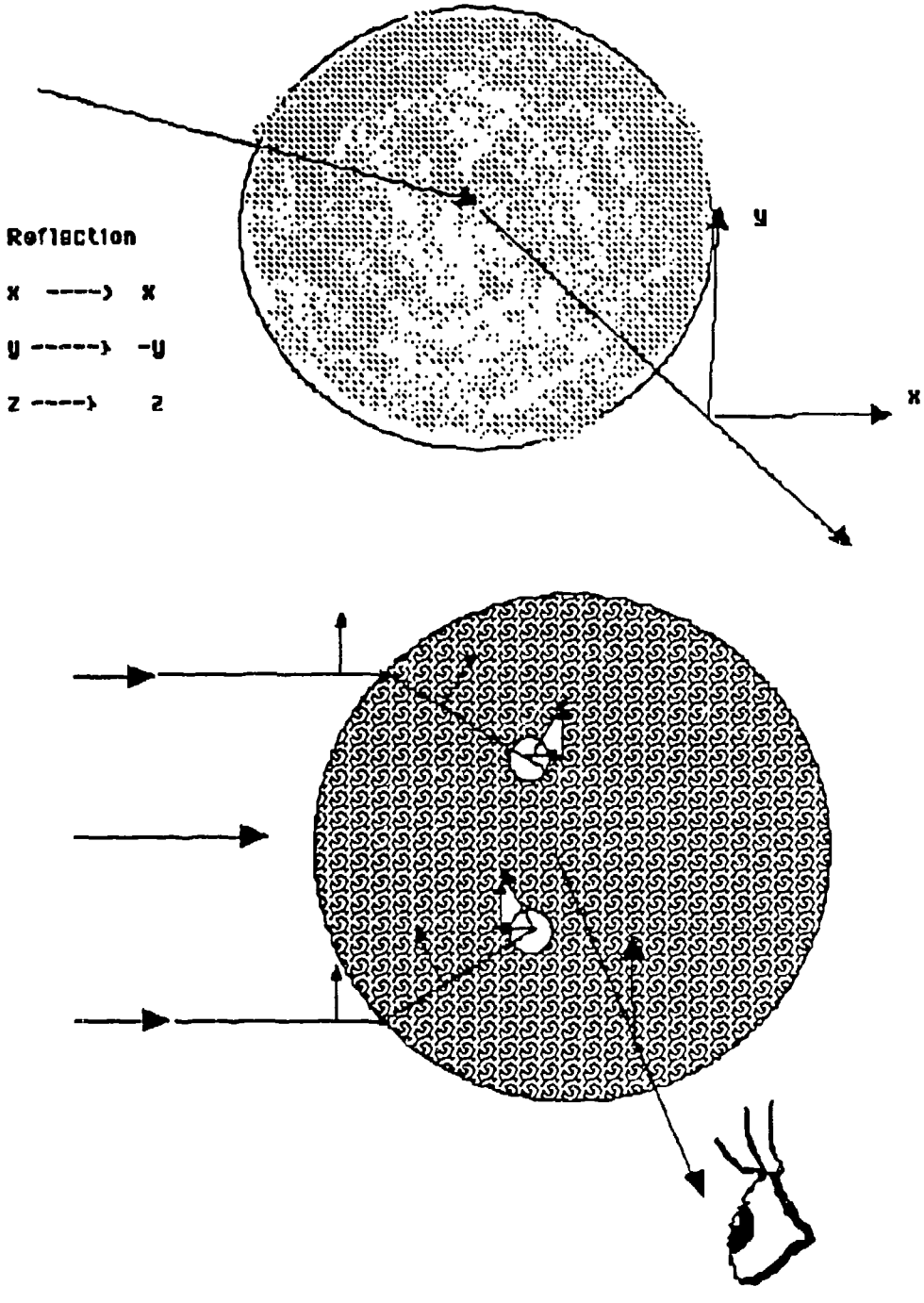

Figure 4: Upper sketch indicates symmetry of spherical droplet which reverts to itself after mirror inversion; Lower sketch shows how depolarized component of light scattered from one particular subelemen of homogeneous sphere cancels in phase with that from another one.

However, consider the case where one of the subspheres shown is a guest particle or other inhomogeneity with different polarizability from the host droplet. Then the cancellation of cross-polarized components no longer works and we should get cross-polarized output.

Figure 5 is a sketch showing what one sees when looking through a microscope at 90 degrees to the input laser light which is located to the viewers left.

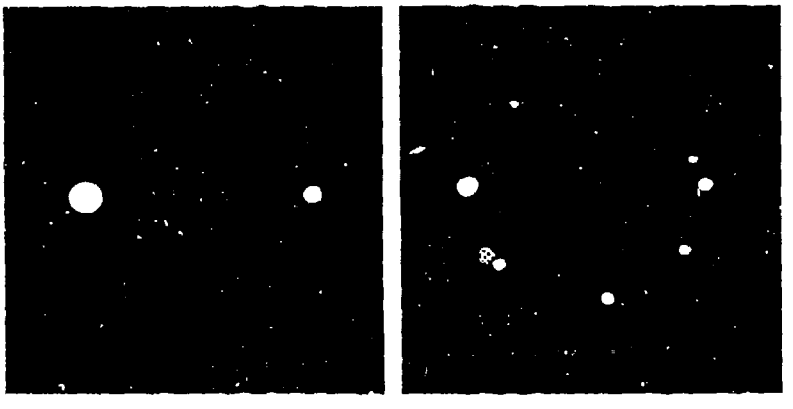

Figure 5 Left --view thru microscope at 90 degrees to input light with no guests or with guests and no cross polarizer. Right--view with guests present through cross polarizer. Laser is to the viewers left (image shown inverted so brighter spot is physically away from laser).

The view on the left shows the familiar glare spots with the brighter spot away from the laser. This is what one sees with or without guests when the output polarizer is in the plane for input polarization in the scattering plane. When guests are present and the output polarizer is crossed to the input one sees a "ring of fireflies" flashing on and off mostly near the periphery of the sphere. The majority of the fireflies were seen near the top of the particle. This is consistent with the equilibrium position of the guests which are 1.7 times as likely to be near the top than near the bottom of the droplet if one calculates the probability using the gravitational potential (density of the guests,1.05, saturated salt water, density, 1.20). The fact that the visible flashes correspond with the gravitational position of the guests suggests that the flashes correspond to the location of the guests rather than an interference phenomenon far from the source.

In Figure 6 we show the photon counts for 90 degree scattering obtained from a 30 micron droplet containing fluoresbrite guests. The

two graphs were taken during consecutive intervals. As noted in Figure 1 for an evaporating droplet with no exit polarizer present, the fluctuations are considerably larger when guest particles are present in the droplet. The coeficient of variation (C.V.) of the fluctuations is ~ 8 percent for the exit polarizer in plane and ~28% for the exit polarizer perpendicular to the input parallel polarization. This is to be compared with Figure 2 (exit polarizer perpendicular) the C. V. was only ~0.6%.

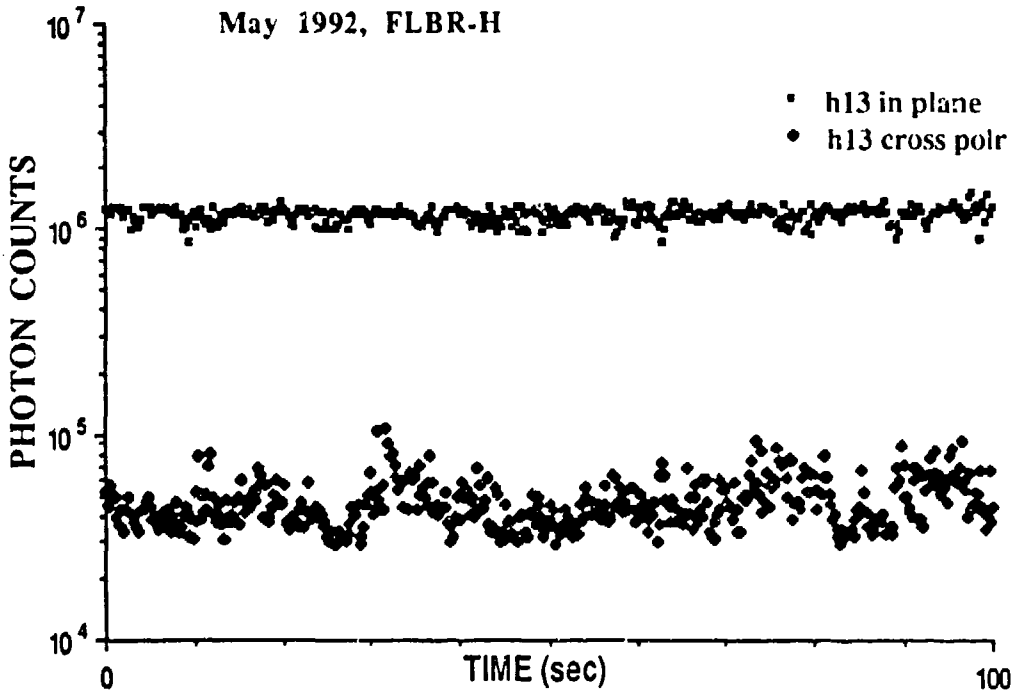

Figure 6 90 degree scattering of 633 nm laser light (polarization in plane) for a 30 micron droplet containing 0.46 micron guest particles. The exit polarizer is parallel (upper) or perpendicular (lower) to the scattering plane.

In Figure 7 we plot the relative correlation function which we define as $<(N(t)-N_{av})\ (N(t+\tau) - N_{av})>/<(N-N_{av})^2>$ where the bra kets denote a time average as does the subscript "av", and N(t) is the photon count during the interval near t. The theoretical model for photon correlation spectroscopy in a cuvette is well established (eg. reference 13), but the present situation of correlations in a droplet is rather more complicated. To take one example we note that for the cuvette, the propagation vector of the incoming light is easily established by the laser, whereas in the

present case, the input direction is affected by the geometry of the chamber (droplet), particularly near the surface of the droplet. Nevertheless we use the standard theory for the present analysis.

If we take the decay as $\exp(-\tau/\tau_i)$ with τ_i a characteristic time, then in Figure 7 we have τ_1, the shortest characteristic time equal to ~ 13 msec If we take $\tau_1 \sim 2q^2D$ where D is the diffusion constant for 1/2 micron spheres in saturated salt solution, and $q = 4\pi/\lambda$ with lamda equal to 633 /1.04 nm and $D = KT/6\pi\eta a$ with the viscosity of saturated salt water

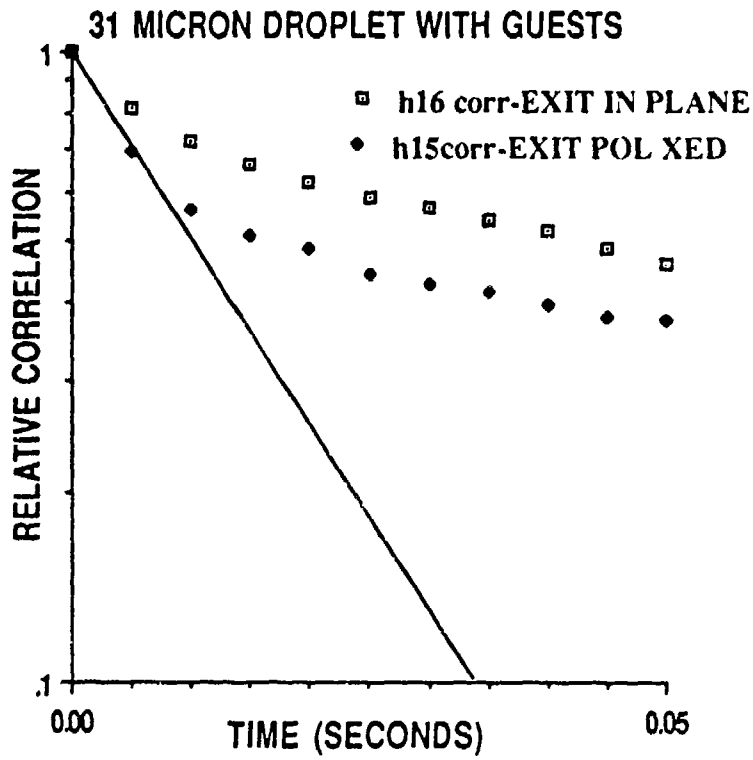

Figure 7. Relative correlation function for an a 31 micron droplet with 0.46 micron guests.

equal to 2.04 cp we may solve for the radius of the guest particles. We obtain a value of about 57 microns for the radius of the guest particles. This is more than twice the nominal radius for single particles. The difference may be due to an increased tendency for guest particles to form multiples when confined inside the host droplet.

In addition to the short characteristic times, we found exponential decay of the relative correlation also occurs on a much longer time scale, up to hundreds of milliseconds and sometimes even as long as several seconds for the same guest particles in the same experiments. An attractive hypothesis is that some of the longer characteristic times may correspond to diffusion of guest particles into and out of small regions of relatively high intensity for the electromagnetic field inside the droplet.

The phenomenon of the "ring of fireflies" is rather intriguiing. First we note that aside from interactions with the gravitational and electric field we would expect the guests to be rather evenly distrubuted throughout the host particle since any charge on them is effectively screened by the many ions present. We have noted that calculation of the probable vertical location accords with the visual evidence indicating that the flashes of light correspond to the location of guest particles relative to the host rather than being an interference phenomenon distant from its source. It has been shown (14) that for droplets with large size parameter the distribution of high intensity regions is not dependent on the exact drop size when the droplet is off resonance for the wavelength used. In this case, there is a concentration of intensity in the border between the "shadow" region and the illuminated region as defined by the geometrical optics model for a plane wave intercepting the sphere. The present host sphere (~30 microns--size parameter `148) is large enough that the distribution shown in reference (14) should still approximate the present case. Whenever a guest comes into these regions of high energy concentration, additional scattering events and occasional depolarization occurs. The location of these regions of high probability of scattering near the spheres surface accounts qualitatively for the appearance of the "ring of fireflies" The visibility of the ring in cross polarization is, we believe due to a great reduction in intensity of the glare spots which are due to the host particle. .

In a perfect sphere, the initial polarization of the scattered light would be completely preserved. In the present case, the presence of a guest of different dielectric polarizability from the host which is not counterbalanced by a similar subsphere in a symmetrical position is not prevented from contributing scattered photons which are depolarized. A clue to the origin of these photons comes from a recent article which shows a concentration for the probability of photons in the region between the shadow and the illuminated region resulting from a plane wave

The initial results of photon correlation spectroscopy inside micron-sized droplets shown in the present report indicates that the properties of host and guest both affect the results. While this complicates

interpretation, it also opens a window for studying internal dynamics of composite particles analogous to the present case.

S. Arnold was supported in part in this research by National Science Foundation Grant, NSF ATM-89-175871. We thank Dr. Stephen Druger, Northwestern University, for the proper references (15,16) for the physical properties of saturated sodium chloride solution.

REFERENCES

1. R. F. Wuerker, H. Shelton, R. V. Langmuir, J.Appl. Phys. 30,342-349 (1959).
2. R. H. Frickel, R. E. Shaffer, J. B. Stamatoff, "Chambers for the Electrodynamic Containment of Charged Aerosol Particles. U.S.Army Chemical Systems Laboratory Report ARCSL-TR-77041; Aberdeen Proving Ground MD 21010 May 1978.
3. E. J. Davis and A. K. Ray, J. Colloid Interface Sci. 75, 566-576 (1980).
4. S. Arnold in *Optical Effects Associated with Small Particles* eds. P. W. Barber and R .K. Chang (World Scientific Publishing, Singapore 1988) Chapter 2, pp 65-137.
5. S. Arnold, M. Neuman, and A. B. Pluchino, Opt. Let. 9, 4-6 (1984).
6. G. S. Grader,S. Arnold,R. Flagan and J. H. Seinfeld, J. Chem.Phys.86,5897-5903 (1987).
7. S. Arnold and L. M. Folan, Rev.Sci.Instrum. 57,2250-2253 (1986).
8. K. H. Fung and I. N. Tang, Chem. Phys. Lett. 147, 509-513 (1988).
9. L. M. Folan, S. Arnold and S. D. Druger, Chem. Phys. Letters 118,322-327 (1985).
10. W. B. Whitten, J. M. Ramsey,S. Arnold, and B. V. Bronk,Anal.Chem 63 1027-1031 (1991).
11. S. Arnold, P. Hendrie and B. Bronk, in preparation 1993, disclosure presented for patent (1992).
12. A. Ashkin and J. M. Dziedzic, Appl.Opt.20,1803-1813 (1981).
13. B. J. Berne and R. Pecora, *Dynamic Light Scattering* (Wiley-Interscience, New York, 1976).
14. D. Q. Chowdhury, P .W. Barber, and S. C. Hill, Appl. Optics 31,3518-3523 (1992)
15. C. R. C. Handbook of Chemistry and Physics, 70thedition, R. C. Weast, editor, (Chemical Rubber Publishing Co., Boca Raton, FL, 1990).
16. W. F. Linke, "Solubilities, Inorganic and Metal-Organic Compounds", (Fourth Edition, American Chemical Soc., Washington, D.C. 1965), Vol. II, p. 960.

* * * * * * * * * * * * * * * *

INCOHERENT SCATTERING OF SEMICLASSICAL PARTICLES AND THE RELAXATION FUNCTION

M. Howard Lee

Department of Physics and Astronomy
The University of Georgia
Athens, Georgia 30602–2451

RECENT PUBLICATIONS, SUBMITTALS FOR PUBLICATION, AND PRESENTATIONS:

1. M.H. Lee and O.I. Sindoni, "Dynamic response function and bounds of the susceptibility of a semiclassical gas and Kramers–Kronig relations in optic–data inversion," Phys. Rev. A 46, 8293 (1992).

2. M.H. Lee, "Comment on velocity autocorrelation function in fluctuating hydrodynamics," J. Phys. Cond. Matter 4, 10487 (1992).

3. M.H. Lee, "Autocorrelation functions for Hermitian many–body systems: Necessary conditions," Phys. Rev. B 47, 8293 (1993).

4. J. Hong and M.H. Lee, Asymptotically exact solution of the dynamic structure factor of an electron gas at rs = 3.5," Phys. Rev. Lett. 70, 1972 (1993).

5. M.H. Lee, "Incoherent scattering of an electron gas," Lecture at the University of Erlangen–Nurnberg, Germany, July 1992.

ABSTRACT

A collection of microdroplets may be regarded as an ensemble of semiclassical gas particles. If such a system is inelastically scattered by light, it is the incoherent scattering which must be considered. The scattering cross section can be computed if the relaxation function is determined. We present the relaxation function for an ensemble of semiclassical particles as a function of the incident wavevector. The same formalism will be applied to study the dynamic behavior of inhomogeneous as well as isotropic systems appropriate to microdroplets and aerosols.

INTRODUCTION

If a particle with mass m is inelastically scattered, it can recoil. It can also suffer an internal excitation if it has a structure. Having been so excited, how does it relax thereafter? It is an interesting question which probes the nature of the particle's "memory." To provide an answer by first–principles calculations is difficult since it involves solving the Heisenberg equation of motion among others. During the 1980's, this kind of physical problem has received considerable attention. Emphasis, however, has been on the coherent scattering in quantum and classical fluids, and magnetic solids. The most successful approach has been that of the memory function in the framework of the generalized Langevin equation, itself formally equivalent to the Heisenberg equation of motion. We shall adopt this approach to study the incoherent inelastic scattering which is all the more difficult owing to the absence of the dispersion relation. For this purpose, we

consider a very elementary model consisting of ideal semiclassical particles in contact with a thermal bath set at temperature T. The principal quantity of theoretical interest is the relaxation function from which the dynamic structure factor may be deduced. One can compare the dynamic structure factor with scattering data. In this presentation, we show some of our calculations for the relaxation function of a single particle as a function of the momentum transfer. In particular, we show the different behavior in the short and long wavelength regimes. We also show the future direction suggested by these solutions.

RELAXATION FUNCTION

Consider an ensemble of N identical particles of mass m. Let r denote the position of a particle at time t = 0, just before scattering, and r(t) its subsequent position. Also let $\hbar k$ and $\hbar\omega$ be the momentum and energy transfers in a scattering process in the usual manner. The relaxation function with respect to one tagged particle is then defined as:

$$R_k(t) = (e^{-ik.r}, e^{ik.r(t)}) \tag{1}$$

where the inner product is the Kubo scalar product. The time evolution is given by

$$e^{ik.r(t)} = e^{itH/\hbar}\, e^{ik.r}\, e^{-itH/\hbar} \tag{2}$$

where H denotes the energy of the ensemble. Note that $[H, r] \equiv Hr - rH \neq 0$. Hence, the time evolution is nontrivial. The noncommutativity implies the existence of the generalized Langevin equation. The Kubo scalar product introduces an ensemble average which is thermal average. For simplicity, we shall assume that the averaging may be taken with respect to the Boltzmann distribution. This combination of the noncommutativity and the Boltzmann averaging is the meaning behind the semiclassical gas.[1] The position of an individual particle, not the density of particles, ensures that we are dealing with an incoherent process.

To connect the relaxation function to scattering, we shall rely on the standard formalism of linear response theory.[1] Let $z = i\omega + \epsilon$, $\epsilon \to 0+$. Then we can define the following:

$$\hat{R}_k(z) = \int_0^\infty e^{-zt}\, R_k(t)\, dt = L.R_k(t),\ \mathrm{Re}\, z > 0. \tag{3}$$

Then it is established that

$$-\pi^{-1}\, \mathrm{Im}\, [1 - z\, R_k(z)]_{z=i\omega+\epsilon} = S_k(\omega) \tag{4}$$

where $S_k(\omega)$ is the dynamic structure function which is proportional to the inelastic scattering cross section. It is also known in the optical parlance as the extinction coefficient, i.e., the imaginary part of the refractive index. Recall that the real and imaginary refractive indices are connected by Kramers–Kronig relations.

We shall now obtain the relaxation function when the scattering particles suffer recoil only which as an ensemble are thermalized according to the Boltzmann distribution. Let $\hbar\omega_0 = \hbar^2k^2/2m$ be the recoil energy. Then, using the commutation relation $[r, P] = i\hbar$ where P is

the momentum of the tagged particle, we find that

$$e^{ik.r(t)} = e^{ik\cdot r}\, e^{iat} \tag{5}$$

where

$$a = \omega_0 + k.P/m. \tag{6}$$

Here the second term on the rhs of eq. (6) represents the Doppler term in the scattering process. To obtain (5) we have used the well–known relation, viz., for any two operators A and B, if their commutator is a c–number,

$$e^A\, e^B = e^{A+B+\frac{1}{2}[A,B]}.$$

Using (5), one can put the relaxation function (1) as follows:[2]

$$R_k(t) = \int_t^\infty X_k(s)\, ds\,. \tag{7}$$

The above integral expression can be evaluated numerically, or asymptotically exactly if k is very small or very large.[3] We shall below give our asymptotic solutions in terms of $u = \hbar\omega_0/k_B T$. In the long wavelength limit,

$$R_k(t) = e^{-t^2/u}. \tag{8}$$

In the short wavelength limit,

$$R_k(t) = \phi(u/8,\tfrac{1}{2},-2t^2/u) \sim t^{-u/4}\,. \tag{9}$$

where ϕ denotes the Kummer function, a special limit of the hypergeometric function. In our solutions, the time t is given in units of its natural time scale, i.e., the mean free time.

In the short wavelength limit one can obtain the dynamic structure function by eq. (4) using our asymptotic solution for the relaxation function. We find that

$$S_k(\omega) = \frac{\omega^{u/4}\; e^{-\omega^2/8u}}{8u\;\Gamma(u/8)}\,. \tag{10}$$

Observe that the scattering function (i.e., the extinction coefficient) is peaked about $\omega = \omega_0$. It is a smooth function of the frequency although not analytic as $\omega \to 0$. This kind of form has been observed in very short wavelength scattering in quantum fluids.

DISCUSSION

We have shown that even in this very elementary model, the relaxation function behaves rather sensitively on momentum transfers. In the long wavelength limit, the system of semiclassical particles will relax rapidly after suffering scattering. But in the short wavelength limit, the system will relax slowly such as to develop long time tails in the autocorrelation function. We consider this different behavior rather remarkable. The mathematical solution cannot be demonstrated here to its full extent in this short note.

As our future direction, we shall consider the scattering when the particles suffer internal excitation in addition to recoil treated here. The system need not be homogeneous. By allowing different masses, we can study the size distributions. We can also allow nonspherical particles. More difficult is to allow some sort of interaction between particles. An interacting system implies that spatial dimensions become an important parameter. Then one can also pursue the study of configurational asymmetry, e.g., layering structure. We are presently studying these problems via a finite model of harmonically coupled classical particles and also of coupled spin--like quantum particles.

ACKNOWLEDGMENT

We gratefully acknowledge the support of this research by the U.S. Army Research Office and the Edgewood Research, Development and Engineering Center.

REFERENCES

1. S.W. Lovesey, Condensed Matter Physics, Dynamic Correlation (Benjamin, Reading 1980).

2. M.H. Lee and O.I. Sindoni, Phys. Rev. A 46, 8293 (1992).

3. J. Hong and M.H. Lee, Phys. Rev. Lett. 70, 1972 (1993).

IDENTIFICATION OF INDIVIDUAL MICROORGANISMS BY A MICROSPHERE FLUORESCENCE IMMUNOASSAY

W. B. Whitten, M. J. Shapiro, J. M. Ramsey
Oak Ridge National Laboratory
Oak Ridge, Tennessee 37831-6142

and B. V. Bronk
U.S. Army Edgewood RDEC
Aberdeen, Maryland 21010

RECENT PUBLICATIONS, SUBMITTALS FOR PUBLICATION, AND PRESENTATIONS

A) W. B. Whitten, J. M. Ramsey, and B. V. Bronk, "Microparticle-Based Fluorescence Immunoassay", Proceedings of the 1992 CRDEC Scientific Conference on Obscuration and Aerosol Research, in preparation.

B) J. M. Dale, M. Yang, W. B. Whitten, and J. M. Ramsey, "Laser Desorption/Mass Spectrometry of Single Microparticles in an Ion Trap Mass Spectrometer", Proceedings of 40th ASMS Conf. on Mass Spectrometry and Allied Topics, Washington, DC May 31-June 5, 1992, p. 450.

C) M. D. Barnes, W. B. Whitten, S. Arnold, and J. M. Ramsey, "Homogeneous Linewidths of Rhodamine 6-G at Room Temperature from Cavity-Enhanced Spontaneous Emission Rates", J. Chem. Phys. 97, 7842 (1992).

D) K. C. Ng, W. B. Whitten, S. Arnold, and J. M. Ramsey, "Digital Chemical Analysis of Dilute Microdroplets", Anal. Chem. 64, 2914 (1992).

E) W. B. Whitten and J. M. Ramsey, "Photocount Probability Distributions for Single Molecules", Appl. Spectrosc. 46, 1587 (1992).

F) M. D. Barnes, K. C. Ng, W. B. Whitten, and J. M. Ramsey, "Detection of Single Rhodamine 6G Molecules in Levitated Microdroplets", Anal. Chem. 65, 2360 (1993).

ABSTRACT

A method is described in which individual microorganisms can be detected by fluorescence immunoassay. Polystyrene microspheres with immobilized antibodies are used for a multicomponent assay whereby a single measurement can analyze for many different species. Results of experiments to determine the sensitivity and specificity of the method are presented.

Timely identification of potential infectious agents has long been a challenge, especially for single organisms. We have obtained some recent results that indicate that an immunoassay technique based on spherical microparticles may permit the recognition of a large number of species of microorganisms with a single measurement.

The methodology is as follows: antibodies for each type of microorganism to be identified will be immobilized on microspheres of different sizes. One or more microorganisms to be identified are stained with a fluorescent dye and incubated with a mixture of the spheres. Fluorescent detection combined with optical determination of the diameter of the microspheres with bound microorganisms permits sensitive detection and unambiguous identification of the microorganisms present in the sample. Because of the precision of the laser size determination, many different species could be tested for in a single measurement. With slight modifications, the technique can be extended to include biomolecules such as toxins as well.

Structural resonances in the light scattering and absorption of transparent microspheres enable us to determine their diameter to about one part in 10^4 (1-3). The fluorescence of species on the surface of the spheres as well as the elastically scattered light is greatly enhanced when the wavelength of the incident exciting light coincides with that of a structural resonance (4,5). Thus, if an exciting laser is scanned in wavelength, a stained fluorescent microorganism bound to a sphere would fluoresce more strongly at certain frequencies characteristic of the sphere's diameter. The size could also be determined by measuring the light scattering as a function of wavelength. The spheres would be initially separated optically into groups with a very narrow size range, depending on the desired number of species to be identified. Each group would be coated with antibodies to one of the desired species (6). The spheres would then be mixed together, suspended in buffered solution. There will be a one-to-one correspondence between sphere resonance wavelength and species of microorganism.

To analyze a small sample containing one or more unknown microorganisms, the sample would first be stained with a fluorescent dye. After incubation with a small batch of the mixed microspheres, the fluorescence of the spheres would be measured. The most sensitive method would be to measure each sphere to see whether a microorganism is attached and then to measure the sphere diameter, hence determine the species. A more rapid method would be to measure the excitation spectrum (scan the wavelength of the laser and measure the total fluorescence of all of the spheres simultaneously). The magnitude of the fluorescence at a wavelength corresponding to a structural resonance would be proportional to the number of microorganisms of that species.

While the concepts presented above, optical size measurement, resonance-enhanced fluorescence, and bonding of microorganisms to immobilized antibodies have been studied individually, the combination of these effects into an integrated procedure for the identification of microorganisms has not been tested. We have made some preliminary measurements, however, that demonstrate the concept.

We tested the above ideas with two species of bacteria, E. coli and Staph. aureus for which antibodies were commercially available. The inert bacteria were obtained from Molecular Probes, Inc., stained with tetramethylrhodamine and Texas Red respectively. Rabbit anti-E. coli and monoclonal anti-Staph. aureus peptidoglycan were obtained from Biodesign International. These antibodies were conjugated to carboxylated polystyrene spheres with carbodiimide reagent (7), with anti-E. coli on 10-μm spheres and anti-Staph. aureus on 6.5-μm spheres. The sphere sizes were selected so that they could be visually distinguished under the microscope. The two species of bacteria could also be recognized by the color of fluorescence, yellow-orange and red.

We first incubated a mixture of the dyed E. coli with spheres coated with anti-E. coli to see how well the bacteria would bind and their detectability. The spheres and bacteria were observed under a binocular microscope with 40X objective, 10X eyepieces, modified for fluorescence measurements as described previously (8). An argon ion laser, at 514-nm wavelength, 10 mW, was used for fluorescence excitation. The first incubations were carried out in a 1.5 mL microcentrifuge tube rotated end for end at 1 min^{-1}. No binding was observed, even after several days. However, after a two-day incubation without stirring, about 95% of the spheres had at least one bacterium attached. In a control experiment with uncoated spheres, only a few spheres were observed with attached bacteria. It was easy to visually discern and also to photograph single bacteria bound to a sphere.

In a second experiment, an excess of the two species of bacteria was incubated with a mixture of the two sizes of antibody-coated spheres. Ideally, the yellow-fluorescing E. coli should bind selectively to the 10-μm spheres and the red Staph. aureus to the 6.5-μm spheres. The statistics obtained from one slide are shown in Table I and Table II. A total of 40 10-μm and 117 6.5-μm spheres were observed. The number and types of bacteria observed to be attached are presented in Table I. There were 98 bound E. coli and 235 bound Staph. aureus, distributed as shown in Table II. These results show that the attachment is indeed selective. In these experiments, no attempt was made to reduce the degree of nonspecific binding by varying the buffer pH or ionic strength, both of which are known to affect adsorption.

ACKNOWLEDGEMENT

Research was supported by the U.S. Department of Energy, Office of Basic Energy Sciences, and by the U.S. Army Edgewood Research and Development Engineering Center. Oak Ridge National Laboratory is managed by Martin Marietta Energy Systems, Inc., for the U.S. Department of Energy under Contract DE-AC05-84OR21400.

Table I. Number of microspheres versus attached species of microorganism.

	10-μm spheres anti-E. coli	6.5-μm spheres anti-Staph.
E. coli	33	5
Staph. aureus	2	105
both	5	7

Table II. Number of bacteria bound to microspheres of a particular size.

	10-μm spheres anti-E. coli	6.5-μm spheres anti-Staph
E. coli	85	13
Staph.	9	226

REFERENCES

1. P. Chylek, J. T. Kiehl, and M. K. W. Ko, Phys. Rev. A 18, 2229 (1978).

2. A. Ashkin and J. M. Dziedzic, Appl. Opt. 20, 1803 (1981).

3. A. K. Ray, A. Souri, E. J. Davis, and T. M. Allen, Appl. Opt. 30, 3974 (1991).

4. R. E. Benner, P. W. Barber, J. F. Owen, and R. K. Chang, Phys. Rev. Lett. 44, 475 (1980).

5. S. C. Hill, R. E. Benner, C. K. Rushford, and P. R. Conwell, Appl. Opt. 23, 1680 (1984).

6. P. Tijssen, "Practice and Theory of Enzyme Immunoassays", Elsevier, Amsterdam, 1985. p. 297.

7. J. Sheehan and G. Hess, J. Am. Chem. Soc. 77,1067 (1955).

8. W. B. Whitten, J. M. Ramsey, and B. V. Bronk, Proceedings of the 1992 CRDEC Scientific Conference on Obscuration and Aerosol Research, in press.

Blank

III. OPTICAL PROPERTIES OF AEROSOLS

Moderator: Orazio I. Sindoni

U.S. Army Edgewood Research,
Development and Engineering Center
Attn: SCBRD-RTB
Aberdeen Proving Ground MD

Blank

REMOTE BIOLOGICAL SENSING BY CIRCULAR POLARIZATION TRANSMISSOMETRY

David L. Rosen
U.S. Army Research Laboratory
Battlefield Environment Directorate
White Sands Missile Range, New Mexico 88002-5501

ABSTRACT

This paper proposes a new method, circular dichroism transmissometry (CPT), for the remote detection of biological organisms. In CPT, a laser pulse passes down through an aerosol plume, scatters off the ground or retroreflector, passes again through the plume, and is detected by a polarization sensitive detector. Microorganisms cause circular dichroism in the plume. Circular dichroism induces circular polarization in the detected light. The shot noise in CPT was numerically modeled. Background radiance does not contribute shot noise because narrow band filters eliminate background radiance. An optical artifact in CPT was studied using a table top experimental simulation. In the future, we will find new methods of eliminating the optical artifact, measure circular dichroism in microorganisms, and evaluate possible field performance.

INTRODUCTION

A remote sensor of biological agents should use an optical property that is specific to biologically derived chemicals. One property that is specific to biologically derived molecules is chirality.[1,2] Chirality is a type of asymmetry where a molecule is different from its mirror image. A molecule and its mirror image are called enantiomers of each other. One way that biological processes are unique is that they produce only one enantiomer of each molecule instead of racemic mixtures (that is, equal amounts of both enantiomers). For example, all living things produce the amino acid l-tryptophan, not its enantiomer d-tryptophan. Chiral molecules cause novel optical properties such as circular dichroism (CD), fluorescence detected circular dichroism, optical activity, and circularly polarized luminescence. This investigation studied potential applications of CD in remote biological detection.

This paper describes a novel method of remote biological detection, called circular polarization transmissometry (CPT), that uses circular dichroism to detect microorganisms. Shot noise and the optical artifact are the two biggest problems for CPT. The next section describes the method of CPT. The Theory section describes signal-to-noise ratio (SNR) calculations. The Experiment section

describes a table top experiment that partly simulates CPT and describes the optical artifact. The discussion section makes a preliminary evaluation.

CIRCULAR POLARIZATION TRANSMISSOMETRY

Figure 1 shows a schematic of circular polarization transmissometry. The user places the remote sensor on some high point looking down at the scene of interest. The lidar operator aims the laser beam at the aerosol plume, which may contain biological agents. The ground or a building behind the plume is also in the path of the laser beam. The laser beam passes through the aerosol plume and reflects from the ground. Part of the reflection is diffuse (that is, in all directions) reflection. Part of this diffuse reflected light passes through the aerosol plume again and a mirror collects it. This sensor return has a nonzero circular polarization, if and only if the aerosol plume has CD at the wavelength of the laser. A polarization modulator interrogates the sensor return. This polarization modulator could be a rotating quarter wave plate for a pulsed laser or a photoelastic modulator for a continuous wave source. The detector measures the left-hand and right-hand components of the sensor return.

A nonzero circular polarization indicates an organism or biochemical substance in the path of the laser beam. The sensor return comes from the backscatter from the ground because the ground backscatter is stronger than the direct elastic scatter from an aerosol.

Ambient light, such as daylight, does not affect CPT for two reasons. First, the laser line is spectrally narrow compared to ambient light. Narrow band filters can filter out ambient light. Second, one can restrict measurements to the solar blind part of the ultraviolet system. The insensitivity to ambient light may be an important advantage of CPT over fluorescence lidar.

The previously described method is single ended because it uses the diffuse ground scatter. Collecting ground scatter is inefficient because diffuse scattering spreads in all directions. A double ended CPT method would have a far greater sensitivity and range. One can place retroreflectors in an area to reflect the laser beam back to the sensor with very little loss. The SNR using retroreflectors would be much larger than the calculated values shown later. However, this study focussed on the single ended method because the user may not have control over the entire area. Retroreflectors would only be practical under some conditions.

SIMULATION

Photon counting (that is, shot noise) will be the largest source of random noise for CPT. This section shows the results of a numerical calculation of the SNR. We adapted lidar equations, including the UVTRAN model,[3] to CPT. A future publication will show the equations in detail.

The calculations shown used a quantity proportional to the dissymmetry ratio, g, the concentration, c, and the path length, L. Tis quantity is called the GCL and is defined as:

$$k_d = 2\int_0^L g\rho\sigma_0 dx \qquad (1)$$

where k_d is the GCL, the total path length is L, the number density of particles is ρ, the mean absorption cross section of each particle is σ_0, and g is the dissymmetric ratio.

The simulation used the following parameters. Recently published measurements of bacterial spore parameters[4] show that the absorption cross section, σ_0, for a wet Bacillus megaterium spore is 6×10^{-9} cm^2 at a 280 nm wavelength. Bacillus megaterium is a harmless bacteria that simulates biological agents in some studies. The dissymmetry ratio, g, was 0.5%. The source energy (that is, time integrated power from the laser) was 900 J. The shot noise comes only from the laser background because solar radiation cannot affect CPT.

Figure 2 shows the functional dependence of SNR to distance for four GCL. The four GCL are 3.4×10^{-3}, 1.9×10^{-3}, 1.1×10^{-3}, and 6.0×10^{-4}. These GCL, in a uniform plume 1 km thick, are equivalent to number densities of 567, 317, 183, and 100 spores/cc. One sees from figure 2 that the maximum range of detection at these values of GCL is greater than 3 km.

EXPERIMENTAL SIMULATION

We did a table top experiment to simulate CPT. The purpose of the experiment was to study how the optical artifact (that is, unwanted birefringence) could bias a CPT measurement.

Figure 3 shows a schematic of the experimental apparatus used to simulate CPT. The scatter plate, Melles-Griote opalized glass, represented the ground. A lens (L1), collected the diffuse scatter at 0° because the small dimensions of the table did not allow convenient collection at 180°. The collected light passed through another lens (L2), a polarizer (P1), a sample holder that contained a removable cuvette, a photoelastic modulator (Hinds PEM-80), another polarizer (P2), a filter holder, a collecting lens (L3), a monochromator, and a photomultiplier.

The samples consisted of saturated solutions of camphoroquinone (R, S, and racemic) with a 16% transmittance. We used a laser wavelength of 496.7 nm.

The distance between the ground and the CPT system will vary. Therefore, polarization signal, proportional to $I_L - I_R$, was measured as a function of distance between the scatter plate and L1. The small dimensions of the experiment did not allow far field conditions, so the intensity did not have an inverse square dependence as in a real lidar. However, the purpose of the experiment was to study the optical artifact.

The signal strength as a function of distance is shown in figure 4 for camphorquinone (R, S, and racemic). Note that we did this experiment under ambient light. The figure shows negative signal of R and the positive signal for S because the signals would be equal in magnitude opposite in sign for the ideal case. Figure 4 shows that the signal for the racemic mixture is much weaker than the other two signals as expected.

The measurements show anomalies at the largest distances (>30 cm). The racemic mixture shows a nonzero signal. Furthermore, the signals for the R and S are not equal in amplitude.

Further studies, not yet published, show that the optical artifact causes these anomalies. A linearly polarized background with an unwanted birefringence in the optical elements causes the optical artifact.[5,6] The unwanted birefringence turns linearly polarized light into circularly polarized light, creating a false signal. The strength of the linearly polarized background changed with distance.

The optical artifact will be an interferant in real CPT measurements because unwanted birefringence are always in optical elements. However, we have found several ways to reduce the optical artifact. The investigator tried subtracting the artifact using a known reference. The reference method reduced the optical artifact by a

large amount. The reference method in the field would consist of monitoring the linear polarization and using an artifact calibration curve. A depolarized laser also will reduce or eliminate the artifact.

CONCLUSIONS

Circularly polarized transmissometry (CPT) has been proposed as a new method of remote biodetection. The insensitivity of CPT to ambient light is an advantage of CPT over fluorescence lidar. However, shot noise and the optical artifact can severely limit CPT.

Shot noise, a fundamental limitation, limits sensitivity and range but can be averaged away. The optical artifact creates false signals. The optical artifact is an instrumental problem that comes from inherent birefringence. Several methods reduce the optical artifact. We will further study the practicality of CPT.

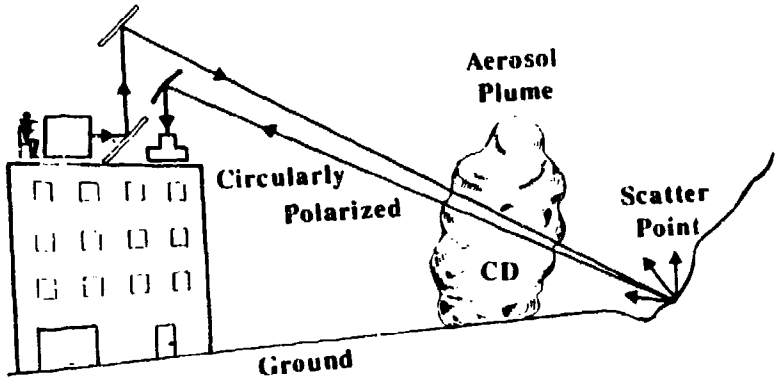

Figure 1. Schematic of circular polarization transmissometry.

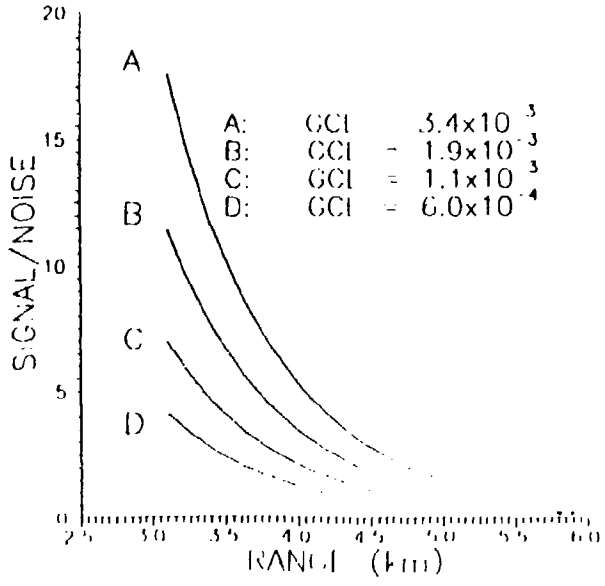

Figure 2. Calculated signal-to-noise ratio as a function of distance for four GCL for a g = 0.5%.

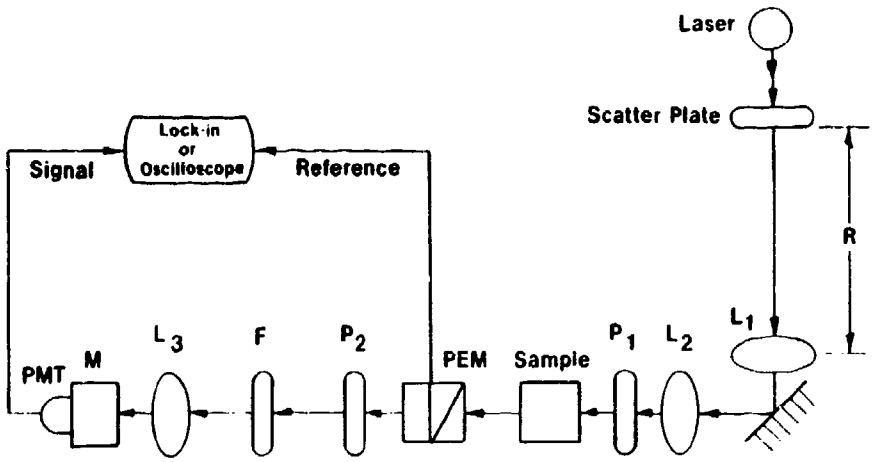

Figure 3. Schematic of optical table simulation of circular polarization transmissometry.

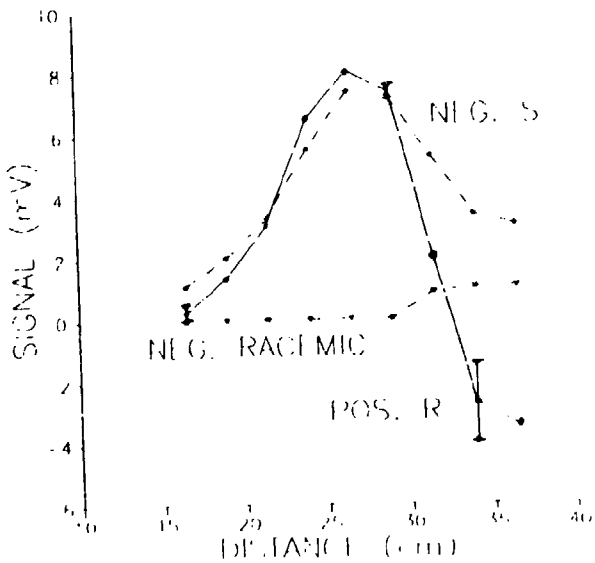

Figure 4. Polarized signal for three types of camphoroquinone (R, S, and racemic).

REFERENCES

1. Petsko, Gregory A., 1992, "On the Other Hand," Science 256, 1403-1404.

2. Avetisov, A. Avetisov, Vitalii, I. G., and V. V. Kuz'min, 1991, "Handedness, Origin of Life and Evolution, Physics Today 7, 33-41.

3. Patterson, Edward M., and James B. Gillespie, "Simplified Ultraviolet and Visible Wavelength Atmospheric Propagation Model," Appl. Opt. 28:425.

4. Bronk, Burt V., and Lou Reinisch, 1993, "Variability of Steady-State Bacterial Fluorescence with Respect to Growth Conditions," Applied Spectroscopy 47, 436-440.

5. James P. Riehl and Frederick S. Richardson, "Circularly Polarized Luminescence Spectroscopy," Chem. Rev. 86, 1-16 (1986).

6. Dekkers, Harry P. J. M., Perry F. Moraal, James M. Timper, and James P. Riehl, "Optical Artifacts in Circularly Polarized Luminescence Spectroscopy," Appl. Spect. 39, 818-821 (1985).

PASSIVE REMOTE SENSING OF MICROORGANISMS USING OPTICAL ACTIVITY AND SUNLIGHT

David L. Rosen and J. David Pendleton
U.S. Army Research Laboratory
White Sands Missile Range, New Mexico 88002-5501

ABSTRACT

Nonracemic mixtures of chiral molecules are almost unique to living things and cause optical activiy. Optical activity induces circular polarization in light scattered from particles. Therefore, optical activity may provide new methods of biodetection. This paper dicusses Mie scattering calculations applied to hypothetical suspensions of optically active spheres that represent microorganisms in different applications. Some applications use solar radiation. In the future, we will do more complete simulations of remote sensing using circularly polarized scattering.

INTRODUCTION

New methods of detecting microorganisms would be useful in both army and civilian applications. The threat of airborne biological weapons creates an army need for early warning detection systems. Both remote and point biosensing systems would be useful to the army for detecting biological threats. Biodetectors also would have peacetime applications. For example, a remote biodetector could sense microorganisms in places that are hard to reach such as in the ocean, high in the atmosphere, or even other planets.

Previous researchers have attempted to identify biological aerosols from the depolarization of elastically scattered, linearly polarized laser pulses.[1] These researchers measured the linear polarization of the elastic scatter from the aerosol plume. Both nonspherical and optically active particles depolarize linearly polarized light.[2,3] However, depolarization of linearly polarized light is not specific to microorganisms because both multiple scattering and the shape of the particle greatly affect linear depolarization. Therefore, we studied the circular polarization induced by an aerosol particle rather than the depolarization of linearly polarized light.

One property that is specific to biologically derived molecules is chirality.[4,5] Chirality is a type of asymmetry where a molecule is different from its mirror image. In nature, only living things produce nonracemic mixtures of chiral molecules. Nonracemic mixtures are materials with an excess of one type of molecule over its

mirror image. Nonracemic mixtures cause optical activity (OA) and other effects. This paper shows how OA could be used for remote biological detection.

Optical activity is a condition where there is a difference between the refractive indices of the two types of circularly polarized light (that is, left- and right-hand polarization). Unpolarized and linearly polarized light are composed of left- and right-hand components of equal intensity. If a particle is optically active, the difference in the refractive index creates a difference in scattering properties. By preferring one scattering one component, the scattering process from optically active particles will often induce a circular polarization. There are no natural sources of circularly polarized light on earth. Therefore, biosensors using circularly polarized elastic scattering can potentially detect microorganisms that are optically active.

We propose some methods of using circularly polarized elastic scattering to detect microorganisms. The theory section describes Mie scattering as applied to optically active spheres. The methods section describes two proposed methods using elastic scattering for detecting microorganisms--remote sensing and point sensing. The results and discussion section describes some numerical simulations of induced circular polarization.

THEORY

This section describes the theory of scattering from individual particles and the scattering from aerosol plumes.

This study uses the approximation that microorganisms are spherical and homogeneous. Mie scattering theory is a well-known method of calculating elastic scattering values from spheres.[6,7]

A generalized Mie-scattering code[8,9] was modified and used to calculate the scattering from an optically active sphere. In this preliminary study, we used a solution based on an approximation by Gordon that involves wave decomposition.[10] The calculations shown later ignore interference between the two circularly polarized components. Ignoring interference means that the total intensity is equal to the sum of the intensities of the two circularly polarized components. Although the codes can calculate interference, this paper ignores interference effects because most polarization measurements use dichroic filters. Polarization measurements using dichroic filters eliminate interference effects.

The codes require as input complex indices of refraction (relative to surrounding medium) for both circularly polarized components, the size parameter of the sphere, and the scattering angle. The size parameter is π times ratio of sphere diameter to wavelength. For this paper, the electric field of the incident light is in the scattering plane. The scattering codes used the following definition of circular polarization, p_c:

$$p_c = \frac{I_L - I_R}{I_L + I_R} \tag{1}$$

where I_L is the intensity of left-hand polarized light and I_R is the intensity of right-hand polarized light.

The code generates a list of intensities and polarizations for different size parameters. Another code calculated an average circular polarization weighted over total intensity and the probability distribution of size parameters. We assumed a lognormal probability size distribution for the microorganisms.

METHODS

This section describes three possible scenarios for using circularly polarized elastic scattering: (1) scattering from an aerosol plume in the atmosphere, (2) scattering from particles in a water-filled cuvette, and (3) backscattering from particles in a large body of water.

Consider the following scenario shown in figure 1. The sun shines overhead on an aerosol plume containing microorganisms. The sun provides strong light in the visible region. A vehicle on the ground a safe distance away collects scattered light. Note that the scattering angle is arbitrary. The circular polarization of the scattered light indicates microorganisms. This system is entirely passive and covert. In this case, the concentration of microorganisms will be small although the path length in the sample may be large.

One could use a laser as a light source instead of the sun. This lidar system would not be sensitive to sky radiance because a narrow band filter would subtract the background. However, this lidar would be an active sensor.

Consider a point sensor where a sample of aerosols is dispersed in water as shown in figure 2. A laser beam enters the cuvette. Particles scatter the light at right angles. Optically active particles induce a circular polarization in the scattered light.

The induced circular polarization is much stronger if the particles are immersed than if the particles are in air. The microorganism is mostly water itself so a larger fraction of light is scattered from chiral molecules. The water acts as an index matching fluid. By matching the index of refraction, the total scattered intensity (that is, the denominator of equation 1) decreases, and the circular polarization increases. Adding the correct solutes to change the liquid's index of refraction can make scattering from nonchiral molecules nearly disappear. The microorganisms can be concentrated in the fluid. However, the cuvette severely limits the path length.

The third scenario concerns a study of microorganisms in a body of water, such as the ocean. Consider a detector looking at backscatter from particles in the water as shown in figure 3. The water provides an index matching liquid, the microorganism density could be very high, and the path lengths in water near 488 nm are reasonable (>30 m). One could probe deeper under water and obtain ranging information by using a laser instead of the sun (that is, use a lidar). Narrow band filters would eliminate ambient light in this lidar (that is, active sensor) case.

RESULTS AND DISCUSSION

In this section, we calculate induced circular polarizations under reasonable conditions for all three scenarios at 488 nm. Argon-ion lasers have a strong line, the sunlight is strong, and the transmission through water is relatively high. Therefore, the scattering wavelength is 488 nm for this study. The index of refraction of water is 1.33. We assume that the index of refraction of the microorganisms is 1.4 and the absorption of the microorganism is zero. The dissymmetry of the index of refraction (that is, optical activity) is assumed to be 0.005. The diameters of the microorganisms are assumed to have a lognormal distribution with a mean of 2.0 μm and a standard deviation of 0.2 μm. For these calculations the angle of scattering was assumed to be 90° for the first two cases and 180° for the third case.

The program averaged polarizations over many radii. The size parameter increment was 0.01 μm. Figure 4 shows polarization and probability distribution as a function of size parameter for the water-filled cuvette (90°) case. The probability distribution is not drawn to scale. This situation has the strongest circular polarization of the three scenarios.

The average polarizations, ignoring the sign, are as follows. The scattered light from the aerosol plume had an average polarization of 0.019. This polarization is small but measurable. The water-filled cuvette had a 0.58 polarization. The large polarization suggests that the optical activity point sensor may be very effective. The marine backscatter had an average polarization of 0.215. Scattering from nonbiological particles will greatly reduce the induced polarization, but the calculation still suggests potential applications. Passive remote biodetection of microorganisms in the water may be possible by the proposed method. Other researchers are exploring circularly polarized scattering for remote biodetection in marine environments.[11,12]

Induced circular polarization does not require the exact conditions simulated in this paper. Further calculations, not shown in this paper, indicate that the circular polarization does not disappear even for wide probability distributions. Induced circular polarization may exist even for nonspherical, optically active particles. Note the large polarization enhancement, from 0.019 to 0.58, caused by an index matching fluid for the right-angle cases. An index matching fluid would increase circular polarization under most conditions.

Active remote biosensors using lasers would not have problems with sky radiance because a narrow band filter can isolate the laser line. The passive remote biosensor using sunlight would have a large problem with background sky radiance. However, noise from sky radiance may be reduced by signal averaging methods. Passive remote biosensors may be practical for some applications.

This study is very preliminary and only suggests potential uses of optical activity for biodetection. In the future, we intend to calculate signal-to-noise ratios, maximum ranges, and sensitivities by using more precise parameters from realistic scenarios. Circular polarization of elastically scattered light may provide valuable methods of biodetection on land, at sea, and in the air.

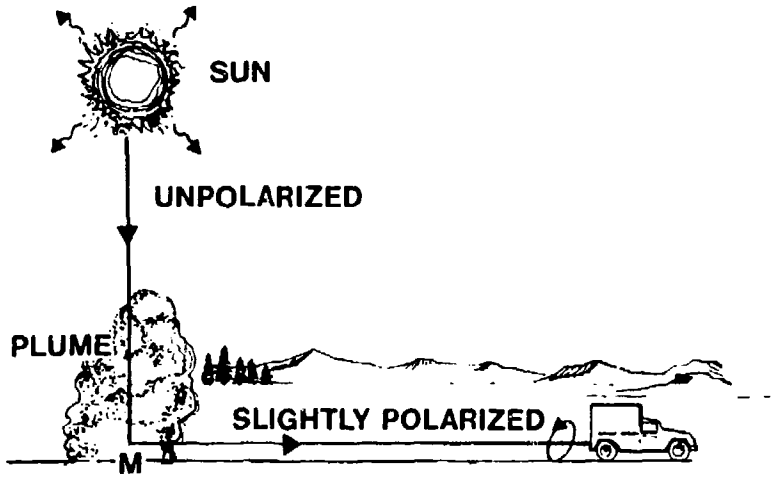

Figure 1. Polarized scattering from an aerosol plume in the atmosphere.

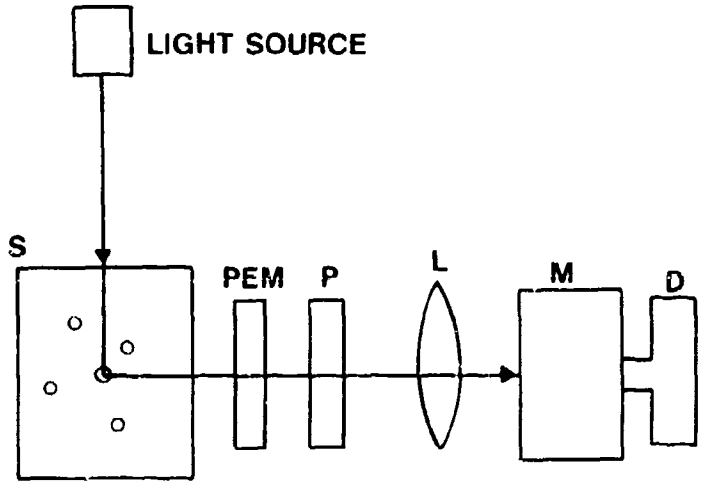

Figure 2. Polarized scattering in a cuvette from an index matched sample. PEM is a photoelastic modulator, P is a polarizer, L is a lens, M is a monochromator, and D is a detector.

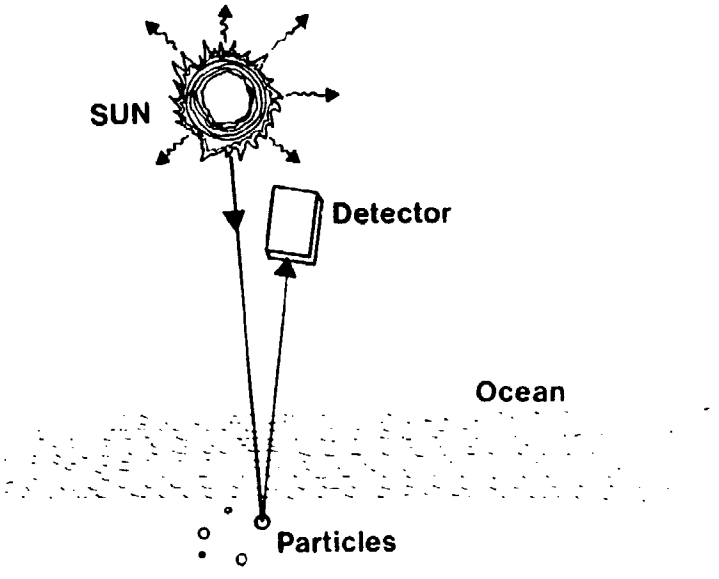

Figure 3. Polarized scattering from particles in a body of water.

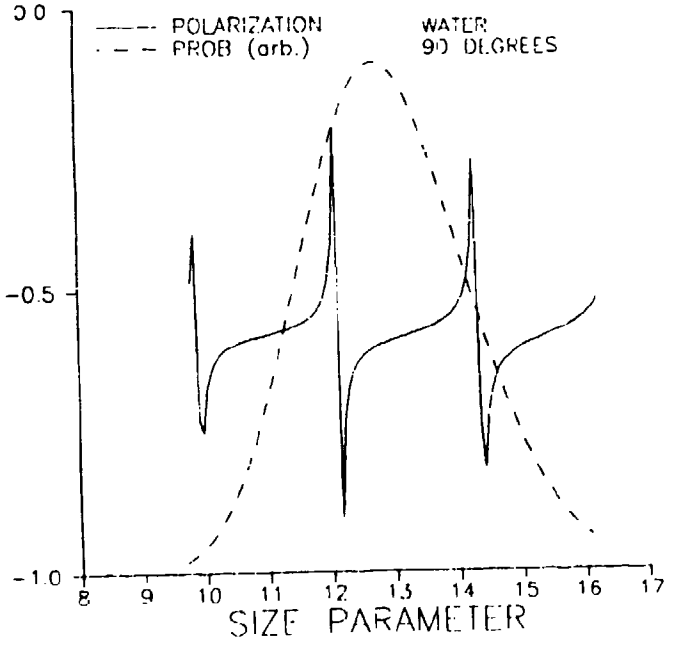

Figure 4. Polarization and probability distribution as functions of size parameter for 90° scattering in water.

REFERENCES

1. Karle, R., 1992, "Linear Depolarization Lidar Measurements of Dugway Clouds," LA-UR-92-1217, LANL technical report.

2. Sassen, K., and G. C. Dodd, 1991, "The Polarization Lidar Technique for Cloud Research: A Review and Current Assessment," Bull. Am. Meteorol. Soc., 72, 1848-1866.

3. Eloranta, E. W., and P. K. Piironen, 1992, "Adaptation of the University of Wisconsin High Spectral Resolution Lidar for Polarization and Multiple Scattering Measurements," Proceedings of 16th International Laser Radar Conference, (NASA Conference Publications 3158) pp 353-356.

4. Petsko, Gregory A., 1992, "On the Other Hand," Science, 256, 1403-1404.

5. Avetisov, A. Avetisov, I. G. Vitalii, and V. V. Kuz'min, 1991, "Handedness, Origin of Life and Evolution, Physics Today, 7, 33-41.

6. Bohren, Craig F., and Donald R. Huffman, 1983, Absorption and Scattering of Light by Small Particles, Wiley, New York, pp. 185-194.

7. Bohren, Craid F., 1974, "Light Scattering by an Optically Active Sphere," Chem. Phys. Lett., 29, 458-462.

8. Pendleton, David J., 1982, "Mie Scattering into Solid Angles," J. Opt. Soc. Am., 72, 1029-1033.

9. Pendleton, David J., 1982, A Generalized Mie Theory Solution and Its Application to Particle Sizing Interferometry, Ph.D Thesis (University of Tennessee, Knoxville).

10. Gordon, David J., 1972, "Mie Scattering by Optically Active Particles," Biochemistry, 11, 413-420.

11. Lofftus, K. D., M. S. Quinby-Hunt, A. J. Hunt, F. Livolant, and M. Maestre, 1992, "Light Scattering by Procentrum Micans: A New Method and Results," Appl. Opt., 31, 2924-2931.

12. Reuter, R., 1980, "Characterization of Marine Particle Suspensions by Light Scattering," Oceanol. Acta., 3, 317-332.

CREEPING WAVES: A MISSING INGREDIENT IN VARIATIONAL TRIAL FIELDS

B. J. Stoyanov and R. A. Farrell
The Milton S. Eisenhower Research Center
The Johns Hopkins University Applied Physics Laboratory
Laurel, MD 20723

RECENT PUBLICATIONS, SUBMITTALS FOR PUBLICATION AND PRESENTATIONS:

A) B. J. Stoyanov and R. A. Farrell, "Variational Scattering Calculations with Impedance Boundary Conditions," in *Proc. of the 1991 CRDEC Scientific Conference on Obscuration and Aerosol Research*, compiled by D. A. Clark, J. E. Rhodes, and B. A. Claunch (U.S. Army CRDEC-SP-036, Edgewood, MD, 1992), pp. 239-255.

B) B. J. Stoyanov, R. A. Farrell, and J. F. Bird, "Asymptotic Expansions of Integrals of Two Bessel Functions via the Generalized Hypergeometric and Meijer Functions," *J. Comp. Appl. Math.* (accepted).

C) B. J. Stoyanov and R. A. Farrell, "Creeping Waves: A Missing Ingredient in Variational Trial Fields," presentation at the 1993 RDEC Scientific Conference on Obscuration and Aerosol Research (U.S. Army Research, Development, and Engineering Center, Aberdeen Proving Ground, MD, 22-24 June 1993).

ABSTRACT

The development of simple and efficient trial fields for a Schwinger-type variational principle for diverse scattering problems has been one of our long-term objectives. Previously devised trial fields that are capable of both satisfying boundary conditions and imitating shadowing effects have proven quite effective for TM polarization. Specifically, comparisons with the exact solutions available for canonical shapes show that such trial fields can yield excellent accuracy for all frequencies/scatterer sizes and all scattering directions.

For TE polarization, such trial fields lead to noticeable inaccuracies in the resonance region for scattering into the backward half-space. As is well known for a smooth sca[illegible], there are pronounced oscillations present in the resonance region caused by [illegible]rence between a specularly-reflected wave and creeping waves that circle the [illegible]tterer's shadowed side and are shed back in the direction of the reflected wave. Guided by this insight, we have earlier conjectured that the discrepancies in the TE variational results are due to the lack of proper creeping-wave effects in the trial fields.

In this paper, we provide an explicit verification of this conjecture for a simple test problem of plane-wave scattering from an infinite cylinder with (TE) Neumann's boundary condition. Namely, we demonstrate that when a creeping-wave contribution, as available from the exact solution, is incorporated into the variationally-derived backscattering amplitude, good accuracy results for all size parameters. The accuracy of this hybrid (variational/exact) solution gradually deteriorates as the scattering angle deviates from the backscattering direction because both its components (i.e., variational and creeping-wave) become increasingly inaccurate for these scattering angles. Using physical insights gained from the hybrid solution as guidance, we are presently developing simple and efficient means for incorporating approximate creeping-wave effects directly into the trial fields to obtain more accurate, consistently-variational solutions.

INTRODUCTION

This work is a continuation of our ongoing effort [1-11] to develop simple and efficient trial functions that, in conjunction with Schwinger-type variational principle [12], yield all-frequency accuracy in variational solutions for electromagnetic and acoustic scattering problems. It has been shown earlier [6-11] that, for transverse-magnetic (TM) polarization and acoustically-soft scatterers with Dirichlet's boundary condition (BC), trial fields that are capable of both satisfying BCs and imitating shadowing effects are very effective in providing accurate variational results. Specifically, comparisons with exact solutions available for canonical shapes [13,14] demonstrate that these so-called shadowed boundary-Born trial fields yield excellent accuracy for all frequencies/scatterer sizes and all scattering directions for impenetrable [6-10] as well as penetrable (with impedance BCs [11]) scatterers.

Such trial fields also provide reasonable broadband accuracy in variational solutions for transverse-electric (TE) polarization and acoustically-hard scatterers with Neumann's BC. However, for scattering into the backward half-space, they lead to noticeable inaccuracies in the resonance region, i.e., for size parameters $1 \lesssim ka \lesssim 20$, where a is the scatterer characteristic size, and $k \equiv 2\pi / \lambda$ is the wavenumber, with λ being the wavelength of incident radiation. In this region, the exact solutions [13,14] exhibit pronounced oscillations that are due [14-16] to

the interference between a direct reflection from the illuminated side of a scatterer and creeping waves that are launched at a shadow boundary, traverse the shadowed side of the scatterer, and are shed in the direction of the specular reflection. Guided by this physical insight, we have made [7,11] a conjecture that the shortcomings of our variational results for TE scattering are due to the lack of proper creeping-wave effects in the shadowed boundary-Born trial fields.

In this paper we explicitly verify this conjecture for a simple test problem of plane-wave scattering from an infinite cylinder with Neumann's BC. Specifically, we demonstrate numerically that incorporating creeping-wave contributions, as available from the exact solutions [13,14], into the variationally-derived backscattering amplitude leads to a hybrid (variational/exact) solution that is accurate for all size parameters. Intuitively appealing explanations based on decomposition of the exact scattering amplitude into optics and creeping-wave contributions, and direct comparison of the variational and optics constituents of the hybrid solution, allow one to readily understand why the hybrid result is so effective for TE backscatter. Good results were also obtained using this procedure for a range of scattering angles around the backscatter. However, as the scattering angle deviates further and further from the backscattering direction, the accuracy of the hybrid solution gradually deteriorates, until at some angle it becomes contaminated with spurious spikes and/or wiggles. Both the variational and the creeping-wave components of the hybrid solution become increasingly inaccurate for such scattering directions, although for different ranges of size parameter: the former for larger and the latter for smaller ka's.

With this added knowledge and further insight into the physics of the problem, the next logical step is to incorporate a simple but efficient approximation for creeping-wave effects directly into the trial fields in order to

obtain accurate, consistently-variational solutions for TE scattering. This is the problem we are still working on, and the results will be reported elsewhere.

It has been noted that unlike the TE case, the creeping-wave contributions [13,14] to TM scattering are numerically insignificant and physically not essential [15,16], as is apparent from the absence of any pronounced oscillatory structure in the exact backscatter. Thus, as should be clear from the above, the shadowed boundary-Born trial fields already contain the essential physical effects required for effective variational approximation of TM scattering from smooth shapes. Since details of our variational solutions for TM scattering from impenetrable and penetrable cylinders were published earlier [6,11], and a more thorough exposition will be published elsewhere [7], here we concentrate on plane-wave scattering from an infinite cylinder with Neumann's BC.

Before proceeding with the problem, we would like to point out that our interest in scattering from canonical separable shapes [13,14] is motivated by the availability of manageable exact solutions against which our variational results can be tested analytically and/or numerically for all size parameters, scattering directions, and polarizations. The approach itself of developing mathematically simple and physically plausible trial fields [17] by incorporating the essential physics inherent in scattering processes [1-11,18] is a generic one and is not limited to particular scattering problems.

SCHWINGER-TYPE VARIATIONAL PRINCIPLE FOR SCATTERING AMPLITUDE

Scattering of a plane wave by an infinitely-long perfectly-conducting cylinder of radius a, whose axis is along the z direction, is depicted in Fig. 1, where $\vec{k}_i, \vec{k}_s$ are the incident and scattered propagation vectors, respectively, and ϕ_s is the scattering angle. The usual polar coordinates ρ, ϕ are used to specify an arbitrary point in a plane normal to the cylinder axis. Only normal plane-wave

incidence is considered because, for the case of perfect conductor, a general three-dimensional (3-D) problem of oblique incidence can be reduced to two scalar (i.e., TM and TE) 2-D scattering problems [13]. This has the additional advantage that physical mechanisms can be evolved without the extra complication brought in by three dimensions. Also, without loss of generality, the incident plane wave propagating in the x direction is assumed to be of unit (dimensionless) amplitude, and the harmonic time dependence $e^{-i\omega t}$ is suppressed everywhere.

For TE polarization, the (total) magnetic field is parallel to the cylinder axis, i.e., in the z direction, depends on $\vec{\rho}$ and $\vec{k}_i$, and has its normal derivative vanishing on the surface (Neumann's BC) of a perfectly-conducting cylinder. Introducing $\psi \equiv \psi(\vec{\rho},\vec{k}_i) = H_z(\vec{\rho},\vec{k}_i)$, the Schwinger-type variational principle [12] for the scattering amplitude for the problem under consideration can be derived in a straightforward manner and written down in the standard form

$$T^V = N\tilde{N} / D \tag{1a}$$

in terms of line integrals along the cylinder circumference

$$N = \frac{ia}{4}\int_0^{2\pi} d\phi\psi(a,\phi)\frac{\partial}{\partial\rho}e^{-ik\rho\cos(\phi-\phi_S)}\Big|_{\rho=a} \tag{1b}$$

$$\tilde{N} = \frac{ia}{4}\int_0^{2\pi} d\phi'\tilde{\psi}(a,\phi')\frac{\partial}{\partial\rho'}e^{ik\rho'\cos\phi'}\Big|_{\rho'=a} \tag{1c}$$

$$D = \frac{a^2}{16}\int_0^{2\pi} d\phi \int_0^{2\pi} d\phi'\psi(a,\phi)\tilde{\psi}(a,\phi')\frac{\partial^2 H_0^{(1)}(k\,|\,\rho-\rho'\,|)}{\partial\rho\partial\rho'}\Bigg|_{\substack{\rho=a\\ \rho'=a}} . \tag{1d}$$

The tilded quantities, $\tilde{N}$ and $\tilde{\psi}$, represent the adjoint solution, i.e., the solution of the reciprocal problem in which the source and observer are interchanged, so that the reciprocity relation [12,17] is satisfied due to the form of Eq. (1a). Thus, the adjoint field $\tilde{\psi} = \psi(-\vec{k}_s)$ follows directly from the original field $\psi = \psi(\vec{k}_i)$ by substitution $\phi \to \phi - \phi_s - \pi$. This relation holds for the exact fields ψ and $\tilde{\psi}$, and we will impose it on the trial field so that our variational solution will satisfy reciprocity. Also, $H_0^{(1)}$, the Hankel function of first kind and zeroth order, represents (up to a constant factor) a two-dimensional free-space Green's function appropriate for this problem. Using Graf's addition theorem [19], the double integral in Eq. (1d) can be reduced to a product of single integrals.

With the correct fields $\psi, \tilde{\psi}$, each of the integrals N, $\tilde{N}$, and D, as well as their ratio Eq. (1a), will yield the correct scattering amplitude T. Then, the normalized differential cross section follows immediately

$$\sigma = \begin{cases} |T|^2/(ka)^2 & , \text{ forward } (\phi_s = 0), \quad (2a) \\ |T|^2(4/\pi ka) & , \text{ otherwise } (\phi_s \neq 0). \quad (2b) \end{cases}$$

Normalization is chosen (as for TM case [6,11]) such that $\sigma \to 1$ for forward- and back-scattering when ka $\to \infty$. On the other hand, when a trial field containing some error is used for ψ (and $\tilde{\psi}$), the variational-approximate T^V given by Eq. (1a) will have errors of the second and higher order. The first order errors in T^V cancel out due to its inherent stationary property [12], and this is potentially advantageous when compared to other, non-variational approximate techniques.

DEVELOPMENT AND TESTS OF TRIAL FIELDS

In developing trial fields for this problem we followed our trial-field design procedure [1,2,6,7,11], which is based on physical insight. Namely, starting with the simple Born approximation, i.e., just the incident plane wave, we augment it by the same expression, but evaluated on the scatterer surface and premultiplied by a simple factor, so that the resulting boundary-Born trial function is capable of satisfying the pertinent BC. To provide for shadowing, which is important for moderate and large size parameters, this trial function is premultiplied by a simple, shadow-imitating function. The following shadowed boundary-Born trial field

$$\psi_t(\rho,\phi) = [1-\beta(ka,\cos\phi)]\left[e^{ik\rho\cos\phi} - f(\rho)\cos\phi\, e^{ika\cos\phi}\right] \tag{3}$$

is capable of satisfying Neumann's BC, i.e. $\psi_t'(a) \equiv \partial\psi_t / \partial\rho\big|_{\rho=a} = 0$, provided $f'(a) = ik$. This approximate field ψ_t is only used in the immediate neighborhood of the cylinder. When this trial field is substituted into Eqs. (1), a variational parameter $f(a)$ resulting from $f(\rho)$ is obtained, with its "optimal" value found from the stationary condition $\partial T^V/\partial f = 0$. Also, it turns out that imposing reciprocity yields $\tilde{f} = f$ and $\tilde{N} = N$.

For TM scattering, the shadow-regulating parameter β in Eq. (3) was adjusted so that the correct large ka-limit of $T^V(\phi_s = 0)$ was obtained [6,7,9,11], i.e.,

$$T^V(\phi_s = 0) \xrightarrow[ka\to\infty]{} T(\phi_s = 0), \tag{4}$$

with the limiting value of T^V derived by employing the asymptotic techniques considered in Refs. 20,21.

Unfortunately, as our asymptotic analysis shows, in the case of TE scattering there is no single value of β in the simple shadowing function of Eq. (3), that would provide both the correct large ka-limit for the forward scattering amplitude as in Eq. (4) and a physically-reasonable $\beta\,(0 < \beta \leq 1)$ to imitate shadowing effects. In view of this, we just set $\beta = 1$ so that at the central point of the illuminated region ($\phi = \pi$) the shadowing factor is two, while at the opposite point in the shadowed region ($\phi = 0$) the shadowing factor is zero. According to the physics of wave scattering [12], shadowing is not present for small size parameters because diffraction causes the entire scatterer to be illuminated. Thus, we set $\beta = 0$ for, say, $ka \leq 0.7$ by introducing a simple ramp function:

$$\beta(ka) = \begin{cases} 0, & ka \leq 0.7, \\ (ka - 0.7)/(1.0 - 0.7), & 0.7 < ka < 1.0, \\ 1, & ka \geq 1.0. \end{cases} \tag{5}$$

With such a ramp function the shadowed trial field in Eq. (3) goes over to the original boundary-Born field for small ka's, which yields exceptionally good results in this ka-region for both TM and TE polarizations.

For TM scattering [6-11], incorporating the simple shadowing into the boundary-Born trial fields not only corrected the large ka-limit of the variational results for forward direction, but also effectively suppressed spurious spikes and/or wiggles for all scattering directions, thereby providing very good accuracy for all size parameters. This is illustrated by Fig. 2 reproduced from Ref. 6.

For TE scattering, due to the above-mentioned lack of physically appropriate β to do this dual job, only for a range of angles ($120° \leq \phi_s \leq 180°$) around the backscatter does the simple shadowing effectively suppress spurious spikes and/or wiggles. The unshadowed boundary-Born variational result for backscatter (derived earlier in Ref. 1) is very accurate for small ka's, but is heavily

contaminated with spurious spikes for moderate and large size parameters, as shown in Fig. 3a. The simple shadowing with β defined in Eq. (5) eliminates the spurious spikes (see Fig. 3b), so that the variational backscatter is now quite accurate for both small ($ka \lesssim 0.7$) and large ($ka \gtrsim 20$) size parameters. However, in between, i.e., in the transition region of moderate ka's the shadowed boundary-Born trial field leads to noticeable inaccuracies. This is the resonance region where the exact solution attains a peak near $ka = 0.8$, and then oscillates about the geometric optics value of $\sigma = 1$ with damped, regularly spaced excursions of notable amplitude that becomes smaller as the cylinder becomes larger. It is well-known [14-16] that these oscillations are due to the interference between the specularly-reflected and creeping-wave contributions to the exact backscatter. To gain a better insight into the physics of this phenomenon, as well as to be able to ascertain explicit implications for improving our trial field, we turn now to a more careful analysis of the exact backscatter solution.

OPTICS AND CREEPING-WAVE CONTRIBUTIONS TO THE EXACT SOLUTION

Applying a sophisticated asymptotic analysis, the **exact** scattering amplitude for $90° < \phi_s \leq 180°$ and values of ka sufficiently large (depending on ϕ_s) can be decomposed as [13-15]

$$T = T^{Opt.} + T^{Creep.}, \tag{6a}$$

where $T^{Opt.}$ and $T^{Creep.}$ are the optical and creeping-wave contributions, respectively (see Fig. 4a). For the exact TE backscatter, a development useful numerically for $ka > 2$ is explicitly given by [13,14]

$$T^{Opt.} = \frac{1}{2}\sqrt{\pi ka}\,\exp[i(\pi/4 - 2ka)]\left[1 - \frac{i11}{16ka} - \frac{353}{512(ka)^2} + O\left[(ka)^{-3}\right]\right] \tag{6b}$$

and

$$T^{Creep.} = 1.531915\sqrt{\pi}(ka)^{1/3}\exp\left[-2.20(ka)^{1/3} - 0.3957635(ka)^{-1/3} + \ldots\right]$$
$$\times \exp\left\{i\left[\pi/3 + \pi ka + 1.2701695(ka)^{1/3} - 0.2284945(ka)^{-1/3} + \ldots\right]\right\}. \tag{6c}$$

It should be noted that the first term in the optical contribution is the standard geometric optics result. One can readily appreciate the accuracy of the creeping-wave approximation represented by Eqs. (6) through inspection of Fig. 4b, where curves of backscattering cross section for the optics and creeping-wave contributions, as well as for the combined optics and creeping-wave contribution, generated by substituting Eqs. (6) into Eq. (2b) are plotted along with the exact solution.

The geometrical optics contribution to the backscattering amplitude is depicted in Fig. 4a as a specularly-reflected ray. The physical interpretation of the origin of the far-field creeping-wave contribution in Eq. (6c) is that the incident rays at their points of tangency to the cylinder (see Fig. 4a, where only one such ray is shown) launch creeping waves emanating from these points. These waves travel along the surface with phase velocity slightly smaller than in free space. As they travel along the surface, they shed radiation along tangential directions, and thus become exponentially damped.

Using heuristic arguments gleaned from the literature, it is possible to qualitatively explain the exponential decay of creeping wave amplitude. Let us consider wave diffraction on a convex polygonal cylinder, first concentrating just on two of its edges. As the wave is scattered on the first edge, its amplitude is decreased. Then a diffracted ray skimming along the cylinder's flat surface impinges on the second edge, and is again diffracted, traveling along a geodesic according to generalized Fermat's principle. Now let us consider m edges. If ϕ is

an overall angle that the wave circumnavigating the scatterer had traversed, then for an elemental angle ϕ/m the wave's amplitude A is decreased by $\gamma(\phi/m)A$, where γ is a proportionality coefficient. To the next edge the wave arrives with the amplitude $A(1-\gamma\phi/m)$, after which the amplitude becomes $A(1-\gamma\phi/m)^2$, and after traveling over m edges it becomes $A(1-\gamma\phi/m)^m$. In the limit $m \to \infty$, we obtain the exponential decay, $A\exp(-\gamma\phi)$, since it is well-known that $\lim_{x\to\infty}(1+1/x)^x = e = 2.718\ldots$. Note that this decay is due entirely to shedding of radiation, as there is no absorption for a perfectly conducting scatterer. Then, according to the classical theory of radiation, the amplitude of the wave shed off the scatterer is proportional to $-(d/d\phi)A\exp(-\gamma\phi) = A\gamma\exp(-\gamma\phi)$.

Let us now find an approximation for the dominant functional form of the phase of a creeping wave at an angular distance ϕ from the point of launching (injection). We note that in a cylindrical coordinate system traveling wave solutions vary as $\exp(i\nu'\phi) = \exp(ik's)$, where ν' is the azimuthal index, and k' is the propagation constant along the surface. Since the arc length $s = a\phi$, this gives $\nu' = k'a$, and the creeping-wave phase factor becomes $\exp(ik'a\phi)$, with $k' \gtrsim k$ because the creeping-wave velocity along the surface is slightly smaller than that in free space. As a first order approximation we set $k' = k$, which leads to $\exp(ika\phi)$.

Thus, a creeping wave traveling along the surface of a scatterer can be represented by the generic form $A\exp(i\nu\phi)$, where $\nu = \nu' + i\nu''$, with $\nu' \approx ka$ and $\nu'' = \gamma$. When this wave is shed off the scatterer at an angle ϕ from the launch point, its form becomes $\sim A\gamma\exp(i\nu\phi)$. It can be shown that the decay coefficient $\gamma \sim (ka)^{1/3}$. For a creeping wave shed off in the backward direction $\phi = \pi$, so that we get $A_0(ka)^{1/3}\exp[i\pi ka - \gamma_0(ka)^{1/3}]$, which correctly reproduces the dominant ka dependence of both the amplitude and phase in Eq. (6c). Specific values of constants A_0 and γ_0 are determined by the geometry and BC of a particular

scatterer, and for canonical shapes they have been derived from rigorous solutions using pertinent asymptotic methods [13,14].

The oscillatory nature of the cylinder **backscatter** is due to the interference between a specularly-reflected wave and a creeping wave that circles the rear of the cylinder and is shed backwards, as is shown in Fig. 4a. To the extent that the creeping wave travels along the surface at the free space velocity, it traverses an additional path length equal to the cylinder diameter plus half the circumference, or a total additional path of $(2+\pi)a$. The damped interference pattern, therefore, should have peak-to-peak spacings in ka that occur when the path length difference is a wavelength, or for $\Delta ka = 2\pi/(2+\pi) \approx 1.22$, which is in close agreement with the actual average spacing in Fig. 3. Because the creeping wave loses energy in proportion to the distance traveled along the cylinder, it becomes weaker as the cylinder becomes larger. Consequently, the interference pattern becomes weaker as the electrical size of the cylinder, i.e., its size parameter ka, increases. Therefore, the creeping-wave contributions are numerically insignificant for $ka >> 1$. Also, the higher-order creeping waves which made one or more additional complete circumnavigations in clockwise and counterclockwise directions around the cylinder are of little value, and were not included in Eq. (6c).

We note in passing [13,14] that, in the corresponding expression for creeping waves with TM polarization, the numerical coefficient (−2.20) in the exponent of the dominant damping factor in Eq. (6c) would be replaced by (≈ -5.05), and the overall constant factor of (≈ 1.53) by (≈ 0.91), among other minor changes. Consequently, the creeping-wave contributions are numerically insignificant for TM polarization, and produce no appreciable oscillatory structure in the backscatter, only a slight wavering (see Fig. 2).

HYBRID (VARIATIONAL/EXACT) SOLUTION

In order to obtain guidance from the above analysis for our objective of improving the TE variational solution in the resonance region, we plotted in Fig. 5a the shadowed boundary-Born result T^V (already shown in Fig. 3b vs. the exact backscatter) together with the **optics** contribution $T^{Opt.}$ from Eq. (6b). An inspection of Fig. 5a reveals that the two curves are in reasonable overall agreement for $1 \lesssim ka \lesssim 10$, and practically coincide for $ka \gtrsim 10$. (Even better agreement has been found between the phases of the complex amplitudes T^V and $T^{Opt.}$.) Because the variational and optics solutions are in good agreement, one can expect that by augmenting the variational backscatter with the creeping-wave contribution from Eq. (6c), a much better accuracy will result in the resonance region.

It is gratifying to see this expectation amply fulfilled, as Fig. 5b attests, where the hybrid solution obtained by substituting [cf. Eq. (6a)]

$$T^{Hybrid} = T^V + T^{Creep.} \tag{7}$$

into Eq. (2b) is compared to the exact backscatter. Not only a remarkable improvement is achieved for $ka \gtrsim 2$, i.e., for the domain where Eqs. (6) hold true, but also the agreement is quite good for $0.7 \lesssim ka \lesssim 2.0$, where the creeping-wave theory is not supposed to be efficient (see Fig. 4b). This somewhat unexpected improvement is, in part, a result of our use of the same ramp function as in Eq. (5) to premultiply $T^{Creep.}$ (which is quite reasonable), but is mostly due to the fact that our variational solution T^V is more accurate than the optics contribution $T^{Opt.}$ in Eq. (6b) for $0.7 \lesssim ka \lesssim 2$ (cf. Figs. 3b and 4b). And since T^V itself is very accurate for $ka \lesssim 0.7$ and ka >> 1, good all-frequency accuracy is achieved with this hybrid solution for TE backscatter

Good results have also been obtained with the hybrid solution for those scattering directions, $120° \lesssim \phi_s \leq 180°$, where the variational component T^V in Eq. (7) is not contaminated by spurious spikes or wiggles, although the accuracy is not as good as for the backscatter for $0.7 \lesssim ka \lesssim 7$ because the creeping-wave contribution [13,14] to Eq. (7) becomes gradually less and less accurate for scattering angles deviating further and further from the backscattering direction. For these scattering angles, the accuracy of T^V alone (i.e., without $T^{Creep.}$) gradually extends to larger ka's, reproducing quite faithfully the first few oscillations, which the representation in Eq. (6a) fails to do. However, beyond this range of scattering angles, T^V becomes quickly contaminated by spurious spikes and/or wiggles, and the hybrid solution completely fails. To remedy such a situation, a better designed trial field is needed, with capability of imitating creeping-wave effects by simple but efficient means akin to those that have been devised to satisfy the boundary condition and shadowing requirements. Investigations in this direction are underway.

SUMMARY AND CONCLUSIONS

The main thrust of this work has been to explicitly verify our earlier conjecture [7,11] based on physical insight that, for TE scattering, creeping waves constitute an essential physical ingredient missing in the shadowed boundary-Born trial fields, as manifested by noticeable inaccuracies in the resonance region. Specifically, we have demonstrated for a simple test problem of plane-wave scattering from an infinite cylinder with Neumann's BC that incorporating the creeping-wave contribution available from the exact solution into the variationally-derived backscattering amplitude yields good accuracy for all size parameters.

In the process of devising this hybrid (variational/exact) solution, physical insights into the creeping-wave phenomena have been provided, and dominant features of a generic creeping wave have been deduced using arguments of a heuristic nature. Intuitively appealing explanations have also been given concerning the effectiveness of the hybrid solution in the entire resonance region and beyond. Additionally, it has been observed that, for TM scattering, the shadowed boundary-Born trial fields lead to very accurate variational results because creeping-wave effects are numerically insignificant in this case.

We expect the hybrid solution to be as effective for scattering from other impenetrable smooth shapes with Neumann's BC, as well as for TE scattering from penetrable scatterers with impedance BCs. Indeed, similar gratifying results have recently been obtained by D. E. Freund for plane-wave scattering from an acoustically-hard sphere using this procedure.

Practical applicability of the hybrid approach is, however, limited to those few problems for which accurate and numerically efficient expressions for creeping-wave contributions are available. Moreover, the hybrid solution cannot provide uniformly accurate results for all scattering directions since its variational and creeping-wave components become increasingly inaccurate for scattering angles further and further away from the backscattering direction. Therefore, guided by knowledge and insights gained from the experience with the hybrid solutions, we are presently trying to derive more accurate, consistently-variational solutions by developing more efficient trial fields. These trial fields will directly accommodate creeping-wave effects through a simple, approximate means similar to those used to satisfy BCs and to imitate the shadowing effects.

ACKNOWLEDGMENTS

We thank S. Favin for his help with the numerical computations. This research was supported by the Navy under contract N00039-91-C-0001.

REFERENCES

1. J. A. Krill, J. F. Bird, and R. A. Farrell, "Trial Functions in Variational Calculations," in *Proc. of the 1982 CSL Scientific Conference on Obscuration and Aerosol Research*, edited by R. H. Kohl and Assoc. (Tullahoma, TN, 1983) pp. 201-209.

2. J. A. Krill and R. A. Farrell, "The Development and Testing of a Stochastic Variational Principle for Electromagnetic Scattering," in *Wave Propagation and Remote Sensing, Proc. of URSI Commission F 1983 Symposium* (European Space Agency, Noordwijk, The Netherlands, 1983), pp. 299-307.

3. J. F. Bird and R. A. Farrell, "Electromagnetic Scattering Theory," *Johns Hopkins APL Tech. Dig.* **7**, 58-72 (1986).

4. B. J. Stoyanov, J. A. Krill, J. F. Bird, and R. A. Farrell, "Broadband Trial Functions for Surface Scattering with Detailed Analysis for a Simple Model," in *Proc. of the 1986 CRDEC Scientific Conference on Obscuration and Aerosol Research* (to appear).

5. J. F. Bird, R. A. Farrell, E. P. Gray, and B. J. Stoyanov, "Trial Functions for Scattering from Surfaces of Arbitrary Roughness and Variational Test Calculations," in *Proc. of the 1986 CRDEC Scientific Conference on Obscuration and Aerosol Research* (to appear).

6. B. J. Stoyanov and R. A. Farrell, "Effects of Simple Shadowing on Variational Calculations," in *Proc. of the 1987 CRDEC Scientific Conference on Obscuration and Aerosol Research*, edited by E. H. Engquist and K. A. Sistek (U.S. Army CRDEC-SP-88031, Edgewood, MD, 1988), pp. 347-356.

7. B. J. Stoyanov and R. A. Farrell, "A Physical Approach to Developing All-Frequency Trial Fields in Variational Wave-Scattering Calculations," in revision.

8. D. E. Freund and R. A. Farrell, "Near Field Variational Principle: Scattering from Spheres," in *Proc. of the 1988 CRDEC Scientific Conference on Obscuration and Aerosol Research*, edited by E. H. Engquist and K. A. Sistek (U.S. Army CRDEC-SP-010, Edgewood, MD, 1989), pp. 217-234.

9. D. E. Freund and R. A. Farrell, "A Variational Principle for the Scattered Wave," *J. Acoust. Soc. Am.* **87**, 1847-1860 (1990).

10. D. E. Freund and R. A. Farrell, "Variational Scattering Calculations for a Prolate Spheroid," in *Program of the 121st ASA Meeting* (Baltimore, 27 April-3 May, 1991), *J. Acoust. Soc. Am.* **89** (No. 4, Pt. 2), 1994 (1991).

11. B. J. Stoyanov and R. A. Farrell, "Variational Scattering Calculations with Impedance Boundary Conditions," in *Proc. of the 1991 CRDEC Scientific Conference on Obscuration and Aerosol Research*, compiled by D. A. Clark, J. E. Rhodes, and B. A. Claunch (U.S. Army CRDEC-SP-036, Edgewood, MD, 1992), pp. 239-255.

12. P. M. Morse and H. Feshbach, *Methods of Theoretical Physics*, Part II, McGraw-Hill, New York (1953).

13. J. J. Bowman, T. B. A. Senior, and P. L. E. Uslenghi, Eds., *Electromagnetic and Acoustic Scattering by Simple Shapes* (North-Holland, Amsterdam, 1969).

14. G. T. Ruck, D. E. Barrick, W. D. Stuart, and C. K. Krichbaum, *Radar Cross Section Handbook* (Plenum, New York, 1970), Vols. 1 and 2.

15. H. C. van de Hulst, *Light Scattering by Small Particles* (Dover, New York, 1981).

16. M. Kerker, *The Scattering of Light and Other Electromagnetic Radiation* (Academic, New York, 1969).

17. D. S. Jones, "A Critique of the Variational Method in Scattering Problems," *IRE Trans. Antennas Propagat.* **AP-4**, 297-301 (1956).

18. M. R. Feinstein and R. A. Farrell, "Trial Functions in Variational Approximations to Long-Wavelength Scattering," *J. Opt. Soc. Am.* **72**, 223-231 (1982).

19. M. Abramowitz and I. A. Stegun, Eds., *Handbook of Mathematical Functions*, AMS 55 (National Bureau of Standards, Washington, DC, 1964).

20. B. J. Stoyanov, R. A. Farrell, and J. F. Bird, "Asymptotic Expansions of Integrals of Two Bessel Functions," in *Asymptotic and Computational Analysis*, edited by R. Wong (Marcel Dekker, Inc., New York, 1990), pp. 723-740.

21. B. J. Stoyanov, R. A. Farrell, and J. F. Bird, "Asymptotic Expansions of Integrals of Two Bessel Functions via the Generalized Hypergeometric and Meijer Functions," *J. Comp. Appl. Math.* (accepted.)

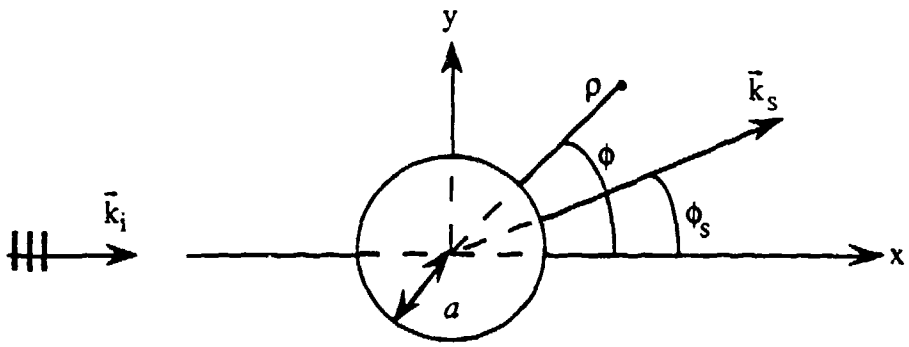

FIGURE 1. SCATTERING CONFIGURATION. Plane-wave scattering by an infinite perfectly-conducting circular cylinder at normal incidence.

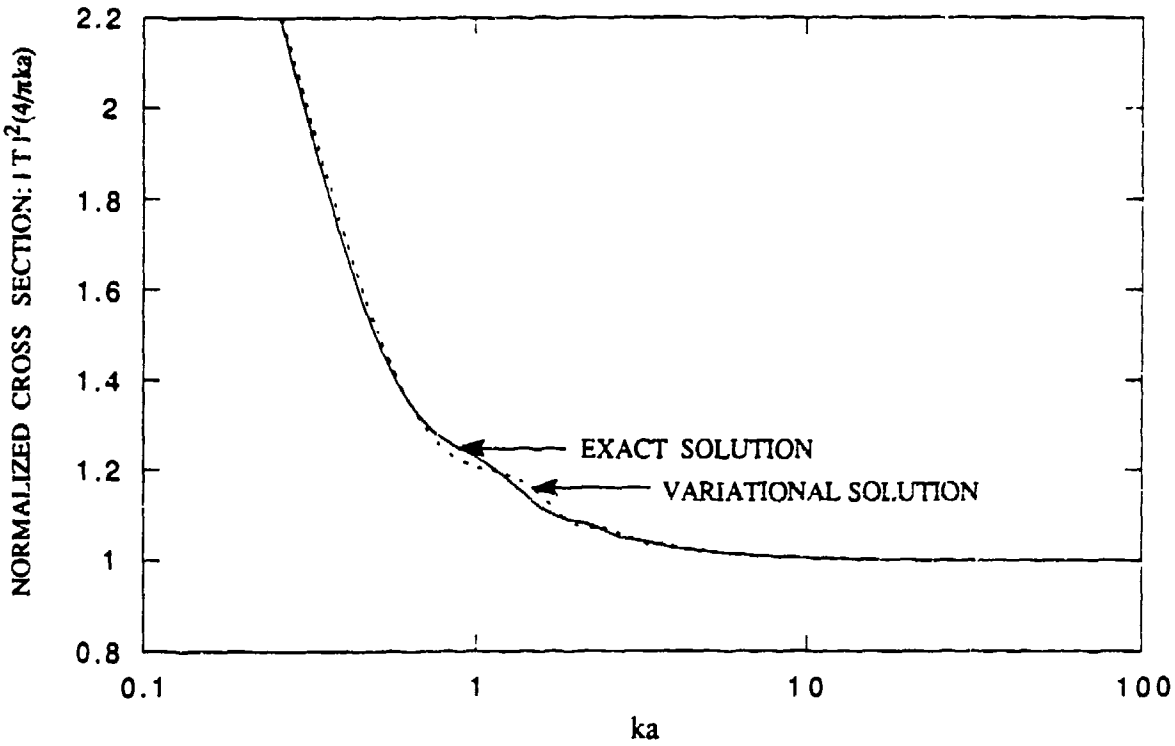

FIGURE 2. TM BACKSCATTERING. The variational cross section obtained with the shadowed boundary-Born trial field is compared with the exact solution. The maximum error is less than 2.5% and occurs at ka ~ 1.5.

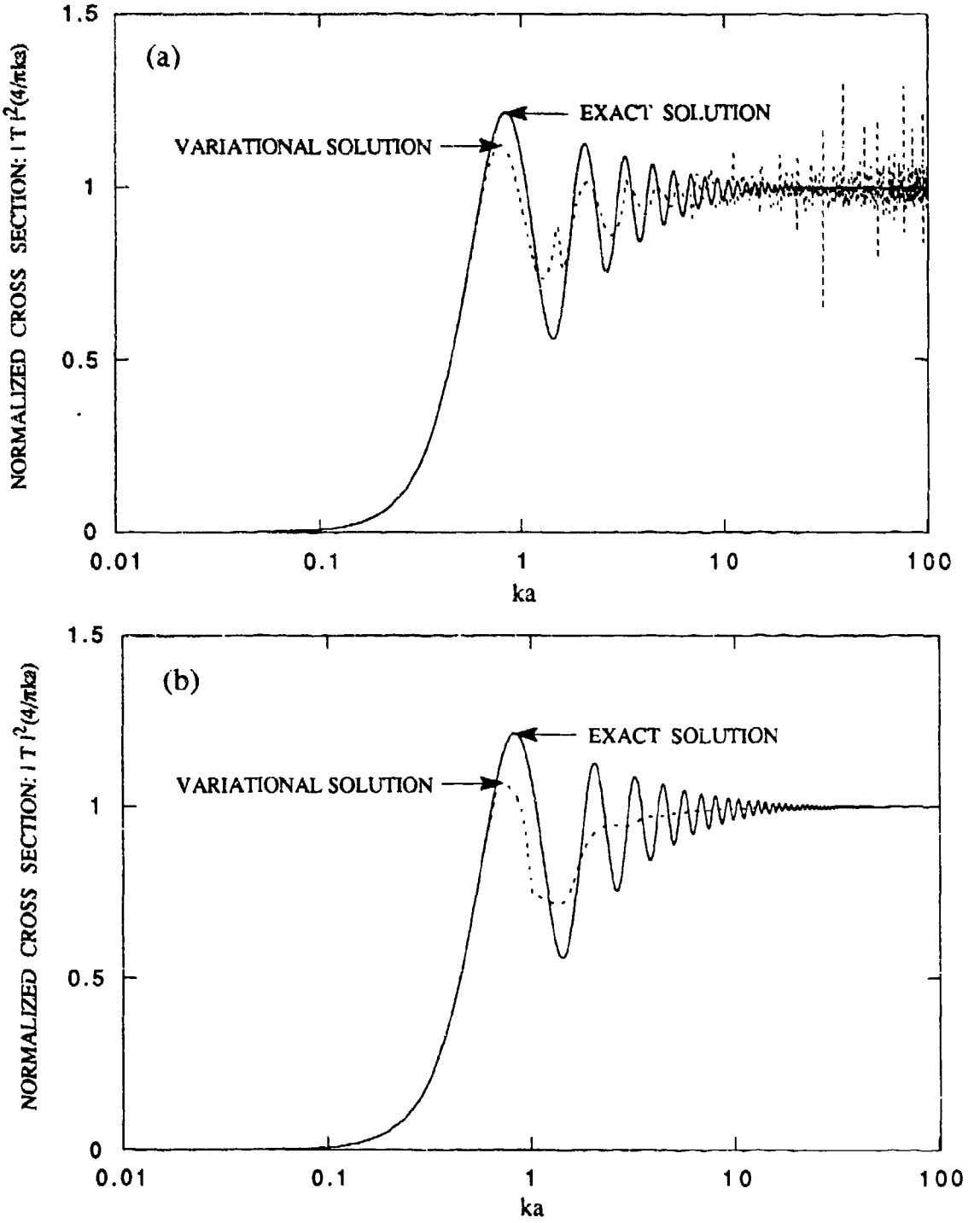

FIGURE 3. TE BACKSCATTERING. The variational solution is obtained with the boundary-Born trial field (no shadowing) in (a), while shadowing is included in (b).

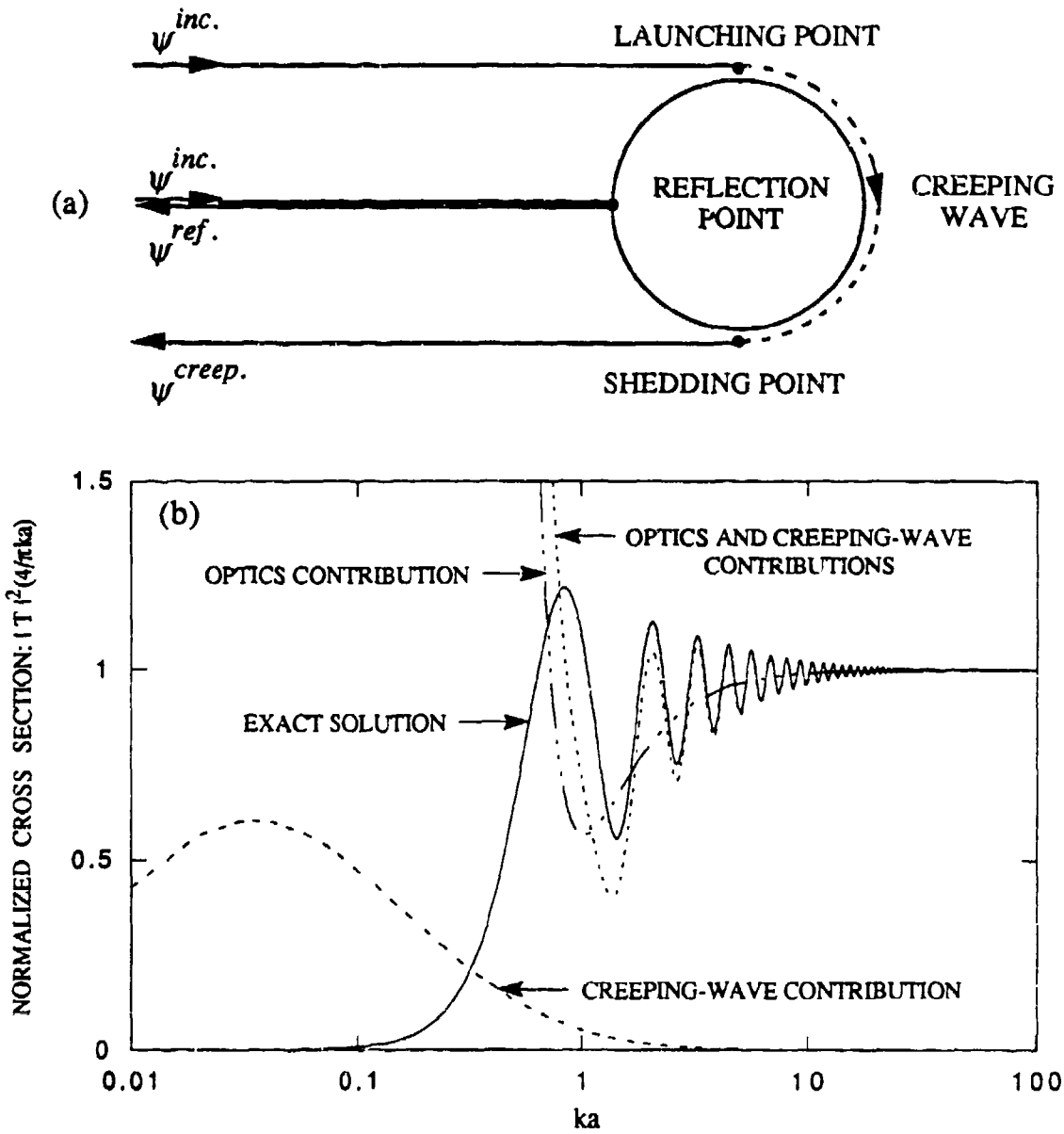

FIGURE 4. TE BACKSCATTERING. (a) Schematic illustrating the ray depiction of specularly-reflected and creeping waves. (b) At large ka, the scattering amplitude can be decomposed into optical and creeping-wave components. The optical and creeping-wave cross sections, along with the cross section from the sum of these two components, are presented as a function of size parameter, ka. The failure of this decomposition at small ka is obvious from comparison with the exact solution.

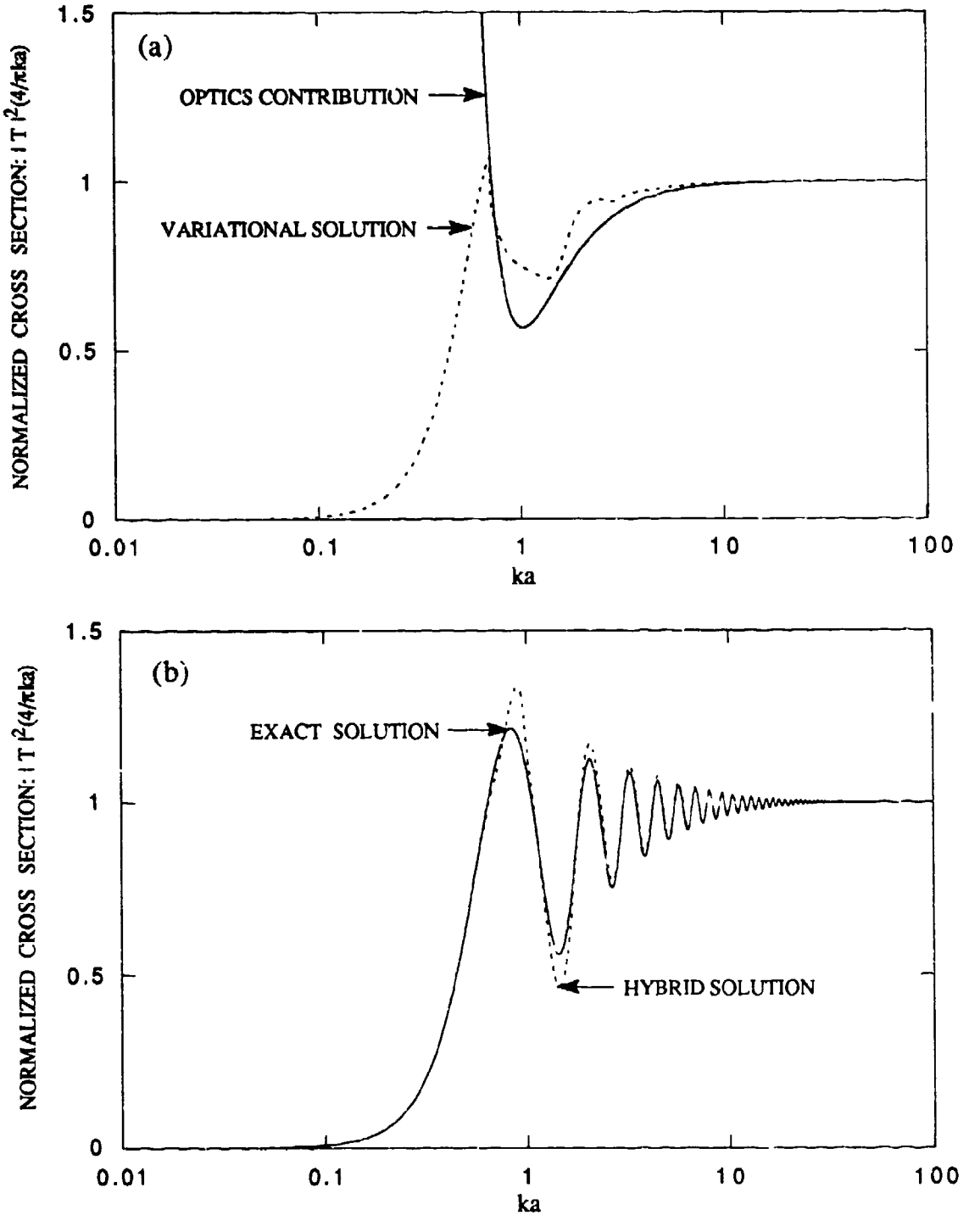

FIGURE 5. TE BACKSCATTERING (a) Comparison of the shadowed boundary-Born variational solution and the optics contribution to the exact solution. (b) The hybrid cross section found by adding the creeeping-wave contribution to the scattering amplitude to that obtained from the shadowed boundary-Born variational solution is compared with the exact solution.

Blank

Application of the Exact Solution for Infinite Cylinder Scattering to Finite Cylinder Problems

Ru T. Wang
Space Astronomy Laboratory, Institute for Space Science and Technology, Inc.
Gainesville, FL 32609

RECENT PUBLICATIONS, SUBMITTALS FOR PUBLICATION AND PRESENTATIONS:

A) Ru T. Wang, "Extinction and Angular Scattering by Rough Particles," submitted to *Proc. of the 1992 CRDEC Scientific Conference on Obscuration and Aerosol Research* (in press).
B) Ru T. Wang, "Scattering by Spheres of Narrow Size Distribution," in *Proc. of the 1991 CRDEC Scientific Conference on Obscuration and Aerosol Research*, Compiled by D. Clark, J.E. Rhodes and B.A. Claunch (Army CRDEC-SP-048, Edgewood, MD, 1992), pp. 227-238.
C) Ru T. Wang and H. C. van de Hulst, "Rainbows: Mie computations and the Airy approximation," Appl. Opt. **30**, 106-117 (1991).

ABSTRACT

The applicability of the exact solution for infinite cylinder scattering to finite cylinder problems is investigated, by comparing the infinite cylinder theory to finite cylinder microwave scattering data. As low as p = 2 for the aspect ratio p = length/diameter = $l/(2a)$ of a finite cylinder, the magnitude as well as the profile of observed scattering can be rather closely approximated by the infinite cylinder theory, if the cylinder orientation is not far from perpendicular incidence. Pertinent formulas and expressions are listed, along with a brief description of a new algorithm for computing cylindrical Bessel functions (an extension of that reported in [Ref. C)]). The appropriate multiplication factors, which depend only on $2\pi a/\lambda$ and/or p, are derived in order to assess the magnitudes of finite cylinder scattering from infinite cylinder expressions. This work, which is planned to be included in a paper for submitting to Applied Optics, represents a part of our continuing effort to systematically catalog existing microwave data, and is also a preparatory work aimed at developing a reliable, but easy to use, approximate solution to the *scattering by finite cylinders*.

I. Introduction

Studies of scattering by a cylinder span a long time, perhaps over a comparable or even longer time than that for sphere/spheroid scattering. Lord Rayleigh solved the *perpendicularly-illuminated infinite* cylinder problem as early as 1881 [Ref. 5], but it took more than 70 years before the appearance of Wait's solution [Ref. 8] for *obliquely-illuminated* cylinders of still unrealistic *infinite* length. The theoretical evaluation of the

scattering quantities deals with complex functions such as cylindrical Bessel functions, and efforts to improve on the calculation algorithms have continued [Refs. 2-4, 7].

It is well known that information on cylinder scattering is needed in a wide variety of disciplines [Ref. 2] and, indeed, it has been one of the major topics in our microwave experiments since the facility's inception by Greenberg in the late 1950's [e.g., see Refs. 1, 3-4, 6, 9, 12]. Comparing these microwave data for finite cylinders with infinite cylinder theory, we have realized that the latter is more useful than previously thought. Over the years our computational algorithm for the infinite cylinder theory has been steadily improved to meet practical applications, and this article is a report of that progress.

Following this brief introduction, the exact infinite cylinder solution as extracted from [Refs. 2-5, 7-8] is outlined in sec. II, for describing: (1) geometry, formulas, symbols and definitions employed in this article, (2) the extension of the *ratio algorithm* for sphere Mie calculation [Ref. C)] to cylinder problems, (3) conversion of the cylinder-geometric-cross-section-normalized complex extinction efficiencies (Q_{ext}, P_{ext}) to equal-volume-sphere-cross-section-normalized efficiencies (Q, P) for theory-experiment comparison, and (4) formulas evaluating the scattering by a *perpendicularly illuminated finite cylinder* via the infinite cylinder solution [Ref. 7]. Sec. III briefs the selected extinction and angular scattering data [Refs. 6, 9, 12] and compares these with the infinite-cylinder theoretical predictions. The summary conclusion is given in sec. IV.

II. The Infinite Cylinder Expressions, the Ratio Algorithm, and the Extension to Finite Cylinders

(1) Geometry, Formulas , Symbols and Definitions

Fig. 1 shows the coordinates which are used. The cylinder has a radius a and consists of a homogeneous material whose dielectric constant is ε and whose magnetic permeability is μ. We follow the notations employed in [Refs. 2-4, 7] closely, and use a Gaussian system of units with $e^{i\omega t}$ as the time factor. The incident wave has a wavelength λ, and the direction of propagation makes an angle of $\chi = 90^{\circ} - \alpha$ with the cylinder axis. In Case E the cylinder axis lies in the plane determined by the propagation vector of the plane wave, **k**, and the electric field **E**. In Case H the cylinder axis lies in the plane determined by **k** and the magnetic field **H**.

The extinction efficiency, Q_{ext}, and the scattering efficiency, Q_{sca}, are usually defined as the corresponding cross section per unit length, C, divided by $2a$, the diameter of the cylinder (normalization via cylinder's lateral geometric cross section). Q_{ext} is the real part of the complex extinction efficiencies (Q_{ext}, P_{ext}), with the imaginary part P_{ext} having a similar definition. The expressions for an infinite cylinder for case E and case H are respectively:

$$Q_{ext}^{E} = \frac{C_{ext}^{E}}{2a} = \frac{2}{ka}\mathrm{Re}\left\{b_0^E + 2\sum_{n=1}^{\infty} b_n^E\right\}, \qquad P_{ext}^{E} = \frac{2}{ka}\mathrm{Im}\left\{b_0^E + 2\sum_{n=1}^{\infty} b_n^E\right\} \tag{II-1}$$

$$Q_{ext}^{H} = \frac{C_{ext}^{H}}{2a} = \frac{2}{ka}\mathrm{Re}\left\{a_0^H + 2\sum_{n=1}^{\infty} a_n^H\right\}, \qquad P_{ext}^{H} = \frac{2}{ka}\mathrm{Im}\left\{a_0^H + 2\sum_{n=1}^{\infty} a_n^H\right\} \tag{II-2}$$

$$Q_{sca}^{E} = \frac{C_{sca}^{E}}{2a} = \frac{2}{ka}\left[\left|b_0^E\right|^2 + 2\sum_{n=1}^{\infty}\left(\left|b_n^E\right|^2 + \left|a_n^E\right|^2\right)\right] \tag{II-3}$$

$$Q_{sca}^{H} = \frac{C_{sca}^{H}}{2a} = \frac{2}{ka}\left[\left|a_0^H\right|^2 + 2\sum_{n=1}^{\infty}\left(\left|a_n^H\right|^2 + \left|b_n^H\right|^2\right)\right] \tag{II-4}$$

The infinite cylinder partial-wave expansion coefficients for the outside fields, a_n, b_n in Eqs. (II-1)-II-4), are determined in the usual way by applying the boundary conditions to the fields at the cylinder surface:

$$a_n^E = in\sin\alpha\left\{\left[B_n(\mu) - A_n(\mu)\right]/\Delta_n\right\}SR_n \tag{II-5}$$

$$b_n^E = R_n\left\{\left[A_n(\mu)B_n(\varepsilon) - n^2S^2\sin^2\alpha\right]/\Delta_n\right\} \tag{II-6}$$

$$a_n^H = R_n\left\{\left[A_n(\varepsilon)B_n(\mu) - n^2S^2\sin^2\alpha\right]/\Delta_n\right\} \tag{II-7}$$

$$b_n^H = -a_n^E \tag{II-8}$$

where

$$\Delta_n = A_n(\varepsilon)A_n(\mu) - n^2S^2\sin^2\alpha \tag{II-9}$$

$$S = 1/v^2 - 1/u^2 \tag{II-10}$$

$$R_n = J_n(v)/H_n(v) \tag{II-11}$$

$$A_n(\xi) = \left[H_n'(v)/(vH_n(v))\right] - \xi\left[J_n'(u)/(uJ_n(u))\right] \tag{II-12}$$

$$B_n(\xi) = \left[J_n'(v)/(vJ_n(v))\right] - \xi\left[J_n'(u)/(uJ_n(u))\right] \tag{II-13}$$

$$u = l_1 a = ka(\mu\varepsilon - \sin^2\alpha)^{1/2}, \qquad v = la = ka\cos\alpha \tag{II-14}$$

$J_n(x)$ = Bessel function of first kind of order n.

$H_n(x) = J_n(x) - iY_n(x)$ = Hankel function of the second kind of order n.

(2) *Ratio Algorithm* for Computing Cylinder Bessel Functions

We found that our ratio method for sphere Mie calculation [Ref. C)] could be extended to cylinder cases to better the numerical stability of computing Bessel functions. Instead of calculating all involved cylindrical Bessel functions $J_n(z)$ and their derivatives $J_n'(z)$, the *ratio algorithm* builds these functions by first computing an array of ratios between 2 consecutive-order $J_n(z)$'s: $p_n(z) = J_n(z)/J_{n-1}(z)$, where $n = 1, 2, 3, \cdots, N$, and then performing successive multiplications, e.g., $J_1(z) = p_1(z) \bullet J_0(z)$, $J_2(z) = p_2(z) \bullet J_1(z)$, $\cdots$,etc.

The well-known recursion formulas for cylindrical Bessel functions:

$$\frac{2n}{z} J_n(z) = J_{n-1}(z) + J_{n+1}(z)$$

$$2J_n'(z) = J_{n-1}(z) - J_{n+1}(z)$$

enable us to write the recursion formulas for the ratio array $p_n(z)$ and the *logarithmic derivative* array $R_n(z)$:

$$p_n(z) = \frac{J_n(z)}{J_{n-1}(z)} = \frac{1}{\frac{2n}{z} - p_{n+1}(z)} \qquad (n = 1, 2, 3, \cdots, N\text{-}1) \qquad \text{(II-15)}$$

$$R_n(z) = \frac{J_n'(z)}{J_n(z)} = -\frac{n}{z} + \frac{1}{p_n(z)} \qquad (n = 1, 2, 3, \cdots, N\text{-}1) \qquad \text{(II-16)}$$

Thus it is seen that only the $p_n(z)$ array needs to be generated, from which the $R_n(z)$ array can also be calculated. For a cylinder of size $x = ka$ and complex refractive index m (here the argument z can be either real: $z = x$, or complex: $z = mx$), the entire $p_n(z)$ array elements are computed via the *downward recursion* formula, Eq. (II-15), by starting from a sufficiently large order N given by

$$N = 1.1 \bullet |z| + 10. \qquad \text{(II-17)}$$

and using thereby the asymptotic value:

$$p_N(z) = \frac{z}{2N} \qquad \text{(II-18)}$$

Only $J_0(z)$ is thence needed to build all $J_n(z)$ and $J_n'(z)$ functions by Eqs. (II-15)-(II-16).

The Neumann functions $Y_n(x)$ needed in the infinite cylinder theory, on the other hand, have to be computed by the *upward recursion* formulas similar to those for $J_n(z)$ above.

(3) Conversion of (Q_{ext}, P_{ext}) to Volume-Equivalent-Cross-Section-Normalized (Q,P)

For a finite cylinder of length l and radius a, Q_{ext} is usually defined as the ratio between the cross section and the normally projected geometric area of the cylinder, $2al$ (as in the infinite cylinder case, Eq. (II-1, where $l = 1$)):

$$Q_{ext} = \frac{C_{ext}}{2al} = \frac{C_{ext}}{4pa^2} \qquad \text{where } p = \text{aspect ratio} = l/(2a) \qquad \text{(II-19a)}$$

However, we have standardized the normalization of our experimental P-Q plot via the *geometric cross section of the sphere equal in volume to the nonspherical particle under*

study [Ref. 9]. This is because of our empirical finding that the particle volume is a more dominant factor in extinction, rather than its geometric cross section. By this definition,

$$Q = \frac{C_{ext}}{\pi a_v^2} = \frac{C_{ext}}{\pi\left[a\left(\frac{3}{2}p\right)^{1/3}\right]^2}, \qquad a_v = a\left(\frac{3}{2}p\right)^{1/3} \tag{II-19b}$$

where a_v is the *radius of the equal-volume sphere*. The above two definitions for the *real part* of the *complex extinction efficiencies* are therefore related by

$$Q = Q_{ext}\frac{4p^{1/3}}{\pi\left(\frac{3}{2}\right)^{2/3}} = Q_{ext} \bullet 0.9716637p^{1/3} \tag{II-20a}$$

Similarly, for the *imaginary part* of the *complex extinction efficiencies*:

$$P = P_{ext}\frac{4p^{1/3}}{\pi\left(\frac{3}{2}\right)^{2/3}} = P_{ext} \bullet 0.9716637p^{1/3} \tag{II-20b}$$

(4) Scattering by a *Perpendicularly Illuminated Finite Cylinder*

For an arbitrarily oriented *infinite cylinder*, the expressions for far-field angular scattering intensities (with respect to cylinder-fixed coordinates) follow those given by Kerker [Ref. 2, pp. 260-261.], using the same expansion coefficients, Eqs. (II-5)-(II-8):

$$I_{11} = \frac{2}{k\pi r}i_{11} = \frac{2}{k\pi r}\left|T_{11}\right|^2 = \frac{2}{k\pi r}\left|b_0^E + 2\sum_{n=1}^{n_{max}} b_n^E \cos(n\theta)\right|^2 \tag{II-21}$$

$$I_{12} = \frac{2}{k\pi r}i_{12} = \frac{2}{k\pi r}\left|T_{12}\right|^2 = \frac{2}{k\pi r}\left|2\sum_{n=1}^{n_{max}} a_n^E \sin(n\theta)\right|^2 \tag{II-22}$$

$$I_{21} = \frac{2}{k\pi r}i_{21} = \frac{2}{k\pi r}\left|T_{21}\right|^2 = \frac{2}{k\pi r}\left|2\sum_{n=1}^{n_{max}} b_n^H \sin(n\theta)\right|^2 \tag{II-23}$$

$$I_{22} = \frac{2}{k\pi r}i_{22} = \frac{2}{k\pi r}\left|T_{22}\right|^2 = \frac{2}{k\pi r}\left|a_0^H + 2\sum_{n=1}^{n_{max}} a_n^H \cos(n\theta)\right|^2 \tag{II-24}$$

Both cross-polarized components I_{12} and I_{21} vanish if the cylinder is perpendicularly illuminated, since $a_n^E = -b_n^H \to 0$ as $\alpha \to 0$.

The above formulas are for *infinite cylinders*, where the scattered cylindrical waves decay as $1/r$ in intensity, instead of the familiar $1/r^2$ decay for spherical waves, at a distance r from the cylinder. The desired *finite cylinder* expression, *assuming the cylinder is perpendicularly illuminated* , is derived in van de Hulst's text [see Ref. 7, pp. 304-306], from which we copy the *dimensionless complex scattering amplitude* $S(\theta,\varphi)$ of the scattered spherical wave:

$$S(\theta,\varphi) = \frac{kl}{\pi} E\left(\frac{kl\varphi}{2}\right) T(\theta) = \frac{2ka}{\pi} pE\left(\frac{kl\varphi}{2}\right) T(\theta) \qquad \text{(II-25)}$$

where $E(u) = \sin u / u$, φ is the elevation angle of the observation point from the equatorial plane of the finite cylinder, and T is either T_{11} (case E, Eq. II-21), or T_{22} (case H, Eq. II-24). If we further assume that the observation is made only in the *finite cylinder's equatorial plane* where $\varphi = 0$ and hence $E(u) = 1$, the expressions for the *dimensionless scattering intensity* from the finite cylinder simplify to

$$I_{11} = |S(\theta,0)|^2_{caseE} = \left(\frac{2ka}{\pi} p\right)^2 |T_{11}|^2 \qquad \text{(II-26)}$$

$$I_{22} = |S(\theta,0)|^2_{caseH} = \left(\frac{2ka}{\pi} p\right)^2 |T_{22}|^2 \qquad \text{(II-27)}$$

where p denotes again the aspect ratio of the finite cylinder.

III. Experimental Data and Comparison with Infinite Cylinder Theory

(1) Retrieval of Microwave Scattering Data and Conversion from *Binary* to *ASCII* Formats

The original microwave data written by PDP computers were all in *binary* formats to save memory space, formats difficult to be compared directly with theoretical computations, which are mostly written in ASCII formats for modern computers. This applies to a personal computer, MS-DOS/386DX, recently purchased for these analysis purposes. We have selected the finite cylinder measurement data from those with the best system stability records, transformed all of them into ASCII formats by a PDP computer, and copied the results into PC floppy disks via a VAX11/750. Table I lists the selected data sets, whose scattering quantities are all calibrated in *absolute magnitudes*, and with the respective target parameters also shown. These magnitudes are directly compared to the theoretical predictions, which are also computed in absolute magnitudes.

(2) Complex Extinction Efficiency (Q, P) versus Cylinder Orientation

The technical detail of the measurement procedures on complex extinction efficiency as a function of particle orientation is referred to in our earlier reports [Refs. 9-11]. We usually call the Cartesian display of such a measurement a microwave P-Q plot. The real (Q) and imaginary (P) part of the complex extinction efficiency are respectively related to the $\theta = 0$ complex scattering amplitude, $S(0)$, through the *Optical Theorem*:

$$Q = \frac{4}{x_v^2}\mathrm{Re}\{S(0)\} \qquad \text{and} \qquad P = \frac{4}{x_v^2}\mathrm{Im}\{S(0)\} \qquad \text{(III-1)}$$

where x_v is defined as the size parameter of the equal-volume sphere [Ref. 9], and the larger the Q is, the more efficiently the particle obscures the incident light (per its unit volume). A vector drawn from the P-Q coordinate origin to a point on a P-Q curve is the Cartesian display of $4S(0)/x_v^2$ at that particle orientation, and the phase shift $\phi(0)$ suffered by the $\theta = 0$ scattered wave with respect to the incident wave is, from Eqs. (III-1),

$$\phi(0) = \tan^{-1}\left[\frac{Q}{P}\right] \qquad \text{(III-2)}$$

A P-Q plot critically depends on target shape, size, refractive property and orientation. In addition, the degeneration of mathematical angular functions at $\theta = 0$, and hence all (Q, P) values hinge most importantly on the partial-wave expansion coefficients, allows us to visualize the convergence in a theoretical calculation. It follows then that the most detailed experiment–theory and/or theory–theory comparisons can be made by overlaying 2 such P-Q plots.

Three such P-Q plots, Figs. 2A-2C, representing the finite cylinders #7 (2:1 Plexiglas cyl.), #18 (4:1 Plexiglas cyl.) and #25 (8:1 Expanded Polystyrene cyl.) respectively in Table I, are displayed so as to compare with the infinite cylinder theoretical predictions. The following summarizes the findings, some of which have not been anticipated:

(A) To compare the magnitudes of infinite-cylinder-theory (Q_{ext}, P_{ext}) as computed by Eqs. (II-1) & (II-2) to finite-cylinder-microwave (Q, P) as represented by Eqs. (III-1), a factor $0.9716637p^{1/3}$ must be multiplied to the former (see Eqs. (II-20a) & (II-20b)).

(B) The infinite cylinder theory can predict a fairly close match with microwave P-Q data, both in *magnitude* and in *phase*, for aspect ratios as low as 2:1, if the cylinder orientation is such that $\alpha < 30^{\circ}$ (i.e., $\chi > 60^{\circ}$). The agreement appears to improve as the aspect ratio p increases.

(C) Although not included in the selected data of Table I due to its dubious measurement stability, the (Q, P) of a nearly perpendicularly illuminated 1:1 Plexiglas cylinder (ka = 2.716) agrees well with the infinite cylinder theory.

(D) The experiment–theory agreement is in general better when the cylinder axis is in the **k**-**E** plane than in the **k**-**H** plane.

(E) As cylinder approaches nose-on incidence ($\alpha \rightarrow 90^{\circ}$), infinite cylinder theory invariably predicts $Q \rightarrow 0$, no matter how large a is. This has never been observed in our experiment, although the cylinder in Fig. 2A came close to it. On the contrary, for a small-radius cylinder such as in Fig. 2B, one may expect unusually large Q (resonance) near end-on incidence, even though the cylinder presents there a small, or even the smallest, geometric cross section with respect to the beam.

(3) Angular Scattering by Finite Cylinders at Normal Incidence

Even though the exact solution to scattering by an infinite cylinder at normal incidence (α = 0) has long been known [Ref. 5], its practical use has been limited to finding scattering profiles, and few attempts have been reported on the magnitudes of scattering from a given finite cylinder. The experiment–theory comparison made in this article may even be the *first* of such attempts.

On the other hand, the microwave data have been measured in absolute magnitudes [Refs. 1, 6, 10, 11], through calibration by standard spheres which are measured in quick succession to the particle under study. We refer again to the measurement procedures in [Refs. 6 10, 11] and point out that the 3 preferential orientations in Table I are such that the cylinder axis is parallel to incident **E** (case E) , **H** (case H) and **k** vectors, which are part of the 44 (or even 272 [Ref. 6]) orientations typically stepped through by computer-controlled target orienting. In the present comparisons, we limit ourselves to the case E and case H orientations only, as displayed in Figs. 3A-3C, for #5 (2:1 Plexiglas cyl.), #19 (4:1 Plexiglas cyl.) and #22 (4:1 Expanded Polystyrene cyl.) in Table I, respectively.

The comparison figures are self explanatory, and we list a few comments:

(A) Eqs. (II-26) & (II-27) with the use of Eqs. (II-21) & (II-22) give the desired formulas for theoretically evaluating the angular scattering from a perpendicularly illuminated finite cylinder, if the observation is to be made on or near the cylinder's equatorial plane.

(B) It is very gratifying that the computer-controlled target-orientation device had performed the intended tasks over protracted periods of orientation stepping. Without this feature it would be very difficult, if not impossible, to retrieve the desired orientation-dependent data, such as case E or case H.

(C) In general the theoretical magnitudes match very well with the observed ones. Certain discrepancies between the two usually occur at $\theta = 0^o$ and at such θ's where the scattered signal is small, or even much smaller than, the residual, fluctuating background which is very difficult to compensate [Ref. 11].

IV. Conclusions

The work in this article is motivated by our wanting to make a systematic catalog of our microwave scattering data so as to test the utility of the long-developed infinite cylinder codes. Although these codes can now be run efficiently in a variety of computers, fast or slow, the use of cylinder codes has not been as popular as Mie codes for spheres because of the simple remaining question: how to apply the codes for *infinite* cylinder to *finite* cylinder scattering? We answer this question by:

(1) For $\alpha < 30^o$ and the aspect ratio p as low as 2:1, the particle-orientation dependent, complex extinction efficiency (Q,P) of a finite cylinder can be closely approximated by the infinite cylinder expression (Q_{ext},P_{ext}) through a multiplication factor which depends only on p (see Eqs. (II-20a) & (II-20b)).

(2) If observation is made only near the *equatorial plane* of a *perpendicularly illuminated* ($\alpha = 0^o$) finite cylinder, the angular scattering intensities can be calculated rather precisely from the infinite cylinder expressions (see Eqs. (II-26) & (II-27)).

(3) Otherwise, infinite cylinder codes cannot be safely employed to finite cylinder problems without substantially modifying the analytical expressions. Near nose-on incidence ($\alpha = 90^o$), e.g., infinite cylinder codes are useless, and we may expect intriguing resonance phenomena. Work is in progress to answer this remaining problem via developing a reliable but easy to use, approximation solution through waveguide mode corrections to the infinite cylinder solution.

ACKNOWLEDGMENTS

Army Research Office's previous supports on our microwave measurement program are very much appreciated. Yu-lin Xu was instrumental in assisting the laboratory work. Special thanks are due to Jerry Weinberg for reviewing this article, and to John Oliver and William Cooke for helps in using personal computers.

References

1 Greenberg, J. M., Pedersen, N. E. and Pedersen, J. C., "Microwave Analog to the Scattering of Light by Nonspherical Particles," J. Appl. Phys. **32**, 233-242 (1961).

2 Kerker, M., *The Scattering of Light and other Electromagnetic Radiation* (Academic, New York, 1969).

3 Lind, A. C. and Greenberg, J. M., "Electromagnetic Scattering by Obliquely Oriented Cylinders," J. Appl. Phys. **37**, 3195-3203 (1966).

4 Lind, A. C., *Resonance Electromagnetic Scattering by Finite Circular Cylinders*, Ph. D.Thesis, Rensselaer Polytechnic Institute, Troy, New York (1966).

5 Rayleigh, Lord, "On the Electromagnetic Theory of Light," Phil. Mag. **12**, 81-101 (1881).

6 Schuerman, D.W., Wang, R.T., Gustafson, B.A.S. and Schaefer, R.W., "Systematic Studies of Light Scattering. 1: Particle Shape," Appl. Opt. **20**, 4039-4050 (1981).

7 van de Hulst, H. C., *Light Scattering by Small Particles* (Wiley, New York, 1957).

8 Wait, J. R., "Scattering of a Plane Wave from a Circular Dielectric Cylinder at Oblique Incidence," Canad. J. Phys. **33**, 189-195 (1955).

9 Wang, R. T., "Extinction Signatures by Randomly Oriented, Axisymmetric Particles," in *Proc. of the 1982 CSL Scientific Conference on Obscuration and Aerosol Research*, R. Kohl, Ed. (Army ARCSL-SP-83011, Aberdeen, MD 1983), pp. 223-242.

10 Wang, R. T., in *Proc. of the 1984 Scientific Conference on Obscuration and Aerosol Research*, R. Kohl and D. Stroud, Eds. (Army CRDC-SP85007, Aberdeen, MD 1985):

(1) "Extinction by Rough Particles," pp. 315-326.

(2) "Angular Scattering by Rough Particles," pp. 327-363.

11 Wang, R. T., "Status of the Microwave Scattering Facility (MSF) Upgrade," in *Proc. of the 1987 CRDEC Scientific Conference on Obscuration and Aerosol Research*, E. H. Engquist and K. A. Sistek, Compilers (Army CRDEC-SP-88031, Edgewood, MD, 1988) pp 323-339.

12 Wang, R. T., *Light Scattering by Irregularly Shaped Particles*, Final Report, ARO Contract DAAL03-86-K0021 (Dec. 12, 1989).

Table I Selected Finite Cylinder Microwave Scattering Data and the Target Parameters

ID #	a radius (cm)	l length (cm)	$p = l/(2a)$ aspect ratio	$ka = 2\pi a/\lambda$ cylinder size parameter	x_v volume-equival. size param.	$m=m'-im''$ refractive index	Extinction P-Q Data	PO Angular Scatt. Data	RO Angular Scatt. Data	Specular Scatt. vs Azimuth Sweep
1	.849	3.400	2.002	1.676	2.418	1.610-i.004	1			
2	.955	3.828	2.004	1.885	2.720	"	1			
3	1.058	4.240	2.003	2.089	3.014	"	1			
4	1.165	4.670	2.004	2.299	3.318	"	1			
5	1.270	5.100	2.008	2.506	3.620	"	1	3	1	6
6	1.376	5.512	2.002	2.717	3.920	"	1			
7	1.482	5.940	2.003	2.926	4.222	"	1			
8	1.590	6.365	2.002	3.137	4.526	"	1			
9	1.799	7.206	2.003	3.551	5.123	"	1			
10	2.012	8.050	2.001	3.970	5.727	"	1			
11	2.118	8.485	2.004	4.179	6.031	"	1			
12	2.328	9.328	2.004	4.594	6.630	"	1			
13	2.540	10.185	2.004	5.014	7.237	"	1			
14	1.304	5.014	1.922	2.574	3.663	1.322-i.005	1			
15	1.302	5.032	1.932	2.570	3.671	1.416-i.005	1			
16	2.490	10.056	2.019	4.914	7.112	1.321-i.005	1			
17	2.512	10.046	2.000	4.958	7.118	1.442-i.005	1			
18	.785	6.282	4.001	1.549	2.816	1.610-i.004	1	3	1	
19	.964	7.712	4.000	1.903	3.457	"	1	3	1	
20	1.204	9.636	4.002	2.376	4.320	"	1	3	1	
21	1.457	11.656	4.000	2.876	5.225	"	1	3	1	
22	1.157	9.256	4.000	2.284	4.150	1.335-i.005	1	3	1	6
23	1.620	12.970	4.002	3.198	5.812	1.390-i.005	1			
24	.635	10.110	7.961	1.253	2.816	1.610-i.004	1 (round-ends cyl.)			
25	1.144	18.334	8.009	2.259	5.174	1.333-i.005	1			
26	.744	18.260	12.26	1.469	3.878	1.327-i.005	1	3	1	6

Note:
PO: Data for preferentially oriented cylinder. RO: Data for randomly oriented cylinder.

FIGURES

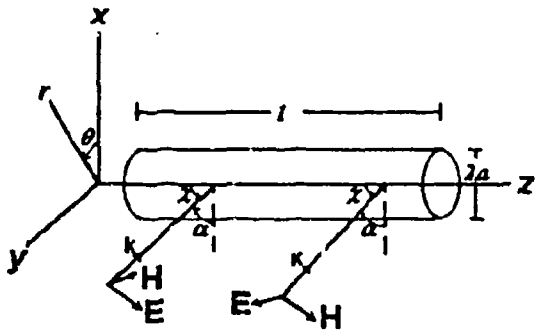

Case E Case H

Fig. 1 Geometry of Scattering by a Cylinder

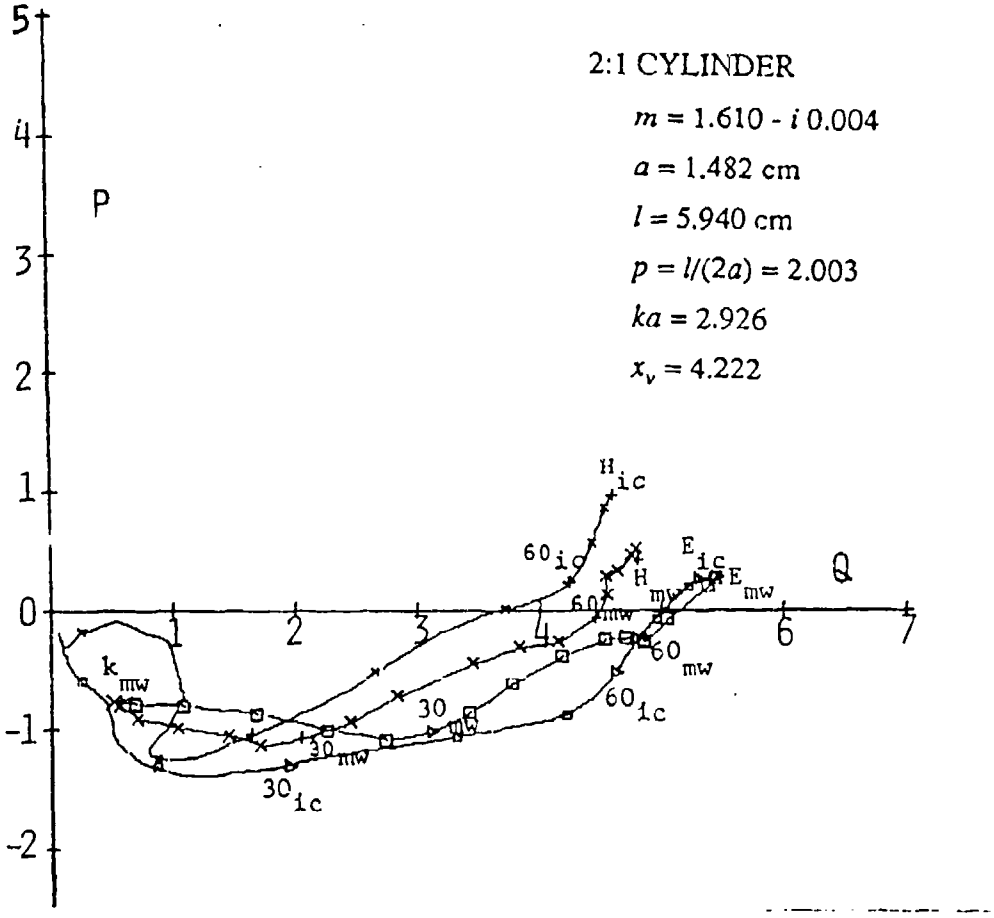

Figure 2A Complex Extinction Efficiency Vs Particle Orientation for a 2:1 Circular Cylinder (Plexiglas)

Suffixes mw and ic respectively denote the microwave data and the infinite cylinder theory result. k, E and H mark the orientations where the cylinder axis is parallel to the incident-wave **k**, **E** and **H**, respectively, and the running numbers show the orientation angle: $\chi = 90^{o} - \alpha$. The orientation angles marked in larger letters are for the axis in the **k**-**E** plane, while for those marked in smaller letters, in the **k**-**H** plane.

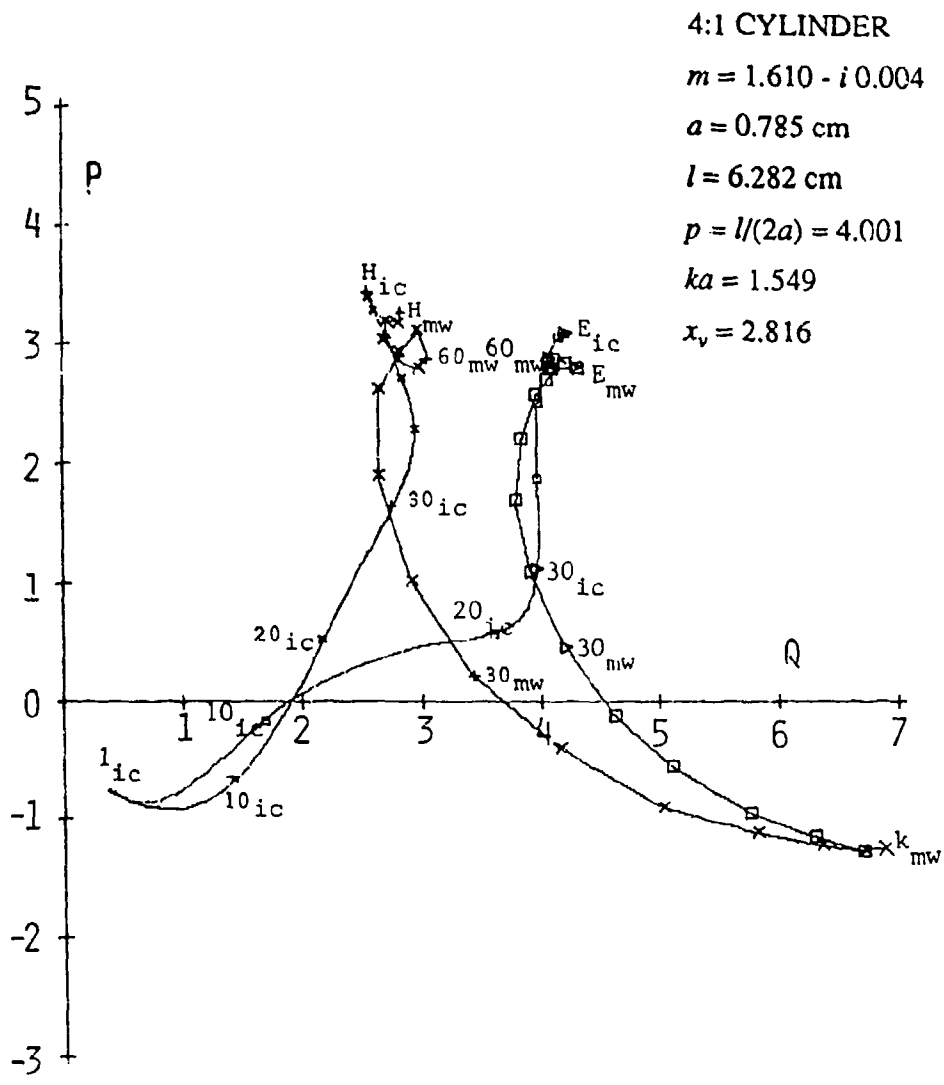

Figure 2B Complex Extinction Efficiency Vs Particle Orientation for a 4:1 Circular Cylinder (Plexiglas)

Suffixes mw and ic respectively denote the microwave data and the infinite cylinder theory result. k, E and H mark the orientations where the cylinder axis is parallel to the incident-wave **k**, **E** and **H**, respectively, and the running numbers show the orientation angle: $\chi = 90^{o} - \alpha$. The orientation angles marked in larger letters are for the axis in the **k-E** plane, while for those marked in smaller letters, in the **k-H** plane.

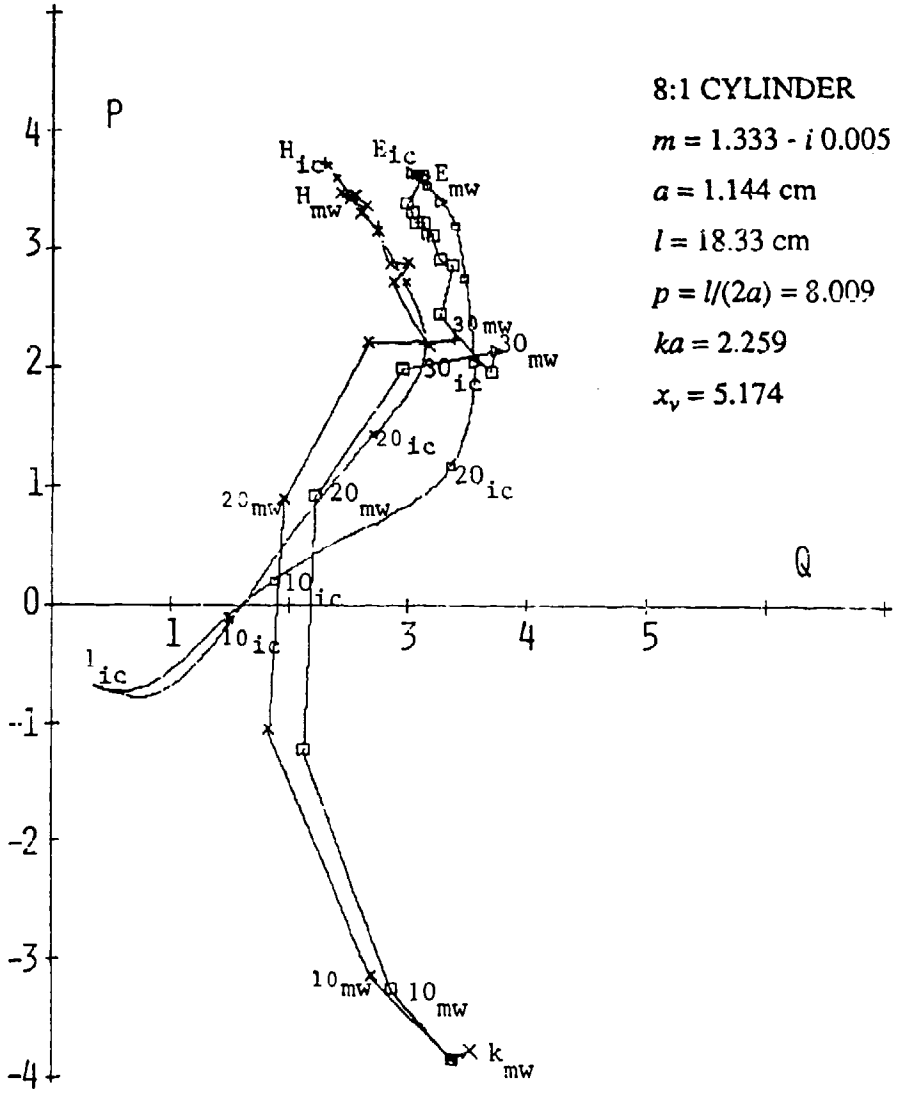

Figure 2C Complex Extinction Efficiency Vs Particle Orientation for a 8:1 Circular Cylinder (Expanded Polystyrene)

Suffixes mw and ic respectively denote the microwave data and the infinite cylinder theory result. k, E and H mark the orientations where the cylinder axis is parallel to the incident-wave **k**, **E** and **H**, respectively, and the running numbers show the orientation angle: $\chi = 90^{o} - \alpha$. The orientation angles marked in larger letters are for the axis in the **k-E** plane, while for those marked in smaller letters, in the **k-H** plane.

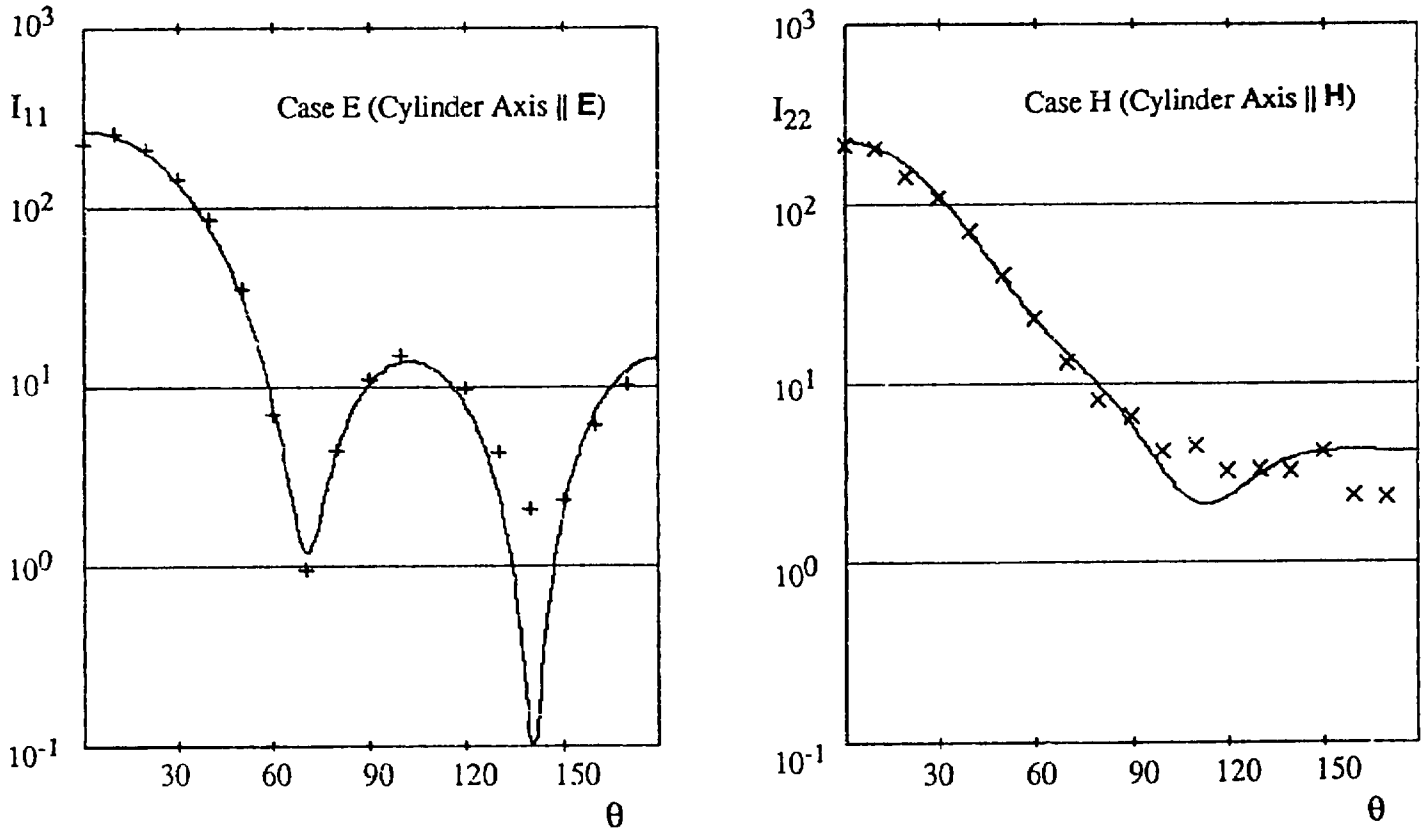

Figure 3A Angular Scattering Intensity Vs Scattering Angle θ for a Perpendicularly Illuminated, 2:1 Circular Cylinder (Plexiglas)

The cylinder has a = 1.270 cm, l = 5.100 cm, m = 1.61-i0.004 (for the Plexiglas material @ λ = 3.1835 cm). Symbols represent the microwave data, and the continuous curves are derived from the infinite cylinder theory.

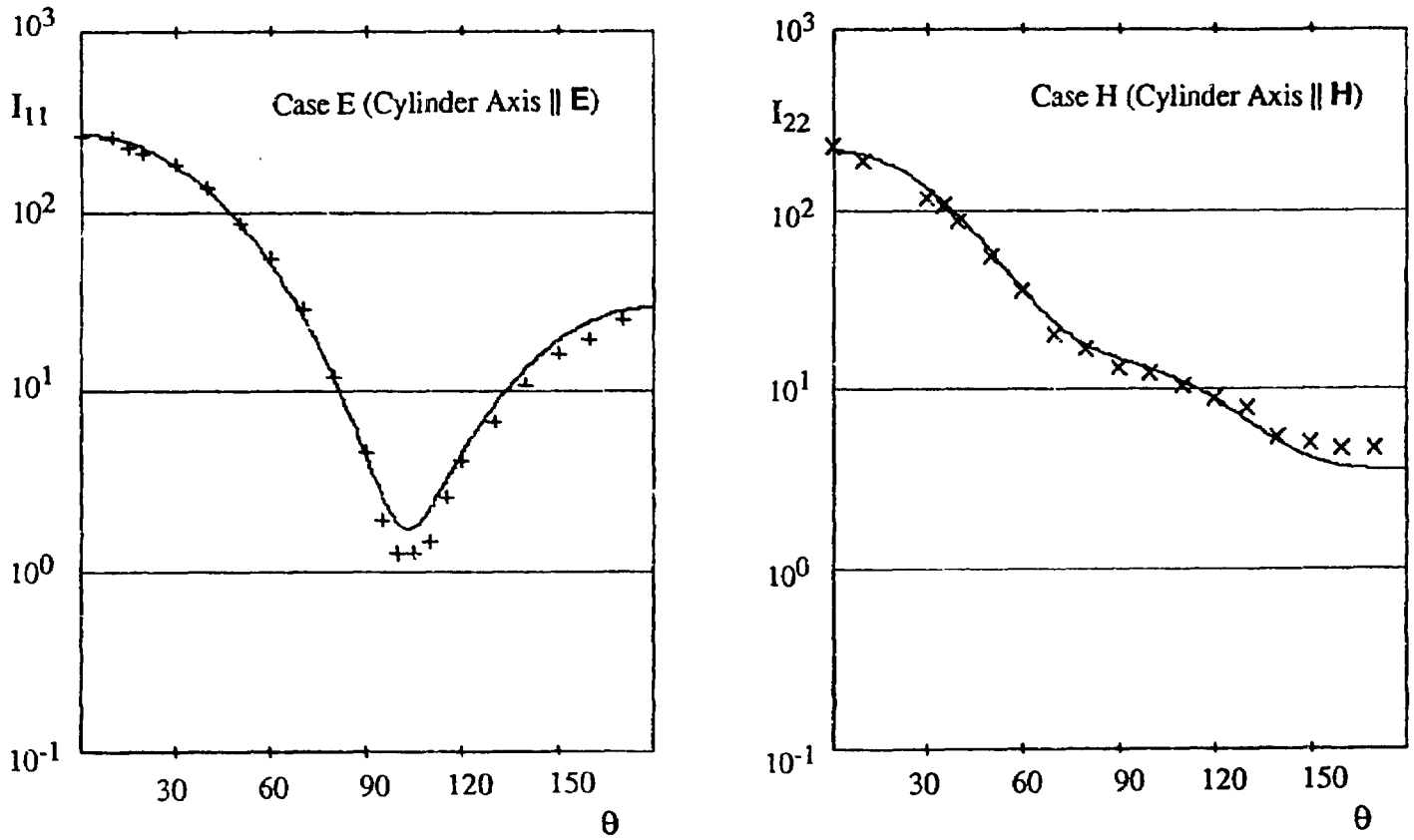

Figure 3B Angular Scattering Intensity Vs Scattering Angle θ for a Perpendicularly Illuminated, 4:1 Circular Cylinder (Plexiglas)

The cylinder has a = 0.964 cm, l = 7.712 cm, m = 1.61-i0.004 (for the Plexiglas material @ λ = 3.1835 cm). Symbols represent the microwave data, and the continuous curves are derived from the infinite cylinder theory.

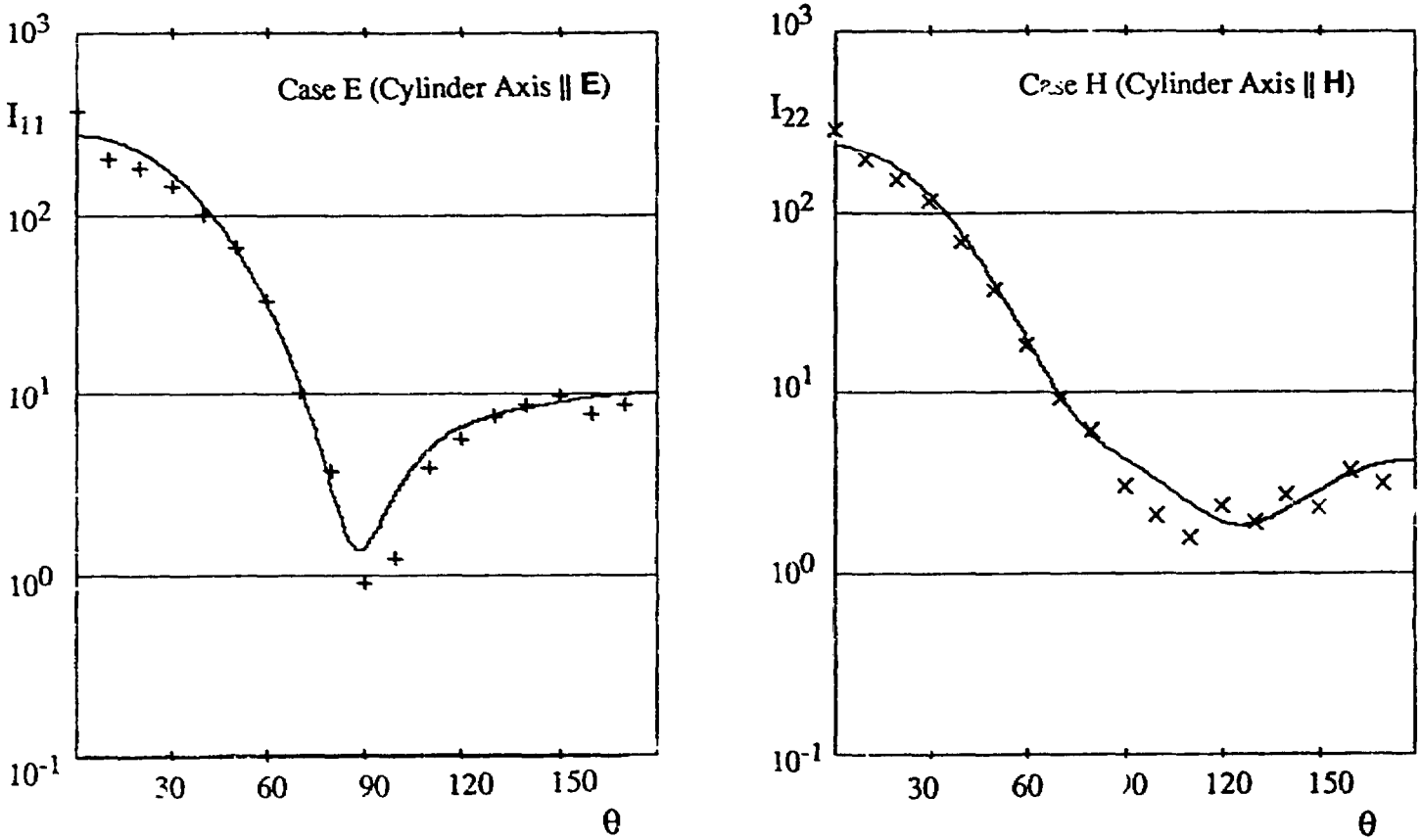

Figure 3C Angular Scattering Intensity Vs Scattering Angle θ for a Perpendicularly Illuminated, 4:1 Circular Cylinder (Expanded Polystyrene)

The cylinder has a = 1.157 cm, l = 9.256 cm, and m = 1.335-i0.005 (for the expanded polystyrene material @ λ = 3.1835 cm). Symbols represent the microwave data, and the continuous curves are derived from the infinite cylinder theory.

Blank

The Response of N layer Bianisotropic Cylindrical Structures to Obliquely Incident Arbitrarily Polarized Plane Wave Electromagnetic Radiation

D. K. Cohoon
43 Skyline Drive
Glen Mills, PA 19342

September 22, 1993

scribe exact formulae for the interaction of obliquely incident electromagnetic radiation with an N layer anisotropic cylinder.

Some new methods of developing the response of a thinly coated metallic cylinder to electromagnetic radiation have been developed. In contrast to theories developed by (Cohen [16], Wait ([52], [55] Chapter 7 pp 152-209) Bohren and Huffman ([9] pp 194-201) and Yeh [59]) the representation of the fields in the thin coating uses no Bessel or Hankel functions. This method eliminated a severe round off error that was incurred when using the traditional solutions (Bussey [11]).

Egon Marx ([34]) considered the interesting problem of scattering by an infinite cylinder that is lying half an a half-space with one electromagnetic property and half in the region from which the stimulating radiation is coming with its axis lying in the plane separating the two regions. Marx's work could be used to help explain the design of the human cornea.

1 Vector Calculus

We will discuss cylindrical coordinates, vector calculus in cylindrical coordinates, and methods of representing vector fields representing electric and magnetic vectors induced within layers of a multilayer cylindrically symmetric structures where the material filling the regions between separating cylinders may possibly have full tensor bianisotropy.

1.1 VECTOR FIELDS IN CYLINDERS

The vector fields in the interior of a penetrable layer and outside the cylinder are represented in terms of the vector fields

$$\vec{A}_{(n,h)} = exp(in\theta)exp(-ihz)\vec{e}_r, \tag{1.1.1}$$

$$\vec{B}_{(n,h)} = exp(in\theta)exp(-ihz)\vec{e}_\theta, \tag{1.1.2}$$

and

$$\vec{C}_{(n,h)} = exp(in\theta)exp(-ihz)\vec{e}_z. \tag{1.1.3}$$

where in terms of the unit vectors $\vec{e}_x$, $\vec{e}_y$, and $\vec{e}_z$ of the cartesian coordinate system we have

$$\vec{e}_r = cos(\theta)\vec{e}_x + sin(\theta)\vec{e}_y \tag{1.1.4}$$

and

$$\vec{e}_\theta = \left(\frac{\partial}{\partial\theta}\right)\vec{e}_r = -sin(\theta)\vec{e}_x + cos(\theta)\vec{e}_y \tag{1.1.5}$$

and

$$\vec{e}_z = \vec{e}_z \tag{1.1.6}$$

Thus, in terms of the unit vectors of cylindrical coordinates after multiplying both sides of equation (1.1.4) by $cos(\theta)$ and multiplying both sides of equation (1.1.5) by $-sin(\theta)$ and adding we obtain

$$\vec{e}_x = cos(\theta)\vec{e}_r - sin(\theta)\vec{e}_\theta \tag{1.1.7}$$

and similarly

$$\vec{e}_y = sin(\theta)\vec{e}_r + cos(\theta)\vec{e}_\theta \tag{1.1.8}$$

Hence, if an arbitrary vector is represented in Cartesian coordinates as

$$\vec{V} = V_x\vec{e}_x + V_y\vec{e}_y + V_z\vec{e}_z \tag{1.1.9}$$

then

$$\begin{aligned}\vec{V} &= (cos(\theta)V_x + sin(\theta)V_y)\vec{e}_r + \\ &(-sin(\theta)V_x + cos(\theta)V_y)\vec{e}_\theta + \vec{V}_z\end{aligned} \tag{1.1.10}$$

and more importantly if a vector $\vec{V}$ has radial, theta and z components given by V_r, V_θ and V_z respectively, then

$$\begin{aligned}\vec{V} &= (V_r cos(\theta) - V_\theta sin(\theta))\vec{e}_x + \\ &(V_r sin(\theta) + V_\theta cos(\theta))\vec{e}_y + V_z\vec{e}_z\end{aligned} \tag{1.1.11}$$

If the electric field is represented in terms of cylindrical coordinates, then

$$curl(V_r\vec{e}_r + V_\theta\vec{e}_\theta + V_z\vec{e}_z) =$$

$$\left(\frac{1}{r}\frac{\partial V_z}{\partial\theta} - \frac{\partial V_\theta}{\partial z}\right)\vec{e}_r + \left(\frac{\partial V_r}{\partial z} - \frac{\partial V_z}{\partial r}\right)\vec{e}_\theta + \frac{1}{r}\left(\left(\frac{\partial}{\partial r}\right)(rV_\theta) - \frac{\partial F_r}{\partial\theta}\right)\vec{e}_z \tag{1.1.12}$$

We will represent the internal and external fields as a linear combination, with coefficients in a ring of functions of the radial variable, of the vector fields defined by equations (1.1.1), (1.1.2), and (1.1.3). The identitities

$$curl(F(r)\vec{C}_{(m,n)}) =$$

$$im\frac{F(r)}{r}\vec{A}_{(m,h)} + ihF(r)\vec{B}_{(m,h)} \tag{1.1.13}$$

$$curl(F(r)\vec{A}_{(m,n)}) =$$

$$-ihF(r)\vec{A}_{(m,h)} + \left(\frac{-F(r)}{r}\right) im\vec{C}_{(m,h)} \tag{1.1.14}$$

$$curl(F(r)\vec{B}_{(m,n)}) =$$

$$ihF(r)\vec{A}_{(m,h)} + \left(\frac{1}{r}\left(\frac{\partial}{\partial r}\right)(rF(r))\right)\vec{C}_{(m,h)} \tag{1.1.15}$$

1.2 COORDINATE FRAMES

Following Ariel Cohen ([16]) we describe coordinate frames which are used to represent incoming, internal, and scattered fields in laboratory, absorber, and detector coordinate frames. The approach taken by Cohen ([16]) enables us to treat the oblique incidence problem and also treat the problem of random orientation. We let $\vec{e}_z$ denote the unit vector along the $z - axis$ of the laboratory frame. We suppose that $\vec{e}_{z_a}$ is the unit vector along the axis of a cylinder which passes through the origin of the original coordinate system. We suppose that

$$\vec{e}_{z_a} = sin(\theta_a)cos(\phi_a)\vec{e}_x + sin(\theta_a)sin(\phi_a)\vec{e}_y + cos(\theta_a)\vec{e}_z \tag{1.2.1}$$

We define the x_a axis by the cross product,

$$\vec{e}_{x_a} = (\vec{e}_{z_a} \times \vec{e}_z)/sin(\theta_0) \tag{1.2.2}$$

so that

$$\vec{e}_{x_a} = sin(\phi_a)\vec{e}_x - cos(\phi_a)\vec{e}_y \tag{1.2.3}$$

$$\vec{e}_{y_a} = cos(\theta_a)cos(\phi_a)\vec{e}_x + cos(\theta_a)sin(\phi_a)\vec{e}_y - sin(\theta_a)\vec{e}_z \tag{1.2.4}$$

We see that we can describe the electric vector of the incoming radiation by the rule,

$$\vec{E}^i = E_0 exp(-ik_0 z + i\omega t)\vec{e}_x \tag{1.2.5}$$

If we do this and transform the variable z to the absorber coordinate frame, we see that

$$z = -sin(\theta_a)y_a + cos(\theta_a)z_a \tag{1.2.6}$$

Letting

$$y_a = rsin(\theta) \tag{1.2.7}$$

in the absorber coordinate frame and making use of the generator function relationship,

$$exp((\tilde{z}/2)(t - 1/t)) = \sum_{n=-\infty}^{\infty} t^n J_n(\tilde{z}) \tag{1.2.8}$$

and letting $t = exp(i\theta)$ and observing that

$$(\tilde{z}/2)(t - 1/t) = i(sin(\theta)\tilde{z}) \tag{1.2.9}$$

we see from (1.2.8) that

$$exp(isin(\theta)\tilde{z}) = \sum_{n=-\infty}^{\infty} exp(in\theta)J_n(\tilde{z}) \tag{1.2.10}$$

We see that if use the fact that

$$y_a \;=\; r \cdot sin(\theta) \tag{1.2.11}$$

and we let

$$isin(\theta)\tilde{z} \;=\; (-ik_0)(-sin(\theta_a)y_a \;=\; (isin(\theta) \cdot (k_0 rsin(\theta)) \tag{1.2.12}$$

we observe that equations (1.2.12), (1.2.11), and (1.2.6) imply first that

$$exp(-ik_0 z) = exp(-ik_0(-sin(\theta_a y_a)) \cdot exp(-ik_0 cos(\theta_a z_a) \tag{1.2.13}$$

and then that

$$exp(-ik_0 z) = [exp(isin(\theta)\,\{k_0 rsin(\theta_a)\})] \cdot exp(-ik_0 cos(\theta_a z_a) \tag{1.2.14}$$

We now use equation (1.2.14) and the definition

$$\tilde{z} = \{k_0 rsin(\theta_a)\} \tag{1.2.15}$$

in equation (1.2.10) to obtain the expression for $exp(-ik_0 z)$ in absorber coordinates that is given by

$$exp(-ik_0 z) = \left[\sum_{n=-\infty}^{\infty} exp(in\theta)J_n(\{k_0 rsin(\theta_a)\})\right] \cdot exp(-ik_0 cos(\theta_a z_a) \tag{1.2.16}$$

This simple notion will help us to obtain an exact solution of the oblique incidence problem for N layer anisotropic cylinders.

2 Representation of Incoming Radiation

We will use three coordinate systems, one is a laboratory system that remains fixed, the other is a coordinate system in which the z axis is the axis of the cylinder.

3 OBLIQUE INCIDENCE

At least two methods have been developed to treat the oblique incidence problem. The classical paper on scattering by cylinders subject to obliquely incident electromagnetic radiation seems to have been due to Wait ([51]) and uses only one coordinate system with a z axis coinciding with the cylinder axis, while the second method ([16], [18]) uses three coordinate systems – a laboratory frame where the direction of propagation of the incoming radiation is that of the unit vector in the direction of the positive z axis, a cylinder frame where the z axis coincides with the cylinder axis, and an observer frame where the measurement device for measuring the scattered radiation is on the z axis with a positive z coordinate.

3.1 Generalized Single Frame Analysis

In ([51]) there is only one coordinated system and the cylinder is oriented with its axis parallel to the z axis of this coordinate system, but the component of the electric vector of the incoming radiation that is parallel to the z axis and lying in the plane $\theta = 0^o$ is given by

$$E_z^i =$$

$$E_0 sin(\zeta) exp(ik_{N+1} r sin(\zeta) cos(\theta)) exp(-ik_{N+1} z cos(\zeta)) exp(i\omega t) \tag{3.1.1}$$

where in Wait ([52]) the angle ζ is the angle that the incoming radiation makes with respect to the negative z axis. This is the same treatment given in chapter 7 of a recent book of Wait ([55]). The radial component of the electric vector of the incoming radiation is

$$E_r^i =$$

$$- E_0 cos(\zeta) exp(ik_{N+1} r sin(\zeta) cos(\theta)) exp(-ik_{N+1} z cos(\zeta)) exp(i\omega t) \tag{3.1.2}$$

We see that both the radial and the z components of the electric vector of the incoming radiation are, in view of the expansion given by equation (1.2.8), given using equations (1.1.1) and (1.1.3) by

$$E_r^i = \sum_{n=-\infty}^{\infty} \left\{ a_n^{(N+1)} F_{(n,N+1)}^{(a)}(r) \vec{A}_{(n,h)}(\theta, z) \right\} \tag{3.1.3}$$

and

$$E_z^i = \sum_{n=-\infty}^{\infty} \left\{ c_n^{(N+1)} F_{(n,N+1)}^{(c)}(r) \vec{C}_{(n,h)}(\theta, z) \right\} \tag{3.1.4}$$

so that the total electric vector is given by

$$\vec{E} = E_r^i \vec{e}_r + E_z^i \vec{e}_z \tag{3.1.5}$$

Equation (3.1.5) and equations (1.1.13) and (1.1.14) imply that the curl of the electric vector is given by

$$curl(\vec{E}) = \sum_{n=-\infty}^{\infty} \left\{ -ina_n^{(N+1)} \frac{F^{(a)}_{(n,N+1)}(r)}{r} \vec{C}_{(m,h)}(\theta, z) \right.$$

$$\left(-iha_n^{(N+1)} F^{(a)}_{(n,N+1)}(r) + inc_n^{(N+1)} \frac{F^{(c)}_{(n,N+1)}(r)}{r} \right) \vec{A}_{(n,h)}(\theta, z)$$

$$\left. + ihc_n^{(N+1)} F^{(c)}_{(n,N+1)}(r) \vec{B}_{(n,h)}(\theta, z) \right\} \tag{3.1.6}$$

For a bianisotropic material, we have

$$i\omega\overline{\overline{\mu}}\vec{H} = \overline{\overline{\alpha}}\vec{E} - curl(\vec{E}) \tag{3.1.7}$$

and using equation (3.1.6)we can even for tensor $\overline{\overline{\mu}}$ and tensor $\overline{\overline{\alpha}}$ solve equation (3.1.7) for $\vec{H}$ Using a general representation of $vecE$ in the interior layer and using equation (3.1.7) we can solve for $\vec{H}$ in each of the layers. By requiring continuity of tangential components of $\vec{E}$ and $\vec{H}$ across the cylindrical surfaces $r = R_p$ which separate regions of continuity of tensorial electromagnetic properties, we develop a system of ordinary differential equations in the radial functions.

4 Coated Cylinders

We consider a metalic structure with an arbitrary coating.

4.1 MAXWELL EQUATIONS

We assume that the coating material is bianisotropic, a material more general than a chiral material. The Maxwell equations are, for time harmonic radiation, given by

$$curl(\vec{E}) = -i\omega\overline{\overline{\mu}}\vec{H} - \overline{\overline{\alpha}}\vec{E} \tag{4.1.1}$$

and

$$curl(\vec{H}) = (i\omega\overline{\overline{\epsilon}} + \overline{\overline{\sigma}})\vec{E} + \overline{\overline{\beta}}\vec{H} \tag{4.1.2}$$

The radiation source term which gives the power density is given by

$$\left(\frac{\partial}{\partial t}\right) Q_{in} =$$

$$(1/2)Re\left\{\vec{E}^* \cdot (i\omega\overline{\overline{\epsilon}} + \overline{\overline{\sigma}})\vec{E} + \vec{E} \cdot \overline{\overline{\alpha}}^* \vec{H}^* - \right.$$

$$\vec{H} \cdot (i\omega\overline{\overline{\mu}}^* \vec{H}^*) + \vec{H} \cdot (\overline{\overline{\beta}}^* \vec{E}^*) +$$

$$\chi_{\partial\Omega}(r)\sigma_s \mid \vec{E}_{tangential} \mid^2\Big\} \tag{4.1.3}$$

where if $\partial\Omega$ is the surface containing the impedance sheet, then

$$\int_{\Omega} \chi_{\partial\Omega}\sigma_s \mid \vec{E}_{tangential} \mid^2 dv = \int_{\partial\Omega} \sigma_s \mid \vec{E}_{tangential} \mid^2 dA \tag{4.1.4}$$

is the characteristic function of the surface supporting the impedance sheet. We consider non plane wave sources such as tightly focused laser beams interacting with these structures ([12], [45], [31], [5], [4]) and use the energy densities as a source term in the energy equation to determine the future state of the cylinder.

4.2 Cross Products

The numerical problem associated with scattering of radiation by thinly coated perfect conductors reduces to the problem of evaluating the cross products of Bessel and Neuman functions (Abramowitz and Stegun [1], page 361 formula 9.1.32),

$$p_\nu = J_\nu(a)Y_\nu(b) - J_\nu(b)Y_\nu(a), \tag{4.2.1}$$

$$q_\nu = J_\nu(a)Y'_\nu(b) - J'_\nu(b)Y_\nu(a), \tag{4.2.2}$$

$$r_\nu = J'_\nu(a)Y_\nu(b) - J_\nu(b)Y'_\nu(a), \tag{4.2.3}$$

and

$$s_\nu = J'_\nu(a)Y'_\nu(b) - J'_\nu(b)Y'_\nu(a), \tag{4.2.4}$$

Observe that the recursion relation is

$$J_{\nu+1}(z)Y_\nu(z) - J_\nu(z)Y_{\nu+1}(z) = \frac{2}{\pi z} \tag{4.2.5}$$

If $\mathcal{G}_\nu(z)$ is one of $J_\nu(z)$ or $Y_\nu(z)$ then we see that

$$\mathcal{G}_{\nu+1}(z) = -\mathcal{G}'_\nu(z) + \frac{\nu}{z}\mathcal{G}_\nu(z) \tag{4.2.6}$$

We see that equations (4.2.5) and (4.2.6) imply that

$$-J'_\nu(z)Y_\nu(z) - J_\nu(z)Y'_\nu(z) = \frac{2}{\pi z} \tag{4.2.7}$$

We expand the Neuman function and obtain

$$Y_\nu(b) = Y_\nu(a) + Y'_\nu(a)(b-a) +$$

$$\sum_{j=2}^{\infty}\left\{(F_{(j,\nu)}Y'_\nu(a) + G_{(j,\nu)}Y_\nu(a))\left(\frac{(b-a)^j}{j!}\right)\right\} \tag{4.2.8}$$

The function $\mathcal{G}_\nu(z)$ satisfies Bessel's differential equation,

$$z^2\mathcal{G}''_\nu(z) + z\mathcal{G}'_\nu(z) +$$

$$(z^2 - \nu^2)\mathcal{G}_\nu(z) = 0 \tag{4.2.9}$$

Dividing all terms by z^2 we see that

$$\mathcal{G}''(z) = -\frac{1}{z}\mathcal{G}'_\nu(z)$$

$$\left(\frac{\nu^2}{z^2} - 1\right)\mathcal{G}_\nu(z) \tag{4.2.10}$$

Differentiating all terms of equation (4.2.10) we see that

$$\mathcal{G}_\nu^{(3)}(z) = \left\{\frac{2+\nu^2}{z^2} - 1\right\}\mathcal{G}'_\nu(z)$$

$$+\left\{-\frac{3\nu^2}{z^3} + \frac{1}{z}\right\}\mathcal{G}_\nu(z) \tag{4.2.11}$$

Differentiating both sides of equation (4.2.11) and using equation (4.2.10) to remove the second derivative terms we find that

$$\mathcal{G}_\nu^{(4)}(z) = \left[\left(\frac{-6\nu^2 - 6}{z^3}\right) + \frac{1}{z}\right]\mathcal{G}'_\nu(z)$$

$$\left[\frac{11\nu^2 + \nu^4}{z^4} - \left(\frac{(1+2\nu^2}{z^2}\right) + 1\right]\mathcal{G}_\nu(z) \tag{4.2.12}$$

We see that there are two forms for the derivatives given by

$$\mathcal{G}_\nu^{(2n)}(z) = \sum_{k=1}^{n}\left(\frac{a_k^{(2n)}}{z^{2k-1}}\right)\mathcal{G}'_\nu(z) +$$

$$\sum_{k=0}^{n}\left(\frac{b_k^{(2n)}}{z^{2k}}\right)\mathcal{G}_\nu(z) \tag{4.2.13}$$

and by

$$\mathcal{G}_\nu^{(2n+1)}(z) = \sum_{k=1}^{n}\left(\frac{c_k^{(2n+1)}}{z^{2k}}\right)\mathcal{G}'_\nu(z) +$$

$$\sum_{k=0}^{n}\left(\frac{d_k^{(2n+1)}}{z^{2k+1}}\right)\mathcal{G}_\nu(z) \tag{4.2.14}$$

We first use the equations (4.2.14) and (4.2.13) and equation (4.2.8) to find an expression for p_ν. We find that

$$\mathcal{P}_\nu(a,b) = p_\nu$$

$$J_\nu(a)Y_\nu(b) - J_\nu(b)Y_\nu(a) =$$

$$J_\nu(a)\left\{\quad Y_\nu(a) + Y'_\nu(a)(b-a) + \right.$$

$$\sum_{j=2}^{\infty}[F_{(j,\nu)}Y'_\nu(a) + G_{(j,\nu)}Y_\nu(a)]\frac{(b-a)^j}{j!}\Bigg\} +$$

$$Y_\nu(a)\Bigg\{ \quad J_\nu(a) + J'_\nu(a)(b-a) +$$

$$\sum_{j=2}^{\infty}[F_{(j,\nu)}J'_\nu(a) + G_{(j,\nu)}J_\nu(a)]\frac{(b-a)^j}{j!}\Bigg\} \tag{4.2.15}$$

Making use of the Wronskian relation (4.2.5) in equation (4.2.15) we see that the expression p_ν defined by equation (4.2.1) is given by

$$\mathcal{P}_\nu(a,b) = (b-a)\left(\frac{2}{\pi a}\right)$$

$$\sum_{j=2}^{\infty} F_{(j,\nu)}\left(\frac{2}{\pi a}\right)\frac{(b-a)^j}{j!} \tag{4.2.16}$$

We next use the expansion (4.2.8) and the Wronskian relation (4.2.5) to evaluate the functions q_ν defined by equation (4.2.2). Substituting the expansions into the expression for the q_ν given by equation (4.2.2) we see that

$$q_\nu = J_\nu(a)Y'_\nu(b) - J_\nu(b)Y_\nu(a) =$$

$$J_\nu(a)\Bigg\{Y'_\nu(a) +$$

$$\sum_{j=2}^{\infty}[F_{(j,\nu)}Y'_\nu(a) + G_{(j,\nu)}Y_\nu(a)]\left(\frac{(b-a)^{j-1}}{(j-1)!}\right)\Bigg\}$$

$$-Y_\nu(a)\Bigg\{J'_\nu(a) +$$

$$\sum_{j=2}^{\infty}[F_{(j,\nu)}J'_\nu(a) + G_{(j,\nu)}J_\nu(a)]\left(\frac{(b-a)^{j-1}}{(j-1)!}\right)\Bigg\}$$

The Wronskian relation implies that

$$q_\nu = \frac{2}{2\pi} +$$

$$\sum_{j=2}^{\infty} F_{(j,\nu)}\left(\frac{2}{2\pi}\right)\left(\frac{(b-a)^{j-1}}{(j-1)!}\right) \tag{4.2.17}$$

In this expression there are no Bessel functions and there is no round off error.

For the function

$$\mathcal{S}_\nu(a,b) = s_\nu \tag{4.2.18}$$

defined by equation (4.2.4) we see that

$$\mathcal{S}_\nu(a,b) = \sum_{j=2}^{\infty} G_{(j,\nu)}(a) \left(\frac{-2}{\pi a}\right) \frac{(b-a)^{j-1}}{(j-1)!} \tag{4.2.19}$$

Finally, for the function

$$\mathcal{R}_\nu(a,b) = r_\nu \tag{4.2.20}$$

defined by equation (4.2.3) we see that

$$\mathcal{R}_\nu(a,b) = \left(\frac{-2}{\pi a}\right) + \sum_{j=2}^{\infty} \left(\frac{-2}{\pi a}\right) G_{(j,\nu)}(a) \left(\frac{(b-a)^j}{j!}\right) \tag{4.2.21}$$

Equations (4.2.16), (4.2.17), (4.2.21), and (4.2.19) give us, for modest values of $b - a$ an error free means of computing the cross products that arise naturally in describing the interaction of electromagnetic radiation with a coated cylinder. When the coating thickness is large, the cross products may be evaluated by direct computation using the Bessel and Neumann functions.

References

[1] Abramowitz, Milton, and Irene Stegun (Editors). *Handbook of Mathematical Functions* New York: Dover (1972)

[2] Agrest, M. M. and M. S. Maksimov. *Theory of Incomplete Cylindrical Functions and their Applications* New York: Springer Verlag (1971)

[3] Armstrong, Robert L. and Andrew Zardecki. "Propagation of High Energy Laser Beams Through Metallic Aerosols" *Applied Optics. Volume 29. Number 12* (April 20, 1990) pp 1786-1792

[4] Barton, J. P., D. R. Alexander, and S. A. Schaub. "Internal fields of a spherical particle illuminated by a tightly focused laser beam: focal point positioning effects at resonance." *Journal of Applied Physics. Volume 65 No. 8* (April 15, 1989) pp 2900-2906

[5] Barton, J. P., D. R. Alexander, and S. A. Schaub. "Internal and near surface electromagnetic fields for a spherical particle irradiated by a focused laser beam" *Journal of Applied Physics. Volume 64, no 4* (1988) pp 1632-1639.

[6] Belts, V. A., O. A. Volkovitsky, A. F. Dobrovolksy, E. V. Ivanov, Y. V. Nasedkin, L. N. Pavlova. "Intensive CO_2 laser pulse transmission through droplet and ice crystal fogs" *IN* Kaye, A. S. and A. C. Walker. *Gas flow and chemical lasers. 1984. Proceedings of the Fifth International Symposium* Oxford, England: Gas Flow and Chemical Laser Symposium (August, 1984) pp 20-24

[7] Biswas, A., H. Latifi, R. L. Armstrong, and R. G. Pinnick. "Time resolved spectroscopy of laser emission from dye doped droplets" *Optics Letters. Volume 14, No. 4* (February 15, 1989) pp 214-216

[8] Bloembergen, N. *Nonlinear Optics* New York: W. A. Benjamin (1965)

[9] Bohren, Craig F. and Donald R. Huffman. *Absorption and scattering of light by small particles* New York: John Wiley and Sons (1983).

[10] Borison, S. L. "Bistatic cross section of a randomly oriented dipole" *IEEE Transactions on Antennas and Propagation* (March, 1967) pp 320-321

[11] Bussey, Howard E. and Jack H. Richmond. "Scattering by a lossy dielectric circular cylindrical multilayer, Numerical Values" *IEEE Transactions on Antennas and Propagation. Volume 23* (1975) pp 723-725

[12] Caledonia, G. E. and J. D. Teare. "Laser beam hygroscopic aerosol interactions" *Transactions of the ASME Journal of Heat Transfer. Vol 99* (May, 1977) pp 281-286.

[13] Chow, S. N., J. Mallet-Paret, and J. A. Yorke. Finding zeros of maps: homotopy methods that are constructive with probability one. *Math. Comp. Volume 32* (1978) pp 887-889.

[14] Chevaillier, Jean Phillipe, Jean Fabre, and Patrice Hamelin. "Forward scattered light intensities by a sphere located anywhere in a Gaussian beam" *Applied Optics. Vol. 25, No. 7* (April 1, 1986) pp 1222-1225.

[15] Chevaillier, Jean Phillippe, Jean Fabre, Gerard Grehan, and Gerard Gousbet. "Comparison of diffraction theory and generalized Lorenz-Mie theory for a sphere located on the axis of a laser beam." *Applied Optics, Vol 29, No. 9* (March 20, 1990) pp 1293-1298.

[16] Cohen, Ariel. "Scattering of a linearly polarized incidence at arbitrary angle to incidence plane of infinite tilted cylinders" *Optics Letters, Volume 5* (1980) pp 150-151.

[17] Cohen, Ariel and Charles Acquista. "Light scattering by tilted cylinders: properties of partial wave solutions" *Journal of the Optical Society of America. Volume 72, No. 5* (May, 1982) pp 531-534

[18] Cohen, Ariel, and P. Alpert. "Extinction efficiency of obliquely and randomly oriented infinite cylinders" *Journal of Applied Physics, Volume 50* (1979) pp 8262-8264.

[19] Cohen, Ariel, Leonard D. Cohen, and Richard D. Haracz. "Double scattering by randomly oriented long cylinders" *Journal of Applied Physics, Volume 57, Number 3* (February, 1985) pp 698-703

[20] Cohen, Ariel, Richard D. Haracz, and Leonard D. Cohen. "Asymmetry factors for randomly oriented infinite cylinders" *Journal of Applied Physics, Volume 58, Number 3* (August, 1985) pp 1135-1140.

[21] English, William J. "Vector variational solutions of inhomogeneously loaded cylindrical waveguide structures" *IEEE Transactions of Microwave Theory and Techniques Volume MTT 19* (January, 1971) pp 9 -18

[22] Flory, E. "Boundary value for a stratified anisotropic ionosphere" *Arch. Elektron. and Uebertragungstech. Volume 34, Number 12* (December, 1980) pp 506-513

[23] Garcia, C. B. and W. I. Zangwill. Pathways to Solutions, Fixed Points, and Equilibria. Englewood Cliffs, NJ: Prentice Hall(1981)

[24] Hammond, W. S. and M. A. K. Hamid. "Diffraction by an infinite dielectric cylinder due to a normally incident cylindrical wave" *Electronics Letters. Volume 6, No. 26* (December 27, 1969) pp 675-676)

[25] Ho, Henry S. "Dose rate distribution in triple layered dielectric cylinder with irregular cross section irradiated by plane wave sources" *Journal of Microwave Power Volume 10. Number 4* (1975) pp 421-432

[26] Hochstadt, Harry. *The Functions of Mathematical Physics.* New York: Dover(1986).

[27] Hörmander, Lars. *Linear Partial Differential Operators* New York: Academic Press (1963)

[28] Jaggard, Dwight L. and Xiaoguang Sun. "Scattering from bandlimmited fractal fibers" *IEEE Transactions on Antennas and Propagation Volume 37. No. 12* (December, 1989) 1591-1597.

[29] Kerker, M., D. Cooke, W. A. Farone, and R. T. Jacobson "Scattering from oblique circular cylinders" *Journal of the Optical Society of America, Volume 56* (1966) pp 487-491.

[30] Kogelnik, H. and T. Li. "Laser beams and resonators" *Applied Optics. Volume 5, Number 10* (October, 1966) pp 1550-1566

[31] Kozaki, Shogo. "Scattering of a Gaussian Beam by a Homogeneous Dielectric Cylinder" *Journal of Applied Physics. Volume 53. No. 11* (November, 1982) pp 7195-7200

[32] Liou, K. N., S. C. Ou Takano, A. Heymsfield, and W. Kreiss. "Infrared transmission through cirrus clouds: a radiative model for target detection" *Applied Optics. Volume 29, Number 13* (May 1, 1990) pp 1886-1896

[33] Mackowski, D. W., R. A. Altenkirch, and M. P. Menguc. "Internal absorption cross sections in a stratified sphere" *Applied Optics, Volume 29, Number 10* (April 1, 1990) pp 1551-1559

[34] Marx, Egon. "Scattering by an arbitrary cylinder at a plane interface" *IN* Stone, Ross (Editor). *Radar Cross Sections of Complex Objects* NY: IEEE Press (1990)

[35] Massoudi, Habib, Carl H. Durney, Peter W. Barber, and Magdy F. Iskander. "Electromagnetic absorption in multilayer cylinder models of man" *IEEE Transactions on Microwave Theory and Techniques. Volume MTT 27, No. 10* (October, 1979) pp 825-830.

[36] Maystre, D. and P. Vincent. "Diffraction d'une onde electromagnetique plane par un objet cylindrique non infiniment conducteur de section arbitraire" *Optics Communications Volume 5, Number 5* (August, 1972) pp 327-330.

[37] Miyazaki, Y. "Scattering and Diffraction of Electromagnetic Waves by an Inhomogeneous Dielectric Cylinder" *Radio Science. Volume 16, Number 6* (November December, 1981) pp 1009-1014

[38] Mugnai, Alberto and Warren J. Wiscombe. "Scattering from nonspherical Chebyshev Particles. I. Cross Sections, Single Scattering Albedo, Asymmetry factor, and backscattered fraction" *Applied Optics, Volume 25, Number 7* (April 1, 1986) pp 1235-1244.

[39] Park, Bae-Sig, A. Biswas, and R. L. Armstrong. "Delay of explosive vaporization in pulsed laser heated droplets" *Optics Letters. Volume 15, No. 4* (February 15, 1990) pp 206-208

[40] Pinnick, R. G., Abhijit Biswas, Robert L. Armstrong, S. Gerard Jennings, J. David Pendleton, and Gilbert Fernandez. "Micron size droplets irradiated with a pulsed CO_2 laser: Measurement of Explosion and Breakdown Thresholds" *Applied Optics. Volume 29, No. 7* (March 1, 1990) pp 918-925

[41] Pinnick, R. G., S. G. Jennings, Petr Chylek, Chris Ham, and W. T. Grandy. "Backscatter and Extinction in Water Clouds" *Journal of Geophysical Research. Vol 88, No. C11* (August 20, 1983) pp 6787-6796

[42] Rainville, Earl D. *Special Functions* New York: The Macmillan Company (1960)

[43] Richardson, C. B., R. L. Hightower, and A. L. Pigg. "Optical measurement of the evaporation of sulfuric acid droplets" *Applied Optics. Volume 25, Number 7* (April 1, 1986) pp 1226-1229

[44] Rosseland, S. *Theoretical Astrophysics: Atomic Theory and the Analysis of Stellar Atmospheres and Envelopes* Oxford, England: Clarendon Press (1936)

[45] Schaub, S. A., D. R. Alexander, J. P. Barton, and M. A. Emanuel. "Focused laser beam interactions with methanol droplets: effects of relative beam diameter" *Applied Optics. Volume 28, No. 9* (May 1, 1989) pp 1666-1669

[46] Schiffer, Ralf. "Perturbation approach for light scattering by an ensemble of irregular particles of arbitrary material" *Applied Optics, Volume 29, Number 10* (April 1, 1990) pp 1536-1550

[47] Tsai, Wen Chung and Ronald J. Pogorzelski. "Eigenfunction solution of the scattering of beam radiation fields by spherical objects" *Journal of the Optical Society of America. Volume 65. Number 12* (December, 1975) pp 1457-1463.

[48] Trefil, J. S. *Introduction to the Physics of Fluids and Solids* New York: Pergamon Press, Inc. (1975)

[49] Tzeng, H. M., K. F. Wall, M. B. Long, and R. K. Chang. "Laser emission from individual droplets at wavelengths corresponding to morphology dependent resonances" *Optics Letters. Volume 9, Number 11* (1984) pp 499-501

[50] Volkovitsky, O. A. "Peculiarities of light scattering by droplet aerosol in a divergent CO_2 laser beam" *Applied Optics. Volume 26, Number 24* (December 15, 1987) pp 5307-5310

[51] Wait, James R. "Scattering of a plane wave from a circular dielectric cylinder at oblique incidence" *Canadian Journal of Physics, Volume 33* (1955) pp 189-195

[52] Wait, James R. *Electromagnetic Radiation from Cylindrical Structures* New York: Pergamon Press (1959)

[53] Wait, James R. "The long wavelength limit in scattering from a dielectric cylinder at oblique incidence" *Canadian Journal of Physics. Volume 43* (December, 1965) pp 2212-2215

[54] Wait, James R. and David A. Hill. "Electromagnetic Surface Fields Produced by a Pulse Excited Loop Buried in the Earth." *Journal of Applied Physics. Volume 43. Number 10* (October, 1972) pp 3988-3989

[55] Wait, James R. *Introduction to Antennas and Propagation* London: Peter Peregrinus (1986)

[56] Wasow, Wolfgang. *Asymptotic Expansions for Ordinary Differential Equations* New York: John Wiley (1965)

[57] Whittaker, E. T. and G. N. Watson. *A Course of Modern Analysis* London: Cambridge University Press (1986).

[58] Wu, Le Kao, and Leonard L. Tsai. "Scattering by Arbitrarily Cross section layered lossy dielectric cylinders" *IEEE Transactions Antennas and Propagation*

[59] Yeh, C. "Scattering of Obliquely Incident Microwaves by a Moving Plasma Column" *Journal of Applied Physics, Volume 40, Number 13* (December, 1966) pp 5066-5075.

[60] Yeh, C. and W. V. T. Rusch. "Interaction of microwaves with an inhomogeneous and anisotropic plasma column" *Journal of Applied Physics, Volume 36, Number 7* (July, 1965) pp 2302-2306

[61] Yeh, C. and P. K. C. Wang. "Scattering of obliquely incident waves by inhomogenous fibers" *Journal of Applied Physics, Volume 43, No. 10* (October, 1972) pp 3999 - 4006.

Blank

SCATTERING AND ABSORPTION BY SPHERES CONTAINING ARBITRARILY LOCATED SPHERICAL INHOMOGENEITIES

Kirk A. Fuller

Department of Atmospheric Science
Colorado State University
Fort Collins, CO 80523
phone:(303)491-8644, fax: (303)491-8449
e-mail: fuller@herschel.atmos.colostate.edu

Recent Publications, Submittals for Publication, and Presentations

K. A. Fuller, "Scattering and absorption cross sections of compounded spheres. I. Theory for external aggregation," submitted for publication in J. Opt. Soc. Am. A. **11** (1994).

K. A. Fuller, "Scattering and absorption cross sections of compounded spheres. II. Calculations for external aggregation," submitted for publication in J. Opt. Soc. Am. A. **11** (1994).

S. Arnold, A. Ghaemi, and K. A. Fuller, "Morphological resonances detected from a cluster of two microspheres," submitted to Opt. Lett.

K. A. Fuller, "Some Advances in Understanding Light Scattering by Nonspherical Particles," to be presented at the 1994 meeting of the American Meteorological Society, Nashville, TN, 1/27/94.

G. W. Mulholland, C. F. Bohren, and K. A. Fuller, Invited Paper, "Light Scattering by Agglomerates: Coupled Electric and Magnetic Dipole Method," presented at the 1993 Workshop on the Electromagnetics of Combat-Induced Atmospheric Obscurants, El Paso, TX, 11/3/93.

K. A. Fuller, Invited Paper, "Light Scattering by Aggregated and Eccentrically Stratified Spheres," presented at the 1993 Workshop on the Electromagnetics of Combat-Induced Atmospheric Obscurants, El Paso, TX, 11/3/93.

G. W. Mulholland, C. F. Bohren, and K. A. Fuller, Poster, "Light Scattering from Agglomerates with Finite Size: Coupled Electric and Magnetic Dipole Method," presented at the 12th Annual Meeting of the American Association for Aerosol Research, Oak Brook, IL 10/13/93.

K. A. Fuller, "Light Scattering by Microdroplets with Internal Structure," presented at the 1993 Meeting of the Optical Society of America, Toronto, Ontario, 10/6/93.

K. A. Fuller, Colloquium, "Scattering and Absorption of Light by Compound Spherical Domains: Beyond Mie Theory," presented to the Department of Physics, New Mexico State University, Las Cruces, NM, 9/9/93.

K. A. Fuller, "Light Scattering by Spheres Containing Spherical Inhomogeneities," presented at the 1993 Conference on Obscuration and Aerosol Research, Edgewood, MD, 6/24/93.

S. Arnold, A. Ghaeme, and K. A. Fuller, "Morphological Resonances Detected from a Cluster of Two Spherical Particles," presented at the 1993 Conference on Obscuration and Aerosol Research, Edgewood, MD, 6/24/93.

K. A. Fuller, "Scattering and absorption by inhomogenous spheres and sphere aggregates," in SPIE Proceedings **1862**, *Laser Applications in Combustion and Combustion Diagnostics*, L. C. Liou, Ed. 249-257(1993).

R. G. Pinnick, G. Fernandez, E. Martinez-Andazola, B. D. Hinds, A. D. A. Hansen, and K. A. Fuller, "Aerosol in the arid southwestern US: measurements of mass loading, volatility, size distribution, absorption characteristics, carbon content, and vertical structure to 7 km ASL," J. Geophys. Res. **98D**, 2651-2666(1993).

K. A. Fuller, "Scattering of light by coated spheres," Opt. Lett. **18** 257-259(1993).

K. A. Fuller, Seminar, "Light Scattering Beyond Mie Theory: Progress in Electromagnetic Scattering from Compound Spherical Domains," presented to the Aerospace Corporation, Los Angeles, CA, 1/21/93.

K. A. Fuller,"Scattering and Absorption by Inhomogeneous Spheres and Sphere Aggregates," presented to the SPIE Conference on Laser Applications in Combustion and Combustion Diagnostics, Los Angeles, CA, 1/20/93.

K. A. Fuller,"A Study of the Possible Alterations of the Radiative Properties of the Atmospheric Aerosol when Sulfate, Silicate, or Aqueous Particles Scavenge Graphitic Carbon," presented at the 11th Annual Meeting of the American Association for Aerosol Research, San Fransisco, CA, 10/13/92.

K. A. Fuller, Invited Paper, "Absorption and Scattering Cross Sections of Carbon Dispersion Aerosols," presented at the 1992 Conference on Obscuration and Aerosol Research, Edgewood, MD, 6/25/92.

K. A. Fuller, Poster, "Absorption Cross Sections for Morphology Dependent Resonances of Two Sphere Systems," presented at the 1992 Conference on Obscuration and Aerosol Research, Edgewood, MD, 6/23/92.

K. A. Fuller, Poster, "Comparison of the Discrete Dipole Approximation and Exact Calculations for Light Scattering by Two Spheres," presented at the 1992 Conference on Obscuration and Aerosol Research, Edgewood, MD, 6/23/92.

Abstract

Theoretical values for absorption and scattering properties of droplets possessing spherical, eccentrically located inclusions are presented. The theory is exact and an outline of it is provided. Particular attention is paid to resonances in glycerol droplets that possess relatively small latex, water, and air inclusions, and to haze elements and cloud droplets that entrain smaller carbon (soot) particles.

I. Introduction

There has arisen, of late, considerable interest in the optical properties of micrometer-sized particles that entrain micrometer- or submicrometer-sized inhomogeneities. One focus of this interest is on the effects that the inhomogeneities might have on phenomena associated with morphology dependent resonances (MDRs) of their hosts. Experimental investigations are being carried out in this context on fluctuations in the intensity of elastically scattered light[1-3] and in the resonance spectra,[4] as well as on the effects of seeding on droplet fluorescence,[5] lasing,[6] and stimulated Raman scattering.[7] Approximations are also being developed for the study of intensity induced inhomogeneities in droplets.[8] Not only are arbitrarily located subparticles of interest; there is still work to be done involving the more familiar concentric core-shell morphology, especially in relation to lasing emission from layered microspheres[9,10] and cladded fibers.[11]

In this report, the theory of light scattering by spheres possessing one or more spherical inhomogeneities is developed. The inhomogeneities, or subspheres, are of uniform but otherwise arbitrary composition and are restricted in size and number only by the volume of the host. Numerical results are presented and discussed in regard to differences between the optical properties of homogeneous and such inhomogeneous spheres as described above. Attention is focused on questions that have arisen in the course of experimental research that is being carried out by Dr. Ronald G. Pinnick of the Army Research Laboratory's Battlefield Environment Directorate, White Sands Missile Range, NM.

It is concluded that, while aggregation of latex inclusions in a glycerol host may interact with the internal fields of the host to produce noticeable time-dependent fluctuations in the light scattered by such a system, it is not yet clear as to what the degree of those fluctuations might be relative to those produced by correlated scattering from the ensemble of inclusions. Furthermore, the addition of inclusions seems to lead to a symmetric broadening of host MDRs, whereas the calculations indicate that only an asymmetric broadening should occur under the given experimental conditions. Further experimental research appears warranted, with added attention being given to the issue of photon correlation spectroscopy.

Another discipline to which structured spheres are of concern is atmospheric science: The ubiquity of soot and its dominance as an absorber of visible radiation in the atmosphere are well known. Soot, in turn, typically occurs as clusters of carbonaceous spherules. In anthropogenic haze, individual haze elements frequently occur in the form of sulfate/soot *composite* particles.[12] Parungo et al.[13] have found that 30% of the particles in the Kuwaiti smoke plumes were SO_4-coated soot particles, and this was in an environment where dust and salt grains could compete equally as condensation sites for the sulfate. Sulfate aerosols are the primary components of haze. In addition to this role, such aerosols can serve as cloud condensation nuclei. Through either nucleation or

impact scavenging, carbon can be incorporated into cloud droplets. The occurrence of carbon on or in cloud droplets is, in turn, of interest as a possible contributor to the so-called cloud absorption anomaly.[14,15] An understanding of the absorption properties of soot that has been scavenged by transparent host particles is thus of considerable importance in assessing the impact of such particles on the earth's radiation balance and on visual air quality.

II. Theory

The vector spherical harmonics (VSH) $\mathbf{N}_{mn}^{(\kappa)}$ and $\mathbf{M}_{mn}^{(\kappa)}$ of order m and degree n can represent, respectively, transverse magnetic (TM) and transverse electric (TE) waves propagating in a homogeneous medium and characterized by spherical surfaces of constant phase. (The harmonic time dependence $\exp(-i\omega t)$ is assumed.) The direction of propagation of these wave fronts is inward when the radial dependence is governed by the spherical Bessel functions, $j_n(kr)$, k being the propagation constant of the medium, and outward when governed by the spherical Hankel functions of the first kind, $h_n^{(1)}(kr)$. This convergence or divergence of the radiation field is indicated by $\kappa = 1$ or $\kappa = 3$, respectively. (The notation is that used by Bruning and Lo,[16] and later, by Fuller.[17])

II.1. Reflection and transmission of an outgoing spherical wave at a concentric, concave spherical boundary.

Consider now the case of an *outgoing* electric partial wave, represented by $\mathbf{E}_{mn} = \mathbf{N}_{mn}^{(3)} + \mathbf{M}_{mn}^{(3)}$, that crosses a spherical dielectric discontinuity of radius ${}^1a$ centered about the coordinate system to which the VSH are referenced. Let the refractive index of the interior region be ${}^1N$ and that of the exterior be unity. The outgoing field will be partially reflected and partially transmitted at the interface. The tangential components of the exterior (transmitted) partial field must match the sum of the interior (incident + reflected) partial fields at the boundary and we may therefore write

$$\left[{}^1\check{c}_n \mathbf{N}_{mn}^{(3)} + {}^1\check{d}_n \mathbf{M}_{mn}^{(3)}\right]_{\theta,\phi} = \left[{}^1\check{a}_n \mathbf{N}_{mn}^{(1)} + {}^1\check{b}_n \mathbf{M}_{mn}^{(1)} + \mathbf{N}_{mn}^{(3)} + \mathbf{M}_{mn}^{(3)}\right]_{\theta,\phi}. \tag{1}$$

Because of the orthogonality properties of the VSH, there is no coupling of mn to $m'n'$ normal modes (nor is there coupling between TE and TM modes) at the boundary. Thus the angular dependence of the $\hat{\mathbf{e}}_\theta$ and $\hat{\mathbf{e}}_\phi$ components of the partial fields cancel algebraically in Eq. (1). Because of the different refractive indices on either side of the boundary, the radial functions, here expressed as Ricatti-Bessel functions, do not cancel and we have

$${}^1N\, {}^1\check{c}_n \xi'_n({}^1\rho) = \xi'_n({}^1\eta) + {}^1\check{a}_n \psi'_n({}^1\eta), \tag{2}$$

where ${}^1\rho = k\,{}^1a$ and ${}^1\eta = {}^1N\,{}^1\rho$. From the magnetic counterpart of Eq. (1) we obtain

$${}^1\check{c}_n \xi_n({}^1\rho) = \xi_n({}^1\eta) + {}^1\check{a}_n \psi_n({}^1\eta). \tag{3}$$

Thus

$$ {}^{1}\check{c}_n = \frac{\psi_n(\underset{\smile}{\eta})\,\xi'_n(\underset{\smile}{\eta}) - \xi_n(\underset{\smile}{\eta})\,\psi'_n(\underset{\smile}{\eta})}{{}^{1}N\xi'_n(\underset{\smile}{\eta})\,\psi_n({}^{1}\eta) - \xi_n(\underset{\smile}{\eta})\,\psi'_n({}^{1}\eta)}. \tag{4} $$

By virtue of the Wronskian,

$$ W\{j_n(z), y_n(z)\} = z^{-2}i \text{ (y_n represents the spherical Neuman functions),} $$

and by denoting

$$ {}^{1}\mathcal{D}_n^M = {}^{1}N\xi'_n(\underset{\smile}{\eta})\,\psi_n({}^{1}\eta) - \xi_n(\underset{\smile}{\eta})\,\psi'_n({}^{1}\eta), $$

we have

$$ {}^{1}\check{c}_n = -i/\,{}^{1}\mathcal{D}_n^M. $$

Precisely the same arguments produce the expressions

$$ {}^{1}\check{a}_n = -\left[{}^{1}N\xi'_n(\underset{\smile}{\eta})\,\xi_n({}^{1}\eta) - \xi_n(\underset{\smile}{\eta})\,\xi'_n({}^{1}\eta)\right]/\,{}^{1}\mathcal{D}_n^M \tag{5} $$

$$ {}^{1}\check{d}_n = \frac{\xi'_n({}^{1}\eta)\,\psi_n({}^{1}\eta) - \xi_n({}^{1}\eta)\,\psi'_n({}^{1}\eta)}{\xi'_n(\underset{\smile}{\eta})\,\psi_n({}^{1}\eta) - {}^{1}N\xi_n(\underset{\smile}{\eta})\,\psi'_n({}^{1}\eta)} \tag{6} $$

$$ = \left[\xi_n({}^{1}\eta)\,\psi'_n({}^{1}\eta) - \psi_n({}^{1}\eta)\,\xi'_n({}^{1}\eta)\right]/\,{}^{1}\mathcal{D}_n^E = i/\,{}^{1}\mathcal{D}_n^E, \tag{7} $$

$$ {}^{1}\check{b}_n = -\left[{}^{1}N\xi_n(\underset{\smile}{\eta})\,\xi'_n({}^{1}\eta) - \xi'_n(\underset{\smile}{\eta})\,\xi_n({}^{1}\eta)\right]/\,{}^{1}\mathcal{D}_n^E \tag{8} $$

as well as the standard Lorenz-Mie coefficients ${}^{1}a_n$, ${}^{1}b_n$, ${}^{1}c_n(= {}^{1}N\,{}^{1}\check{c}_n)$, and ${}^{1}d_n(= {}^{1}N\,{}^{1}\check{d}_n)$.[18]

For incoming spherical waves, the Lorenz-Mie coefficients of order n for the scattered and internal partial fields are the spherical wave analogues to the Fresnel coefficients for reflection and refraction of a plane wave at a planar boundary. With the derivation of the '$\check{}$' (hacek) coefficients, the analogy can now be extended to the case of *outgoing* spherical waves reflected and transmitted by *concave* spherical surfaces. A simple illustration of the above points leads to an elegant solution of the standard concentrically stratified sphere problem.

II.2. A novel solution for light scattering by stratified spheres.

The crux of the Lorenz-Mie theory lies in finding the projections of a plane wave onto vector spherical harmonics centered about a spherical scatterer, as is depicted in Fig. 1. The incident field may then be expanded in the VSH basis with the expansion coefficients (projections) of the TM and TE modes denoted, in order, as p_{mn} and q_{mn}. The coefficients of reflection (a_n, b_n) and transmission (c_n, d_n) serve as complex amplitudes of the (TM, TE) vector partial waves in terms of which the scattered and internal fields are expanded, as illustrated in Fig. 2.

Consider now a wavefront incident on a stratified sphere of which the core (shell) has a refractive index ${}^{2}N$ (${}^{1}N$) and size parameter $\underset{\smile}{\eta}$ ($\underset{\smile}{\eta}$). The incident wavefront will couple to the normal modes of the shell. The strength of this coupling is still given by the expansion coefficients p_{mn} and q_{mn}. The shell will produce a scattered and a transmitted field with associated partial wave amplitudes $p_{mn}\,{}^{1}a_n$, $q_{mn}\,{}^{1}b_n$ and $p_{mn}\,{}^{1}c_n$, $q_{mn}\,{}^{1}d_n$, just as though it was homogeneous. The transmitted partial fields of degree n couple directly to the normal modes of the same degree associated with the core particle, producing a scattered field with amplitudes $p_{mn}\,{}^{1}c_n\,{}^{2}a_n$ and $q_{mn}\,{}^{1}d_n\,{}^{2}b_n$, where

the ${}^2a_n$ and ${}^2b_n$ are the Lorenz-Mie coefficients of a core particle immersed in an infinite medium of refractive index ${}^1N$. From the discussion surrounding Eq. (4), it is seen that the fields transmitted to the exterior of the mantle will have amplitudes $p_{mn}\,{}^1c_n\,{}^2a_n\,{}^1\check{c}_n$ and $q_{mn}\,{}^1d_n\,{}^2b_n\,{}^1\check{d}_n$, and the internally reflected fields will have amplitudes $p_{mn}\,{}^1c_n\,{}^2a_n\,{}^1\check{a}_n$ and $q_{mn}\,{}^1d_n\,{}^2b_n\,{}^1\check{b}_n$.

A multiple scattering series is thus constructed and the scattering amplitudes of the coated sphere are found to be

$$
\begin{aligned}
{}^1AE_{mn} &= p_{mn}\left[{}^1a_n + {}^1c_n\,{}^2a_n\,{}^1\check{c}_n \sum_{k=0}^{\infty}({}^2a_n\,{}^1\check{a}_n)^k\right] \\
&= p_{mn}\left[{}^1a_n + \frac{{}^2a_n\,{}^1c_n\,{}^1\check{c}_n}{1-{}^1\check{a}_n\,{}^2a_n}\right]
\end{aligned}
\tag{9}
$$

and

$$
\begin{aligned}
{}^1AH_{mn} &= q_{mn}\left[{}^1b_n + {}^1d_n\,{}^2b_n\,{}^1\check{d}_n \sum_{k=0}^{\infty}({}^2b_n\,{}^1\check{b}_n)^k\right] \\
&= q_{mn}\left[{}^1b_n + \frac{{}^2b_n\,{}^1d_n\,{}^1\check{d}_n}{1-{}^1\check{b}_n\,{}^2b_n}\right],
\end{aligned}
\tag{10}
$$

provided, of course, that the moduli of the quantities in parentheses are less than one. This process is illustrated in Figs. 2 and 3.

The problem of scattering from a sphere containing multiple spherical inhomogeneities must, as a special case, be reducible to the problem considered above. Eqs. (9) and (10) have not only been shown to agree numerically with the scattering coefficients of Aden and Kerker,[19] but a reduction of the multiple inclusion problem to the coated sphere problem, outlined below, provides an independent verification of the order-of-scattering (OS) argument.

II.3. Light scattering from an eccentrically stratified sphere.

Now let a wavefront be incident on a composite particle made from a sphere of refractive index ${}^2N$ and size parameter $\hat{\mathfrak{p}}$ located arbitrarily within a spherical and otherwise homogeneous host of refractive index ${}^1N$ and size parameter $\mathfrak{p}$. The incident wavefront will still couple to the normal modes of the host with a strength determined by p_{mn} and q_{mn}. The shell will produce a scattered and a transmitted field with associated partial wave amplitudes $p_{mn}\,{}^1a_n \equiv {}^1a^{(1)}_{mn}$, $q_{mn}\,{}^1b_n \equiv {}^1b^{(1)}_{mn}$ and $p_{mn}\,{}^1c_n$, $q_{mn}\,{}^1d_n$. Since the spherical surfaces are not concentric, *each* of the transmitted partial fields couples to *every* normal mode associated with the inclusion, producing a scattered field with amplitudes ${}^2a^{(1)}_{mn}$ and ${}^2b^{(1)}_{mn}$. For example, the TM coefficient is

$$
{}^2a^{(1)}_{mn} = {}^2a_n \sum_{\nu}\sum_{\mu}\left(p_{\mu\nu}\,{}^1c_\nu \widetilde{A}^{\mu\nu}_{mn} + q_{\mu\nu}\,{}^1d_\nu \widetilde{B}^{\mu\nu}_{mn}\right),
\tag{11}
$$

where the ${}^2a_n$ are the TM Lorenz-Mie coefficients of a core particle immersed in an infinite medium of refractive index ${}^1N$. References for the quantities $\widetilde{A}^{\mu\nu}_{mn}$ and $\widetilde{B}^{\mu\nu}_{mn}$ are given in the next

section. The fields scattered by the inclusion are then transmitted to the exterior of the mantle or internally reflected by its surface with the respective amplitudes ${}^1a_{mn}^{(2)}$, ${}^1b_{mn}^{(2)}$ and ${}^1c_{mn}^{(2)}$, ${}^1d_{mn}^{(2)}$. The internally reflected fields will in turn be scattered by the inclusion, and so on. The coefficients for the total scattered field may thus be constructed as

$$ {}^1\mathcal{A}E_{mn} = \sum_{j=1}^{\infty} {}^1a_{mn}^{(j)} \quad \text{and} \quad {}^1\mathcal{A}H_{mn} = \sum_{j=1}^{\infty} {}^1b_{mn}^{(j)}, \tag{12} $$

where, for the TM normal modes,

$$ {}^1a_{mn}^{(j)} = {}^1\check{c}_n \sum_{\nu}\sum_{\mu}\left({}^2a_{\mu\nu}^{(j)}\widetilde{A}_{mn}^{\mu\nu} + {}^2b_{\mu\nu}^{(j)}\widetilde{B}_{mn}^{\mu\nu}\right) \tag{13} $$

$$ {}^2a_{mn}^{(j+1)} = {}^2a_n \sum_{\nu}\sum_{\mu}\left({}^1c_{\mu\nu}^{(j)}\widetilde{A}_{mn}^{\mu\nu} + {}^1d_{\mu\nu}^{(j)}\widetilde{B}_{mn}^{\mu\nu}\right) \tag{14} $$

$$ {}^1c_{mn}^{(j)} = {}^1\check{a}_n \sum_{\nu}\sum_{\mu}\left({}^2a_{\mu\nu}^{(j)}\widetilde{A}_{mn}^{\mu\nu} + {}^2b_{\mu\nu}^{(j)}\widetilde{B}_{mn}^{\mu\nu}\right), \tag{15} $$

for $j > 1$. Expressions for the TE modes are readily derived from similar arguments. This process is illustrated in Figs. 4 and 5. Calculations based on this order-of-scattering (OS) treatment are in agreement with those obtained by Borghese et al.,[20] who solved a system of linear equations to obtain the scattering coefficients. For a concentric inclusion, Eqs. (12) reduce to Eqs. (9) and (10).

II.4. The solution for an arbitrary number of inclusions.

The multiple inclusion problem closely parallels the problem of scattering by sphere clusters, an overview of which is provided in Ref. 17. The spheres in the host particle are centered about the origins ${}^\ell O$, where ℓ is an index identifying a specific constituent in a set of L spheres. The index $\ell = 1$ is reserved for the host itself. The host and inclusions (with radii ${}^\ell a$) are characterized by the size parameters $k\,{}^\ell a \equiv {}^\ell\underline{p}$ and complex refractive indices ${}^\ell N$. It is assumed that the total electric field at points exterior to the host, inside the host but outside the inclusions, and in the inclusions can be expanded, respectively, as

$$ {}^{\mathcal{E}}\mathbf{E} = \sum_{n=1}^{\infty}\sum_{m=-n}^{n}\left(p_{mn}\,{}^1\mathbf{N}_{mn}^{(1)} + q_{mn}\,{}^1\mathbf{M}_{mn}^{(1)} + {}^1\mathcal{A}E_{mn}\,{}^1\mathbf{N}_{mn}^{(3)} + {}^1\mathcal{A}H_{mn}\,{}^1\mathbf{M}_{mn}^{(3)}\right), \tag{16} $$

$$ {}^{\mathcal{H}}\mathbf{E} = \sum_{n=1}^{\infty}\sum_{m=-n}^{n}\left(\mathcal{C}E_{mn}\,{}^1\mathbf{N}_{mn}^{(1)} + \mathcal{C}H_{mn}\,{}^1\mathbf{M}_{mn}^{(1)} + \sum_{\ell>1}\left[{}^\ell\mathcal{A}E_{\mu\nu}\,{}^\ell\mathbf{N}_{mn}^{(3)} + {}^\ell\mathcal{A}H_{\mu\nu}\,{}^\ell\mathbf{M}_{mn}^{(3)}\right]\right), \tag{17} $$

$$ {}^{\mathcal{I}}\mathbf{E} = \sum_{n=1}^{\infty}\sum_{m=-n}^{n}\left(\mathcal{C}E_{mn}\,{}^\ell\mathbf{N}_{mn}^{(1)} + \mathcal{C}H_{mn}\,{}^\ell\mathbf{M}_{mn}^{(1)}\right), \tag{18} $$

where the expansion coefficients ${}^\ell\mathcal{A}E_{mn}$ and ${}^\ell\mathcal{A}H_{mn}$ correspond, respectively, to the TM and TE modes of the ℓth sphere, and ${}^\ell\mathbf{N}_{mn}^{(3)}$ and ${}^\ell\mathbf{M}_{mn}^{(3)}$ are vector spherical harmonics centered about the ℓth inclusion.

The boundary conditions of the multiple inclusion system can be satisfied with the aid of the addition theorem for VSH, and one is led to a self-consistent set of linear equations for the scattering coefficients:

$$ {}^{\ell}AE_{mn} = {}^{\ell}a_n \sum_{\nu\mu} \left[{}^{1}CE_{\mu\nu} \widetilde{A}^{\mu\nu}_{mn} + {}^{1}CH_{\mu\nu} \widetilde{B}^{\mu\nu}_{mn} + \sum_{\ell' \neq \ell} \left({}^{\ell'}AE_{\mu\nu} A^{\mu\nu}_{mn} + {}^{\ell'}AH_{\mu\nu} B^{\mu\nu}_{mn} \right) \right] \tag{19} $$

$$ {}^{\ell}AH_{mn} = {}^{\ell}b_n \sum_{\nu\mu} \left[{}^{1}CH_{\mu\nu} \widetilde{A}^{\mu\nu}_{mn} + {}^{1}CE_{\mu\nu} \widetilde{B}^{\mu\nu}_{mn} + \sum_{\ell' \neq \ell} \left({}^{\ell'}AH_{\mu\nu} A^{\mu\nu}_{mn} + {}^{\ell'}AE_{\mu\nu} B^{\mu\nu}_{mn} \right) \right] \tag{20} $$

$$ {}^{1}CE_{mn} = {}^{1}c_n p_{mn} + {}^{1}\check{a}_n \sum_{\ell \neq 1} \sum_{\nu\mu} \left({}^{\ell}AE_{\mu\nu} \widetilde{A}^{\mu\nu}_{mn} + {}^{\ell}AH_{\mu\nu} \widetilde{B}^{\mu\nu}_{mn} \right) \tag{21} $$

$$ {}^{1}CH_{mn} = {}^{1}d_n q_{mn} + {}^{1}\check{b}_n \sum_{\ell \neq 1} \sum_{\nu\mu} \left({}^{\ell}AH_{\mu\nu} \widetilde{A}^{\mu\nu}_{mn} + {}^{\ell}AE_{\mu\nu} \widetilde{B}^{\mu\nu}_{mn} \right) \tag{22} $$

$$ {}^{1}AE_{mn} = {}^{1}a_n p_{mn} + {}^{1}\check{c}_n \sum_{\ell \neq 1} \sum_{\nu\mu} \left({}^{\ell}AE_{\mu\nu} \widetilde{A}^{\mu\nu}_{mn} + {}^{\ell}AH_{\mu\nu} \widetilde{B}^{\mu\nu}_{mn} \right) \tag{23} $$

$$ {}^{1}AH_{mn} = {}^{1}b_n q_{mn} + {}^{1}\check{d}_n \sum_{\ell \neq 1} \sum_{\nu\mu} \left({}^{\ell}AH_{\mu\nu} \widetilde{A}^{\mu\nu}_{mn} + {}^{\ell}AE_{\mu\nu} \widetilde{B}^{\mu\nu}_{mn} \right), \tag{24} $$

where the translation coefficients $A^{\mu\nu}_{mn}$, $B^{\mu\nu}_{mn}$, $\widetilde{A}^{\mu\nu}_{mn}$, and $\widetilde{B}^{\mu\nu}_{mn}$ are defined by the addition theorem for VSH,[16,17,21,22] and ${}^{1}CE_{mn}$, ${}^{1}CH_{mn}$ are the TM, TE coefficients of the electric field in the host material. A detailed derivation of these equations will be the focus of an upcoming publication.

It is worth noting that when the separation between two coordinate origins, in this case the centers of the host and inclusion, tends to 0, $\widetilde{A}^{\mu\nu}_{mn}$ and $\widetilde{B}^{\mu\nu}_{mn}$ tend to $\delta_{m,\mu}\delta_{n,\nu}$ and 0, respectively, and the set of Eqs. (19)–(24) is greatly simplified. A bit of algebra then leads to Eqs. (9) and (10). Arriving at Eqs. (9) and (10) from the self-consistent set of Eqs. (19)–(24) shows that the former are valid even in the event that the multiple reflection series fail to converge. Such a problem with convergence can arise when dealing with optical resonances of externally aggregated two-sphere systems[17] but this matter is still under investigation for the case of included spheres.

III. Calculations

An illustrative sample of recent experimental data is presented in Fig. 6. In the experiment, measurements are made of the intensity of light scattered from an evaporating glycerol droplet into a small solid angle centered near 90° from the direction of forward scattering. The glycerol droplet may be homogeneous, or it may be host to large numbers of latex inclusions. The radius of the host is on the order of 3.25 μm and that of the inclusions ranges from 15–52.5 nm. Two features seen in this figure that are of particular interest in the current study are (1) the increasing fluctuations in the scattered intensity with increasing sizes of the latex inclusion, and (2) the broadening and ultimate suppression of morphology dependent resonances, also with increasing inclusion size. Not apparent in Fig. 6 is an observed tendency of these two features to become enhanced with increasing inclusion concentration.

III.1. Fluctuations off resonance.

A likely contributor to the fluctuations is dynamic light scattering or photon correlation, but it is also likely that this is not the only contributor. Acccording to the calculations displayed in Fig. 7, a latex inclusion with a diameter of 105 nm can cause about an 8% fluctuation in side-scattered intensity as it passes through the geometric hot spot of the host. (The term *geometric* hot spot is used here to distinguish it from the much more intense hot spots that are associated with MDRs.) This is somewhat surprising since such an inclusion has only about 2.5×10^{-5} the volume of the host. (Note that the inset in the figure is not drawn to scale—the inclusion would not be visible if it were.) Now, the fluctuations that arise when 105 nm inclusions are involved are certainly larger than 8%. In fact, an 8% fluctuation is more in line with those observed when 64 nm inclusions were used. Also seen in Fig. 7, however, is that 64 nm inclusions are predicted by theory to produce fluctuaions that are only on the order of a percent or so. Agglomeration of the inclusions has been invoked to explain this discrepancy, but, as is discussed below, the spheres do not even need to come in contact in order for 64 nm inclusions to exibit 105 nm-type fluctuations.

In cases where the dimensionless center-to-center distance, kd, between two sufficiently small spheres is less than one, the particles are not significantly out of phase in their response to an oscillating field and will behave approximately as a single scatterer with twice the volume of a single sphere. The scattering efficiency of such a particle is proportional to the square of its volume, and this leads to a scattering efficiency that is four times that of the isolated spheres. It has been shown[21] that the scattering cross section of a pair of identical, closely spaced, noninteracting Rayleigh spheres can be written as

$$\sigma_s = {}^{11}\sigma_s + {}^{22}\sigma_s + 2Re\left({}^{12}\sigma_s\right) = 2\left[{}^{11}\sigma_s + Re\left({}^{12}\sigma_s\right)\right]. \tag{25}$$

When the incident electric field is polarized perpendicular to the line of centers, ${}^{12}\sigma_s$ reduces to

$$\begin{aligned} Re\left({}^{12}\sigma_s\right) &= \frac{9\pi|{}^1a_1|^2}{k^2}\cos\left(kd\cos\alpha\right)\left[2a(1,1,-1,1,0)j_0\left(kd\right) + a(1,1,-1,1,2)j_2\left(kd\right)\right] \\ &= \frac{-9\pi|{}^1a_1|^2}{k^2}\frac{\cos\left(kd\cos\alpha\right)}{kd}\left[\left(\frac{1}{kd^2}-1\right)\sin kd - \frac{\cos kd}{kd}\right], \end{aligned} \tag{26}$$

and the coefficients $a(m,n,\mu,\nu,p)$ represent Gaunt integrals.[17] The ratio of the scattering efficiency of the pair to the sum of those of the individuals can now be written as

$$\frac{Q_s}{({}^1Q + {}^2Q)} = 1 - \frac{3}{2}\frac{\cos\left(kd\cos\alpha\right)}{kd}\left[\left(\frac{1}{kd^2}-1\right)\sin kd - \frac{\cos kd}{kd}\right]. \tag{27}$$

For sufficiently small kd this ratio is 2, as expected. Any variation from this expression is a measure of the strength of electrodynamic coupling between the spheres.

Given the number density of inclusions, it is likely that more than one inclusion resided in the geometric hot spot at one time. It is therefore likely that the proximity effects outlined above contributed significantly to the scattered intensity of radiation, without any actual agglomeration having taken place.

III.2. Broadening of resonance spectra.

In order to better understand the effects of guest particles on the resonance spectra of their hosts, a number of calculations were carried out that involved differing sizes and locations of the inclusions. The major findings from these runs are outlayed in Figs. 8–13.

In Fig. 8, the simulation that produced Fig. 7 was rerun, but with the host now tuned to a TE^2_{36} resonance. A 32 nm inclusion is not seen to effect side scattering to a significant degree. The 64 nm inclusion, however, is now seen to produce about a 15% decrease in the scattered intensity. The 105 nm inclusion reduces that intensity by 60%, or, more importantly, it is seen to reduce the scattered intensity almost to its noresonant value. These reductions occur as the inclusion passes through the hot spots of the resonating sphere. Examination of Figs. 7 and 8 shows that the position of the inclusion that causes the greatest change in scattering intensity differs slightly between the resonant and nonresonant cases—this is because the distribution of energy density within the sphere is radically different between the two cases. It is somewhat fortuitous that the two positions are as close as they are.

At first, it was believed that an inclusion with a diameter as small as 64 nm could, if passing through a hot spot, appreciably degrade the quality of the resonance; reducing the energy density in the host to such a degree that the above decreases in scattered intensities could be observed. A study of the resonance spectra of a glycerol droplet with such inclusions centered in a hot spot reveals, however, that this is not the case: Fig. 9, wherein the size of the inclusion is given by its *radius*, makes it clear that the resonance is not spoiled to a significant degree by the presence of either a 64 or 105 nm latex subsphere, but rather, the inclusion causes the resonance to be redshifted. This is consistent with the phase-matching conditions that photons traversing an 'orbit' inside the host must meet in order for a resonance to be sustained. A blue shift of the resonance is predicted if the optical density of the inclusion is *less* than that of the host. This is borne out in the case of water inclusions, also depicted in Fig. 9.

An important point to make in regard to the calculations is that, even though the order-of-scattering method is applicable to cases involving nonresonant hosts, it will break down if the host is on resonance and the inclusion surpasses a critical size. In the present study, this critical size was found to be at a diameter of slightly more than 64 nm. The solution for arbitrarily placed inclusions involves simultaneously matching boundary conditions at all surfaces in the ensemble, including, of course, that of the host. The system of equations layed out in Eqs. (19)-(22) can be solved to yield the coefficients associated with the inclusions; these coefficients are then used in Eqs. (23) and (24) to determine the scattering coefficients of the field exterior to the host. This method of solution has been stable under all conditions encountered thus far. The spectra, in Fig. 9, of the glycerol droplet with 30 nm (radius) inclusions were found from the order-of-scattering method, the calculations for the 50 and 100 nm inclusions were made with the use of a biconjugate gradient linear equation solver.

Given the fact that intense fields can be generated in microdroplets, it is plausible that vapor bubbles could be formed in regions of strong localized heating, especially when such regions are colocated with a latex (or other) 'impurity.' It is therefore worth comparing the changes in resonance spectra due to the presence of latex inclusions to those brought on by the presence of small vapor bubbles. In Fig. 10, the effects of various sizes of air bubble on the TE^2_{46} resonance of glycerol is studied. Since the optical contrast of an air bubble is greater than that of one composed

of water or latex, the spectra are seen to be more sensitive to the size of the air inclusions: The resonance can be effectively destroyed by a 100 nm bubble, whereas the resonance can be sustained (albeit degraded) in the presence of water or latex inclusions of this same size, as was seen in Fig. 9.

Although the inclusions can clearly change the profile of an MDR, the experimental data indicate that a symmetrical broadening of the resonance is occurring. The above calculations indicate, however, that an inclusion centered in an MDR-induced hot spot can only produce an asymmetric shift in the resonance. The effects of locating the inclusion off the center of the hot spot are examined in Figs. 11 and 12. The heaviest solid curves in both figures correspond to the case of a homogeneous sphere. The other solid curves are resonance spectra produced by inclusions located at several radial positions that are slightly larger than that of the center of the hot spot. The dotted curves are for inclusions located at several radial positions that are slightly smaller. In all cases, the resonances are seen to be shifted to lower size parameters.

One last possible condition that might lead to symmetric broadening that was considered here is that where the inclusion comes in contact with the surface of the host, although it had to be assumed, for the sake of calculation, that such contact did not actually perturb that surface. Given that, as seen in Fig. 8, the scattered intensity could be greatly effected in such cases, it seemed possible that this case could lead to some kind of leakage of radiation that could produce a blue shift in the resonances. As seen in Fig. 13, however, only shifts toward the red could be produced under such conditions. (The dashed curve corresponds to the case of an inclusion slightly removed from contact with the surface.)

Thus, no satisfactory explanation for symmetric broadening has been found. The only possibile source of such broadening, assuming that it is real, unearthed in the present study is the production of vapor bubbles in the seeded host. There is no direct evidence that this has occurred, though the possibility may be worth pursuing.

IV. Effects of Scavenging on the Specific Absorption of Soot

Illustrative results for absorption by carbon spheres located in transparent hosts are displayed in Figs. 14–17. The scattering geometry of the eccentric inclusion problem as posed in this section is depicted in the insets of Figs. 14 and 15. All calculations presented henceforth are based on the order-of-scattering method. The radii of the host and inclusion are, respectively, ^{1}a and ^{2}a.

It is popular (and, at times, useful) to define the efficiency factors for extinction, scattering and absorption to be, in order,

$$Q_e = \frac{\sigma_e}{G}, \quad Q_s = \frac{\sigma_s}{G}, \quad \text{and} \quad Q_a = \frac{\sigma_a}{G}, \tag{28}$$

where G is the geometric shadow of the particle and σ denotes the respective cross sections. In view of the more complex morphologies of sphere aggregates, however, a better choice for efficiency factors is the gram-specific cross section, $\mathcal{A}$, the units of which are m^2/g:

$$\mathcal{A} = \frac{\sigma_a}{m} = \frac{\sigma_a}{(\text{specific gravity})(\text{ particle volume})}. \tag{29}$$

The basic features of the dependence of $\mathcal{A}$ on orientation can be understood from geometric optics: An optically large sphere with a refractive index of ≈ 1.5 will focus light into a region near its surface. If the refractive index is ≈ 1.33 then light will be focused into a volume slightly less than half a radius from the sphere surface. The refractive effects of the sphere will prevent most of the incident radiation from reaching regions other than the focal volume in the 'shadowed' hemisphere. Reflections from the shadow surface of the sphere will produce a secondary focal volume narrowly centered about the illuminated side of the droplet. Such features of a spherical lense are manifested in the behavior of the absorption cross sections of the carbon grains as a function of particle position in both Figs. 14 and 15. The larger the optical size of the host particle, the more accurate the geometric optics picture. When carbon grains are found within the focal volumes of the larger particles, their absorption cross sections can be enhanced by well over an order of magnitude. Carbon spheres with radii of 0.01, 0.05, and $0.10\mu m$ have been considered. In Figs. 14 and 15, $\mathcal{A}(\alpha)$ is displayed for unpolarized light.

The refractive index of the host particles considered in Figs. 14 and 16 is taken to be $1.52 + 0.0i$; appropriate for sulfuric acid droplets or ammonium sulfate particles at moderate relative humidities. The absorption cross sections of carbon spheres entrained in other particles not only depend on the orientation of the system relative to the incident beam, but on the polarization of the beam, as well. This is primarily because the stucture of the electric fields in the host have a strong polarization dependence. In fact, the smaller carbon grains can act as probes of the source function, $\mathbf{E}\cdot\mathbf{E}^*$, in the sphere. (The magnetic fields are not probed since the absorption arises only from the coupling of the local electric field to current densities which are themselves proportional to that field.) The larger the grain, the less sensitive its $\mathcal{A}$ to rapid variations in $\mathbf{E}\cdot\mathbf{E}^*$. This effect of an increasing grain size is reminiscent of the convolution of a noisy function with a Gaussian profile of increasing width.

Similar results from calculations of the absorption cross sections of carbon particles contained in cloud droplets are displayed in Figs. 15 and 17. There is a strong enhancement of $\mathcal{A}$ near $\alpha = 0$, as expected, and the caustic becomes evident in Fig. 15 as the grain approaches the surface of the droplet.

The lensing effect of the water droplets does not enhance the absorption cross sections to as great of a degree as it does in the case of the smaller sulfate particles, primarily because the sulfates have a higher refractive index and hence their focal volume is centered at or very near the surface. The caustic more sharply defines a boundary between regions with high values of $|E|^2$ and those where $|E|^2 \approx 0$ for the optically large water droplets than for the smaller sulfate particles and hence refractive shielding of carbon grains by cloud droplets is seen in Fig. 16 to be more pronounced than is the shielding in haze elements.

In order to better understand the effects that scavenging of soot by transparent droplets may have on the optical properties of haze and clouds, it is necessary to consider orientation averages of cross sections. Orientation averages require a high resolution in α. (The calculations summarized in Figs. 16 and 17 were based on a sampling frequency of 1°.) It is here, perhaps, that the order-of-scattering approach plays its most important role, from a numerical standpoint, since the smaller the adsorbed grain, the fewer terms are needed in the multiple scattering series from which the scattering coefficients and cross sections are found. In fact, only one exchange between the $0.01\mu m$ carbon grains and droplets was necessary in order to determine σ_a to the required precision. For larger grains, no more than five orders of scattering were needed. For a given polarization, the

orientation-averaged $\mathcal{A}$ is taken to be

$$\langle \mathcal{A} \rangle = \frac{1}{2} \int_0^{\pi} \mathcal{A}(\alpha) \sin(\alpha)\, d\alpha. \tag{30}$$

Fig. 16 shows $\langle \mathcal{A} \rangle$ of carbonaceous spheres at various displacements, d, from the center of a sulfate host. Fig. 17 displays the dependence of $\langle \mathcal{A} \rangle$ on d when the carbon is entrained in a cloud droplet. Given that $\mathcal{A} = 3.7$, 4.6, and 5.3 m^2/g for, respectively, ^{2}a= .01, .05, and .10 μm when the carbon is isolated, scavenging is indicated to generally enhance absorption by soot. It is noteworthy, however, that for cloud droplets, the *concentric* spheres model (J=0) commonly applied to this problem tends to overestimate this enhancement. This is because the refractory properties of the droplet can shield the inclusions from sunlight to a degree that cannot be offset by the presence of caustics.

V. Summary and Conclusions

The theory of light scattering by spherical hosts that entrain one or more spherical inclusions has been presented and applied to calculations of the scattering properties and resonance spectra of glycerol droplets seeded with latex inclusions and to a study of the aborption properties of soot that is internally mixed in haze and clouds.

It has been demonstrated that a single inclusion, though very small compared to the host, can create large ($\approx 10\%$) fluctuations in the scattering of light from such particles. Such fluctuations are consistent with experimental data, but it is not clear what the contribution of this process might be relative to photon correlation effects. It is demonstrated that small particles may have anamolously large effects when their center-to-center separation is less than the wavelength of light in the inclusion, but without the occurrence of true aggregation. The effects of inclusions can be much greater when the host is tuned to a morphology dependent resonance. The type of broadening that seems to be discernable in experimental data has not yet been satisfactorily explained by the calculations presented in this study.

The effects of scavenging of atmospheric carbon by haze and cloud droplets has been considered in terms of the orientations of the resulting composite particles—carbon grains residing in droplets—with respect to the incident fields. Orientation- and polarization-averaged absorption efficiencies were then determined. Carbon scavenged into cloud droplets appears thus far to absorb significantly more light when it is located near the center of the droplet than when it is found at other locations, especially near the surface. If there is no preferred radial position for the carbon, then the concentric sphere models overestimate $\langle \mathcal{A} \rangle$. This overestimation should become even more pronounced in cloud droplets if there is a tendency, owed perhaps to capillary or van der Waals effects, for the soot to reside near the surface of the host.

4. Acknowledgements

The author wishes to thank Dr. Ronald G. Pinnick for many stimulating conversations. This work was supported in part by National Science Foundation grant ATM-9204146. Additional support for the research on resonances was provided by U. S. Army Research Office contract DAAL03-91-C-0034, Delivery Order 763, and additional support for the research on absorption by entrained carbon grains was provided by National Park Service grant NA90RAH000077.

References

1. Burt. V. Bronk, Michael J. Smith, and S. Arnold, "Photon-correlation spectroscopy for small spherical inclusions in a micrometer-sized electrodynamically levitated droplet," Opt. Lett. **18**, 93-95(1993).

2. J. Gu, T. E. Rukgauer, J.-G. Xie, and R. L. Armstrong, "Effect of particulate seeding on microdroplet angular scattering," Opt. Lett. **18**, 1293-1295(1993).

3. Petr Chýlek, Dat Ngo, and R. G. Pinnick, "Resonance structure of composite and slightly absorbing spheres," J. Opt. Soc. Am. A **9**, 775-780(1992).

4. Dat Ngo and R. G. Pinnick, "Suppression of scattering resonances in inhomogeneous microdroplets," submitted to J. Opt. Soc. Am. B.

5. H.-B. Lin, A. L. Huston, J. D. Eversole, A. J. Campillo, and P. Chýlek, "Internal scattering effects on microdroplet resonant emission structure," Opt. Lett. **17**, 970-972(1992).

6. R. L. Armstrong, J.-G. Xie, T. E. Ruekgauer, J. Gu, and R. G. Pinnick, "Effects of submicrometer-sized particles on microdroplet lasing," Opt. Lett. **18** 119-121(1993)

7. J.-G. Xie, T. E. Ruekgauer, R. L. Armstrong, and R. G. Pinnick, "Suppression of stimulated Raman scattering from microdroplets by seeding with nanometer-sized latex particles," Opt. Lett. **18**, 340-342(1993).

8. Md. Mohiuddin Mazumder, "Morphology-dependent resonances in inhomogeneous spheres: comparison of the layered T-matrix method and the time-independent perturbation method," J. Opt. Soc. Am. A **9**, 1844-1853(1992).

9. James A. Lock, "Interference enhancement of the internal fields at structural resonances of a coated sphere," Appl. Opt. **29**, 3180-3187(1990).

10. M. Essien, R. L. Armstrong, and R. G. Pinnick, "Lasing Emission from an evaporating layered microdroplet," Opt. Lett. **18**, 762-764(1993).

11. J. C. Knight, H. S. T. Driver, and G. N. Robertson, "Interference modulation of Q values in a cladded-fiber whispering-gallery-mode laser," Opt. Lett. **18**, 1296-1298(1993).

12. J. Podzimek, "Physical properties of coarse aerosol particles and haze elements in a polluted urban-marine environment," J. Aerosol Sci. **21**, 299–308(1990).

13. F. Parungo, B. Kopcewicz, C. Nagamoto, R. Schnell, P. Sheridan, C. Zhu, and J. Harris, "Aerosol Properties in the Kuwait Oil Fire Plumes: Their Morphology, Size Distribution, Chemical Composition, Transport, and Potential Effects on Climate," J. Geophys. Res. **97** D, 15867-15882(1992).

14. P. Chýlek, V. Ramaswamy, and R. J. Cheng, "Effect of graphitic carbon on the albedo of clouds," J. Atmos. Sci. **41**, 3076-3084(1984).

15. G. L. Stephens and S.-C. Tsay, "On the cloud absorption anomaly," Q. J. R. Meteorol. Soc. **116**, 671–704(1990).

16. J. H. Bruning and Y. T. Lo, "Multiple scattering of em waves by spheres parts I & II," IEEE Trans. Ant. Prop. **AP-19**, 378–400 (1971), J. H Bruning and Y. T. Lo, "Multiple Scattering by Spheres," Antenna Laboratory Report No. 69-5, Antenna Laboratory, Department of Electrical Engineering, Engineering Experiment Station, University of Illinois, Urbana, Illinois.

17. K. A. Fuller, "Optical resonances and two-sphere systems," Appl. Opt. **30** 4716–4731 (1991)

18. H. C. van de Hulst, *Light Scattering by Small Particles*, (Dover Publications, 1981).

19. A. Aden and M. Kerker, "Scattering of electromagnetic waves from two concentric spheres," J. Appl. Phys. **22**, 1242–1246(1951).

20. F. Borghese, P. Denti, R. Saija, and O. I. Sindoni, "Optical properties of spheres containing a spherical eccentric inclusion," J. Opt. Soc. Am. A **9**, 1327–1335(1992).

21. K. A. Fuller, "Scattering and absorption cross sections of compounded spheres. I. Theory for external aggregation," submitted to J. Opt. Soc. Am. A. **11**, 1994.

22. K. A. Fuller, "Scattering and absorption cross sections of compounded spheres. II. Calculations for external aggregation," submitted for publication in J. Opt. Soc. Am. A. **11**, 1994.

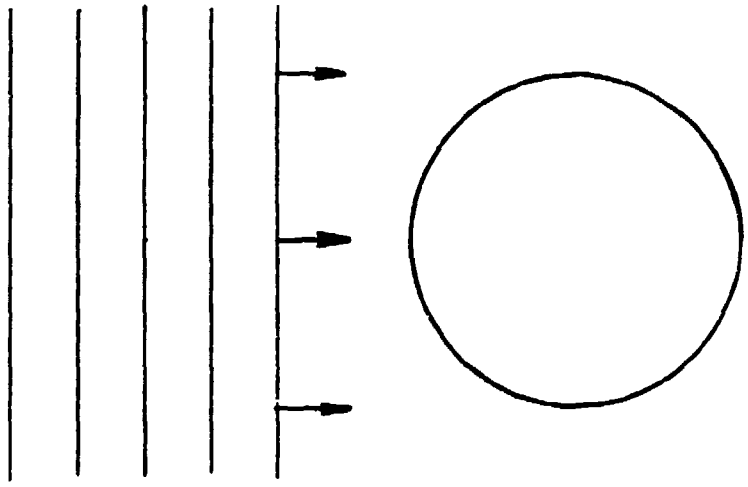

$$\mathbf{E}_i = \sum_{n=1}^{\infty} \sum_{m=-n}^{n} \left(p_{mn} \mathbf{N}_{mn}^{(1)} + q_{mn} \mathbf{M}_{mn}^{(1)} \right)$$

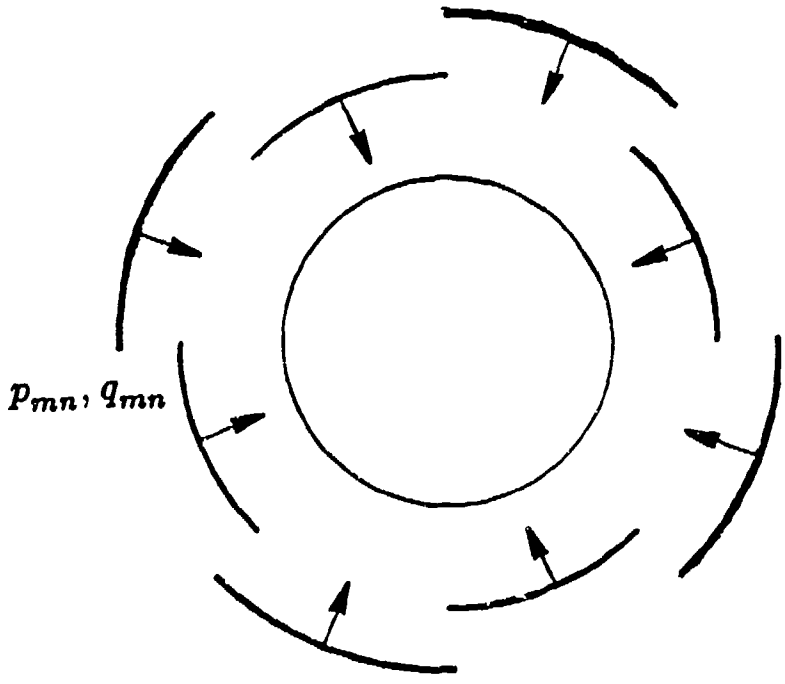

Figure 1. A wave front incident on a sphere (top) is decomposed into components of vector spherical harmonics that are concentric with the sphere (bottom), i.e., the projections of the incident field onto these basis functions serve as the coefficients for the expansion of the incident wave in VSH.

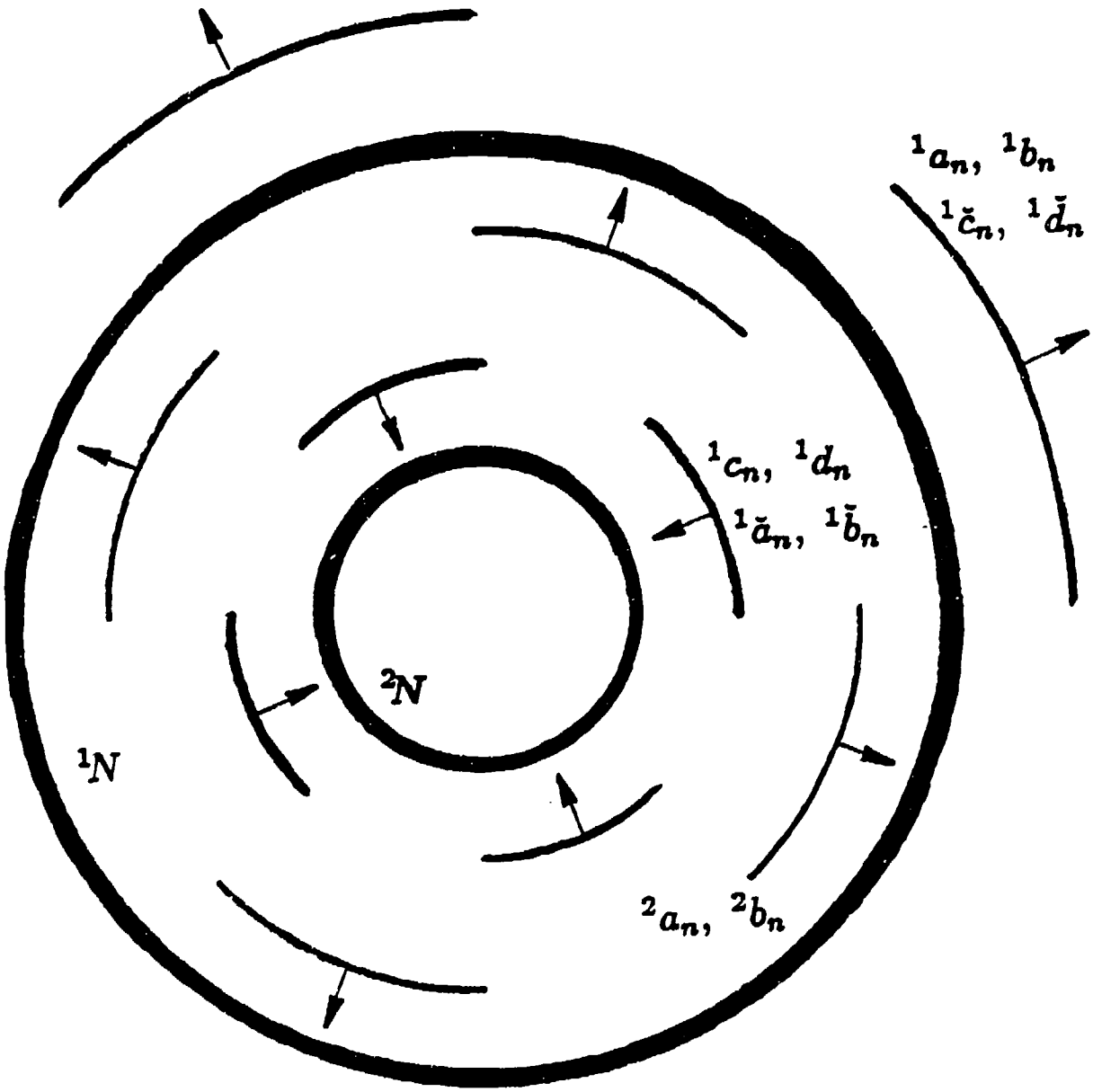

Figure 2. Transmitted and reflected nth partial waves arising from scattering by a layered sphere. The complex amplitudes (^1c_n, ^1d_n) and (^1a_n, ^1b_n) are those associated with, respectively, reflection and transmission of the nth incoming VSH component of the plane wave at a convex spherical surface. The coefficients (^2a_n, ^2b_n) likewise correspond to reflections from the core. Transmission and reflection of these outgoing partial waves accross the concave outer surface of the shell are represented, in order, by ($^1\check{c}_n$, $^1\check{d}_n$) and ($^1\check{a}_n$, $^1\check{b}_n$).

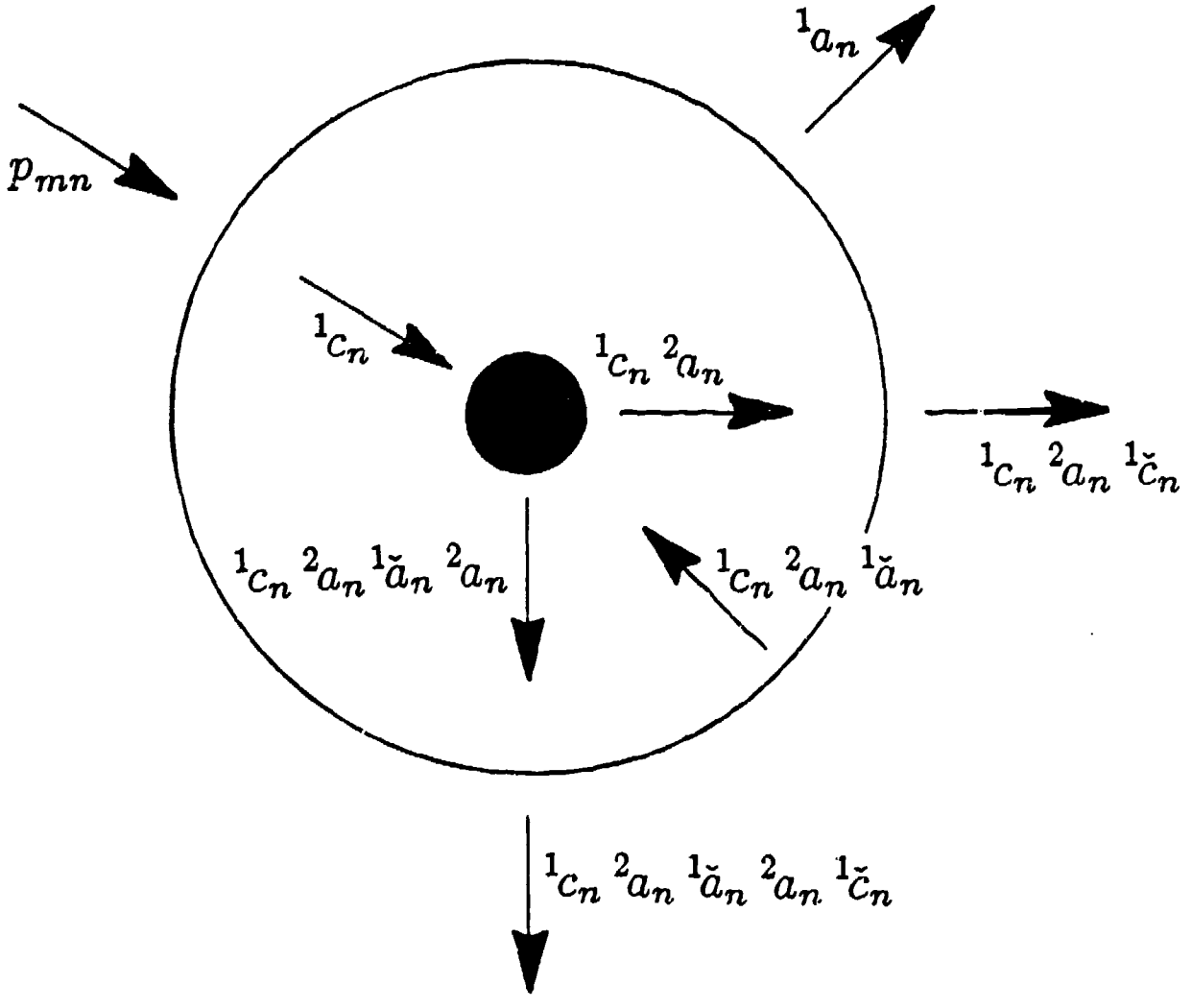

$$\overline{AE}_{mn} = p_{mn}\left[\,{}^1a_n + {}^1c_n\,{}^2a_n\,{}^1\check{c}_n \sum_{k=0}^{\infty}\left({}^2a_n\,{}^1\check{a}_n\right)^k\right]$$

Figure 3. Illustration of the multiple scattering calculation of the scattering coefficients of a coated sphere. Shown are the first three TM contributions. Note that the incident field is illustrated in its vector spherical harmonic representation.

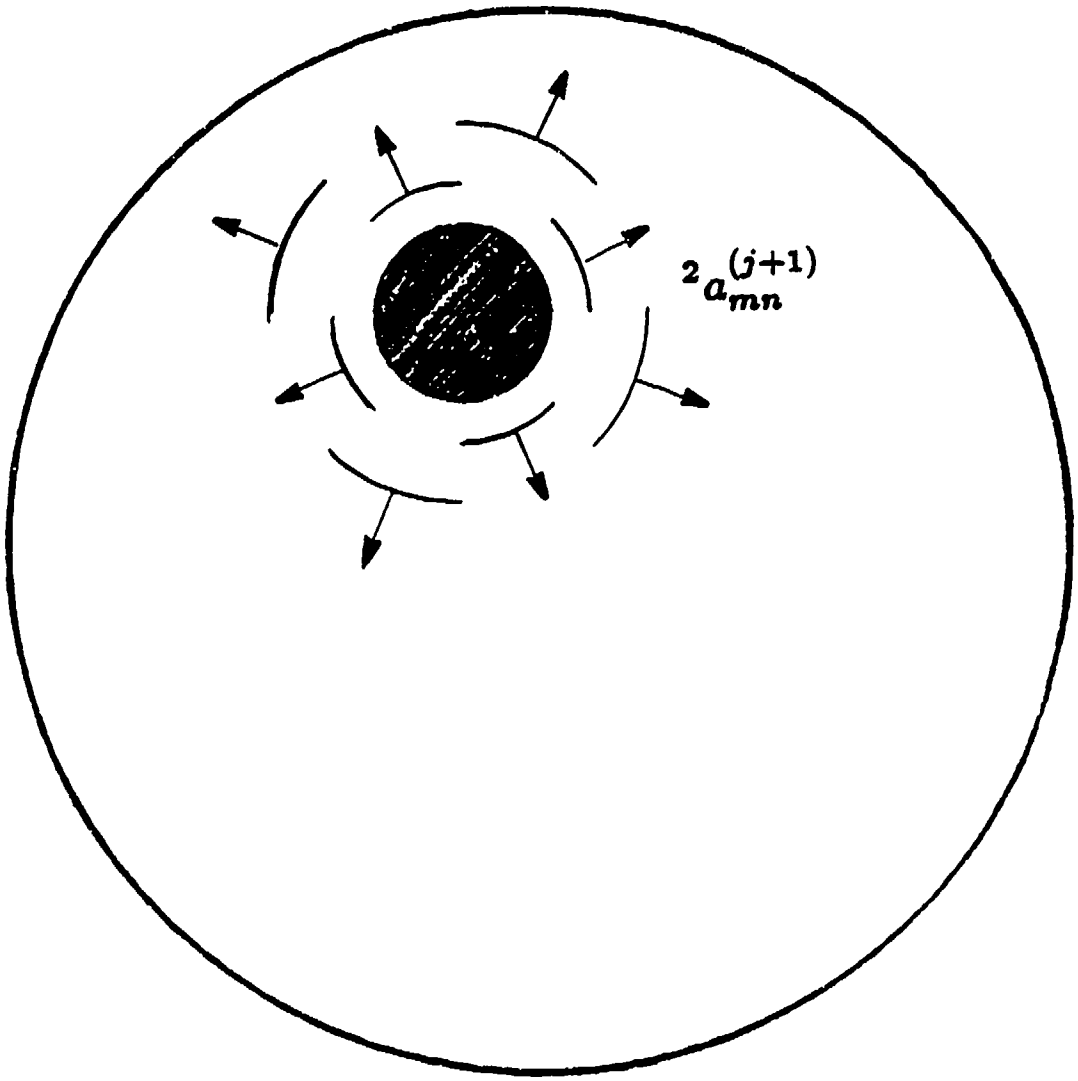

$$^2a_{mn}^{(1)} = {}^2a_n \sum_{\nu} \sum_{\mu} \left(p_{\mu\nu}\, {}^1c_\nu \widetilde{A}_{mn}^{\mu\nu} + q_{\mu\nu}\, {}^1d_\nu \widetilde{B}_{mn}^{\mu\nu} \right)$$

$$^2a_{mn}^{(j+1)} = {}^2a_n \sum_{\nu} \sum_{\mu} \left({}^1c_{\mu\nu}^{(j)} \widetilde{A}_{mn}^{\mu\nu} + {}^1d_{\mu\nu}^{(j)} \widetilde{B}_{mn}^{\mu\nu} \right)$$

Figure 4. Scattering from an arbitrarily located spherical inclusion in an otherwise homogeneous spherical host. To find the coefficients of the partial fields scattered by the inclusion, the projections onto the normal modes of the inclusion are found for incoming partial waves concentric with the host. The sum of these projections is then multiplied by the Lorenz-Mie coefficient (reflection coefficient) of the inclusion.

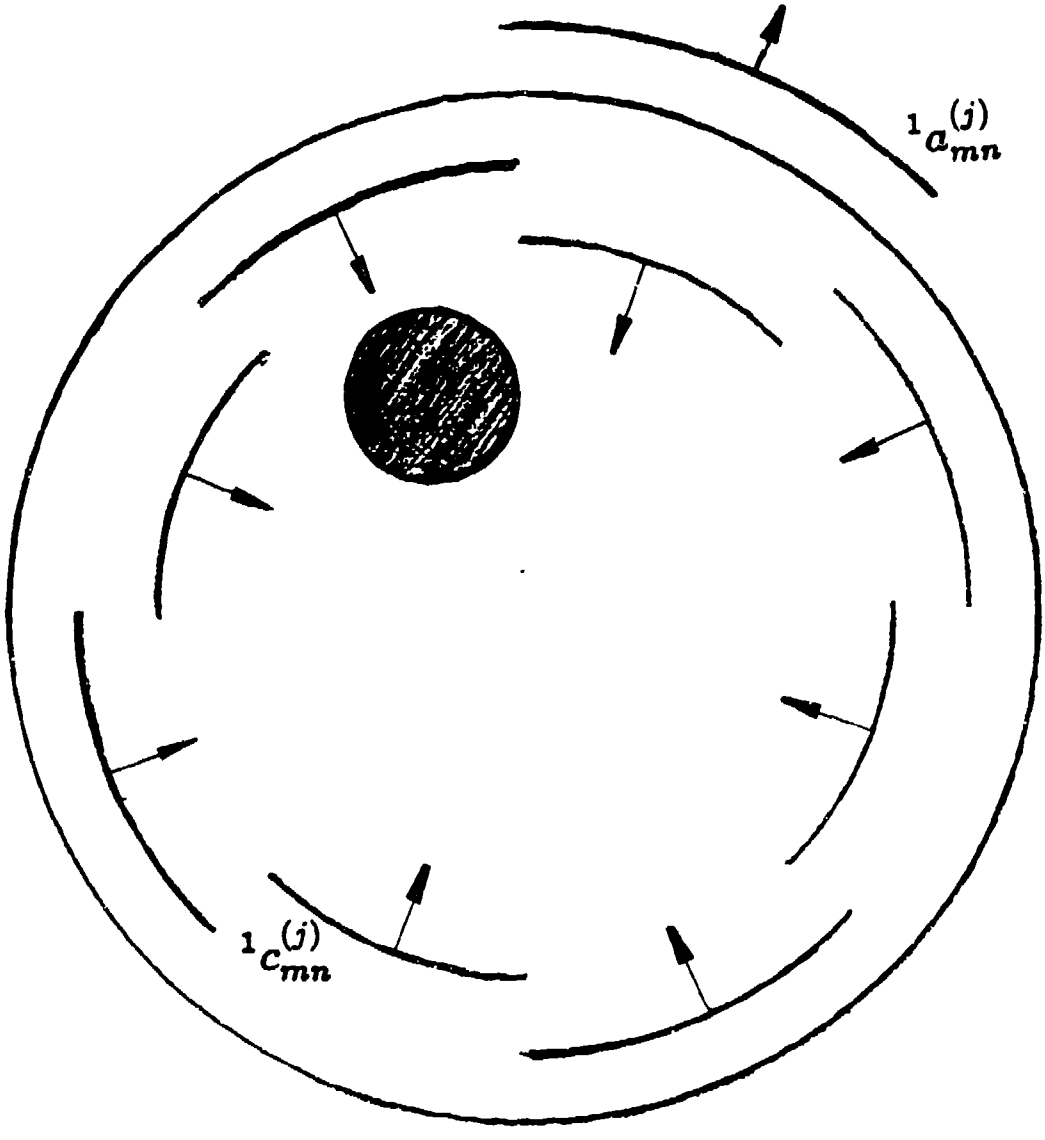

$$ {}^{1}a_{mn}^{(j)} = {}^{1}\check{c}_n \sum_{\nu} \sum_{\mu} \left({}^{2}a_{\mu\nu}^{(j)} \widetilde{A}_{mn}^{\mu\nu} + {}^{2}b_{\mu\nu}^{(j)} \widetilde{B}_{mn}^{\mu\nu} \right) $$

$$ {}^{1}c_{mn}^{(j)} = {}^{1}\check{a}_n \sum_{\nu} \sum_{\mu} \left({}^{2}a_{\mu\nu}^{(j)} \widetilde{A}_{mn}^{\mu\nu} + {}^{2}b_{\mu\nu}^{(j)} \widetilde{B}_{mn}^{\mu\nu} \right) $$

Figure 5. Transmission and reflection, at the surface of the host, of the scattered field of an arbitrarily located spherical inclusion is determined from the projections of those scattered fields onto the basis functions of the host as a product of the sum of those projections and the concave Lorenz-Mie coefficients of the host.

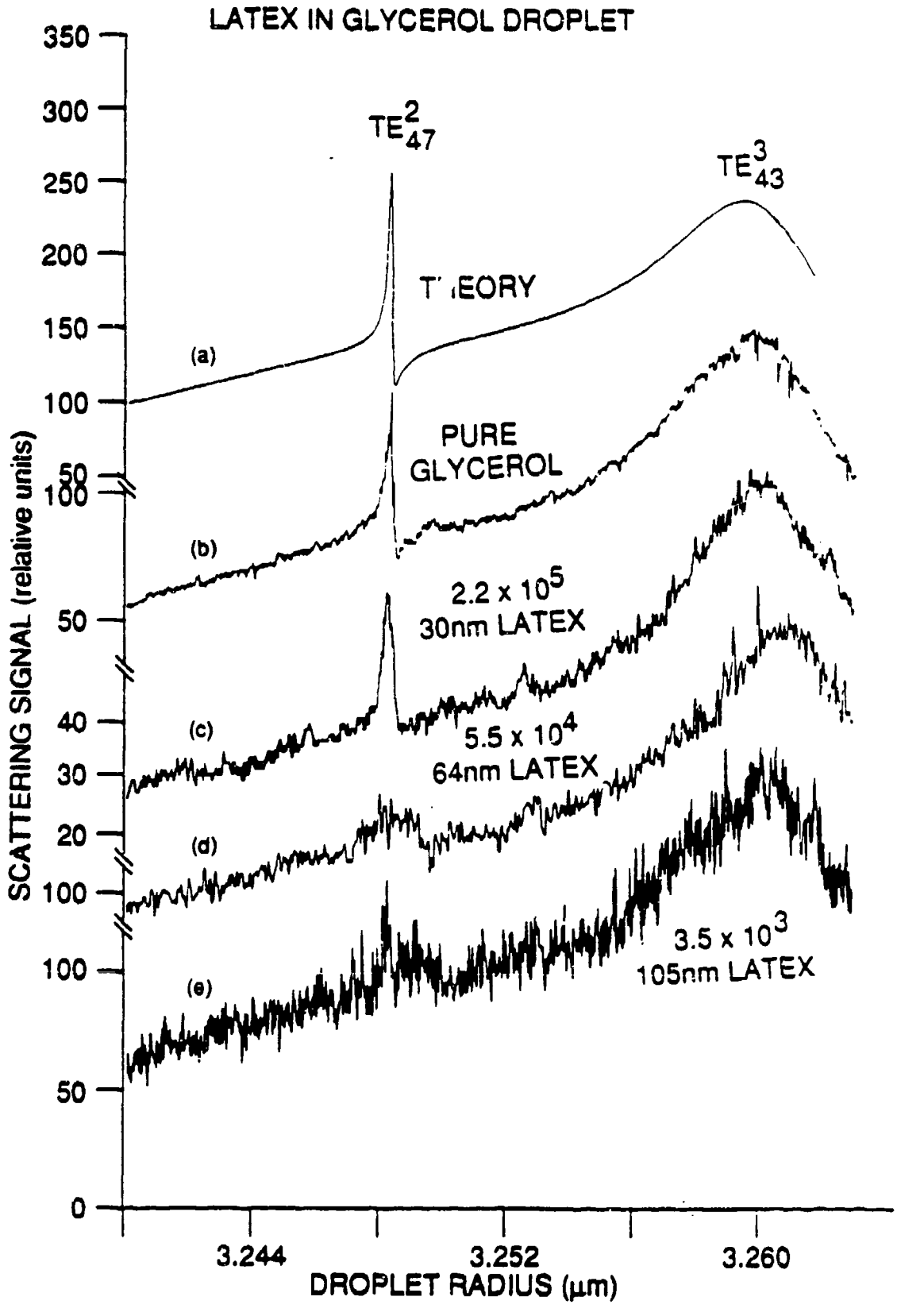

Figure 6. A sample of the experimental data collected by Dr. Ronald Pinnick and Dat Ngo. Lorenz-Mie theory for and experimental measurements of light scattering by an evaporating homogeneous glycerol droplet are compared with measurements made on glycerol hosts that had been seeded with latex spheres of various size and concentration.

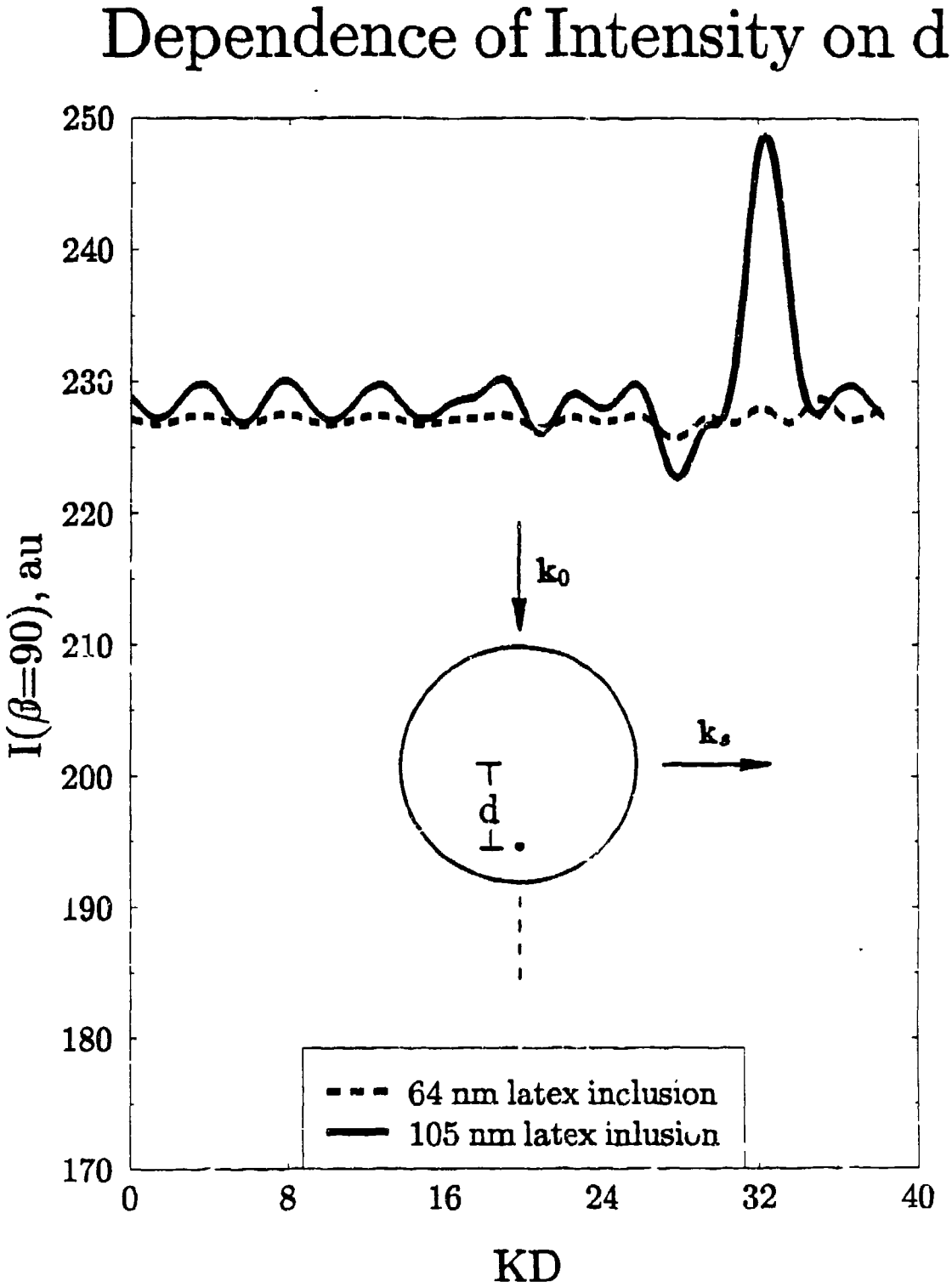

Figure 7. The dependence of scattered intensity, observed at 90° from the direction of incidence, on the axial position of two sizes of latex inclusions. The host sphere is not on an MDR.

Dependence of Intensity on d

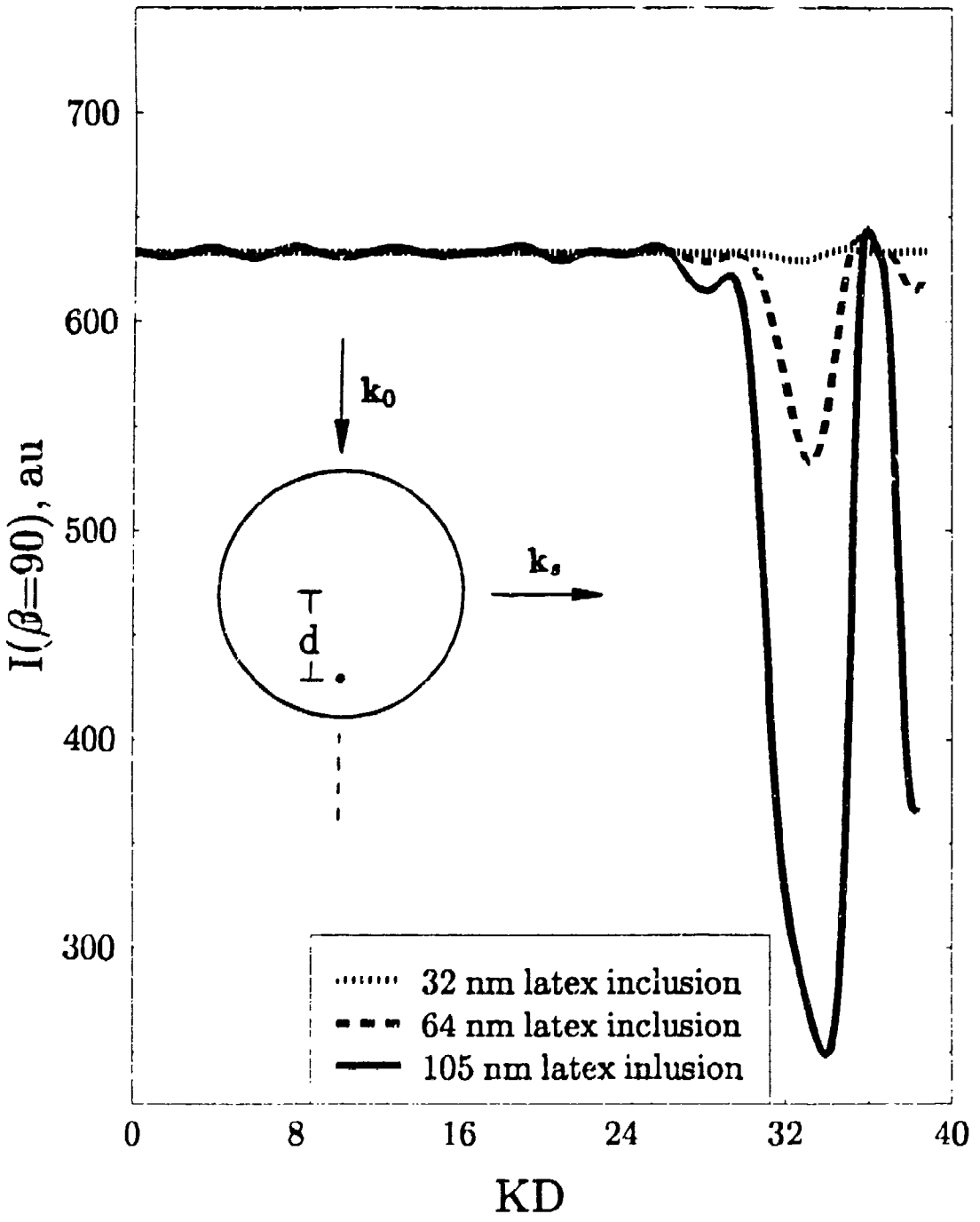

Figure 8. The same as Fig. 6, but with the host tuned to a resonance, and with three sizes of inclusion.

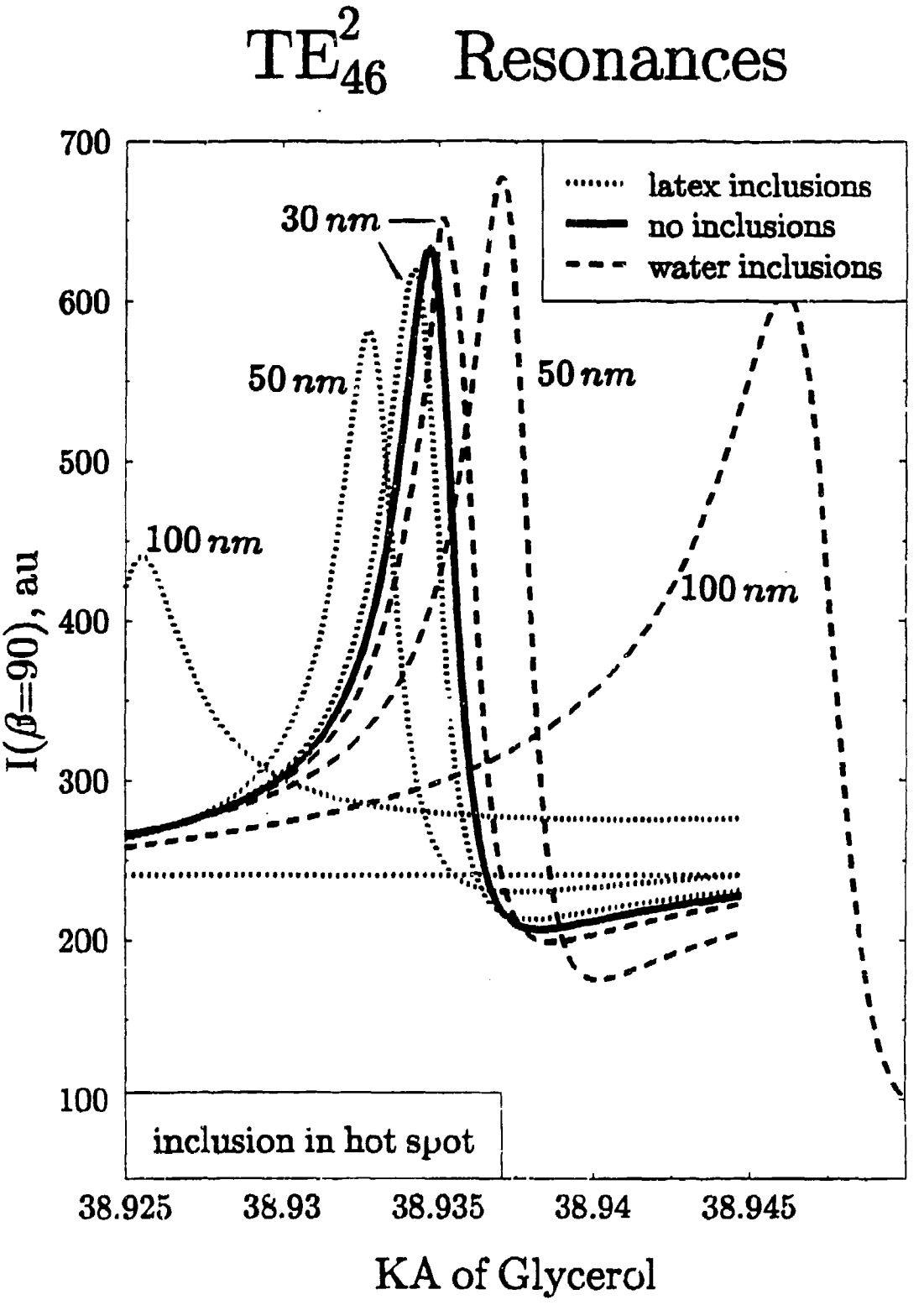

Figure 9. The TE^2_{46} resonance spectrum of a glycerol droplet for three different sizes of latex and water inclusions. The inclusions are in the forward hot spot of the resonating droplet.

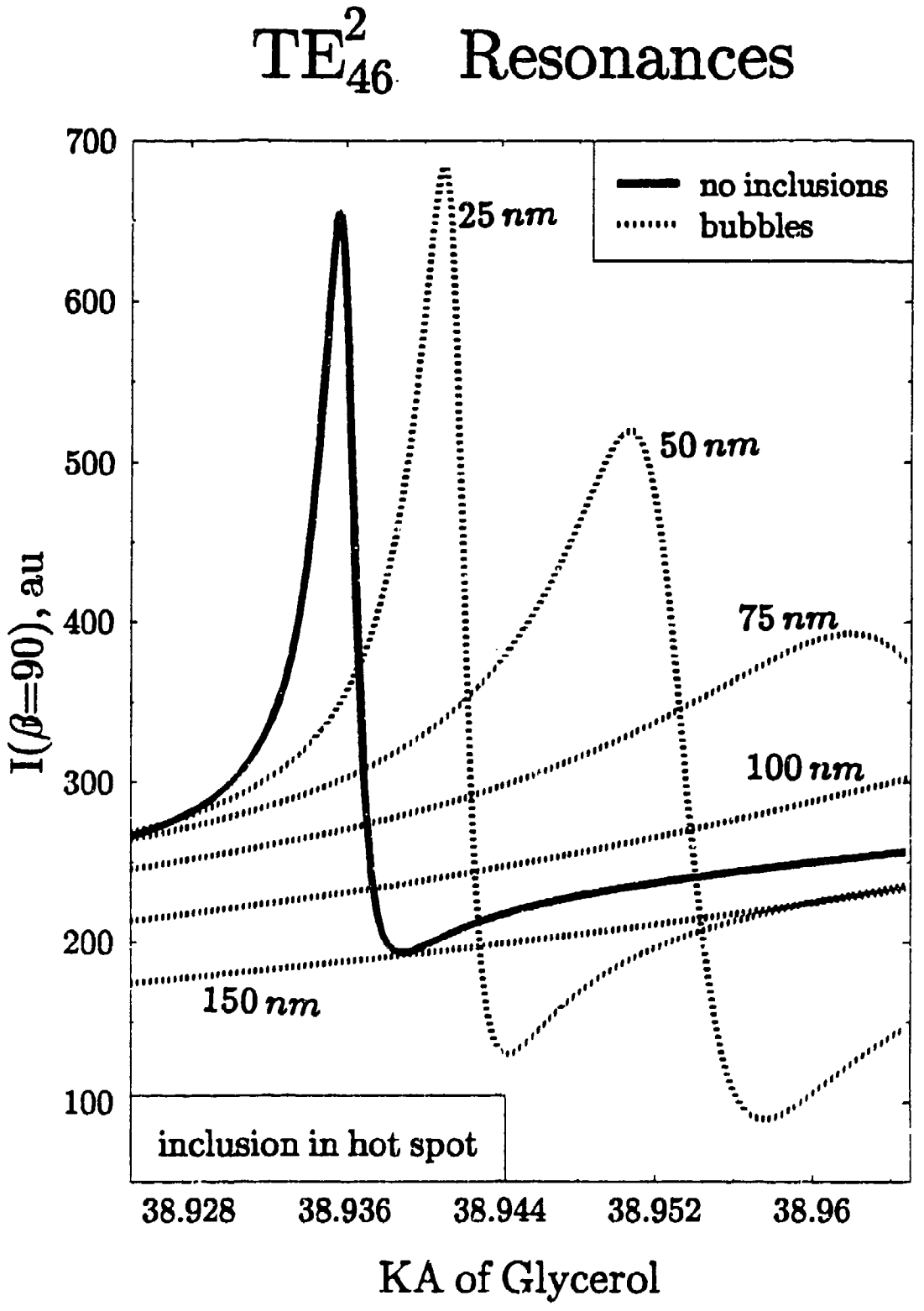

Figure 10. The same as Fig. 8, but for five sizes of air bubbles in the glycerol.

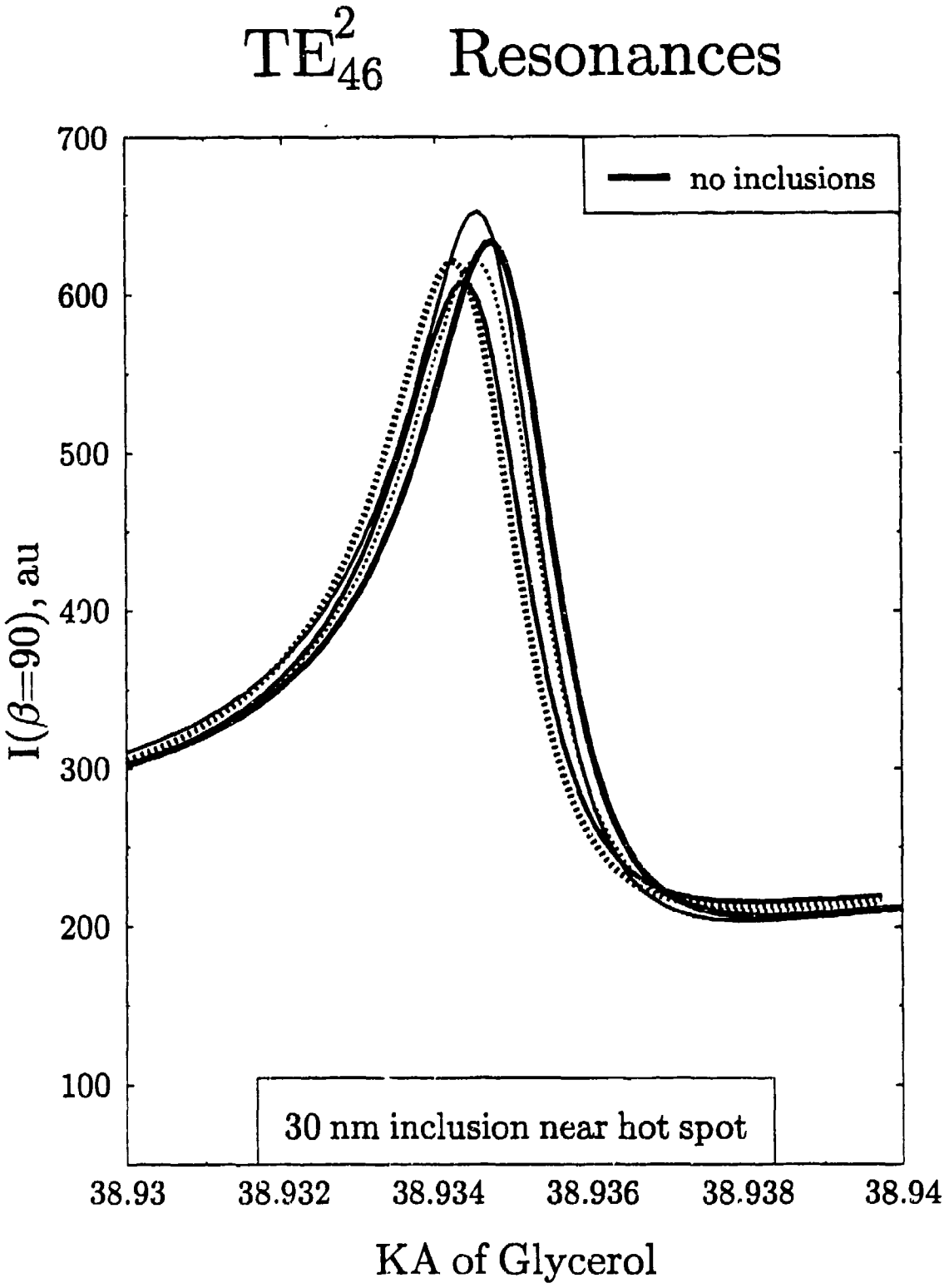

Figure 11. Variations in the resonance spectrum of a glycerol droplet as a latex inclusion having a radius of 30nm is located at several positions near the center of the forward hot spot. The heaviest solid line represents the spectrum of a homogeneous host.

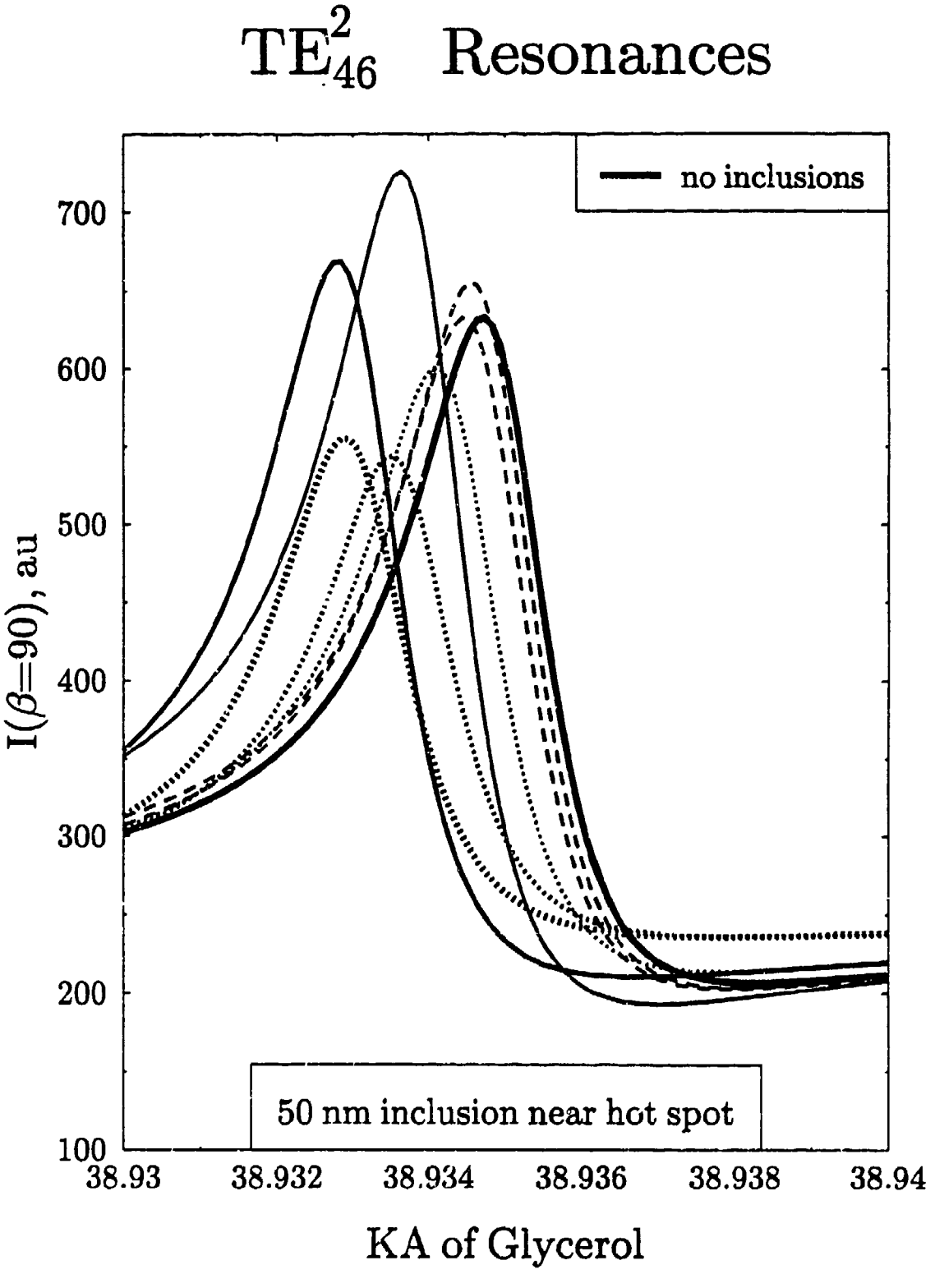

Figure 12. Same as Fig. 10, but for a latex inclusion having a radius of 50 nm.

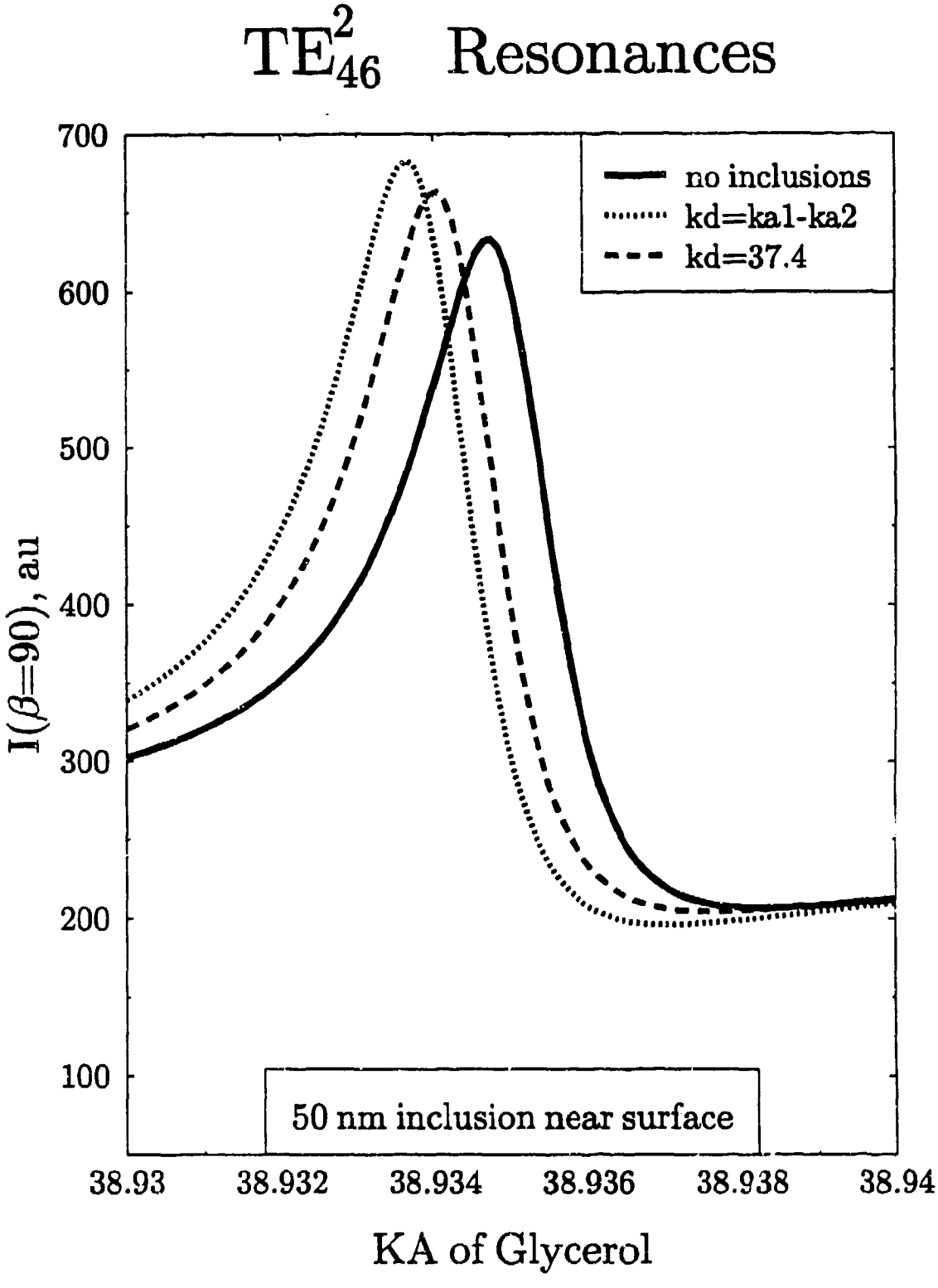

Figure 13. Variations in the resonance spectrum of a glycerol droplet with a 50 nm latex inclusion located near the forward surface of the droplet. (This is near the focal volume of the host.)

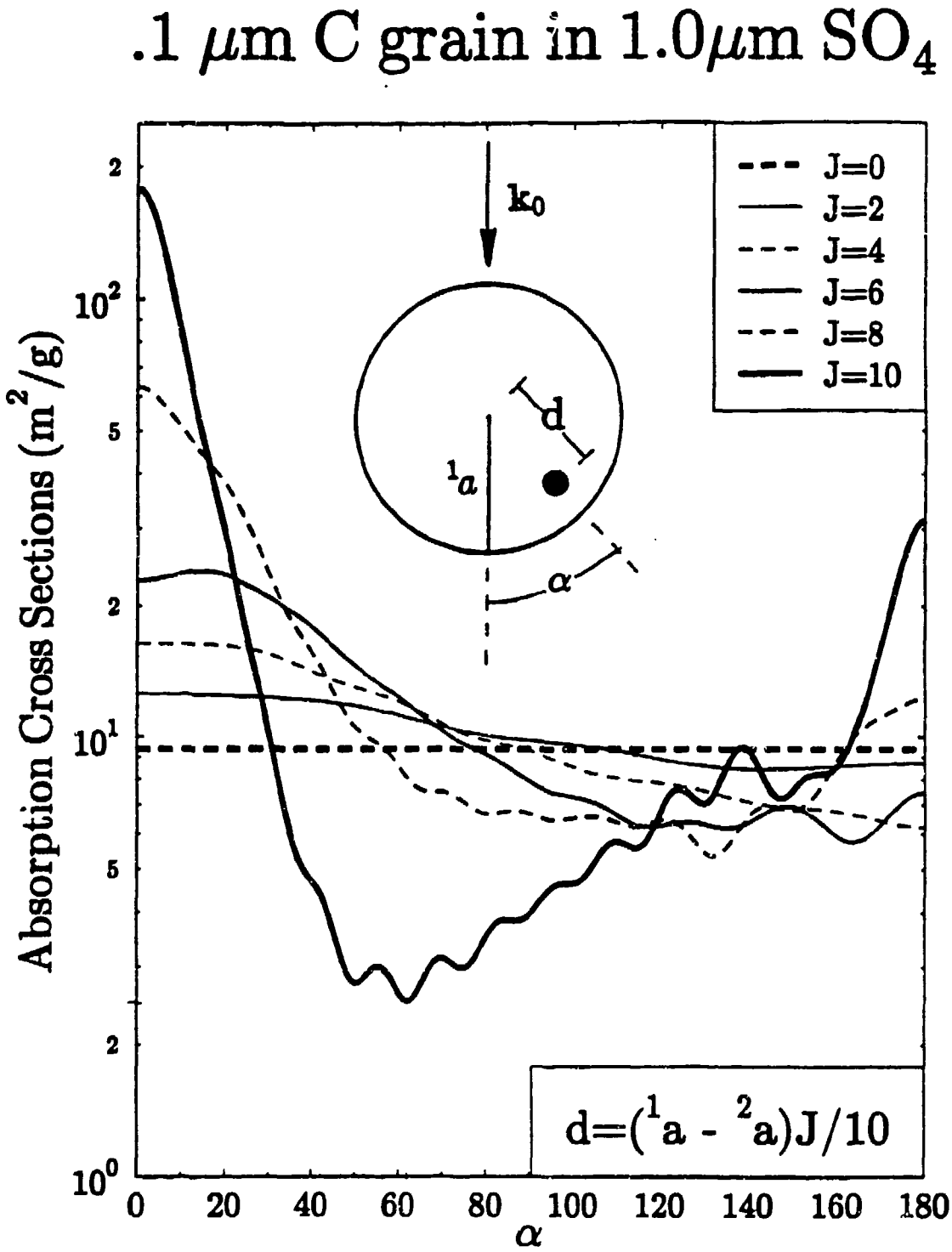

Figure 14. Orientation dependence of the gram-specific absorption cross sections of a carbon grain located at various radial distances from the center of a sulfate host. The refractive index of the sulfate and carbon particles is taken to be 1.52+0.0i and 1.8+0.5i, respectively. In the example shown, an average over polarization has been taken.

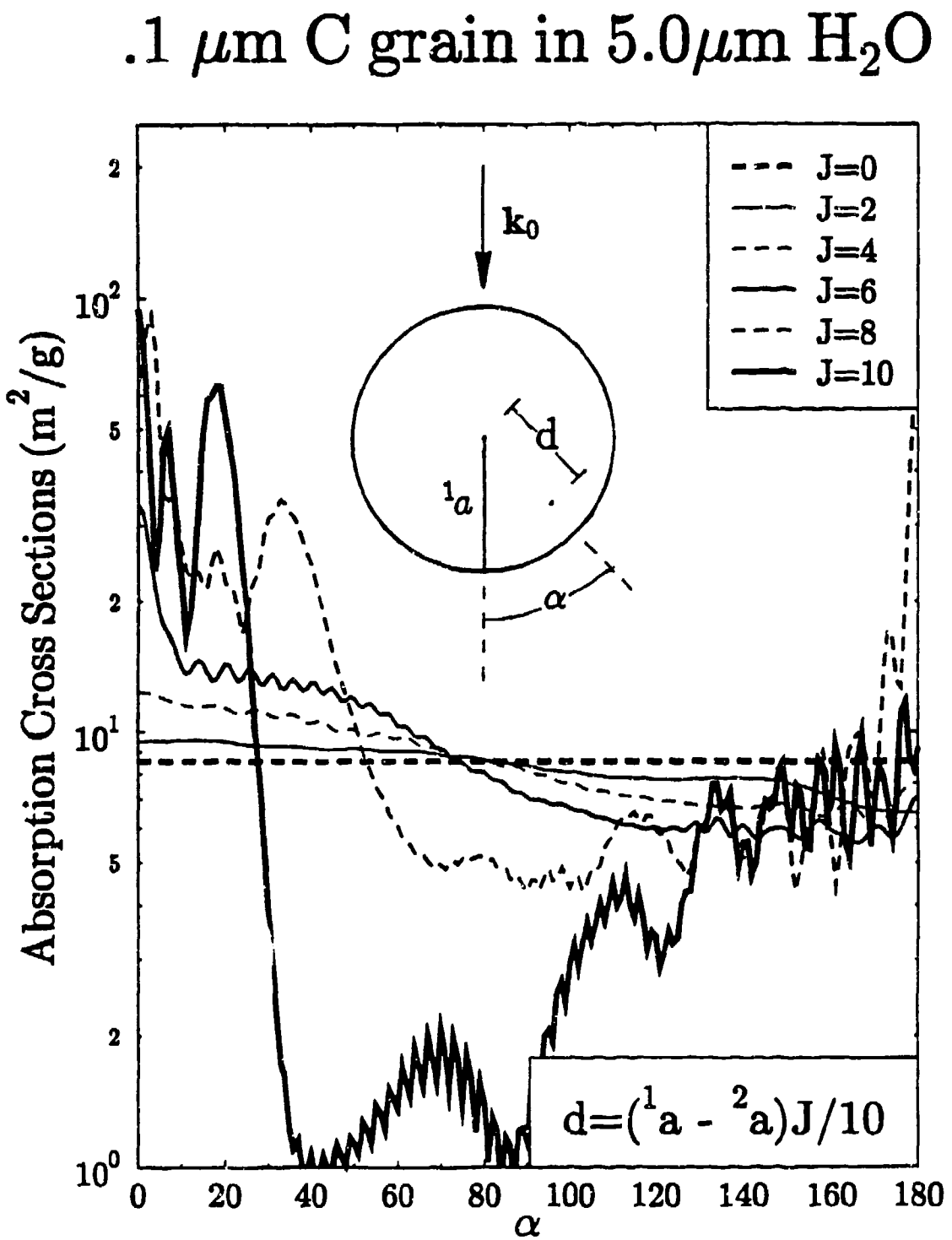

Figure 15. Same as Fig. 14, but with the carbon entrained in a cloud droplet of radius 5 μm. The refractive index of water is taken here to be 1.33+0.0i.

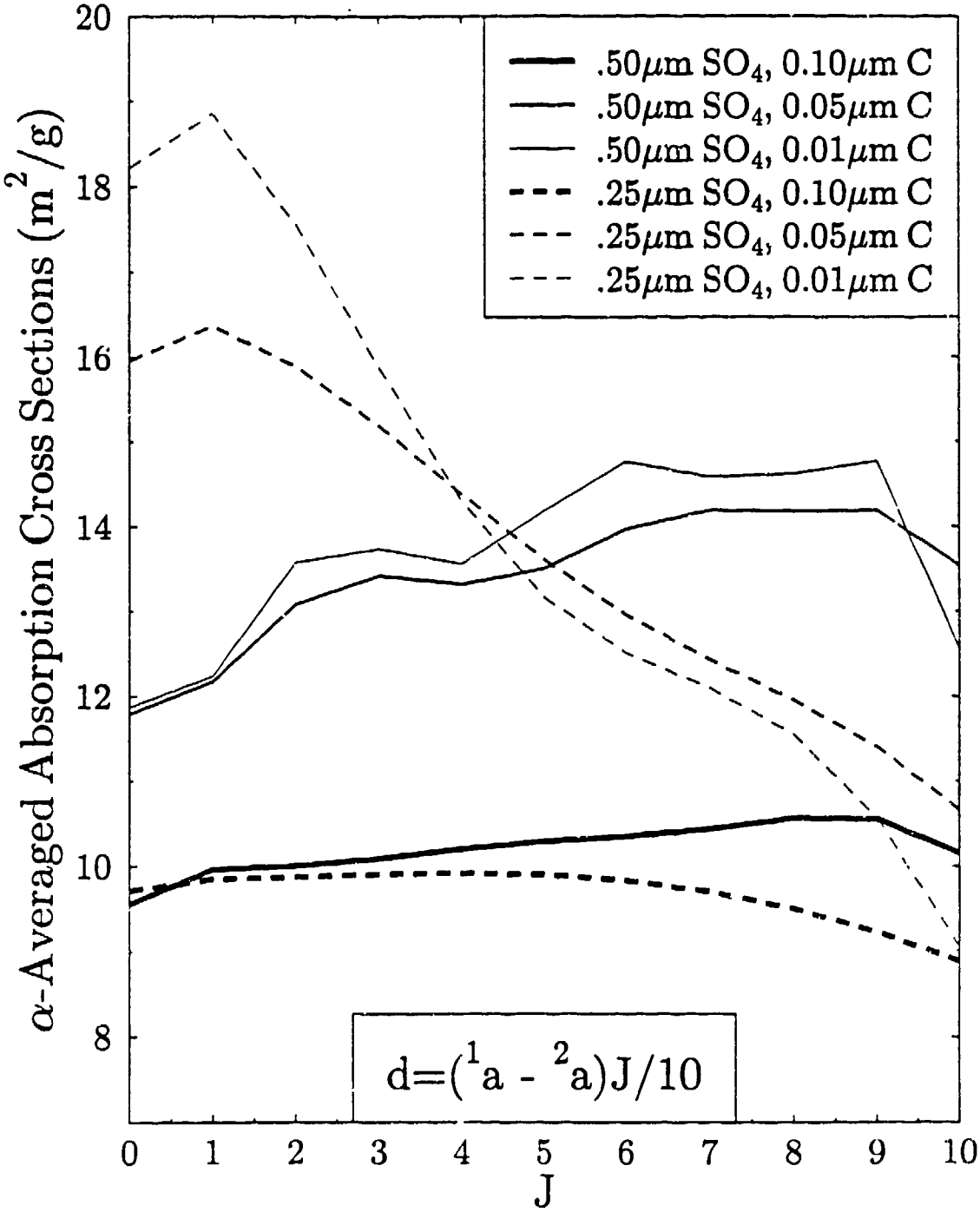

Figure 16. Orientation-averaged absorption cross sections for carbon spheres at different radial distances from the center of sulfate haze elements.

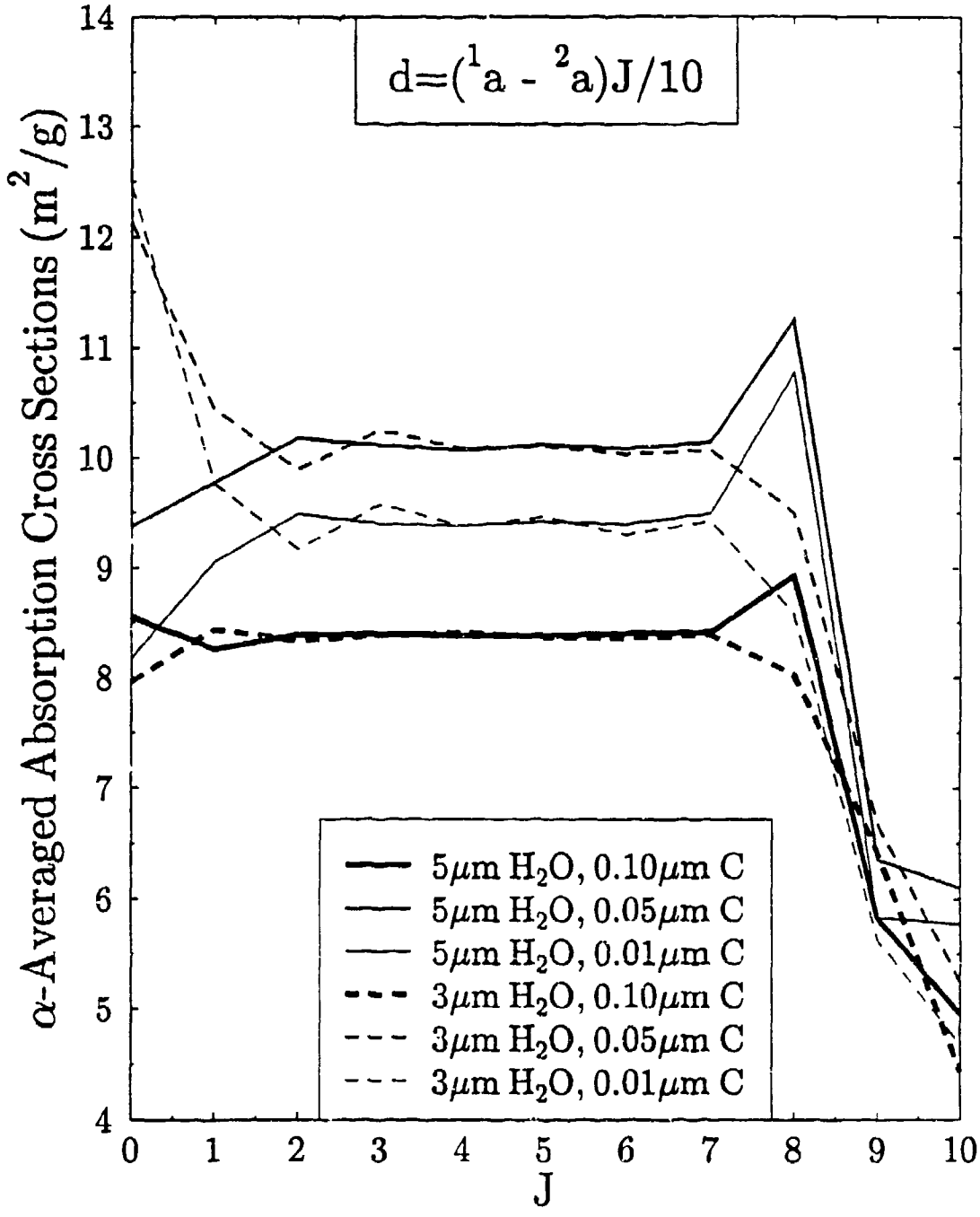

Figure 17. Same as Fig. 16, but for carbon grains entrained in cloud droplets.

INDEX A

INDEX OF AUTHORS

Akinyemi, A. 165

Allison, E.E. 41

Andrews, K.T. 155

Arnold, S. 347

Banks, D.R. 129

Barnes, M.D. 329

Benner, R.E. 115

Berg, O. 21

Birenzvige, A. 165

Bonfante, R. 129

Brock, J.R. 11, 49

Bronk, B.V. 347, 363

Bussoletti, E. 31

Cai, W. 101

Carotenuto, L. 31

Catalano, E. 129

Choi, M.K. 49

Cohoon, D.K. 65, 173

177, 305, 427

Colangeli, L. 31

Dell'Aversana, P. 31

Dunning, G.J. 155

Faris, J. 21

Farrell, R.A. 387

Ferguson, F. 31

Frenklach, M. 305

Fry, E.S. 5

Fuller, K.A. 43

Hadad, A. 37

Kendall, B.R.F. 41

Kretzschmar, J. . . . 11

Lax, M. 101

Lee, M.H. 359

Li, X. 101

Lilleleht, L.U. 31

Littman, H. 47

Marshall, M.S. 115

Mele, F. 31

Mennella, V. 31

Meyer, R.K. 115

Minden, M.L. 155
Mirra, C. 31
Morgan, M.H. 47
Nuth, J.A. 21, 31
Oh, C. 147, 155
Padmabandu, G.G. 147
Pendleton, J.D. 379
Pepper, D.M. 155
Poreh, M. 37
Ramsey, J.M. 329, 363
Rosen, D.L. 371, 379
Rouse, W.G. 129
Sehmel, G.A. 129
Shapiro, M.J. 363
Sindoni, O.I. 173
Smith, M.J. 347
Stephens, J.R. 31
Stiassnie, M. 37
Stoyanov, B.M. 387
Sun, S. 305
Torres, R. 165
Wang, R.T. 409
Wasilewski, P. 21
Whitten, W.B. 329, 363
Zaromb, S. 165

INDEX B

INDEX OF AUTHOR'S ORGANIZATIONS

- Calvert Institute 21
- City College of the City University of New York
  Department of Physics 101
- Colorado State University 443
- Hughes Research Laboratories 155
- Institute for Space Science and Technology, Inc.
  Space Astronomy Laboratory 409
- Instituto Universitario Navale
  Naples, Italy 31
- MARS Center
  Naples, Italy 31
- Matrix 31
- NASA-Goddard Space Flight Center 31
- NASA-Goddard Space Flight Center
  Astrochemistry Branch, Code 691 21
- N.Y. Polytechnic University 347
- Oak Ridge National Laboratory 329, 363
- Osservatorio Astronomico di Capodimonte
  Naples, Italy 31
- Pacific Northwest Laboratory 129
- Rensselaer Polytechnic Institute
  Department of Chemical Engineering 47
- Technion-Israel Institute of Technology
  Department of Civil Engineering 37
- Temple University/NRC Fellow Associate
  @ Edgewood RDEC 65, 173, 177, 305, 427

- Texas A & M University
  Department of Physics 147, 155

- The Johns Hopkins University
  Applied Physics Laboratory
  The Milton S. Eisenhower Research Center 387

- The Pennsylvania State University
  Department of Physics 41

- The University of Georgia
  Department of Physics and Astronomy 359

- Universita di Cassino
  Cassino, Italy 31

- University of Texas/Austin
  Department of Chemical Engineering 11, 49

- University of Utah
  Electrical Engineering Department 115

- University of Virginia, Charlottesville 31

- U.S. Army Dugway Proving Ground
  Instrumentation Branch 115

- U.S. Army Edgewood Research, Development
  & Engineering Center 129, 165, 173, 347, 363

- U.S. Army Research Laboratory
  Battlefield Environment Directorate 371, 379

APPENDIX A
PHOTOGRAPH OF 1993 CONFERENCE ATTENDEES

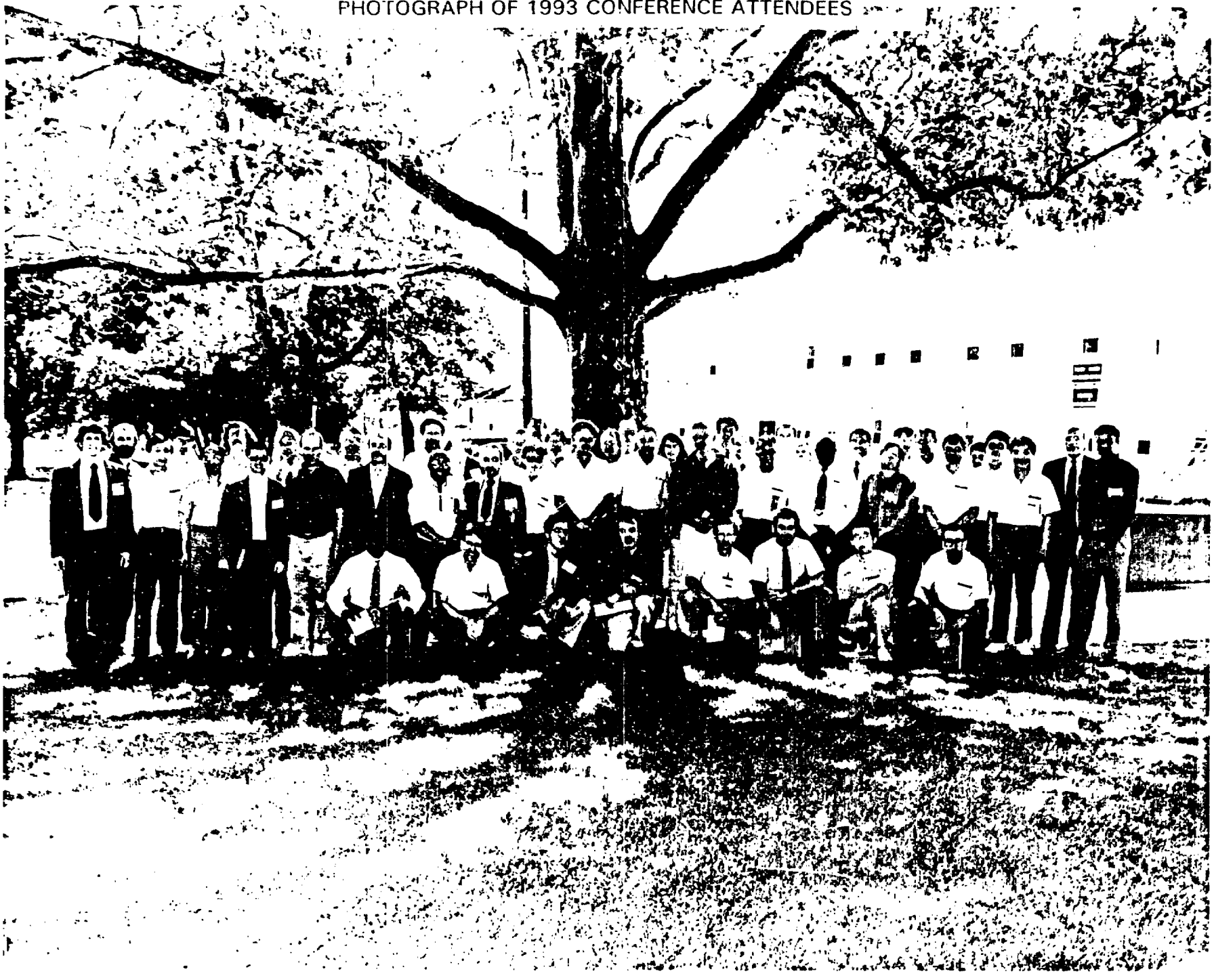

1993 EDGEWOOD RDEC SCIENTIFIC CONFERENCE ON OBSCURATION AND AEROSOL RESEARCH

Pictured from left to right are:

First Row

Mike Smith

Norman M. Witriol

Richard K. Chang

Steve Arnold

Ron Pinnick

James Dimmette

Jungshik Shin

Bob Sutherland

Second Row

Cary Presser

Xiaoshen Li

Wei Cai

Stanley Niles

Dave Pendleton

David Rosen

Ammon Birenzvige

Sol Zaromb

Joseph Hodges

George Mulholland

Bill Whitten

Burt V. Bronk

Ru Wang

George Randall

Jerold Bottiger

Blair Evans

Gang Chen

Md. Mohiuddin Mazumder

Third Row

Kirk Fuller

Jim Gillespie

Joe Nuth

M. Howard Lee

Melvin Lax

Edward Stuebing

David Cohoon

Frank Poleski

R. Morris

Bruce Kendall

James T. Brown

Howard Littman

Amy Hamilton

Dan Magnus

John Carpin

Ed Fry

Ivy Sindoni

Ricardo Torres

Steve Hill

George Sehmel

Michael D. Barnes

Keng Leong

Paul Morgan

APPENDIX B

1993 EDGEWOOD RDEC SCIENTIFIC CONFERENCE ON OBSCURATION AND AEROSOL RESEARCH

ATTENDEES LIST

Agnes Akinyemi
Edward E Allison
Stephen Arnold
Michael D Barnes
Amnon Birenzvige
Jerold R Bottiger
James R Brock
Burt V Bronk
James Brown
Wei Cai
Anthony J Campillo
John C Carpin
Elizabeth S Catalano
Richard K Chang
Gang P Chen
David K Cohoon
Galen Daum
Robert W Doherty
Denis J Donohue
Janon Embury
Blair Evans
Jay D Eversole
Richard Farrell
Dennis F Flanigan
David Freund
Robert H Frickel
Edward Fry
Kirk A Fuller
James B Gillespie
Dick Haracz
Steven Hill
Joseph T Hodges
Sidney A Katz
Bruce Kendall
James D Klett
Paul L Koehmstedt
Melvin Lax
M Howard Lee
Keng H Leong
Xiaoshen Li
Horn-Bond Lin
Howard Littman
Daniel L Magnus
Martin S Marshall
MD Mohiuddin Mazumder
Morris H Morgan
Robert Morris
George W Mulholland
Stanley Niles
Joseph A Nuth
J David Pendleton
Ronald Pinnick
Franklin A Poleski
Cary Presser
Madhav Ranade
George Randall
Asit Ray
Lou Reinisch
David L Rosen
Harry Salem
Mark Seaver
George Sehmel
Jungshik Shin
Orazio I Sindoni
Michael J Smith
Douglas R Sommerville
Basil J Stoyanov
Edward W Stuebing
Arthur K Stuempfle
Robert A Sutherland
Ricardo Torres
Ru T Wang
W B Whitten
Norman M Witriol
S Zaromb

Blank

APPENDIX C

CONFERENCE AGENDA

TUESDAY, 22 JUNE

9:00 Registration

10:10 Opening: ***Dr. Edward W. Stuebing,*** Team Leader, Aerosol Sciences and Technology, Edgewood RDEC

Welcome: ***Mr. Joseph Vervier,*** Technical Director, Edgewood RDEC

Announcements: ***Mr. Elmer H. Engquist,*** Battelle Edgewood Operations

I. AEROSOL DYNAMICS

A. Particle Formation and Transport *(Moderator: Janon Embury)*

10:30 ***J.R. Brock*** and Kwang-ho Song (Univ. of Texas/Austin), Generation of Graphitic Carbon Fibers in Corona Discharge

10:50 ***G. Chen*** and R.K. Chang (Yale Univ.), Techniques to Measure the Evaporation Rate, Drag, and Shape Distortion of Droplets in a Segmented Stream

11:10 ***M.B. Ranade***, J.W. Gevling and R.J. Han (Particle Technology, Inc.), Sorting of Fibers and Flakes by Aspect Ratio Using Electrostatic Separation

11:30 ***A.K. Ray*** (Univ. of Kentucky), Formation, Characterization and Behavior of Emulsion Droplets

11:50 **LUNCH** (Sign up for dinner at Josef's)

B. Particle Dissemination, Transport and Deposition *(Moderator: Janon Embury)*

1:15 ***E. Allison*** and B.R.F. Kendall (Penn State Univ.), Dynamics of Levitated Microparticles in a Gas Flow

1:35 ***J.R. Brock*** (Univ. of Texas/Austin), Stochastic Model for Windows in Dispersing Aerosol Plumes

1:55 ***M.B. Ranade***, R.V. Calabrese (Particle Technology, Inc.) and M.H. Wang (Univ. of Maryland), Aerodynamic Factors in Pneumatic Dispersion of Fine Powders

2:15 ***H. Littman***, M.H. Morgan III, J. D. Paccione and S. DJ. Jovanovic (RPI), Modeling Dilute Phase Flow in a Vertical Transport Pipe

2:35 **BREAK** (Sign up for dinner at Josef's)

TUESDAY, 22 JUNE (cont.)

II. AEROSOL CHARACTERIZATION METHODS

A. Sampling, Nephelometry and Inversion *(Moderator: Jerold Bottiger)*

3:15 ***K. Leong***, M. Jones and D. Holdridge (Argonne), Calibration and Performance of a Polar Nephelometer

3:35 ***M. Lax***, W. Cai and X.S. Li (CCNY), Quasi-Binary Decision Making: A Speedup

3:55 ***M.S. Marshall*** and R.E. Benner (US Army DPG), Spherical and Nonspherical Aerosol and Particulate Characterization Using Optical Pattern Recognition Techniques

4:15 ***G.A. Sehmel***, R. Bonfante, D.R. Banks, E. Catalano and W.G. Rouse (PNL), Operation of the Breeze Tunnel at Edgewood Area of Aberdeen Proving Ground to Determine Mass Extinction Coefficients

4:35 **ADJOURN** (Suggested restaurant for dinner: Josef's)

WEDNESDAY, 23 JUNE

II. AEROSOL CHARACTERIZATION METHODS (cont.)

A. Sampling, Nephelometry and Inversion *(Moderator: Jerold Bottiger)*

8:30 ***E.S. Fry***, G.G. Padmabandu, and C. Oh (TAMU), Angular Distribution of Electromagnetic Scattering Near Zero Degrees

8:50 ***D. Magnus*** (KLD Labs, Inc.), PC-Based Hot-Wire Aerosol Sampling Technique

9:10 ***S. Zaromb***, R. Torres, A. Birenzvige, and A. Akinyemi (Edgewood RDEC), Portable High-Throughput Liquid Absorption Aerosol Sampler

9:30 **BREAK - GROUP PHOTO**

III. OVERVIEW & DISCUSSION

10:30 ***E.W. Stuebing*** (Edgewood RDEC), Directions for Future Research in the Edgewood RDEC Aerosol Science Program

11:45 **LUNCH**

II. AEROSOL CHARACTERIZATION METHODS (cont.)

B. Spectroscopy of Single Particles and Aerosols *(Moderator: Mike Smith)*

1:15 ***J. Hodges*** (NIST), Elastic Light Scattering in a Gaussian Beam

II. AEROSOL CHARACTERIZATION METHODS (cont.)

B. Spectroscopy of Single Particles and Aerosols *(Moderator: Mike Smith)*

1:35 ***M.M. Mazumder***, S.C. Hill and R.K. Chang (Yale Univ.), Intensity-dependent Shifts of Cavity Resonances: Effects on Nonlinear Processes in Droplets

1:55 ***M.D. Barnes***, W.B. Whitten and J.M Ramsey (ORNL), QED - Enhanced Fluorescence Yields in Levitated Microdroplets

IV. POSTER PROGRAM

2:15 **POSTER PREVIEWS** (Auditorium)

J.A. Mirth, F. Ferguson, L. Lilleleht and J. Stephens (NASA - GSFC), Microgravity Nucleation and Particle Coagulation Experiments on the KC-135 Aircraft

J.D. Pendleton (ARL/White Sands), Characterizing Layered Spheres with Particle Sizing Instruments

R.T. Wang (ISST - SAL), Obscuration and Scattering by Finite Cylinders - Microwave Experiment and Theoretical Explanation

W.B. Whitten, M.J. Shapiro and J.M. Ramsey (ORNL), Multianalyte Immunoassay Based on Size Discrimination of Microspheres

H-B. Lin, J.D. Eversole and A.J. Campillo (NRL), Correlation of Emission MDR Spectroscopy with Emission Excitation Selection (Input Pump Resonance) in Microdroplets

D. Magnus (KLD Labs, Inc.), PC-Based Hot-Wire Aerosol Sampling Technique

A.E. Carver and J.P. Kahler (OptiMetrics, Inc.), Deriving the Mean 3-D Concentration Distribution of Initial Puffs Produced by Graphite Fiber Sources Utilizing Video Imagery, Multipath Transmissometry, and the RADON Transform

S. Arnold, L.M. Folan and A. Korn (Polytechnic Univ.), Optimal Long-term Imaging of a Charged Aerosol Particle at the Center of an Electrodynamic Levitator - Trap

S. Zaromb, R. Torres, A. Birenzvige, and A. Akinyemi (Edgewood RDEC), Portable High-Throughput Liquid Absorption Aerosol Sampler

N.M. Witriol (LA Tech Univ.), D.K. Cohoon (Temple Univ./NRC Fellow Assoc. @ Edgewood RDEC), O.I. Sindoni (Edgewood RDEC), A More Realistic Determination of Layered Aerosol Particle Properties from Scattering Data; Noise Introduction

D.K. Cohoon (Temple Univ./NRC Fellow Assoc. @ Edgewood RDEC), An Exact Analytical Solution of a Model of Explosive Dispersal of an Electromagnetic Wave Obscurant in a Steady Wind Assuming Constant Settling Velocity, Transverse and Vertical Eddy Current Diffusivity and Rate Constant for Species Removal

3:00 **POSTER SESSION** (Seminar Area)

5:00 **ADJOURN**

II. AEROSOL CHARACTERIZATION METHODS (cont.)

B. Spectroscopy Of Single Particles and Aerosols *(Moderator: Burt Bronk)*

8:30 ***J.D. Eversole***, H-B Lin, A.L. Huston, A.J. Campillo (NRL) and H.M. Lai, P.T. Leung, S.Y. Liu, K. Young (Chinese University of Hong Kong), High Resolution Spectroscopy and Precise Identification of Morphology Dependent Resonances in Microdroplets

8:50 ***A.J. Campillo*** and H-B. Lin (NRL), CW Stimulated Rayleigh-Wing Scattering and Four-Wave Parametric Oscillation in Carbon Disulfide Microdroplets

9:10 ***S. Arnold***, N.B. Hessel (Polytechnic Univ.), Photoemission from Single Particles in an Electrodynamic Levitator - Trap

9:30 ***L. Reinisch*** (Vanderbilt Univ. Medical Center), M. Smith and B.V. Bronk (Edgewood RDEC), Fluorescence Methods Applied to Aerosols

9:50 **BREAK**

10:30 ***M.H. Lee*** (Univ. of Georgia), Incoherent Scattering of Semiclassical Particles and the Relaxation Function

V. OPTICAL PROPERTIES OF AEROSOLS

Moderator: Orazio I. Sindoni

10:50 ***J.R. Brock*** and Moon-kyu Chei (Univ. of Texas/Austin), Finite Element Calculation of Absorption and Scattering of Electromagnetic Radiation by Coated Spheres

11:10 ***D. Rosen*** (BED/ARL), Remote Biological Sensing by Circular Polarization Transmissometry

11:30 ***D. Rosen*** and J.D. Pendleton (BED/ARL), Passive Remote Sensing of Microorganisms Using Optical Activity and Sunlight

11:50 **LUNCH**

1:15 ***K. Fuller*** (Colorado State Univ.), Light Scattering by Spheres Containing Multiple Spherical Inhomogeneities

1:35 ***B.J. Stoyanov*** and R.A. Farrell (The Johns Hopkins Univ. APL), Creeping Waves: A Missing Ingredient in Variational Trial Fields

1:55 ***R.T. Wang*** (ISST - SAL), Application of the Exact Solution for Infinite Cylinder Scattering to Finite Cylinder Problems

2:15 ***D. Haracz***, A. Cohen, L. Cohen (Drexel Univ.), Angular Scattering Curves for Rain Droplet Shaped Nonspherical Particles

2:35 **ADJOURN**

END

FILMED

DATE: 6-94

DTIC